University of Strathclyde

Department of Naval Architecture, Ocean and Marine Engineering

Marine propeller hydrodynamic and hydroacoustic performance with roughness effects

Savas Sezen

A thesis presented in fulfilment of the requirements for the degree of Doctor of Philosophy

2022

This thesis is the result of the author's original research. It has been composed by the author and has not been previously submitted for examination which has led to the award of a degree.

Signed: Savas Sezen Date: 08.06.2022

(The Princess Royal starboard propeller operating in 1200/685.7 Engine/shaft rpm)

Cavitation is almost inevitable for ship propellers due to their wide operational profiles, and it brings several adverse side effects such as performance degradation, URN and erosion. The author was inspired by this phenomenon, as shown above in the real environment, to explore cavitation modelling and its side effect URN using CFD methods.

Acknowledgements

My PhD journey started three years ago in Glasgow with passion and excitement. It has also been an adventure starting a new life in a new country, although it did come with its challenges. I would like to thank everyone who contributed to completing this journey with their support and companionship.

First of all, I would like to express my deep and sincere gratitude to my primary supervisor, Prof. Mehmet Atlar, for giving me this opportunity and providing invaluable guidance throughout this research study. His continuous support, encouragement and motivation have deeply inspired me throughout my PhD. Furthermore, I appreciate him for being a supervisor of my research study and mentoring me for the last three years by giving me several opportunities and responsibilities. It has been a great privilege for me to do my research under his supervision.

I would also like to express my gratitude to Prof. Patrick Fitzsimmons for his advice. I will never forget his help in understanding the real physics of the numerical world, particularly for propeller cavitation and noise. I have always benefited from his academic and professional background to widen my knowledge and complete this research study.

Additionally, I would like to acknowledge the sponsorship of the University of Strathclyde and Stone Marine Propulsion for providing me with a scholarship at the University of Strathclyde.

I would also like to thank Dr Dogancan Uzun, who helped me understand the roughness and its applications. It would not have been possible to include the roughness in this research study without his experimental work and interesting discussions with him. I would also like to thank Dr Giorgio Tani and Dr Mario Felli, who provided me with experimental data and explained the experiments' details for validating my numerical results.

I also gratefully acknowledge Dr Refik Ozyurt for his kind support and friendship during my research study. I would like to also thank my esteemed friend Callum Stark for his kind friendship and for making my life enjoyable in Glasgow.

My acknowledgement extends to my colleagues and friends, who are known as the old “Yildiz Mafia” in Turkey, for their continuous support and morale during my study: Dr Omer Kemal Kinaci, Dr Taner Cosgun, Dr Ahmet Yurtseven, Dr Ali Dogrul, Dr Ferdi Cakici, Dr Emre Kahramanoglu.

I want to express my deepest gratitude to my father, mother, brother, sister-in-law, nephew and niece for their continuous support of my decisions and for believing in me.

Last but not least, my deepest appreciation to my wife, Ezgi Sezen, for her sacrifice, invaluable support and for changing her life to accompany me on this journey. It would not have been possible to complete this journey without her support. Also, our little wee one, Mehmet Ege, who was born in Glasgow, made this journey unforgettable and helped me complete this thesis with his long nights of sleep and good behaviour.

Contents

List of Figures

List of Tables

Abstract

Shipping noise is considered a primary contributor to anthropogenic noise in oceans. With an expansion of the world fleet, the Underwater Radiated Noise (URN) levels have increased considerably, especially in the low-frequency band of the noise spectrum. As marine animals generally use sound in the low-frequency region, URN has been a major factor adversely affecting marine life. This potential harmful impact of URN on marine fauna has been commonly investigated in many research projects using experimental methods since the prediction of URN using numerical methods are rather new research field in marine applications. Therefore, in recent years, the accurate prediction of propeller URN has become of great importance to obtain the acoustic signature of the vessel and apply further noise mitigation concepts.

Although several research studies have recently been carried out to predict the propeller URN using numerical methods, the verification and validation studies are still rare. Thus, the validity of the current numerical methods, together with the acoustic analogies for the prediction of propeller URN, is not yet fully understood. Also, the research studies are generally conducted for the propellers in model scale operating under non-cavitating conditions. Although several studies have been for predicting cavitating propeller URN, these research studies are still limited to sheet cavitation modelling due to the modelling complexity of the tip vortex cavitation (TVC). Moreover, the influence of roughness applied on the propeller blades and hub on propeller hydrodynamic and hydroacoustic performance has not been explored yet using Computational Fluid Dynamics (CFD) methods.

Based on the above background, this PhD thesis aims to develop a mathematical model to investigate the propeller hydrodynamic performance, including cavitation and hull pressure fluctuations, and propeller URN in the presence of roughness using advanced numerical modelling and developed meshing techniques. This aim has been accomplished by using the validated state-of-art CFD tools.

In the thesis, firstly, the effects of grid resolution on the accurate prediction of propeller URN and the contribution of nonlinear noise sources on overall propeller URN under non-cavitating conditions were explored. Secondly, the newly developed Vorticity-based Adaptive Mesh Refinement (V-AMR) technique was developed for accurate solution of the tip vortex flow and hence better realisation of TVC in the propeller slipstream. The V-AMR technique was also

utilised to include the contribution of TVC on overall propeller URN for both model and full-scale propellers. Then, comprehensive verification and validation study was conducted to explore the effectiveness of the developed CFD approach through the propeller hydrodynamic performance, cavitation extension, hull pressure fluctuations and propeller URN for model and full-scale propellers operating under uniform and non-uniform flow conditions. Finally, the influence of roughness applied on the propeller blades and hub on propeller hydrodynamic and hydroacoustic performance was investigated.

The numerical investigations conducted with the developed CFD method in this thesis demonstrated the satisfactory capability and effectiveness of the method for predicting the propeller hydrodynamic performance, including cavitation extension, hull-pressure fluctuation and URN, combined with the acoustic analogy for the URN. Thus, similar to other ship hydrodynamic problems (e.g., ship resistance, propulsion), CFD can also be reliably used, particularly for predicting the propeller URN, under non-cavitating and cavitating conditions. Also, the application of a new meshing technique, V-AMR, can be a practical way to investigate the tip vortex flow, TVC and include its effects on propeller URN effectively. Finally, the roughness application can also be an attractive method for mitigating the cavitation and hence propeller URN, especially for retrofit applications.

1 Introduction

1.1 Introduction

This chapter aims to make an introduction to the research study conducted in this PhD thesis. In Section 1.2, a general perspective of the subjects explored in the thesis is given. The author's motivation for the research study is described in Section 1.3. The study's main aim and specific objectives are presented in Section 1.4, and this is followed by the structure of the thesis chapters in Section 1.5. Consequently, the summary of the chapter is given in Section 1.6.

1.2 General perspectives

Anthropogenic noise levels have shown an increasing trend in the last two decades as industrial activities (e.g., oil, gas, renewable energy, transport industries and commercial vessel traffic) in the oceans have become more widespread. Industrial noise sources can be classified as incidental and deliberate. The commercial vessel traffic, oil and gas drilling activities, etc., can be considered incidentally radiated noise sources. On the other hand, the sonar systems, oil & gas seismic surveys, etc., can be deemed to be deliberate noise sources in the oceans (Chou et al., 2021; Brooker and Humphrey, 2016). The incidentally radiated noise sources negatively influence the communication, breeding and day-to-day living circumstances of some marine animal species, especially mammals. The possible long and short term influences of deliberate noise sources (e.g., ship-related operational noises) on different marine species are unknown, and investigations have still been carried out (Kellett et al., 2013). Thus, Underwater Radiated Noise (URN) has been addressed by the European Marine Strategy Framework Directive (MSFD) to protect the ecosystem and reduce noise pollution. The noise radiated by the shipping traffic is considered to be the main source contributing to the anthropogenic noise levels, particularly at low frequencies (Erbe et al., 2019).

A ship represents a very complex noise source, mainly machinery noise, hydrodynamic flow noise, and propeller radiated noise (ITTC, 2017a). The latter could be the most important contributing sources (i.e., non-cavitating and cavitating propeller URN), especially from a cavitating propeller, and hence they are investigated in this thesis. The propeller URN can be predicted using numerical methods, empirical formulations, and experiments. The numerical prediction of the propeller URN using hybrid methods (i.e., hydrodynamic method and acoustic analogy) is a relatively new research field for hydroacoustic studies. As there are no consolidated procedures for the implementation of acoustic analogy for the propeller URN

studies using viscous flow-based Computational Fluid Dynamics (CFD), the effectiveness of the hybrid methods, several issues related to the application of acoustic analogy (e.g., permeable surface dimension/location, timestep, turbulence modelling, etc.) have still been investigated in the literature, particularly for the propellers operating under non-cavitating conditions (e.g., Lidtke et al., 2019; Testa et al., 2021). Amongst the different parameters, the adaptation of suitable grid structures, possible non-physical numerical noise sources in the numerical calculations for propeller URN's accurate prediction and exploring the nonlinear noise sources further in the propeller's wake remain to be explored.

Almost all commercial ship propellers are operating under cavitating conditions to reach optimum performance, and avoidance of non-erosive cavitation is almost inevitable. Depending on the operating conditions, various cavitation forms (e.g., sheet, bubble, cloud, vortex cavitation) can be observed on the ship propellers, and their effects on the propeller hydrodynamic and hydroacoustic performance are different. The most commonly observed cavitation types on the ship propellers and most relevant for the URN are the sheet and tip vortex cavitation (TVC) (Bosschers, 2018). Although sheet cavitation can be modelled accurately using existing numerical methods and associated numerical parameters, modelling the TVC emanating from all propeller blades is a challenging task. In order to model the TVC in the propeller slipstream, advanced meshing techniques (e.g., AMR) were applied for different propellers on model scale (e.g., Shin and Andersen, 2018; Yilmaz et al., 2019 and Krasilnikov 2019). However, existing techniques are still computationally expensive, and it is not possible to implement these techniques for the full-scale propellers and incorporate them with the propeller URN predictions. Therefore, a computationally affordable and practical TVC modelling technique must be developed using CFD.

When the propeller operates under cavitating conditions, the cavitation will be the dominant noise source contributing significantly to the overall URN levels for both tonal and broadband parts of the noise spectrum and hull pressure fluctuations (Kellett et al., 2013). Therefore, the understanding and accurate prediction/modelling of the propeller cavitation, associated URN and hull pressure fluctuations is crucial. In the current literature, there are several research studies investigating the cavitation, propeller URN and hull pressure fluctuations in open water and behind hull conditions on a model scale using CFD (e.g., Lidtke et al., 2015; Bagheri et al., 2017). However, accurate solutions of the tip vortex flow and better TVC modelling are generally disregarded due to the modelling difficulties. Also, the lack of verification and validation is still present in these studies for the propeller URN predictions. Therefore, the

validity of the CFD approach, together with the acoustic analogy, is required to be investigated comprehensively with an accurate solution of the tip vortex flow, including the TVC, and replicating the experimental conditions under uniform and non-uniform flow conditions using CFD.

Although there are several studies exploring the propeller hydrodynamic and hydroacoustic performance under non-cavitating and cavitating conditions, these studies are generally carried out on a model scale (e.g., Bensow and Liefvendahl, 2016; Ianniello et al., 2013; Testa et al., 2018). Inevitably, predicting the propeller URN in model scale and extrapolating the results from the model to full-scale are still challenging due to the different flow properties between the model and full-scale. Due to this fact, there are limited studies investigating the propeller URN in full-scale under cavitating conditions (e.g., Fujiyama and Nakashima, 2017; Li et al., 2018). Therefore, the applicability of the CFD methods still needs to be demonstrated in full-scale and validated with the full-scale measurements at several operating conditions.

The propeller URN is usually predicted under cavitating conditions by taking only the sheet cavitation into account due to the difficulties of TVC modelling as stated above. TVC is one of the most important noise sources and increases the URN levels considerably when the vortex dynamics experience the bursting/collapsing phenomenon. In the past, some cavitation tunnel experiments were conducted to understand the tip vortex dynamics and associated TVC noise using the hydrofoils and propellers (e.g., Higuchi et al., 1989; Strasberg, 1986). However, the contribution of TVC noise on overall propeller URN was not investigated in detail. The use of viscous CFD solvers enables exploration of the TVC noise by modelling only the sheet as well as the sheet and TVC together in a wide range of operating conditions. Therefore, the contribution of TVC on overall propeller URN and understanding its dynamics need to be investigated using CFD.

The propeller hydrodynamic and hydroacoustic performance are always predicted when the blade surfaces are clean (i.e., in smooth condition), and the roughness is ignored in the majority of investigations. Yet, when the vessel is in service condition, the accumulation of the marine organisms, which is defined as biofouling, on the hull, propeller and hub surfaces will influence the ship and propeller performance. In order to investigate these physical realities, the wall function approach of the current CFD solvers, which is an alternative and effective approach to replicate the roughness in the numerical calculations, can be utilised. The wall function approach has been used to explore the effects of biofouling roughness on ship performance

using CFD in several studies in the literature (Uzun et al., 2021a; Uzun et al., 2021b). However, its applications for marine propellers are rather rare to investigate its possible detrimental and favourable impacts on propeller hydrodynamic performance, including cavitation. In fact, the investigation of the effect of the biofouling on the propeller and hull URN is non-existent, requiring novel investigation. Therefore, the influence of homogeneously and heterogeneously distributed roughness on the propeller blades and hub on propeller hydrodynamic and especially on hydroacoustic performance needs to be explored for model and full-scale propellers using CFD.

1.3 Motivation

The author's motivation behind the present research study is summarised as follows.

- With the development of numerical tools, the prediction of propeller URN using the CFD becomes appealing. However, the effectiveness of the acoustic analogy, numerical models and associated numerical parameters have still been investigated in the literature as there is no practical guideline and procedures in this field. Amongst the several key numerical parameters affecting the accuracy of the propeller URN, the grid resolution is one of the important parameters for the sound propagation from near field to far-field. Also, the acoustic analogy is considered to be more sensitive to the grid resolution as it affects the accuracy of the hydrodynamic inputs and possible numerical noise sources in the numerical calculations. As this issue has not been investigated in the current literature, this gap can be filled by more in-depth investigations using CFD.

- The role of nonlinear noise sources, mainly represented by vorticity and turbulence, has been shown in different studies in the literature for the accurate prediction of propeller URN. Inevitably, the detailed investigation of the propeller's wake enables an understanding of the flow details and hence possible nonlinear noise sources. Nowadays, several research studies have been conducted to explore the propeller hydrodynamic performance and propeller's wake using different numerical methods and turbulence models. However, these investigations have not been combined with the propeller URN predictions to understand the contribution of nonlinear noise sources to the overall propeller URN. Therefore, this research gap can be filled by investigating the flow field in the propeller's wake and associating them with the propeller URN predictions using CFD.

- Propeller cavitation is generally modelled by only taking the sheet cavitation into account due to the modelling difficulties of TVC in numerical calculations. Some recent advanced meshing techniques are used to model the TVC in the propeller slipstream by tackling these difficulties. However, the computational cost of these studies is still high, and it is not practical to implement these techniques for full-scale propellers and combine them with the propeller URN prediction methods using CFD. Thus, developing a TVC modelling technique with minimal computational cost increase is important. This research gap can be filled by developing a new technique to model the TVC emanating from all propeller blades in the propeller slipstream.

- Although several recent numerical studies have been predicting the cavitating propeller URN, these studies have been generally conducted by only modelling the sheet cavitation and ignoring the nonlinear noise sources. Also, the verification and validation of these studies are rather scarce. This makes the effectiveness of the current CFD methods are still questionable. In order to show the validity and capabilities of the current propeller URN prediction methods, comprehensive verification and validation studies are required for the propellers operating under uniform and non-uniform flow conditions by including the nonlinear noise sources and TVC. Therefore, this research gap can be filled with comprehensive verification and validation studies by replicating the realistic test configurations using CFD as in the cavitation tunnels. This will also show the accuracy of the CFD methods, which are relatively recently applied for propeller URN predictions, compared to noise measurements conducted in the cavitation tunnels or depressurised towing tanks.

- The propeller URN is generally predicted in model scale and then extrapolated to the full-scale. As the scale effects are not completely eliminated due to the different flow fields and cavitation dynamics between the model and full-scale, it is important to conduct the propeller URN predictions in full-scale. To the best of the author's knowledge, there are only two studies available in the current literature investigating the propeller URN in full-scale and comparing the numerical results with the full-scale measurements under cavitating conditions (e.g., Fujiyama and Nakashima, 2017; Li et al., 2018). However, in these studies, an adequate solution of tip vortex and hence TVC modelling is not present, and the noise comparisons are not carried out in the far-field where the noise data is collected. Due to this reason, the validity of the CFD approach

is not yet completely understood for the full-scale cavitating propellers in the far-field. Therefore, this research gap can be filled with the full-scale propeller URN predictions in the far-field by including the TVC.

- TVC is one of the important noise sources contributing to the propeller URN significantly. To the best of the author's knowledge, specific studies exploring the contribution of such a critical noise source using CFD are scarce. Therefore, it is worthwhile to show the effects of TVC on propeller URN predictions in a wide range of operating conditions for model and full-scale propellers using CFD.

- The effects of roughness on ship performance have been widely investigated in the literature using CFD. Also, to the best of the author's knowledge, only one study investigates the effects of roughness on propeller cavitation, emphasising only the TVC under uniform flow conditions. However, its effects on propeller hydrodynamic performance, hub vortex and tip vortex cavitation and propeller URN have not been investigated yet under different operating conditions. Therefore, this research gap can be filled by applying homogenous and heterogenous distributed roughness on propeller blades and hub to explore its detrimental and favourable impacts on propeller performance, cavitation and propeller URN.

1.4 Aims & Objectives

1.4.1 Aims

Within the framework of the above motivation, this research study's ultimate aim is to contribute to the accurate prediction of the propeller hydrodynamic performance, cavitation, and propeller induced hull pressures and URN by accounting for more realistic physics using CFD methods. More realistic physics can be accounted for by including nonlinear noise sources with the permeable formulation of the FWH equation, better resolution of tip vortex flow and TVC, and reflecting the blade and hub roughness conditions for different benchmark propellers in model and full-scale. This is achieved through the validated state-of-the-art commercial CFD tools, which are the essential pillars of the aims.

1.4.2 Specific objectives

The above-stated aims of the research study can be met through the following specific objectives:

1. To conduct a state-of-the-art literature survey related to the cavitation, propeller URN and roughness by identifying the current research gaps and hence justify the aims and objectives of the study (Chapter 2)

2. To develop a CFD method for investigating the influence of grid resolution on propeller hydrodynamic and hydroacoustic performance and understanding the nonlinear noise sources under non-cavitating conditions (Chapter 4)

3. To develop a new advanced meshing technique to solve the tip vortex flow accurately and model the TVC emanating from all propeller blades in a better way in the propeller slipstream (Chapter 5).

4. To develop a more accurate and basic mathematical model for investigating the propeller hydrodynamic performance, cavitation and propeller URN using CFD, including comprehensive verification and validation study for the benchmark propeller operating under uniform, inclined and non-uniform flow conditions (Chapter 6)

5. To apply the developed CFD methodology to a full-scale benchmark vessel at several operating conditions and validate the numerical results with the full-scale measurements (Chapter 7).

6. To explore the influence of TVC on propeller URN using the developed CFD model and advanced meshing technique in a wide range of operating conditions in model and full-scale (Chapter 8).

7. To develop a CFD method of a model and full-scale propellers to investigate the effects of roughness applied on the propeller blades and hub on propeller hydrodynamic performance, cavitation and propeller URN under uniform, inclined and non-uniform flow conditions (Chapter 9)

1.5 Structure of the thesis

The above-stated aim and objectives are achieved within the ten chapters of this thesis. These are briefly described as follows.

Chapter 1 presents the general perspective, motivation of the author, aims and objectives of this research study. Also, the thesis structure is presented to describe the chapters briefly to achieve the aim and objectives of this research study.

Chapter 2 provides a comprehensive literature review on propeller hydrodynamics, cavitation, propeller URN and roughness to identify the research gaps and justify the aims and objectives of the PhD thesis. First of all, this chapter presents the shipping noise and research studies in the field of cavitation, particularly for TVC. The propeller URN prediction methods are then explained. Eventually, the state-of-art research studies investigating the non-cavitating, cavitating propeller URN and the influence of roughness on propeller hydrodynamic and hydroacoustic performance are given to predict.

Chapter 3 presents the methodology and general outline of the PhD thesis.

Chapter 4 explains the basic mathematical model established for predicting the propeller hydrodynamic and hydroacoustic performance under non-cavitating conditions using the INSEAN E779A model scale propeller. The numerical investigations are carried out to explore the influence of grid resolution on propeller hydrodynamic performance characteristics (i.e., thrust, torque and efficiency) and URN. Further analyses are also performed for investigating the flow details in the propeller's wake and its relationship with the propeller URN to understand the influence of nonlinear noise sources on overall propeller URN predictions.

Chapter 5 develops a new advanced meshing technique (V-AMR) to solve better tip vortex flow and TVC modelling in the propeller slipstream using the INSEA E779A model scale propeller. The different numerical methods (i.e., RANS (Reynolds-averaged Navier Stokes, DES (Detached Eddy Simulation) and LES (Large Eddy Simulation)) and significant crucial numerical modelling parameters are explored for enhanced modelling of TVC in the propeller slipstream.

Chapter 6 presents a comprehensive verification and validation study using the benchmark propeller of a research vessel, "*The Princess Royal"*, operating under uniform, inclined, non-uniform flow conditions and in the presence of a 3D model of the vessel. The numerical

calculations are validated with the experimental data through the propeller hydrodynamic performance, cavitation extensions, hull-pressure fluctuations and propeller URN in various operating conditions.

Chapter 7 further explores the validity and capabilities of the developed CFD model using the full-scale benchmark vessel, *The Princess Royal*. The numerical results are validated with the full-scale measurements (i.e., sea trial data) through the propeller hydrodynamic performance, cavitation extension and propeller URN at four different operating conditions.

Chapter 8: utilises the developed CFD model to understand the contribution of TVC on overall propeller URN using *The Princess Royal* propeller operating under uniform, inclined and non-uniform flow conditions in model and full-scale. Akin to Chapters 5, 6 and 7, the developed advanced meshing technique (V-AMR), as explained in Chapter 5, is utilised for this investigation. The numerical calculations are conducted in conditions by modelling only the sheet cavitation and the sheet and tip vortex cavitation together. The numerical results are validated with the experiments and full-scale measurements through the propeller hydrodynamic performance, cavitation extension and propeller URN.

Chapter 9 investigates the influence of biofouling type roughness on the propeller hydrodynamic performance, including cavitation and URN, by using the benchmark propellers, *INSEAN E779A* and *The Princess Royal*. The wall function of the CFD model is utilised to represent the surface roughness on the blades and hub. The numerical calculations are performed using the homogenously and heterogeneously distributed roughness under uniform, inclined and non-uniform flow conditions in model and full-scale. The favourable and degradation effects of roughness on propeller hydrodynamic performance, cavitation extension and propeller URN are examined extensively.

Chapter 10 provides a summary of the PhD thesis. The achievement of the aim and objectives, main conclusions, research outputs, and recommended future works are given.

1.6 Chapter summary

This chapter presented a general introduction to the research study conducted in this thesis in terms of the general perspectives and motivation of the research, its aim & objectives and the structure of the thesis chapters to achieve the aims and objectives.

2 Literature Review

2.1 Introduction

A comprehensive literature survey was carried out in the fields of propeller hydrodynamics, cavitation, URN and roughness to identify the literature gaps and justify the aims and objectives of the PhD thesis.

Section 2.2 presents the shipping noise, its importance and the main URN components within a ship. The literature survey related to propeller hydrodynamic performance and cavitation, emphasising the TVC, is given in Section 2.3. Section 2.4 presents the state-of-art research studies regarding the propeller URN, and this section is mainly divided into two sub-sections: non-cavitating and cavitating propeller URN. The research studies on cavitating propeller URN are categorised for model and full-scale propellers. Also, the research studies regarding the TVC noise are given in Section 2.4. A brief review of the marine biofouling and relevant studies regarding the roughness application for submerged bodies (e.g., marine propellers and hydrofoils) are given in Section 2.5. The identified literature gaps are presented in Section 2.6. Finally, the chapter summary and concluding remarks are provided in Section 2.7.

2.2 Shipping noise

The mechanical disturbance of a body in an elastic medium like fluid creates a sound due to the relative motion between the fluid and body, and the sound propagates. The unwanted sound is defined as noise. When considering the noise generated by the ships, the noise can be divided into self-noise and propagating or radiated noise. All shipboard noise sources within the ship are considered self-noise, and their effects are on the vessel's own personnel and equipment. However, the radiated noise can be defined as recognisable and detectable underwater noise (URN) at a distance from the ship (Carlton, 2018; ITTC, 2017a). A ship's URN can be classified into three main components according to Urick, 1983 and Ross, 1976:

- Machinery noise because of the propulsion system and auxiliary equipment within the ship
- Hydrodynamic flow noise created by the flow around the hull
- Propeller noise

Understanding and interpreting different noise sources are crucial for monitoring ship-generated noise. Amongst different noise sources, propeller noise, which is the main interest of this PhD thesis, can be classified as non-cavitating and cavitating propeller URN. Additionally, it is considered that the propeller is an important noise source contributing to the overall URN levels, particularly when the propeller is operating under cavitating conditions (Abrahamsen, 2012; ITTC, 2017a). The pressure waves, which are mainly created in four different mechanisms in water, generate the propeller URN. These four different mechanisms can be summarised as follows (Carlton, 2018).

- Displacement of water with rotating propeller blades
- The pressure difference between the pressure and suction sides of the propeller
- The periodic fluctuations of the cavity volumes due to the operation of the blades in a non-uniform wake field
- The sudden bursting/collapsing phenomenon associated with the cavitation dynamics

Over the years, the URN levels induced by shipping activities have increased significantly (Hildebrand, 2009). Considerable growth in maritime transport and commercial shipping between 1950 and 2000 increased the low-frequency ambient noise levels by approximately 10 dB or more in the oceans (Ross, 1976). The rising concern about the potential environmental impacts of noise pollution caused by the shipping activities has forced governments, national & international regulatory bodies, classification societies and IMO (International Maritime Organisation) to study and mitigate its impact on the marine ecosystem. This is because marine animals use sound at a certain frequency range for their various fundamental living activities such as communication, interaction and feeding. The sudden increase in URN levels may disorient them and destroy their communication with each other and even cause their local extinction. For this reason, several notations (e.g., the Det Norske Veritas Germanisher Loyd (DNV-GL) QUIET class, Registro Italiano Navale (RINA)) were published to emphasise this issue. For instance, DNV GL issued SILENT class notations in 2010 to highlight the noise-related issues and urge ship owners to take precautions to reduce the URN emissions (DNV, 2010). Also, in order to address the increased URN levels due to commercial shipping, the International Maritime Organisation (IMO) recognised this issue and published a non-mandatory guideline to mitigate the URN levels radiated by commercial ships to decrease the short and long term negative impacts on marine life (IMO, 2014). This guideline identified several alternative ways to reduce the URN levels for retrofit and new built commercial vessels.

Also, it was stated that there are still some research and knowledge gaps to identify the contribution of different sources on URN levels.

So far, shipping noise is being low prioritised compared to other sustainability concerns in the shipping industry (e.g., Greenhouse Gas Emissions (GHG)). Also, the lack of mandatory international regulations and noise limits makes progress slow for the URN mitigation investigations. However, the steady increase in URN levels in the oceans has further escalated interest in this field. Recently, the Marine Environment Protection Committee of the IMO has accepted the proposal from Australia, Canada and the United States to review the existing 2014 Guidelines (IMO, 2014) for the mitigation of URN by commercial vessels (Cruz et al., 2021). The effort in this field is getting more attention to highlight the possible short and long term detrimental impacts of ship URN on marine mammals. For example, the hearing ranges of the marine animals, particularly cetacean species, and their overlap with the shipping noise sources are shown in Figure 2.1.

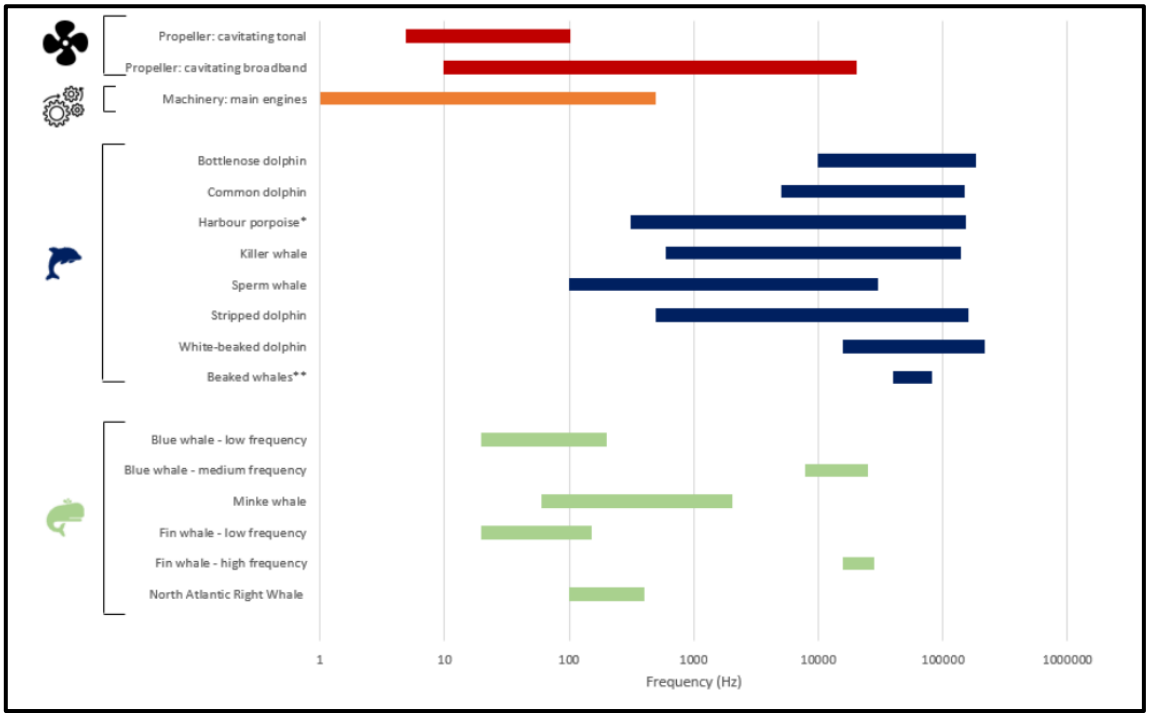

Figure 2.1. The frequency range of marine animals and shipping noise sources (Cruz et al., 2021).

2.3 Cavitation

Due to the resulting performance degradation, blade erosion, vibration, and the URN, propeller cavitation is of great interest for ships. The type, extension, and dynamics of the cavitation depend on the propeller geometry, its operating condition, water quality, and the wake flow of the ship's hull in front of the propeller. Figure 2.2 shows the cavitation types observed on and

off the propeller blades. Amongst the different propeller cavitation types, such as bubble, sheet, cloud, and vortex, the ship propellers commonly operate in conditions where the sheet and tip vortex cavitation are present (Bosschers, 2018). Thus, in this PhD thesis, the main focus will be to model the sheet, tip vortex cavitation and associated URN accurately using CFD. Also, hub vortex cavitation will be of interest.

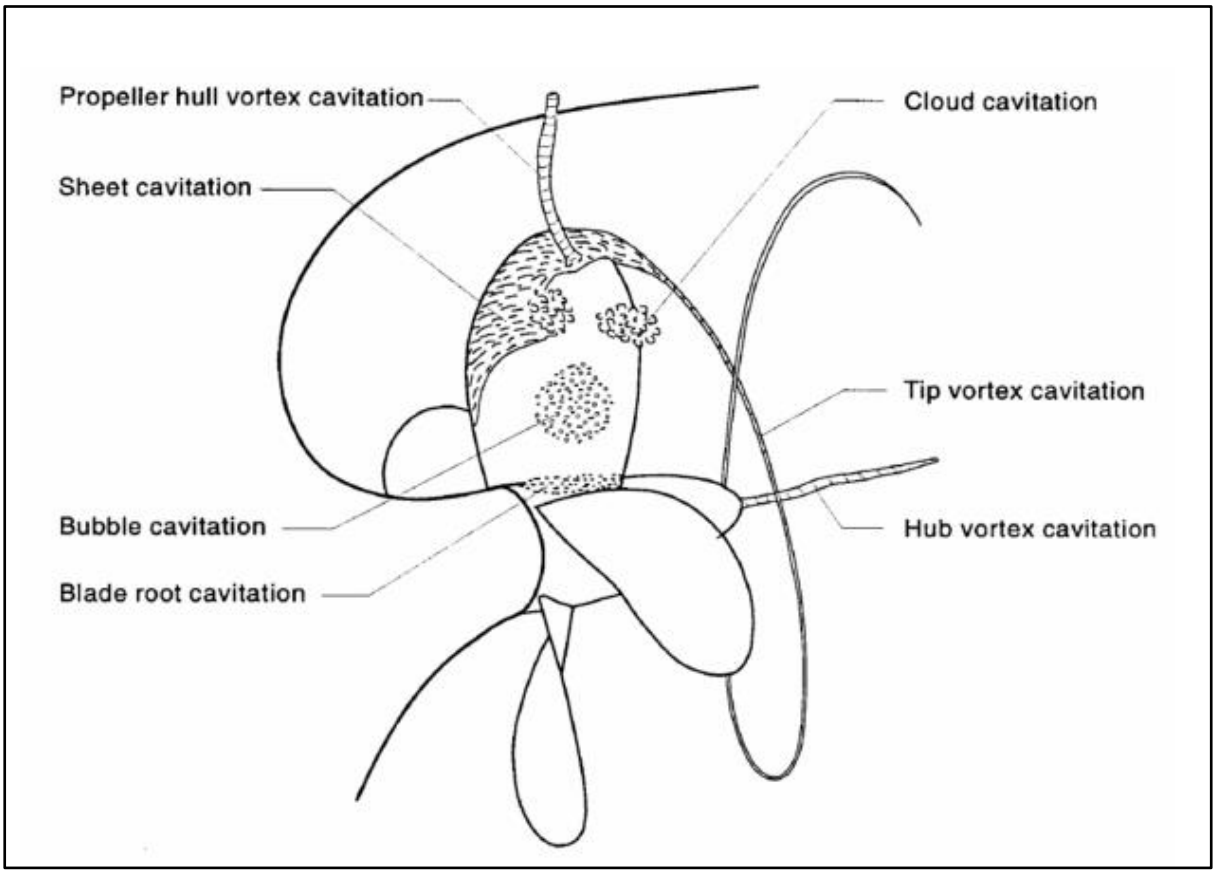

Figure 2.2. Cavitation formations observed on and off the propeller blades (ITTC, 2002a).

The numerical studies related to cavitation have mainly focused on sheet cavitation due to the modelling complexities of the TVC using numerical methods. In this regard, the potential flow-based solvers (i.e., lifting surface and panel methods) are generally used in the propellers' early design stage to account for the sheet cavitation and its effects on the propeller hydrodynamic performance (e.g., Fine and Kinnas 1993; Lee and Kinnas 2004). However, the potential flow solvers may have some drawbacks for accurately predicting the cavitation dynamics compared to viscous flow solvers. The reason is that they ignore the effects of viscosity even though the empirical method is used to add the viscous drag in the calculations. Including the viscosity in the computations enables predicting the shedding of the sheet and tip vortex cavities in a more accurate way (Sipilä, 2012). Therefore, different viscous flow methods, e.g., RANS, DES and

LES, are alternative ways to model the cavitating flow around the marine propellers (e.g., Bensow and Bark 2010; Gaggero et al., 2014; Viitanen and Siikonen, 2017).

The numerical prediction of cavitation phenomena is complicated compared to non-cavitating conditions, not only because of the multi-phase nature of cavitation but also due to the strong interactions between the turbulent flow and cavitation dynamics. Thus, the selection of different numerical methods (e.g., RANS, DES, LES) and modelling parameters (e.g., timestep, grid resolution, water quality, etc.) used in the CFD solver are important (Lloyd et al., 2017). One of the main difficulties in the cavitating propeller flow computations is to model the TVC. The prediction of the strength and size of a tip vortex, which is driven by both viscous diffusion and vortex lines, along its trajectory is a complex flow phenomenon. The anisotropic turbulence and higher velocity gradients in all directions inside the vortex core make the evaluation of the tip vortex flow difficult. This is further complicated by the complex physical dynamics between the vortex structures and different pressure fields created within the surrounding and inside the vortex core (Hunt et al., 1988; Asnaghi, 2018; Asnaghi et al., 2020a). Hence, a realistic solution of the flow inside the vortex core enables accurate modelling of the TVC in the propeller slipstream.

TVC is also one of the important URN sources, especially in the presence of the bubble collapse or bursting phenomenon in the non-uniform wake (Konno et al., 2002). It consequently influences the overall noise spectrum and hull-pressure fluctuations. Thus, physical understanding and numerical modelling of the TVC is still important in propeller hydrodynamics.

In recent years, several studies have been conducted to investigate the tip vortex flow under non-cavitating conditions using experimental and numerical methods in the literature (e.g., Felli et al., 2011; Qiu et al., 2013; Muscari et al., 2013; Guilmineau et al., 2015). As well as these investigations, the inception of TVC has been studied with hydrofoil geometries and marine propellers using different numerical methods. Hsiao and Chahine 2008 performed a numerical study to examine the TVC inception for marine propellers. RANS and DNSS (Direct Navier Stokes Simulations) methods were utilised together to increase the accuracy of the RANS solution for the tip vortex flow. DNSS was performed in a reduced domain by taking the boundary conditions from the initial RANS solution. The results showed that the RANS solution was inadequate to resolve the continuous roll-up process, except for the initial roll-up, due to the averaging nature and insufficient turbulence modelling. Gaggero et al., 2014

investigated the inception of tip vortex and tip leakage vortex cavitation for conventional and two ducted propellers using the RANS method with the Schnerr-Sauer cavitation model. Their results showed that the RANS method could be reliably used as a primary design tool for engineering purposes to predict the inception of TVC. Also, the solution of the tip vortex flow inside the vortex core was found to be more sensitive to the grid resolution than the cavitation model parameters (i.e., nuclei density and diameter). Asnaghi et al., 2020a performed a comprehensive numerical study to investigate tip vortex flow under cavitating and non-cavitating conditions for an elliptical foil. The grid resolution requirements were assessed using LES for the flow solution inside the vortex core. The numerical results showed that it was important to adopt sufficient cells for the accurate solution of tip vortex flow.

As stated in the above review of some relevant studies, the solution of the tip vortex requires an accurate calculation of the minimum pressure inside the vortex. Thus, the realistic solution of the tip vortex flow is strongly dependent on the grid resolution inside the vortex and numerical modelling techniques. In the numerical computations, priory local mesh refinements (i.e., tube and spiral) are generally adopted at the propeller blade tips to decrease the numerical diffusion for tip vortex formation; hence, TVC (e.g., Usta and Korkut 2018; Zhu and Gao 2019). However, these approaches have not been sufficiently successful, and they are computationally expensive due to the excessive number of cells used to model the TVC in the propeller slipstream. Also, it is not practical to adopt high-resolution grids in the entire propeller slipstream as the computational cost would be escalated. Therefore, the grid refinement should be implemented locally at the tip vortex regions to decrease the computational cost and predict the minimum pressure inside the vortex core. This can be achieved using the Adaptive Mesh Refinement (AMR) technique, implemented relatively recently in the hydrodynamic field for isolated propeller cases and complete models (i.e., propeller and hull). In the studies of Wackers et al., 2010 and Queutey et al., 2012, the flow around the hull and propeller was solved using an in-house unsteady RANS method, which was integrated with AMR. The AMR technique was successful for the solution of the free surface and vorticity field. Windt and Bosschers 2015 performed AGR (Adaptive Grid Refinement) technique and local mesh refinement to investigate the minimum pressure in the tip vortex core for a rectangular wing and single propeller blade in open water conditions. The computations showed that both methods improved the accuracy of the solution, but the total number of cells in AGR was found three times lower than the local mesh refinement. Yvin and Muller, 2016 studied the TVC inception assessment without the cavitation model for a marine

propeller. In their model, an automated mesh refinement technique was used to evaluate the minimum pressure inside the vortex core using the RANS based EASM (Explicit Algebraic Stress Model) method. Lloyd et al., 2017 employed the local mesh refinement and AGR technique using RANS and DES methods by modelling a single blade of INSEAN E779A benchmark propeller. The results showed that the details of the vortex roll-up using the AGR technique were predicted better than using the local mesh refinements. Also, the different types of AMR techniques have been recently implemented by Shin and Andersen, 2018; Yilmaz et al., 2019, Krasilnikov 2019 and Kimmerl et al., 2021a to model TVC.

Although there have been recent numerical studies to model the TVC in the propeller slipstream, the computational cost of the current methods are still high (e.g., Yilmaz et al., 2019, Krasilnikov 2019); thus, a single blade is usually modelled (e.g., Lloyd et al., 2017). Modelling the single blade, extensive grid numbers and associated computational resources used in the current methods would inevitably limit expanding these techniques for the complex scenarios (e.g., full-scale propellers), which is one of the aims of this PhD thesis. Therefore, this present study aims to present a more computationally efficient new TVC modelling technique emanating from all propeller blades using the CFD solver. Also, to the best of the author's knowledge, the influence of the different numerical methods (e.g., RANS, DES, LES) and that of some key computational prediction parameters such as grid resolution, timestep and water quality parameters (e.g., nuclei number and nuclei density) on the TVC has not been comprehensively investigated together yet. Therefore, this study aims to fill these research gaps by introducing an alternative vorticity-based AMR, the V-AMR technique, for a more accurate solution of tip vortex flow as a better representation of the TVC in the propeller slipstream, exploring the effects of the different numerical methods and other key modelling parameters.

2.4 Propeller URN

While experiments conducted in cavitation tunnels, depressurised towing tanks, and empirical/semi-empirical methods are common approaches for propeller URN predictions, the efforts to predict propeller URN using the CFD methods have escalated with the development of computational tools. Also, understanding the complex flow phenomena around the propeller affecting the propeller URN is improving using the CFD methods. Therefore, in the future, similar to other ship hydrodynamic problems, the CFD based methods will be expected to become the frontline for the propeller URN prediction and hence propeller design/optimisation

studies (Stark and Shi, 2021). The CFD methods used for the propeller URN predictions both in the near and far-field can be classified as follows:

- Direct Numerical Simulation (DNS) to solve all turbulent scales
- Direct viscous-based CFD methods (i.e., LES, DES and RANS)
- Viscous-based hybrid methods (i.e., hydrodynamic method with the acoustic analogy)
- Potential-based hybrid methods (i.e., hydrodynamic method with the acoustic analogy)

DNS is computationally expensive, and it is not possible to perform such a hydroacoustic simulation with the current resources as all turbulent scales need to be solved. The alternative CFD methods can be utilised to predict the propeller hydroacoustic performance. Amongst them, LES is a capable method for directly solving the large turbulence scales and modelling the small scales, whereas the RANS is based on the solution of time-averaged equations. DES is an alternative method, and it uses the advantages of LES and RANS methods. However, any direct solution requires governing equations based on compressibility assumptions. This is because the sound is defined as a pressure fluctuation, and it propagates at a finite speed in a medium. Under the isentropic flow hypothesis, the speed of sound is defined by $({c_0}^2 = dp/d\rho)$ and hence the incompressibility assumption $(d\rho = 0)$, used for propeller hydrodynamic performance prediction, makes the sound speed infinite $(c_0 = \infty)$. This results in ignoring the sound propagation from near to far-field. Due to this fact, any direct methods under the incompressibility assumption are unsuitable for URN predictions in the far-field (Ianniello et al., 2013). Implementing the direct CFD methods under compressibility assumption for the propagation of the sound to the desired location is an expensive approach, especially for high Reynolds number flows, because the high-fidelity and high order methods are required to prevent dissipation or dispersion of the acoustic field. For this reason, in general, the source and propagation fields are decoupled using hybrid methods (Nitzkorski, 2015). Once the source field is solved and the sound source is predicted using the high-fidelity CFD methods, the acoustic analogies are used to propagate sound from near to far-field (Ianniello et al., 2013). In other words, the acoustic analogy adds compressibility effects to the incompressible hydrodynamic solver (Sezen and Kinaci, 2019).

Although potential flow methods have been generally used together with the acoustic analogy for the propeller URN predictions because of their low computational cost, particularly in the preliminary design stage, they are not as capable as viscous based methods. The reason is that the turbulence and viscosity effects are disregarded; hence, the potential-based methods are

inadequate for capturing the complex flow details, which are important for the accurate prediction of propeller URN. Therefore, viscous based CFD methods (e.g., RANS, DES, and LES) and together with the acoustic analogy as a hybrid method are considered to be the state-of-art propeller URN prediction methods (ITTC, 2017a).

The most commonly used acoustic analogy is the Ffowcs-Williams Hawkings (FWH) (Ffowcs Williams and Hawkings, 1969) equation in both aeroacoustics and hydroacoustic fields. In the aeroacoustics field, the impermeable formulation of the FWH equation has been generally used, and only linear noise terms of the FWH equation (i.e., monopole and dipole noise terms) are taken into account for the noise predictions. The reason is that the flow regime is often assumed as subsonic due to the low rotational speed of the blades. The nonlinear noise sources (i.e., quadrupole noise terms) become important at high supersonic or transonic regimes. However, unlike the aeroacoustics field, the linear terms show rapid decay as far away from the noise source in the hydroacoustic field. The contribution of nonlinear noise sources, mainly represented by vorticity and turbulence, including TVC, becomes important, particularly in the far-field. Hence, the nonlinear noise sources need to be included in the calculations to accurately predict propeller URN under non-cavitating and cavitating conditions (Ianniello et al., 2013). This can be achieved by either solving the direct volume integrals in the generalised FWH equation or using the porous/permeable formulation of the FWH (P-FWH) equation. However, the solution of direct volume integrals is computationally expensive and more sensitive to the accuracy of the input data in the generalised FWH formulation. Due to this reason, the P-FWH equation becomes attractive as the quadrupole volume integrals are evaluated with the solution of surface integrals.

2.4.1 Non-cavitating propeller URN

As stated in Section 2.2, the propeller noise can be considered non-cavitating and cavitating. The non-cavitating propeller URN mainly occurs due to the fluctuation of the hydrodynamic forces on the propeller blade, and it is classified into three parts, low-frequency tonal noise, low-frequency broadband noise and high-frequency broadband noise. The low-frequency tonal noise (i.e., discrete frequencies) is created with the propeller's action in the presence of a non-uniform wake field as the propeller is generally operating behind a ship. The fluctuating turbulent flow creates low-frequency broadband noise, whereas the local boundary layer and vortex flow interacting with the trailing edge of the blade cause the high-frequency broadband

noise (ITTC, 2017a). Predicting non-cavitating propeller URN is critical for naval vessels and submarines to prevent acoustic detection, particularly by sonars.

The propeller URN studies were first conducted using potential solvers and the acoustic analogy under non-cavitating conditions. In this way, the feasibility of the acoustic analogy, main numerical issues and pros & cons were examined in the literature. Seol et al., 2002 conducted a numerical study to predict non-cavitating propeller URN using the impermeable formulation of the FWH equation coupled with a BEM (Boundary Element Method) solver in a wide range of operating conditions. The authors investigated the effects of duct geometry on overall URN by taking sound reflection and scattering effects into account. The results showed that the influence of duct geometry on overall URN was small in the far-field since the same directivity pattern was observed w/o ducted propellers. Testa et al., 2008 investigated the hydroacoustic performance of a marine propeller using the FWH equation and Bernoulli-based methodology. The method applied by the authors was based on boundary element formulation. The study aimed to compare FWH and Bernoulli equations to assess the pressure in the far-field. It was shown that the FWH acoustic analogy was more robust and attained many advantages compared to the Bernoulli-based method. Thus, FWH equations were suggested for predicting the noise generation and propagation phenomena around the ship.

In addition to the studies conducted using potential based solvers and the acoustic analogy, viscous-based methods became popular and widely used for hydroacoustic problems in the maritime field. The hydrodynamic flow field is analysed through the RANS, DES or LES methods and then required inputs are provided to the acoustic analogy for the prediction of URN both in near and far-field. Ianniello et al., 2012 explored the non-cavitating propeller hydroacoustic performance using the RANS method with different formulations of the FWH equation (i.e., impermeable and permeable) to examine the contribution of linear and nonlinear noise terms on overall acoustic pressure for the isolated case and a complete ship model. The numerical results showed that the URN field was considerably affected by the contribution of nonlinear noise sources, and they needed to be included in the calculations for the reliable prediction of propeller URN. Later on, the authors conducted a comprehensive study to predict INSEAN E779A propeller hydroacoustic performance under non-cavitating conditions using the RANS method (Ianniello et al., 2013). Time-based acoustic pressure signals were computed at different blade loading conditions and compared with the hydrodynamic pressures. The results also proved the importance of the nonlinear noise' contributions to overall propeller URN. Lloyd et al., 2014 compared two numerical solvers (i.e., ReFRESCO with porous FW-

H and EXCALIBUR with Kirchhoff formulation) for the two-bladed model propeller (i.e., S6666) in open water conditions. The study's main aim was to verify the FWH analogy and investigate the behaviour of the porous surface at different receiver locations. The results showed that FWH results agreed with the measured data, but the 1st BPF value was underpredicted. Lloyd et al., 2015a examined the propeller hydroacoustic performance using the RANS method with the porous FWH formulation, utilising two different CFD codes (i.e., ReFRESCO and OpenFOAM). The authors' study evaluated the effects of permeable surface closure on the propeller hydroacoustic performance at two receivers located in the propeller slipstream. The results revealed that the acoustic pressures at the receivers, close to the end-cap of the porous surface, were more sensitive to the inclusion of the downstream side end-cap. Nevertheless, it remained unclear whether the considerable contribution to the acoustic signals at the receivers was mainly due to the nonlinear noise sources in the propeller slipstream. Ianniello and De Bernardis, 2015 investigated the hydroacoustic performance of INSEAN E779A model propeller in uniform flow using RANS and DES methods and the FWH equation. In the numerical calculations, the RANS method exhibited three subsequent spirals of tip vortex in the propeller's wake before fading, whereas DES showed persistent tip vortex distribution in the propeller slipstream. Thus, it was considered that RANS methods became inadequate for hydroacoustic purposes, particularly for the receivers where the turbulent fluctuating component of the velocity field was relevant. Testa et al., 2018 compared DES and BEM methods, coupled with the porous FWH equation, for the INSEAN E779A propeller under uniform and non-cavitating conditions. The study's main purpose was to present the capabilities of the BEM for the propeller URN predictions in open water conditions. The results showed that an important vorticity field in the propeller slipstream predicted by the DES method characterised the overall sound pressure level. Yet, the BEM was found to be inadequate to reflect the effects of nonlinear noise sources on overall acoustic pressure for the receivers located downstream of the propeller. Hence, the BEM was found to be inappropriate for more in-depth hydroacoustic investigations. Cianferra et al., 2019 focused on the hydrodynamic noise radiated by a ship propeller in open water and non-cavitating conditions. In the numerical calculations, the LES method and FWH equation were utilised. In the authors' study, different noise generation mechanisms were examined separately. As a result of the study, it was found that the nonlinear quadrupole term dominated the broadband noise spectrum. In a very recent study by Testa et al., 2021, a comprehensive numerical investigation was carried out using the porous formulation of the FWH equation. In the authors' study, the issues regarding the pseudo-compressible solvers, end-cap problem, and placement/sizing of

the permeable surface were examined. The most important finding was that accurate noise predictions could be achieved using the special CFD grid stretching to avoid boundary reflections.

All studies above investigated the propeller URN using the potential/viscous based methods and FWH acoustic analogy under non-cavitating conditions. The contribution of nonlinear noise sources, key simulation parameters, and the sensitivity of the acoustic analogy were commonly investigated using the RANS method because of its low computational cost. As stated in the study by Lloyd et al., 2015b, the FWH equation was considered more sensitive to hydrodynamic inputs; hence, grid resolution. Also, the required grid resolution for the hydroacoustic simulations was discussed in the 27th ITTC (International Towing Tank Conference) Noise discussion Forum (ITTC, 2014). This is because it is unclear if the grid applied for traditional propeller hydrodynamic simulations is enough for sound propagation. The grid should be designed to improve the accuracy of the hydrodynamics inputs and mitigate the nonphysical numerical noise, which might deteriorate the overall acoustic pressure. In this regard, to the best of the author's knowledge, there is no specific study to explore the effects of grid resolution and nonphysical numerical noise issues in the numerical solvers. Thus, this research study aims to fill this research gap by conducting more in-depth investigations and developing a numerical technique to visualise the nonphysical numerical noise in the numerical solvers.

As stated above, the role of nonlinear noise sources is crucial for the accurate prediction of propeller URN. Within this framework, several numerical studies were conducted to explore the flow field around the propeller, particularly the propeller's wake, using the different eddy viscosity turbulence models. Wang and Walters (2012) solved the flow around the model propeller (i.e., P5168) using a three-equation transition-sensitive k-ω and standard k-ω SST models. The study's main objective was to compare the flow characteristics obtained by two different turbulence models. The numerical results showed that the sensitive k-ω turbulence model captured blade-surface stresses, flow separations, and vortex cores' flow properties more accurately. In contrast, the standard k-ω SST model induced excessive dissipation in the vortex cores. Also, the thrust and torque coefficients were predicted with good accuracy using a transition-sensitive turbulence model, especially at high blade loading conditions. Ji et al. (2012) solved the flow around the marine propeller using a modified k-ε turbulence model, which was named as Partially-Averaged Navier–Stokes (PANS) model. The results indicated that the modified turbulence model solved the flow field better than the k-ε turbulence model

in the propeller slipstream. Peng et al. (2013) examined the effects of turbulence models on the tip vortex flow for a marine propeller under non-cavitating conditions. The numerical results indicated that eddy viscosity turbulence models predicted the tip vortex flow and global performance characteristics slightly better than Reynold Stress Turbulence Models (RSM). In addition, it was found that the circumferentially averaged velocities, which were outside of the tip vortex region, were not significantly affected by the different solutions of turbulence models. Muscari et al. (2013) solved the flow around the non-cavitating marine propeller using the DES and RANS methods with the Spalart-Allmaras turbulence model. The study's main aim was to investigate the hydrodynamic characteristics of the propeller and wake instability in the propeller slipstream at two different loading conditions. The numerical calculations with the RANS method were conducted in a steady manner, whereas unsteady simulations with DES method were performed. As a result of the study, the RANS method predicted thrust and torque values better than the DES method. However, vortex instability in the propeller wake was predicted with good accuracy in the DES compared to RANS. Guilmineau et al., (2015) examined propeller hydrodynamic performance and propeller's wake instability in a wide range of advance coefficients under non-cavitating conditions. In the numerical calculation, the k-ω SST and EARSM (Explicit Algebraic Reynolds Stress Model) and DES with k-ω SST were utilised. The numerical results were compared with the experiment through the vorticity distribution and global performance characteristics. While thrust and torque values were found in good agreement with the experiment using different models, dissipation of the flow properties in the propeller's wake was found higher in steady k-ω SST and EARSM RANS models. Baek et al. (2015) investigated the effects of the advance ratio on the evolution of a propeller's wake instabilities using an unsteady RANS method for the KP505 model propeller in open water conditions. The numerical calculations were performed in a wide range of advance ratios from J=0.2 to J=0.6. Based on the numerical results, empirical models for the 3-D helices of tip vortices were proposed. It was stated that the propeller's wake could be reliably modelled using empirical models.

The effects of different eddy viscosity models on propeller hydrodynamic performance and flow details in the propeller's wake were investigated in several studies in the literature. According to these research studies conducted by different eddy viscosity turbulence models and advanced methods (e.g., DES), the flow details in the propeller's wake (e.g., vortex structures) were predicted to be dissimilar. However, these dissimilarities in the propeller's wake field, which are important as the nonlinear noise sources, have not been associated with

the propeller URN predictions yet. Thus, the research study in this thesis also aims to fill this research gap by investigating the flow field, particularly the propeller's wake and understanding the primary nonlinear noise sources in the propeller URN predictions using the different eddy viscosity turbulence models.

2.4.2 Cavitating propeller URN

This section gives the research studies on cavitating propeller URN for the model and full-scale propellers, respectively. The studies related to cavitation, hull pressure fluctuations and propeller URN in model scale are also given separately for the propellers operating under uniform and non-uniform flow conditions. Finally, the studies solely focussing on the propeller TVC noise are presented. The classification of the sub-sections will ease the understanding of the research gaps.

2.4.2.1 Model scale propeller

- **Uniform flow conditions**

As reviewed in Section 2.2., the main hydroacoustic noise source radiating from a commercial ship is the cavitating propeller, even if the hydrodynamic flow noise and machinery noise can significantly contribute to the overall noise levels at certain operating conditions. When the cavitation occurs on and off the blades, the cavitating propeller will dominate all relevant noise sources radiated by the ships. The avoidance and delay of the cavitation on marine propellers can be possible for warships and submarines. Hence, considerable effort is given at the design stage to increase the cavitation inception speed (CIS) to avoid cavitation. On the other hand, the complete elimination of the cavitation is not possible for the commercial vessel's propeller to meet the required speed and power criteria (Leaper et al., 2014). Therefore, the accurate prediction of cavitating propeller URN became an important research area in the hydrodynamic field.

Cavitation dynamics is an extremely complex flow phenomenon that dominates the broadband noise characteristics as well as the discrete peaks at the blade passage frequencies. The growth and collapse of individual bubbles in the water create broadband noise, whereas the volume variation of the sheet and tip vortex cavitation generates discrete peaks (IMO, 2014 and ITTC, 2017a).

In order to have a better understanding of the cavitation dynamics, cavitation-induced propeller URN, and the developing URN mitigation techniques, the universities, conventions, regulatory bodies, experts national and international agencies have participated in different research projects supported by the EU (European Union) (Chou et al., 2021). Between 2012 and 2015, the FP7 AQUO (Achieve QUiter Oceans, (AQUO, 2012)) and SONIC (Suppression of Underwater Noise Induced by Cavitation, (SONIC, 2012)) projects were conducted in parallel to investigate the ship URN, its prediction and mitigation methods. In recent years, SATURN (Solutions @ Underwater Radiated Noise, (SATURN, 2021)) project, which is aimed to finish in 2025, has been underway to explore ship URN's detrimental effects on marine animals and develop effective mitigation techniques.

Additionally, as there is no universal procedure for measuring the propeller URN in the experimental facilities, this required investigations on the accuracy and reliability of the URN measurement techniques in the model scale. For this purpose, the Joint Research Programme (JRP), named Noise Measurements, was established within the Hydro Testing Alliance Network of Excellence (HTA-NoE) to assess the propeller URN and investigate the experimental methods. This programme was completed successfully in 2011 (AMT'11, 2011). Later on, the members of JRP came together and decided to create a new research group, called Noise Community of Practice (Noise CoP) of the Hydro Testing Forum (HTF), which was initially named Noise Working Group (NWG). The Noise CoP has performed a round-robin test (RR) campaign to explore the cavitation and hydroacoustic performance of the newly introduced Newcastle University (UNEW) 's Deep-V type catamaran research vessel, The Princess Royal, propeller (Atlar et al., 2013). The RR test campaign aims to explore the URN measurement techniques and compare the results obtained by different test facilities using the same benchmark propeller (i.e., The Princess Royal) (Aktas et al., 2016a; Tani et al., 2020).

In general, numerical calculations have been conducted for predicting the cavitating propeller URN under uniform flow conditions to simplify the calculations. In this regard, Ye et al., 2012 examined the blade frequency noise of a cavitating propeller under uniform flow conditions using the potential based panel code and impermeable formulation of the FWH equation. The time-dependent pressure and the cavity volume data were used as inputs for the FWH equation to predict the propeller URN. The numerical results showed that cavitation noise decreased relatively slower than the non-cavitating noise. Also, it was found that the thickness noise term was dominant in the presence of sheet cavitation. Lidtke et al., 2015 presented preliminary results for the cavitating Potsdam Propeller Test Case (PPTC) propeller in open water

conditions using the RANS method and permeable/porous formulation of the FWH equation. The results showed that the RANS method accurately predicted the blade rates. However, its capability for predicting the broadband part of the noise spectrum was not enough. The numerical results were not validated with the experiment due to the lack of URN data for the selected propeller. Bagheri et al., 2017 examined the propeller hydrodynamic and hydroacoustic performance under non-cavitating and cavitating conditions. In the numerical calculations, only sheet cavitation was considered. The propeller hydrodynamic coefficients and cavitation extensions were compared with the experiment, and good agreement was found. However, the noise predictions obtained by the RANS and impermeable FWH equation were not validated with the experiment. In the authors' study, the inception and development of sheet cavitation were examined to understand the effects of propeller rotational speed on propeller URN. In a very recent study by Kimmerl et al., 2021b, the propeller URN was predicted using ILES (Implicit Large Eddy Simulation) and porous formulation of the FWH equation under uniform flow conditions at three different operating conditions. The hydroacoustic results showed discrepancies at certain frequencies compared to experimental data.

Despite the research studies investigating the cavitating propeller URN in open water conditions, the verification and validation of studies with the available experimental data are rather scarce due to the lack of experimental data for the benchmark propellers in the literature. This makes the capabilities of the hybrid CFD methods questionable for the propeller URN predictions. For this reason, the reliability of the CFD tools for the propeller URN predictions has not been completely understood compared to model scale experiments performed in either cavitation tunnels or depressurised towing tanks. Also, the propeller URN predictions have been generally predicted in the presence of only sheet cavitation due to the modelling complexity of TVC, as explained in Section 2.3. Therefore, there is a need for a computationally efficient advanced mesh refinement technique for TVC modelling (i.e., V-AMR) to include its contribution in the propeller URN, as it is aimed in this thesis. Furthermore, the thesis aims to validate the developed CFD model comprehensively under the uniform and inclined flow conditions using the state-of-art hybrid method (i.e., DES with the permeable formulation of the FWH equation) with the available experimental data through the propeller hydrodynamic characteristics, cavitating extensions, hull pressure fluctuations and propeller URN.

- **Non-uniform flow conditions**

The application of permeable FWH formulation for hydroacoustic problems is a relatively new approach, and there is no standard practice yet. Despite this, there are several studies conducted using the permeable FWH formulation using the different CFD methods for investigating the propeller URN under non-cavitating and cavitating conditions as given above (e.g., Ianniello et al., 2013; Ianniello and De Bernardis, 2015; Lloyd et al., 2015b; Testa et al., 2018). It is worth mentioning that the research in this field was mainly conducted under uniform flow conditions to eliminate the influence of hull wake and shaft inclination for the validation and investigation purposes of the hybrid methods before the complex scenarios (e.g., in the presence of hull wake). In reality, the marine propellers are always operating behind the ship, hence in the presence of a non-uniform wake. The interaction between the wake of a ship and the propeller alters the blade loading, cavitation dynamics and hence associated pressure pulse and URN characteristics. Thus, the propeller URN prediction will be more important in the presence of a non-uniform wake than the predictions conducted under uniform flow conditions. In this regard, Seol et al., 2005 predicted the non-cavitating and cavitating propeller URN in the presence of only sheet cavitation under non-uniform flow conditions. In the numerical calculations, the potential solver and the impermeable formulation of the FWH equation were used to predict the propeller URN in the low-frequency region of the noise spectrum. The circulation distribution and cavity volume change with the time were compared with other numerical studies, and experimental data and good agreement was found. It was stated that more study was needed to include the nonlinearities and complexities created by sheet cavitation break-off and formation of the tip vortex cavitation to predict the high-frequency band of the noise spectrum. Ianniello et al., 2014a predicted the hydroacoustic performance of a complete-scale ship model using RANS and different formulations of the FWH equation. In the numerical calculations, the scattering effects created by the hull surface, the influence of sound refractions at the free surface and the importance of nonlinear noise sources were explored. The numerical results showed that the hull scattered pressure was one of the dominant linear noise components affecting the overall propeller URN prediction. Bensow and Liefvendahl, 2016 predicted the cavitating propeller URN in the presence of a hull using the LES method together with the porous FWH equation. The numerical results, including cavitation patterns and propeller URN, were validated with the experimental data measured in the cavitation tunnel. The results showed good agreement with the experimental data after 1kHz, whereas the numerical calculations underpredicted the noise levels in the low-frequency

region. The differences between numerical prediction and experiment were mainly deemed to the lack of sheet and tip vortex cavitation predicted in the numerical calculations compared to the measured data. Kowalczyk and Felicjancik, 2016 studied the hydroacoustic performance of a marine propeller under non-uniform flow conditions both experimentally and numerically. In these authors' study, the flow field around the propeller blades was solved by the RANS method, and acoustic pressure fluctuations were assumed as hydrodynamic pressure without using the acoustic analogy. The noise levels were calculated at four-receiver locations. The sheet cavity patterns and noise levels up to 1000 Hz were compared with the experimental data. Due to the adopted grid resolution and insufficient TVC modelling, the difference between numerical and experimental results was found around 20-30 dB after 100Hz. Fujiyama and Nakashima, 2017 explored the cavitating propeller URN using the hybrid method for both model and full-scale ships. The cavitation patterns at different blade angles were compared with the experimental observations. The sheet and tip vortex cavitation could be observed successfully in the numerical calculations in model scale, whereas the interaction between the sheet and TVC could not be captured in full-scale. The noise predictions were in good agreement with the experimental data up to 5^{th} BPF for model scale and 1^{st}-2^{nd} BPF for the full-scale propeller, respectively. In the study by Lidtke et al., 2019, the hydrodynamic performance of the INSEAN E779A propeller was investigated under non-cavitating and cavitating conditions in the presence of a non-uniform wake field using the RANS method and permeable FWH equation. This study investigated several noise modelling parameters (e.g., the definition of the porous surface, and the influence of the time step). The pressure amplitude comparisons between the numerical results and experiments showed good agreement with the receivers located sides and above the propeller, whereas the pressures in the numerical calculations were overpredicted compared to experimental data for the receivers located downstream. It was also stated that the future work will focus on the further refinement for the modelling of tip vortex dynamics as the current method suffered from insufficient tip vortex modelling in the propeller slipstream.

Although several studies were conducted for predicting the cavitating propeller URN under non-uniform flow conditions, similar to uniform flow conditions, the numerical propeller URN predictions still need more validation and verification studies to understand the capabilities of the CFD tools and acoustic analogy. For this reason, this thesis aims to make a further contribution by filling this research gap using the state of art CFD method together with the permeable formulation of the FWH equation for the benchmark propeller (i.e., The Princess

Royal) operating in open water conditions in the presence of non-uniform wake field. Akin to the uniform flow conditions, the thesis also aims to incorporate the advanced meshing technique (i.e., V-AMR) with the noise modelling of the CFD approach by modelling the tip vortex flow accurately and hence better representing the TVC in the propeller slipstream to include its effects on the propeller URN.

In addition to the research studies focussing on the cavitation and propeller URN under non-uniform flow conditions, there are also some research studies investigating the hull pressure fluctuations in the presence of cavitation. The pressure fluctuations induced by the propeller and amplitudes are predicted with the potential based methods. These methods are not computationally expensive compared to viscous methods (e.g., Kanemaru and Ando, 2013). However, they can only predict sheet cavitation, and TVC could not be modelled sufficiently compared to viscous methods. Moreover, when the blade is covered by a large cavitation volume, these methods may overestimate the influence of cavitation on pressure fluctuations, particularly for the first blade harmonic (e.g. Gaggero and Villa, 2016). Thus, better results can be obtained for TVC modelling and accurate pressure fluctuations using the viscous methods (i.e., RANS, DES and LES). Amongst them, the RANS method is commonly used to predict the hull pressure fluctuations despite several drawbacks for modelling the tip vortices. Therefore, it is believed that the accuracy of the numerical predictions conducted with the RANS methods is limited up to 2^{nd}-order BPF (Blade Passage Frequency) as the high order BPF values are considerably affected by the TVC dynamics, as shown in Konno et al., 2002 (Ge et al., 2020). For this reason, DES and LES are the more accurate methods for the prediction of hull-pressure fluctuations. Vaz et al., 2015 investigated the propeller performance characteristics, pressure fluctuations and cavitating volumes using E779A propeller in open water and behind wake conditions in the scope of the Cooperative Research Ships (SHARCS) project. Ten institutions joined the workshop, and eight different flow codes were utilised. Although the cavitation extensions on the blades were successfully modelled, the pressure fluctuations were generally overpredicted. Fujiyama, 2015 predicted the hull pressure fluctuations using the SST-SAS turbulence model. The unsteady cavitation dynamics were well captured in the numerical calculations, resulting in a good prediction of hull pressure fluctuations compared to the experimental data. Shin and Andersen, 2018 simulated the flow around the marine propeller behind-hull condition using the DES method. In the numerical calculations, Adaptive Mesh Refinement (AMR) was adopted to model the TVC in the propeller slipstream better. The results were compared between the base mesh and AMR. The

results showed that 1st and 2nd order BPF pressure fluctuations with the AMR technique were predicted closer to the experimental measurements. In a recent study by Ge et al., 2020, the propeller hull fluctuations induced by the propeller and interaction of sheet and tip vortex cavitation behind-hull conditions were investigated using the RANS method. The numerical calculations explored the influence of grid resolution, timestep, and the Reynolds number. Additional mesh refinement was performed to reduce the numerical diffusion at the tip. The results were compared between the base and refined mesh regarding tip vortex generation, its interaction with sheet cavitation, and pressure fluctuations. The results showed that 1st and 2nd order BPF pressure fluctuations were considerably affected by the sheet cavitation, while its closure contributed to high order pressure fluctuations.

In general, the flow around the propeller is investigated in open water conditions using the non-uniform wake field due to the dimensions of the cavitation tunnels and in the CFD calculations Tani et al., 2019a. In order to achieve model scale propeller inflow as similar as possible to the full-scale propeller inflow conditions, in large cavitation tunnels, the tests in model scale are also conducted with the 3D model hull, which is geometrically scaled. In the scope of the SONIC project (SONIC, 2012), the experiments in the cavitation tunnels and depressurised towing tanks were conducted in the presence of a 3D model hull of The Princess Royal vessel by different facilities (e.g., MARIN, CNR-INSEAN, ROLLS-ROYCE AB) to explore the cavitation, hull pressure fluctuations, and propeller URN. The access to such a comprehensive model test database motivated the author further to verify and validate the cavitation extensions, hull pressure fluctuations, and propeller URN. Thus, the thesis aims to further contribute to this field and show the prediction capabilities of the CFD and acoustic analogy by further validation to provide growing confidence in the CFD methods.

2.4.2.2 Full-scale propeller

The cavitating marine propeller URN is predicted in model scale with the experiments conducted in the cavitation tunnels and numerical methods (e.g., Aktas et al., 2016a; Tani et al., 2019a). Then, the hydroacoustic results are extrapolated to full-scale using the proposed extrapolation techniques (ITTC, 2017b). However, scaling the results from the model to full-scale brings some difficulties. For instance, viscous effects influence the flow characteristics and the cavitation dynamics on and off the propeller blades. In particular, the tip vortex cavitation (TVC) is delayed in model tests compared to the sea trials because the propellers are generally operating at a lower Reynolds number in the model test. In this case, the development of TVC and associated noise prediction will be more critical and different extrapolation

techniques might be required for the accurate prediction of propeller URN in full-scale (e.g., Park and Seong, 2017). Furthermore, the additional issues related to cavitation inception & development, such as water quality between the model and full-scale propellers, were also explained and discussed in ITTC, 2002b and Tani et al., 2019a.

Several studies were conducted to predict cavitation extensions, hull-pressure fluctuations, and propeller URN using the CFD methods. However, these studies are still limited in model-scale. The results are needed to be extrapolated to full-scale with the extrapolation techniques despite the several issues stated before. Due to this fact, either the URN predictions should be conducted in full-scale to avoid scale effects using CFD methods, or URN measurements need to be undertaken for the full-scale ship in real sea state conditions. Inevitably, the sea trial URN measurements are the foundation for the accurate prediction of full-scale propeller noise levels, and they have been generally conducted for military and research purposes; hence the results are often restricted for validation purposes. Also, there are a few numerical studies in the literature for predicting the full-scale propeller URN and validating the numerical results with the full-scale measurements, especially under cavitating conditions. Hallander et al., 2012 investigated the propeller URN for the full-scale LNG ship under non-cavitating and cavitating conditions. In the numerical calculations, the unsteady RANS method, impermeable formulation of the FWH equation, two different potential based solvers and semi-empirical formulation were used. The obtained results were validated with the experimental data. The numerical calculations performed by the RANS method and FWH equation underpredicted the results up to 20dB for the frequency range until 100Hz. This underprediction was associated with insufficient grid resolution, the RANS method's limitations, and the ignoring of nonlinear noise sources. Later on, the authors repeated the calculations using the advanced CFD method (i.e., DES) and FWH acoustic analogy to predict propeller URN in model and full-scale (Li et al., 2015). In their previous study, due to the capabilities of the RANS, the contribution of nonlinear noise sources originating from the instantaneous stress tensor and turbulent eddies could not be predicted accurately. However, with the application of the DES method, this issue was rather solved, and the results showed better agreement with the experimental and sea trial data up to the mid-frequency region. Nevertheless, due to the insufficient modelling of TVC, the numerical results deviated compared to full-scale measurements at a certain frequency range. Kellett et al., 2013 predicted the propeller URN of LNG carrier under non-cavitating conditions. The numerical calculations were performed with 6.4 million cells using the RANS with the porous formulation of the FWH equation. In the numerical calculations, the effects of

propeller rotational techniques (i.e., MRF (Moving Reference Frame), RBM (Rigid Body Motion) and the free surface were investigated. The predicted propeller URN results were validated with the full-scale measurements, and a significant deviation (i.e., 40dB and 80dB) was found between the CFD and full-scale measurements. The numerical results also showed that the free surface did not affect the overall propeller URN predictions. Thus, neglecting the free surface in the CFD calculations was suggested for the propeller URN predictions. Ianniello et al., 2014b explored the capabilities of the FWH equation for the full-scale RO-PAX vessel under non-cavitating conditions using the RANS method. The numerical results were underpredicted up to 30dB at certain frequencies compared to the full-scale measurements. The results showed that the contribution of nonlinear noise sources is required for the accurate prediction of the propeller URN. In the study by Fujiyama and Nakashima, 2017, the CFD calculations were performed to predict the cavitation extensions and propeller URN both in model and full-scale. The model scale predictions were in good agreement with the experimental data and semi-empirical formulations. In contrast, the full-scale propeller URN was underpredicted between 10dB to 30dB depending on the receiver location. This underprediction was considered due to the insufficient grid resolution adopted in the numerical method for the sound propagation and the lack of TVC dynamics modelled in the CFD compared to sea-trial data. Li et al., 2018 investigated the model and full-scale propeller hydrodynamic and hydroacoustic performance using the DES and permeable formulation of the FWH equation. The hydrodynamic results and hull pressure fluctuations were first validated with the model experiments, and then propeller URN predictions were compared with the full-scale measurements. In the numerical calculations, the sheet cavitation was predicted similar to the experimental and sea trial observations, whereas the strength and extension of TVC could not be observed in the numerical calculations as in the sea trial. The hydroacoustic results were found to be in good agreement with the full-scale measurements up to 5^{th} BPF, but the lack of TVC dynamics in the CFD calculations resulted in an underprediction of URN levels, approximately after 200Hz, in the numerical calculations compared to full-scale measurements.

The present literature indicates that there are a few studies investigating the propeller URN in full-scale, particularly operating under cavitating conditions. Also, these studies mainly suffer from the inadequate solution of tip vortex flow and grid resolution. In the EU-funded SONIC project (SONIC, 2012), full-scale measurements were performed at different operating conditions for the Newcastle University's Research Vessel, The Princess Royal (Atlar et al., 2013). As a result of the full-scale measurements, the comprehensive ship URN database,

including the cavitation observations, was generated. The full-scale sea trial data collected during the SONIC project gave the author an excellent opportunity to show the capabilities of the CFD methodology used in this PhD thesis. Thus, the thesis aims to fill the research gap by predicting the propeller hydrodynamic performance, cavitation extensions and propeller URN in full-scale using the state-of-art CFD method (i.e., DES and permeable FWH equation). In this way, the effectiveness of the CFD methodology, the acoustic analogy and the newly developed TVC modelling technique (i.e., V-AMR, in Chapter 5) will be explored for the full-scale application.

2.4.2.3 TVC noise

As shown in Figure 2.2, various cavitation forms (e.g., sheet, bubble, cloud, vortex cavitation) can be observed on the ship propellers, depending on the operating conditions. Their effects on propeller hydrodynamic and hydroacoustic performance are different. As stated in Section 2.3, the most commonly observable cavitation types on the ship propellers and most relevant for URN are the sheet and tip vortex cavitation. Although sheet cavitation is more harmful than the TVC, understanding and accurately predicting its noise is of great interest in the hydroacoustic field. This is because it is the first type of cavitation observed on well-designed propellers and is deemed the main cavitation type controlled in the propeller design stage (Asnaghi et al., 2021). TVC is generally associated with broadband hull-pressure fluctuations, broadband noise, and rudder erosion in many cases (Bosschers, 2018).

The propeller URN is generally predicted in a condition where only the sheet cavitation is modelled using the numerical methods due to difficulties in modelling the TVC, as explained in Section 2.3. Additionally, the influence of developed TVC on broadband and narrowband noise is not yet fully understood both numerically and experimentally (Higuchi et al., 1989; Strasberg, 1986). In the past, only a few experimental studies were conducted to address the TVC noise for marine propellers and foils specifically. As stated in Pennings et al., 2016, Barker, 1976 studied the source of cavitation noise experimentally and found out that the steady tip vortex cavity did not show the strong collapse of other types of cavitation and thus produced less sound. The findings were also observed in other studies solely focusing on steady cavitating trailing tip vortices (e.g., Higuchi et al., 1989; Maines and Arndt, 1997; Astolfi et al., 1998). Konno et al., 2002 conducted a comprehensive experimental study to investigate the bursting or collapsing phenomenon of TVC by changing the wake distributions, thrust coefficients and cavitation numbers using two different marine propellers. The pressure fluctuations were measured to understand the effects of systematic investigations. The results

showed that large pressure hull fluctuations occurred twice in the bursting phenomenon, and they strongly depended on the wake distribution. Also, it was found that the stabilisation of TVC or total cavitation volume reduction needed to be achieved to suppress the TVC. Pennings et al., 2016 explored whether the resonance tip vortex cavity was the main source of high-amplitude broadband pressure fluctuations for a full-scale propeller. This investigated by conducting series of experiments in the cavitation tunnel. Additionally, the Proctor vortex model was used to determine the resonance frequency of the tip vortex cavity. The experimental measurements showed that steady tip vortex cavitation in the propeller slipstream did not yield a significant sound in uniform flow in the range of 0.5-1.2kHz. In contrast, the noise levels increased in the presence of the upstream wake. It was found out that dominant sound frequency was directly associated with the resonance of the tip vortex cavity.

Similar to experimental studies, various semi-empirical formulations have also been utilised to predict TVC noise in the literature. Raestad, 1996 developed a semi-empirical formulation called Tip Vortex Index (TVI) based on the pressure field generated by the cavity volumes on the propeller blades using the measurements conducted for Queen Elizabeth 2. The results obtained by the semi-empirical formulation were found in line with the measurements. Lafeber et al., 2015 studied the cavitating propeller URN for the container, cruise and catamaran vessels using different computational models (i.e., propeller flow panel method (PROCAL), tip vortex noise model (ETV), sheet cavitation noise model (Matusiak and Brown)). The numerical results were compared with the full-scale sea trials and measurements conducted in the depressurised water tunnel in MARIN. The results showed that the ETV model predicted the noise in good agreement with the sea-trial data for the cruise liner as the vortex cavitation was expected to be dominant. However, ETV underpredicted the noise levels for a container vessel compared to experimental data measured in the cavitation tunnel as there was significant sheet cavitation observed on the blades. In a recent comprehensive study, Bosschers, 2018 developed prediction methods for broadband noise, including hull pressure fluctuations generated by the developed TVC using the full-scale and model scale data. In the author's model, the vortex cavity size was the principal parameter. It was predicted with the boundary element method and together with the semi-empirical vortex model. Also, a novel method was developed to correct the scale effects due to the Reynolds number on broadband noise of TVC. The developed model could predict the broadband hull-pressure fluctuations and URN using the inputs provided by the boundary element method (BEM). The results were compared to experimental, and sea trial data for different propellers and operating conditions, and agreement

was good. Sezen and Bal, 2020 investigated the TVC noise at the inception stage using the potential based semi-empirical TVI (Tip Vortex Index), developed by Raestad, 1996 and hybrid viscous methods in open water conditions. The numerical results showed that the TVI and hybrid method gave the same results once the TVC started. Thus, it was stated that the TVI method could be reliably applied instead of the hybrid method at the inception stage of the TVC.

In recent years, as reviewed above, cavitating propeller URN has been predicted using the hybrid CFD method. However, the cavitating propeller URN is generally predicted by modelling only the sheet cavitation on the propeller blades (e.g., Lidtke et al., 2016; Stark and Shi, 2021). Also, the lack of reproduction of cavitating tip vortices in the numerical calculations is considered to be the main reason for the underprediction of propeller URN levels in the numerical calculations compared to experimental data (e.g., Bensow and Liefvendahl, 2016; Fujiyama and Nakashima, 2017; Li et al., 2018). To the best of the author's knowledge, the influence of TVC on the propeller hydroacoustic performance has not been explored thoroughly using CFD methods. Thus, the thesis also aims to understand the contribution of TVC on overall propeller URN levels at different operating conditions in model and full-scale.

2.5 Roughness

The accumulation of marine organisms on a submerged/floating body surface is defined as marine biofouling (Uzun, 2019). Although several types of marine organisms create biofouling, marine organisms can be divided into microfouling and macrofouling, depending on their size (Atlar, 2008). Figure 2.3 shows the marine fouling types. In this PhD thesis, the barnacle type biofouling was utilised as the experimental data was generated based on this type of particular roughness (Uzun et al., 2020).

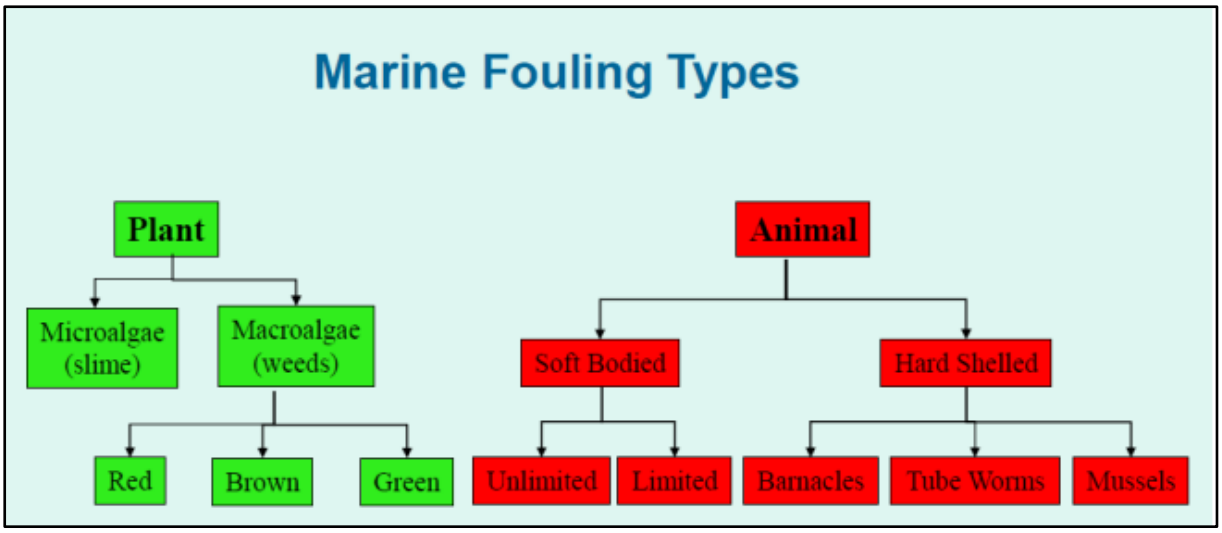

Figure 2.3. Categorising the marine fouling types (Atlar, 2008).

Marine biofouling is identified as one of the essential problems in economic and ecologic aspects by IMO. Biofouling causes performance degradation in the hydrodynamic performance of ships by increasing the hull resistance. This escalates fuel consumption and hence GHG emissions.

Although the effects of biofouling roughness on ship performance have been investigated profoundly in the literature (e.g., Schultz, 2007; Schultz et al., 2011; Demirel et al., 2017; Yeginbayeva and Atlar, 2018; Speranza et al., 2019; Uzun et al., 2019; Song et al., 2020), there is a lack of investigations on the roughness effects on propeller hydrodynamic performance (Owen et al., 2018). According to the American Bureau of Shipping (ABS) (ABS, 2013) report, fouling accumulates on a propeller within a year shows a wide range of diversity, including slime, algae and even barnacles and tube worms. For example, fouling accumulation over a year of operation on a propeller can be seen in Figure 2.4. The ITTC (ITTC, 2011) suggested that new methods and strategies need to be developed to understand the effect of coatings and biofouling roughness on overall ship performance, including the propeller.

Figure 2.4. Biofouling after a year of operation on a propeller.

While the concern is the efficiency and fuel consumption for the shipping industry, the effects of roughness on the propeller cavitation and URN are also important. Townsin et al., 1981 drew attention to penalties caused by propeller roughness. Moreover, a cost-efficiency analysis was conducted to compare hull and propeller cleaning operations. Additionally, Mosaad, 1986 highlighted the energy loss per unit area due to the rough propeller and explained the importance of propeller roughness compared to hull roughness. Atlar et al., 2002 investigated the influence of foul release coatings on propeller hydrodynamic performance. The authors showed that the propeller blade roughness caused significant penalties in ship performance due to the changes in torque and thrust of the propeller. In the following study, Atlar et al., 2003 conducted a similar analysis to examine the efficiency loss due to the roughness of the high-speed vessel. The authors' study showed that preventing biofouling on propeller blades had the potential to increase propeller efficiency. As stated in Atlar et al., 2003 and Anderson et al., 2003 a clean propeller had favourable cost benefits compared to a roughened propeller. Seo et al., 2016 developed an algorithm and investigated the impacts of biofouling on propeller

performance in open water. The results showed that biofouling on the propeller increased the torque with an increase in fouling rate, resulting in efficiency loss.

With an increasing interest in CFD methods, Owen et al., 2018 investigated the impacts of fouling on the performance of a Potsdam Propeller Test Case (PPTC) in model scale using CFD. In their study, the authors stated that the wall function of the CFD approach was a very practical way to predict the penalties caused by fouling accumulation on a propeller. Song et al., 2019 examined the deteriorating effects of biofouling roughness on ship propellers in open water conditions at different advance ratios. The results showed that the roughness led to performance degradation. A very recent and comprehensive numerical and experimental study was conducted by Asnaghi et al., 2020b for elliptical foil. This study explored the mitigation of tip vortex cavitation inception by applying different roughness configurations. The results showed that applying roughness on a small area of the foil section could prevent performance degradation, and TVC inception could be reduced around 33% compared to the smooth condition.

There are limited studies in the literature investigating the impacts of the roughness on propellers in terms of noise and cavitation characteristics. One of the earliest studies was conducted by Van der Kooij, 1986 with a comparison between roughened and smooth propeller blades. In the author's study, cavitation bubbles were generated by electrolysis currents varying from 0 to 2.4A for the smooth blades. Additionally, the artificial roughness was used with an electrolysis current of 2.4A on the leading-edge part of the propeller blades for the roughened blades. Furthermore, generated noise fluctuations through increasing cavitation bubble densities were investigated in the model scale. The results showed that with the rising number of bubbles at the beginning, there was an increase in the noise levels; however, there was a remarkable drop when the numbers of bubbles became larger for both roughened and smooth cases until 63Hz. Krüger et al., 2016 stated that Philipp and Ninnemann, 2007's study showed that the application of roughness on a small area at the suction side of the blade close to the trailing edge could destabilise the tip vortex formation, hence its early breakdown. Cong et al., 2019 conducted an experimental study and tested the cavitation characteristics of a composite coating on a propeller. Their results presented that there was not a significant impact on the thrust and torque characteristics of the propeller.

As reviewed above, there are limited numerical and experimental research studies investigating the propeller hydrodynamic and hydroacoustic performance under non-cavitating and cavitating conditions. However, the effects of roughness on the propeller hydrodynamic performance in the presence of sheet and tip vortex cavitation (TVC) have not been investigated adequately using CFD, and hence its impact on the URN characteristics of a propeller is totally unknown. Hence, the thesis also aims to fill this research gap by investigating the propeller hydrodynamic performance, cavitation extension and propeller URN characteristics in the presence of roughness using the wall function of the CFD approach and the experimental roughness data.

There are different methods to modify, delay or mitigate the TVC on marine propellers. They can be identified as active and passive control methods (Yakushiji, 2009). In the active control methods, TVC can be suppressed by the polymer or water injection inside the tip vortex (e.g., Yakushiji, 2009; Fruman and Aflalo, 1989; Chahine et al., 1993; Platzer and Souder, 1981). On the other hand, as a passive control method, the most common approach is modifying the blade geometry by reducing the tip region's circulation to unload the propeller tip. In this way, the circulation decreases, and pressure inside the vortex also increases (Carlton, 2018). In addition to this, the inclusion of additional geometry at the propeller blade tips, drilling holes and application of extra roughness on the propeller blades can be considered as alternative passive TVC mitigation methods (e.g. Chekab et al., 2013; Aktas et al., 2020; Asnaghi et al., 2020b; Asnaghi et al., 2021). Among the different passive methods, roughness on the propeller blades becomes an appealing and suitable method to reduce the cavitation, hence propeller URN, particularly for retrofit projects. In this regard, several experimental studies have been conducted using hydrofoil and propellers to understand the influence of roughness on the hydrodynamic performance of these submerged bodies and associated tip vortex flow.

In the past, Platzer and Souders, 1979 showed that roughness on the hydrofoil tip had a favourable impact on delaying the TVC inception. Katz and Galdo, 1989 conducted an experimental study in a towing tank using a rectangular NACA-66 hydrofoil in smooth and rough conditions. The experimental observations showed that the tip vortex's physical dimension was not affected considerably by the roughness application, while the pressure changed significantly. Thus, it was concluded that an increase in surface roughness enabled a reduction in the tip vortex strength. Johnsson and Rutgersson, 1991 explored the influence of leading-edge roughness on the tip vortex roll-up phenomenon at different angles of attack. The results showed that the roughness applied on the pressure side and near the leading edge

delayed the TVC, whereas it increased the drag up to 10%, depending on the propeller operating condition, and hence efficiency loss was observed. Korkut and Atlar, 2012 performed another comprehensive experimental study. In the authors' study, the hydrodynamic performance, including cavitation, and URN levels of the coated and uncoated propellers, were investigated in the Emerson Cavitation Tunnel. Considerable differences were not observed between coated and uncoated propellers in terms of cavitation. However, the noise levels decreased for the coated propeller at a higher advance coefficient, while the noise levels increased for the coated propeller compared to the uncoated one at lower advance coefficients. A recent and comprehensive experimental study was conducted by Svennberg et al., 2020 for an elliptical foil to investigate the effects of uniform and non-uniformly distributed roughness on cavitation inception and tip vortex flow. The cavitation inception properties of the foil were found similar by applying both uniform and non-uniformly distributed roughness, whereas the drag force was found to be higher for the non-uniformly distributed roughness in comparison with the uniformly distributed roughness.

Despite some favourable experimental reports for the influence of roughness on the propeller and hydrofoil cavitation in model scale, particularly for the TVC inception, similar investigations using the CFD in the model and full-scale are scarce. As stated in Section 2.3, tip vortex flow is a complex phenomenon with the challenging task of predicting its strength and size along its trajectory. It becomes further complicated with the application of roughness (Hunt et al., 1988; Asnaghi et al., 2020a). Krüger et al., 2016 investigated roughness effects on propeller hydrodynamic performance under non-cavitating conditions using RANS and LES methods. Their study modelled the roughness using the wall function approach and physical dimple elements on the propeller blades by modelling a single propeller blade. Their study aimed to explore the effects of propeller tip roughness and application area on the tip vortex flow. The results showed that the strength of the tip vortex decreased with the application of suction side tip roughness. Asnaghi et al., 2019 investigated the probability and effectiveness of varying roughness characteristics (e.g., roughness height and roughness coverage area) for elliptical foil using CFD. The authors' study demonstrated that cavitation inception could be delayed with the application of roughness. Asnaghi et al., 2020b conducted a comprehensive numerical and experimental study to explore the impact of roughness on tip vortex and TVC using roughness for an elliptical foil. Several roughness configurations and sizes were tested, and hydrodynamic performances were investigated. The roughness was modelled using a wall function approach and resolving the flow around the roughness elements with the LES method.

The authors showed that the TVC inception could be decreased around 33% with a minimal drag increase (i.e. less than 2%). Following this study, the authors extended their investigation for the marine propellers using CFD (Asnaghi et al., 2021). The authors achieved the suppression of TVC considerably by keeping the efficiency loss as small as possible both in the model and full-scale propeller with the application of roughness on the strategic areas at the blade surfaces under the uniform flow conditions.

Although a few studies have been conducted to investigate the influence of the roughness on tip vortex flow (e.g. Krüger et al., 2016), those studies are generally limited to the model scale propeller under non-cavitating conditions. Also, the investigation of the influence of roughness on the cavitating full-scale propeller is very scarce. Tip vortex flow requires detailed knowledge to understand where and how the tip vortex formation occurs, especially under non-uniform flow conditions. To the best of the author's knowledge, the influence of the roughness on propeller hydrodynamic performance and the potential use of this roughness to mitigate the TVC has not been explored yet under inclined and non-uniform flow conditions for both model and full-scale propellers. Therefore, the thesis aims to fill this research gap by applying uniformly and non-uniformly distributed roughness to examine the propeller hydrodynamic performance and TVC using the existing benchmark research vessel propeller, The Princess Royal, in model and full-scale.

Similar to TVC, hub vortex cavitation, another main interest of this PhD thesis, is also practically important. First of all, the waste energy is spent by the excessive swirl of the flow in the propeller slipstream near the propeller rotational axis. This swirl will result in a pressure reduction with respect to ambient pressure, and hence it will generate an undesirable drag force on the propeller. Also, when the swirl is large, the energy given to the fluid near the hub will not produce axial thrust, and the mixing of turbulence will dissipate it. Secondly, the hub vortex cavitation is a large cavity. Thus, if the rudder or any control surfaces are positioned in line with the propeller-shaft system axis, they can lose the lift force which is aimed to be produced. The vortices around the hub reduce the propeller efficiency by increasing the energy loss depending on the axial load distribution on the propeller and hub geometry. Hub vortex cavitation can also be associated with undesirable vibration, noise and, in some cases, erosion on the rudder (Atlar et al., 1998; Ghassemi et al., 2012; Carlton, 2018).

In order to mitigate the cavitation and associated URN, as summarised above, several active and passive noise control methods are applied, mainly for TVC mitigation. In addition to passive noise control methods, propeller boss cap fins (PBCF), primarily designed to improve the propeller performance characteristics, have been commonly utilised as an Energy Saving Device (ESD). Also, with this concept, the strength of the hub vortex is weakened, and the kinetic energy of the flow around the boss can be recovered by applying the same number of fins corresponding to the propeller blade number. Thus, it can also be used as a passive noise control concept to mitigate hub vortex cavitation, associated URN and rudder erosion. The PBCF investigations were carried out by Ouchi et al., 1988; Ouchi et al., 1989; Ouchi, 1992. The authors found that thrust increased, whereas the torque reduced with the application of PBCF. This resulted in a favourable impact on propeller efficiency. Since then, there have been several experimental, and numerical investigations conducted using different PBCF concepts to investigate its effects on propeller hydrodynamic performance, including cavitation and URN (e.g., Kawamura et al., 2012; Xiong et al., 2013; Mizzi et al., 2017; Sun et al., 2020; Gaggero and Martinelli, 2021).

Applying the roughness on the blades and its favourable impacts on cavitation and propeller URN encouraged the author to apply this novel concept as an alternative to the PBCF on the propeller hub to mitigate the propeller hub vortex and hence its cavitation. Also, to the best of the author's knowledge, this novel concept (i.e., roughness application on the propeller hub) has not been investigated using the CFD. Hence, this thesis aims to present the alternative passive noise control concept for mitigating the propeller hub vortex and its cavitation.

2.6 Identification of literature gaps

The following research gaps were identified based on the broad literature review in propeller hydrodynamics, cavitation, URN, and roughness fields.

- As the application of the acoustic analogy is a relatively new research area in the hydroacoustic field, the effectiveness of the acoustic analogy, including key simulation parameters, has still been investigated in the literature. Amongst these parameters, the grid resolution, which is crucial for the sound propagation and overall noise levels, is important since the prediction by the FWH equation is considered to be sensitive to the grid resolution. However, this important topic has not been explored satisfactorily in the current literature. Therefore, a comprehensive investigation of the grid resolution effect on propeller URN predictions and possible nonphysical numerical sources in the numerical calculations is needed to be explored using the CFD method and acoustic analogy.

- Several studies have been conducted using different numerical methods to investigate the propeller hydrodynamic performance with a special emphasis on flow details in the propeller's wake under non-cavitating conditions. Although the propeller's wake field is one of the major factors contributing to the nonlinear noise sources, the dissimilarities in the propeller's wake field predicted by different numerical methods have not been related to the propeller URN predictions to understand the nonlinear noise sources in detail. Thus, the nonlinear noise sources affecting the propeller URN predictions need to be investigated to understand the further details.

- The numerical studies are generally conducted by only modelling the sheet cavitation due to the difficulties of the TVC modelling. Even though some advanced meshing techniques are available in the literature for modelling the TVC, the computational cost of these methods is still high. These disadvantages of the current few methods limit the incorporation of advanced meshing techniques for the propeller URN predictions in full-scale. Therefore, developing a new meshing technique for TVC modelling emanating from all propeller blades with a low computational cost is required.

- Although there have been several numerical studies investigating the propeller URN in model scale using different numerical methods under cavitating conditions, the verification and validation of these studies with the available experimental data are relatively rare. For this reason, the capabilities of the current CFD approaches have not been fully understood. Besides, in these studies, cavitation modelling is still limited to sheet cavitation only. Hence, the CFD method can be effectively used to make extensive verification and validation studies through the propeller hydrodynamic characteristics, cavitation extensions, hull-pressure fluctuations and propeller URN by including the TVC by making use of the recently introduced benchmark propeller model and full-scale test data operating under uniform, inclined and non-uniform flow conditions.

- The numerical studies are generally conducted in model scale for predicting the propeller URN. Although there are limited studies conducted in full-scale under cavitating conditions, these studies mainly suffer from insufficient TVC modelling, and the validity of the methods are shown in the relatively near field. Therefore, it is worthwhile to show the effectiveness of the CFD approach for the full-scale propeller URN predictions in the far-field where the noise data is collected.

- Although TVC is one of the important noise sources affecting the overall propeller URN, no study has been devoted to investigating the contribution of TVC to propeller URN using the CFD method. Therefore, the CFD method, including the V-AMR technique, can be utilised to understand and separate the contribution of TVC noise on overall propeller URN prediction.

- To the best of the author's knowledge, there is no specific study exploring the effects of roughness on propeller URN. Also, only one study is presently investigating the effects of homogenously and heterologously distributed roughness on propeller cavitation in model and full-scale. Moreover, no study is present for applying the roughness on the propeller hub for mitigating the hub vortex cavitation. Therefore, it is important to perform CFD calculations in the presence of roughness applied on the blades and hub to investigate its impacts on propeller hydrodynamic performance, cavitation and propeller URN for model and full-scale propellers.

2.7 Chapter summary and concluding remarks

A comprehensive literature survey was carried out in the fields of propeller hydrodynamics, cavitation, URN and roughness in this chapter to identify the current literature gaps in these fields and hence to justify the aims and support the specific objectives of the PhD thesis.

Overall, it can be safely stated that the URN from commercial shipping is another global pollution concern threatening the world's oceans and occupying the political agenda. This requires the accurate prediction of the URN in full-scale by using state of the art validated numerical tools and the development of novel mitigation techniques using these tools.

Within the above context, the prediction of the underwater radiated noise induced from the cavitating propeller in full-scale and by using the CFD methods has been emerging as a powerful tool, but it requires further developments, which are identified as the research gaps in this chapter to form the basis for the aim and objectives of this thesis.

3 Methodology

3.1 Introduction

In order to ease the reader to follow the methodology used in the thesis, this chapter presents a general outline and brief insight into the computational, experimental and full-scale approaches used in this research study. The general methodology utilised throughout this PhD thesis is briefly explained, and the methodology used in each chapter is presented in detail.

3.2 Methodology

Figure 3.1 shows a chart to outline the general methodology used in this PhD thesis. As shown in Figure 3.1, the PhD thesis mainly consists of four main parts, namely Part I, II, III, and IV. Chapter 4 in Part I focuses on non-cavitating propeller hydrodynamic and hydroacoustic performance prediction in open water conditions, and the influence of grid resolution (in Chapter 4.2) and non-linear noise sources (in Chapter 4.3) on propeller URN predictions are presented. Chapter 5 in Part II describes the developed CFD-based numerical technique for accurate solution of the tip vortex flow and better modelling TVC in the propeller slipstream for the propeller operating in open water conditions. Also, the important cavitation modelling parameters affecting the cavitation phenomenon are explored. Chapters 6, 7 and 8 in Part III present the comprehensive validation of the CFD approach applied with the experimental and sea trial data for the model (in Chapter 6) and full-scale (in Chapter 7) propellers in open water and behind ship conditions. Also, the contribution of TVC on overall propeller URN predictions is presented in Part III (in Chapter 8). Finally, Chapter 9 in Part IV presents the effects of roughness applied on the blades and hub on the propeller operating in open water and behind ship conditions on propeller hydrodynamic and hydroacoustic performance. Chapter 9 also investigates the determination of the most effective roughness application area on the propeller blades.

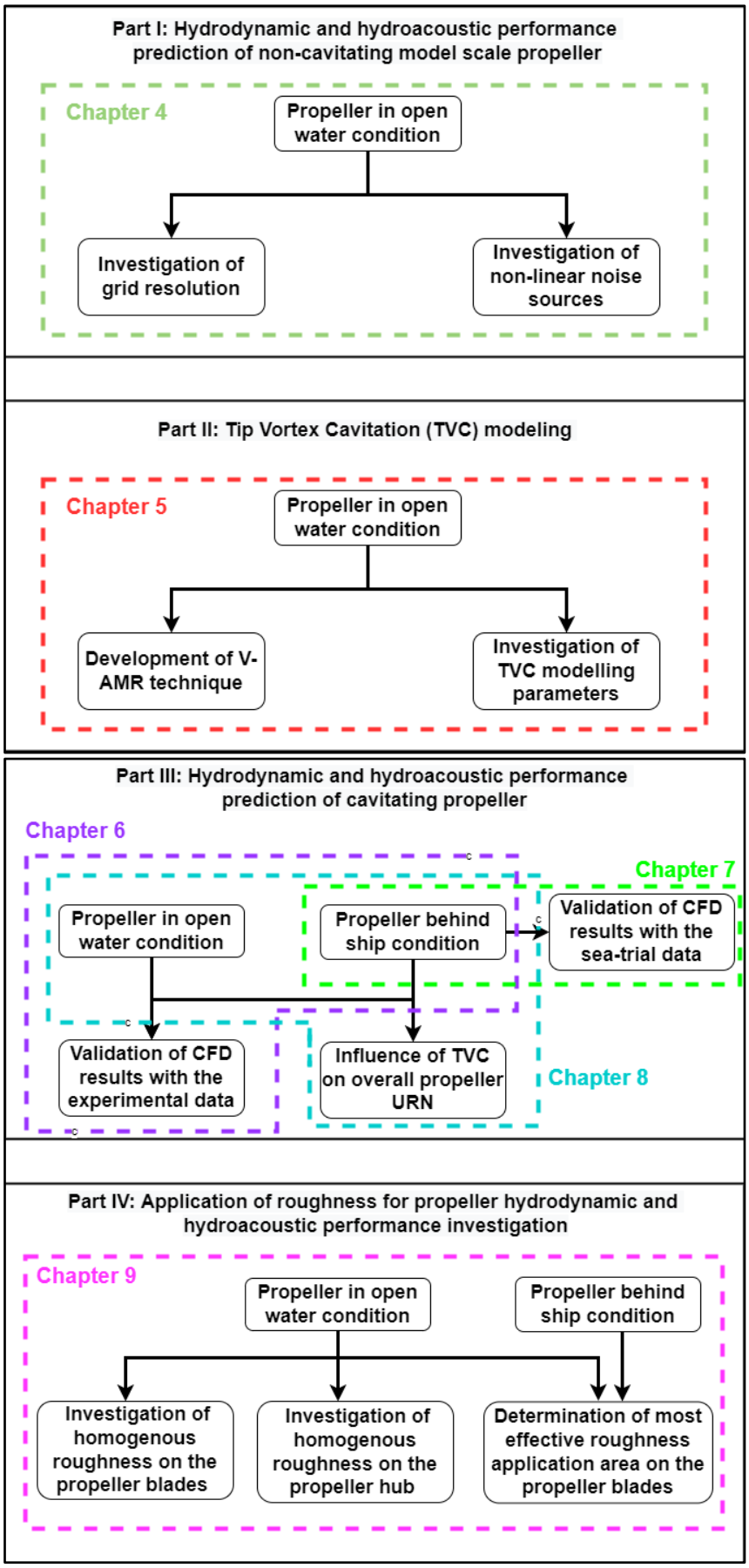

Figure 3.1. The methodology followed in the PhD thesis.

To give further insight into the methodology outlined in Figure 1, the hydrodynamic performance of the model scale INSEAN E779A propeller operating under uniform flow conditions (i.e., open water) was investigated. The CFD model of this propeller was established in Chapter 4 to predict propeller hydrodynamic performance and URN accurately. Chapter 4 also presents a numerical investigation into the influence of grid resolution and non-linear noise sources on propeller hydroacoustic performance using RANS and permeable FWH formulation. More specifically, in Chapter 4.2, the grid resolution used in the numerical calculations was changed to explore the influence of grid resolution on the propeller URN predictions in the near field. In Chapter 4.3, the different eddy viscosity turbulence models, namely k-ε, k-ω SST, and Spalart-Allmaras, were used to examine their capabilities in predicting the non-linear noise sources in the propeller slipstream at high and low blade loading conditions. The flow details in the propeller slipstream were associated with the propeller URN predictions. The obtained hydrodynamic results were validated with experimental data, while the URN predictions were compared with other numerical studies in the literature due to the lack of experimental URN data for the selected propeller in Chapter 4.

Chapter 5 focuses on developing the CFD approach for the investigation of cavitating flow around the benchmark model scale INSEAN E779A propeller operating in open water conditions using RANS, DES, and LES methods. One of the aims of Chapter 5 is to develop a CFD-based numerical technique for accurate solution of the tip vortex flow and enhanced modelling of the TVC in the propeller slipstream to include its effects on propeller URN predictions. In the numerical calculations, the Schnerr-Sauer cavitation model based on the reduced Rayleigh Plesset equation was utilised for sheet, hub, and tip vortex cavitation modelling. The obtained numerical results were validated with the experimental data for the hydrodynamic performance coefficients and cavitation extension.

Validation of the CFD approach for predicting the propeller hydrodynamic characteristics, including cavitation and URN, is presented in Chapter 6. In the numerical calculations, DES with permeable FWH equation was used to predict propeller hydrodynamic performance characteristics, cavitation extensions, hull-pressure fluctuations, and propeller URN. The newly introduced benchmark propeller, The Princess Royal propeller, was used in Chapter 6 as comprehensive validation data is available for this propeller. The developed CFD-based TVC modelling technique, explained in Chapter 5, together with the Schnerr Sauer cavitation model, was used in the CFD approach to better solve the tip vortex flow and represent the TVC in the propeller slipstream. The numerical results were validated with the experimental data

under uniform (in Chapter 6.1) and non-uniform flow conditions (in Chapter 6.2 and Chapter 6.3) to show the capability and validity of the CFD approach developed in this PhD thesis.

Chapter 7 presents the full-scale application of the developed CFD approach using the benchmark vessel, The Princess Royal. In the numerical calculations, DES and permeable FWH formulation was used for the propeller URN predictions. The developed CFD-based TVC modelling technique, as given in Chapter 5, was applied with the Schnerr Sauer cavitation model to show the capability of the technique for the full-scale propeller. The hydrodynamic performance characteristics and cavitation extensions, and far-field URN predictions obtained by the CFD approach were validated with the sea-trial data at different operating conditions of the benchmark vessel.

The investigations into the influence of TVC on the hydroacoustic performance of the model and full-scale benchmark propeller of The Princess Royal are presented under the uniform, inclined shaft, and non-uniform flow conditions in Chapter 8. The DES method was used to solve the flow field around the cavitating propeller, whereas the permeable FWH formulation was utilised for the URN predictions. The Schnerr Sauer cavitation model and the developed CFD-based TVC modelling technique, as given in Chapter 5, were used to model the cavitation. The numerical calculations were carried out in conditions where only sheet cavitation was modelled, and sheet and tip vortex cavitation were also modelled together to show the contribution of TVC on the propeller URN.

In Chapter 9, the influence of biofouling type (representative barnacle) roughness on the propeller hydrodynamic performance characteristics, including cavitation and URN, is presented using the CFD approach. The roughness functions of barnacles (Uzun et al., 2020) were employed in the wall function of the CFD model to represent the surface roughness with different sizes and coverage. In the numerical calculations, both RANS and DES methods were used to solve the flow around the non-cavitating and cavitating propellers. For the URN predictions, permeable formulation of the FWH equation was used. The cavitation on and off the blades was modelled using the Schnerr-Sauer cavitation model together with the developed CFD-based TVC modelling technique, as given in Chapter 5. In Chapter 9.1., the homogenous roughness was applied to the blades using the RANS method, and its influence on propeller hydrodynamic performance characteristics, cavitation extensions, and propeller URN for the model scale INSEAN E779A propeller was examined. In Chapter 9.2, the investigations were further extended to determine the most effective roughness application area on the blades for

the model and full-scale The Princess Royal propeller using the DES method. Finally, in Chapter 9.3, the same roughness model was applied to the propeller hub for the INSEAN E779A model scale propeller to explore its impact on the hub vortex cavitation using the RANS method. The numerical results were validated with the experimental data in a wide range of operating conditions.

3.3 Chapter summary

In order to ease the reader to follow the methodology used in the thesis, this chapter presented a general outline and associated insight into the computational, experimental and full-scale approaches used in this research study.

4 Hydrodynamic and hydroacoustic performance prediction of a non-cavitating marine propeller

4.1 Introduction

This chapter aims to investigate the importance of the computational parameters, grid resolution, turbulence modelling and nonlinear noise sources (i.e., wake instability) on the overall propeller URN within the context of CFD modelling and acoustic analogy for the accurate prediction of the propeller URN.

The chapter, therefore, investigates the effects of grid resolution and the contribution of nonlinear noise sources on propeller URN predictions in Section 4.2 and Section 4.3, respectively. For this purpose, the theoretical background, including hydrodynamic and hydroacoustic models, is explained in Sections 4.2.1 and 4.3.1. In Sections 4.2.2 and 4.3.2, the propeller geometry, test matrix and numerical modelling regarding the computational domain, boundary conditions, grid resolution, and solution strategy are described. The detailed hydrodynamic and hydroacoustic results are presented in Sections 4.2.3 and 4.3.3. Finally, the summary and concluding remarks of the chapter are given in Section 4.4.

4.2 Investigation of grid resolution on propeller hydrodynamic and hydroacoustic performance

4.2.1 Theoretical background

The numerical background of this study is based on the Navier-Stokes equations. Here, hydrodynamic and hydroacoustic acoustic models are presented separately.

4.2.1.1 Hydrodynamic model

The hydrodynamic model uses the continuity and momentum equations in an incompressible form. The incompressible form of the continuity equation is given as:

$$\nabla . \mathrm{V} = 0 \tag{4.1}$$

The incompressible form of the momentum equation is also given as:

$$\rho \frac{DV}{Dt} = -\nabla \mathrm{P} + \vartheta \nabla^2 \mathrm{V} + F \tag{4.2}$$

Here, V is the velocity (m/s), $\nabla^2 V$ is the Reynolds stress tensor (N), P is the pressure (Pa), and F is the body forces (N).

4.2.1.2 Hydroacoustic model (FWH equation)

Numerical CFD methods (i.e., potential or viscous) are used to assess the flow field. Once the sound source is identified in the fluid domain, several acoustic analogies can be used for sound propagation from the near to far-field. Lighthill (1952) pioneered the development of acoustic analogy by ignoring the presence of a solid surface in the flow field. Following this, a more general formulation was developed by Curle (1955) for the cases where a stationary solid surface is available in the flow field. Later on, the formulation was generalised by Ffowcs Williams Hawkings (FWH) (Ffowcs Williams and Hawkings, 1969) for moving and permeable/porous surfaces. In numerical calculations, FWH formulation has been generally applied as an integral method for predicting the noise in the near and far-field both in aeroacoustics and hydroacoustic fields (Lyrintzis, 2003; Najafi-Yazdi et al., 2011; Nitzkorski, 2015).

The FWH equation rearranges the continuity and momentum equations into wave equations (Ffowcs Williams and Hawkings, 1969). The integral solution of the FWH equation is based on the use of Green's functions. In this equation, three different noise generation mechanisms are present. The generalised formulation of the FWH equation is given as follows.

$$\begin{aligned}\left(\frac{1}{{c_0}^2}\frac{\partial^2}{\partial t^2} - \nabla^2\right) p(x,t) = \frac{\partial}{\partial t}\{[\rho_0 v_n + \rho(u_n - v_n)]\delta(f)\} - \\ \frac{\partial}{\partial x_i}\{[\Delta P_{ij} n_j + \rho u_i (u_n - v_n)]\delta(f)\} + \frac{\partial}{\partial x_i \partial x_j}\{T_{ij} H(f)\}\end{aligned} \tag{4.3}$$

Here, the first term indicates the thickness term (i.e., monopole); the second one is the loading (i.e., dipole) term, and the latter one is the nonlinear (i.e., quadrupole) term at the right-hand side of Equation 4.3. Additionally, in Equation 4.3, p identifies the acoustic pressure disturbance, ∇^2 is Laplace operator, ρ is density, t is observer time, x is location, T_{ij} ($T_{ij} = \rho u_i u_j + P_{ij} - {c_0}^2 \tilde{\rho} \delta_{ij}$) is Lighthill stress tensor, u_i and v_i are the fluid and surface velocity components, respectively. $\tilde{\rho} = \rho - \rho_0$ is the density perturbation for the undisturbed medium, n indicates the projection along the outward normal to the surface, c_0 is the sound speed, P_{ij} represents the compressive stress tensor ($\Delta P_{ij} = P_{ij} - p_0 \delta_{ij}$). δ is the Kronecker operator, H is a Heaviside function. The derivation of the FWH equations and comprehensive mathematical formulations can be found in the studies of Farassat, 2007 and Brentner and Farassat, 2003.

If the impermeable condition is imposed on the calculations ($i.e. u_n = v_n$), a generalised formulation of the FWH equation (i.e., Equation 4.3) simplifies, and two linear terms can be written in the integral form. This form of the FWH equation is known as Farassat 1A (Farassat, 2007) solution. The impermeable form of the FWH equation is commonly used in the aeroacoustics field. In contrast, as stated in the study by Ianniello et al. (2013), the underwater field is considerably affected by the contribution of quadrupole (nonlinear) noise sources for hydroacoustic applications; thus, the porous or permeable type of the FWH equation can be used effectively to include the nonlinear contributions, including TVC. The porous formulation, which was applied by Ffowcs Williams and Hawkings (1969) in their original study and also proposed as a possible numerical solution of the FWH equation by Di Francescantonio (1997), was used in this study. The main advantage of using porous FWH is that the direct solution of the volume integrals is more computationally expensive. Thus, porous FWH reduces the cost of the numerical solution. Also, the solution of the volume integrals in the generalised FWH equation is more sensitive to the numerical errors and accuracy of the hydrodynamic data than the solution of surface integrals in the permeable formulation.

In the porous formulation of the FWH equation, an integral domain (i.e., porous or permeable surface) is defined around the body (i.e., around the propeller blades) to include all relevant nonlinear contributions as much as possible for the numerical calculations. When the porous formulation of FWH is used, the nonlinear terms inside the integral domain are evaluated by solving the surface integrals instead of the volume integral. In this way, the thickness and loading terms lose their physical meanings in the impermeable approach, and they become

pseudo thickness and pseudo loading noise terms. In this formulation, two new variables (U_i and L_i) as modified velocity and modified stress tensor are defined as follows.

$$U_i = u_i + (\frac{\rho}{\rho_0} - 1)(u_i - v_i) \tag{4.4}$$

$$L_i = P_{ij}\hat{n}_j + \rho u_i\,(u_n - v_n) \tag{4.5}$$

The generalised FWH equation can be rearranged by changing u_n and P_{ij} with U_i and L_i, respectively. The porous formulation of the FWH equation can be written in Equation 4.6 for the stationary integral domain under incompressibility and $M = |v|/|c_0| \ll 1\ (i.e. Mach\ Number)$ assumptions (Di Francescantonio 1997).

$$4\pi p(x,t) = \int_S \frac{\rho_0 \dot{U}_n}{r}\,dS + \int_S \frac{\dot{L}_r}{c_0 r}\,dS + \int_S \frac{L_r}{r^2}\,dS + p_Q(x,t) \tag{4.6}$$

Here, in Equation 4.6, r (m) is the distance between the noise source and the receiver; subscripts r and n define the dot product of a quantity with a unit vector in either radiation or normal directions, respectively.

In this equation, the first term is pseudo-thickness, whereas the second and third terms are the pseudo-loading noise terms. The last term represents the quadrupole noise sources outside of the integral surface. The undamped fluctuating pressure and momentum as nonlinear noise sources pass through the boundaries of permeable surfaces can produce spurious noise that can contaminate the overall acoustic pressures. This spurious noise occurs because of the truncation errors of the source terms at the permeable surface boundary. This problem is also known as the "end cap" or closure problem (Nitzkorski, 2015). The receivers located upstream are less sensitive to spurious noise as the linear thickness, and loading terms are dominant. However, the receivers located downstream of the propeller can be affected by spurious noise. The end-cap problem is associated with the differences between acoustic and hydrodynamic pressure distributions described in Ffowcs Williams, 1992 (Testa et al., 2021). Several approaches are used to correct the end cap problem in the near field using the corrected volume terms (e.g., Wang et al., 1996 and Ikeda et al., 2017).

Nevertheless, the applications of these alternative approaches may not be practical for different problems (Lidtke et al., 2019). In order to reduce the spurious noise, the permeable surface can be placed far from the flow region where the vorticity is still present. However, this leads to the risk of information loss because of the numerical dissipation and discretisation errors. Even if one attempts to adopt fine grid resolution for the entire large permeable surface to minimise the numerical dissipation, this will inevitably increase the computational cost of the solution, and it is not practical. Alternatively, this issue can be completely eliminated by solving the full FWH equation, including the nonlinear noise sources outside the permeable surface. However, calculating volume terms to account for the contribution of nonlinear noise sources outside of the permeable surface is computationally expensive and difficult to compute and retain data. Thus, similar to other studies in the literature (e.g., Ianniello et al., 2013; Lloyd et al., 2015b; Lidtke, 2017), to reduce the computational cost of the solution, the contribution of possible nonlinear noise sources outside of the permeable surface was neglected. Also, the end-cap problem was left out of the scope of this PhD thesis.

4.2.2 Numerical modelling

4.2.2.1 Propeller geometry and test case

The numerical calculations were conducted using a well-known model scale INSEAN E779A propeller, which is widely used in hydrodynamic and hydroacoustic fields. The experimental hydrodynamic data is also available for the selected propeller (Salvatore et al., 2006). 3D view of the propeller and its main parameters are indicated in Figure 4.1 and Table 4.1, respectively.

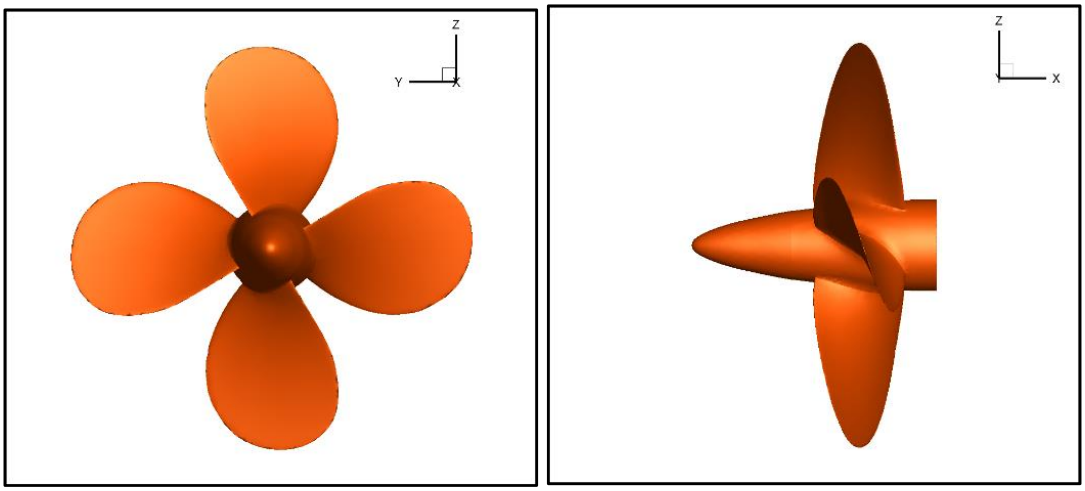

Figure 4.1. Back and side views of the INSEAN E779A model propeller.

Table 4.1. Main particulars of INSEAN E779A model propeller.

Number of Blades	Z	4
Diameter (m)	D	0.227
Pitch Ratio	P/D	1.1
Expanded Area Ratio	A_E/A_0	0.69

In the numerical calculations, the same operational condition (i.e. J=0.88 and n=25rps) was selected with those of other studies in the literature to compare the numerical results (e.g., Ianniello et al., 2013; Lidtke, 2017; Testa et al., 2018). It should be noted that experimental URN data is not available for the selected propeller in the current literature.

4.2.2.2 Computational domain and boundary conditions

The computational domain and boundary conditions are given in Figure 4.2. The computational domain was extended by 7D downstream of the propeller from the propeller blades centre, enabling wake evolution before reaching the outlet. Additionally, the computational domain was extended by 4D both in the upstream and radial directions from the propeller centre. The transition between the rotating and static regions was provided by a rotating interface (i.e., a sliding interface).

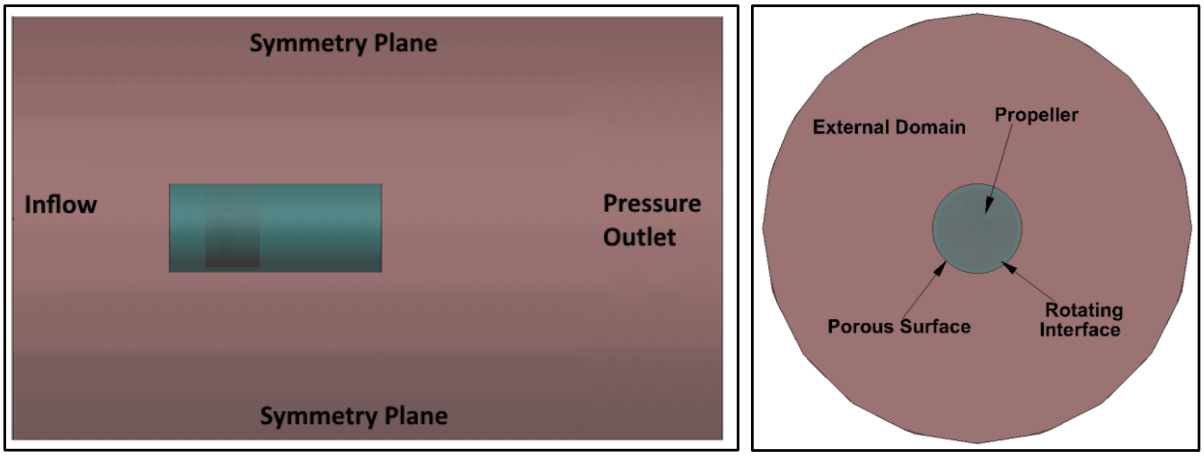

Figure 4.2. The computational domain used in the numerical calculations (Figure is not scaled).

An integral surface (i.e., porous or permeable surface) was used in the numerical calculations to compute the hydroacoustic pressures at different receiver locations. As seen in Figure 4.3, the integral surface consists of the main cylinder and two end-caps (i.e., upstream and downstream end-caps). As expected, the downstream end-cap of the integral surface cuts the tip vortex and changes the overall acoustic pressure behaviour. Therefore, an open-ended integral surface, which was proposed in the study by Ianniello and De Bernardis, (2015), was used to minimise the possible spurious noise sources outside of the permeable surface.

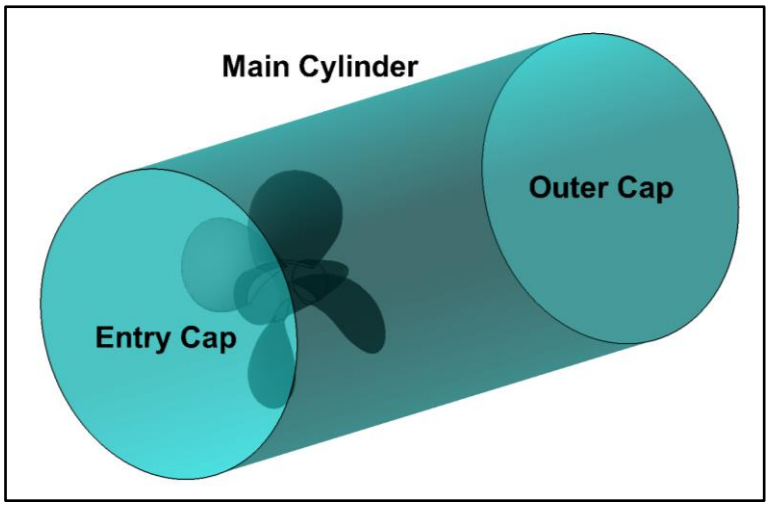

Figure 4.3. Representation of integral (i.e., porous) FWH surface.

The exact dimension and location of the permeable surface have not been defined clearly in the present literature, and it is still being investigated (Bensow and Liefvendahl, 2016; Li et al., 2018; Lidtke et al., 2019). Nevertheless, the convergence study was conducted by varying the length and dimensions of the permeable surfaces in this study. Table 4.2 summarises the geometrical properties of the integral surfaces. It should be noted that the dimensions of the base integral surface, which was used in this study, were set according to similar studies in the literature to compare the present numerical results with other numerical results in the literature (e.g., Ianniello et al., 2013; Lloyd et al., 2015b; Lidtke, 2017).

Table 4.2. Geometrical features of the integral surfaces.

ID	L/D	$D_{integral}$
1	2.5	1.23D
Base (2)	3.0	1.25D
3	3.5	1.28D
4	4.0	1.32D

4.2.2.3 Grid resolution

Hydroacoustic simulations are deemed to be more sensitive to mesh quality and density than traditional hydrodynamic simulations. Hence, a suitable grid structure should be adopted to increase the accuracy of the URN predictions. The applied grid structure should meet two main principles (Star CCM+ 14.06, 2019);

- The grid should be adequate to resolve/model the sound generating turbulence scales, particularly in the propeller's slipstream, where the contributions of nonlinear noise sources are dominant over blade dynamics.

- The grid should be able to resolve the propagation of the acoustic waves towards the locations of the receivers.

In this study, the unstructured grid was used to discretise the computational domain within the facilities of Star CCM+ 14.06, 2019. The region-based mesh technique was implemented with the cells, which have minimal skewness, by using the trimmer mesh algorithm. In this way, the numerical dissipation was prevented, and the accuracy of the solution was increased with a reasonable computational cost. The hexahedral elements were used to discretise the computational domain as the application of the tetrahedral cells can deteriorate the accuracy of the solution (Jonas and Clarke, 2010). Besides, during the mesh adaptation process, the cell sizes inside the integral surfaces were kept constant to prevent the additional non-physical noise, contaminating the overall acoustic pressures (Star CCM+ 14.06, 2019). Cells inside the noise source region were aligned at the interfaces to facilitate the smooth transition between the two regions. Besides, the grid quality at the interfaces was increased by identifying a layer of prismatic cells to reduce the numerical noise as much as possible. Moreover, almost uniform cell size, particularly in the X direction, was used to reduce the numerical diffusion. Different integral surfaces were placed inside the finer grid resolution to minimise information loss.

Table 4.3 presents the different grid resolutions generated to investigate the numerical noise and contribution of tip vortex on overall acoustic pressure. The general view of the finest grid resolution is given in Figure 4.4

Table 4.3. Total element counts of different grid resolutions (N; millions of cells).

Grid	N
Coarse	2.8
Medium	4.9
Fine	10.3
Finer	17
Finest	31.6

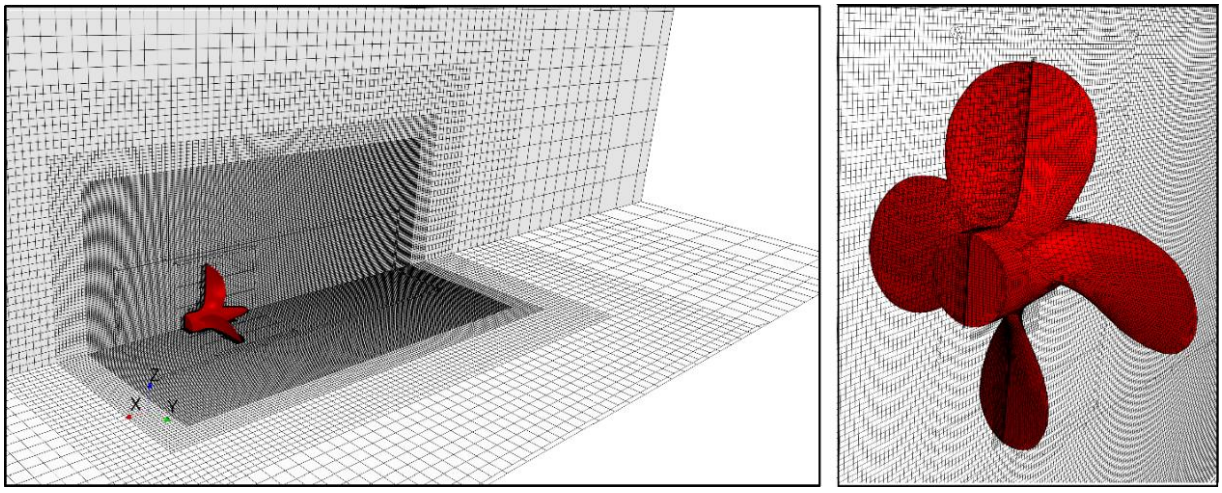

Figure 4.4. General view of the grid structure around the propeller blades (Finest Grid).

4.2.2.4 Solution strategy

The commercial CFD solver Star CCM+ was utilised (Star CCM+ 14.06, 2019). RANS equations were discretised using the finite volume method in the numerical calculations. The near wall-boundary layer was solved using the wall function. The convective and temporal terms in the momentum equations were discretised with 2nd order scheme. The equations were coupled using a segregated SIMPLE type of solution algorithm. The k-ω SST (Shear Stress Transport) turbulence model, commonly used for propeller hydrodynamic and hydroacoustic simulations, was used for turbulence modelling. During the simulations, the inner iteration was set to 8. The simulations were first initiated in a steady manner to accelerate the convergence. After that, the unsteady simulations were conducted with 1^{o} of propeller rotational rate. After 20 propeller revolutions, it increased gradually to 5^{o} of propeller rotational rate to eliminate the high-frequency noise. Consequently, the acoustic pressures were collected at 15 propeller revolutions.

In this study, steady initialisation was conducted by MRF (Moving Reference Frame), whereas RBM (Rigid Body Motion, also known as Sliding Mesh) was used in unsteady simulations. In the RBM technique, unsteady governing equations are solved at every timestep. In contrast, unsteady components of the flow field are not considered in the MRF technique. Therefore, the RBM technique produces more accurate results. In addition to this, it has been widely used for hydrodynamic simulations when the unsteady flow features in the flow region are of great interest (Moussa, 2014).

4.2.3 Numerical results

4.2.3.1 Hydrodynamic results

As a first validation of the numerical results with different grid resolutions, the propeller's open water characteristics (i.e., thrust, torque and efficiency values) were compared with the experimental data at J=0.88. The non-dimensional thrust (K_T), torque (K_Q) and efficiency (η_0) values are calculated as follows.

$$K_T = \frac{T}{\rho n^2 D^4} \tag{4.7}$$

$$K_Q = \frac{Q}{\rho n^2 D^5} \tag{4.8}$$

Here; ρ is the water density (kg/m^3), n is the propeller rotational speed (rps), D is the diameter of the propeller (m), T is thrust (N), and Q is the torque (Nm).

$$\eta_0 = \frac{J}{2\pi}\frac{K_T}{K_Q} \tag{4.9}$$

Advance ratio (J) is defined by:

$$J = \frac{V_A}{nD} \tag{4.10}$$

where V_A (m/s) is the average flow velocity at the propeller plane. The hydrodynamic results are given together with the experimental data at J=0.88 for different grid resolutions in Table 4.4. The uncertainty study was conducted via the GCI (Grid Convergence Index) method based on the Richardson extrapolation technique (Richardson, 1911) for thrust and torque values in Table 4.5. GCI method, which is recommended for CFD verification studies in the ITTC procedure (ITTC, 2008; ITTC, 1999), was first proposed by Roache (1998) and applied in several studies in the literature. The main procedure can be summarised as follows (Celik et al., 2008).

- Refinement factor (r) was selected for different solutions.
- The difference between results of solution scalars (ε) was calculated for thrust and torque.
- Solution type was determined with the convergence condition (R), which is calculated as the ratio of solution scalars in the GCI method.

- Convergence condition (R) indicates the solution criteria, which can be classified into oscillatory, monotonic convergence or oscillatory and monotonic divergence. In our case, R was calculated in the range of monotonic convergence (0<R<1).
- As the last step, the numerical uncertainty of the solution was calculated.

Table 4.4. Computed performance coefficients for different grid resolutions.

	Numerical Results			**Difference (%, EFD-CFD)**	
Grid	K_T	$10K_Q$	η_0	K_T	$10K_Q$
Coarse	0.1532	0.3103	0.6915	1.46	1.74
Medium	0.1531	0.3105	0.6906	1.39	1.80
Fine	0.1527	0.3108	0.6881	1.12	1.90
Finer	0.1525	0.3112	0.6863	0.99	2.03
Finest	0.1524	0.3115	0.6852	0.93	2.13
Experiment	0.151	0.305	0.718		

Table 4.5. Uncertainty values of the numerical solution.

Results	**(Finest-Finer-Fine)**	**(Finer-Fine-Medium)**	**(Fine-Medium-Coarse)**
% GCI (K_T)	0.07	0.25	0.37
% GCI ($10K_Q$)	0.12	5.20	5.52

As given in Table 4.4, from the global hydrodynamic performance point of view (i.e., thrust and torque values), the difference between the numerical and experimental results is found to be quite good, even if the coarse grid resolution is adopted in the numerical solvers. However, the prediction of vortex structures in the propeller's slipstream with different grid resolutions is entirely different if one looks at further details of the performance. In this respect, Figure 4.5 shows the vorticity distributions (i.e., ω_Y) in the propeller's slipstream, obtained by experiment and numerical calculations with different grid resolutions. As seen in Figure 4.5, the tip vortex can be extended downstream of the propeller with an increase in grid resolution. In contrast, the tip vortex disappears rapidly with the relatively coarse grid resolutions due to the numerical diffusion. Although the tip vortex can be extended with the grid resolution, the accuracy of the flow details inside the vortex core might be still questionable for the standard RANS methods.

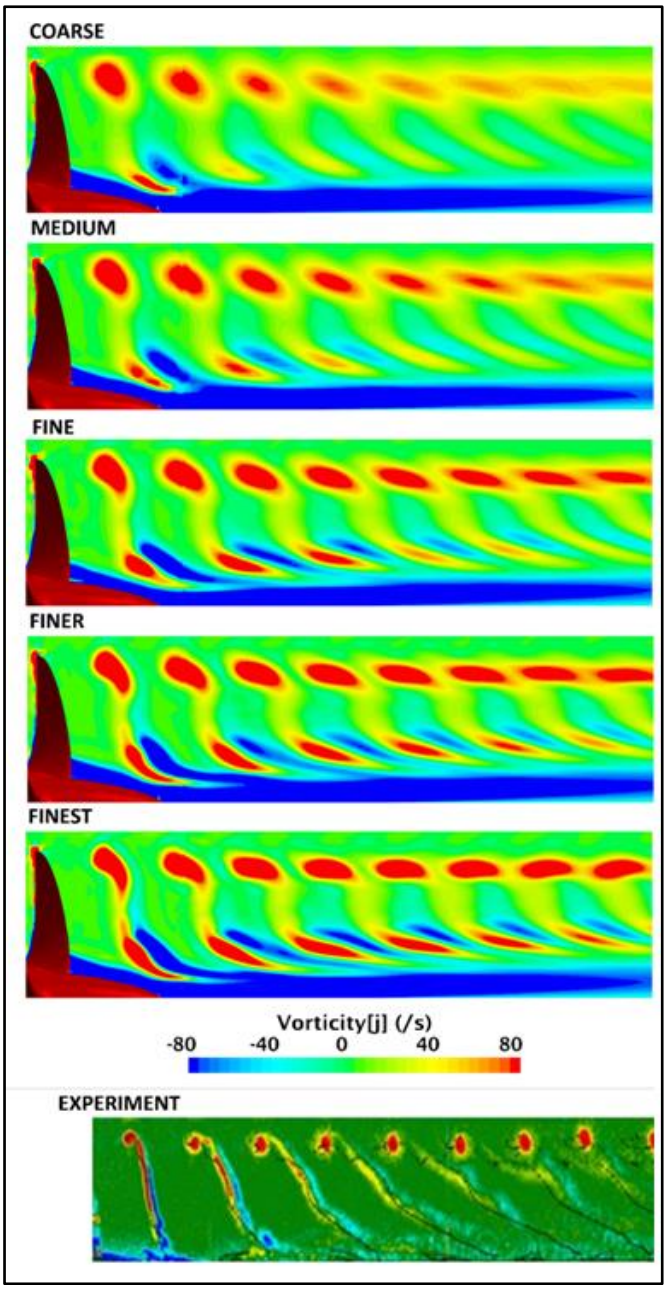

Figure 4.5. Comparison of the vorticity Y component $\boldsymbol{\omega_Y}$ with the experiment (Salvatore et al., 2006) on the plane (y=0) for different grid resolutions.

4.2.3.2 Hydroacoustic results

In this section, hydroacoustic results are presented to investigate the effects of grid resolution on propeller URN. The following subsections are devoted to showing the numerical noise associated with the sliding interfaces and visualisation of the tip vortex in the propeller's slipstream. Furthermore, hydrodynamic and hydroacoustic pressures are compared at different receiver locations.

- **Visualisation of numerical noise in hydroacoustic simulations**

The grid structure should be well designed in the numerical solver to calculate hydrodynamic inputs accurately; hence, propeller URN. Additionally, numerical disturbances such as reflections from the domain boundaries, non-physical numerical noise generated by sliding (or rotating) interfaces, and inappropriate pressure correction methods can be considered as the key issues that require in-depth investigation. The artificial reflections created by the boundaries of the computational domain can be considerably reduced by selecting suitable domain dimensions. It is to be noted that this thesis only focuses on the investigation of the non-physical numerical noise created by the grid resolution.

In the propeller hydrodynamic and hydroacoustic simulations, the sliding interface mesh technique (i.e., RBM) is widely used to model the propeller's rotational motion. From the hydroacoustic point of view, one of the main disadvantages of this technique can be considered to cause additional numerical noise. The interface is mainly used to transfer the data and solution quantities, such as pressure, velocity, temperature, etc., between the neighbouring regions. Thus, the suitable grid resolution is more important to increase the accuracy of the input data for hydroacoustic predictions. In particular, this issue might be more critical in the far-field where pressure fluctuations are smaller; hence, it may lead to pollution of the overall acoustic pressures. It should be pointed out that the numerical noise issue can also be faced at the interface of the integral (or porous) surface. However, as the static (i.e., non-rotating) porous surface was used in this study, any additional numerical noise was not observed from the interface of the integral surface (see Figure 4.8). Additionally, as stated in Section 4.2.2, smooth mesh transitions were provided between the inside and outside of the integral surface to minimise the numerical noise.

In this study, the numerical noise associated with the sliding interfaces is observed using the time derivative of the pressure. For this purpose, a user-based field function and additional pressure monitor are introduced to the solver using the following formulation.

$$\frac{dP}{dt} = \frac{P^n - P^{n-1}}{\Delta t} \tag{4.11}$$

Here, P is acoustic or hydrodynamic pressures, and Δt is timestep. The pressure difference between consecutive time steps is computed using the stored pressure value of every node point at the previous time step. Once the flow field converges, this function is activated to visualise the pressure variation with time in the flow field.

Coloured rectangles (i.e., blue and red regions) show the additional sound sources induced by the rotating interfaces for different grid resolutions in Figure 4.6. There is no noise source within the computational domain that would cause rapid pressure variations on either side of the interface boundaries. Thus, acoustic pressure is expected to propagate downstream of the propeller without deterioration. However, the strong pressure fluctuations occurring at the interfaces can be proof of the non-physical numerical noise. As shown in Figure 4.6, even though an increase in grid resolution enables a reduction in numerical noise at the sliding interfaces, it does not disappear entirely using the sliding mesh approach. Hence, it consequently might lead to a change in either amplitude or overall shape of the pressure signal.

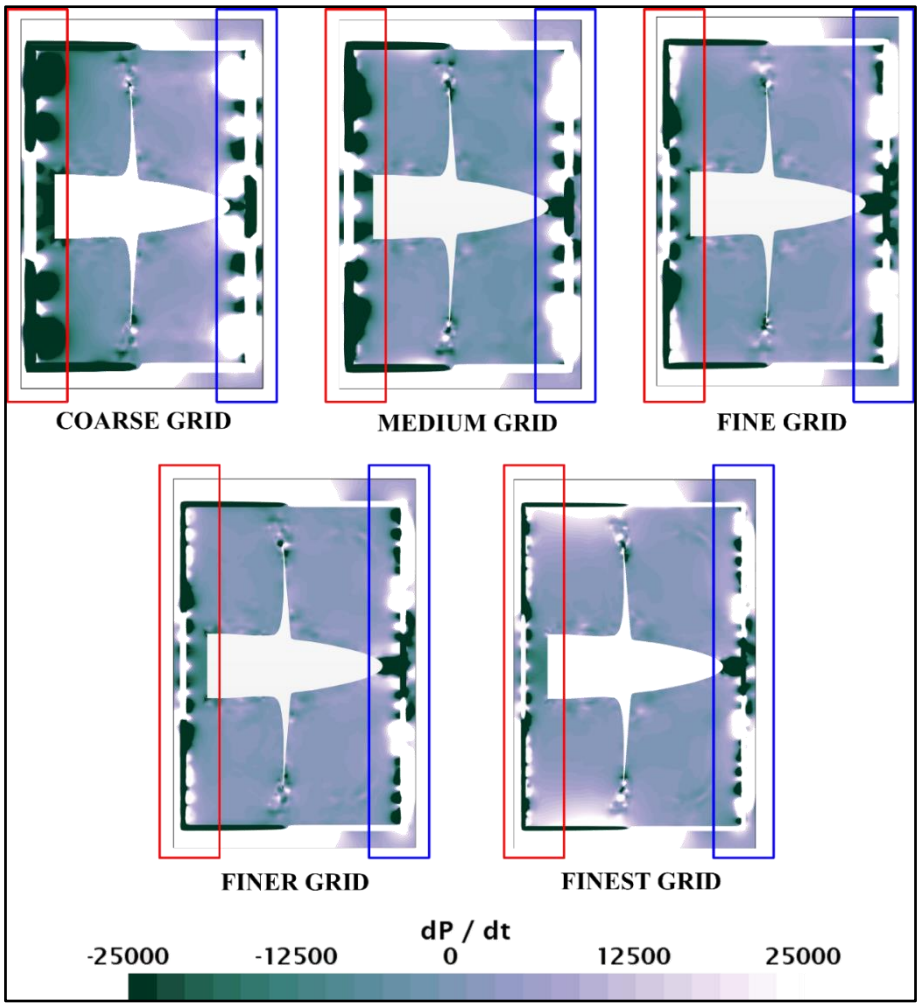

Figure 4.6. Numerical noise induced by rotating interfaces for different grid resolutions.

- **Visualisation of tip vortex extension**

The coherent vortical structures in the propeller's slipstream are generally visualised in different numerical methods (e.g., RANS, DES, and LES) using either Q or λ_2 criteria, which are based on the velocity gradient tensor. In this way, the comparison of the hub and tip vortices with the experiment can be performed to show the capabilities of the numerical solution and a detailed investigation of the vortical structures in the wake of the propeller. In the numerical solver, Q criterion is defined by the following formulation;

$$Q = 1/2[(|\Omega|^2 - |S|^2)] \tag{4.12}$$

Where S denotes the strain rate tensor, and Ω is the angular rotation rate tensor (or vorticity tensor). According to Q criterion magnitude, the dominant parameter in the flow field can be determined. When its value is positive, the vorticity dominates the flow field, whereas strain rate dominates when its value is negative (Star CCM+ 14.06, 2019). Similar to Q-criterion, λ_2

criterion, which is based on the mathematical formulation proposed in Jeong and Hussain (1995), is another technique for detection of the vortex structures in the flow field. In this technique, the velocity gradient (J) is first calculated, and then it is assessed for each point in the domain. It is decomposed as symmetric (S) and anti-symmetric part (O) and defined as;

$$S = \frac{J + J^T}{2} \tag{4.13}$$

$$O = \frac{J - J^T}{2} \tag{4.14}$$

Following the symmetric and anti-symmetric calculation, a matrix is obtained with three eigenvalues. The value of the second eigenvalue shows the scalar quantity of λ_2. When the value of λ_2 is negative, the vortex structures can be detected in the flow region. Detailed information about the vortex identification methods can be found in the studies of Kolář (2007), Epps (2017) and Jeong and Hussain (1995).

In the numerical solvers, the visualisation of the vortex distribution in the propeller's slipstream strongly depends on the threshold value of the criteria $(i.e. Q$ and $\lambda_2)$, which results in a different prediction of tip and hub vortices extensions downstream of the propeller. However, an accurate prediction of the extension of the vortical structure in the propeller's wake can be important for a detailed flow field investigation. For this reason, the time derivative of the pressure technique, which was explained in the previous section, can also be used to determine the more realistic extension of the vortex distributions. As a spatial and temporal derivative of the pressure shows the change in pressure with time and position in the flow field, different pressure fields are created around the vortex because of its physical dynamics (Hunt et al., 1988). Therefore, the tip and hub vortex regions can be first detected with the time derivative of the pressure technique on the longitudinal plane since the contribution of the tip vortex is dominant in the propeller's slipstream (Jang et al., 2001; Felli et al., 2006).

Figure 4.7 shows the change in extension of tip vortex distributions in the propeller's slipstream through the different threshold values of the Q criteria and time derivative of the pressure technique. As can be seen in Figure 4.7, the location and extension of the pressure fluctuations do not change with the selection of different threshold values (e.g., 10000, 25000 and 50000 $1/s^2$) in the time derivative of the pressure technique, while the pressures intensities in the vortex regions show a small variation. However, the extension of the tip vortex changes

significantly with the selection of various threshold values (e.g., 500, 1500, 3000 $1/s^2$) in Q criterion. It consequently leads to a misprediction of tip vortex extension in the numerical calculations. Therefore, the time-derivative of the pressure technique can be reliably used to determine the exact location and extension of the tip vortex. This approach can also be used together with the Q criterion to determine the threshold value in the Q criterion. In this way, the spiral tip vortex can be observed.

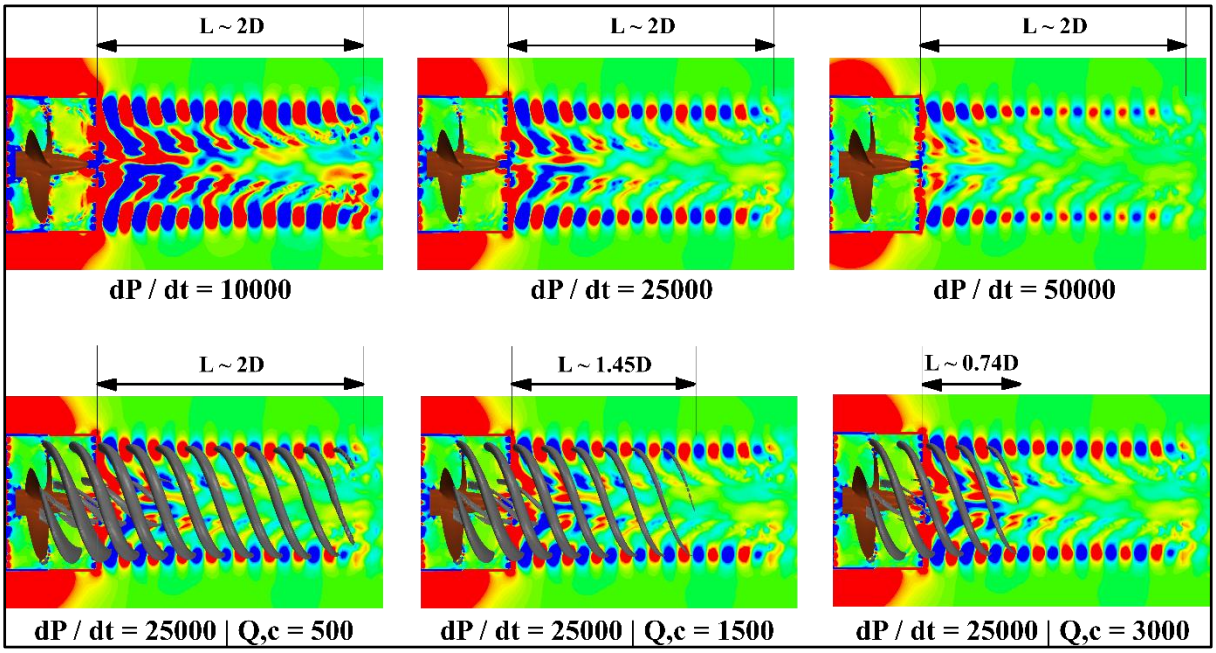

Figure 4.7. Change in tip vortex extension with the time derivative of the pressure technique and $\boldsymbol{Q}$ criterion (finer grid resolution).

In this study, the proposed technique is used to visualise the tip vortex in the propeller's slipstream for several grid resolutions, as shown in Figure 4.8. It is a known fact that the RANS method suffers from both turbulence modelling and discretisation errors; thus, it produces a higher amount of numerical diffusion. Due to this fact, the vortical structures in the propeller's slipstream disappear rapidly (Feder and Abdel-Maksoud, 2016; Duraisamy and Baeder, 2006). The numerical dissipation of the vortices can be deemed to be directly related to grid resolution and mainly occurs due to the insufficient discretisation of the nonlinear convective term (Ramponi and Blocken, 2012). However, this can be reduced by increasing grid resolution in the numerical solvers, and the tip vortex can be further extended downstream of the propeller (Duraisamy and Baeder, 2006).

Figure 4.8 indicates the tip vortex extension with different grid resolutions. As shown here, a finer grid resolution results in a greater tip vortex extension in the propeller's slipstream. Furthermore, grid resolution changes the pressure field inside the tip vortex. The magnitude of the pressure is high in the vicinity of the propeller blade, whereas it reduces gradually as far away from the downstream, especially for coarse, medium, and fine grid resolutions. In contrast, the pressure inside the tip vortex reduces considerably for the finest grid resolution. Hence, an increase in grid resolution would also facilitate the observation of tip vortex cavitation in the propeller's slipstream since the aim is to decrease the pressure below the saturation pressure inside vortex cores.

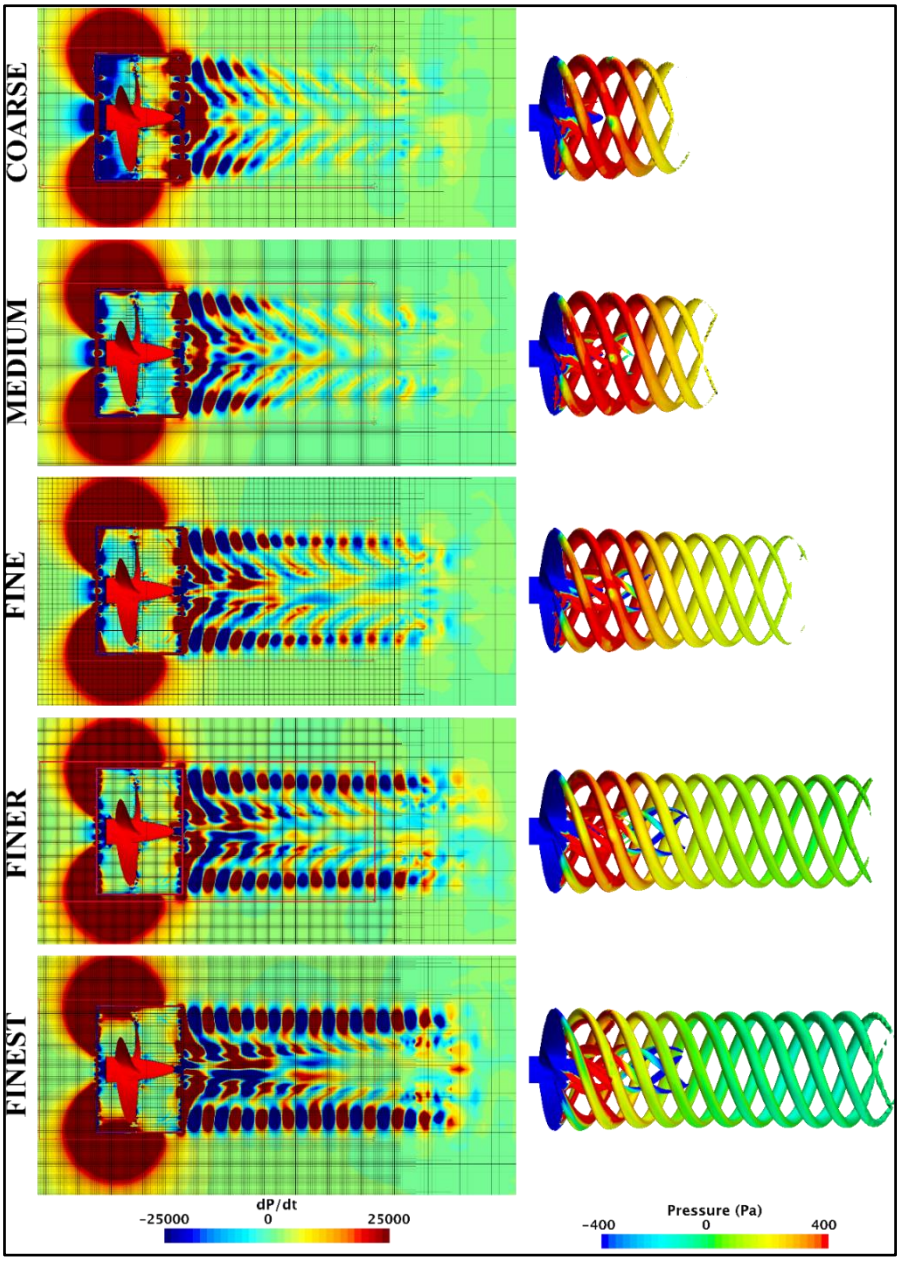

Figure 4.8. Change in vortex distributions with different grid resolutions (Right figure is coloured by pressure, $\boldsymbol{Q_c}$=500 1/s^2).

- **Hydrodynamic and hydroacoustic pressures**

Figure 4.9 and Table 4.6 show the receiver locations and coordinates in the near field, respectively. The origin of the coordinate system was set to the centre of the propeller blades. Receiver 1 (R1) was located upstream, whereas R3, R4 and R5 were located downstream of the propeller. R2 and R6 were also located on the propeller plane. Since there is no experimental noise data for the selected propeller, the numerical results at R2, R4 and R6 were compared with other numerical studies in the literature conducted by Ianniello et al. (2013) and Testa et al., 2018. It should be mentioned that the numerical results in the reference studies were obtained using data digitiser software.

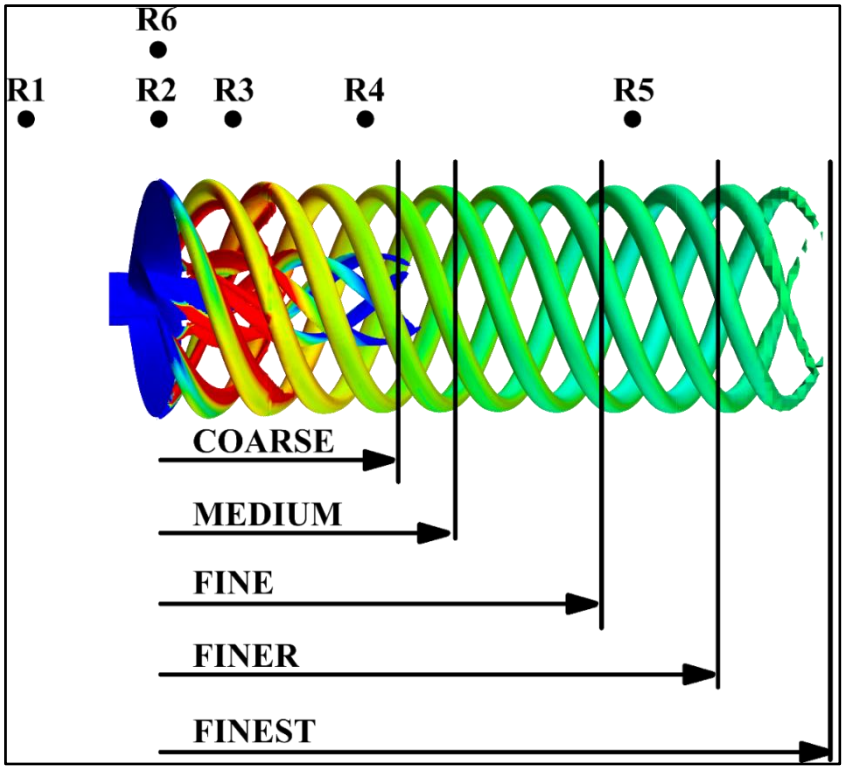

Figure 4.9. Receiver locations (Q_c=500 1/s^2, the figure is coloured by pressure and not scaled).

Table 4.6. Receiver coordinates.

Receiver	X (m)	Y (m)	Z (m)
1	0.1403		0.1703
2	0		0.1703
3	-0.0800	0	0.1703
4	-0.2270		0.1703
5	-0.4569		0.1703
6	0		0.2648

As the receivers were positioned in the vicinity of the propeller where the incompressibility assumption is still not visible, the hydrodynamic and hydroacoustic pressures can be compared to verify the numerical solution. However, with an increase in distance between the noise source and receiver, hydrodynamic pressures tend to deteriorate due to the numerical diffusion. For this reason, the acoustic analogy is required for the prediction of far-field noise since the linear terms of FWH is only dependent on blade shape and hydrodynamic load (Ianniello et al., 2013; Sezen and Kinaci, 2019)

Figure 4.10A-C compares hydrodynamic and hydroacoustic pressures at R1 with different grid resolutions. At this receiver location, the contribution of linear noise terms (i.e., thickness and loading) to the overall acoustic pressure is dominant, whereas the contribution of the nonlinear noise term is almost negligible. The hydrodynamic pressures obtained with different grid resolutions are compared with each other in Figure 4.10A. The results show that the hydrodynamic pressure amplitude changes slightly with the different grid resolutions in Figure 4.10A. The overall hydroacoustic pressure is purely characterised by BPF (Blade Passage Frequency) at R1 in Figure 4.10B due to the dominant contribution of linear noise terms. As seen in Figure 4.10B, the inadequate grid resolution triggers the numerical noise, which is probably induced by sliding interfaces (see Figure 4.6) and causes deterioration of the overall shape of the acoustic signal. Additionally, a good agreement is found between hydrodynamic and hydroacoustic pressures in Figure 4.10C. Therefore, the hydrodynamic pressure may be used instead of hydroacoustic pressure at this receiver location to evaluate the propeller URN.

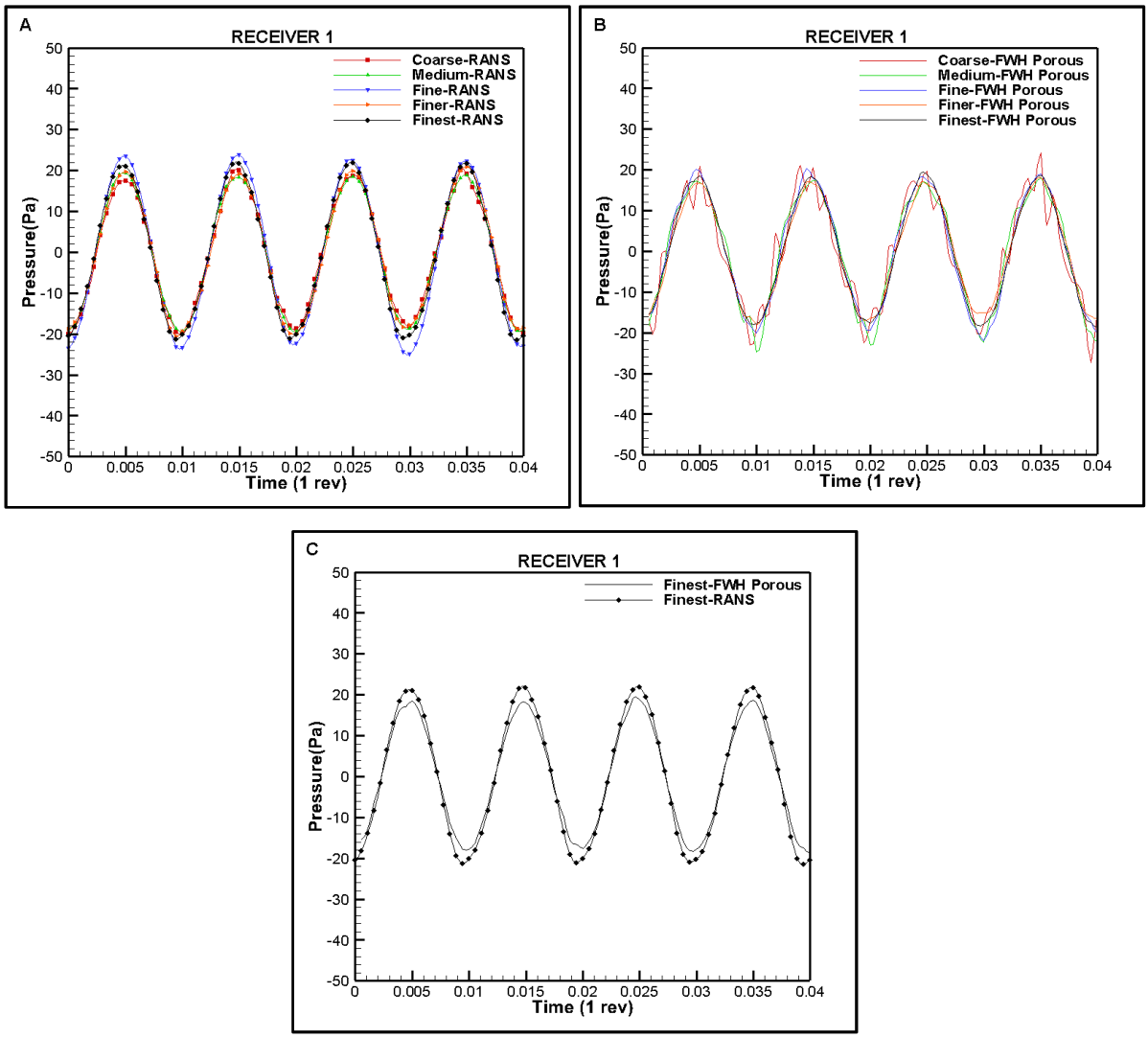

Figure 4.10. RANS pressures (A), FWH pressures (B) and RANS versus FWH pressures (C) at R1.

Figure 4.11 shows the comparison between hydrodynamic and hydroacoustic pressures at R2. Akin to the previous receiver location, the amplitude of the hydrodynamic pressure does not change considerably with the different grid resolutions in Figure 4.11A. Unlike the previous receiver location, the overall shape of the acoustic signal is not strongly affected by the numerical noise in Figure 4.11B. Potentially, the reason could be that R2 is closer to the propeller when compared to R1. Similar to R1, the overall shape of the signal is dominated by the blade harmonics. Furthermore, the amplitude of the acoustic pressure at R2 is higher than at R1 due to the decreased distance from the noise source. Figure 4.11C shows the comparison of hydrodynamic and hydroacoustic pressures, and the agreement is found to be quite good. Additionally, the numerical results are compared with another numerical study in the literature, performed by DES together with porous FWH equation, by Testa et al., 2018 in Figure 4.11D. As shown in Figure 4.11D, the present study (i.e. RANS) slightly overestimated the acoustic pressure compared to the DES method at the R2.

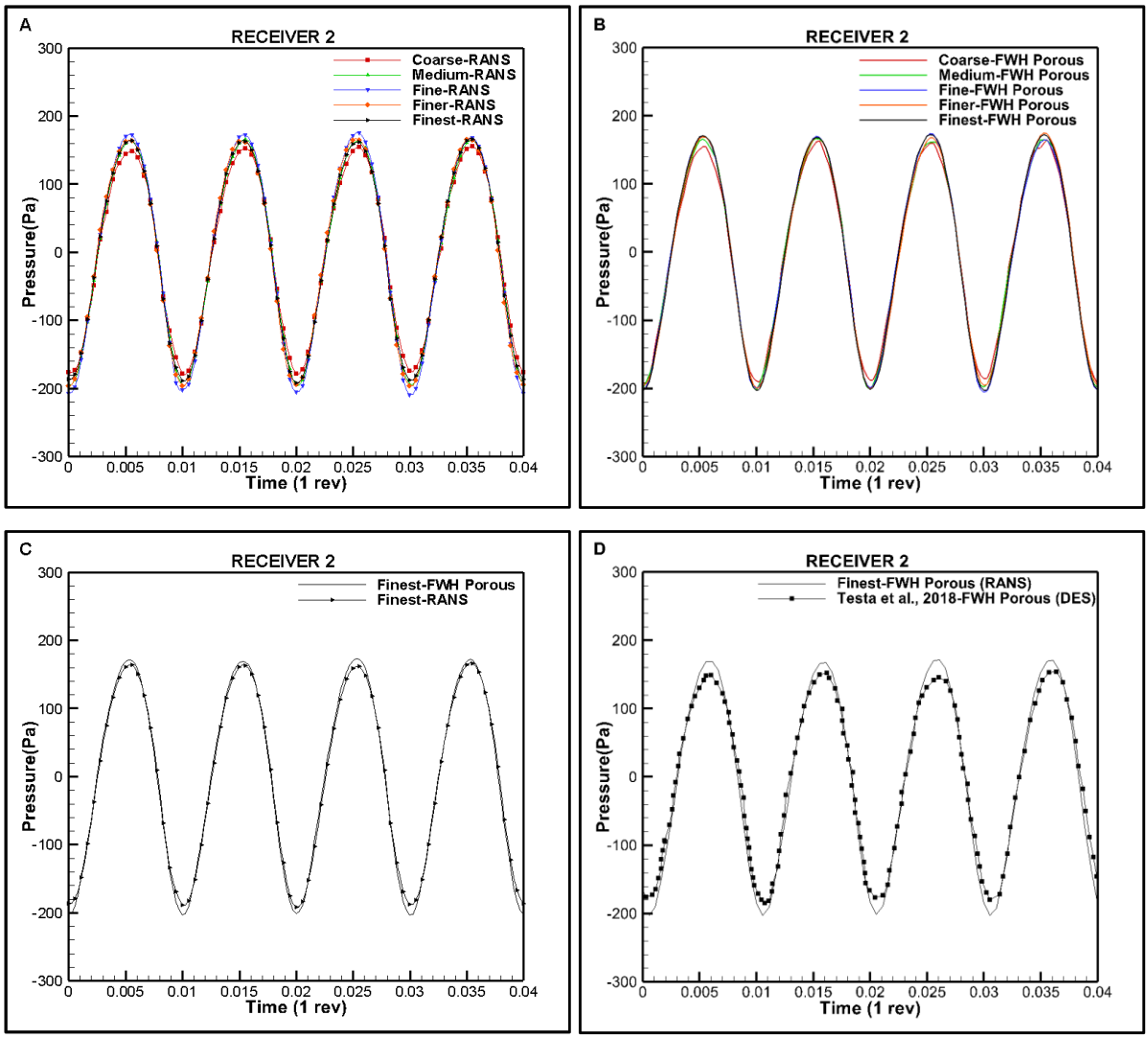

Figure 4.11. RANS pressures (A), FWH pressures (B) and RANS versus FWH pressures (C) and comparison of the numerical results (D) at Receiver 2.

The comparison of the pressures is presented in Figure 4.12 for the R3, located downstream of the propeller. Similar to R1 and R2, the effects of grid resolution on hydrodynamic pressure are found to be low at R3 (Figure 4.12A). However, the numerical noise, probably created by the sliding interfaces, starts to appear in the hydroacoustic pressures with a decrease in grid resolution in Figure 4.12B. Thus, with a decrease in grid resolution, the magnitude and shape of the overall acoustic pressure deteriorate, resulting in unreliable propeller URN prediction. As the R3 is still close to the propeller, hydrodynamic and hydroacoustic pressures can be directly compared. As shown in Figure 4.12C, a satisfactory agreement between the RANS and porous FWH pressures is found.

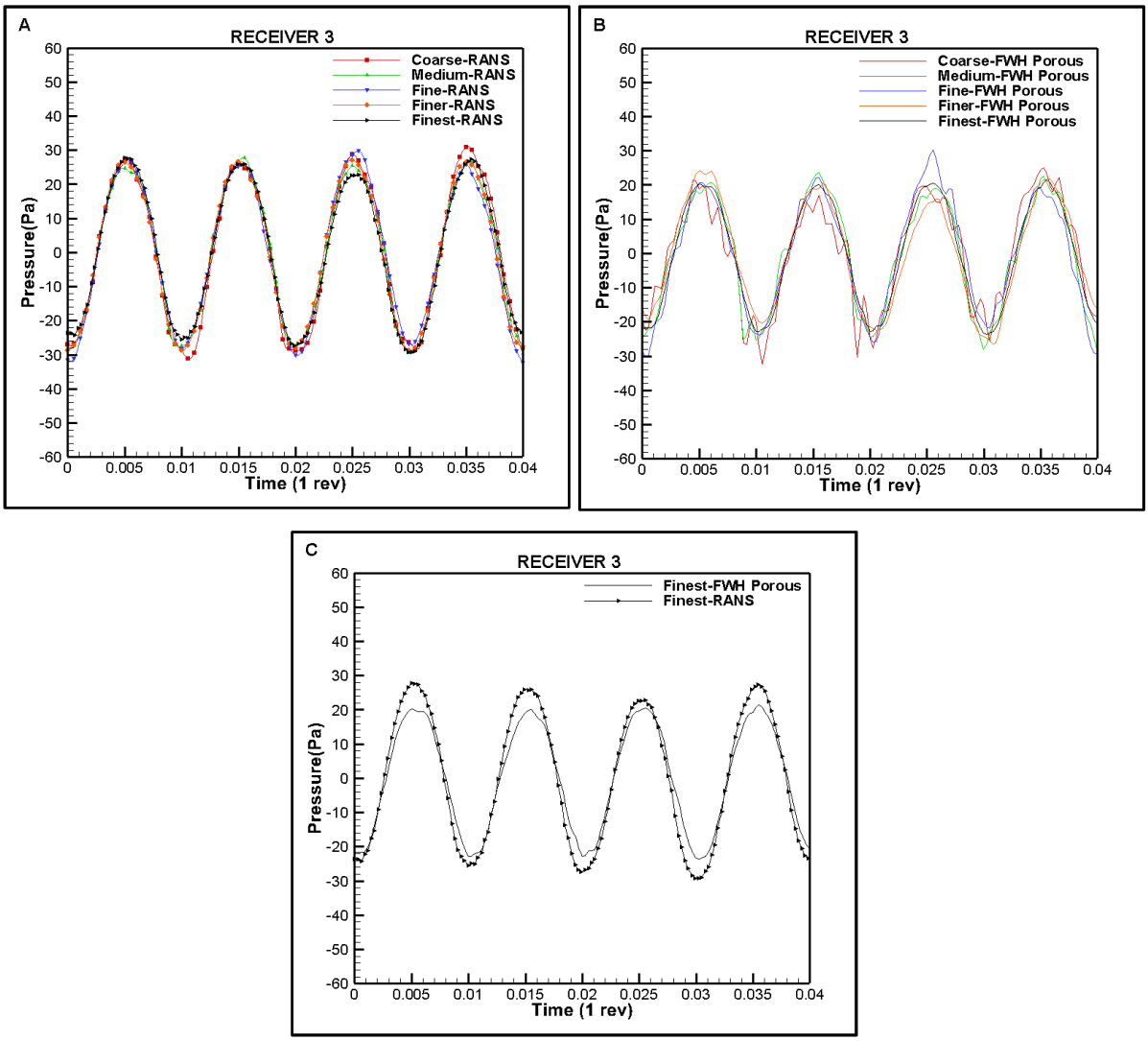

Figure 4.12. RANS pressures (A), FWH pressures (B) and RANS versus FWH pressures (C) at Receiver 3.

Increasing the distance from the propeller, hydrodynamic and hydroacoustic pressures start to become completely different at R4 and R5 in terms of magnitude and overall shape of the signal, as shown in Figure 4.13 and Figure 4.14. The total pressures show a rapid decrease (i.e. from approximately ∓ 30 to ∓ 1) at R4 compared to R3. The variation of hydrodynamic pressures with the different grid resolutions is given in Figure 4.13A. As shown in Figure 4.13A, an increase in grid resolution (i.e. more extension of tip vortex downstream) does not provide a significant change in the amplitude of hydrodynamic pressures. Hence, these results lead the RANS method to be questioned for the receivers located downstream of the propeller even if the numerical diffusion is significantly reduced for the receivers located downstream of the propeller.

The change in hydroacoustic pressures with different grid resolutions is also given in Figure 4.13B. Similar to hydrodynamic pressures, the magnitude of the acoustic pressures is too small. In other words, a few diameters away from the propeller downstream, the total noise tends to disappear, which is not realistic. In the study by Testa et al., 2018, the propeller URN was predicted using DES and the porous FWH equation at R4. Although the low level of pressure fluctuations coming from the direct DES solution was considered as a result of the reflection of numerical disturbances from the computational domain in their study, the hydrodynamic and hydroacoustic pressure fluctuations were detected between around ∓ 8 using the DES method. As depicted in Figure 4.13C, the RANS method underestimated the hydroacoustic pressures compared to the DES method during a propeller revolution. Due to the substantial contribution of the nonlinear noise term to the overall acoustic pressure, the overall shape of the signal is no longer characterised purely by BPF.

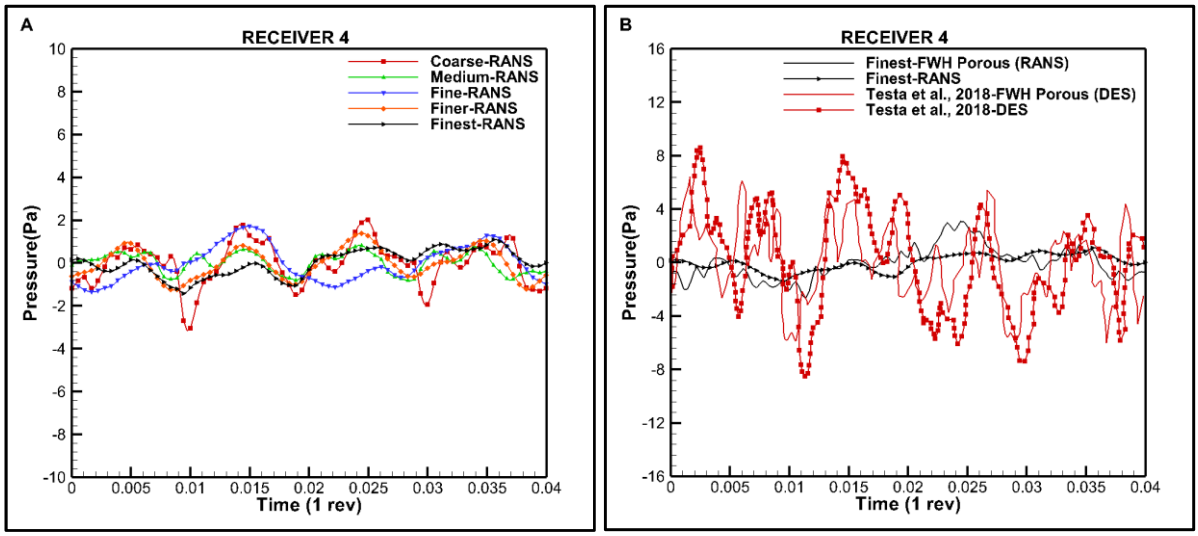

Figure 4.13. RANS pressures (A), RANS versus FWH pressures and comparison of the results (B) at Receiver 4.

Another comparison of the pressures with different grid resolutions is performed at R5 in Figure 4.14. Similar to R4, a decrease in numerical diffusion does not positively impact hydrodynamic and hydroacoustic pressures (Figure 4.14A and Figure 4.14B). Additionally, the amplitudes of the pressure signal at R5 are expected to be lower than at R4. There could be numerous reasons why an incorrect prediction occurs at R5. This could be caused by the numerical noise induced by the sliding interfaces, mesh transitions, numerical errors, or strong vortex-vortex interactions in the propeller's slipstream. The same issue was also observed in Lloyd et al., 2015a and Testa et al., 2018.

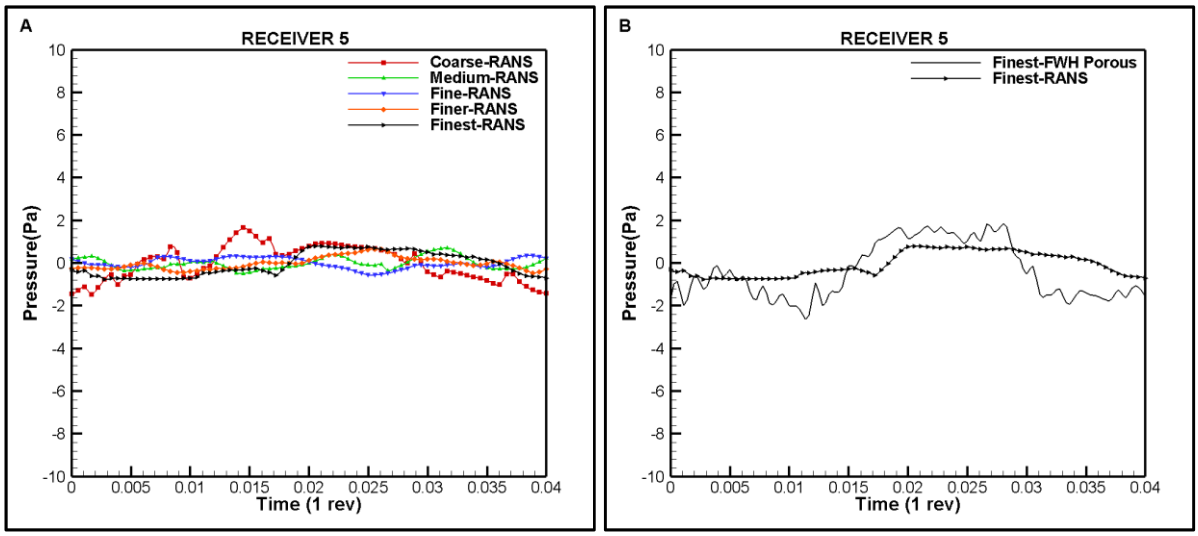

Figure 4.14. RANS pressures (A), RANS versus FWH pressures (B) at Receiver 5.

In addition to the comprehensive investigation of the hydrodynamic and hydroacoustic pressures at different receiver locations, the convergence study was also conducted with different integral (i.e., permeable/porous) surfaces using the fine grid resolution, as given in Table 4.2. Figures 4.15A, 15B and 15C show the change in hydroacoustic pressures with different porous surfaces at R1, R2 and R3 receiver locations, respectively. As shown in Figures 4.15A-C, all of them superimpose each other.

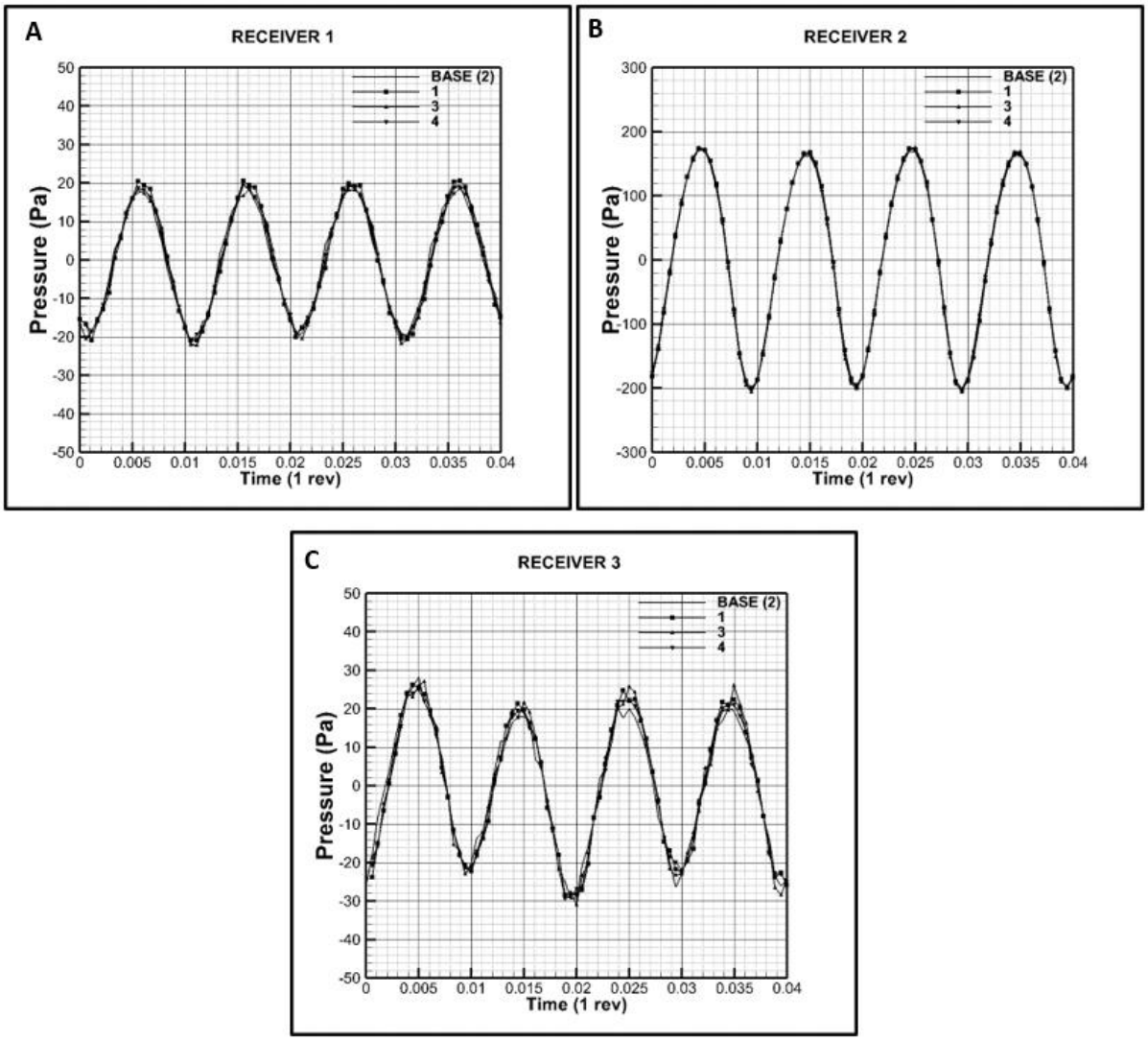

Figure 4.15. Comparison of hydroacoustic pressures with different integral surfaces at Receiver 1(A), 2(B), and 3(C).Understanding the nonlinear noise contribution on propeller URN

4.3 Understanding the nonlinear noise contribution on propeller URN

4.3.1 Theoretical background

In this chapter, the mathematical formulations given for hydrodynamic and hydroacoustic models are identical to those used in Section 4.2, and the details of the turbulence models are provided.

4.3.1.1 k-ε turbulence model and its variants

k-ε turbulence model might be considered the most popular turbulence model in engineering calculations, probably the first applied one in practice. It mainly focuses on the processes that cause a change in the turbulent kinetic energy (Versteeg and Malalasekera, 2007). In this

model, two transport equations (i.e., turbulence kinetic energy and dissipation rate) are computed to represent the effects of turbulent stresses on eddy viscosity. The earlier proposed coefficients were revised with those suggested by Launder and Sharma (1974), and it was started to be referred to Standard k-ε turbulence model (Wilcox, 2006). Following that, the application of the Standard k-ε turbulence model became popular, and it was integrated with many commercial CFD codes (Pope, 2000). The Standard k-ε turbulence model uses the wall functions to model the universal behaviour of the near-wall flows at high Reynolds numbers. In contrast, the drawback of the Standard k-ε turbulence model is that it is not suitable for the low Reynolds number type flows since the log-law is not valid near solid boundaries. Therefore, several modified versions of the Standard k-ε model were proposed for both low and high Reynolds number type flows (Versteeg and Malalasekera, 2007).

One of the modified versions of the standard model is the Realisable k-ε model, which has been extensively used for practical ship hydrodynamic problems (Shih et al., 1995). In this model, a new transport equation was proposed for the turbulent dissipation rate. Besides, a new formulation was introduced to calculate the turbulent viscosity coefficient, which is constant in Standard k-ε. Thus, it became a nonlinear version of the Standard k-ε model, and additional effects were included to account for Reynolds stress anisotropy (Sadrehaghighi, 2019). As a result, the Realisable k-ε model provides better predictions in many applications, particularly for separating and unconfined flows, compared with the Standard k-ε model (Bulat and Bulat, 2013; Tu et al., 2018).

Another variant of the Standard k-ε model is the Abe-Kondoh-Nagano (AKN) k-ε model, proposed for the low-Reynolds number type flows (Abe et al., 1994). AKN k-ε model has different coefficients and damping functions compared to other models. It is considered that the AKN k-ε model predicts average flow and turbulent quantities in separating flows better than the standard model. Another widely used turbulence model is the v^2f k-ε turbulence model (Durbin, 1991). It is the improved version of the Standard k-ε model, and it combines the anisotropy of the near-wall turbulence and non-local pressure-strain effects (Sundén and Fu, 2017). In addition to the kinetic and dissipation rate equations, the v^2f k-ε model also solves two more transport equations: wall-normal stress component 'v^2' and elliptic relaxation parameter 'f'. Also, it solves the near-wall flow without the need of using a wall function. Some modifications were applied for the source terms and non-isotropic turbulence viscosity to improve the model's capabilities (Davidson et al., 2003). It is claimed that the v^2f k-ε turbulence model is more accurate than traditional two-equation eddy viscosity models for the solution of

flow separation, wall friction, and representation of the near-wall turbulence effects (Star CCM+ 14.06, 2019; Luo and Razinsky, 2008).

4.3.1.2 k-ω turbulence model and its variants

The second widely used two-equation transport model is the k-ω model and its variants. Similar to k-ε models, the Standard k-ω model solves a transport equation for turbulence kinetic energy 'k' to determine turbulent eddy viscosity (Wilcox, 2006). However, the dissipation rate (ε) is replaced with turbulence frequency (ω), which is the dissipation rate per unit of turbulent kinetic energy. According to Sadrehaghighi (2019), the main difference between k-ε and k-ω turbulence models are dissimilar trends of ε and ω at the solid walls and different descriptions of the wall boundary conditions for the same variables. It is believed that the superiority of the k-ω model is to show better performance for the solution of the boundary layer under adverse pressure gradients (i.e. separated or swirled flows) (Star CCM+ 14.06, 2019). Nevertheless, the k-ω turbulence model is sensitive to the free stream value of ω; hence, it needs to be described carefully (Tu et al., 2018).

The k-ω SST (Shear Stress Transport) model was derived by Menter (1994) as the modified version of Wilcox's k-ω model. In this model the robust & accurate formulation of the Standard k-ω model in the near solid surfaces and the benefits of the free stream independence of the k-ε model in the outer region were combined (Poncet et al., 2010). The k-ω SST model is available in many commercial CFD tools. The popularity of the model increases for the solution of the hydrodynamic problems because of the several advantages (e.g., the prediction flow separation, good behaviour in adverse pressure gradient, etc.) compared to other models. For this reason, it was selected to investigate its capabilities in predicting propeller's wake instability and propeller URN at two different loading conditions in this thesis.

4.3.1.3 One equation turbulence models

One equation turbulence closure models were proposed as an alternative to the two equations turbulence models to calculate the eddy viscosity. The most popular one-equation model is the Spalart-Allmaras model (Spalart and Allmaras, 1992). This closure uses a transport equation for the calculation of eddy viscosity. The Spalart-Allmaras model is more computationally affordable than the other two-equation models since it only solves one additional equation. While the Spalart-Allmaras model is suitable for free-shear and boundary-layer flows, it is claimed that it may have disadvantages for the computations of shear flow, separated flow, or decay of turbulence (Zhai et al., 2007; Sadrehaghighi, 2019). It should be noted that this model

was initially developed for aerodynamic applications. As there are several studies in the literature, especially in the propeller hydrodynamic and hydroacoustic fields, its capabilities were investigated through the propeller URN in the scope of this thesis.

The summary of the implemented turbulence models is also presented in Table 4.7. Detailed mathematical descriptions and references about these models can be found in the user guide of the CFD solver (Star CCM+ 14.06, 2019).

Table 4.7. Selected turbulence models.

One equation turbulence model	Spalart-Allmaras
Two Equations turbulence models	k-ω SST Realisable k-ε

4.3.2 Numerical modelling

4.3.2.1 Propeller geometry and test case

In this section, the selected model scale propeller geometry is identical to those used in Section 4.2. Thus, the details of the propeller's main characteristics can be found in Section 4.2.2. In the numerical calculations, the propeller rotational speed was kept constant at 25rps. The inflow velocities were set to V_A=5 and 1.7m/s corresponding to J=0.88 and J=0.3, respectively.

4.3.2.2 Computational domain and boundary conditions

The computational domain and boundary conditions used here are the same as in Section 4.2. Hence, the details can be found in Section 4.2.2.

4.3.2.3 Grid resolution

The unstructured grid with hexahedral elements was employed to discretise the computational domain, similar to Section 4.1..Based on the important findings in Section 4.2, the suitable grid structure is adopted in the computational domain, as shown in Figure 4.16.

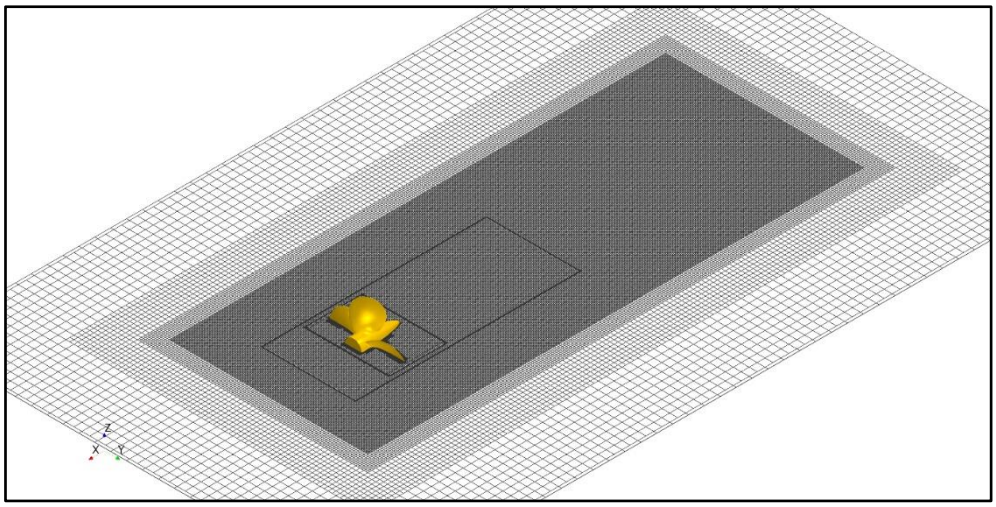

Figure 4.16. Grid structure around the propeller blades (Finest Grid).

An uncertainty study was conducted using the methodology proposed by Roache (1998) for propeller global performance characteristics (i.e. non-dimensional thrust and torque), similar to Section 4.2. In the proposed methodology, three different solutions are desired to assess the numerical solution accurately. However, according to Roache (1998), two solutions can also be used to calculate the uncertainty level of the solution. Therefore, the numerical solution's uncertainty was evaluated using two different grid resolutions, which have 18.5M and 7M total element counts. The solution scalars were selected for both thrust and torque coefficients at J=0.88. Furthermore, the k-ω SST turbulence model was utilised for the uncertainty study.

The solution variation can be estimated in the proposed uncertainty methodology as follows.

$$E = \frac{f_2 - f_1}{1 - r^p} \tag{4.15}$$

Here, f_1 and f_2 represent fine and coarse grid solutions, respectively. r is the refinement factor, and p is the formal order of accuracy. In the numerical calculations, r was selected $\sqrt{2}$, whereas p was selected 2. Then, the uncertainty of the numerical solution can be calculated with the following equation.

$$U_N = F_s|E| \tag{4.16}$$

where F_s is a safety factor, and it was taken as $F_s = 3$, according to Roache (1998).

Non-dimensional K_T and $10K_Q$ values and the uncertainty value of the solution can be seen in Table 4.8. As a result of the uncertainty study and the findings in Section 4.2, a fine grid structure was employed for the calculations carried out using three different turbulence models at two different loading conditions.

Table 4.8. Uncertainty of the numerical solution.

Grid	K_T	$10K_Q$	U_N (%)
Coarse	0.152	0.310	0.9
Fine	0.149	0.306	1.2

4.3.2.4 Solution strategy

As followed in Section 4.2, the same solution strategy was adopted in this section. The details can be found in Section 4.2.2.

4.3.3 Numerical results

4.3.3.1 Hydrodynamic results

Table 4.9 compares non-dimensional thrust and torque values with the experimental data for different turbulence models at two different loading conditions. As shown in Table 4.9, propeller performance characteristics are predicted with good accuracy using different turbulence models. It can be concluded that there is no significant difference between turbulence models for the prediction of thrust and torque values.

Table 4.9. Comparison of propeller hydrodynamic characteristics at two different loading conditions.

	J=0.88			J=0.3		
Quantity	Spalart Allmaras	k-ω SST	Realisable k-ε	Spalart-Allmaras	k-ω SST	Realisable k-ε
K_T (CFD)	0.152	0.149	0.150	0.424	0.425	0.426
K_T (EFD)		0.151			0.430	
ΔK_T (%)	0.662	1.325	0.662	1.395	1.162	0.930
$10K_Q$ (CFD)	0.309	0.306	0.308	0.712	0.721	0.723
$10K_Q$ (EFD)		0.305			0.707	
$\Delta 10K_Q$ (%)	1.311	0.328	0.983	0.707	1.980	2.263

- **Investigation of the flow field in the propeller slipstream**

The flow field analysis in the propeller's slipstream is performed at two different advance coefficients (i.e., J=0.88 and J=0.3), and the numerical results are compared with the available experimental data.

***J*=0.88**

The flow around the marine propeller is a complex phenomenon both in open water and behind hull conditions. Therefore, a detailed investigation of the flow field in the propeller's slipstream is of great importance as it is directly related to the marine propellers' noise, vibration, and propulsion performance. The propeller's wake consists of two systems of vortex structures, which are mainly generated at the blade's root and tip sections. The tip vortices originate from the pressure difference between the face and back sides of the blades. A sheet of trailing vortices and axial hub vortex can be considered additional vortex structures. Besides, vortex/vortex interactions may cause vortex instabilities, which are still investigated using experimental and numerical techniques (e.g., Felli et al., 2011; Muscari et al., 2013; Kumar and Mahesh, 2017).

The vorticity distribution in the Y direction is given in Figure 4.17 for three different turbulence models with the experimental visualisation at J=0.88. The extension of tip vortices in the propeller's slipstream agrees with the experimental measurement using different turbulence models.

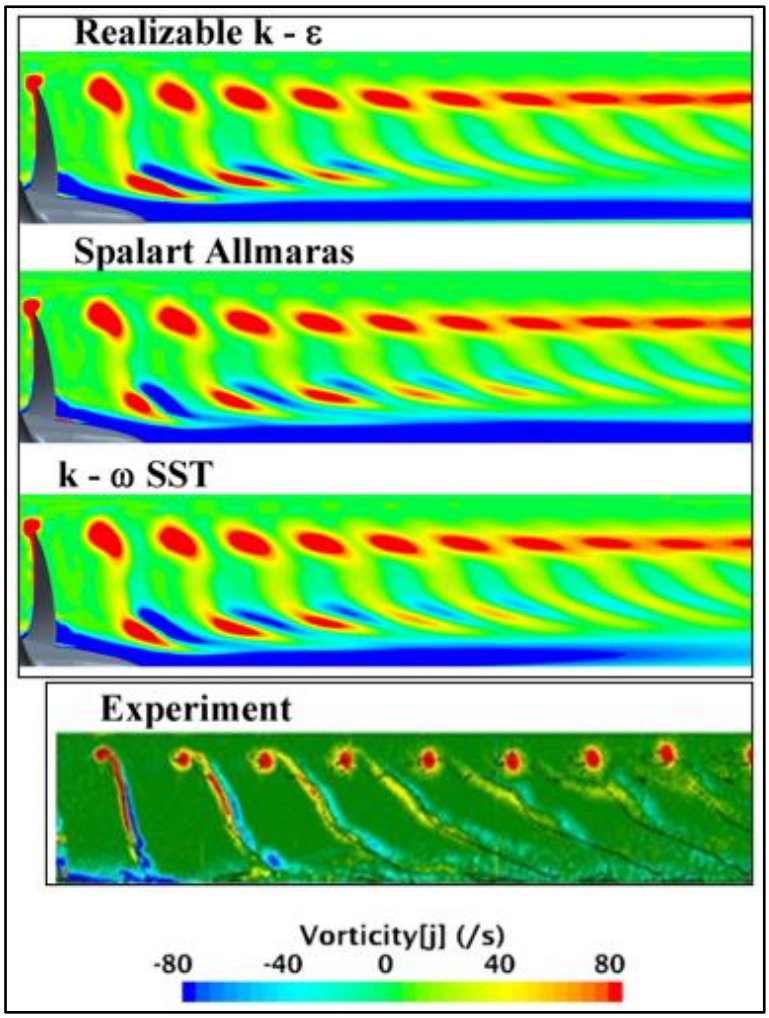

Figure 4.17. Comparison of vorticity in the Y direction (ω_Y) with the experiment (Calcagno et al., 2003)

The general view of the vorticity distribution in the propeller's slipstream is given in Figure 4.18. The coherent vortical structures in the propeller's slipstream are visualised using the Q criterion, which shows the vorticity regions where the vorticity magnitude is higher than the strain rate magnitude. Figure 4.18 is coloured by helicity by using the following formulation;

$$H = V_r \Omega / (|V_r||\Omega|) \tag{4.17}$$

where V_r is the relative velocity vector in the rotating reference frame. Helicity indicates the cosine angle between the absolute vorticity vector and the corresponding velocity. Helicity becomes ± 1 in the vortex core, and the sign shows the swirl direction.

The threshold value of the Q criterion (i.e., Q_c=500 1/s^2) was determined using the time derivative of the pressure, as explained in Section 4.2. The helices, mainly formed by tip vortices, remain almost at a constant radius downstream of the propeller in Figure 4.18. As shown in Figure 4.18, tip and hub vortices in the propeller's slipstream are predicted to be

slightly different by using different turbulence models. As the blade loading is low (i.e. J=0.88), significant destabilisation (or instability) of the vortex structures is not present at the tip and hub vortex in compliance with the experimental findings by Felli et al., 2011. It should be noted that tip vortices can be maintained much further downstream using more advanced models (e.g., DES and LES).

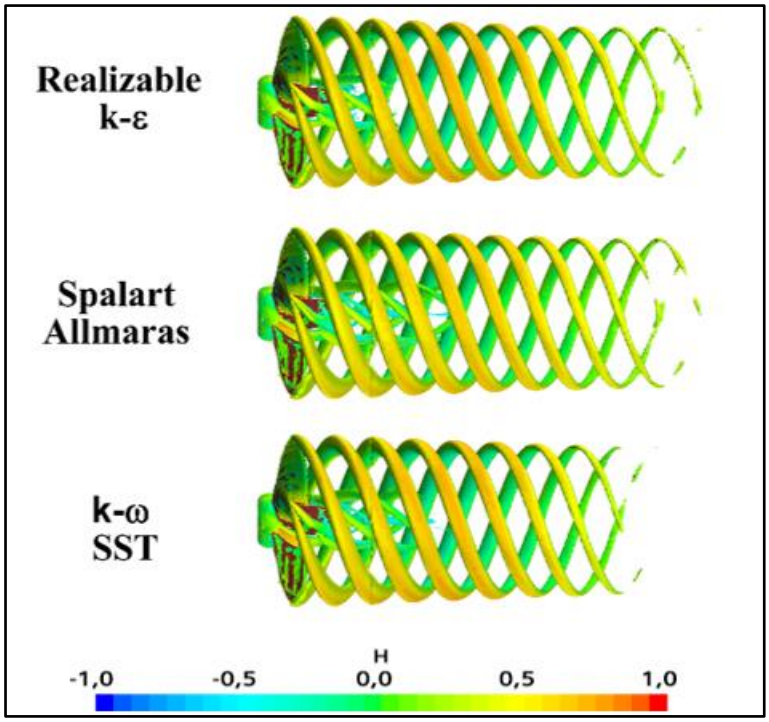

Figure 4.18. Comparison of tip and hub vortex in the propeller's slipstream at J=0.88 ($Q_c = 500\ 1/s^2$).

Further detailed flow investigation is conducted at four different planes located near, intermediate, and far fields of the propeller's slipstream, as shown in Figure 4.19.

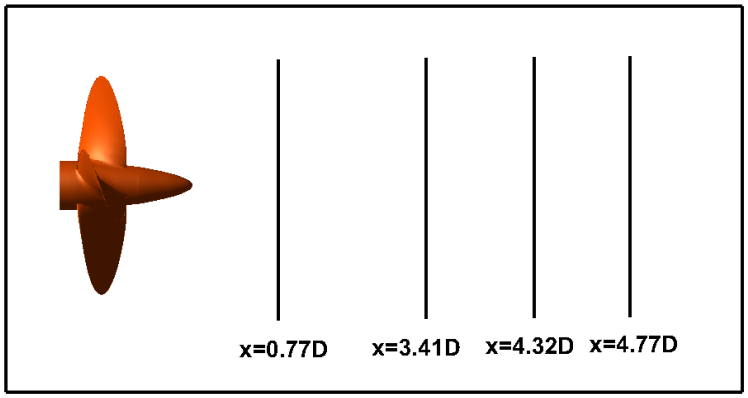

Figure 4.19. Representation of plane locations (Figure is not scaled).

Figure 4.20 shows the longitudinal view of the non-dimensional axial velocity distributions at different locations. As shown in Figure 4.20, the visual inspection of axial velocity does not present any out-of-phase unsteadiness. It indicates almost uniform behaviour at different locations for all turbulent models. Hence, it can be considered that the velocity field around the propeller is predicted similarly using different turbulence models.

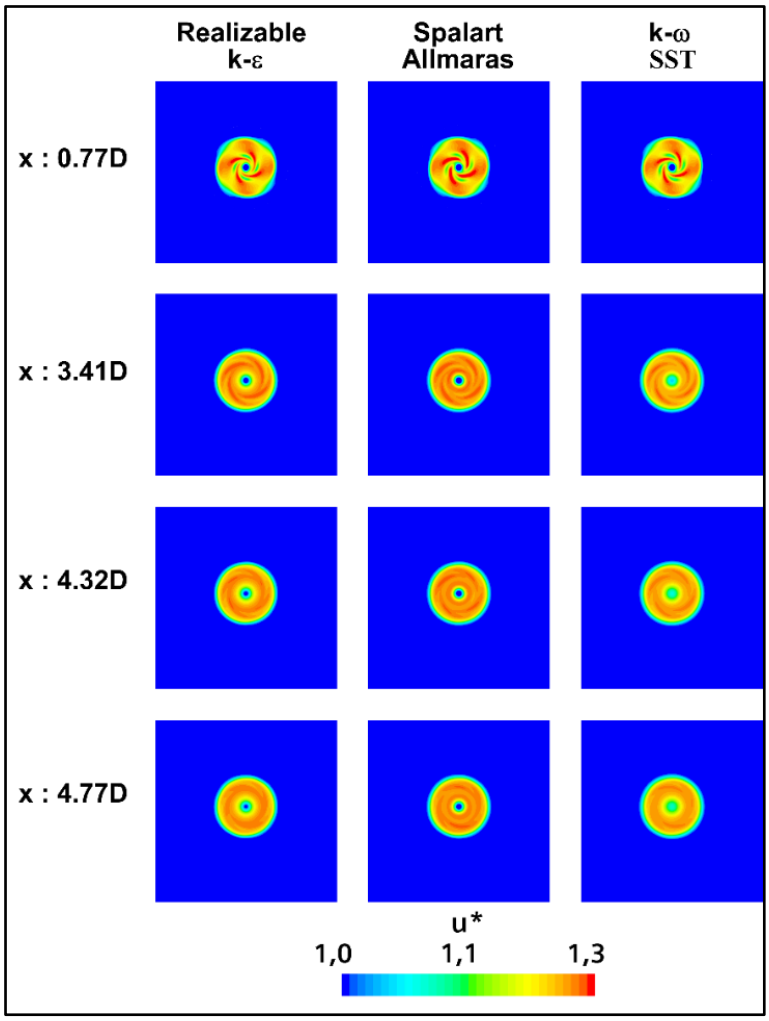

Figure 4.20. Comparison of non-dimensional axial velocity distributions at different sections in the propeller's slipstream at $\boldsymbol{J}$=0.88.

Variation of turbulent viscosity ratio (TVR), also known as eddy viscosity ratio, is given in Figure 4.21 for different turbulence models. TVR is the ratio between turbulent viscosity (μ_t) and molecular dynamic viscosity (μ). Also, turbulence viscosity (eddy viscosity) can be considered as the contribution of turbulence to the mean momentum equation. Generally speaking, turbulence is expected to increase at the flow regions where velocity changes occur. Due to the strong vortex structures, velocities and their components are high in the propeller's slipstream. Thus, vortex structures cause a change in velocity, pressure field and TVR. The computation of TVR in the vortex depends on the turbulence model and its mathematical

background. Even though similar coherent vortex structures in the propeller's slipstream are predicted at J=0.88 with different turbulence models (see Figure 4.18), TVR levels are found dissimilar in Figure 4.21. As shown in Figure 4.21, TVR is small in the near field of the propeller's slipstream, but its magnitude increases rapidly for Realisable k-ε and k-ω SST turbulence models in the far-field of the propeller's slipstream. Additionally, TVR presents nearly stable behaviour after the near field of the propeller's slipstream (i.e., x/D=0.77) due to the consistent tip vortex structure at J=0.88. As shown in Figure 4.21, the TVC is predicted small using the Spalart-Allmaras turbulence model, while the Realisable k-ε turbulence model produces the highest TVR.

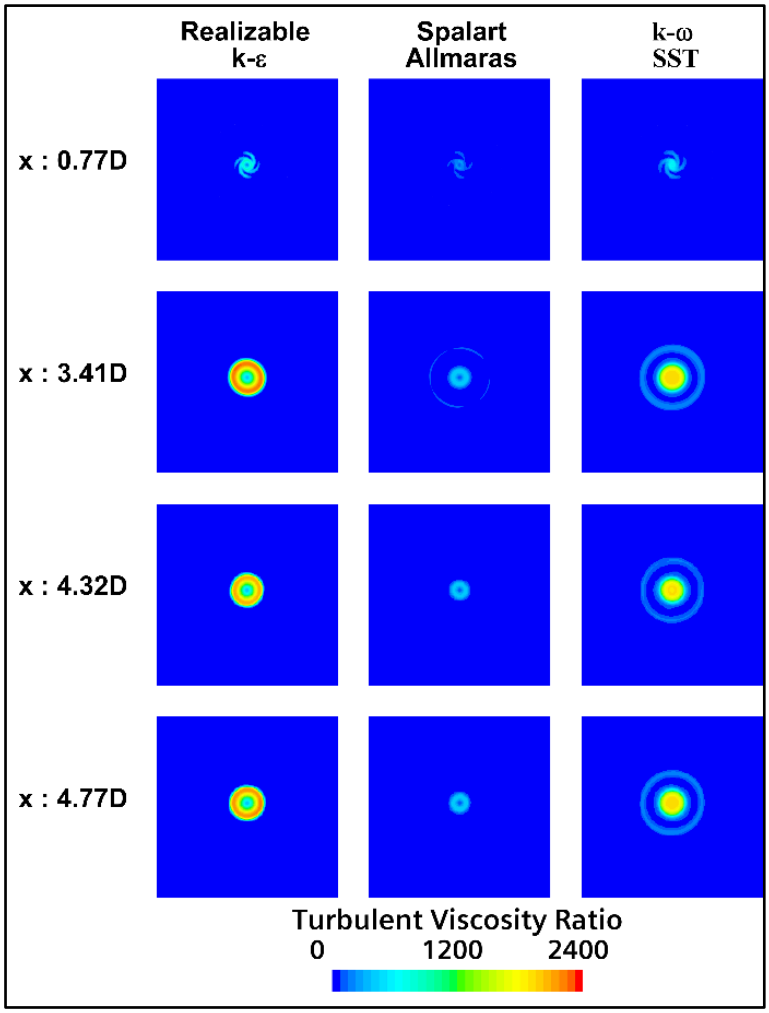

Figure 4.21. Comparison of TVR at J=0.88.

***J*=0.3**

A high propeller loading condition (i.e., J=0.3) is selected to investigate the capabilities of turbulence models to follow the onset of the instability process in the propeller's slipstream. It should be noted that experimental vorticity distribution is not available at J=0.3. The vorticity distribution in the Y direction (ω_Y) can be seen in Figure 4.22 using different turbulence

models. As shown in Figure 4.22, the instability process of the tip vortex initiates with an increase in blade loading. Tip vortices start to deform from the helical path, and the break-up process develops in the far-field of the propeller's slipstream, particularly for the predictions obtained by Realisable k-ε and Spalart-Allmaras turbulence models. Furthermore, the break-up of vortices predicted using the Spalart-Allmaras turbulence model is more pronounced and extends towards the far-field. The destabilisation of the tip vortex may also play a role in the instability process of the hub vortex, as explored by Felli et al. (2011). As shown in Figure 4.22, the k-ω SST turbulence model smoothes out the vortex/vortex interactions and does not show any pronounced instability compared to other turbulence models. Similar comments for the k-ω SST turbulence model can be found in the study by Guilmineau et al., (2015).

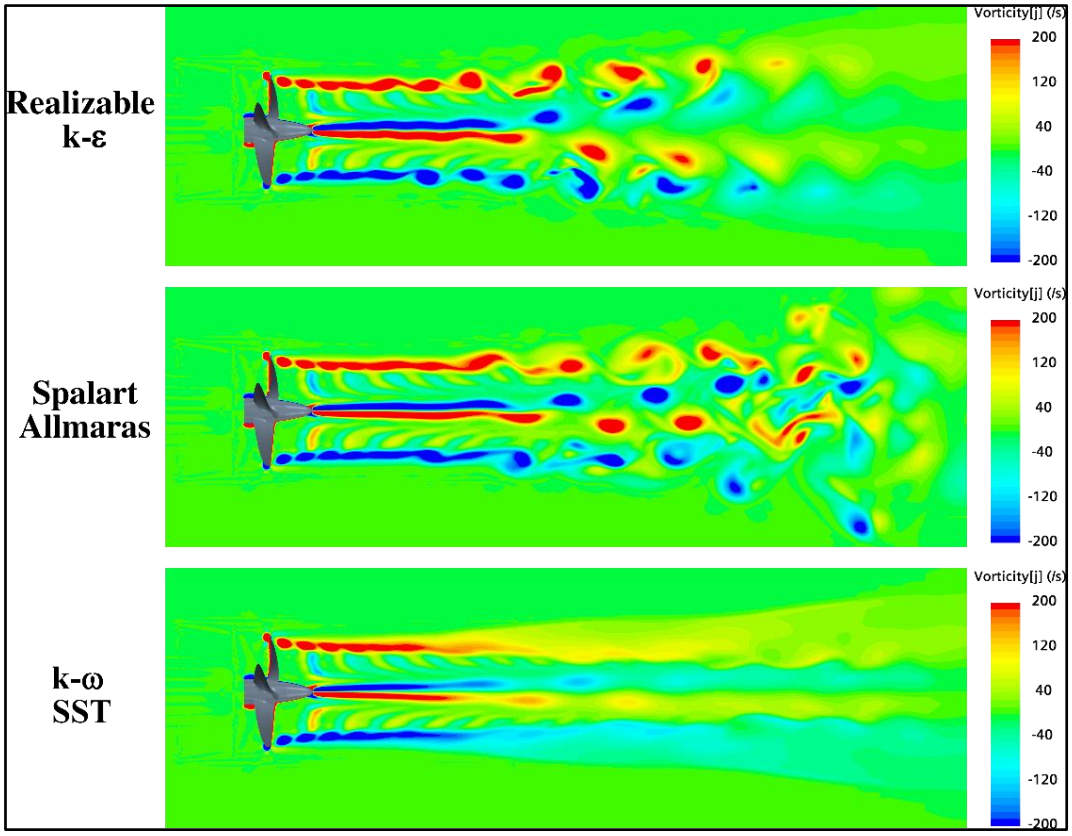

Figure 4.22. Comparison of vorticity distributions in the Y direction (ω_Y) at J=0.3.

The general view of the vortex structures in the propeller's slipstream is given in Figure 4.23. The vortex characteristics show rapid deformation in the propeller's slipstream, and more intense tip vortices occur compared to J=0.88 using all turbulence models. Although the tip vortices are stronger at J=0.3 than J=0.88, it extends to a short distance before the instability occurs. Tip vortices combine and form a larger vortex with adjacent trailing vortices in the far-field of the propeller's slipstream. The contraction ratio of tip vortex trajectory at J=0.3 is found to be higher than J=0.88.

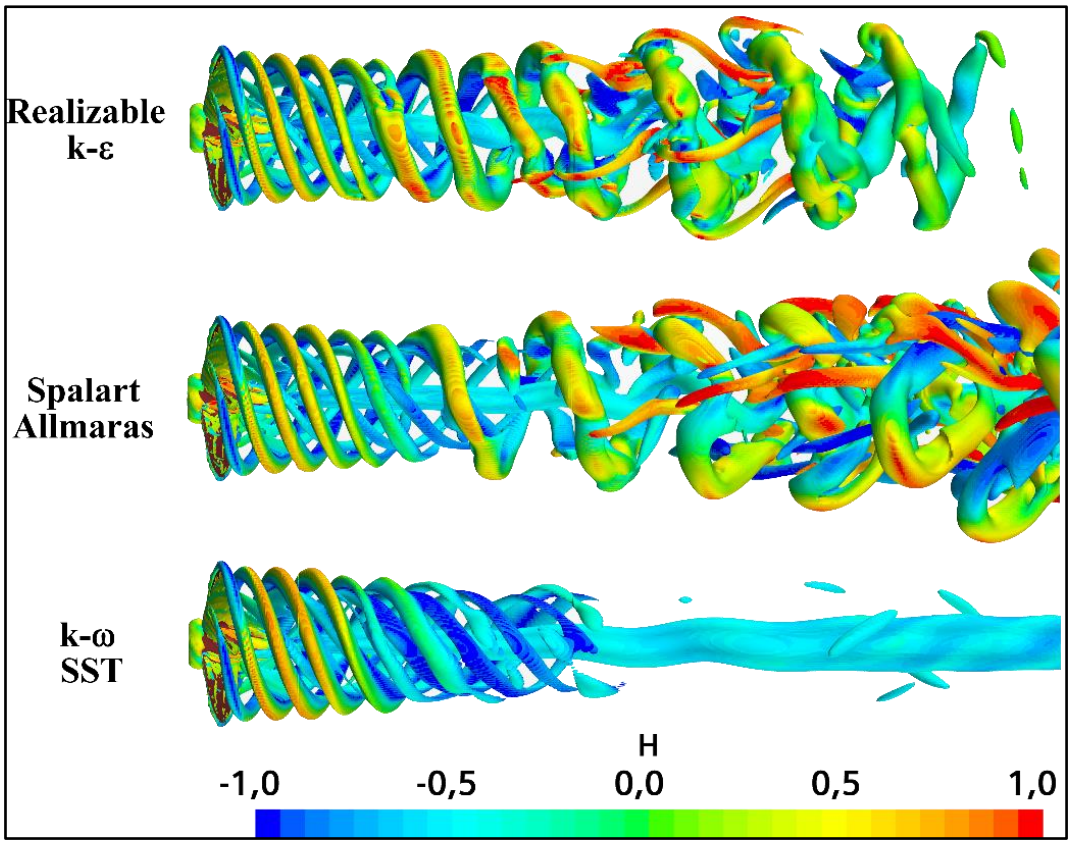

Figure 4.23. Comparison of tip and hub vortex in the propeller's slipstream at J=0.3 ($Q_c = 1500\ 1/s^2$).

Vortices create different velocity and pressure fields in their surroundings and dominate the turbulent flow due to their chaotic motions and coherent structures (Hunt et al., 1988). Thus, as the tip vortex is the dominant parameter to identify the pressure field in the propeller's slipstream, the break-up mechanism considerably affects the pressure or velocity variations in the flow region (Felli et al., 2006; Jang et al., 2001). Figure 4.24 shows the non-dimensional axial velocity distributions near and far-field of the propeller's slipstream. Unlike the low loading condition (i.e., J=0.88), strong vortex structures, detected by Realisable k-ε and Spalart-Allmaras turbulence models, deteriorate the homogenous axial velocity distribution in the far-field of the propeller's slipstream.

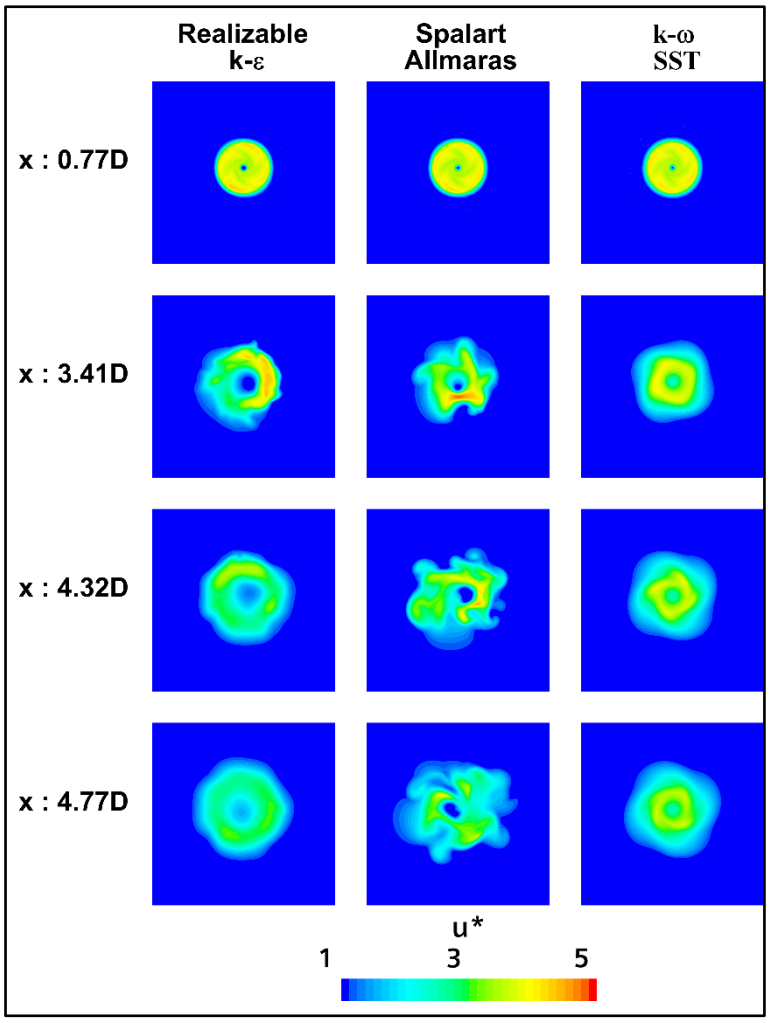

Figure 4.24. Non-dimensional axial velocity distributions at different sections in the propeller's slipstream at J=0.3.

With an increase in blade loading, the instability process caused by the break-up mechanism increases TVR, which results in the rapid growth of TVR in the far-field of the propeller's slipstream. Figure 4.25 shows the change of TVR with different turbulence models at different locations. As shown in Figure 4.25, Realisable k-ε produces the highest level of TVR, while the lowest level of TVR is found in the Spalart-Allmaras turbulence model. Similar to J=0.88, TVR is small in the near field of the propeller's slipstream, whereas it increases further downstream of the propeller. Similar findings can also be found in Guilmineau et al., (2015). and Kumar and Mahesh (2017).

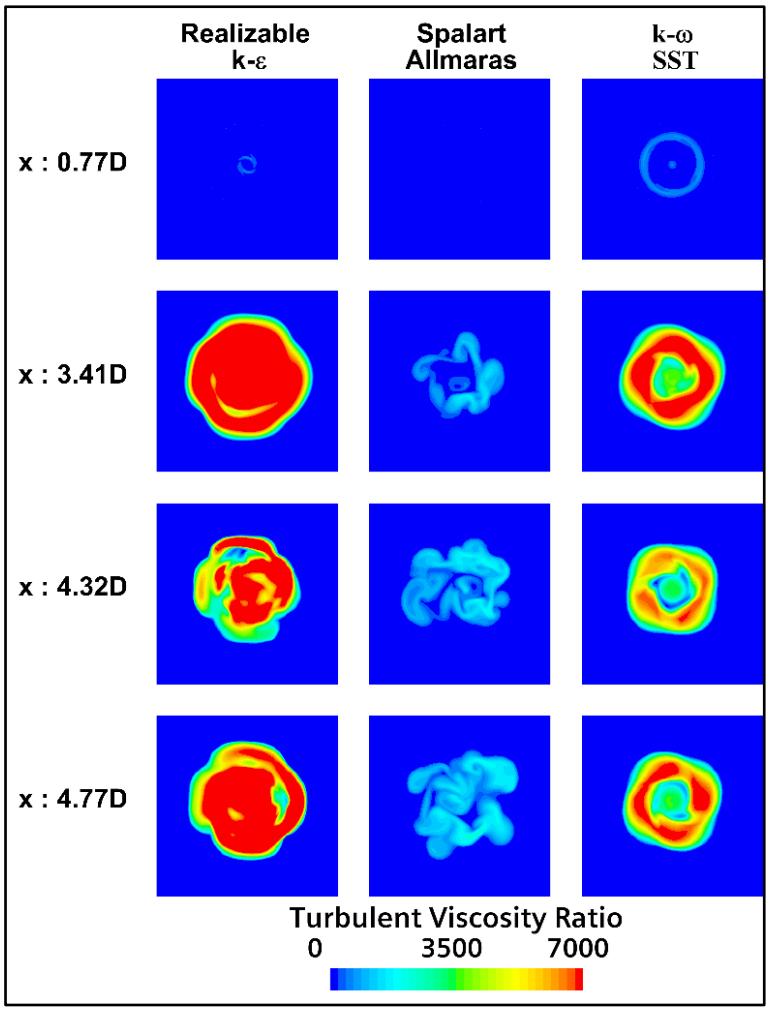

Figure 4.25. Comparison of TVR at J=0.3.

4.3.3.2 Hydroacoustic results

In this section, hydroacoustic results are presented at J=0.88 and J=0.3, respectively, both in near and far-field.

- ***J*=0.88 near field**

Figure 4.26 shows the receiver locations in the near field of the propeller. The receiver locations are also given in Table 4.10. It should be noted that the coordinate system (i.e., origin) is located at the centre of the propeller blades.

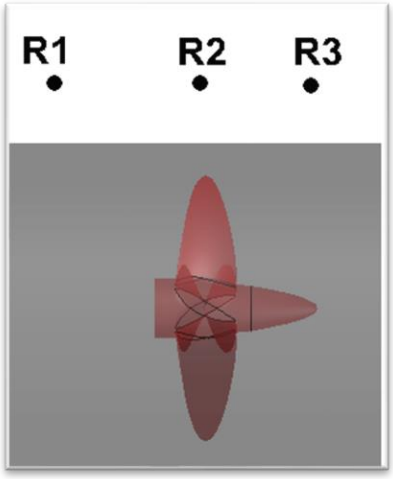

Figure 4.26. Representation of near-field receivers (Figure is not scaled).

Table 4.10. Location of near-field receivers.

Receiver	X (m)	Y (m)	Z (m)
1	0.1403		
2	0	0	0.2648
3	-0.1279		

Hydrodynamic and hydroacoustic pressures should be compatible in the near field for reliable assessment of the propeller URN in the far-field. Akin to Section 4.2, hydrodynamic pressures directly calculated from the solution of the Navier-Stokes equation and hydroacoustic pressures obtained using the acoustic analogy were compared.

Figure 4.27 compares hydrodynamic and hydroacoustic pressures at Receiver 1, located upstream of the propeller. The calculated hydrodynamic pressures are given in Figure 4.27A using different turbulence models, whereas the hydroacoustic pressures are presented in Figure 4.27B. As shown in Figures 4.27A and 4.27B, hydrodynamic and hydroacoustic pressures show the same amplitude and are deeply characterised by BPF (Blade Passage Frequency) of the four-bladed model propeller. The comparison of hydrodynamic and hydroacoustic pressures is also given in Figure 4.27C. The agreement between the two pressure fluctuations is quite good. Furthermore, due to the lack of experimental hydroacoustic results for the benchmark propeller, numerical results are compared with another numerical study in the literature presented by Ianniello et al. (2013) using RANS with the FWH equation in Figure 4.27D. As can be seen in Figure 4.27D, the numerical results are in good agreement with those of Ianniello et al. (2013).

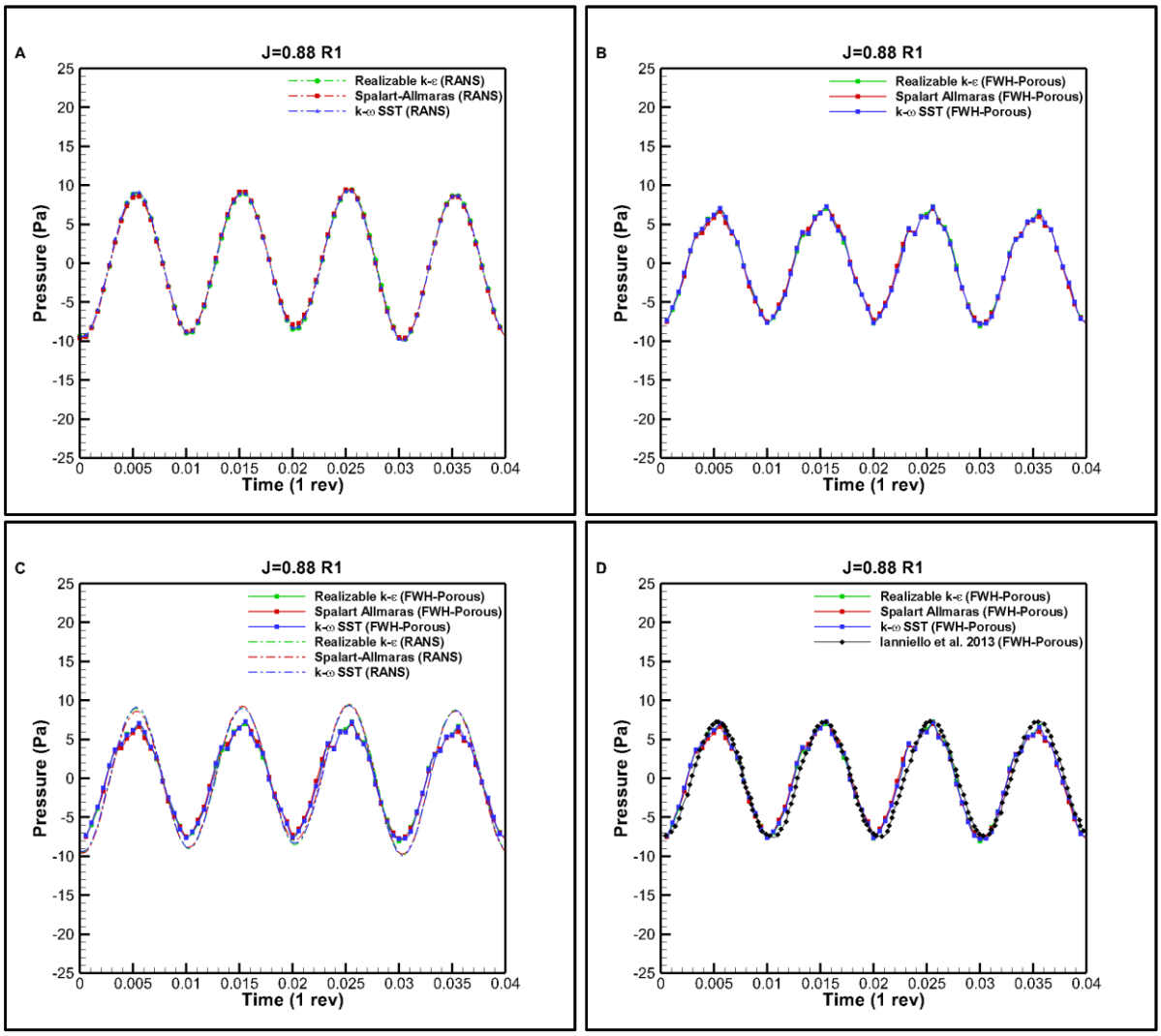

Figure 4.27. Comparison of hydrodynamic and hydroacoustic pressures at Receiver 1 (J=0.88).

Figure 4.28 compares hydrodynamic and hydroacoustic pressures at Receiver 2, located at the propeller plane. Akin to the previous receiver location, the linear contribution of the FWH terms is more dominant, and pressures are characterised purely by BPF. The amplitude of the signal is higher due to the contribution of blade harmonics compared to Receiver 1. Figures 4.28A and 4.28B show the hydrodynamic and hydroacoustic pressures for three different turbulence models. Similar to Receiver 1, hydrodynamic and hydroacoustic pressures are in quite good agreement with each other. The comparison between the present numerical results and Ianniello et al. (2013) shows a good agreement at this receiver location (Figure 4.28D).

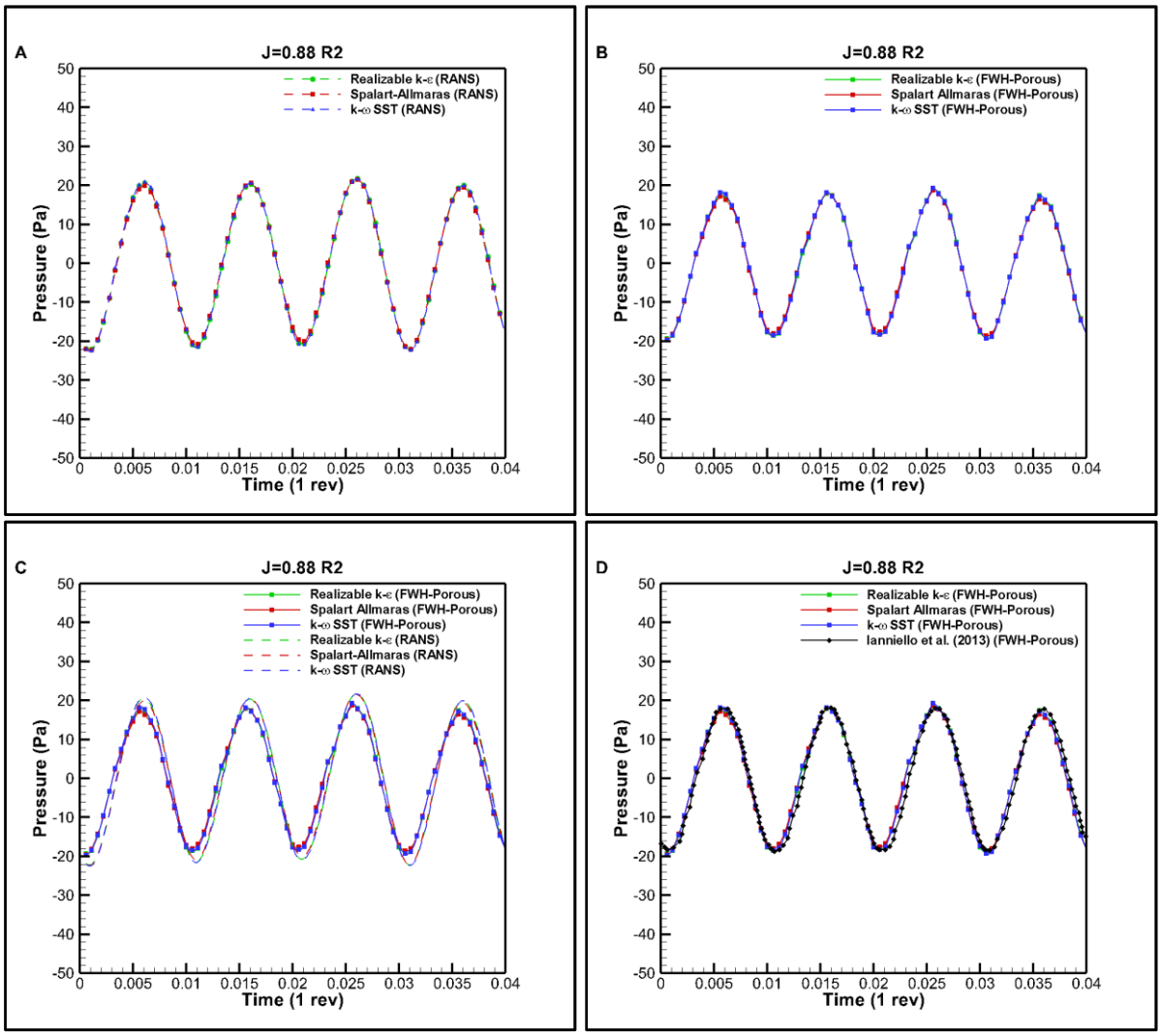

Figure 4.28. Comparison of hydrodynamic and hydroacoustic pressures at Receiver 2 (J=0.88).

Hydrodynamic and hydroacoustic results are also compared at Receiver 3, located downstream of the propeller. As Receiver 3 is still close to the propeller, the overall shape of the acoustic signal is still dominated by the contribution of the linear noise terms. Figures 4.29A and 4.29B show hydrodynamic and hydroacoustic pressures for three different turbulence models at Receiver 3, whereas Figure 4.29C indicates the comparison of these pressures. The agreement between hydrodynamic and hydroacoustic pressures is satisfactory with a minimal phase shift. Despite the fact that the location of the Receiver 3 is nearly symmetrical with Receiver 1, pressure fluctuations compared to Receiver 1 decreased from ∓ 8 to ∓ 5. In Figure 4.29D, numerical results at Receiver 3 are slightly lower than those of Ianniello et al. (2013) in Figure 4.29D.

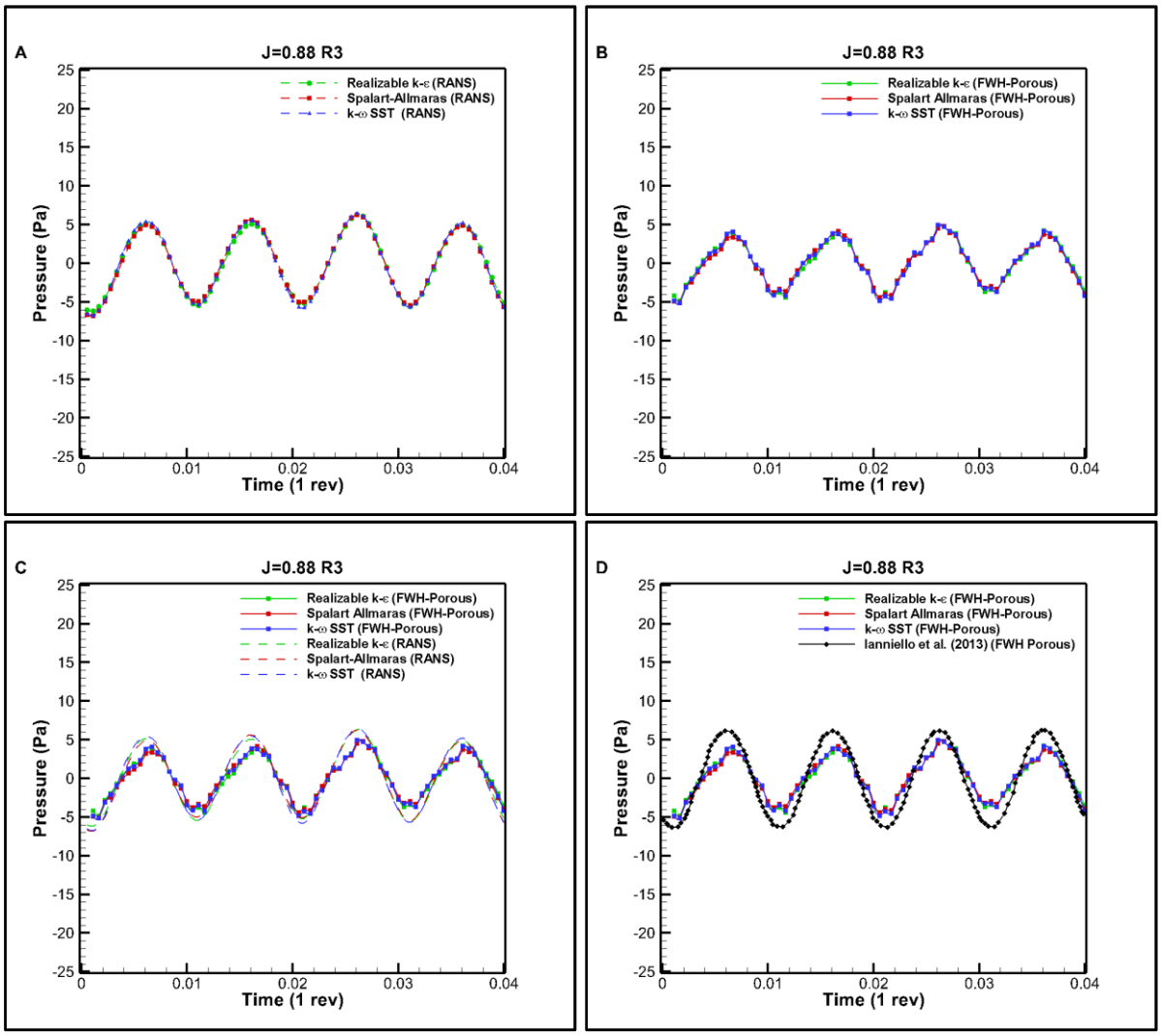

Figure 4.29. Comparison of hydrodynamic and hydroacoustic pressures at Receiver 3 (***J***=0.88).

- ***J*=0.88 far field**

Three arrays of receivers are placed outside the computational domain at a distance of 25D, 100D and 200D from the propeller's blade centre with an equal angular increment (i.e., 15^{o}) to investigate the propeller URN in the far-field, as shown in Figure 4.30. Also, receivers are located at both X, Y and Z-axis. The location of the receivers at the propeller plane (i.e., X-axis) can be seen in Figure 4.30. In the literature, the FWH acoustic analogy has been generally used with the hydrodynamic method to predict the propeller URN in the near field to compare hydroacoustic and hydrodynamic pressures. However, one of the main reasons for applying the FWH acoustic analogy is to predict URN in the far-field. Therefore, investigating propeller URN in the far-field would give an insight into strong debates for applying acoustic analogy.

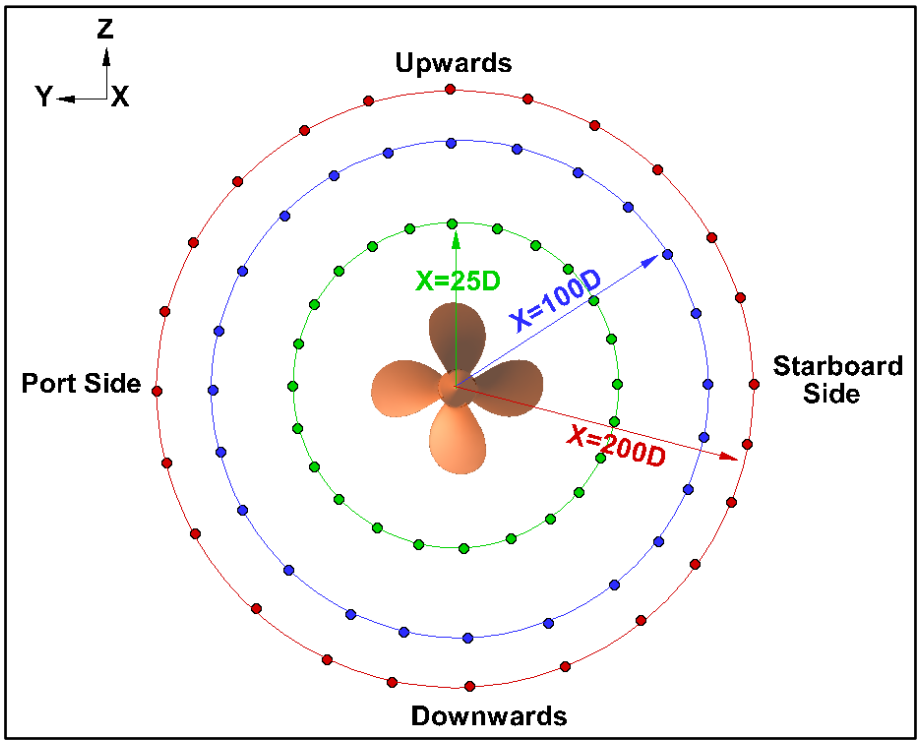

Figure 4.30. Representation of far-field receivers at 25D, 100D and 200D at the X-axis (Figure is not scaled).

Overall acoustic pressures are calculated in the time domain and transferred to the frequency domain using Fast Fourier Transform (FFT) for each receiver. Sound Pressure Level (SPL) can be calculated by using the following equation;

$$SPL = 20\log\left(\frac{p_{rms}}{p_{ref}}\right) \tag{4.18}$$

Here, p_{rsm} is the acoustic pressure in Pa and p_{ref} is the reference pressure and 10^{-6}Pa for water.

Figure 4.31 indicates directivity patterns predicted by FWH acoustic analogy together with three different turbulence models at the propeller plane (i.e., 25D, 100D and 200D). Additionally, the numerical results show that acoustic analogy, coupled with varying turbulence models, predicts the same noise directivity pattern regardless of the distance at low loading conditions (i.e., J=0.88). As shown in Figure 4.21, the overall URN levels predicted by different turbulence models are found to be similar at low blade loading conditions. This can be associated with a similar prediction of vorticity structures in the propeller slipstream (see Figures 4.17 and 4.18).

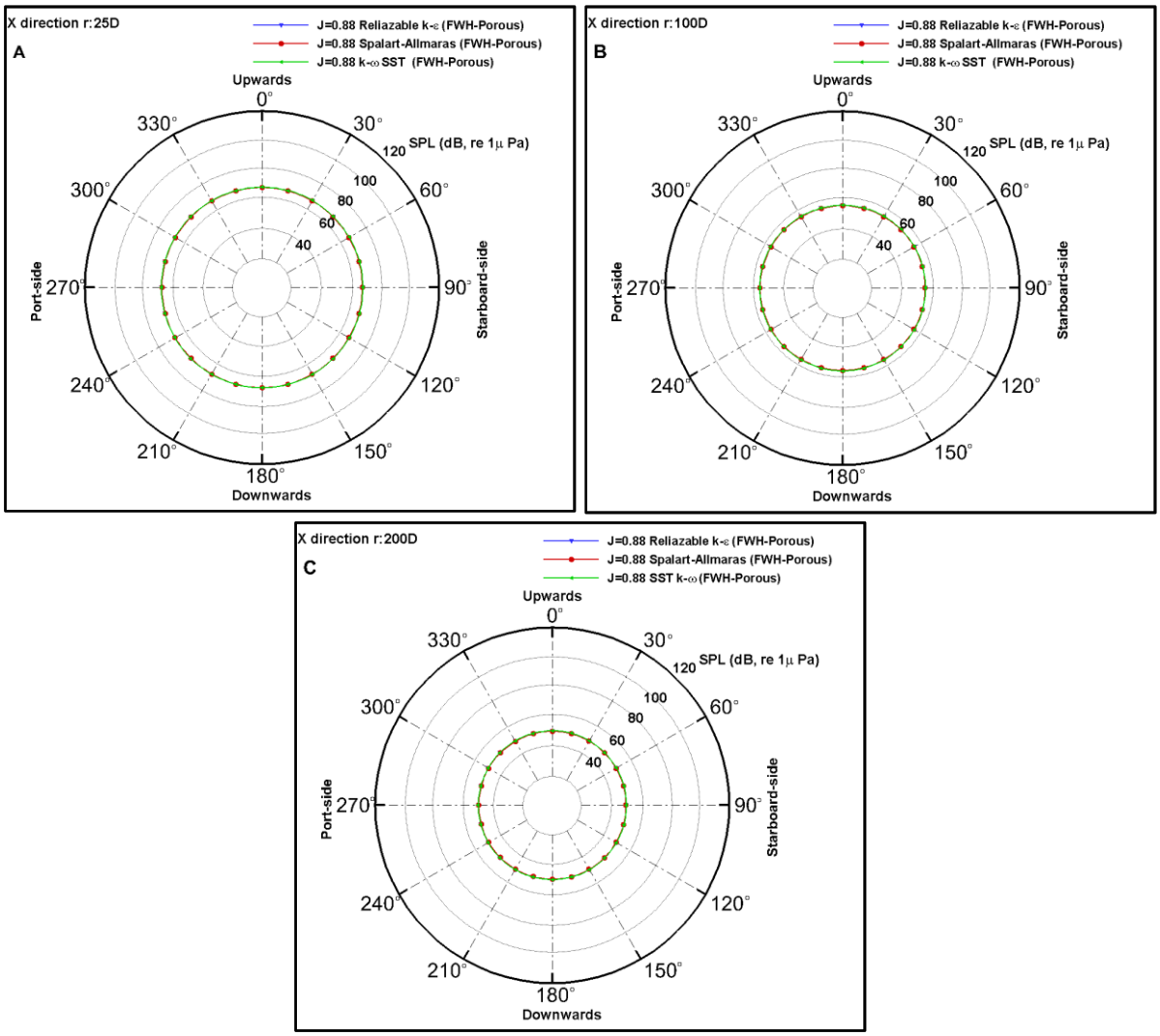

Figure 4.31. Noise directivity predicted at ***J***=0.88 (A: 25D, B:100D and C:200D).

On the other hand, noise levels can be extrapolated to the desired distance using the ITTC distance normalisation formulation (ITTC, 2017b), which is given below;

$$SPL_{ITTC} = SPL + 20\log\left(\frac{d}{d_{ref}}\right) \tag{4.19}$$

In this formulation, SPL_{ITTC} is the extrapolated noise level at the desired distance, SPL is the measured noise level at the reference distance, d is the receiver distance from the noise source and d_{ref} is the reference distance. ITTC formulation is generally applied in the experimental facilities to transfer the measured value from the confinement region to free field conditions. As clearly stated in the author's previous study (i.e., Sezen and Kinaci, 2019), extrapolation of the noise results from the near field to the far-far field with the aid of ITTC distance formulation does not yield satisfactory results for the far-field noise predictions. However, in this study, ITTC distance formulation can also be used for the extrapolation of the numerical results from far-field to far-field. In this regard, overall URN results predicted with the k-ω SST turbulence

model at 25D and 180^o can be taken as a reference result and extrapolated to 100D and 200D using ITTC distance formulation. Table 4.11 shows computed and extrapolated data. As shown in Table 4.11, unlike the extrapolation of URN results from near field to far-field, ITTC distance formulation can be reliably used to extrapolate noise results from far-field to far-field. It should be noted that this is also valid at every receiver position and different turbulence models, as given in Figure 4.31.

Table 4.11. Extrapolated and predicted noise results at 25D and 180^o (J=0.88).

Receiver	SPL_{FWH} (dB)	SPL_{ITTC} (dB)	Difference %
25D	68.26	-	-
100D	56.21	56.22	0.02
200D	50.18	50.20	0.02

- **J=0.3 near field**

The hydroacoustic analysis is also conducted at J=0.3. As expected, an increase in the blade loading causes an increase in propeller URN. The main features of the vorticity field in the propeller's slipstream remarkably change due to the rapid increase of hydrodynamic gradients between the face and back sides of the propeller blade at J=0.3 (see Figures 4.22 and 4.23).

Similar to the previous advance coefficient (i.e., J=0.88), hydrodynamic and hydroacoustic pressures are compared for the receivers (see Figure 4.26) located around the propeller in Figure 4.32. Figures 4.32A and 4.32B show hydrodynamic and hydroacoustic pressures at Receiver 1, respectively. The hydrodynamic and hydroacoustic pressures predicted by different turbulence models agree with each other, as shown in Figure 4.32C. The pressure fluctuations increase from approximately $\mp$8 to $\mp$18 at J=0.3 compared to J=0.88 due to the higher blade loading (see Figure 4.27).

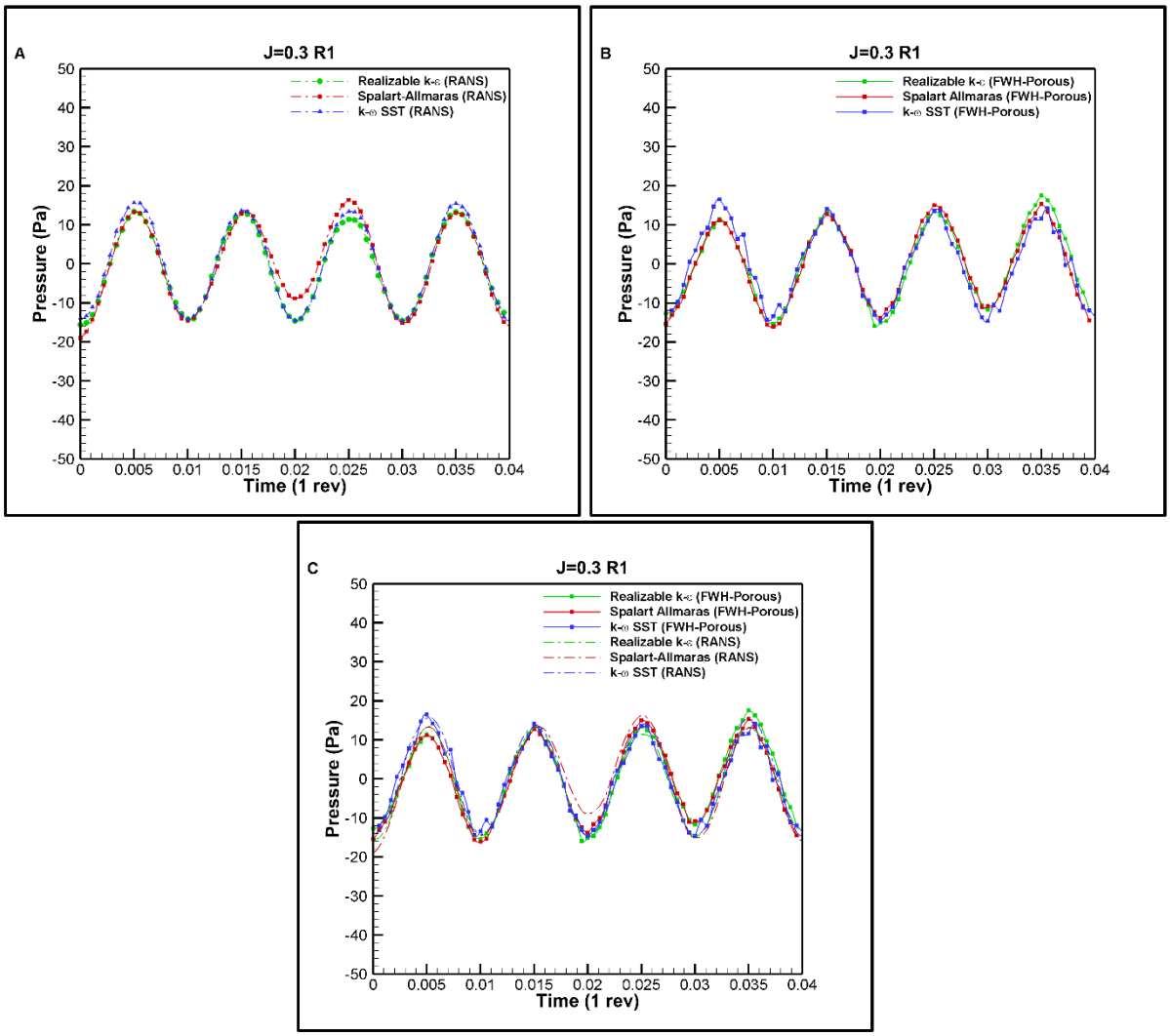

Figure 4.32. Comparison of hydrodynamic and hydroacoustic pressures at Receiver 1 (J=0.3).

A similar comparison between hydrodynamic and hydroacoustic pressures is performed at Receiver 2, as shown in Figures 4.33A and 4.33B. The agreement between hydrodynamic and hydroacoustic pressures is good using different turbulence models, as shown in Figure 4.33C. Also, the hydroacoustic results are compared with another numerical study conducted by Ianniello et al. (2013) in Figure 4.33D, and good agreement is found.

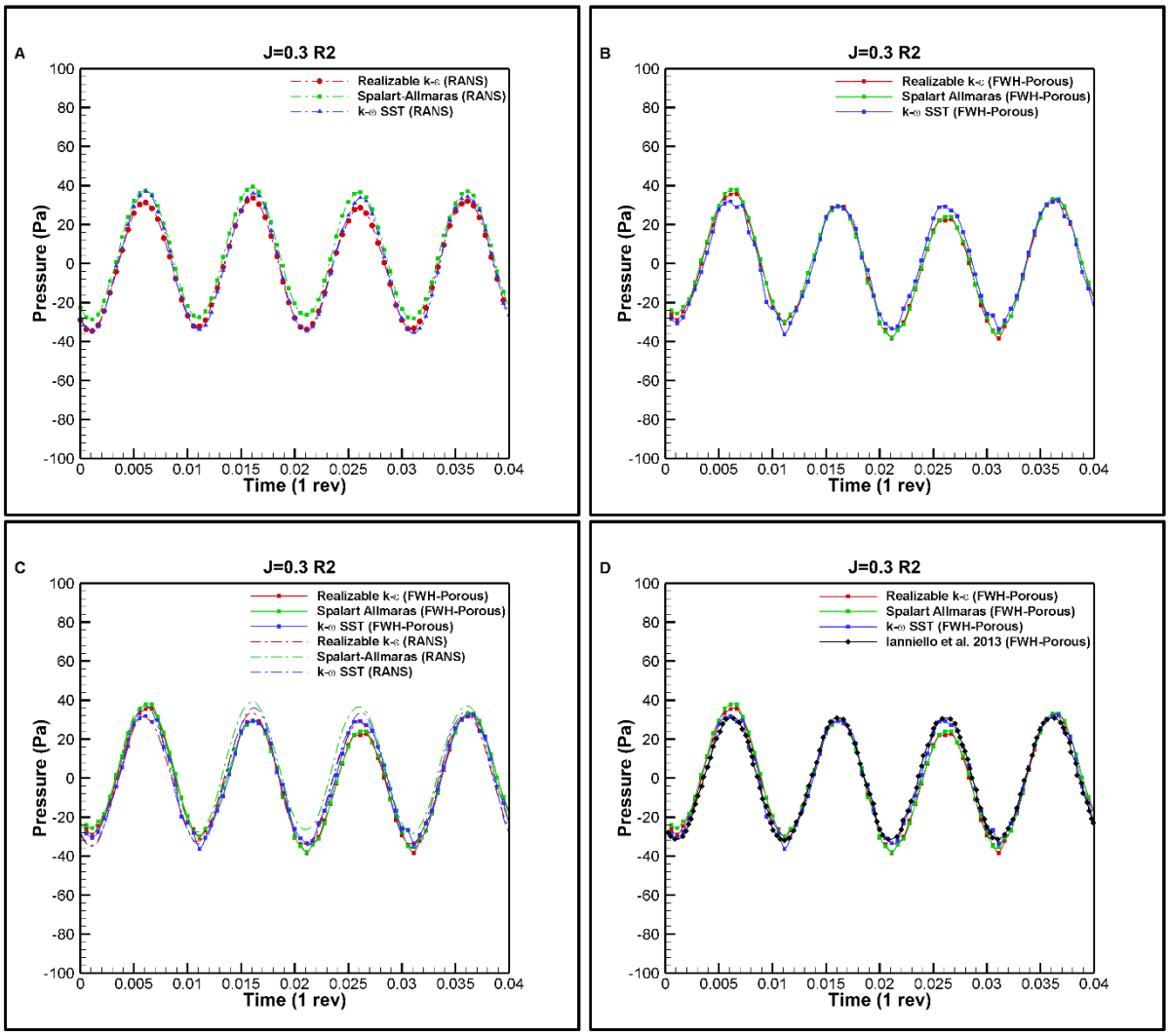

Figure 4.33. Comparison of hydrodynamic and hydroacoustic pressures at Receiver 2 (***J***=0.3).

- ***J*=0.3 far field**

Noise directivity of the propeller is presented under high blade loading conditions in Figure 4.34. Unlike the low blade loading condition (i.e., J=0.88), hydroacoustic results notably change using different turbulence models with the acoustic analogy at J=0.3 in Figure 4.34. This is because flow details in the propeller's slipstream, especially vortex structures, are predicted differently, resulting in dissimilar propeller URN predictions. The previous section shows that the increased blade loading triggers the instability process, and vortices breaks-up in the propeller's slipstream (see Figure 4.23). The k-ω SST turbulence model fails the capture the instability process and smoothes out the vorticity field rapidly compared to the Realisable k-ε and Spalart-Allmaras turbulence models. Thus, the URN levels predicted by different turbulence models with the acoustic analogy are different because of capturing the instability process in the propeller slipstream. The acoustic analogy coupled with the Spalart-Allmaras

turbulence model predicts the highest URN compared to other predictions conducted by Realisable k-ε and k-ω SST turbulence models. As shown in Figure 4.34, the difference between the overall noise levels predicted by using the Spalart-Allmaras turbulence and k-ω SST models together with the acoustic analogy is around 10-15 dB. In contrast, 2-3 dB noise differences are found for the predictions conducted by the Spalart-Allmaras and Realisable k-ε turbulence models. Similar to J=0.88, ITTC distance formulation gives compatible results for extrapolating the results from far-field to far-field at high blade loading conditions at J=0.3. It should be noted that the considerable differences in terms of the overall SPL between J=0.8 and J=0.3 and different turbulence models originate from the prediction of SPL at sub-harmonics in the far-field. When considering the general noise spectrum (i.e., SPL-f), the differences between noise levels decrease at each discrete frequency, especially after the 3rd BPF.

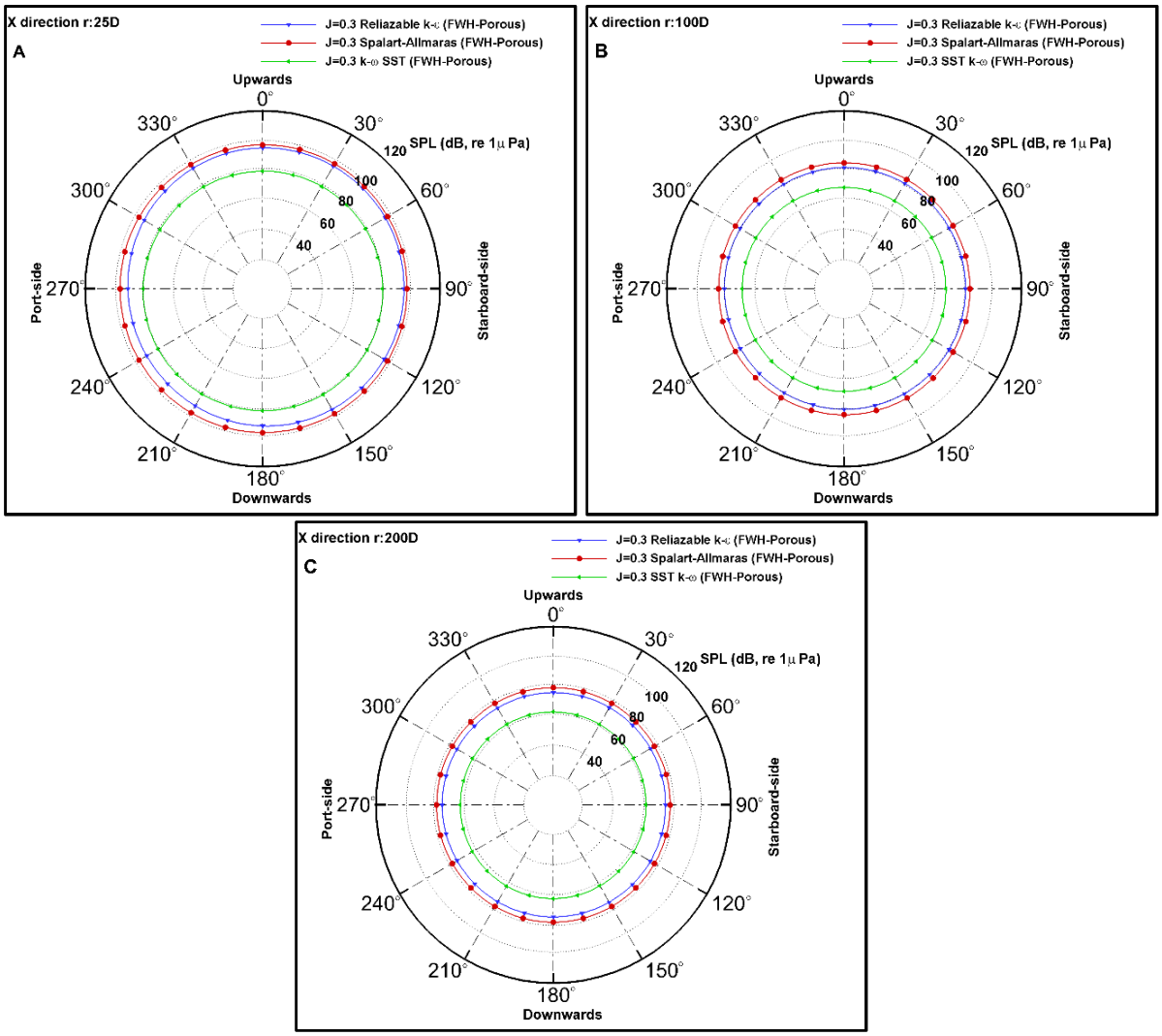

Figure 4.34. Noise directivity of the propeller at J=0.3 (A: 25D, B:100D and C:200D).

4.4 Chapter summary and concluding remarks

This chapter aimed to investigate the importance of the grid resolution, turbulence modelling and nonlinear noise sources (i.e., wake instability) on the overall propeller URN within the context of CFD modelling and acoustic analogy for the accurate prediction of propeller URN. Hence, it presented the benchmark INSEAN E779A model scale propeller hydrodynamic and hydroacoustic performance under non-cavitating conditions. In the numerical calculations, the RANS method, together with k-ω SST, Realisable k-ε and Spalart-Allmaras turbulence models, were utilised to solve the flow field around the propellers, and the source field was determined for the propeller URN predictions. The permeable formulation of the FWH equation was used for the sound propagation to predict the propeller URN both in the near and far-field at low and high blade loading conditions.

The verification study was carried out to evaluate the uncertainty of the numerical solution for the hydrodynamic part of the solution using the GCI method. The propeller open water characteristics and vorticity distribution in the propeller slipstream were validated with the experimental data, and the results showed good agreement. As the experimental propeller URN data was not available for the selected propeller, the numerical predictions were compared with those of other numerical studies conducted with different numerical studies conducted at the same operating condition and receiver location in the literature. The time-based acoustic pressures agreed with other numerical studies regarding amplitude and waveform. The numerical investigations conducted in this chapter, therefore, led to the following conclusions:

- The hydroacoustic analysis was found more dependent on the grid resolution than the prediction of propeller performance characteristics due to the numerical noise mainly induced by the sliding interfaces. Therefore, the grid resolution, specifically designed for the prediction of global hydrodynamic performance characteristics purposes, is not suitable for the accurate prediction of the propeller URN.

- An increase in the grid resolution enabled a considerable reduction in the non-physical numerical noise for the accurate propeller URN prediction. This non-physical numerical noise sources in the flow domain can be visualised successfully using the proposed time derivative of the pressure technique.

- Even though the sliding mesh has been widely used for hydrodynamic studies in the literature, the results showed that this approach suffered from the additional numerical noise induced by the interfaces. The results also indicated that this numerical noise issue in the sliding mesh originates from the grid resolution, and it is independent of the selected numerical methodology (i.e., RANS, DES and LES).

- The time derivative of the pressure technique can also be a more efficient way to determine the accurate extension of vortex structures in the propeller's slipstream. This approach can be beneficial for further in-depth studies using advanced models (i.e., DES and LES). Also, from the hydroacoustic point of view, this approach may provide a basis to determine the integral (permeable/porous) surface location that includes the most energetic part of the relevant nonlinear noise sources.

- An increase in grid resolution reduced the numerical diffusion, allowing for an extended tip vortex. However, it was found that an increase in tip vortex extension and intensity is not sufficiently adequate to make a reliable prediction of propeller URN with the standard RANS methods. A more accurate prediction of the propeller URN can be achieved using the advanced models (i.e., DES and LES), particularly if the receivers located downstream are of great interest.

- With an increase in the blade loading, the flow properties in the propeller slipstream significantly changed. In particular, the vortex structure lost its stability and evolved into the far-field. This instability process in the propeller slipstream was predicted alternatively using the different eddy viscosity turbulence models.

- The numerical results showed that the similar vortex structure in the propeller slipstream predicted by different eddy viscosity turbulence models resulted in similar propeller URN prediction at low blade loading conditions. However, an increase in the blade loading (i.e., at high blade loading conditions) triggered the vorticity break-up phenomenon, which was dissimilar to the ones caused by different eddy viscosity turbulence models at high blade loading conditions.

- The results showed that the acoustic pressures were dominated by the contribution of linear noise sources in the near field, where the receivers were located in the proximity of the propeller. Thus, the different predictions of vortex structures, particularly at high blade loading conditions, did not change the overall acoustic pressures in the near field.

Yet, as the contribution of nonlinear noise sources became dominant in the far-field, the dissimilar prediction of vortex structures caused a difference in the overall propeller URN levels at high blade loading conditions in the far-field. Eventually, the numerical results suggested that the instability process, vortex instability and break-up phenomenon can be the major nonlinear noise source contributing to the overall propeller URN levels at high blade loading conditions.

- The numerical results showed that the ITTC distance formulation could be reliably used to extrapolate the URN levels from far-field to far-field.

5 Enhanced tip vortex cavitation modelling of a marine propeller

5.1 Introduction

Cavitation for marine propellers is the most important phenomenon affecting the propeller URN apart from its powering performance, vibrations and material integrity. Therefore, this chapter aims to develop an advanced meshing procedure in CFD, called the Vorticity-based Adaptive Mesh Refinement (V-AMR) technique, for the accurate solution of tip vortex flow and propeller cavitation with a specific emphasis on the TVC modelling. Most of the time, TVC is the earliest type of cavitation to incept on a propeller, and its contribution to URN can be significant and complex.

The chapter first briefly explains the theoretical background used in the numerical calculations within the above framework. This is followed by the details of the numerical CFD modelling, including the propeller geometry, test matrix, computational domain, boundary conditions, grid resolution and analysis properties. The chapter then presents the numerical results, including the effects of key numerical modelling parameters (e.g., time step, grid resolution, turbulence modelling, cavitation modelling parameters, and boundary layer resolution) by comparing the CFD approach with the experimental data. Finally, the chapter summary and concluding remarks are given in the last section.

5.2 Theoretical background

The simulations were conducted using the Star CCM+ commercial solver under cavitating conditions (Star CCM+ 14.06, 2019). Cavitation is a phase change and is assumed to occur when the static pressure at a particular location within the liquid becomes equal to or smaller than the saturation vapour pressure, depending on the water quality. Cavitation bubbles are assumed to be consist of cavitation nuclei which are tiny bubbles filled with vapour or gas or a combination of them. The number of small nuclei is higher than those of larger nuclei in the fluid due to the stable nature of the small bubbles under their higher surface tension (Sipilä, 2012). In this study, the Schnerr-Sauer cavitation model based on the reduced Rayleigh Plesset equation was used to model sheet and tip vortex cavitation within the facilities of the commercial solver (Star CCM+ 14.06, 2019). In this model, seeds are assumed to be spherical and uniformly distributed in the liquid, and all seeds initially have the same radius. The Volume of Fluid (VOF) method, first introduced by Hirt and Nichols 1981, was used to describe the phase transition of liquid into vapour or vice versa. Detailed information about the VOF and

cavitation model can be found in Star CCM+ 14.06, 2019 and Schnerr and Sauer 2001, respectively.

In the numerical simulations, the three different simulation methods, RANS, DES and LES, and the associated approaches were used to solve the flow around the cavitating propeller. The RANS method is based on the solution of the time-averaged equations in the fluid domain, whereas LES is based on filtered differential equations. DES is a hybrid method combining the RANS in the boundary layer and LES in the free field region. The improved formulation of DES (i.e., DDES) was used in this study. The k-ω SST turbulence model was selected for the RANS and DDES methods.

Additionally, the WALE (Wall-Adapting Local-Eddy viscosity) subgrid-scale model was used to close the filtered Navier-Stokes equations for the LES. Also, the large scales of the turbulence are directly resolved everywhere in the flow domain in the LES, while the small scales are modelled. Despite its several limitations, the RANS method is still used for many engineering problems due to its lower computational cost compared to scale resolving simulations (i.e., DES and LES), particularly in the design stage. The detailed information about the numerical methods can be found in Spalart et al., 2006 and Star CCM+ 14.06, 2019.

In the above described three different methods, the segregated flow model was used with a SIMPLE type algorithm between the continuity and momentum equations. The second-order implicit unsteady scheme was employed for the time discretisation. As well as this, the convection term was discretised using the second-order scheme in the RANS and DES methods, whereas its discretisation was provided with the bounded central scheme for the LES. The propeller rotational motion was modelled using the RBM (Rigid Body Motion) approach in an unsteady manner, while the MRF (Moving Reference Frame) approach was also used as an initial solution in a steady manner for the unsteady simulations. The simulations were initially started without a cavitation model using the MRF approach to avoid any numerical stability problems due to the cavitation. The inner iteration was set to 7 for all models.

5.3 Numerical modelling

5.3.1 Propeller geometry and test case

The benchmark INSEAN E779A model propeller was selected in this chapter, similar to Chapter 4. The cavitating flow around this model propeller was compared with the numerical solutions conducted by different facilities in the scope of the Rome 2008 Workshop in uniform flow under non-cavitating and cavitating conditions (Salvatore et al., 2009). The non-cavitating results were found to be in good agreement with each other, whereas some discrepancies were observed for the cavitating flow case. Also, the TVC could not be predicted successfully using different flow methods. Thus, this propeller was deemed to be a suitable test case to show the capabilities of the proposed V-AMR technique. The numerical simulations were performed in the presence of sheet, hub and tip vortex cavitation and only included the sheet and hub vortex cavitation. In this way, the capabilities of the V-AMR technique would be proven at different levels. Table 5.1 summarises the properties of the test case.

Table 5.1. Test case description.

Parameter	Symbol and Unit	Value
Advance ratio	J (-)	0.71
Rotation Rate	n (rps)	36
Inflow averaged velocity	V_A (m/s)	5.8
Cavitation number	σ (-)	1.763
Vapour pressure	P_V (Pa)	2337

Various non-dimensional coefficients were used to present the propeller performance in presenting the test results. The cavitation number is defined with respect to the propeller rotational rate as in Equation 5.1.

$$\sigma = \frac{P_0 - P_V}{\frac{1}{2}\rho(nD)^2} \tag{5.1}$$

where P_0 is the static pressure (Pa), P_V is the vapour pressure (Pa), ρ is the density of the fluid (kg/m^3), n is the propeller rotational rate (rps), and D is the propeller diameter (m).

5.3.2. Computational domain and boundary conditions

Figure 5.1 shows the computational domain used in the numerical calculations. The domain was extended by 3D and 7D upstream and downstream from the propeller centre, respectively, whereas the radius of the domain was set to 4D. The red surface of the domain was the velocity inlet, whereas the green surface was the pressure outlet. The remaining surfaces of the domain were defined as symmetry planes. In addition, the propeller blades and hub were identified as a wall with the no-slip condition to satisfy the kinematic boundary condition. The transition between the rotating and static regions was provided with the sliding interfaces.

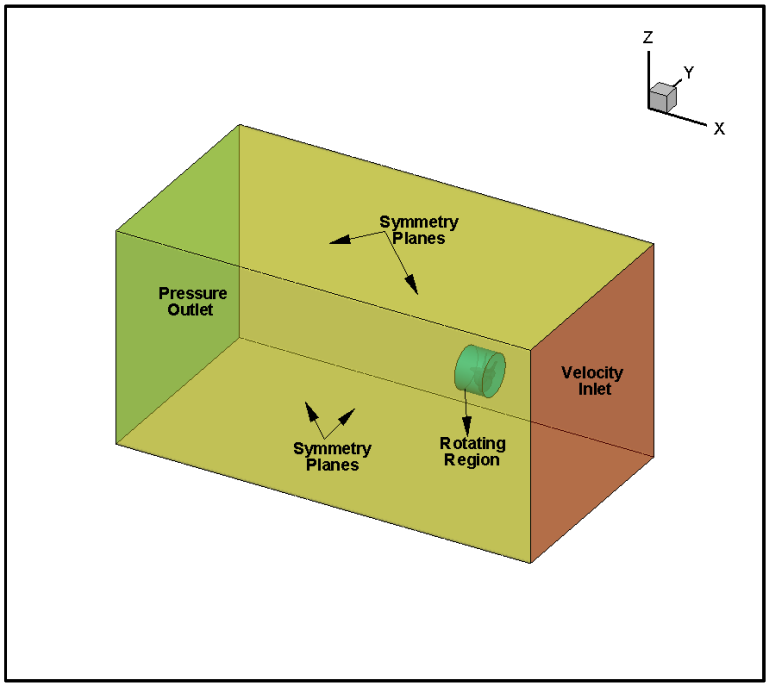

Figure 5.1. Representation of computational domain.

5.3.2 Grid Structure and Vorticity-based Adaptive Mesh Refinement (V-AMR) Technique

The implementation of a suitable grid structure is important for the accuracy of the numerical solution. Thus, the grid should be as adequate as possible to solve the flow around cavitating propellers but in an efficient manner to avoid impracticalities. In particular, the solution of the tip vortex is more dependent on the grid resolution inside the vortex, and it requires high-resolution grids in all directions. However, the application of high-resolution grids in the entire propeller slipstream would inevitably increase the total cell number in the numerical calculations, resulting in an increased computational cost. Thus, AMR becomes appealing as

it can decrease the computational cost considerably while still accurately predicting the area of interest.

AMR is a mesh technique, and it refines or coarsens the cells in the specified regions of the computational domain according to the adaptive mesh criteria. The solution quantities are automatically interpolated to the new adapted mesh locations. One of the challenges in the AMR technique is the selection of an appropriate refinement criterion. The refinement criterion can be selected either as a scalar (e.g., pressure) or as a gradient (e.g., vorticity) quantity to create the cells in the tip vortex trajectory. As stated in the study by Yvin and Muller, 2016, the shape of the pressure field in the transversal direction looked like a Gaussian function; thus, it was difficult to conclude whether the location of the minimum pressure inside the vortex was in the centre or not. For this reason, it was suggested that the refinement criterion should not be chosen value of pressure itself (Yvin and Muller, 2016). Hence, the vorticity based Q criterion was selected as the refinement criterion for the AMR application in this study.

As well as the refinement criterion, it is also important to select the suitable cell size for the accurate flow solution inside the vortex. In this regard, Asnaghi, 2018 and Asnaghi et al., 2020a performed a comprehensive numerical study to investigate the cell numbers per vortex radius for the accurate solution of the tip vortex flow for an elliptical foil. Kuiper 1981 also conducted a series of experimental tests using different model scale propellers for investigating the bubble, sheet and tip vortex cavitations. Kuiper, 1981 studied the relationship between cavitation index (σ) and core radius (a_c). According to his experimental results, the core radius was measured around 0.25mm at the cavitation inception for the model scale propellers. Hence, based on the analysis of these investigations (Asnaghi, 2018; Asnaghi et al., 2020a; Kuiper, 1981) , the vortex's cell size was set to be changed from 0.2mm to 0.3mm to detect the influence on TVC.

The proposed V-AMR technique involves two main steps. Once the flow field converges using the initial mesh (i.e., without AMR), the tip vortex areas can be visualised using the threshold value of Q-criterion (see Figure 5.2A). In this study, the threshold value of the Q-criterion was selected as $Q = 400.000\ 1/s^2$ at the 1st stage to allow for sufficient extension of the helical structure to the downstream of the rotating region boundary using the LES method. As can be seen in Figure 5.2A, the helical structure of the tip vortex shows the regions where the magnitude of the Q criterion is higher than the selected threshold value ($i.e. Q = 400.000\ 1/s^2$). It is also important to note that the determined refinement area with the

threshold value of Q criterion shows the cells around the hub, which is not of interest. Hence, the additional user-based field functions were also imposed on the V-AMR solution algorithm to avoid the generation of redundant cells, with the sole refinement located in the tip vortex trajectory (see Figure 5.2B). When the field of interest was determined, the refinement table was generated in all directions with the user-based field functions. In the 1st stage of the V-AMR procedure, the tip vortex trajectory was revealed using relatively coarse grids. Following the 1st stage of the V-AMR (i.e., after two or three propeller revolutions), the 2nd stage of the V-AMR procedure was implemented with the new threshold value of Q criterion ($Q = 5.000.000\ 1/s^2$) in our case, see Figure 5.2C). The advantage of this two-stage application of the V-AMR procedure is to decrease the total element count in the numerical solver and hence, the computational cost. The reason is that the actual tip vortex radius is small when compared to the helical structure of the tip vortex radius, which was determined in the 1st stage of V-AMR (see Figure 5.2A). If the V-AMR application were directly implemented with smaller cell size (i.e., 2nd stages of V-AMR) without determination of the tip vortex trajectory in the 1st stage of the V-AMR, the total element count would increase excessively. The adopted grid refinements can be seen in Figure 5.2D using the V-AMR procedure's two stages. It is to be noted that the above procedure can be repeated three or four times to observe the TVC. However, from the author's experience and some test studies, it was found that any more than two stages do not give considerable benefit in terms of the extension of the TVC in the model scale for the application of the V-AMR procedure. Thus, two steps of V-AMR were implemented in this PhD thesis. It is to be noted that the threshold value of the Q criterion is dependent on the operating condition. Hence, it should be set based on the visualisation of the tip vortex trajectory in the propeller slipstream.

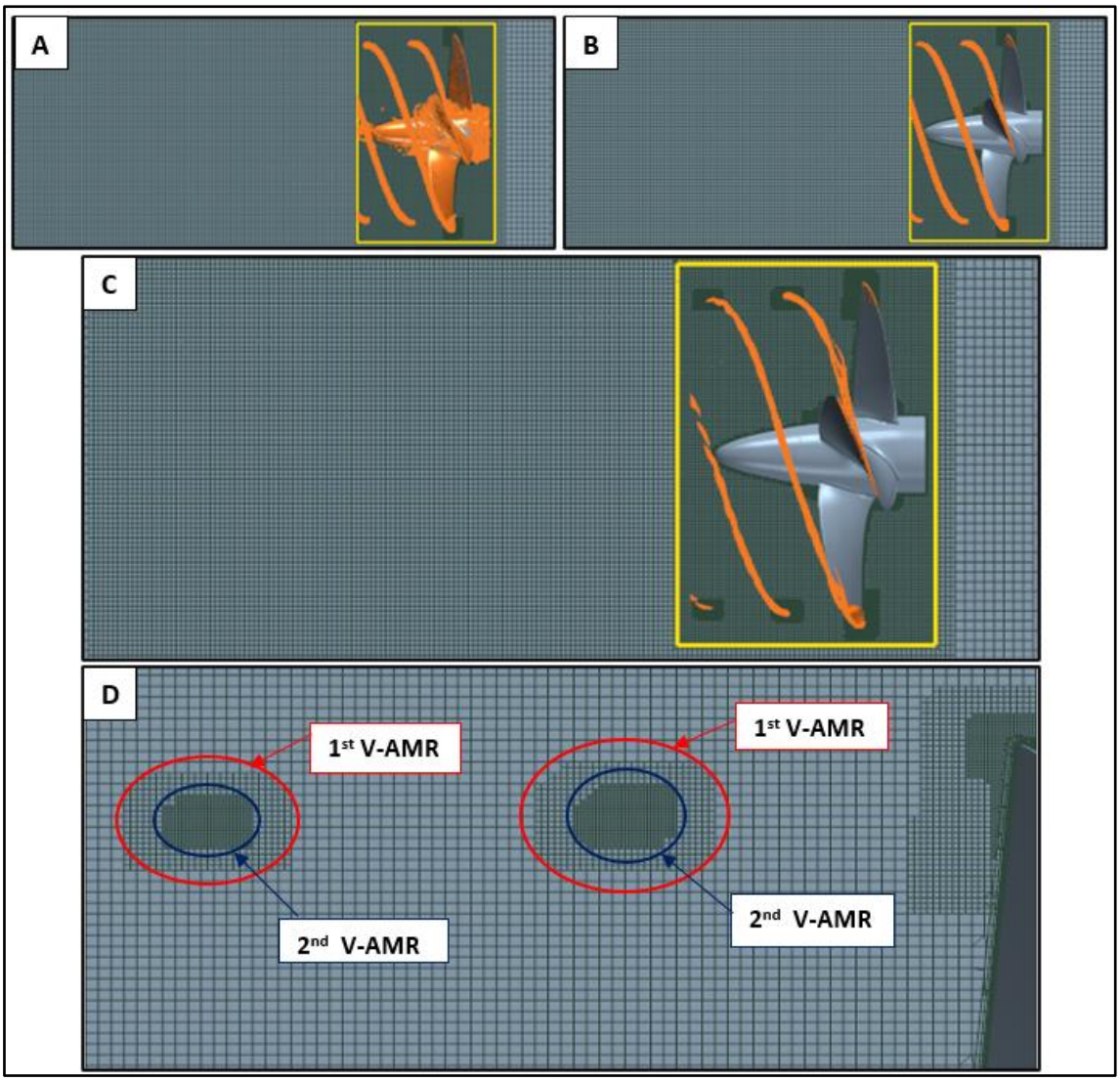

Figure 5.2. Refinement regions with the V-AMR technique.

The unstructured grid was used in the numerical calculations to discretise the computational domain using the trimmer mesh approach in Star CCM+ 14.06, 2019. The same grid structure and refinement table were used for the RANS, DES and LES methods. Later on, the effects of the grid on the extension of TVC were examined using different grid structures by the LES method. The average y^+ value on the propeller blades was kept under 1 for all methods. In this way, the boundary layer was directly resolved without using the wall function approach. A flow chart for the developed V-AMR technique is also given in Figure 5.3 to summarise the algorithm used.

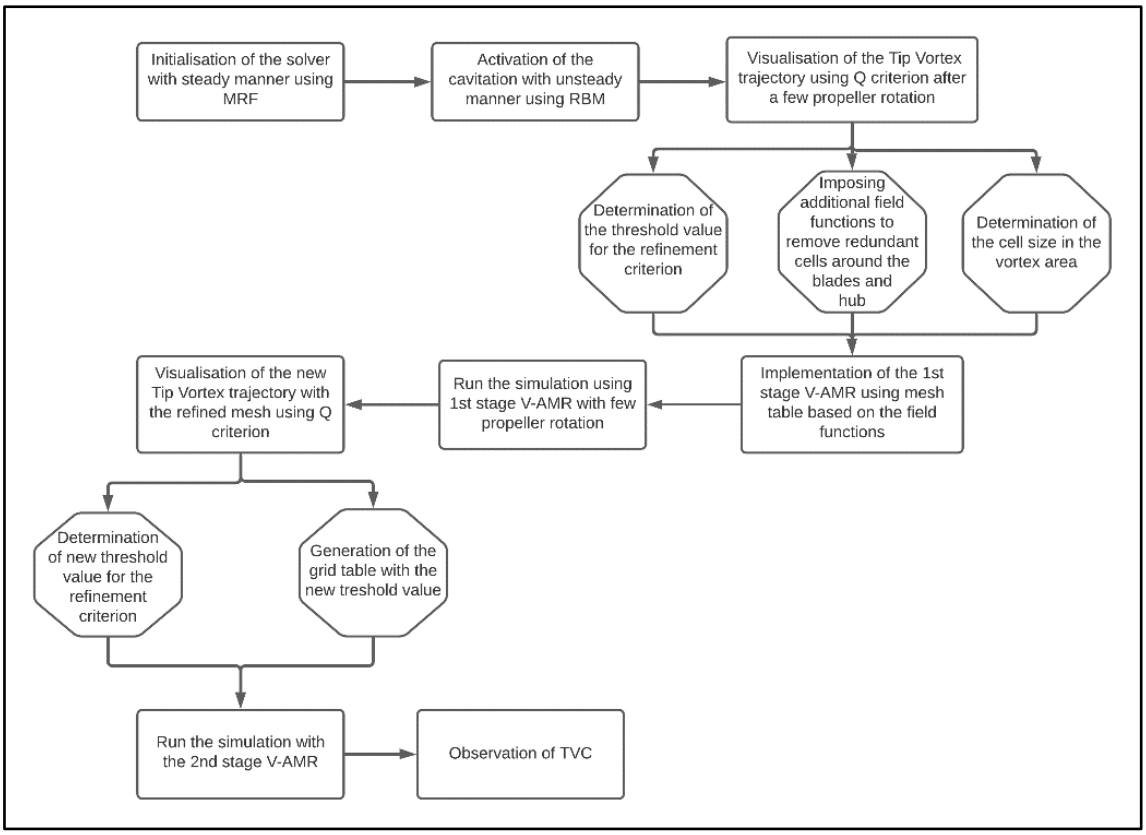

Figure 5.3. The flow chart of the algorithm used in the V-AMR procedure.

5.4 Numerical results

5.4.1 Influence of AMR on hydrodynamic field and cavitation

In this section, the results were presented with the initial mesh and further refinement of the mesh to see the effect of the V-AMR technique on the hydrodynamic field around the propeller, hydrodynamic performance characteristics of the propeller, and TVC formation using the RANS, DES and LES methods. It is to be noted that the same grid structure, including the same cell size in the tip vortex region (i.e., 0.2mm), the timestep (i.e., 0.5^{o} of propeller rotation rate) and the default cavitation parameters (i.e., water quality) were used. In this way, the capabilities of different numerical methods were compared.

The effects of the V-AMR technique on the hydrodynamic field were compared with the two axial planes located at x/D=0.05 and x/D=0.1 in the propeller's slipstream using the three different methods. Figures 5.4 and 5.5 show the change in the non-dimensional pressure coefficient at the propeller blade tips, where the tip vortex is more pronounced for x/D=0.05 and x/D=0.1, respectively. As shown in Figures 5.4 and 5.5, the pressure inside the vortex core is lower than its surroundings, and it increases gradually outside of the vortex region. The

overall distribution of the pressure field is found to be similar without the application of the V-AMR technique for different models at x/D=0.05. As further away in the propeller downstream, the low-pressure region is slightly more distinct using the LES method without the V-AMR technique. However, the low-pressure region becomes more prominent with the RANS, DES and LES methods applying the mesh refinement. Additionally, the low-pressure field is more stretched in the LES when compared to the RANS and DES at two different sections.

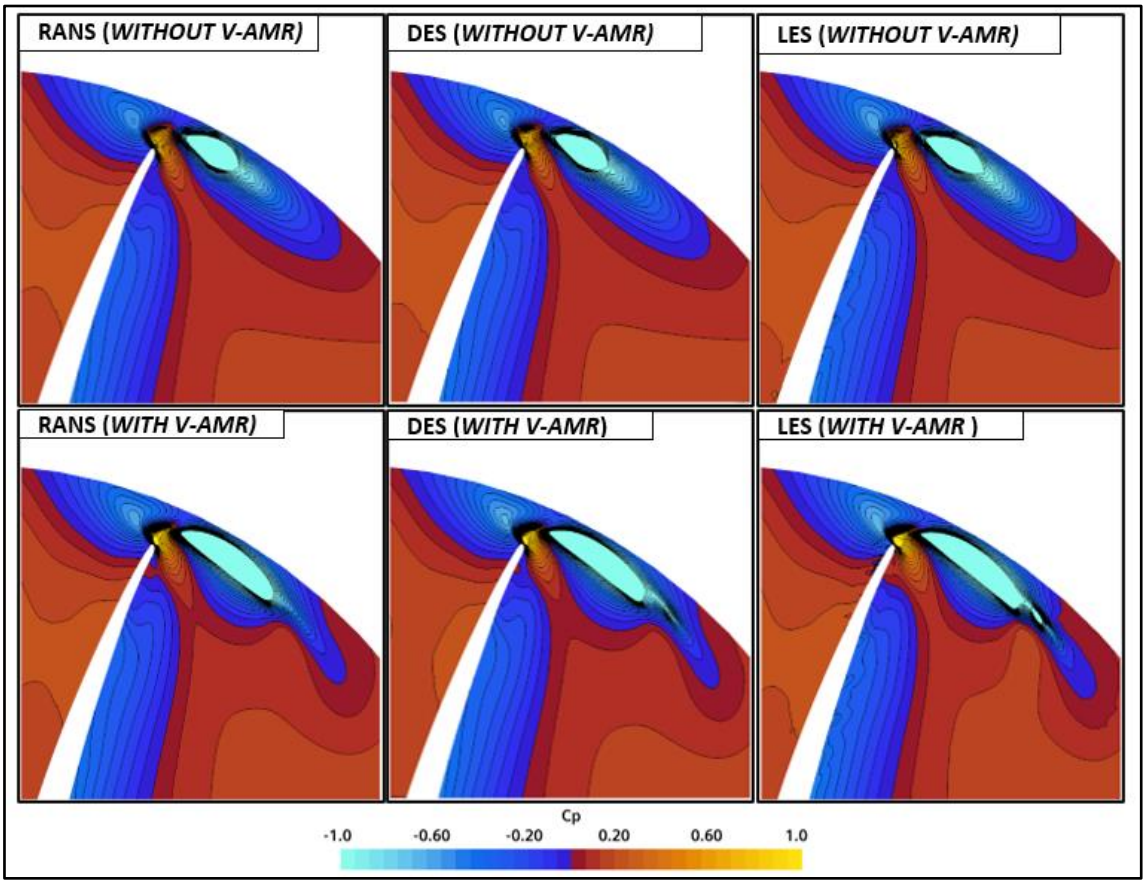

Figure 5.4. The change in the pressure field at x/D=0.05 ($C_p = \frac{P}{0.5\rho(nD)^2}$).

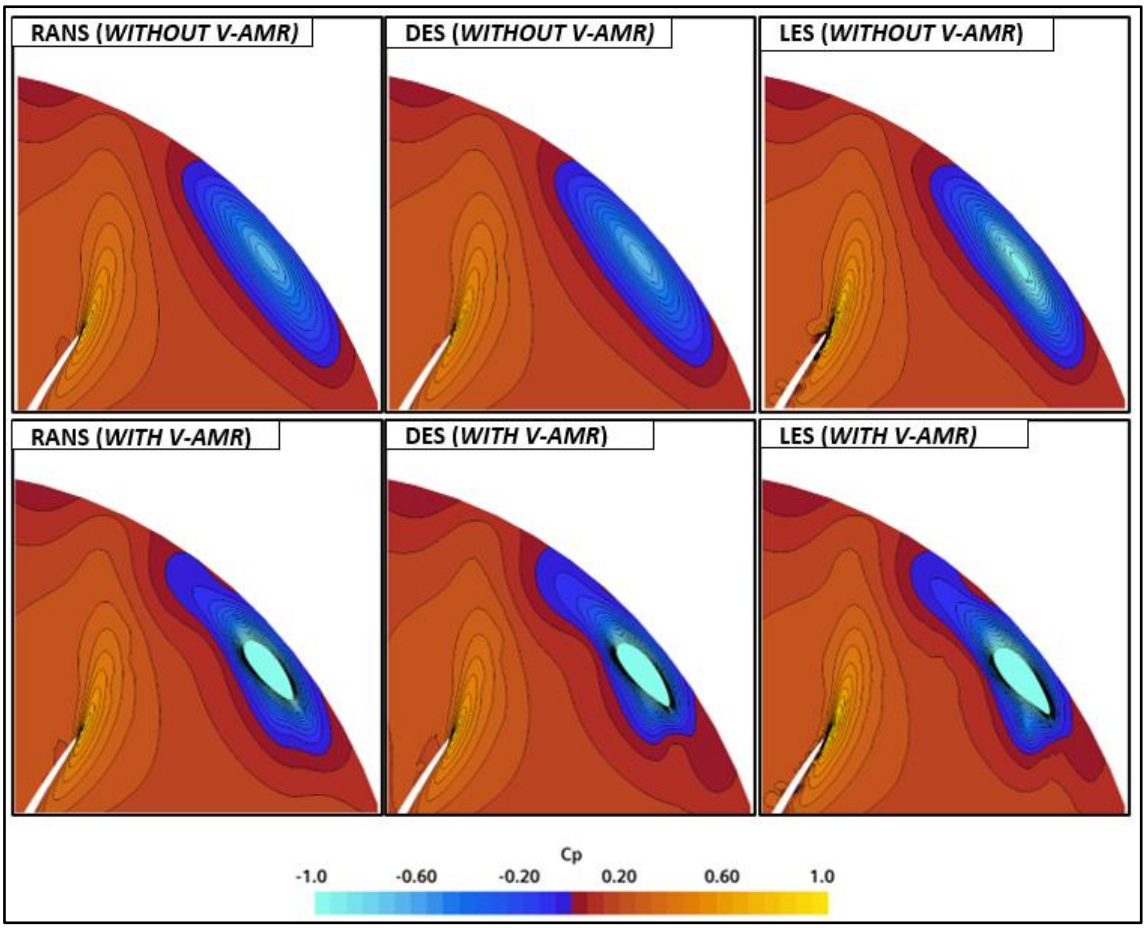

Figure 5.5. The change in the pressure field at x/D=0.1 ($C_p = \frac{P}{0.5\rho(nD)^2}$).

Further comparisons were performed to investigate the turbulent eddy viscosity ratio patterns, as shown in Figures 5.6 and 5.7, between the RANS and DES-based results as the same turbulence model was used. The turbulent eddy viscosity ratio (also known as eddy viscosity ratio) is the ratio of the turbulent viscosity (μ_t) and dynamic molecular viscosity (μ). This ratio can also be considered an indication of the additional dissipation created by the turbulence model. As shown in Figures 5.6 and 5.7, when the V-AMR technique is applied, the RANS method presents an excessive eddy viscosity compared to that predicted by the DES method, which is expected to lead to rapid dissipation of the tip vortex in the propeller slipstream. This is because the standard RANS methods use the eddy viscosity concept to model the Reynolds stress tensor. This concept, also called Boussinesq approximation, assumes that the anisotropic part of the Reynolds stress tensor is linearly proportional to the time-averaged strain rate tensor, and the turbulence is presumed locally isotropic (Pope, 2000). Thus, the standard RANS methods are not successful for the accurate solution of the anisotropic turbulence inside the vortex core compared to scale resolving simulations (i.e., DES and LES). This leads to an insufficient extension of TVC in the propeller slipstream (Wang et al., 2015). However, the V-

AMR technique reduces the eddy viscosity ratio with the DES, which is expected to result in further extension of TVC downstream of the propeller since all turbulent scales are not modelled in the DES method compared to the RANS.

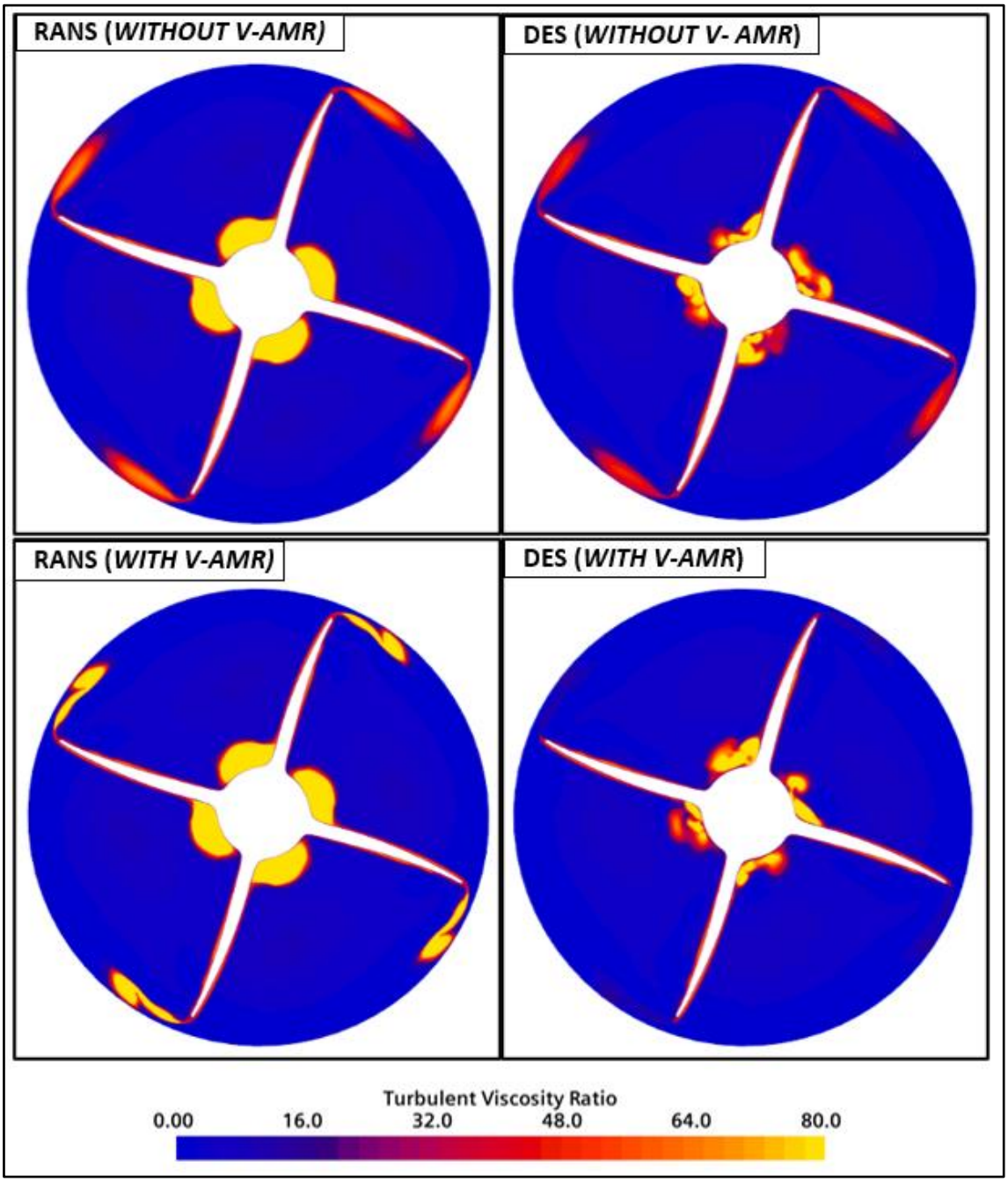

Figure 5.6. The change in eddy viscosity ratio at x/D=0.05.

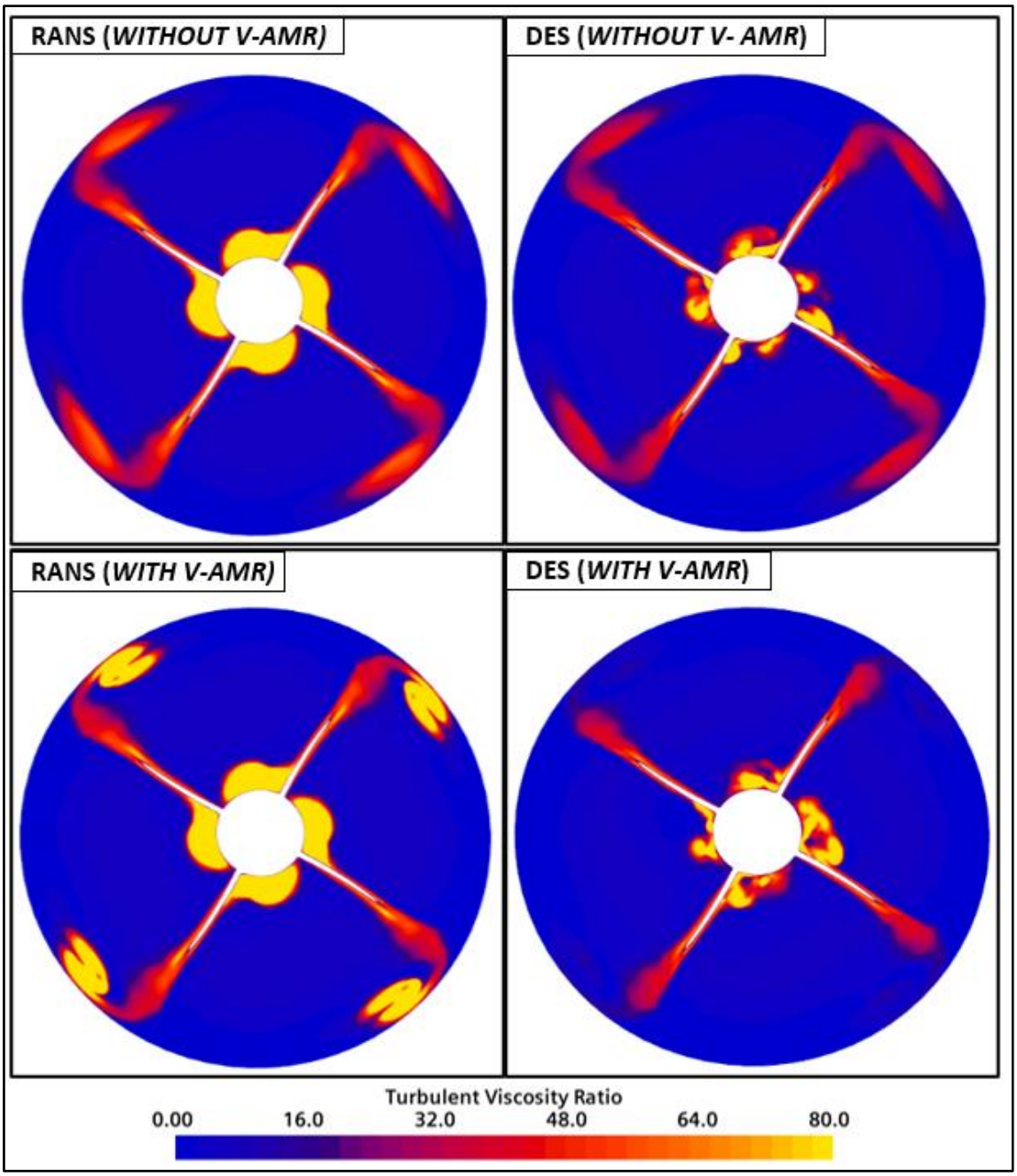

Figure 5.7. The change in eddy viscosity ratio at x/D=0.1.

Following the investigation of the hydrodynamic field in the propeller slipstream with and without applying the V-AMR technique, the cavitation extensions predicted by the different methods were compared with the experimental cavitation observation. Figure 5.8 shows the cavitation extension observed in the experiment, which involves sheet, tip vortex and hub vortex cavitation at the specified operating condition.

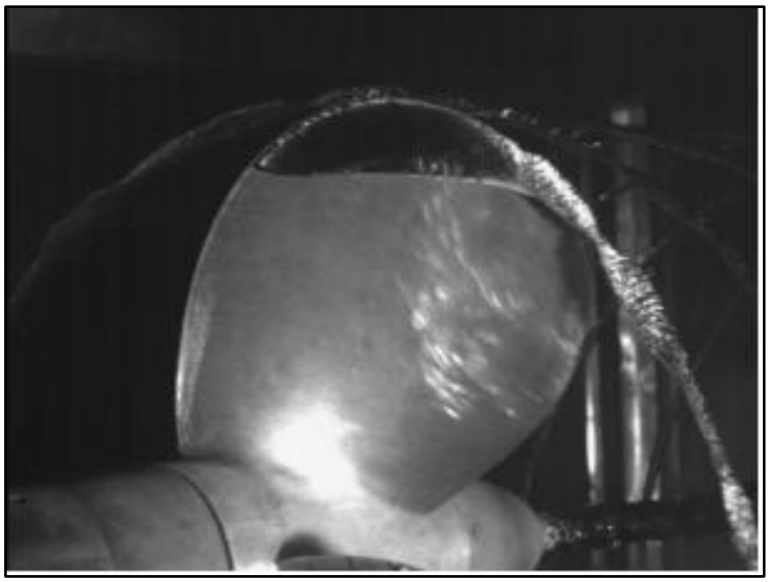

Figure 5.8. Experimental observation of cavitation pattern at J=0.71 and $\sigma = 1.763$ (Salvatore et al., 2009).

Figure 5.9 compares the three cavitation types observed in the model tests with their counterparts predicted by the RANS, DES and LES methods with and without applying the V-AMR technique. The red lines indicate the isosurface of α_v=0.1 (volume fraction of vapour). As shown in Figure 5.9, the sheet cavitation extensions are predicted similar by all three methods without the V-AMR technique, whereas the extension of the hub vortex cavitation is predicted differently. This is due to the superiority of the LES and DES methods through the solution of vortex structures compared to the RANS method. In the numerical calculations, the sheet cavitation is slightly overpredicted using different methods compared to the experimental observation (see Figure 5.8). If one considers the three simulation results using the V-AMR technique, an accurate representation of the tip vortex cavitation can be observed by capturing reduced minimum pressure inside the vortex and the roll-up of the tip vortex cavitation by all three numerical methods. The application of the V-AMR technique does not change the sheet cavity pattern and hub vortex cavitation. However, large differences are observed between the RANS and DES & LES in terms of the extension of TVC in the propeller slipstream with the application of the V-AMR technique. The excessive eddy viscosity predicted inside the vortex by the RANS method results in an inadequate (shorter) extension of the TVC in the propeller slipstream compared to the DES and LES methods. This overprediction of the turbulent viscosity around the cavity region is one of the deficiencies of the standard RANS methods, apart from the inadequate turbulence modelling. This consequently influences the accurate prediction of unsteady cavitation behaviour and the development of the re-entrant jet

(Goncalves et al., 2010 and Bensow, 2011). Nevertheless, this needs to be further investigated in a study solely focused on this subject.

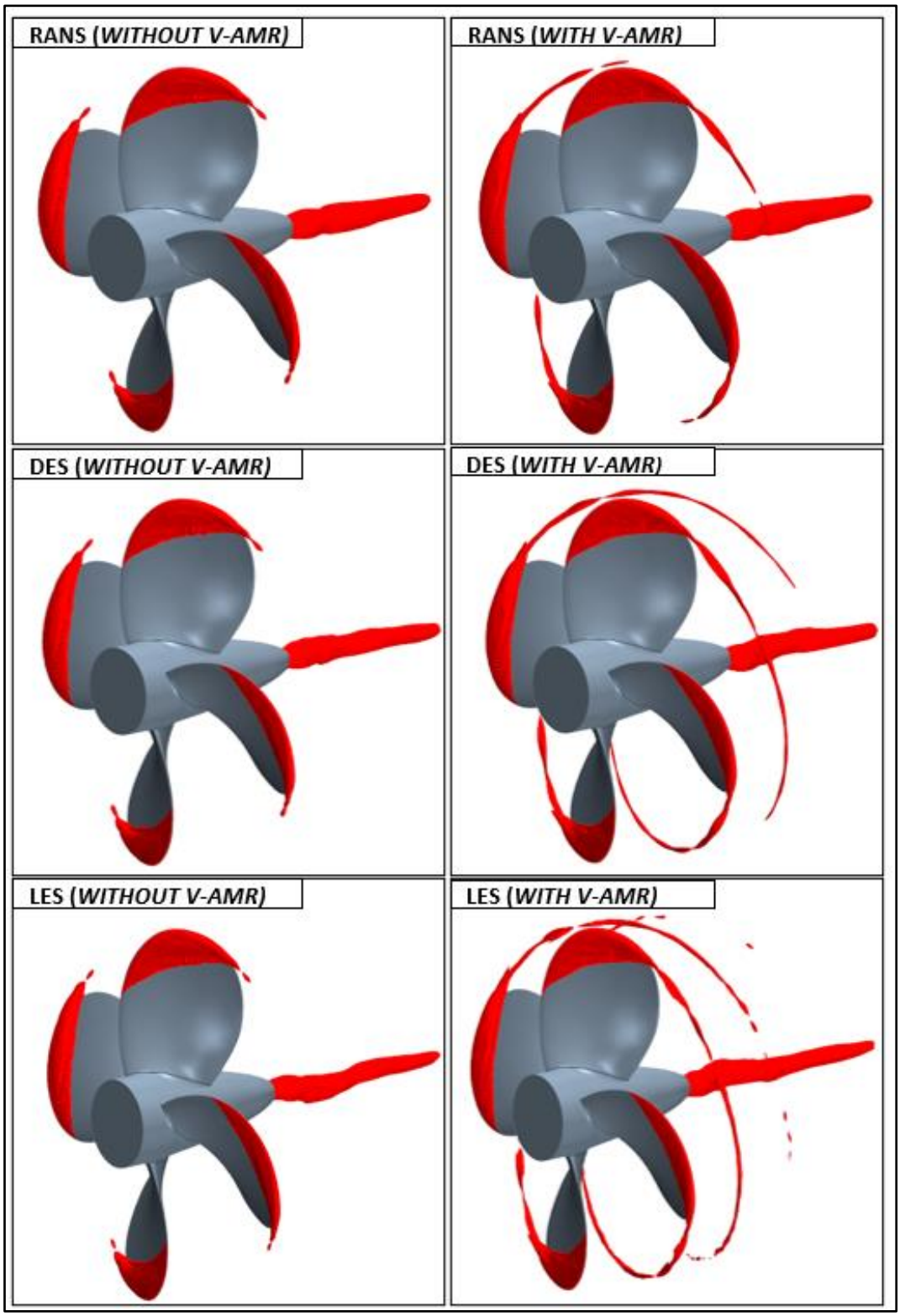

Figure 5.9. Comparison of sheet, tip and hub vortex cavitation with RANS, DES and LES methods ($\alpha_v = 0.1$).

The comparison of the propeller thrust, torque and efficiency predicted by the three numerical methods against the experimentally measured values is given in Table 5.2. As expected, the TVC has a negligible influence on the hydrodynamic coefficients for all models. Also, the thrust and torque coefficient values are predicted similarly by the RANS and DES methods. In contrast, these values are different by around 3% compared to those predicted by the LES method, as given in Table 5.2.

Table 5.2. Comparison of propeller hydrodynamic coefficients.

	LES			DES			RANS		
	K_T	$10K_Q$	η_0	K_T	$10K_Q$	η_0	K_T	$10K_Q$	η_0
WITHOUT V-AMR	0.245	0.421	0.658	0.241	0.431	0.632	0.241	0.432	0.630
WITH V-AMR	0.245	0.422	0.656	0.241	0.431	0.632	0.242	0.433	0.632
EXPERIMENT (Salvatore et al., 2009)	0.255	0.460	0.626	0.255	0.460	0.626	0.255	0.460	0.626

5.4.2 Effects of key simulation parameters on TVC with the LES method

In this section, the effects of the grid resolution and timestep on the prediction accuracy of the TVC are investigated. For this purpose, the LES method is used with default cavitation parameters (i.e., water quality) since the sufficient extension of the TVC is obtained by the LES and DES methods compared to the RANS as indicated in the previous section.

5.4.2.1 Influence of grid structure

As stated in Section 5.3.3, the accurate solution of the tip vortex is sensitive to the selection of the numerical techniques and grid resolution in the vortex region. Thus, as shown in Table 5.3, three different grid resolutions are utilised to investigate the effect of the grid resolution on the TVC extension in the propeller slipstream. It is to be noted that the time step was kept constant as 0.5^o of the propeller rotational rate and default cavitation parameters were selected for this investigation.

Table 5.3. Grid parameters for TVC extension investigation.

Grid Type	1st Refinement Cell Size (mm)	Refinement Factor (1st Refinement)	2nd Refinement Cell Size (mm)	Refinement Factor (2nd Refinement)	Total Number of Cells (Millions)
Fine w/o V-AMR	-	-	-	-	8.842.287
Fine with V-AMR	0.40	Cell Size/4	0.20	Cell Size/8	17.721.807
Medium with V-AMR	0.50	Cell Size/4	0.25	Cell Size/8	11.637.147
Coarse with V-AMR	0.60	Cell Size/4	0.30	Cell Size/8	9.083.751

Figure 5.10 shows the predicted TVC extensions with the application of the 1st and 2nd stages of the V-AMR technique, respectively, using a fine grid resolution. As shown in Figure 5.10, in the 1st refinement stage, the trajectory of TVC is determined using a relatively coarse grid (i.e., 0.4mm). Then the total extension of TVC is obtained by applying the 2nd refinement stage of the V-AMR technique to make the solution more computationally affordable.

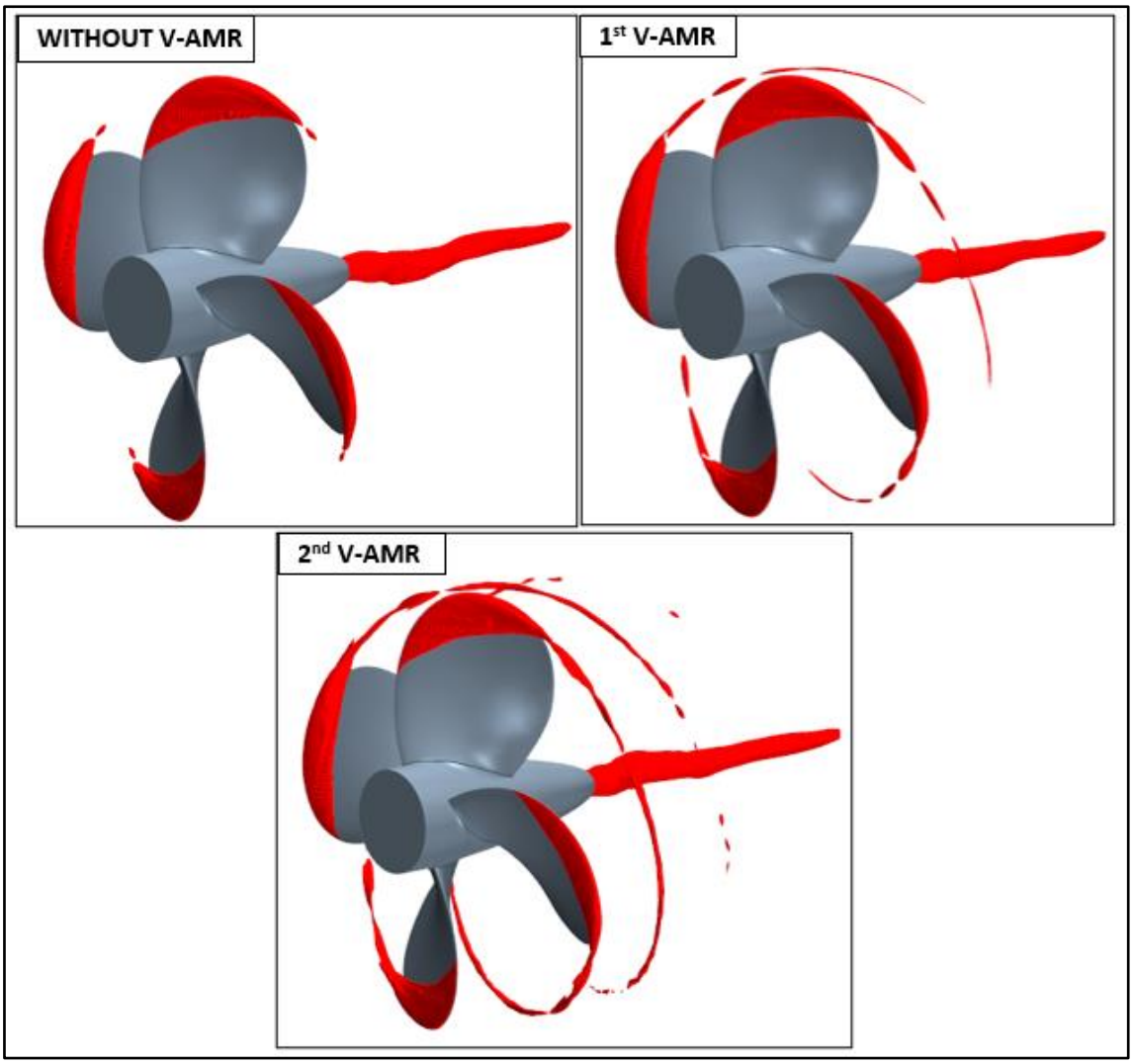

Figure 5.10. Development of TVC in the propeller's slipstream with two stages of the V-AMR technique using the LES method ($\alpha_v = 0.1$).

Figure 5.11 shows the change in the extensions of TVC in the propeller slipstream with an increase in the grid resolution inside the vortex. As shown in Figure 5.11, the TVC becomes more stretched downstream with an increase in the refinement level. No discernible differences could be observed between the results of the medium and fine grid structure applications. Thus, one may assume that the accurate solution of the TVC can be achieved by creating approximately 3M additional cells (i.e., medium mesh) by modelling the TVC emanating from all propeller blades. This proves the feasibility of the proposed V-AMR technique for numerical applications. In addition to this, the roll-up phenomenon of the tip vortex is well captured using the different grid resolutions compared to that observed by the experiment, as shown in Figure 5.8.

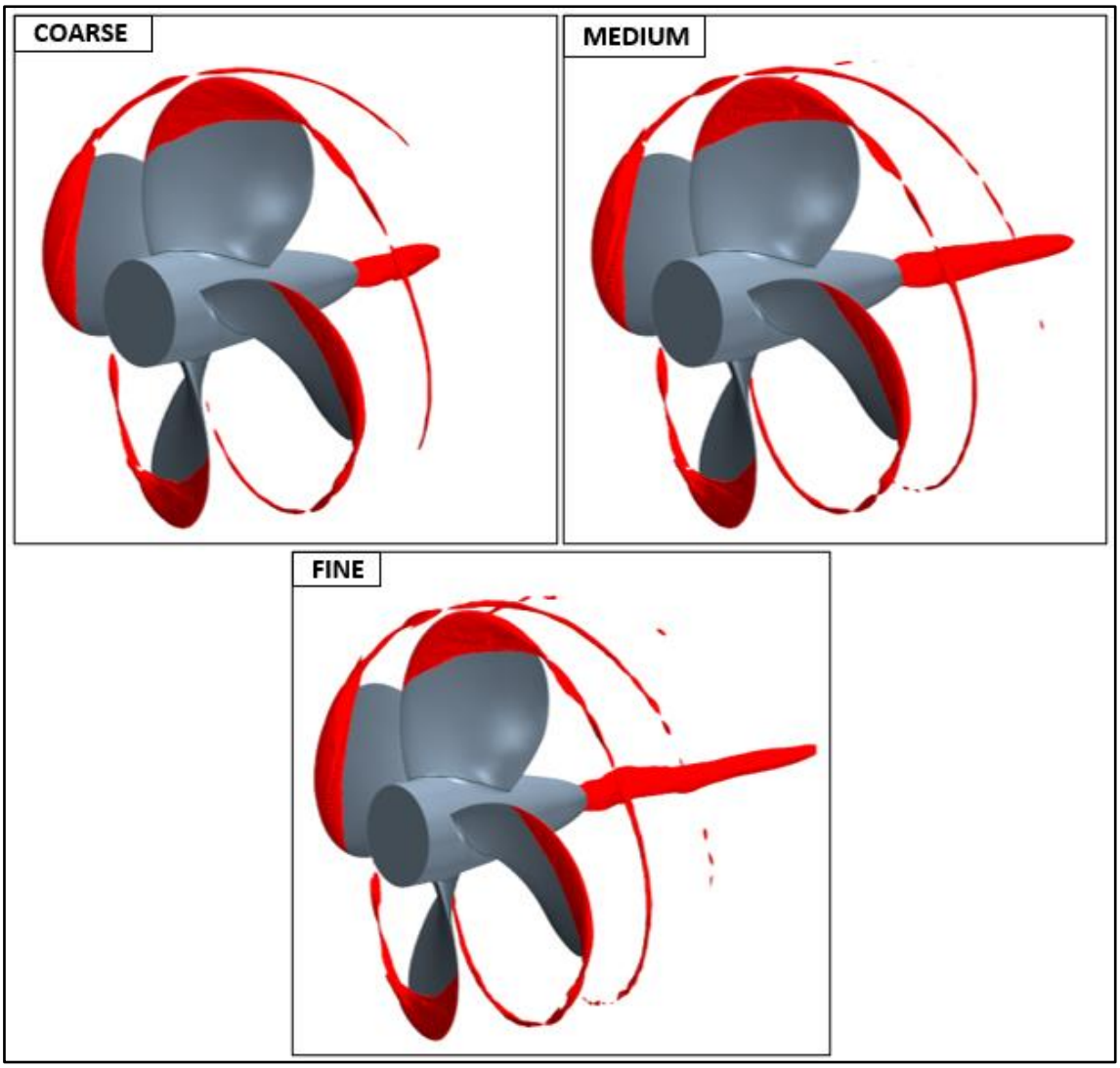

Figure 5.11. Comparison of TVC extension with different grid resolutions using the LES method ($\alpha_v = 0.1$).

In order to calculate the numerical uncertainty of the solution due to the grid spacing, the GCI (Grid Convergence Index) method was performed by following the ITTC guideline (ITTC, 1999), as used in Chapter 4. Table 5.4 shows the solution scalars computed by different grid resolutions at constant timestep (i.e., 0.5^o of propeller rotational rate). Here, φ is the solution scalar, R is the convergence condition, e_a is the discretisation error due to the extrapolated zero grid spacing, and GCI_{FINE} is the uncertainty level of the solution. As given in Table 5.4, the uncertainty level of the solution due to the grid spacing is calculated below than 1% for both thrust and torques coefficients. Additionally, the convergence condition (i.e., R) is found below than 1 which determines the solution type as monotonic convergence. It should be noted that the CFL (Courant–Friedrichs–Lewy) number was not kept constant during the uncertainty study as the GCI method is implemented using one variable. As the numerical approach is implicit, the CFL requirement is not associated with the stability of the time scheme.

Nevertheless, CFL number was kept below 1, particularly in the propeller slipstream, for the accuracy of the solution for different grids.

Table 5.4. The results of the spatial convergence study.

J=0.71, σ=1.763	K_T	$10K_Q$
φ_1 (Fine)	0.245	0.422
φ_2 (Medium)	0.246	0.425
φ_3 (Coarse)	0.248	0.429
R	0.500	0.750
e_{ext}^{21}	2.63E-3	8.03E-3
e_{ext}^{32}	1.11E-2	2.11E-2
GCI_{FINE} (%)	0.327	0.996

5.4.2.2 Influence of timestep

Apart from the grid structure and numerical modelling, another key simulation parameter is the time step for the TVC. The influence of the timestep on TVC is examined using the fine grid structure and four different time step values with default cavitation parameters, as shown in Table 5.5.

Table 5.5. The details of the selected timestep values.

Grid Type	Δt (°)	Δt (s)
Fine	0.25	$1.959*10^{-6}$
Fine	0.5	$3.858*10^{-5}$
Fine	1	$7.716*10^{-5}$
Fine	2	$1.543*10^{-4}$

Figure 5.12 shows the change in the sheet, tip and hub vortex cavitation with the timestep. As shown in Figure 5.12, the shape of the sheet cavitation is found to be similar using the different timestep values. However, the extension of the hub and TVC is found to be sensitive to the selection of the timestep. The values between 0.25° and 0.5° do not create considerable differences in terms of the TVC extension in the propeller slipstream. Nevertheless, slight differences are observed in the hub vortex cavitation.

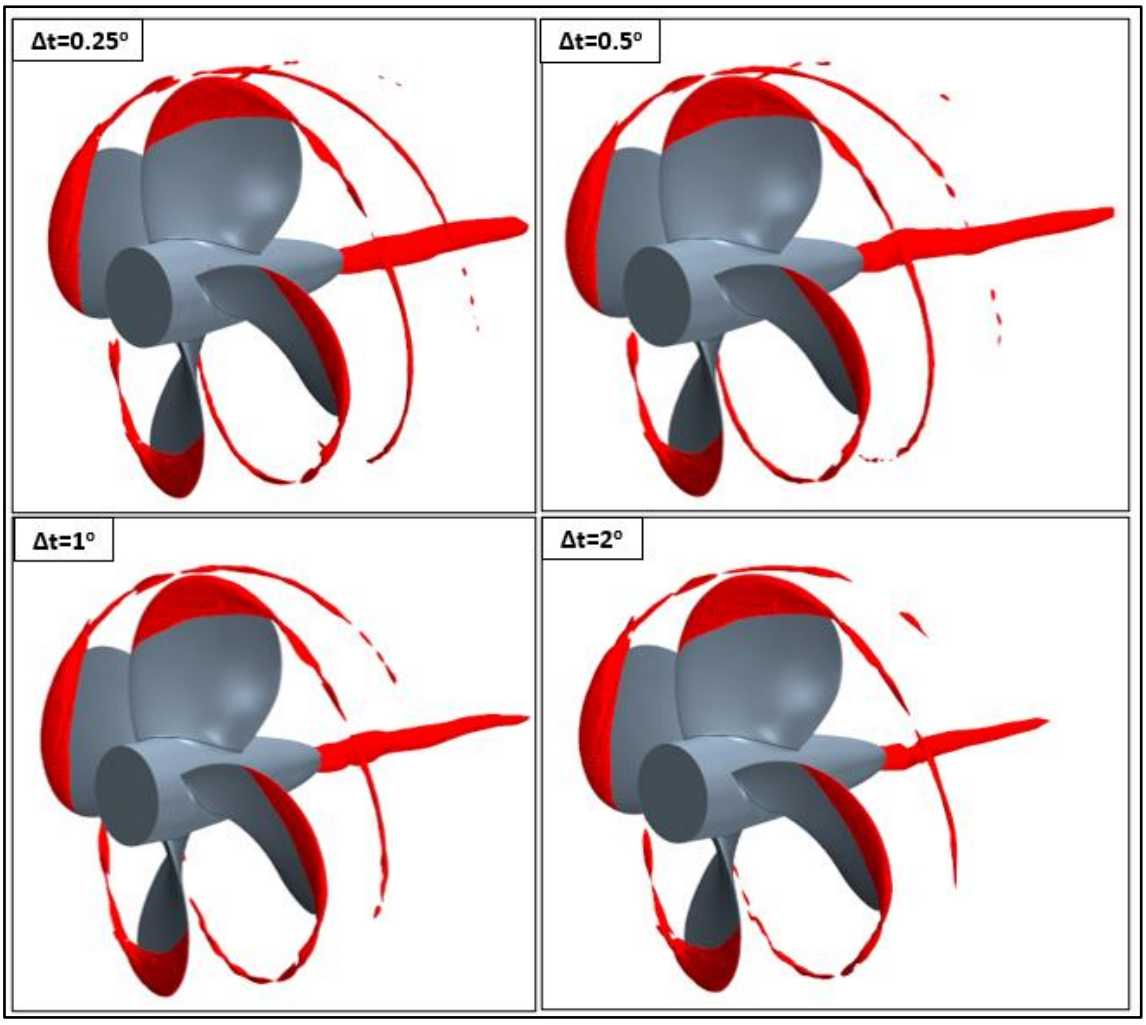

Figure 5.12. Comparison of TVC extension with different timesteps using the LES method ($\boldsymbol{\alpha_v = 0.1}$).

The variation of the total cavity volume with the different time steps is shown in Figure 5.13. As shown in Figure 5.13, the total cavity volume decreases dramatically with the selection of timestep as 1^o and 2^o of propeller rotational rate. This can be associated with the TVC and hub vortex cavitation reduction.

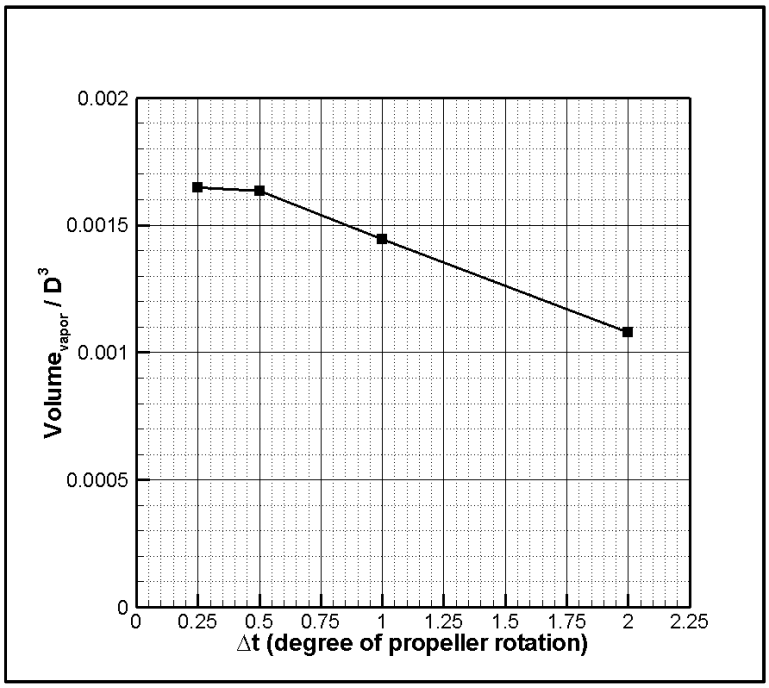

Figure 5.13. Comparison of total cavity volume obtained by using the LES method.

The change in the thrust and torque values with different timesteps is given in Table 5.6. The uncertainty of the numerical solution due to the temporal discretisation was assessed with the GCI approach. The uncertainty level of the solution is found between 0.5% and 2% for thrust and torque values in Table 5.6.

Table 5.6. The obtained hydrodynamic values and uncertainty results using a fine grid with the LES method.

	K_T	$10K_Q$
Δt_1 (°)	0.25	0.25
Δt_2 (°)	0.5	0.5
Δt_3 (°)	1	1
Δt_4 (°)	2	2
φ_1	0.246	0.423
φ_2	0.245	0.422
φ_3	0.243	0.420
φ_4	0.240	0.417
$R(\Delta t_1, \Delta t_2 . \Delta t_3)$	0.500	0.500
$R(\Delta t_2, \Delta t_3 . \Delta t_4)$	0.666	0.666
e_{ext}^{21}	4.05E-3	2.36E-3
e_{ext}^{32}	8.10E-3	4.72E-3
e_{ext}^{43}	2.41E-2	1.41E-2
$GCI_{FINE\ (\Delta t_1 - \Delta t_2 - \Delta t_3)}$ (%)	0.508	0.296
$GCI_{FINE\ (\Delta t_2 - \Delta t_3 - \Delta t_4)}$ (%)	2.041	1.185

5.4.2.3 Influence of cavitation parameters

Cavitation inception is a complex flow phenomenon, and it is strongly affected by the water quality, the growth of the boundary layer and cavitation type (e.g., Korkut and Atlar, 2012). Cavitation nuclei, which are tiny bubbles filled with water or gas or a combination of them, form the cavitation. Thus, cavitation does not incept in water, in which there are no nuclei (i.e., filtered and degassed) (Sipilä, 2012). The filtered and degassed water cavitates alternatively depending on the filtration and degassing process.

In order to perform the comparison between the numerical methods and experiments for the cavitation investigations, the water quality (i.e., nuclei density and nuclei number) should be the same. However, these values are not generally measured during the measurements in the cavitation tunnels introducing some uncertainty in the inception level predicted. Hence, commercial numerical solvers use their default values for cavitation modelling. For instance, the FLUENT solver uses 10^{13} for the nuclei density, whereas Star CCM+ suggests using 10^{12} and 10^{-6} for the nuclei density and diameter, respectively. Additionally, several studies use different values (e.g., Cazzoli et al., 2016 and Shin, 2019). and hence the selection of these values is quite scattered. The effects of these parameters on TVC were investigated in the following.

Table 5.7 shows the selected nuclei diameters for the analysis using the LES method. Figure 5.14 shows the effects of the change in the nuclei diameter from 10^{-5} to 10^{-8} at the constant nuclei density (i.e., 10^{12}) on the cavity volume and extent of the sheet, hub and tip vortex cavitation. As shown in Figure 5.14, the variation of the nuclei diameters has a negligible influence on the sheet and tip vortex cavitation. At the same time, slight differences can be observed in the hub vortex cavitation.

Table 5.7. The selected nuclei diameter values.

Case Number	Grid Type	Δt (°)	Analysis Type	Density ($1/m^3$)	Diameter (m)
1	Fine	0.5	Nuclei Diameter	10^{12}	10^{-8}
2	Fine	0.5	Nuclei Diameter	10^{12}	10^{-7}
3	Fine	0.5	Nuclei Diameter	10^{12}	10^{-6}
4	Fine	0.5	Nuclei Diameter	10^{12}	10^{-5}

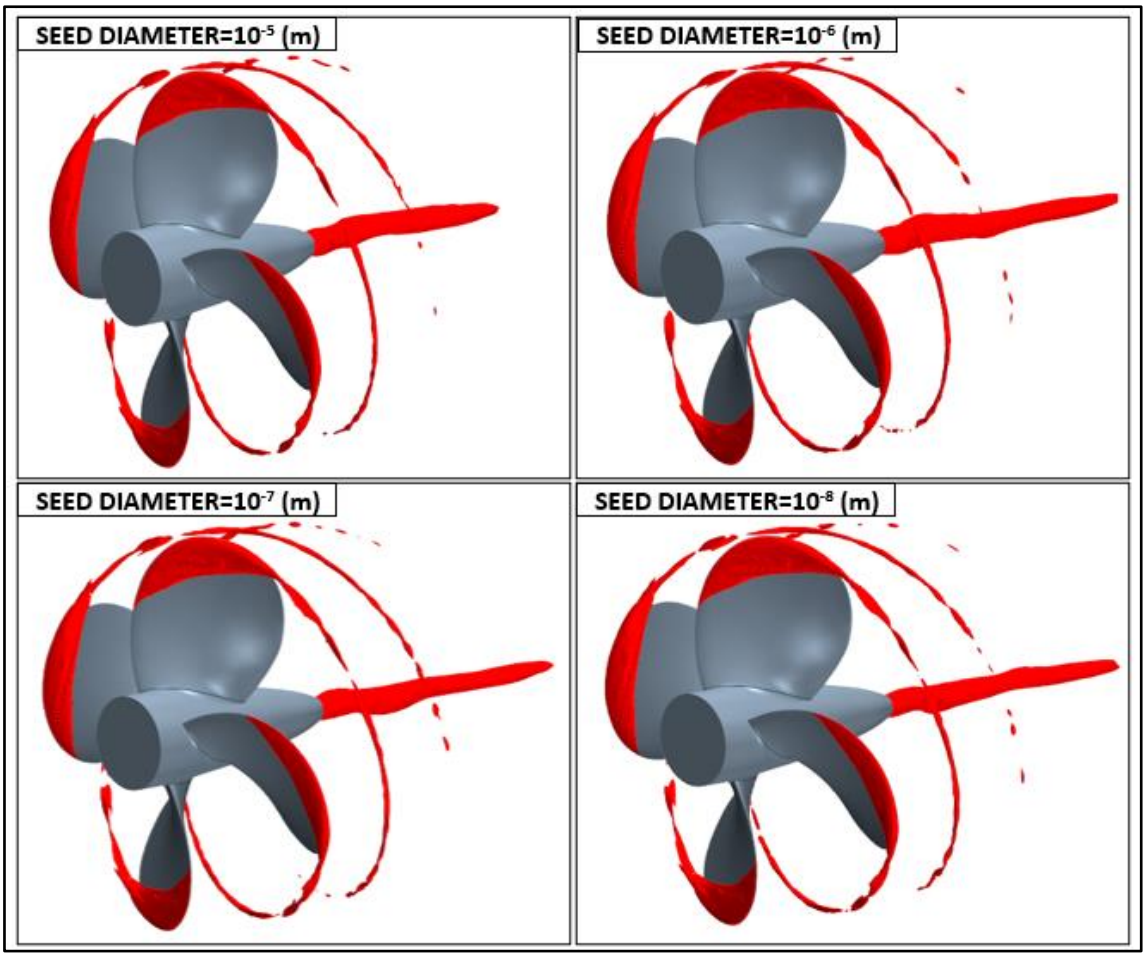

Figure 5.14. Variation of cavitation volume with different nuclei diameters using the LES method ($\alpha_v = 0.1$).

Next is the investigation of the effect of different nuclei density values on the cavitation extensions. The used and selected values used for this investigation are presented in Table 5.8. In this investigation, the nuclei diameter was kept constant at 10^{-6} (i.e., default value). Figure 5.15 shows the resulting effect on the three cavitation extensions. As shown in Figure 5.15, the effects of the nuclei density are more pronounced on the tip and hub vortex cavitation; as such, with the selection of higher nuclei density values (i.e., 10^{14}), the tip and hub vortex cavitation disappear rapidly. Thus, the results suggest that higher values of nuclei density should not be selected for the tip and hub vortex cavitation investigations in the numerical studies using the Schnerr-Sauer cavitation model unless experimental values are available.

Table 5.8. The selected nuclei density values.

Case Number	Grid Type	Δt (°)	Analysis Type	Density ($1/m^3$)	Diameter (m)
1	Fine	0.5	Nuclei Density	10^{11}	10^{-6}
2	Fine	0.5	Nuclei Density	10^{12}	10^{-6}
3	Fine	0.5	Nuclei Density	10^{13}	10^{-6}
4	Fine	0.5	Nuclei Density	10^{14}	10^{-6}

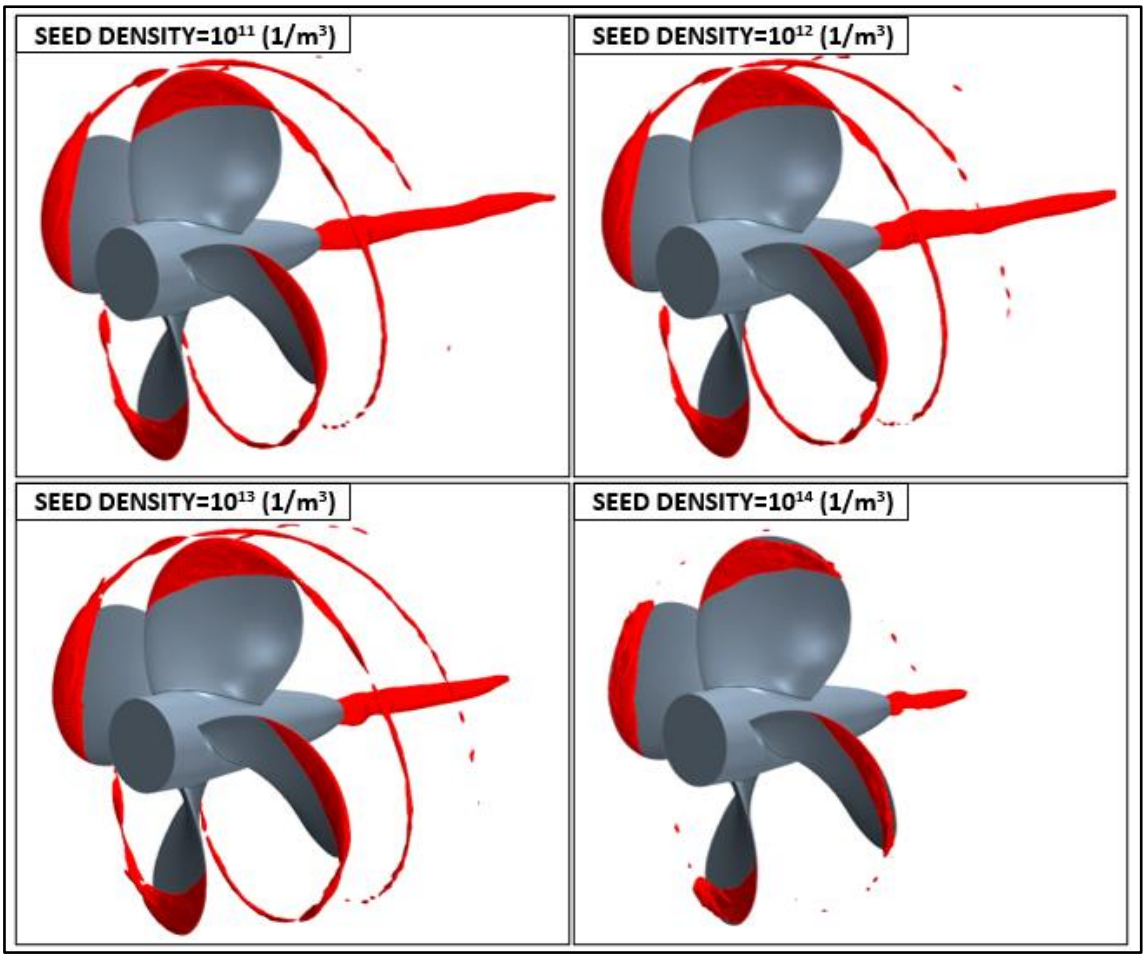

Figure 5.15. Variation of cavitation volume with different nuclei densities using the LES method ($\alpha_v = 0.1$).

Figure 5.16 shows the change in the total cavitation volume by selecting different nuclei densities and numbers. Although the effects of cavitation parameters on the hydrodynamic performance coefficients are negligible, the total cavitation volume changes significantly, particularly with the selection of higher nuclei densities. This analysis confirms the reliability of the default values applied in the Schnerr-Sauer cavitation model in the commercial solver for model scale propellers (i.e., Star CCM+ 14.06, 2019). It is recommended that these values need be explored with the full-scale investigations in further studies as the cavitation dynamics will be different in full-scale compared to the model-scale.

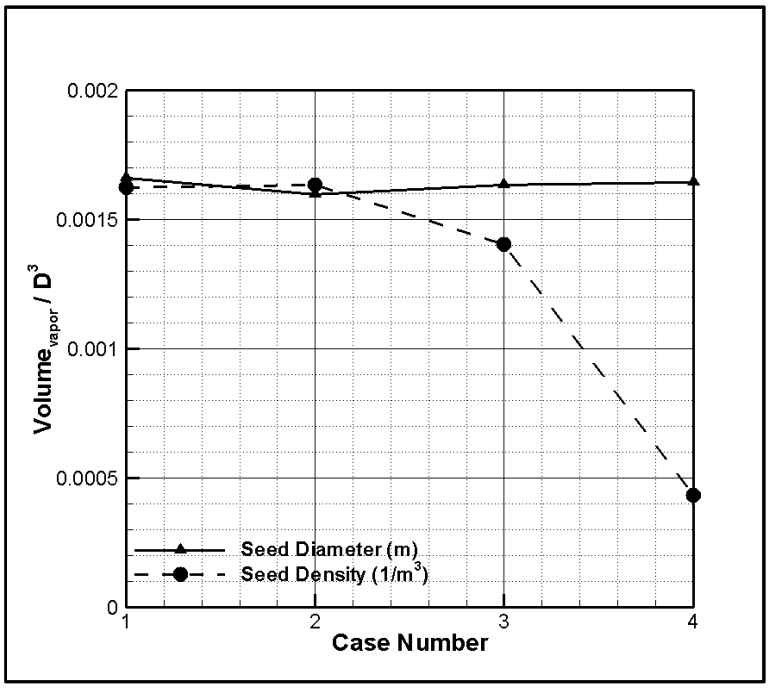

Figure 5.16. Change in total cavitation volume with different nuclei densities and diameters using the LES method.

5.4.3 Influence of boundary layer resolution on TVC for standard RANS method

As demonstrated in the previous sections, scale resolving simulations (i.e., DES and LES) are more successful in predicting the TVC than predictions with the standard RANS methods. Despite this fact, the standard RANS methods have been generally implemented for representing cavitating flows around the propellers, particularly in the preliminary design stage. Therefore, the evolution of the tip vortex was examined by changing the boundary layer resolution as the initial roll-up phenomena, and the sensitivity of the evolution of the TVC to the boundary layer solution was demonstrated in the literature (e.g., Hsiao and Chahine 2008; Gaggero et al., 2014). Here, in this section, the author also explored such capability of the standard RANS methods using the subject model propeller. In this investigation, the timestep was kept constant at 0.5^o and cavitation parameters were taken as default values (i.e., nuclei density= 10^{12} and nuclei diameter=10^{-6}) in the numerical calculations.

Accurate computation of the flow near-wall is important in many turbulent flows modelling. However, this requires a higher grid resolution to resolve all turbulence boundary layer details, especially in high Reynold numbers. In the standard RANS methods, this issue is commonly tackled by implementing the wall-function approach and considering the universal behaviour of the near-wall flows to reduce the computational cost. The wall-function approach models the flow variables near the wall by keeping the first cell of the prism layer in the log-law region

(where 30< y^+<500) instead of resolving (Versteeg and Malalasekera, 2007; Craft et al., 2002). On the other hand, resolving the boundary layer without using the wall function increases the accuracy of the solution (Defraeye et al., 2011). To implement the latter approach, the y^+ value was kept between 0 and 5. Table 5.9 shows the details of the grid resolution in the boundary layer. By keeping the constant prism layer thickness and overall grid structure, only the prism layer numbers are changed from 14 to 4 with a stretching ratio of 1.5, as shown in Table 5.9.

Table 5.9. The details of the mesh properties in the near-wall for the RANS method.

Grid Type	Averaged y^+ on the blades	Prism Layer Number	Prism Layer Thickness (mm)
Fine	0.67	14	0.0013
Fine	2.7	11	0.0013
Fine	39	5	0.0013
Fine	64	4	0.0013

Figure 5.17 shows the change in the sheet, hub and tip vortex cavitation with different near-wall resolutions. The overall pattern of the sheet and hub vortex cavitation remains the same, both using the wall function approach and resolving the boundary layer itself. With an increase in the averaged y^+, the TVC becomes intermittent, and the extension of TVC reduces gradually. As experienced by the author, the further increase in the average y^+ values lead to the deterioration of the roll-up phenomena; thus, the considerable reduction in the extension of TVC. Due to this reason, an accurate solution of the near-wall is important to predict the TVC using the RANS methods.

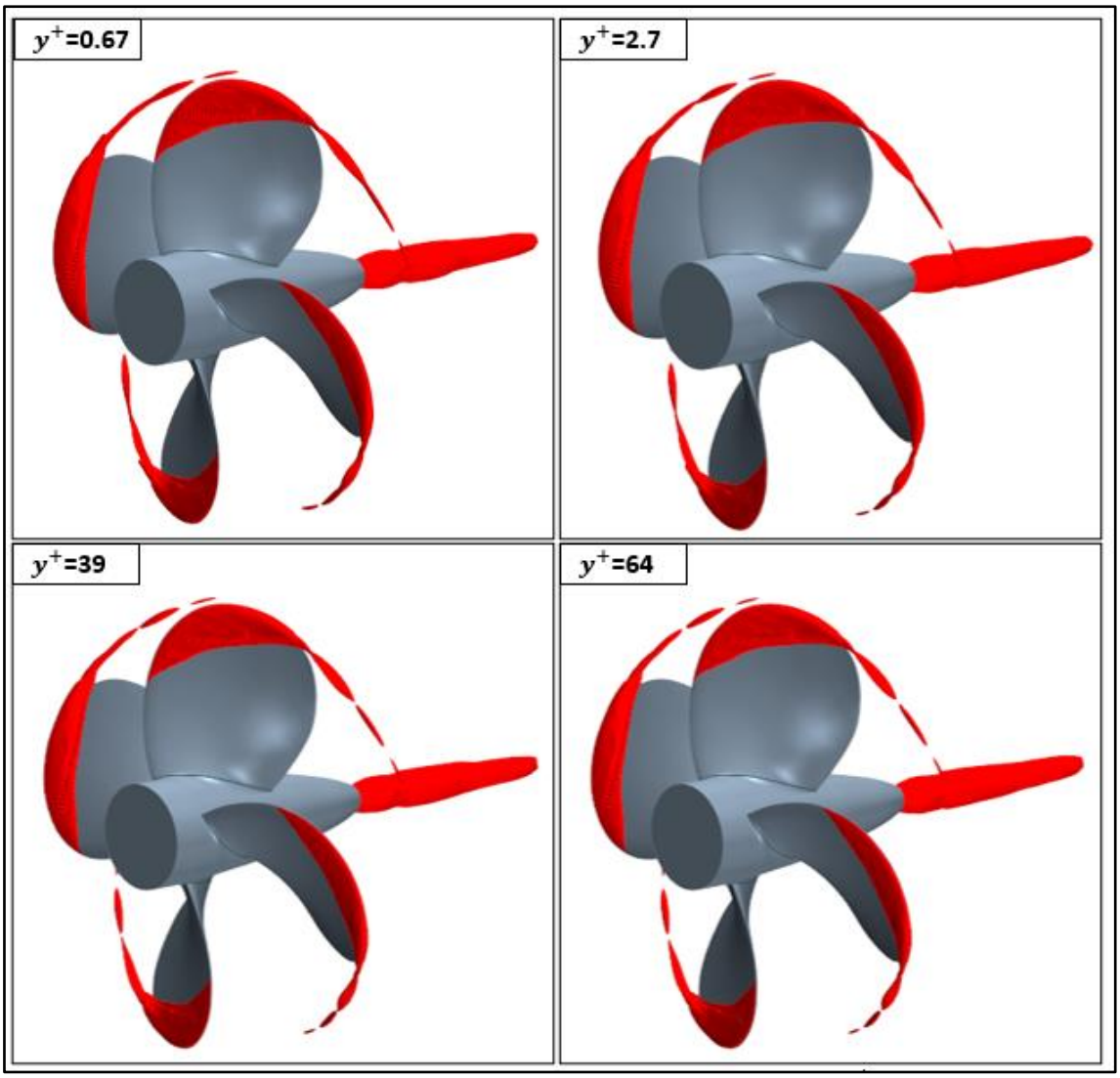

Figure 5.17. Variation of cavitation pattern with change in near-wall properties using the RANS method.

5.5 Chapter summary and concluding remarks

This chapter focused on the cavitation modelling for the benchmark INSEAN E779A propeller using RANS, DES and LES methods. Also, a new and alternative AMR technique (V-AMR) for the accurate solution of tip vortex flow and realisation of TVC in a computationally efficient manner was introduced to help wider applications of the CFD method involving TVC modelling. The technique was applied to the selected model propeller in open water and uniform flow conditions. The uncertainty study was conducted for grid spacing and temporal discretisation using the GCI technique. The hydrodynamic results obtained by the RANS, DES and LES methods were compared with the experimental data with and without the TVC modelling through the propeller hydrodynamic performance characteristics and cavitation

extensions. The influence of key simulation parameters on the representation of the TVC modelling was comprehensively investigated. Based on the investigations, it was found that:

- As the accurate solution of the TVC requires a higher grid resolution in the tip vortex regions, the proposed V-AMR technique enabled the prediction of TVC in the propeller slipstream with a minimal computational cost. The TVC was successfully observed with additional 3M cells (i.e., cell size: 0.25mm) by modelling all propeller blades. This proves the applicability of the proposed method compared to other recent AMR techniques in the literature. The minimal cost of the current V-AMR technique enables it to widen its applications to full-scale propellers.

- As far as the different simulation methods (i.e., RANS, DES and LES) are concerned, the overall pattern of the sheet cavitation predicted was found to be similar using the three numerical methods. In contrast, the TVC and hub vortex cavitation differed.

- With the implementation of the proposed V-AMR technique, the RANS method presented an insufficient extension of the TVC in the propeller slipstream compared to the DES and LES predictions due to the capabilities of the standard RANS methods for the solution of tip vortex flow. The more realistic TVC extension in the propeller slipstream was obtained by the DES and LES methods.

- The influence of TVC on the global performance characteristics (i.e., thrust and torque) was found negligible. However, the accurate prediction of the TVC was found to be significantly affected by the selection of numerical method (i.e., RANS or DES & LES), grid resolution, timestep and water quality (i.e., nuclei density) parameters. The results suggested that the cell size inside the vortex should be between 0.2mm and 0.25mm for the realistic formation of TVC in the propeller slipstream for model scale propellers. Also, the timestep should be kept between 0.25^{o} and 1^{o} of propeller rotational rate in terms of the realisation of TVC. Even though the nuclei diameter did not influence the sheet, hub and tip vortex cavitation, the hub and tip vortex cavitation were strongly dissipated with the selection of higher nuclei density values in the numerical calculations.

- The optimum cell size inside the vortex can be implemented as 0.2mm-0.25mm for the model scale propellers when the diameter of the propeller is between 0.2m and 0.3m. However, for full-scale applications, the grid size inside the vortex should be enlarged with the scale ratio for the observation of TVC in the numerical solvers.
- As the standard RANS methods are still commonly used for practical engineering applications, the representation of the TVC by using the standard RANS methods was found to be affected by the near-wall solution.

6 Hydrodynamic and hydroacoustic performance prediction of benchmark ship propeller in model scale

6.1 Introduction

As reviewed in Chapter 2, predicting the propeller URN is an important and complex topic, and there have been relatively few studies conducted to predict the propeller URN and validate the results with the experimental and full-scale data comprehensively. Therefore, the aim of this chapter is to demonstrate the capability and validity of the developed procedures using the CFD and acoustic analogy to predict the propeller hydrodynamic performance, including the cavitation, fluctuating hull pressures and URN for the realistic benchmark model test cases both in open water and behind conditions, including the effect of shaft inclination and non-uniform wake.

This chapter consists of three sections. In Section 6.2, the numerical investigations are conducted under uniform and inclined flow conditions, whereas in Section 6.3, the effect of a non-uniform wake field on the propeller hydrodynamic performance, cavitation and propeller URN is explored. Section 6.4 presents the numerical results in the presence of a 3D scaled (demi) hull model of the benchmark vessel to explore hull pressure fluctuations, cavitation, and propeller URN. All the sections start with the theoretical background, including the hydrodynamic and hydroacoustic models. The following are the numerical modelling (i.e., propeller geometry, test matrix, computational domain, boundary conditions, grid structure, and analysis properties). The results are presented at the end of each section. Finally, the overall chapter summary and conclusions are given in Section 6.5.

6.2 Under uniform and inclined flow conditions

6.2.1 Theoretical background

6.2.1.1 Hydrodynamic model

In the numerical calculations, the Delayed Detached Eddy Simulation (DDES) variant of the DES method, together with the k-ω SST turbulence model, was utilised due to the drawbacks of RANS and the higher computational cost of the LES methods. DES method uses the RANS method's features for the attached boundary layer and irrotational flow regions and the LES method for the unsteady separated regions. The switch from RANS to LES is driven by the

local grid spacing relative to the distance to the wall, and thus suitable grid design is crucial for the accuracy of the DES solution. The DES formulation of the k-ω SST turbulence model is derived by changing the dissipation term in the transport equation for the turbulent energy. In this method, the specific dissipation rate ω in the transport equations is replaced by $\tilde{\omega}$,

$$\tilde{\omega} = \omega\phi \tag{6.1}$$

and ϕ can be defined as;

$$\phi = \max(l_{ratio}F, 1) \tag{6.2}$$

where, l_{ratio} (i.e., length scale ratio) is calculated as;

$$l_{ratio} = \frac{l_{RANS}}{l_{LES}} \tag{6.3}$$

Here, l_{RANS} and l_{LES} can be written as;

$$l_{RANS} = \frac{\sqrt{k}}{f_{\beta^*}\beta^*\omega} \tag{6.4}$$

$$l_{LES} = C_{DES}\Delta \tag{6.5}$$

Here, k is the turbulent kinetic energy, f_β is the free-shear modification factor, β^* is a model coefficient of turbulence model, Δ is the biggest distance between the cell centre of neighbour cell centre and cell centre under consideration, and C_{DES} is the model coefficient, which blends the values obtained from the independent calibration of the k-epsilon and k-ω versions of the k-ω SST model. In Equation 6.2, the F can be defined as;

$$F = 1 - F_2 \tag{6.6}$$

where F_2 is the blending function defined in the turbulent eddy viscosity formulation for the k-ω SST turbulence model. In Equation 6.2, when the $\phi = 1$, the solution is provided by the RANS method, whereas $\phi > 1$ shows the regions where the LES method is used in the DES method (Spalart et al., 1997 and Star CCM+ 14.06, 2019). In our case, the suitability of the adopted cells for the boundary layer and propeller slipstream (i.e., to understand where the

RANS and LES methods are used) can be visualised using the DES correction factor (i.e., F_{DES}). As shown in Figure 6.1, the boundary layer solution is provided by RANS, whereas LES is used for the flow field solution in the propeller slipstream, as expected. Also, the far-field where the coarse grid is present is solved using the RANS method.

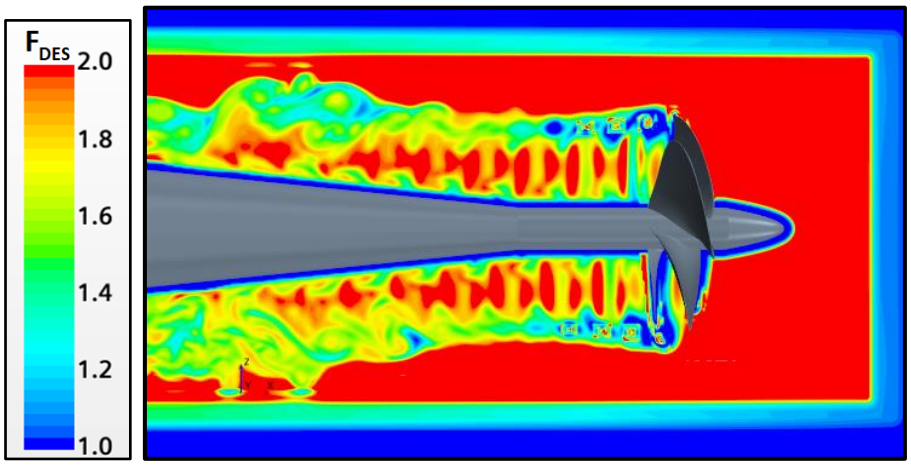

Figure 6.1. Contour plots of DES Correction Factor (RANS is $F_{DES} = 1$ and LES is $F_{DES} > 1$).

As used in Chapter 5, the Schnerr-Sauer cavitation model, based on the reduced Rayleigh-Plesset equation, was used in this Section. The details of the model were already given in Section 5.2

6.2.1.2 Hydroacoustic model

As in Chapter 4, the same permeable formulations of the FWH equation was used in this Section for the propeller URN predictions. The details of the formulations were already given in Section 4.2.1.

6.2.2 Numerical modelling

6.2.2.1 Propeller geometry and test matrix

The new benchmark propeller, i.e., Newcastle University's (UNEW) Deep-V type catamaran research vessel, The Princess Royal's propeller, was selected in this study to take advantage of the large international round-robin (RR) test campaign results that were produced by many different participating facilities (i.e., MARIN, UNIGE, SSPA, UNEW, KRISO, NMRI and CNR-INM). The five-bladed model propeller's main particulars and 3D view are given in Table 6.1 and Figure 6.2, respectively.

Table 6.1. The main particulars of the propeller (Atlar et al., 2013).

Parameters	Model Scale Princess Royal Propeller
Diameter, D (m)	0.22
P/D at 0.7R	0.8475
Expanded Blade Area Ratio (EAR)	1.057
Blade Number, Z	5
Rake (^{o})	0
Skew (^{o})	19

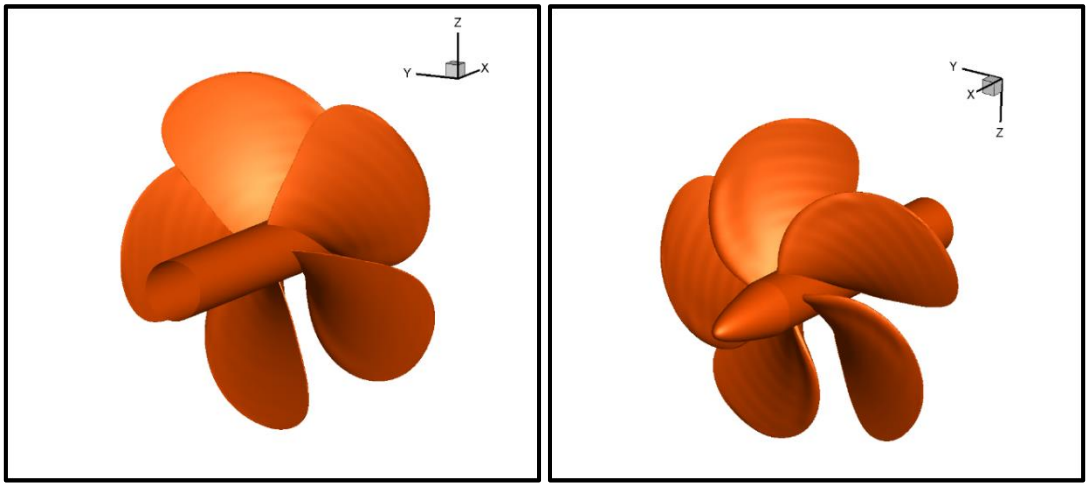

Figure 6.2. 3D view of the benchmark Princess Royal propeller.

Tests have been carried out for the cavitation observations and noise predictions for the selected propeller in the scope of the ongoing RR test campaign. The model scale propeller's diameters used in different facilities are slightly different, and they are taken as 0.25m, 0.22m, 0.214m. So far, the tests were conducted under uniform and inclined flow conditions by taking either the thrust coefficient identity (i.e., K_T) or advance ratio (i.e., J) identity (Tani et al., 2019b and Tani et al., 2020). The operational conditions set according to the RR test campaign are described in Table 6.2. As shown in Table 6.2, uniform (i.e., straight) and inclined shaft flow configurations (β) together with six operating conditions are explored in this study through hydrodynamic performance prediction, cavitation observation and noise prediction. The operating conditions were changed according to advance ratio (i.e., J) and cavitation number based on propeller rotational speed (n).

Table 6.2. Test matrix.

Test Condition	J	β (°)	σ_N	V_A	$n\ (rps)$
C1	0.4	0	2.223	3.08	35
C2	0.4	0	1.311	3.08	35
C3	0.4	0	0.721	3.08	35
C4	0.5	0	3.486	3.85	35
C5	0.5	0	2.024	3.85	35
C6	0.5	0	1.137	3.85	35
C7	0.4	5	2.223	3.08	35
C8	0.4	5	1.311	3.08	35
C9	0.4	5	0.721	3.08	35
C10	0.5	5	3.486	3.85	35
C11	0.5	5	2.024	3.85	35
C12	0.5	5	1.137	3.85	35

Here, V_A is the inflow speed, n is the propeller rotation rate, P_0 is the static pressure, P_V is the vapour pressure, ρ is the water density and β is the shaft inclination angle.

6.2.2.2 Computational domain and boundary conditions

In the numerical calculations, the computational domain dimensions were set according to the dimensions of the GENOA cavitation tunnel measurement section, which has a 2.2m total length and 0.57m x 0.57m square test section. Similarly, the upstream and downstream of the computational domain from the propeller blade's centre were extended around 2.5D and 7.5D, respectively. The width and height of the domain were also set to 0.57m x 0.57m, respectively. As shown in Figure 6.3, the positive X direction was identified as velocity inlet, whereas the negative X direction was defined as pressure outlet. The remaining surfaces of the domain, propeller, shaft, and hub were defined as no-slip walls. The computational domain consisted of three different regions: static, rotating, and noise. These regions connected each other with the internal interfaces. The rotating region was used for the propeller motion, whereas the noise region (or permeable surface) was utilised for the propeller URN predictions. For the inclined shaft conditions, the same computational domain was used with shaft inclination.

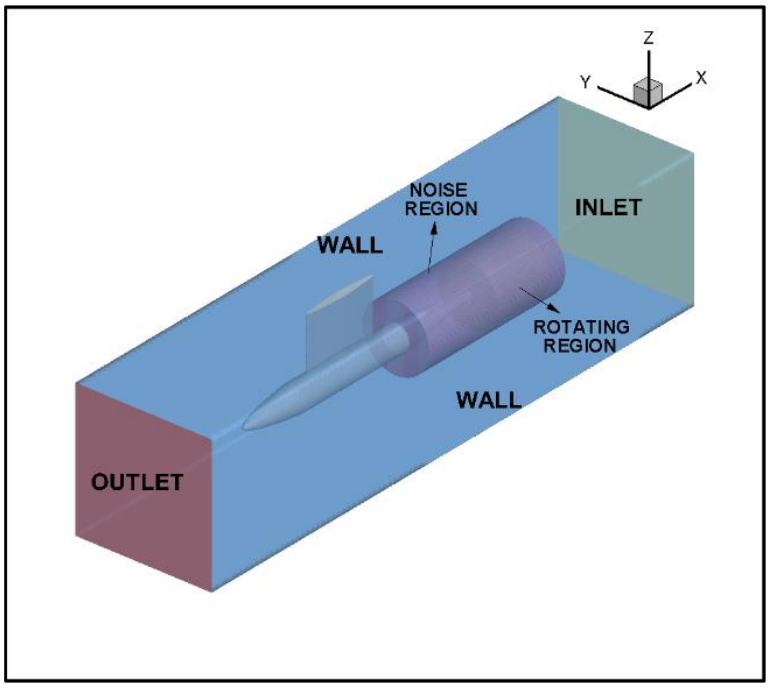

Figure 6.3. Representation of computational domain used in the numerical calculations.

6.2.2.3 Grid generation

The grid quality used in numerical calculations is of paramount importance for representing the complex geometry and the accurate solution of the flow field. In order to reduce the discretisation errors, the grid resolution should be sufficient enough to resolve all the relevant flow features, including cavitation dynamics, around the propeller. The numerical modelling of cavitation phenomena is complicated compared to non-cavitating conditions because of the cavitation dynamics and turbulence interactions. Thus, a suitable grid resolution should be adopted in numerical calculations. In particular, an accurate solution of tip vortex flow is strongly dependent on grid resolution. For this reason, advanced mesh techniques should be implemented around the tip vortex regions to predict the minimum pressure inside the vortex accurately. In this regard, the author has introduced the Vorticity-based Adaptive Mesh Refinement (V-AMR) technique for the solution of the tip vortex flow and hence tip vortex cavitation (TVC) observation in the propeller slipstream, as described in detail in Chapter 5. Using the V-AMR technique, the grid is refined as local as possible in the vicinity of tip vortex areas to reduce the computational cost of the solution. As stated in Chapter 5, this technique consists of two stages: the 1st stage V-AMR and the 2nd stage V-AMR to reduce the computational cost of the solution. In the 1st stage, the relatively coarse grid reveals the tip vortex trajectory in the propeller slipstream. Following this, 2nd stage V-AMR is implemented using the fine grid resolution.

The grid quality is also crucial for the accurate prediction of propeller URN as the sound is propagated from near field to far-field. Thus, the numerical diffusion should be as minimum as possible. Also, the insufficient grid resolution and abrupt mesh changes inside the noise surface can lead to non-physical numerical noise, which is mainly created by the sliding mesh interfaces, and they can contaminate the overall acoustic pressure. Based on the findings in Chapter 4, the uniform grid resolution in all directions was applied, and the permeable surface was located inside the fine grid region to minimise the information loss because of the numerical dissipation. The adopted grid structure can be seen in Figure 6.4.

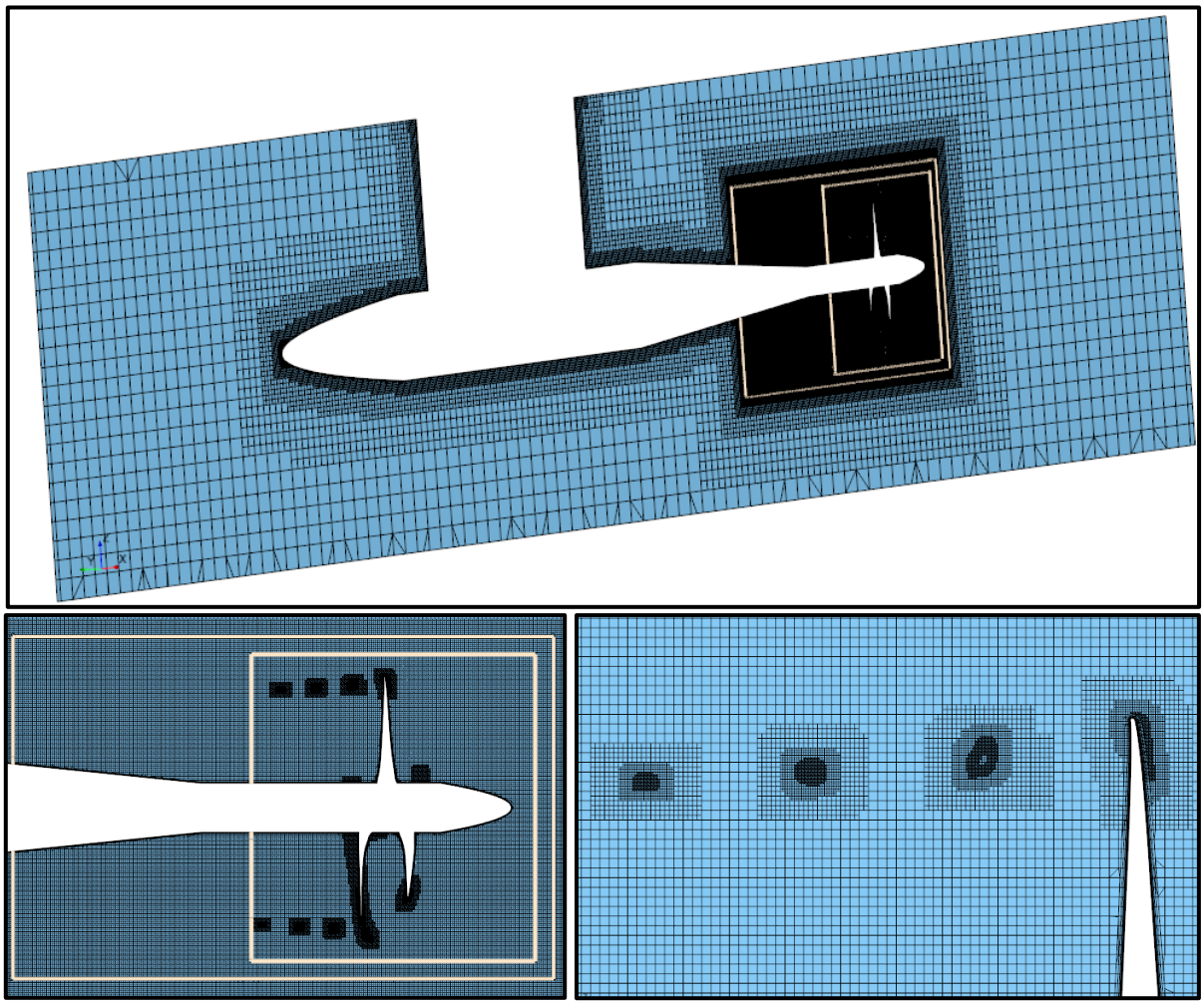

Figure 6.4. Representation of grid resolution in the computational domain, permeable surface, and tip vortex areas.

In this study, the trimmer mesh with hexahedral elements was adopted using the Star CCM+ automated mesh tool to solve the flow around the cavitating propeller and URN predictions at various operating conditions given in Table 6.2 (Star CCM+ 14.06, 2019). The grid was refined in all directions to achieve the $y^+ < 1$ to resolve the boundary layer itself to increase the accuracy of the solution. In order to observe the TVC, the V-AMR technique was also

implemented using the user-based field functions. In order to reduce numerical noise, the high-quality cells with minimum skewness were utilised in all directions. The grids were also aligned at the transition regions to decrease the possible numerical noise sources arising from the internal interfaces. The total element count was calculated at approximately 23M.

6.2.2.4 Analysis properties

The application of the DES method can be challenging unless suitable simulation properties are selected. A segregated flow solver and a SIMPLE algorithm were used to compute the velocity and pressure in the numerical calculations. The Hybrid Bounded Central Differencing Scheme (Hybrid-BCD) was used for the segregated solver to discretise convection terms in the momentum equations. This scheme blends second-order upwind and bounded central differencing, and the blending factor is calculated according to the flow field features. This discretisation scheme is also advisable for DES methods. Furthermore, the second-order discretisation scheme was also utilised for the convection of turbulence terms (Star CCM+ 14.06, 2019).

The second-order implicit numerical scheme was used for the time discretisation. The time step selection is also an important parameter linked to the CFL number inside the domain for the DES method. In this regard, the timestep was selected as 0.5^{o} of the propeller rotational rate at different operating conditions. As the implicit scheme was utilised, the CFL number is not associated with the stability of the time scheme, but keeping the CFL around 1, especially in the propeller slipstream, enabled to increase the accuracy of the numerical solution.

The multiphase VOF (Volume of Fraction) approach was coupled with the cavitation model for modelling the cavitation phenomena. For the convection term of the VOF approach, High-Resolution Interface Capturing (HRIC) was used to track the sharp interfaces between phases. The Schnerr- Sauer mass transfer model based on the reduced Rayleigh-Plesset equation was used to model the cavitation. In this model, the customisable cavitation parameters (i.e., nuclei density and diameter) were taken as default values based on our investigation of its effects on the sheet and tip vortex cavitation formation, as given in Chapter 5. Thus, the nuclei density and diameter were set to 10^{12} ($1/m^3$) and 10^{-6} (m), respectively. The DES method was initialised with a steady-state RANS method using the k-ω SST turbulence model. In this way, the DES method's robustness was increased, and the RANS solution provided a consistent initial guess that ensured that the problem was mathematically well-posed. After initialising with the RANS method, the solver was switched to the DES method by activating the cavitation. When the

flow field converged, the acoustic analogy was started to collect the acoustic pressures at the specified points using the receivers. The acoustic data were collected during the six propeller revolutions.

At the initialisation stage with the steady RANS method, the Moving Reference Frame (MRF) technique was used to model the propeller rotational motion. When the solver was switched to the DES method, the propeller rotational motion technique was changed with the Rigid Body Motion (RBM). During the first propeller rotation, the timestep was set to 1^o of propeller rotational rate and then reduced to 0.5^o of propeller rotational rate. In this way, any possible stability issues related to cavitation phenomena were avoided.

6.2.3 Numerical results

In this Section, the hydrodynamic and hydroacoustic results, including cavitation observations, are given for the model scale propeller. The numerical results are then extrapolated to full-scale using the ITTC scaling procedure as in the experiment and compared with obtained results by different facilities in the scope of the RR campaign under uniform flow (i.e., straight shaft) conditions.

6.2.3.1 Model scale propeller

- **Hydrodynamic results**

In the scope of the RR test campaign, the participants carried out the tests at thrust coefficient identity (i.e., K_T= 0.242 and K_T=0.192, corresponding to J=0.4 and J=0.5, respectively) or J identity. Thus, this resulted in slightly different thrust and torque values and hence operating conditions (Tani et al., 2020). Also, in order to keep the J constant, the slightly different cavitation numbers (σ_n) were used when the thrust identity was adopted during the tests, as given in Table 6.3. In CFD calculations, the J identity was adopted as several iterations were required to equal the thrust coefficients (i.e., for thrust identity) between CFD and experiment. This would increase the computational cost of the solution for twelve operating conditions. As the model scale hydrodynamic and hydroacoustic results obtained by CFD were mainly compared with the data obtained by the University of Genoa Cavitation tunnel (UNIGE), the same cavitation numbers as in the UNIGE tunnel were adopted in CFD computations at different operating conditions.

Table 6.3. Adapted cavitation numbers for different operating conditions in the scope of the RR test campaign (Tani et al., 2020) and CFD.

	σ_N							
Condition	MARIN	UNIGE	SSPA	UNEW	KRISO	NMRI	CNR	CFD
C1	2.57	2.223	2.340	2.220	2.140	3.081	2.730	2.223
C2	1.296	1.311	1.410	1.300	1.300	1.442	1.590	1.311
C3	0.720	0.721	0.790	0.720	1.130	0.801	0.880	0.721
C4	3.475	3.486	3.630	3.480	3.320	2.978	3.890	3.486
C5	2.025	2.024	2.130	2.030	2.030	2.173	2.270	2.024
C6	1.125	1.137	1.180	1.130	1.120	1.207	1.260	1.137
C7	-	2.223	-	-	-	-	-	2.223
C8	-	1.311	-	-	-	-	-	1.311
C9	-	0.721	-	-	-	-	-	0.721
C10	-	3.486	-	-	-	-	-	3.486
C11	-	2.024	-	-	-	-	-	2.024
C12	-	1.137	-	-	-	-	-	1.137

Table 6.4 shows the thrust coefficients obtained by CFD and experiments performed by different facilities. As shown in Table 6.4, CFD results are in good agreement with those of experimental data obtained by SSPA and NMRI, as they mainly used the J identity throughout the tests. Also, the comparison of CFD results with experimental data obtained by other facilities (i.e., MARIN, UNIGE, UNEW, KRISO and CNR) shows that the deviation is between 5% and 7% in terms of thrust coefficient, depending on the operating conditions. It should be noted that similar to other facilities, except CNR, the propeller was operating in pulling configuration in the CFD computations.

Table 6.4. The comparison of thrust coefficients between experiments (Tani et al., 2020) and CFD at different operating conditions.

	K_T							
Condition	MARIN	UNIGE	SSPA	UNEW	KRISO	NMRI	CNR	CFD
C1	0.223	0.244	0.260	0.242	0.255	0.243	0.245	0.262
C2	0.243	0.244	0.262	0.242	0.255	0.243	0.245	0.262
C3	0.222	0.226	0.236	0.242	0.255	0.243	0.232	0.237
C4	0.192	0.190	0.203	0.190	0.203	0.191	0.189	0.202
C5	0.193	0.189	0.204	0.190	0.203	0.191	0.191	0.203
C6	0.195	0.191	0.206	0.190	0.203	0.191	0.195	0.207
C7	-	0.245	-	-	-	-	-	0.261
C8	-	0.245	-	-	-	-	-	0.257
C9	-	0.226	-	-	-	-	-	0.237
C10	-	0.189	-	-	-	-	-	0.202
C11	-	0.190	-	-	-	-	-	0.204
C12	-	0.192	-	-	-	-	-	0.207

- **Cavitation extensions**

The cavitation observations obtained by CFD are first compared in Figure 6.5 to show the change in cavitation extensions at different operating conditions (i.e., straight and inclined shaft configurations) before comparing them with the experimental data obtained by different facilities. The general comments for the cavitation observations at all operating conditions can be summarised as follows:

- The suction side sheet cavitation is present at all operating conditions, except C4.
- With an increase in blade loading from C1 to C3 at J=0.4 and C4 to C6 at J=0.5, the sheet cavitation extension and its thickness increase.
- Similar sheet cavitation phenomena and dynamics are observed at C1, C2, C5 and C6, with differences in their extensions.
- The leading-edge vortex cavitation is observed at C1, C2, C3 and C6.
- The stable TVC is present at C1, C2 and C6 with different extensions in the propeller slipstream. The strongest TVC in the propeller slipstream is observed at C2.
- The largest sheet cavitation is observed at C3 with rather unstable vortex cavitation. This unsteadiness affects the vortex structure considerably, resulting in the tip vortex core disruption.

- The cavitation extensions in inclined shaft configurations are slightly different from straight shaft configurations.

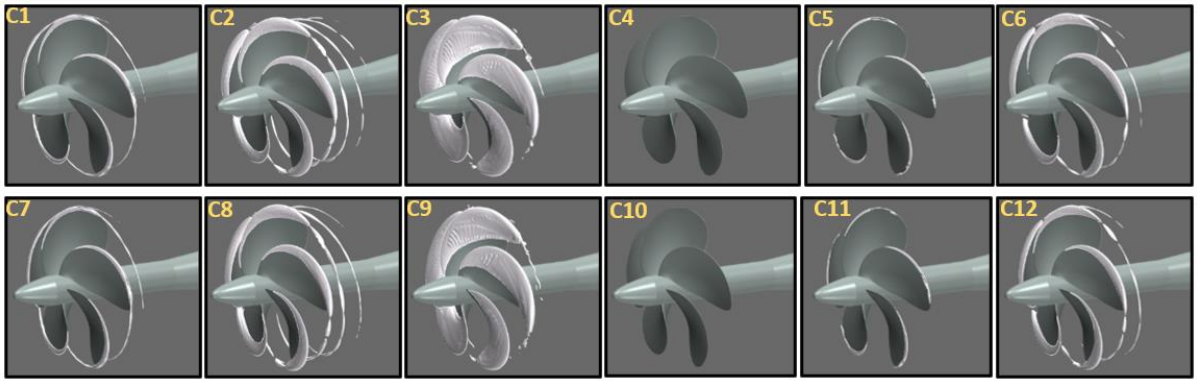

Figure 6.5. Comparison of cavitation extensions between the uniform and inclined flow conditions obtained by CFD ($\alpha_v = 0.1$).

Following the comparison of cavitation extensions obtained by CFD at different operating conditions, the numerical results were also compared with the experimental observations obtained by different facilities within the scope of the RR test campaign. Figure 6.6 compares cavitation extensions for C1, C2 and C3 at J=0.4. As shown in Figure 6.6, similar sheet and tip vortex cavitation are observed in the CFD compared to the experiments with slight differences. The sheet cavitation is slightly more extended towards the inner radii in CFD at C1, C2, whereas it is overpredicted at C3 compared to experimental observations. Applying the V-AMR technique in the numerical calculations enables better modelling of the TVC in the propeller slipstream. Nevertheless, the TVC observed in the CFD is less extended in the propeller slipstream than in the experiments. Amongst the conditions, the more extended TVC in the propeller slipstream is captured at C2 as the vortex diameter is sufficiently bigger than those of C1 and C3. The unstructured and cloudy appearance of TVC at C3 could not be observed in CFD as in the experiments.

Figure 6.7 compares cavitation extensions between CFD and experiment for C4, C5 and C6 at J=0.5. Similar sheet cavitation dynamics and extensions are observed in CFD compared to experiments for C5 and C6. In the experiments, the weak TVC, which is attached to the blade leading edge (i.e., NMRI) or appears incipient in the propeller slipstream, is observed for C4 by other facilities. Unlike the experiments, the weak TVC formation could not be observed in CFD for C4 and C5. The reason is that the diameter of the tip vortex is rather small at these conditions. Due to this fact, the adopted grid size inside the vortex core (i.e., 0.2mm) using the V-AMR technique may not be sufficient to capture the weak cavitation TVC dynamics in the CFD.

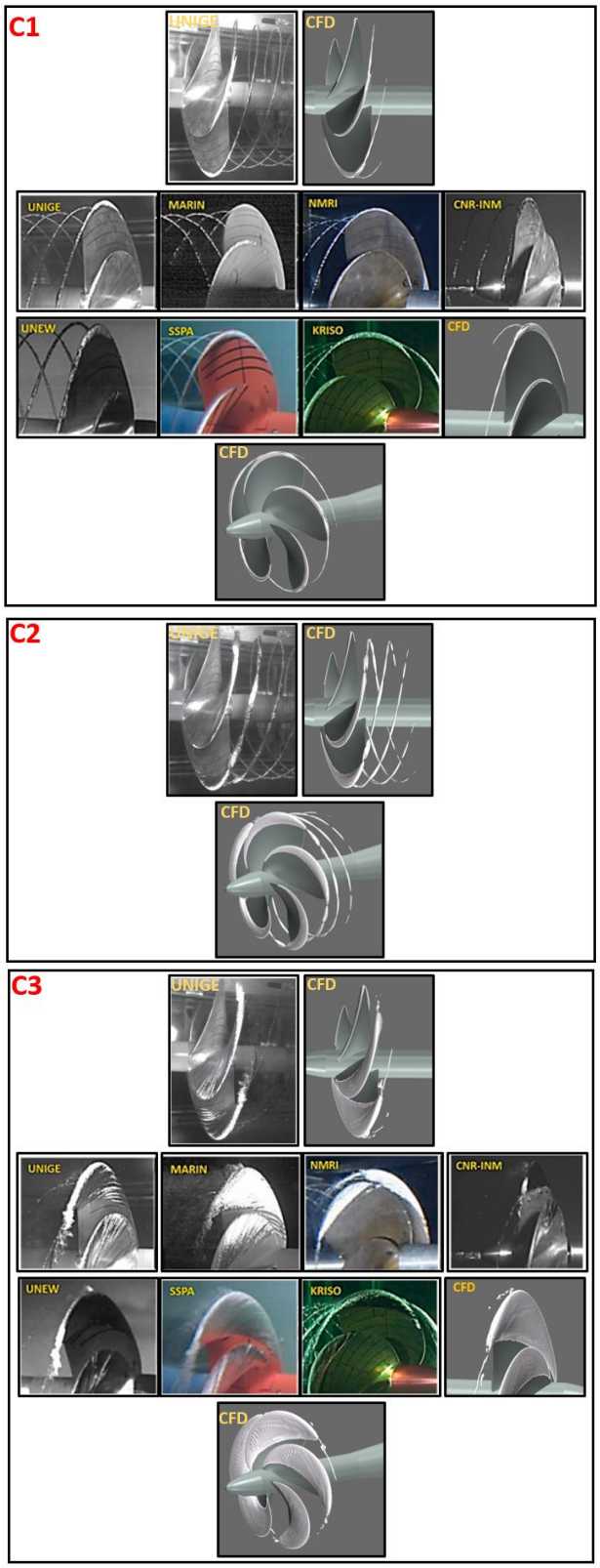

Figure 6.6. Comparison of cavitation extensions at J=0.4 for straight shaft configuration (C1, C2 and C3) ($\alpha_v = 0.1$).

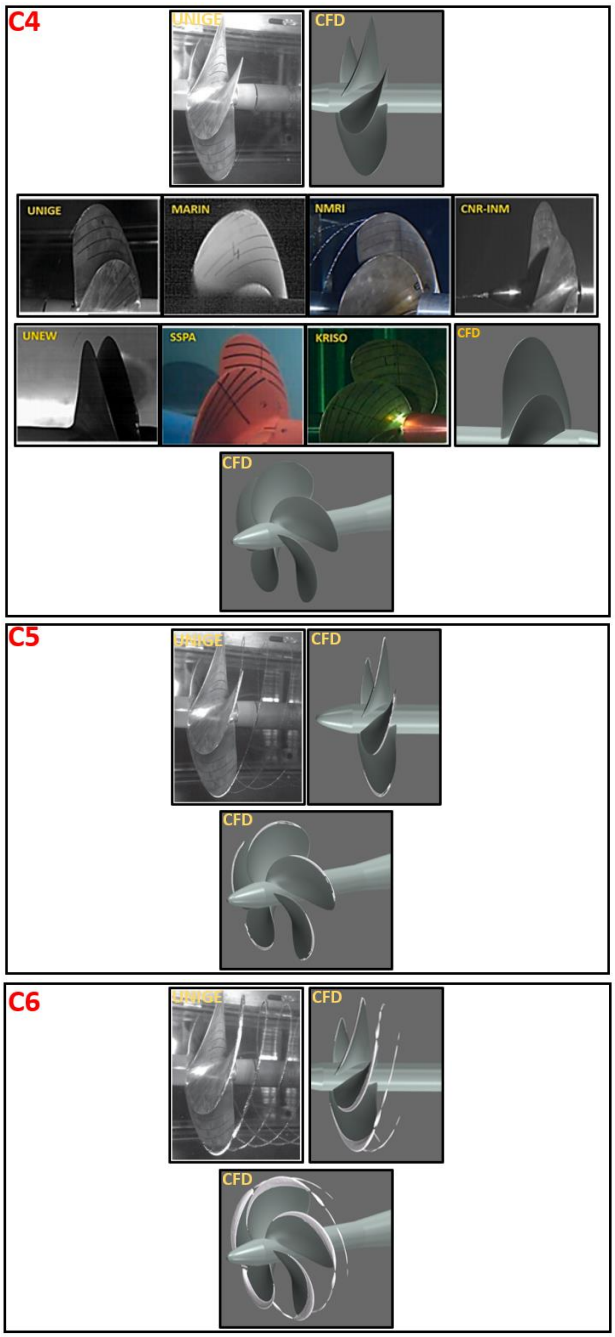

Figure 6.7. Comparison of cavitation extensions at J=0.5 for straight shaft configuration (C4, C5 and C6) ($\alpha_v = 0.1$).

Similar to straight shaft configuration, the cavitation observations are compared between CFD and experiment for the inclined shaft configurations in Figure 6.8. As the RR test campaign data is not yet published for inclined shaft configuration, the numerical results are only compared with the experiments performed in UNIGE. Akin to the straight shaft configuration, analogous sheet cavitation extensions are observed. The sheet cavitation is generally more extended towards inner radii in CFD compared to experiments. Also, the same TVC dynamics in the propeller slipstream could not be captured for C10 and C11 due to the small diameter of TVC in the propeller slipstream observed in the experiment.

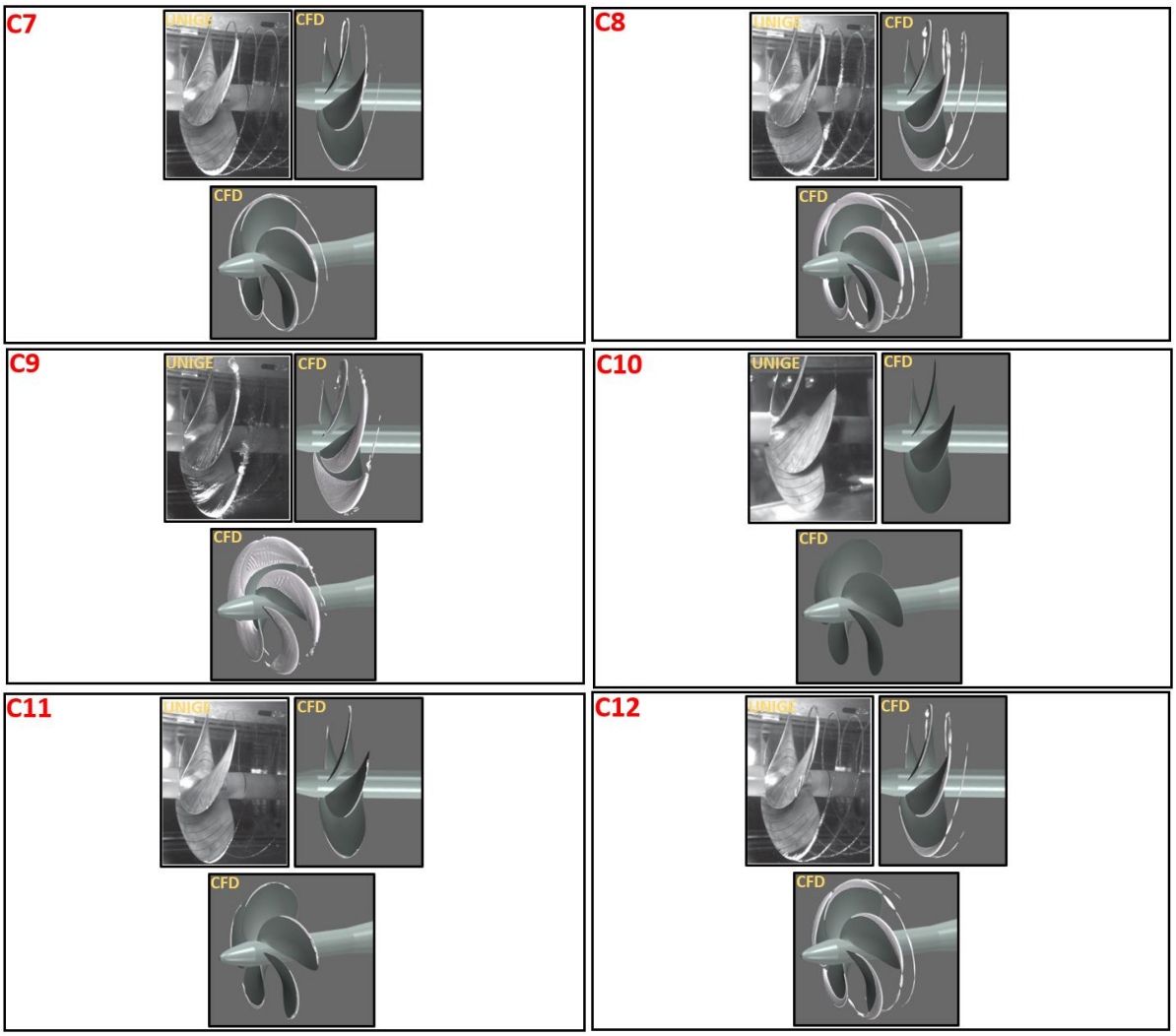

Figure 6.8. Comparison of cavitation extensions for inclined shaft configuration (C7, C8, C9, C10, C11 and C12) ($\alpha_v = 0.1$).

Investigating the cavitation phenomena such as thickness and chordwise extensions between CFD and experiment is rather difficult as the cavitation patterns were observed at different angles by different facilities during the experiments, as stated in Tani et al., 2020. Nevertheless, similar sheet cavitation and shorter TVC extensions are observed in CFD compared to experiments. The differences between the experiments and CFD can be associated with several effects: the development of boundary layer, Reynolds number, water quality, and freestream turbulence. A detailed comparison of the cavitation observations obtained by each facility can be found in the study by Tani et al., 2020.

- **Hydroacoustic results**

In the hydroacoustic simulations, incompressible hydrodynamic solver (i.e., DES method) and permeable/porous FWH formulation were utilised for the propeller URN prediction. The sound speed propagates with a finite speed in a medium under the isentropic flow hypothesis ($c_o^2 = dp/d\rho$). The incompressibility assumption ($d\rho = 0$) denies the acoustic propagation phenomena, and so the simultaneous combination of noise sources overlaps and creates acoustic pressure. This is because the computed pressure at a location is not the resultant value, including all possible pressure waves travelling in the fluid. The acoustic delay affects the contribution of sources in computed pressure and characterises the overall signature of the pressure in terms of amplitude and waveform. This effect is dependent on the relative motion between each source, receiver and sound of speed. As the marine propeller is operating at a much lower rotational speed compared to the sound propagation speed, the acoustic delays became negligible, as shown in the studies of Testa, 2008 and Ianniello et al., 2013. Therefore, the instantaneous propagation of sound does not influence the resulting signal considerably in near and mid-field. As a result, despite the theoretical inconsistency of the incompressibility assumption, the comparison of hydrodynamic and hydroacoustic pressures collected close to the noise source can be compared to each other to show the reliability of the hydrodynamic and hydroacoustic solution (Testa et al., 2021).

In our study, several receivers are located close to the noise source and porous surface to compare both pressures in the near field for Condition 2. Figure 6.9 compares the hydrodynamic and hydroacoustic pressures at the propeller plane (i.e., z=0.17m from the propeller blades' centre). As shown in Figure 6.9, the hydrodynamic and hydroacoustic pressures are in good agreement with each other in terms of amplitude and waveform. The agreement between both pressures is present for other receivers located both upstream and downstream of the porous surface.

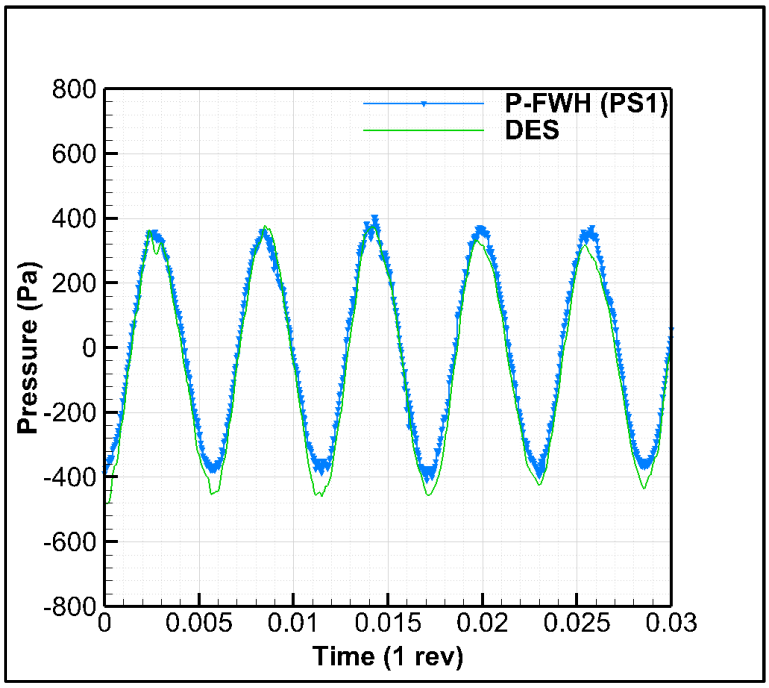

Figure 6.9. Comparison of hydrodynamic and hydroacoustic pressures in the near field at the propeller plane (z= 0.17m from the propeller blades' centre) for Condition 2.

The placement of porous surfaces is still under debate in the scientific community, and there is no practical guideline for the surface placement and dimensions. Nevertheless, few studies have recently focused on this subject (e.g., Lidtke et al., 2019; Testa et al., 2021). The porous surface needs to include all relevant possible nonlinear noise sources, mainly represented by vorticity and turbulence, including TVC within the flow domain, especially in the propeller slipstream. For this reason, the permeable surface should be placed in a region where the fine grid resolution is present. The reason behind this is that numerical diffusion in the CFD domain created by the grid resolution can affect the accuracy of the acoustic pressures. In our study, three different permeable surfaces, which have different dimensions and placed in fine grid resolution region, are tested to show the convergence of the solution for Condition 2, as given in Table 6.5.

Table 6.5. Geometrical properties of selected porous surfaces (L is the length of the Porous Surface (PS), D_{PS} is the diameter of the PS).

PS ID	L/D	D_{PS}
1	3.0	1.26D
2	2.5	1.25D
3	2.0	1.24D

The acoustic pressures obtained by different porous/permeable surfaces are first compared in the near field, where the hydrodynamic and hydroacoustic pressures are compared in Figure 6.10. As can be seen in Figure 6.10, the acoustic pressures are similar in the near field and low-frequency region of the noise spectra.

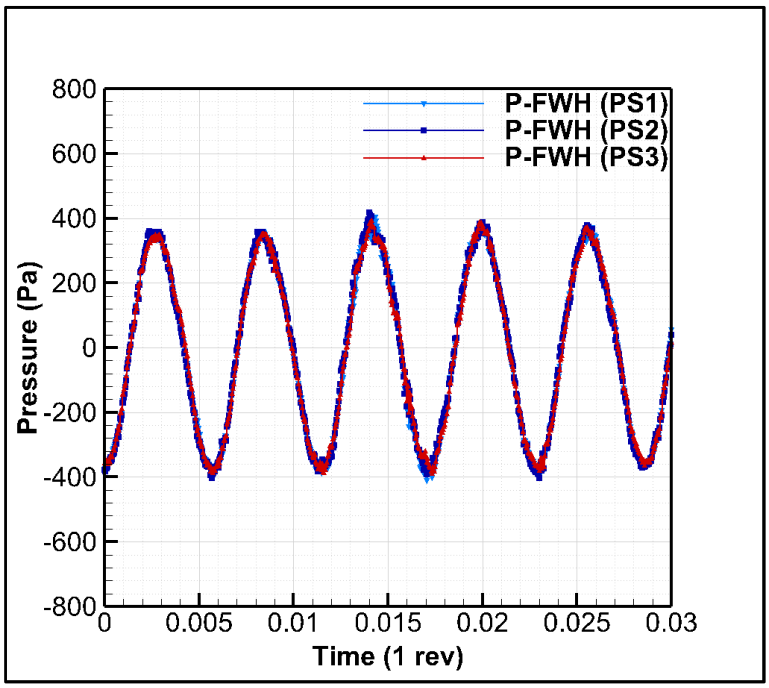

Figure 6.10. Comparison of hydroacoustic pressures obtained by different porous surfaces in the near field at the propeller plane (z= 0.17m from the propeller blades' centre) for Condition 2.

The acoustic pressures are recorded at the receivers located around the propeller to obtain the noise spectra in narrowband and one-third octave (OTO) band representation. In this study, the propeller URN predictions in model scale were compared with the experiments performed by UNIGE. Hence, the receivers are located in the CFD calculations according to the experimental setup of the UNIGE cavitation tunnel measuring section, as shown in Figure 6.11.

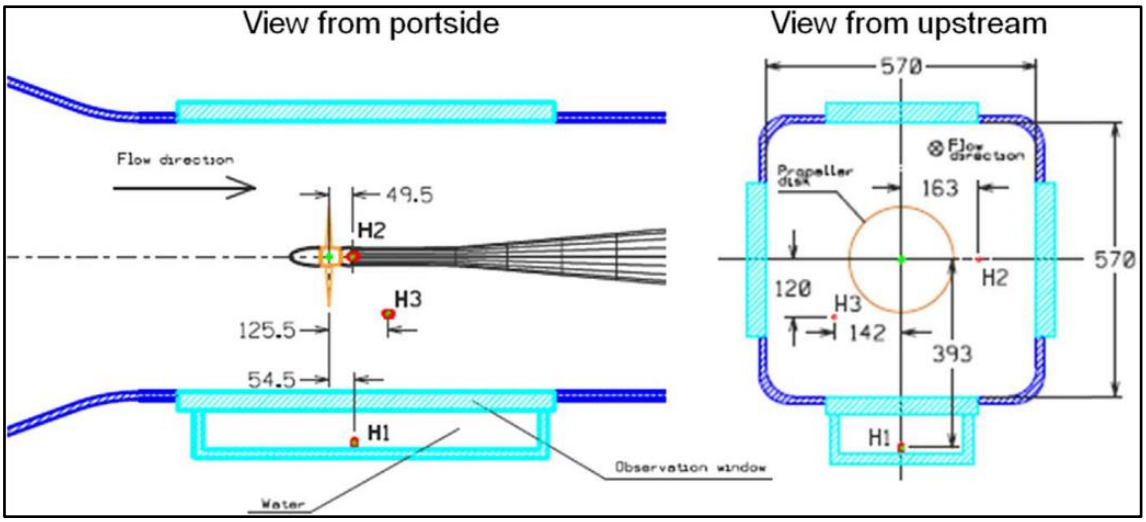

Figure 6.11. The receiver locations for the URN measurements during the experiments in UNIGE (Tani et al., 2017).

The measurements were conducted using the receivers H1, H2, and H3. The measurements were presented on both averages of three receivers and only H3. The data were then extrapolated to 1m reference distance using the transfer functions. Akin to the measurements, the CFD calculations were performed using the three receivers and presented accordingly. The transfer functions were utilised in the measurements to obtain the source strength level (SL), whereas the spherical spreading loss definition (i.e., $20\log(d/d_{ref})$) was adopted in the CFD calculations to extrapolate the results from near (i.e., measured distance, d) to reference distance (i.e., d_{ref} =1m). This is because the details of the transfer function are not available. Additionally, one more receiver was located at 1m in the CFD to compare the results directly without extrapolation from near to far-field. The noise spectrums were given in power spectra in the experiments, and the frequency resolution was df=6.1Hz. Hence, post-processing of the acoustic predictions obtained by CFD was performed similarly for both narrowband and OTO comparison with the measurements.

Before comparing the CFD predictions with the measurements, the convergence of the solution is also shown at Condition 2 using the permeable surfaces, as given in Table 6.5. In this way, the change in the low-and high-frequency part of the spectrum with the application of different permeable surfaces can be seen using the average of three receivers as in the measurements (see Figure 6.11). As shown in Figure 6.12, the overall trend of the noise spectrums obtained using the three different permeable surfaces is similar for both narrowband and OTO. Yet, some slight differences were observed at some BPF values predicted by different permeable surfaces. Among them, the PS3 predicted the BPF values as slightly more distinct. Thus, it can be concluded that a relatively smaller porous surface (i.e., PS3), which was placed to capture

the most energetic part of the vortex and turbulence structures in the propeller slipstream, is likely to capture more noise information than those of relatively bigger porous surfaces. Eventually, the PS3 was used to compare the CFD predictions with the experimental data for the following part of this Section.

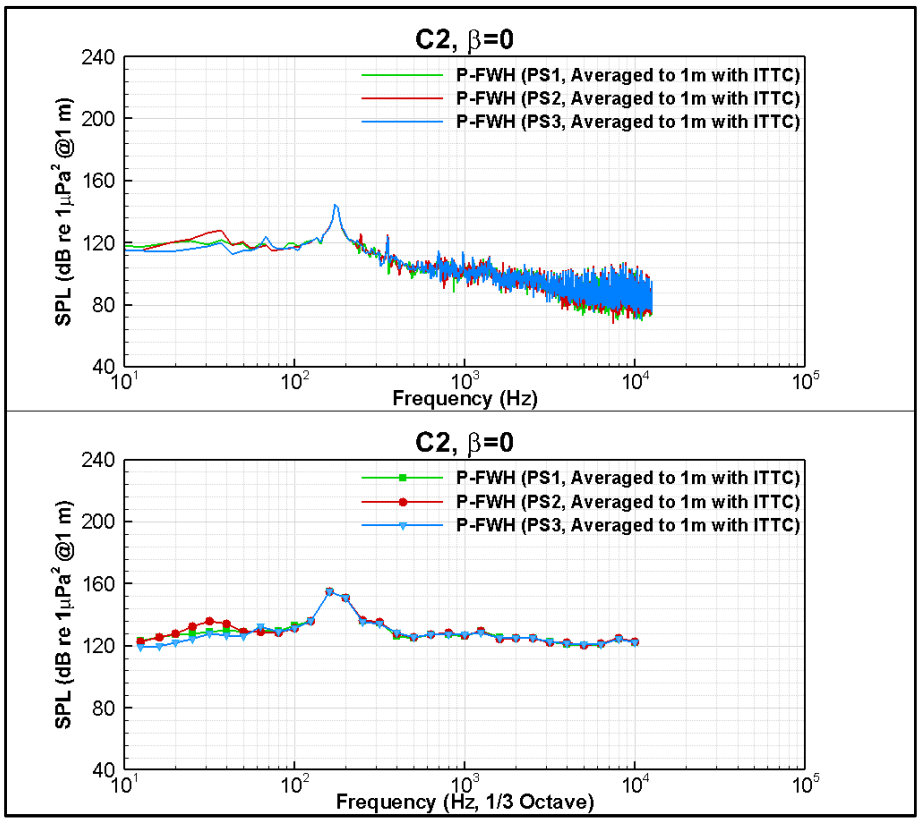

Figure 6.12. Comparison of noise spectrums obtained by different porous surfaces using the average of three receivers for Condition 2.

Figure 6.13 compares the predicted noise levels by CFD (i.e., PFWH) and measurements performed by UNIGE for straight shaft configurations. The results are presented in both narrowband and OTO for all operating conditions using the average of three receivers and the additional receiver placed at 1m. As shown in Figure 6.13, the numerical results underpredict the noise levels between approximately 5dB and 10dB in the frequency resolution between 300Hz and 1kHz for C1, C2, C4, C5 and C6 compared to measurements. This discrepancy between the numerical prediction and measurements is further reduced after 1kHz. Unlike the C1, C2, C4, C5 and C6, the numerical results are in good agreement with the measurements at C3, particularly until 1kHz. However, after 1kHz, the numerical calculations overpredict the noise levels up to approximately 8kHz. This is because the large and strong sheet cavitation is observed in the CFD calculations compared to experimental observations obtained in UNIGE. Hence, these cavity dynamics lead to an increase in noise levels between 1kHz and 8kHz at C3. In all operating conditions, the 1st BPF (Blade Passage Frequency) values are more distinct

at 175Hz in the numerical calculations, whereas the 2nd, 3rd and other peaks are also present with small amplitudes. The differences between the average of three receivers and the receiver located at 1m are because of the extrapolation from near to far-field using the ITTC distance normalisation. Also, the near field effects created by the receiver H2 and H3 can characterise the average of data, especially when the cavitation is not dominant.

In the measurements, the high-amplitude peak was observed at around 740Hz, which was also present in the background noise measurements in the tunnel. According to a detailed investigation conducted by Tani et al., 2017, it was stated that the mechanical vibration of one of the receiver supports created this noise component, and it could not be eliminated during the background noise measurements. Also, some other tonal components are also distinguishable between 6kHz and 12kHz. It was considered that the driveline of the dynamometer probably created these tones, and their amplitude was higher when the propeller was switched to a dummy hub because of the higher loading occurring on the driveline. Thus, these noise components are not relevant for comparing numerical calculations with the measurements. A detailed investigation and discussion of the measurements can be found in the study by Tani et al., 2017.

The measured noise data are characterised by a medium-low frequency hump associated with the pressure fluctuations generated by the tip vortex. This spectral hump is present at C1, C2, C3, C5 and C6 in the measured data between 300Hz and 1000Hz, although this hump partially overlaps with the irregular peaks due to the tunnel characteristics stated before. However, the same hump with high amplitude occurs due to the tip vortex pulsation could not be captured in the numerical prediction even though the TVC is modelled in the propeller slipstream using the V-AMR technique. This might be because of the lack of flow instability in the numerical calculations that may affect the cavity volume pulsations and structure of the cavity vortex using the DES method and Schnerr-Sauer cavitation model under uniform flow conditions compared to the experiments. The similar phenomenon was also observed under uniform flow conditions, resulting in a lack of instability of the cavity and hence URN (Kimmerl et al., 2021b). It is to be noted that the noise predictions for the inclined shaft configurations were not carried out as similar cavitation extensions and hydrodynamics characteristics were obtained in the CFD calculations similar to experiments.

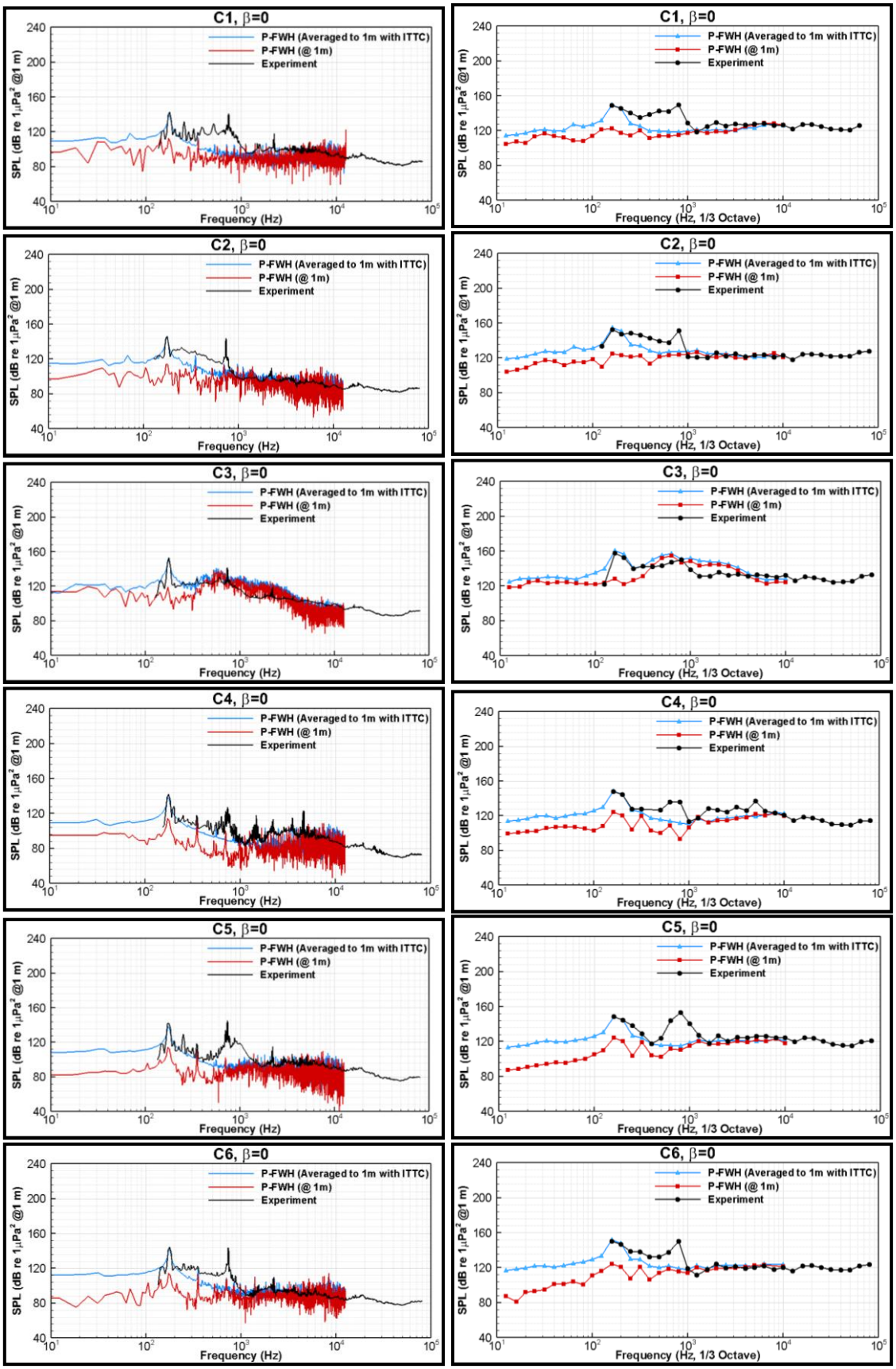

Figure 6.13. Comparison of predicted and measured noise levels for straight shaft conditions in model scale at all operating conditions.

6.2.3.2 Full-scale propeller

In order to compare the numerical results with the measurements performed by different facilities in the scope of the RR test campaign, the URN data needs to be extrapolated from model to full-scale, similar to the experiments. The full-scale condition corresponds to the benchmark propeller's higher operating condition with maximum speed and shaft rotation rate. The details of the operating conditions in full-scale are given in Table 6.6.

Table 6.6. Full-scale propeller operating conditions.

D_S (m)	0.75
n_S (rps)	19.025
σ_s (-)	1.06

where D_S is the diameter, n_S is the propeller rotational rate and σ_{ns} is the cavitation number based on the propeller rotational speed of a full-scale Princess Royal propeller. The prediction of the full-scale propeller URN is made using the procedure given in ITTC, 2017b. In this procedure, the frequency scaling between model and full-scale is given as follows.

$$\frac{f_s}{f_m} = \frac{n_s}{n_m}\sqrt{\frac{\sigma_s}{\sigma_n}} \tag{6.7}$$

An increase in Sound Pressure Level (SPL) from model to full-scale is given as:

$$\Delta SPL = 20\log\left[\left(\frac{\sigma_s}{\sigma_n}\right)^w \left(\frac{r_m}{r_s}\right)^x \left(\frac{n_s D_s}{n_m D_m}\right)^y \left(\frac{D_s}{D_m}\right)^z\right] \tag{6.8}$$

Here, the subscripts s and m refer to full-scale and model scale propellers, respectively. r is the distance between the noise source and receiver. In this procedure, two sets of parameters (w, x, y, z) can be used for the extrapolation, and the selection of parameters is dependent on the variation of acoustic efficiency. When the acoustic efficiency is constant, the formulation is known as the high-frequency formulation. Yet, if there is a linear change in acoustic efficiency with the Mach number, the formulation is known as the low-frequency formulation in the extrapolation procedure (ITTC, 2017b).

During the RR test campaign, the low-frequency formulation was used. Hence, the exponents used in the RR test campaign and this study are given in Table 6.7 for constant and proportional bandwidth spectra.

Table 6.7. Exponents for the low-frequency formulation.

Bandwidth	w	x	y	z
Constant	0.75	1	1.5	1.5
Proportional	1	1	2	1

The noise spectrums are given in OTO band representation in full-scale and Power Spectral Density (PSD). The full-scale noise spectrums are derived using the scaling procedure of ITTC, 2017b, which is briefly explained above, by different facilities and CFD calculations.

Before comparing the numerical predictions with measurements performed by different facilities, the first comparison is carried out using CFD predictions (i.e. PFWH) for all operating conditions to understand the effects of cavitation dynamics and extensions (see Figure 6.5) on propeller URN levels in Figure 6.14. The general conclusions can be summarised as follows:

- In general, the increase in cavitation extensions from C1 to C3 and C4 to C5 increases the noise levels accordingly.
- 1st BPF values are generally predicted at all operating conditions with different amplitudes and centred at a slightly different frequency.
- At high blade loading (i.e. J=0.4) conditions, the URN levels suddenly increase from C1 to C3.
- The largest sheet cavitation observed in C3 manifests itself with higher noise levels among the other conditions.
- At low blade loading conditions (i.e., J=0.5), the highest noise levels are predicted at C6, whereas the lowest noise levels are predicted at C4. The results are in line with the cavitation observations given in Figure 6.5.

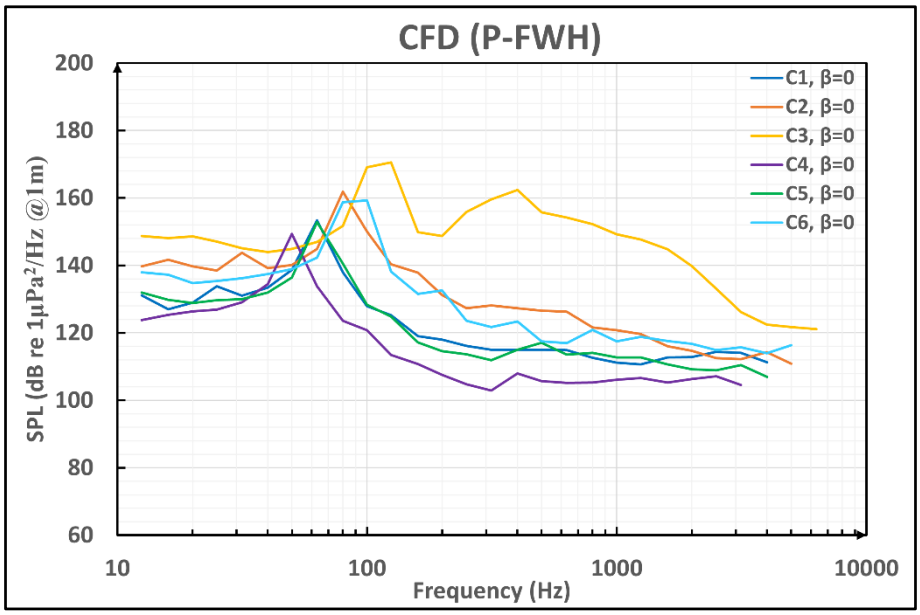

Figure 6.14. Comparison of predicted noise levels by CFD for all operating conditions using the average of three receivers.

The comparison of noise predictions obtained by CFD with the measurements carried out by different facilities is given in Figure 6.15 for all operating conditions. It should be noted that the measured data were obtained using the data digitiser software. Looking at the comparison of noise data from different facilities reveals that the discrepancies between the noise levels are quite considerable. The distinct tonal components caused by propeller singing, mechanical vibrations, drive train noise etc., contributed these discrepancies between the measurements in the low-frequency region of the noise spectrum apart from the slightly different operating conditions used in different facilities. The contributions of additional noise sources could not be eliminated by the background noise corrections. Similarly, the other noise components (e.g., propeller singing) could not be eliminated as they are part of the overall noise levels (Tani et al., 2019b).The numerical results generally underpredict the URN levels compared to measurements by different facilities at C1, C2, C4, C5 and C6, especially until 1kHz. The predicted noise levels are quite close to the measurements performed by UNIGE, UNEW, MARIN, CNR for C1, C2 and C6 after 1kHz. Remarkably, the numerical results slightly overpredict the noise levels at C3 compared to measurements until 1kHz, whereas the noise levels show a sudden decrease in CFD prediction compared to measurements after 1kHz. This might be because of the lack of unstructured and cloudy TVC dynamics in the CFD compared to the experiment, which can be the main driving noise source after 1kHz.

The interpretation of the CFD results in comparison with the experimental data obtained by different facilities is rather difficult. Even though the cavitation extensions between CFD and experiments are important for the noise predictions, inevitably, there are several possible issues related to the noise propagation process, reverberations and tunnel characteristics, etc., in the experimental facilities. These differences in the experimental results might be the another reason for the noise discrepancies between the measurements and CFD. Nevertheless, the CFD results might be evaluated as acceptable in comparison with the measurements by taking the measured margins by all facilities and the uncertainty levels estimated for ship noise predictions based on model tests, which are expected to be 3–5 dB (ITTC, 2017b) into account.

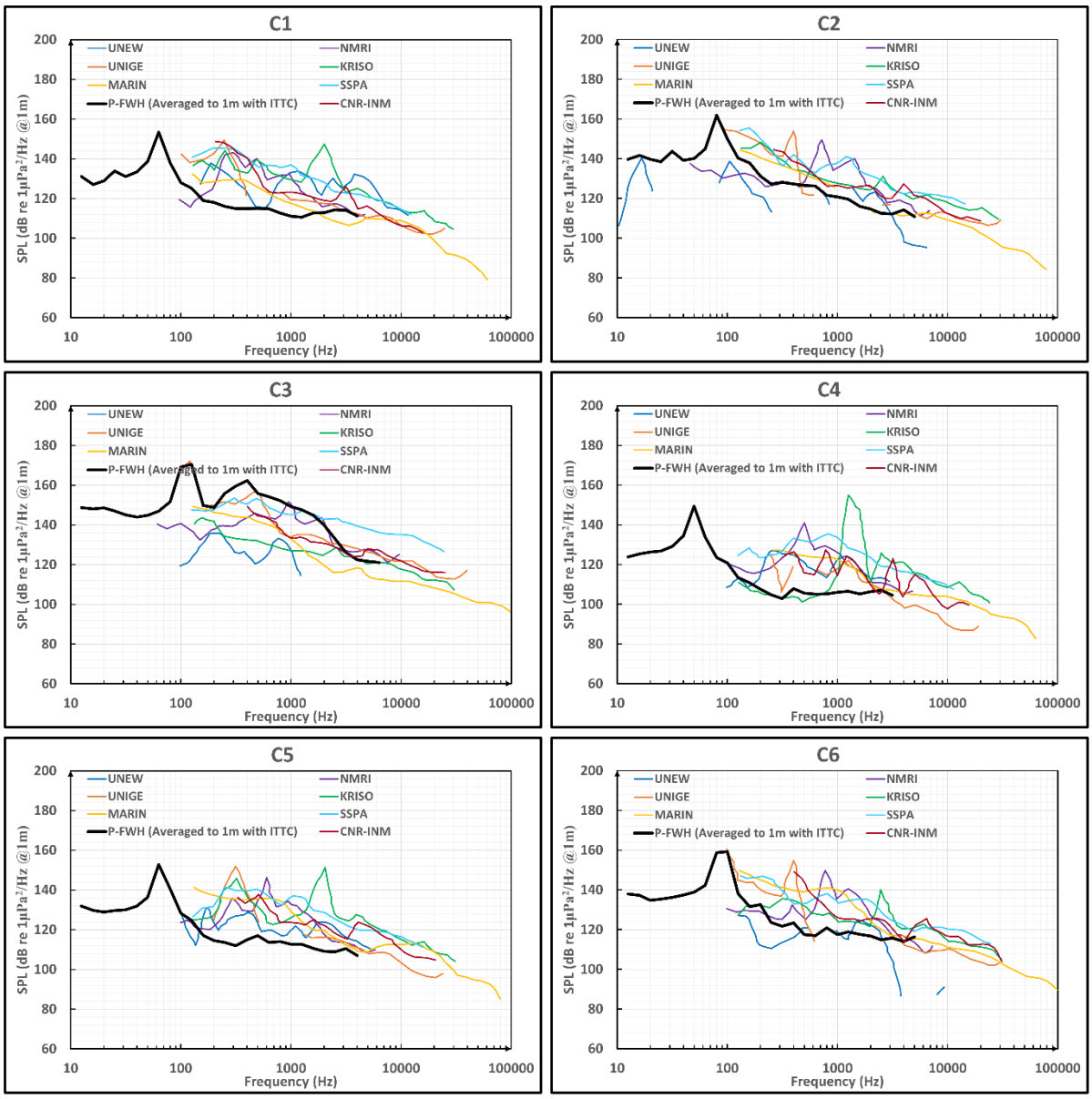

Figure 6.15. Comparison of predicted noise and measured noise levels by different facilities (Tani et al., 2019b) in the scope of RR for all operating conditions in full-scale.

6.3 Under non-uniform flow conditions

6.3.1 Theoretical background

6.3.1.1 Hydrodynamic model

The same hydrodynamic model (i.e., DDES method together with k-ω SST model) was utilised in this Section, similar to Section 6.2.

6.3.1.2 Hydroacoustic model

The permeable formulation of the FWH equation was used in this Section, as used in Chapter 4 and Section 6.2. Thus, the detailed formulations can be found in Section 4.2.1.

6.3.2 Numerical modelling

6.3.2.1 Propeller geometry and test matrix

Akin to Section 6.2, the benchmark Princess Royal propeller was used in this Section to predict the propeller hydrodynamic characteristics, cavitation extensions, and propeller URN.

The propeller operating conditions were defined according to torque and cavitation number identity during the measurements at the University of Genova (UNIGE) cavitation tunnel to reproduce the full-scale operating conditions model scale (Aktas et al., 2016b; Tani et al., 2019a). The experimental setup and tests details can be found in the study by Tani et al., 2019a. The operating conditions investigated in this study are summarised in Table 6.8.

Table 6.8. Test matrix.

	FULL-SCALE				MODEL-SCALE	
Test Condition	Engine RPM	Shaft RPM	Shaft rate (RPS)	STW (knot)	$n\ (rps)$	$\sigma_N(nD)$
C1	900	514	8.6	7.1	25	5.28
C2	1200	685	11.4	9.4	35	3.00
C3	1500	856	14.3	10.5	35	1.91
C4	2000	1142	19.0	15.1	35	1.07

During the experiment, a wire screen was built iteratively to measure the resulting flow field using a 2D-LDV device until a similar non-uniform wake field was found compared to the target wake field measured at Ata Nutku towing tank at Istanbul Technical University (Korkut and Takinaci, 2013). As shown in Figure 6.16, the resulting wake field is compared with the target wake field. As stated in the study by Tani et al., 2019a the reason for missing values on

the left side of the polar graph was the LDV beams' inaccessibility to the measuring area in the tunnel. The target wake field measured at the towing tank was used in the numerical calculations at different operating conditions.

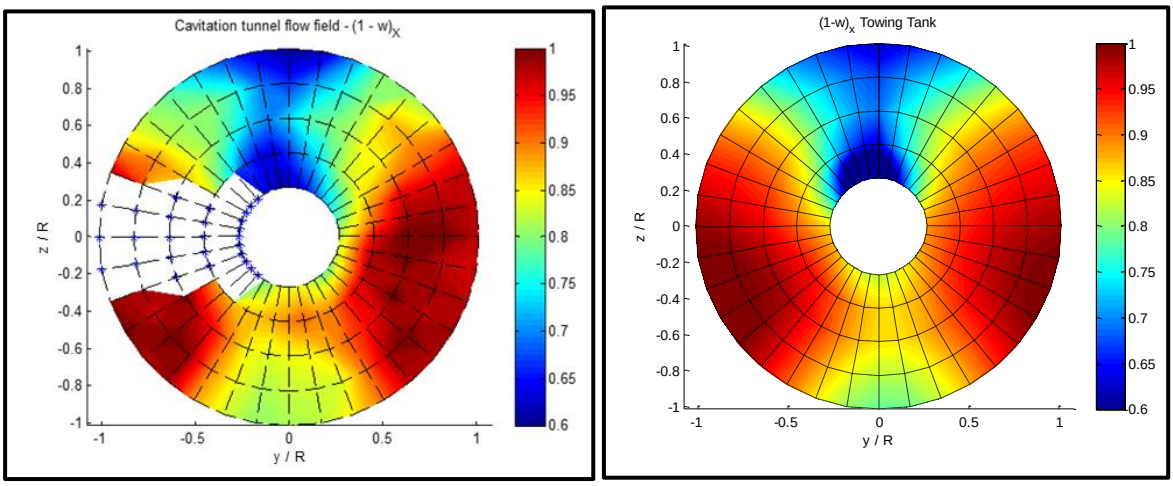

Figure 6.16. Nominal wakefield at the propeller plane (Left: simulated wakefield in the cavitation tunnel, right: target wakefield measured in the towing tank) (Tani et al., 2019a).

6.3.2.2 Computational domain and boundary conditions

The test section of the cavitation tunnel was replicated in the numerical calculations, as in Section 6.2. Also, the same computational domain and boundary conditions were used here, as described in Section 6.2. The wake field was imposed on the inlet to operate the propeller under non-uniform flow conditions.

6.3.2.3 Grid generation

The same meshing techniques, together with the V-AMR technique, as described in Chapter 5, were used, as in Section 6.2. Further details can be found in Section 6.2.2 and Section 5.3.3. The total element count was calculated at around 24M. The grid structure used in the numerical calculations can be seen in Figure 6.17.

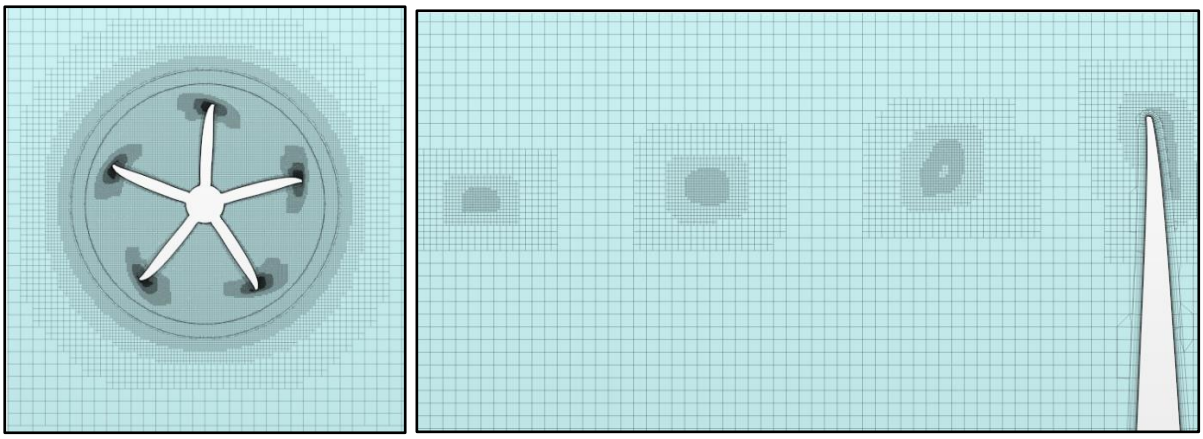

Figure 6.17. Representation of grid resolution in the computational domain, permeable surface, and tip vortex areas.

6.3.2.4 Analysis properties

Akin to Section 6.2, the same solution strategy was adopted in the numerical calculations. The details of the analysis properties can be found in Section 6.2.2.

6.3.3 Numerical results

6.3.3.1 Model scale propeller

- **Hydrodynamic results**

Table 6.9 compares hydrodynamic performance characteristics between CFD, experiment and sea trial. Thrust and torque identity was applied separately during the experiments as the thrust and torque coefficients derived from sea trials do not correlate accurately with the propeller open water curve. Thus, in this study, experimental data obtained by torque identity was used to validate CFD results. The thrust coefficients are determined based on the torque coefficients using the open water characteristics of the propeller. In the CFD calculations, the torque identity was somewhat tried to replicate, but it could not be entirely done as it required several iterations to find the equal torque values with the sea trial and experiment at four different operating conditions.

As shown in Table 6.9, the maximum difference between the sea trial and experiments is 8.805% in Condition 4, whereas the minimum difference is around 1% in Condition 1 for torque coefficient.

Table 6.9. Comparison of global performance characteristics between CFD, experiment and sea trial data for all operating conditions.

	SEA TRIAL AND EXPERIMENTS		CFD		Δ (%)	
Condition	$10K_Q$ (sea trial)	K_T(from $10K_Q$)	K_T	$10K_Q$	K_T	$10K_Q$
C1	0.336	0.237	0.239	0.339	0.844	0.893
C2	0.318	0.221	0.236	0.340	6.787	6.918
C3	0.323	0.225	0.237	0.342	7.239	5.882
C4	0.318	0.221	0.237	0.346	5.333	8.805

- **Cavitation observations**

Figures 6.18, 6.19, 6.20 and 6.21 show the comparison of cavitation extensions between CFD, experiment and sea trial data. The experimental figures were taken from Tani et al., (2019a), whereas the sea trial observations were taken from Sampson et al. (2015) for all operating conditions.

Figure 6.18 shows the cavitation extension observed when the engine speed was 900rpm (i.e., C1). The full-scale propeller cavitation mainly consists of leading-edge tip vortex cavitation. The relatively stable tip vortex cavitation, which is less intermittent, emanating from the blade's suction side, is present in full-scale. This stable leading-edge vortex cavitation extends through the propeller slipstream. Also, the cavitation dynamics seem to be experienced with bursting phenomena, as shown in Figure 6.18. At C1, the model scale observations are characterised by the leading-edge vortex cavitation when the propeller passes at 0^o, similar to the full-scale. Unlike the sea trials, the vortex cavitation is not persistent in the model scale. Compared to the sea trial and experiment, relatively less leading-edge vortex cavitation is observed in the CFD calculations. As the vortex diameter is quite small, the CFD predictions could not capture the vortex cavitation as in the sea trial. Nevertheless, the cavitation observations on the blades obtained by CFD, experiment and sea trial are similar, except for the leading-edge vortex cavitation in the propeller slipstream.

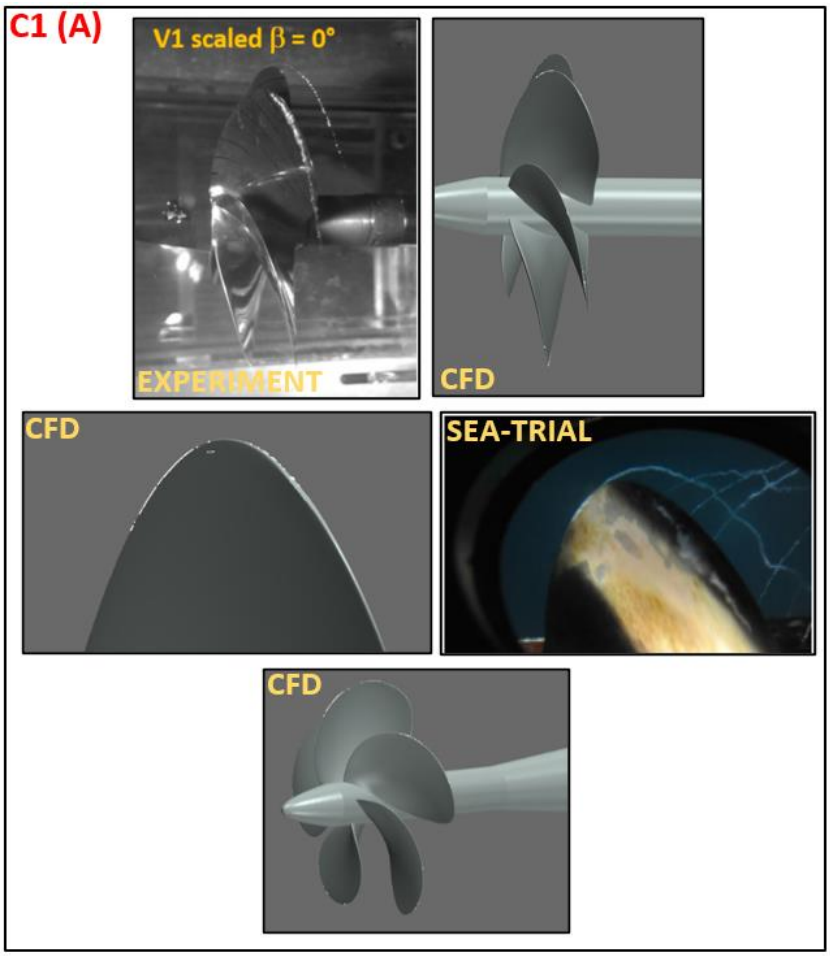

Figure 6.18. Comparison of cavitation observations between CFD, experiment and sea trial at C1 ($\alpha_v = 0.1$).

The cavitation observations are compared at 1200rpm engine speed (i.e., C2) in Figure 6.19. As shown in Figure 6.19, with an increase in engine loading from 900rpm to 1200rpm, the strong suction side sheet cavitation appears on the blades in the full-scale. Also, the sheet cavitation breaks up partially and shedding bubble and vortex structures extending downstream of the propeller can be observed. The experiments and CFD predictions show the analogous feature of the cavitation, except for complex cavity structures. Unlike the experiment, the sheet cavitation is observed at inner radii in the CFD calculations, similar to sea trial observations. Both experiment and sea trial observations show trailing vortices in the propeller slipstream, whereas the extension of vortices in the CFD is almost non-existent.

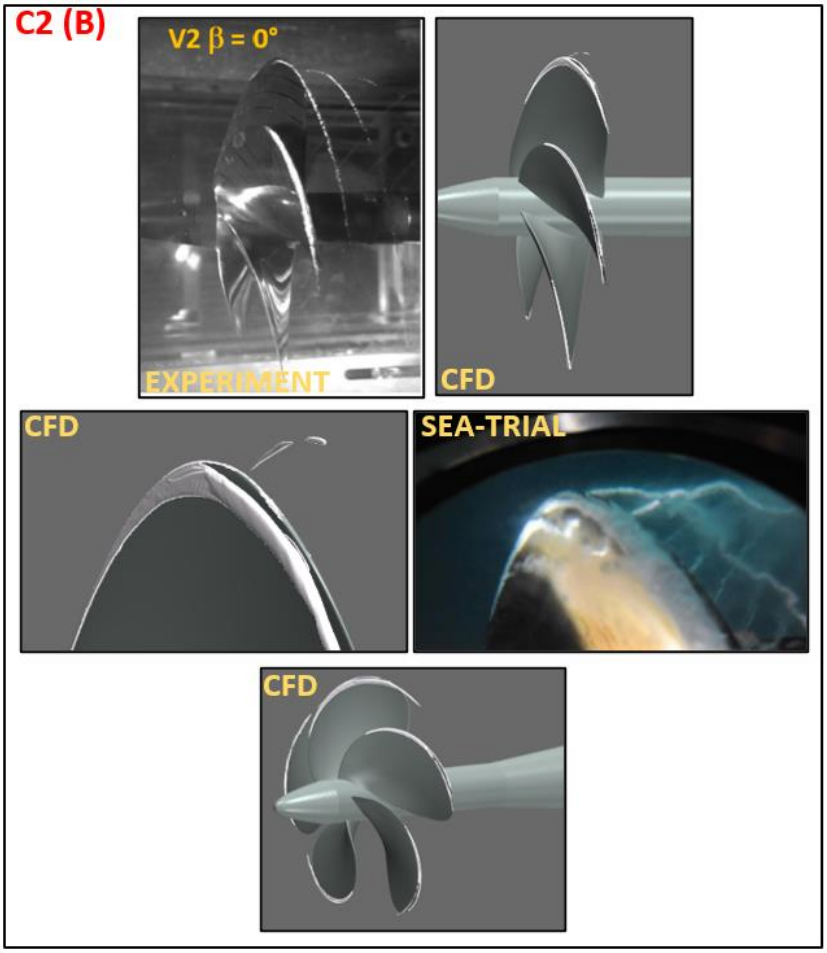

Figure 6.19. Comparison of cavitation observations between CFD, experiment and sea trial at C2 ($\alpha_v = 0.1$).

Looking at the other full-scale operating condition (i.e., 1500rpm, C3) in Figure 6.20, the cavitation structures vary considerably compared to the previous operating condition (i.e., Figure 6.19). The sheet cavitation becomes unstable, and its volume, intensity and chordwise extension on the blades increase significantly. The unsteady structures concentrate at the blade tip where the roll-up mechanism terminates the sheet cavity, resulting in TVC formation. Similar to sea trials, the extension and volume of sheet cavitation increase in the experiment and CFD. The break-up of tip vortices is not present, and its diameter is clearly defined in the CFD. The TVC extension in the propeller slipstream in the CFD is not as same as the model experiment and sea trial observation. This is because the V-AMR technique was applied inside the rotating region with reasonable extension to keep the computational cost reasonable. Also, the diameter of the TVC reduces further downstream and additional refinements with reduced mesh size might be required.

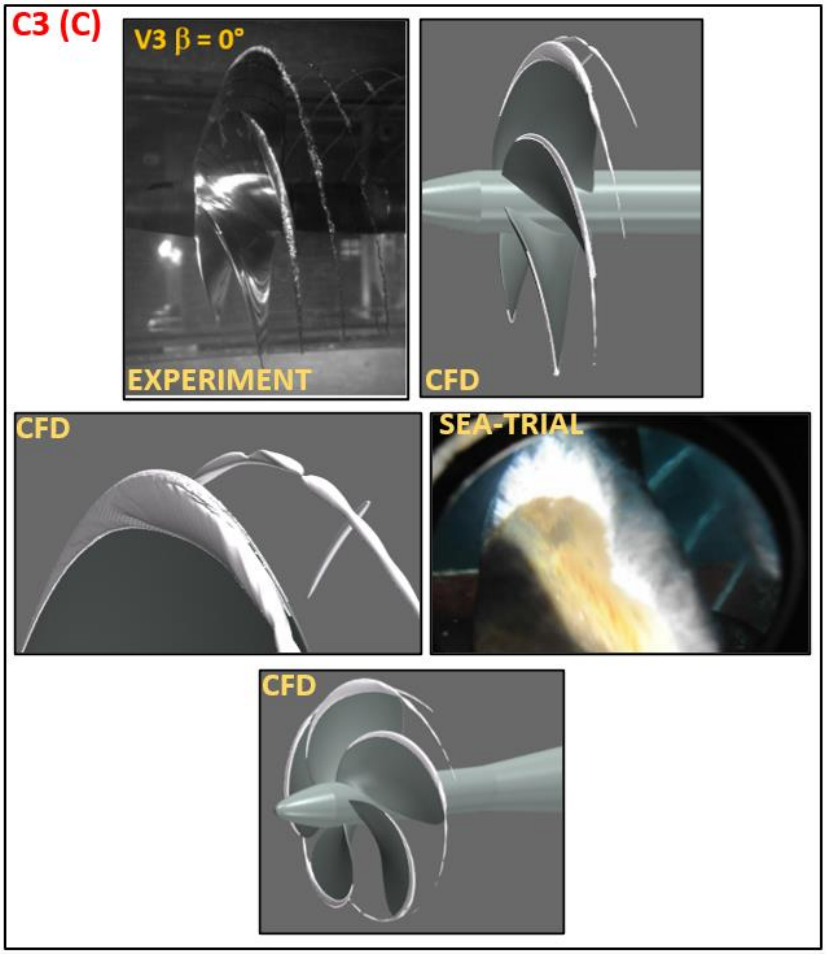

Figure 6.20. Comparison of cavitation observations between CFD, experiment and sea trial at C3 ($\alpha_v = 0.1$).

The cavitation extensions observed at the highest loading condition (i.e., C4 at 2000 engine rpm) are given in Figure 6.21. The cavitation volume and intensity increase rapidly at this operating condition, and the sheet cavitation covers approximately 25-30% of the blade. As shown in Figure 6.21, the unsteady sheet cavitation and the cloudy formation are present. Similar to C2 and C3, the roll-up terminates the sheet cavitation at the propeller's blade tip, and thick, cloudy and unstructured TVC occurs and extends downstream of the propeller. The experiment and CFD calculations could not capture the cloudy appearance of the sheet and TVC as in the sea trial. Additionally, the coverage of sheet cavitation on the blades is underpredicted in the experiment and CFD compared to the sea trial observations. Despite the lack of cloudy TVC dynamics observed in the experiment and CFD, the unstable behaviour of TVC dynamics is observed partially in comparison with the sea trial data. The sheet cavitation is present at inner radii in the CFD, and overall cavitation volume seems to be higher in the CFD observations compared to the experiment.

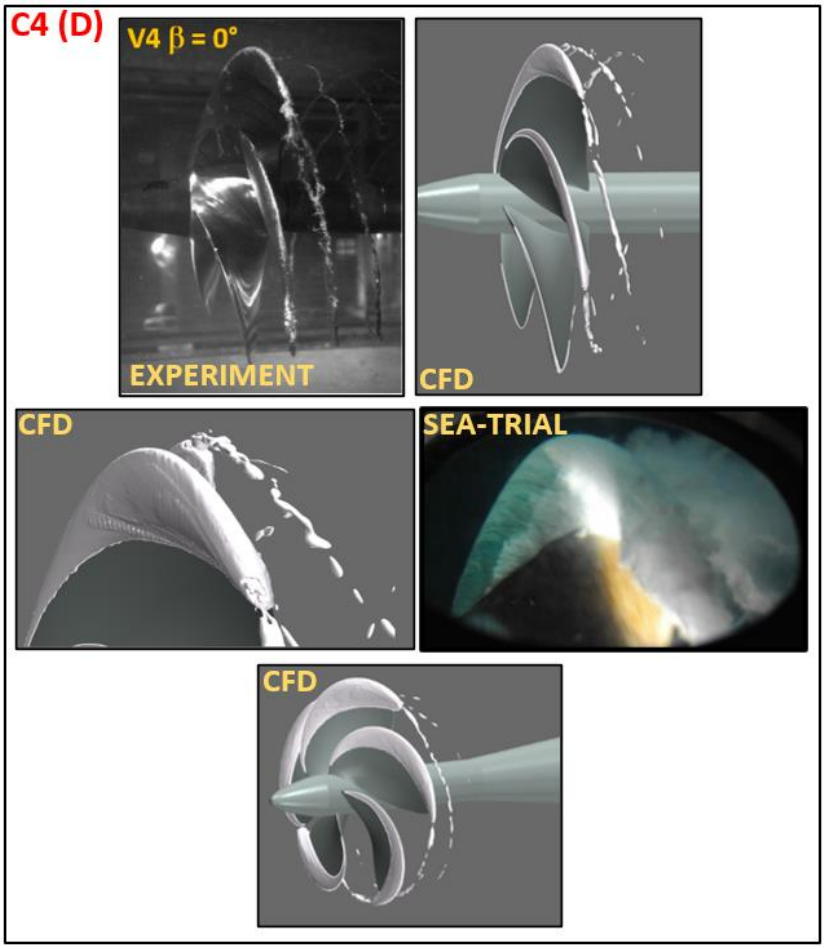

Figure 6.21. Comparison of cavitation observations between CFD, experiment and sea trial at C4 ($\alpha_v = 0.1$).

- **URN predictions**

Verification of the results

The verification study is generally conducted for hydrodynamic performance coefficients (e.g., thrust, torque and efficiency) for marine propellers using different grid spacing. According to the uncertainty of the numerical solution, suitable grid spacing is found in the numerical calculations. However, the hydrodynamic and hydroacoustic solutions differ considerably. The hydrodynamic performance coefficients can be predicted accurately with relatively coarse grid numbers. In contrast, the hydroacoustic results dependent on more grid resolution than the hydrodynamic solution, as shown in Chapter 4. The relatively coarse grids used in the hydrodynamic simulations are not suitable for the hydroacoustic part of the solution. This is because the insufficient grid resolution for the hydroacoustic part can create non-physical numerical noise and contaminate the overall acoustic pressure levels. Due to this fact, the verification of propeller URN predictions can be carried out by comparing hydrodynamic and

hydroacoustic results in the near-field (i.e., in the vicinity of the propeller and porous surface) as in Section 6.2.

Figure 6.22 and Table 6.10 show the location of the receivers and their coordinates, respectively. The NHP1 is positioned upstream of the propeller, whereas the NHP3 is located downstream of the propeller. The NHP2 is located at the propeller plane. The origin of the coordinates is defined as the centre of the propeller blades.

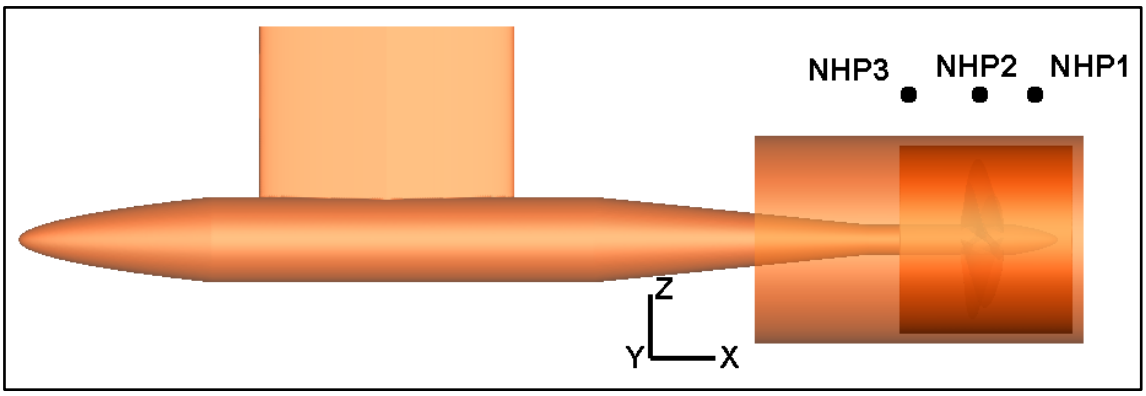

Figure 6.22. Representation of receivers around the porous region (Figure is not scaled).

Table 6.10. Receiver coordinates.

Receiver	X (m)	Y (m)	Z (m)
NHP1	0.05	0	0.171
NHP2	0	0	0.171
NHP3	-0.06	0	0.171

Figures 6.23 and 6.24 show the hydrodynamic and hydroacoustic pressures computed at the C1 (i.e. 900rpm) and C2 (i.e., 1200rpm) loading conditions, respectively, for three receivers located in the vicinity of the propeller. In the near field, the overall pressures are mainly characterised by BPF (Blade Passage Frequency) for C1 and C2. For both operating conditions, the contribution of linear noise sources to the overall acoustic pressure level is dominant, particularly for NHP1 and NHP2. Further downstream (i.e., NHP3), the contribution of nonlinear sources coming from the propeller slipstream can start to appear. Hence, the pressure increases with respect to the receiver located upstream of the propeller (i.e., NHP1) though their locations from the noise source are quite similar. The maximum hydrodynamic and hydroacoustic pressures are computed at NHP2 as it is located at the propeller plane, where the linear noise terms are more dominant than those of upstream and downstream. As shown in the previous Section, the considerable increase in cavitation volume increases the pressure levels

from C1 to C2 for each receiver. The agreement between both pressures at each receiver location shows the accuracy of the hydrodynamic and hydroacoustic solutions.

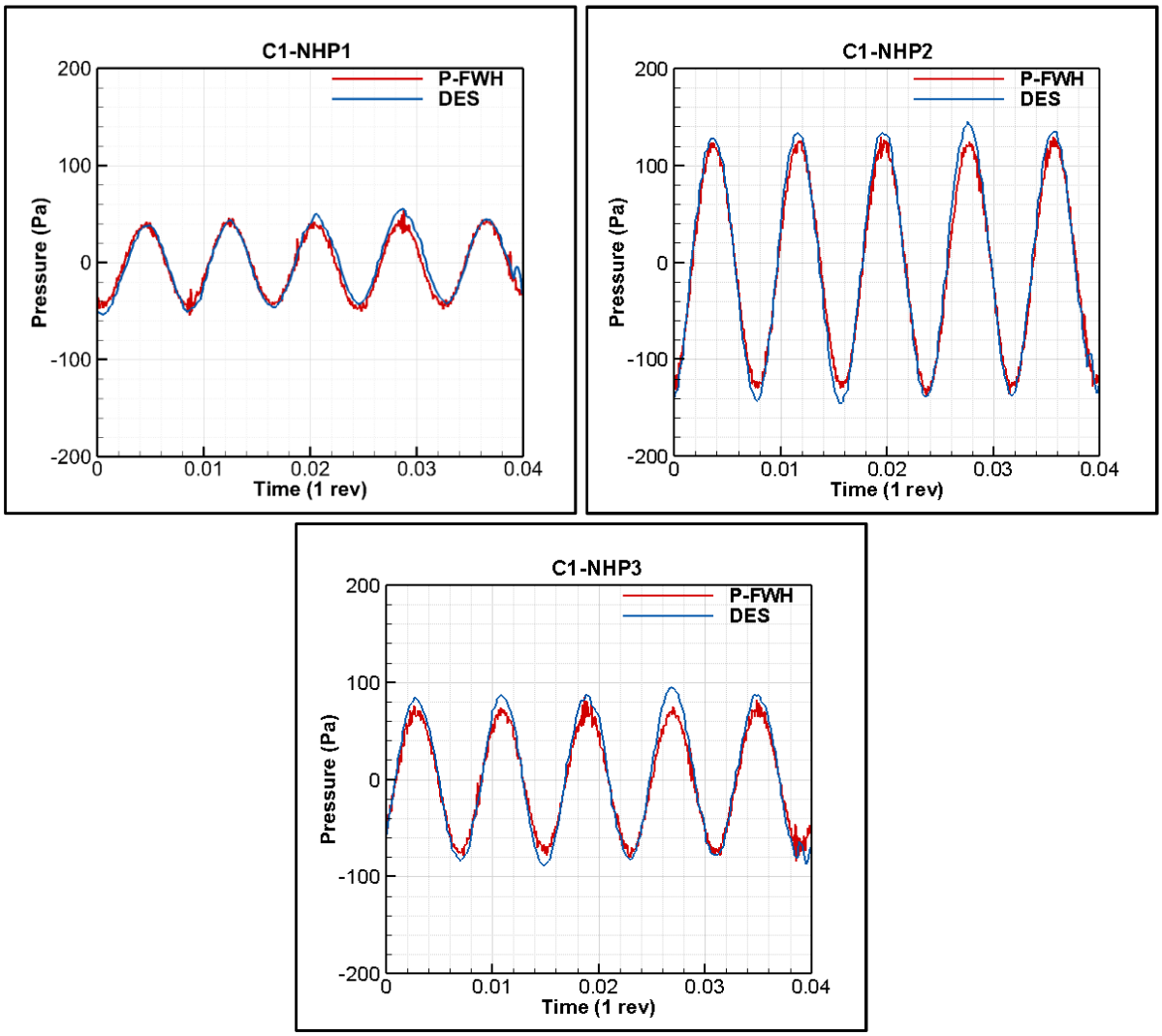

Figure 6.23. Comparison of hydrodynamic and hydroacoustic pressures at C1 for three receivers located in the near-field.

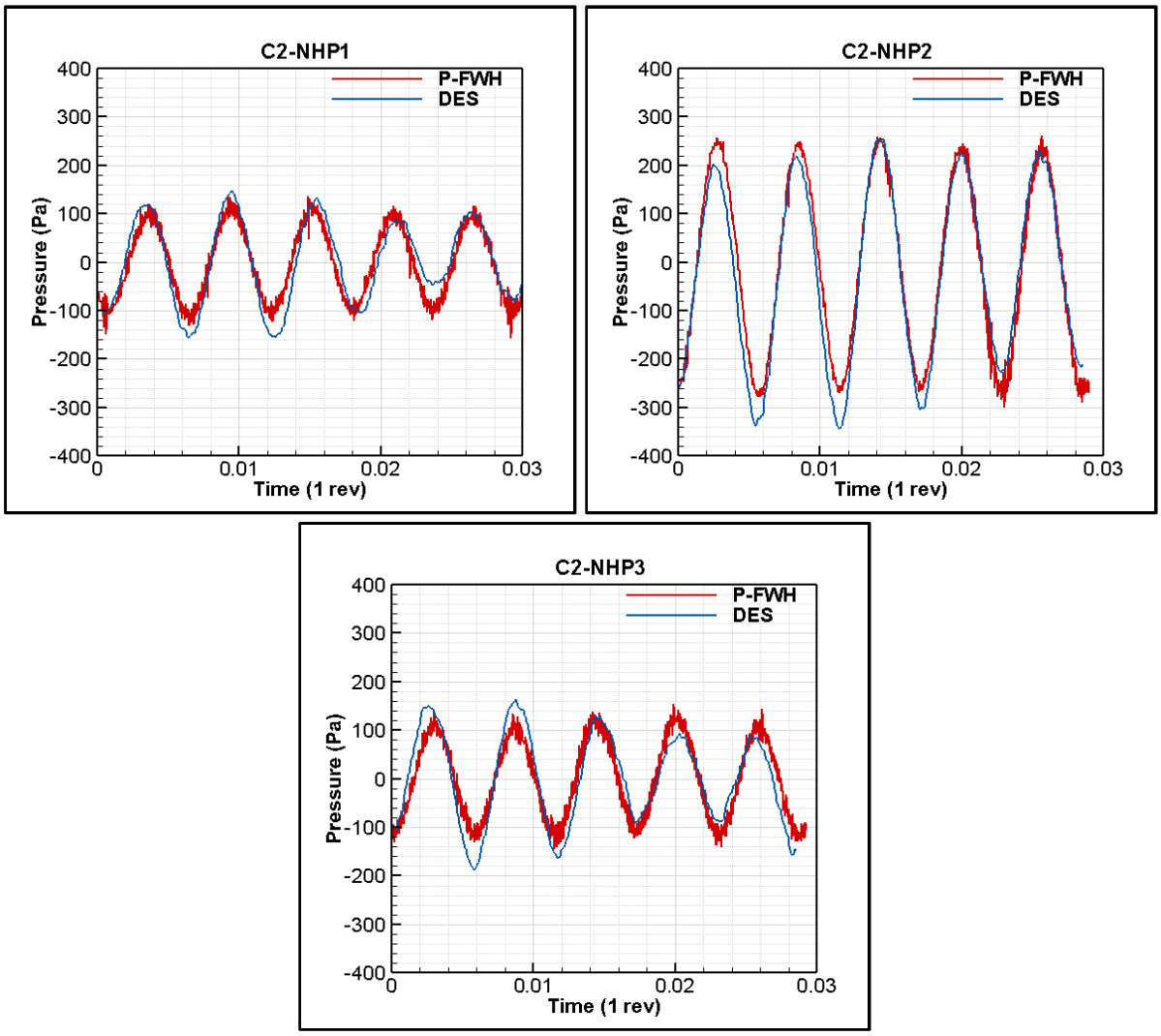

Figure 6.24. Comparison of hydrodynamic and hydroacoustic pressures at C2 for three receivers located in the near-field.

Comparison of numerical URN predictions with the measurements

The noise measurements were conducted in the UNIGE using three different receivers, as shown in Figure 6.11. The Source Strength Levels (SL) were computed from the measured Sound Pressure Levels (SPL), and noise spectrums were derived in one-third octave (OTO). The propeller URN predictions in model scale between the CFD and experiment were carried out using the H1 receiver.

Figure 6.25 compares predicted URN levels with the measured data in the cavitation tunnel at four different operating conditions. The general comments regarding the comparison between CFD and the experiment can be summarised as follows:

- As explained in Section 6.2, there is a peak around 740Hz and it is considered that it is related to the vibration of receiver support during the measurements.
- The CFD predictions agree with the measured data, particularly at C1, C2 and C3. However, unlike these conditions, the propeller URN levels are overpredicted up to 10dB between 1kHz and 4kHz using CFD compared to measured data at C4. This can be associated with the larger sheet cavitation observed in the CFD than in experimental observations.
- There is a discrepancy around 1kHz between CFD and experiment for all operating conditions. This deviation seems to be because of the vibration of receiver support during the measurements, as explained above.
- The URN levels predicted by CFD using the receiver located at 1m and shifted to 1m using the HP1 and the ITTC distance normalisation show similar values as the near-field effects are not present at HP1 compared to HP2 and HP3 under non-uniform flow conditions.
- C2, C3 and C4 conditions slightly show a spectral hump in the CFD predictions due to the TVC modelled using the V-AMR technique between 400Hz and 1kHz, similar to experiments.
- The 1st BPF value is well predicted in the CFD predictions for all operating conditions.
- With increased engine loading, more extended cavitation is seen on and off the blade. This resulted in increased URN levels from C1 to C4.

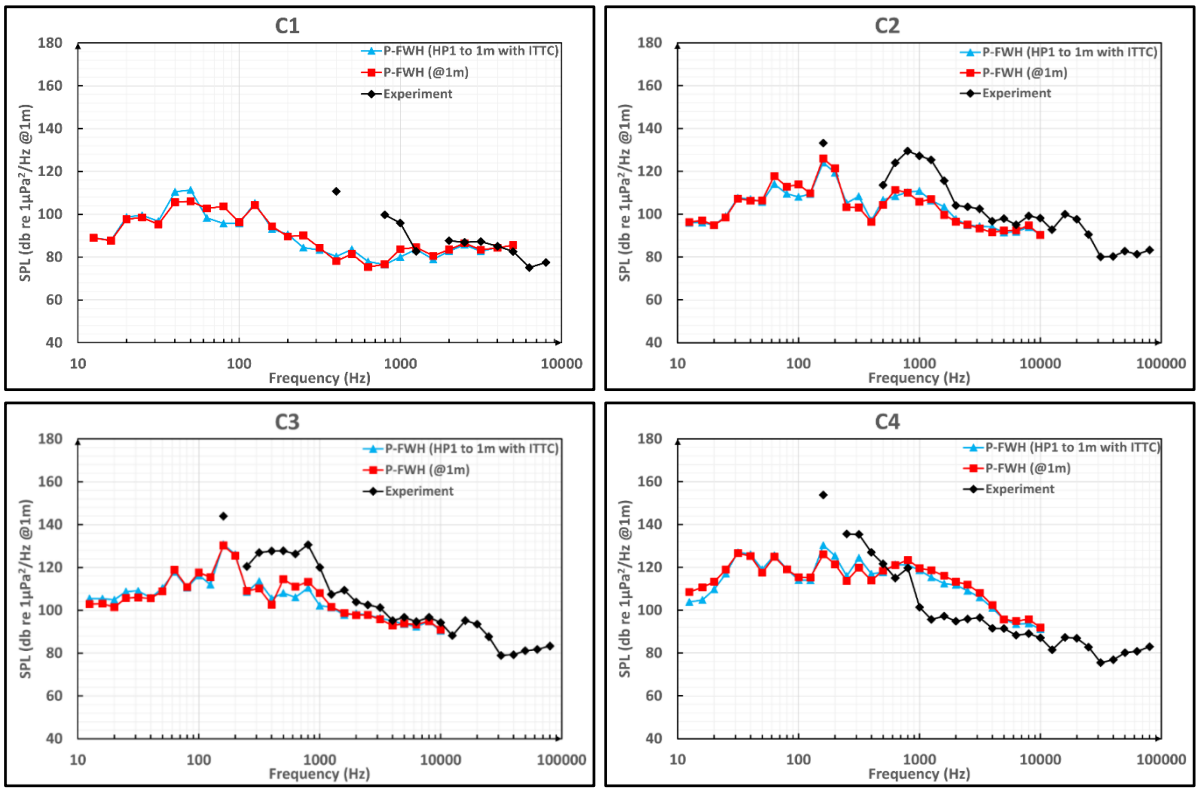

Figure 6.25. Comparison of predicted URN levels with measured data at C1, C2, C3 and C4 in model scale.

6.3.3.2 Full-scale propeller

- **URN predictions**

The sea trials for the Princess Royal vessel were carried out to measure the URN in full-scale in the scope of the SONIC project at different operating conditions, and a comprehensive database was created (SONIC, 2012). During the sea trials, different receiver arrays were utilised by SOTON and CETENA and data was presented both in narrowband and OTO. Hence, the numerical results were compared with the full-scale data collected by CETENA and SOTON in this study. The details of the full-scale measurements conducted by SOTON can be found in Brooker and Humphrey, 2014; Brooker and Humphrey, 2016; Humphrey and Brooker, 2019. It should be noted that the full-scale noise spectra are derived using the average of three receivers and the receiver located at 1m, as shown in Figure 6.11. The noise spectrums are given in OTO band representation in full-scale at 1m.

As given in Section 6.2.3, the same extrapolation technique was used by following the ITTC procedure (ITTC, 2017b). The noise spectrums are given in OTO band representation in full-scale at 1m, and spectra are presented as Power Spectral Density (Pa^2/Hz). The details of the formulation and selected parameters can be found in Equations 6.7 and 6.8 and Table 6.7.

Figure 6.26 compares extrapolated results using the CFD and experiment with the full-scale measurements performed by SOTON and CETENA. As shown in Figure 6.26, the numerical results are extrapolated to full-scale using both the average of three receivers and the receiver located directly at 1m. The numerical results underpredicted the URN levels at certain frequencies compared to sea trials at C1. According to cavitation extensions, the weak leading-edge vortex cavitation, which extends in the propeller slipstream, is observed during the sea trials. However, this TVC could not be observed in the CFD calculations, including possible bursting phenomena (see Figure 6.18). Thus, the lack of leading-edge vortex cavitation dynamics captured in the CFD calculations and many other full-scale factors can cause the differences between predicted and measured URN levels in full-scale. Similar to CFD predictions, the URN levels are underpredicted up to 10dB using the extrapolated measured data obtained by the cavitation tunnel measurements at certain frequencies. The 1st BPF value is captured in the CFD calculations in the low-frequency region of the noise spectrum. The extrapolated data at 1m using the average of three receivers and the receiver located directly at 1m show a different behaviour, particularly until 1kHz. The reason can be because the near-field effects are more dominant at receivers H2 and H3 than H1. Thus, the dominant near field effects for H2 and H3 characterise the receivers' average, particularly when the cavitation is not strong, resulting in a noise difference compared to the receiver located directly at 1m.

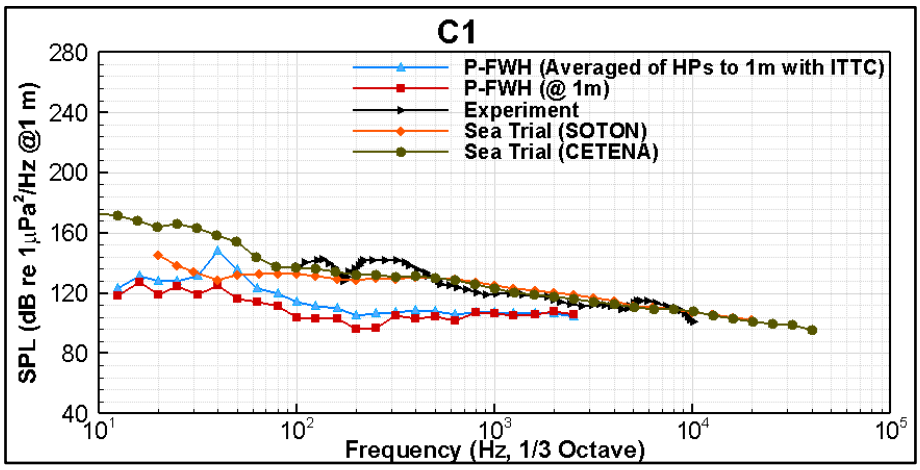

Figure 6.26. Comparison of predicted noise levels using CFD, measured data using the cavitation tunnel with full-scale measurements at URN at C1 in full-scale.

Figure 6.27 compares CFD predictions, cavitation tunnel measurements and full-scale measurements in full-scale at C2. As shown in Figure 6.27, the discrepancy between the CFD prediction and full-scale measurements is around 15dB between approximately 100Hz and 3kHz at C2. The complex cavity dynamics, including break-up phenomena and TVC extension in the propeller slipstream, could not be observed in the CFD calculations, although similar

sheet cavitation extensions are present between CFD, experiment and full-scale observations (see Figure 6.19). Therefore, these dissimilarities between the CFD predictions and full-scale observations are probably the main reason for the URN difference. The extrapolated data using the tunnel measurements show that URN levels are underpredicted in full-scale compared to sea trial data. Nevertheless, the extrapolated data using the tunnel measurements are closer to the full-scale measurements than those of extrapolated data based on CFD predictions.

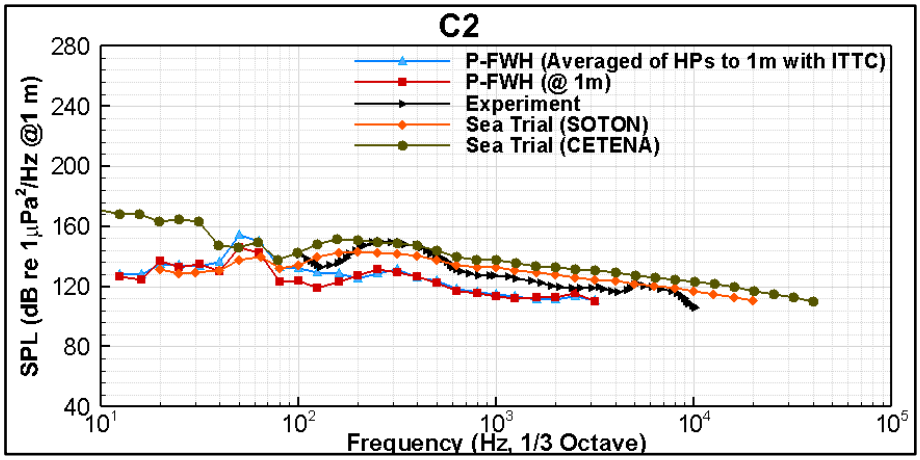

Figure 6.27. Comparison of predicted noise levels using CFD, measured data using the cavitation tunnel with full-scale measurements at URN at C2 in full-scale.

Similar to C2, the measured full-scale URN levels are higher than those of extrapolated URN levels using CFD at C3, as shown in Figure 6.28. The discrepancy of URN levels is around 10dB between both approaches. Akin to the previous conditions, the numerical calculations underpredicted the URN levels up to 15dB compared to full-scale measurements at C3, as shown in Figure 6.28. The unstable sheet cavitation with the cloudy formation and periodic vortex break up phenomenon is not present in CFD observations. Hence, this lack of cavitation dynamics leads to the URN differences between the CFD and full-scale measurements.

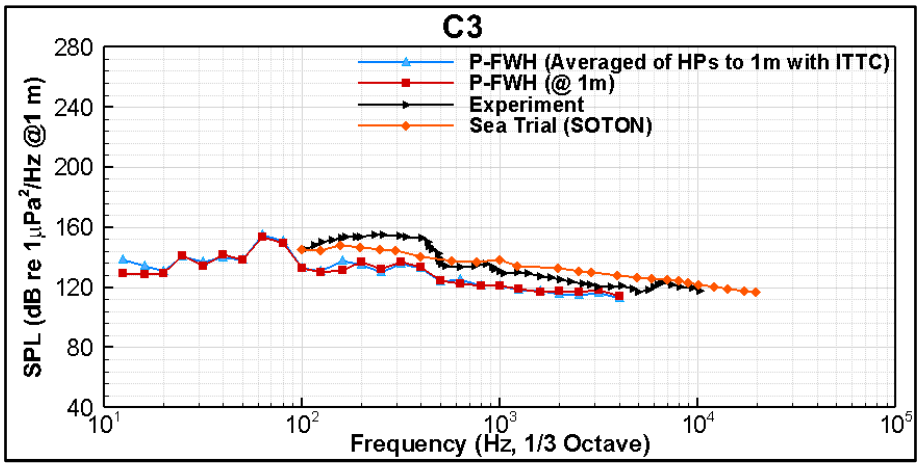

Figure 6.28. Comparison of predicted noise levels using CFD, measured data using the cavitation tunnel with full-scale measurements at URN at C3 in full-scale.

The last comparison between the CFD, tunnel measurements and sea trial data is carried out at the highest loading condition (i.e., C4) in Figure 6.29. Unlike the other operating conditions (i.e., C1, C2 and C3), the numerical predictions are in good agreement with the full-scale measurements up to around 2kHz. Akin to the other operating conditions, the 1st BPF value is well captured in the CFD. The numerical results show sudden decay after 2kHz. The reason is that the strong TVC dynamics observed during the sea trials at C4 and these dynamics can dominate the broadband part of the noise spectrum. Also, the interaction between sheet and TVC is rather complex at C4. Thus, the lack of reproduction of cavity dynamics and their interactions can cause the underprediction of URN levels after 2kHz.

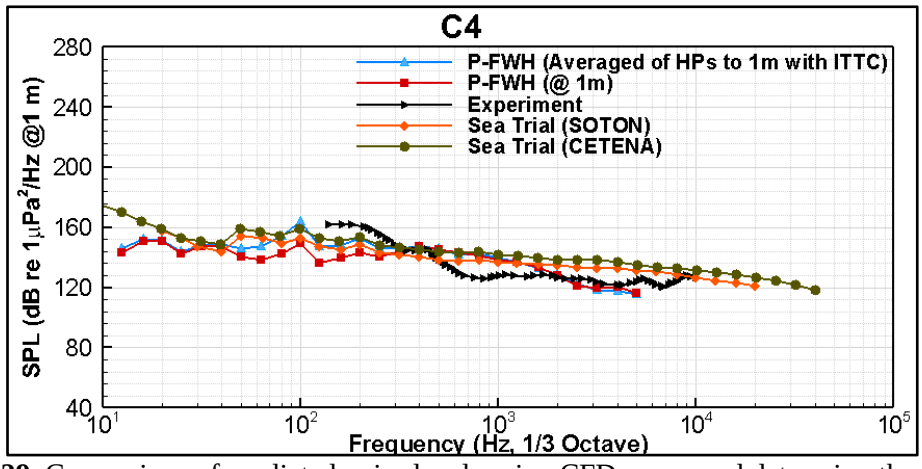

Figure 6.29. Comparison of predicted noise levels using CFD, measured data using the cavitation tunnel with full-scale measurements at URN at C4 in full-scale.

The underprediction of propeller URN levels between the sea trial and extrapolated data based on CFD predictions can also be related to different flow field modelling and, hence, the Reynolds number. This different flow field between the model and full-scale propeller inevitably affects the cavitation dynamics; hence, the propeller URN. This can be further related to the interaction between the hull and propeller, which is not present in the present case.

6.4 In the presence of a scaled hull model

6.4.1 Theoretical background

6.4.1.1 Hydrodynamic model

The same hydrodynamic model (i.e., DDES method together with k-ω SST model) was utilised in this Section, as used in Section 6.2 and Section 6.3. To observe the flow regions where the RANS and LES methods are actively employed, the DES correction factor (i.e., F_{DES}), which is an available tool for the DDES variant, can be used, similar to Section 6.2. As shown in Figure 6.30, a thin unsteady RANS region is attached to the ship hull, which means that unsteady RANS provided a boundary layer solution. Also, the LES method is utilised in the propeller slipstream, especially inside the permeable surface, to account for nonlinear noise contributions on overall noise levels for noise predictions. When the grid is coarsened far-field of ship wake, the solution is also provided by the unsteady RANS solution, similar to the open water propeller, as shown in Section 6.2.

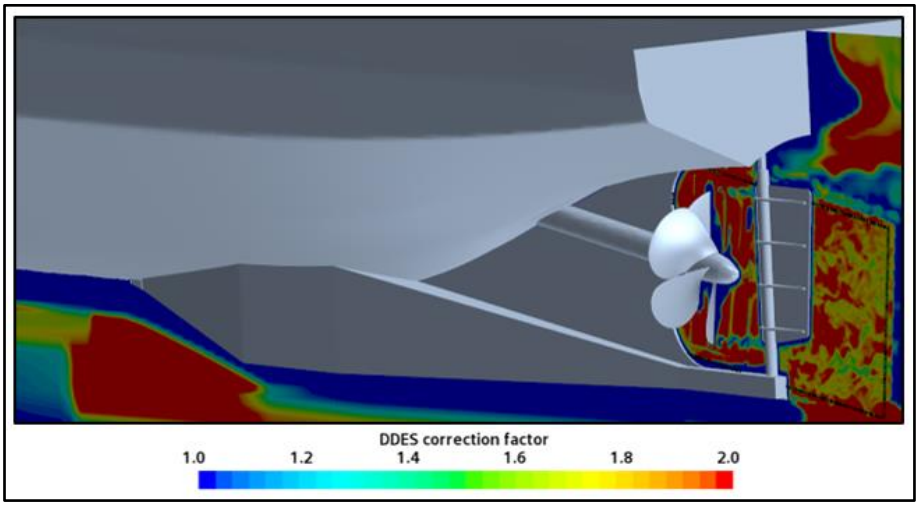

Figure 6.30. Contour plots of DES Correction Factor (RANS is $F_{DES} = 1$ and LES is $F_{DES} > 1$).

6.4.1.2 Hydroacoustic model

The permeable/porous formulation of the FWH equation was used in this Section, as in Chapter 4, for Sections 6.2 and 6.3. Thus, the detailed formulations can be found in Section 4.2.1.

6.4.2 Numerical modelling

6.4.2.1 Propeller geometry and test matrix

In the scope of the SONIC project (SONIC, 2012), model tests of The Princess Royal vessel were carried out by several facilities to collect a database of hull pressure fluctuation, cavitation and URN characteristics of the propeller at different operating conditions. Amongst the different experiments conducted in different cavitation tunnels, the properly scaled full model (i.e., not a dummy body but with a demi-hull) of The Princess Royal vessel was also tested in the Large Circulation Water Channel of CNR INSEAN. Thus, this makes The Princess Royal vessel's model scale a strong candidate for validating current numerical results with the experimental data obtained in CNR-INSEAN. The experiments were conducted using a scaled model of the Princess Royal vessel with a scale ratio of 3.4. The main geometrical characteristics of the ship and propeller are given in Table 6.11, whereas the demi-hull model is shown in Figure 6.31.

Table 6.11. Main geometrical characteristics of the vessel and propeller both in full and model scale (Felli et al., 2014).

Properties	Full-Scale	Model Scale
L_{OA} (m)	18.88	5.55
L_{BP} (m)	16.45	4.84
Breadth moulded at design waterline (B) (m)	7.03	2.07
Breadth extreme (B) (m)	7.34	2.16
Depth moulded (D) (m)	3.18	0.93
Demi-hull separation (m)	4.9 (CL)	0.72 (to symmetry plane)
Draught (lightship) Amid (T) (m)	1.65	0.48
Draught (lightship) AP T_{AP} (m)	1.70	0.5
Draught (lightship) FP T_{FP} (m)	1.60	0.47
Number of propellers	2	1
Propeller Diameter, D (m)	0.75	0.22
Chord @ 0.7R	0.352	0.103
Number of blades	5	5
Nominal pitch ratio (FPP)	0.8475	0.8475
Skew angle (^{o})	19	19
Rake angle (^{o})	0	0
Expanded area ratio	1.057	1.057
Boss-Diameter ratio	0.18	0.18

Figure 6.31. Model scale vessel tested in the cavitation tunnel (Felli et al., 2014).

During the experiments, several operating conditions corresponding to the full-scale operating conditions were tested for cavitation observation, measurement of pressure hull fluctuations and URN. These operating conditions, investigated in this Section, are summarised in Table 6.12. Here, U is the vessel speed in full-scale, V_M is the model testing velocity, n is the propeller rotational rate, J is the advance ratio, P_0 is static pressure, σ_n is the cavitation number based on propeller rotational rate. In the cavitation tunnel, the oxygen content was set to 0.25 mg/l at the 14^o C water temperature throughout the experiments.

Table 6.12. The test matrix used (Felli et al., 2014).

Condition	U (kn)	V_M (m/s)	n (rps)	J	P_0 (mbar)	σ_n
1	4.775	1.33	10.53	0.57	70	11.07
2	5.200	1.45	12.26	0.54	70	8.17
3	7.100	1.98	15.80	0.57	80	5.09
4	9.350	2.61	20.96	0.56	70	2.81

6.4.2.2 Computational domain and boundary conditions

In the numerical calculations, the test section of the large circulation tunnel of CNR INSEAN was replicated with extended upstream and downstream. A tunnel is a vertical plane, and it has a free surface and 4 million litres capacity. The test section of the facility has 10m length, 3m width and 2.25m maximum water depth. In the measurements, the demi-hull of the model was placed close to the right vertical wall of the tunnel measuring section to represent the symmetry (centre) plane for the Princess Royal. In the numerical calculations, the computational domain was extended to $2L_P$ from the FP (fore-peak) and $4L_P$ from the AP (aft peak). The domain width was set to 3.6m. The origin was located on the free surface at 2.25m water depth as in the tunnel. The tunnel setup and computational domain used in the numerical calculations are given in Figures 6.32 and 6.33, respectively. As shown in Figure 6.33, the vessel is trimmed according to the tested conditions in the tunnel, and hence free surface is neglected to simplify the problem to decrease the computational cost. The inlet of the computational domain was defined as velocity inlet, whereas the outlet side was defined as pressure outlet. The side and bottom surfaces of the domain were defined as a wall. The free surface was defined as a symmetry boundary condition. The no-slip boundary conditions were also defined for the hull, including appendages and the propeller.

The computational domain is divided into three regions: rotating, static, and noise, as shown in Figure 6.33. These regions connected each other with internal interfaces. The rotating region provided the propeller rotational motion, whereas the noise region was used to compute the acoustic pressures at every timestep.

Figure 6.32. Tunnel setup for the measurements (Felli et al., 2014).

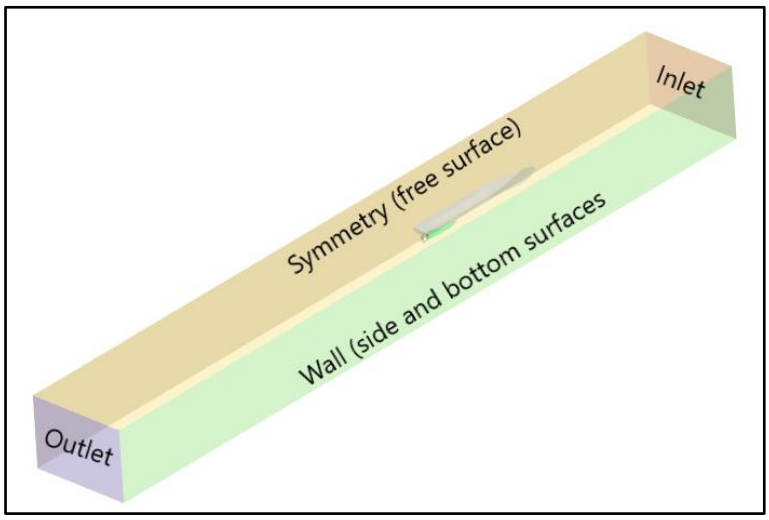

Figure 6.33. The computational domain used in the numerical calculations.

In the numerical calculations, first, the rudder was neglected to simplify the meshing process for the permeable surface, which encapsulates the propeller and its slipstream. Then, the rudder was refitted into the vessel as in the experiment to explore its influence on propeller URN. These two configurations are given in Figure 6.34.

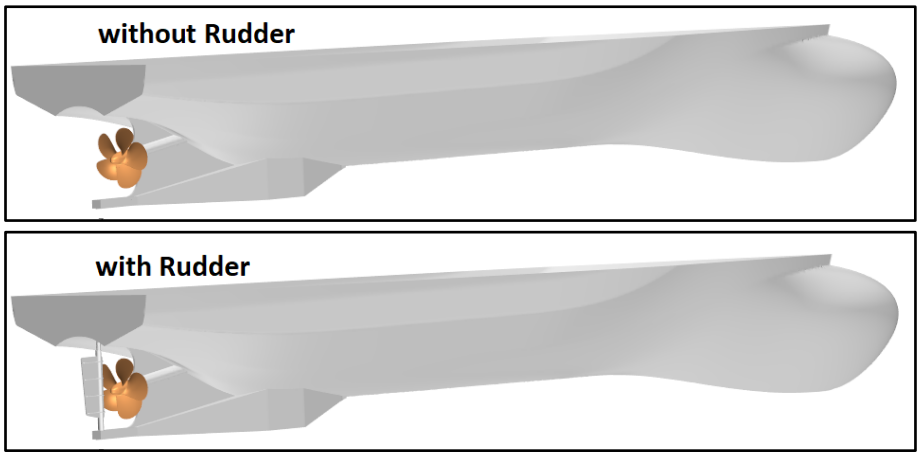

Figure 6.34. Tested configurations with and without a rudder.

6.4.2.3 Grid generation

The same grid properties were used in this Section, as given in Sections 6.2 and 6.3. The grid structure used in the numerical calculations can be seen in Figure 6.35. As shown in Figure 6.35, the local mesh refinements in the propeller slipstream are applied using the V-AMR technique, which was explained in Chapter 5, for better modelling of tip vortex flow and hence TVC. Also, the permeable/porous surface was located inside the fine grid region, which covers the important part of the slipstream to include the nonlinear noise contributions in the propeller slipstream.

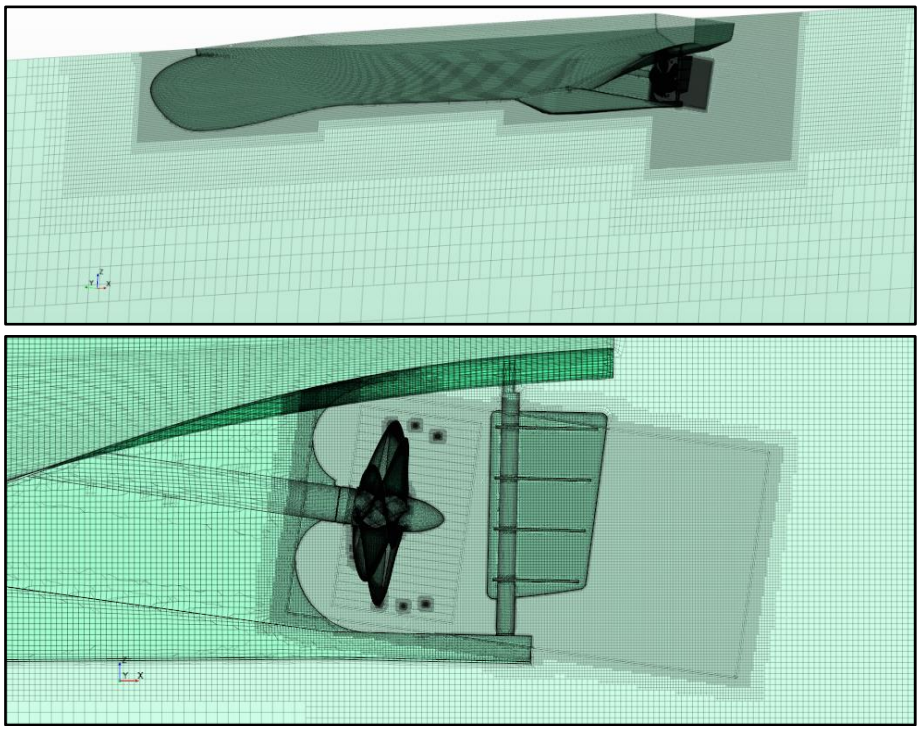

Figure 6.35. Representation of grid resolution in the computational domain.

6.4.2.4 Analysis properties

The same solution strategy was followed in this Section, as explained in Sections 6.2 and 6.3. Therefore, the details of the analysis properties can be found in Section 6.2.2.

6.4.3 Numerical results

6.4.3.1 Hydrodynamic results

During the experiments carried out in the CNR-INSEAN Large Cavitation Tunnel, the thrust and torque were not measured in a wide range of operating conditions. Due to this reason, the CFD results are only presented in Table 6.13. In the scope of the SONIC project (SONIC, 2012), the tests were also conducted at different facilities corresponding to the full-scale operating conditions. Amongst them, Rolls-Royce AB performed the test at $10K_Q$=0.322 for C3 condition and similar cavitation observations were obtained compared to CFD and the tests performed at CNR-INSEAN. Additionally, another CFD calculation was carried out by Bensow and Liefvendahl, 2016 in the absence of a rudder, and the authors calculated the K_T=0.193 for the C3 condition. Therefore, the present results are in good agreement with another experiment and CFD calculation.

Table 6.13. The non-dimension thrust and torque coefficients obtained by CFD at four different operating conditions.

Condition	K_T	$10K_Q$
C1 w/ rudder	0.187	0.307
C2 w/ rudder	0.204	0.322
C3 w/ rudder	0.189	0.304
C3 w/o rudder	0.184	0.297
C4 w/ rudder	0.191	0.304

Figure 6.36 shows the overview of the vortex structures in the propeller slipstream at C1 with and w/o rudder configurations. The focus is given on the vortex structures aft of the ship. This is because the permeable surface is placed around the propeller, and hence the vortex structures in the propeller slipstream are expected to have an impact on the URN predictions as nonlinear noise sources. The vortex structures are visualised with the threshold value of Q criterion 1000 $1/s^2$. The tip and hub vortex structures are rather persistent in the propeller slipstream for both configurations at C1. Hence, it shows the adequacy of the grid resolution applied around the hull in the near field. However, further downstream, the numerical dissipation starts to be seen, which results in the disappearance of vortex structures. As shown in Figure 6.36, the rudder causes the tip and hub vortices to break up in the propeller slipstream compared to the

configuration without the rudder. Thus, it is considered that this breakup phenomenon can have an impact on the URN levels as nonlinear noise sources, as shown in Chapter 4. Based on the observations obtained in Figure 6.36, the permeable surfaces are placed in the propeller slipstream to cover the most energetic part of the vortex structures.

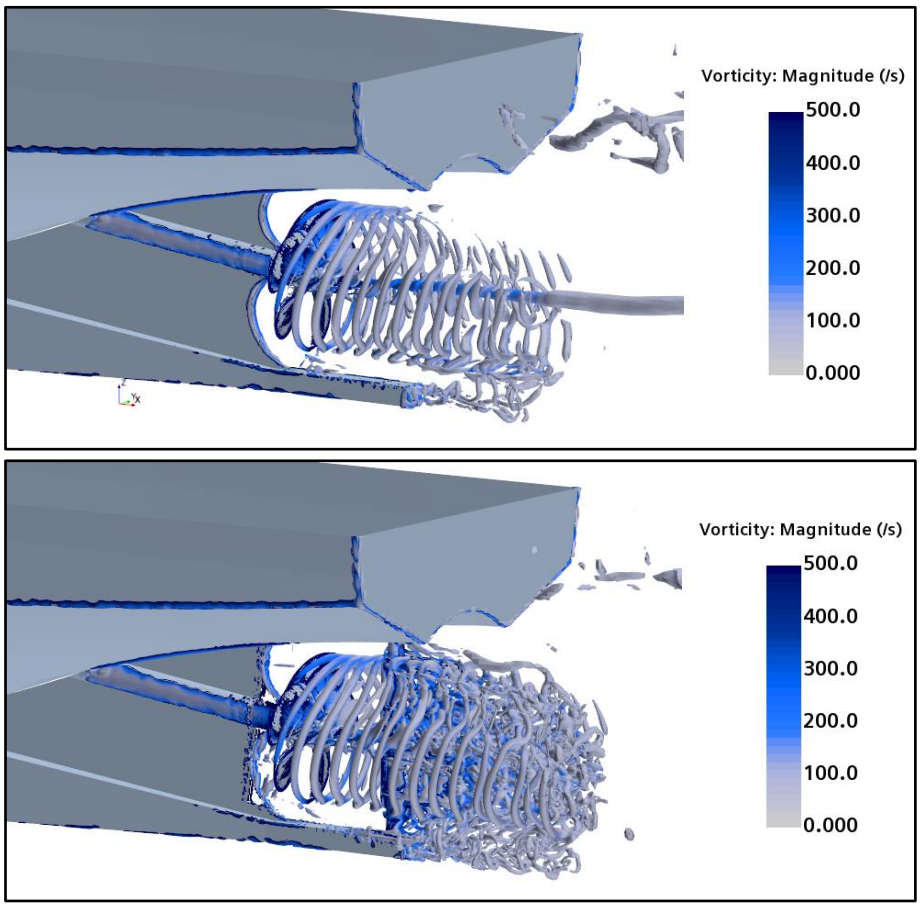

Figure 6.36. The vortex structures in the propeller slipstream for two configurations (above: without rudder, below: with rudder) at C1 (Q =1000 1/s^2).

6.4.3.2 Cavitation observations

The cavitation extensions between the CFD using the iso-surface 10% volume of fraction and experiments were compared at different operating conditions. Apart from comparing the numerical results with the experiments conducted in CNR-INSEAN, the numerical results were also compared with those of other facilities' observations during the SONIC project (SONIC, 2012) at the same operating conditions.

The predicted cavitation extensions using the CFD are first compared with the experimental observations at C1 in Figure 6.37. At this operating condition, the cavitation is not present in the experiments performed by CNR-INSEAN, MARIN and predictions obtained by CFD calculations.

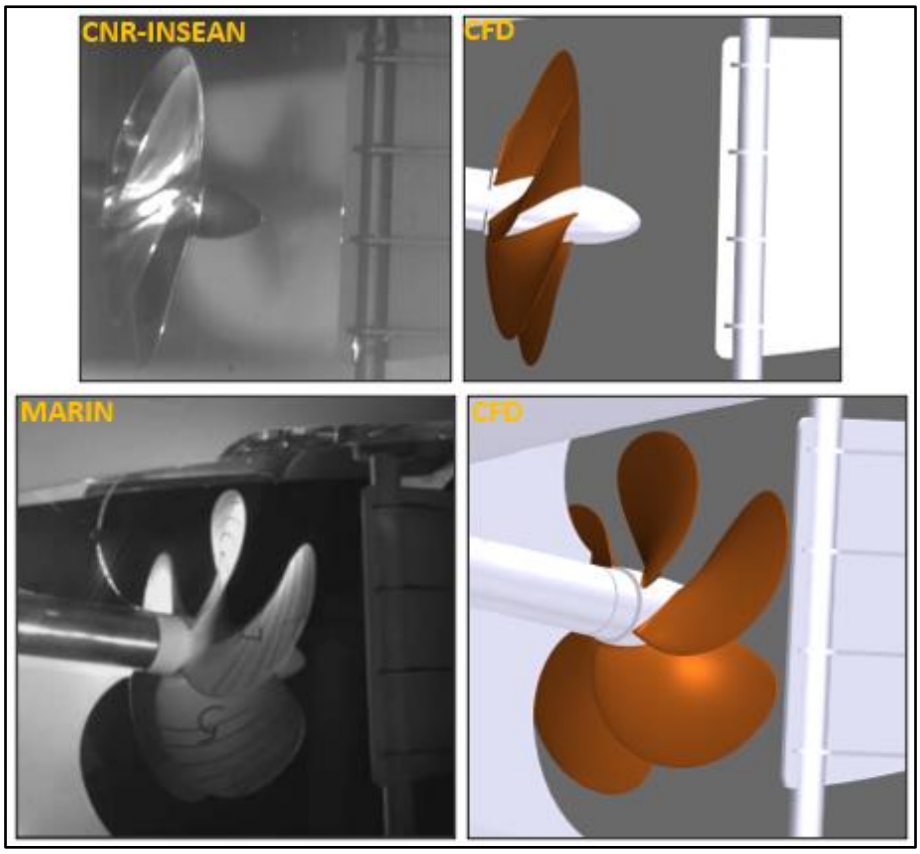

Figure 6.37. Comparison of cavitation extensions at C1 ($\alpha_v = 0.1$).

Figure 6.38 shows the comparisons of cavitation extensions at C2. The incipient TVC appears when the blade passes the hull perturbation and the blade is in the 12 o'clock position. However, unlike the experiment, the same incipient TVC is not present in the CFD predictions. Also, there is no sheet cavitation on the blades, according to the experimental observations. Akin to the experiment, the sheet cavitation is not present in the CFD calculations.

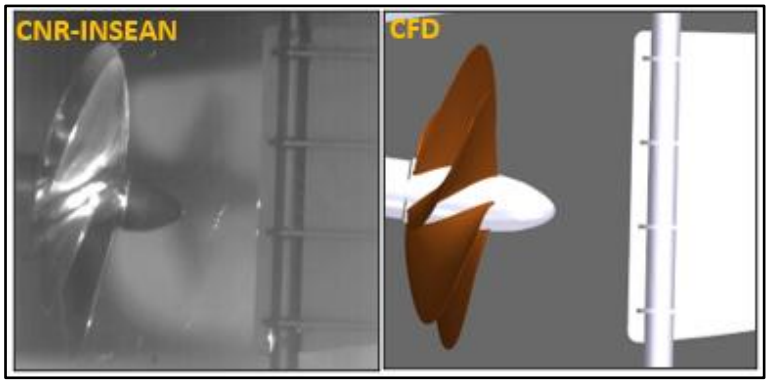

Figure 6.38. Comparison of cavitation extensions at C2 ($\alpha_v = 0.1$).

At C3, there is a very weak TVC and the least amount of blade cavitation when the propeller blade is in the 12 o'clock position, according to the experiment performed by CNR-INSEAN, as shown in Figure 6.39. Also, the blade cavitation disappears, and TVC gets weaker when the blade is rotating after the 12 o'clock blade position. The weak intermittent tip vortices are

present at this operating condition, whereas the least amount of sheet cavitation is not present according to the experiments conducted by MARIN and Rolls-Royce AB. The minor differences in terms of TVC between the facilities can be because of the slightly different Reynolds numbers used in the measurements. In the CFD predictions, the least amount of sheet cavitation and intermittent or very weak TVC is not present.

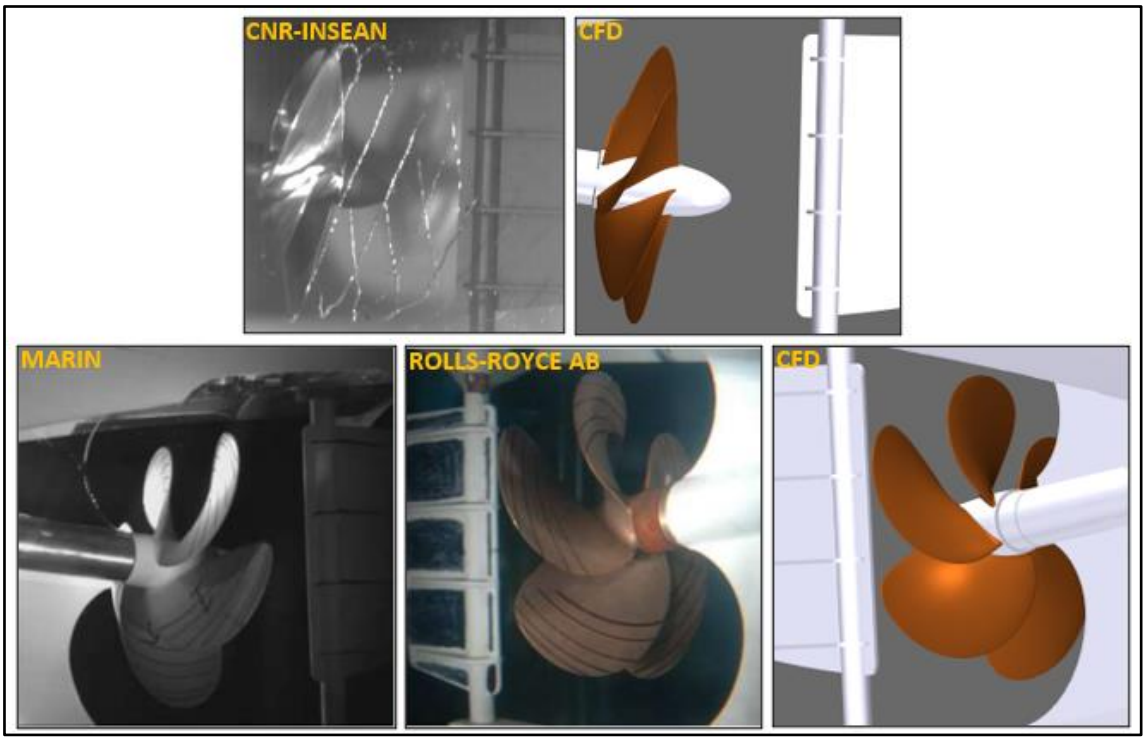

Figure 6.39. Comparison of cavitation extensions at C3 ($\alpha_v = 0.1$).

Figure 6.40 compares the predicted and observed cavitation extensions at C4. As shown in Figure 6.40, there is a clearly visible TVC with a small diameter according to the experimental observations. Apart from the TVC, the sheet cavitation is also visible in some blade passages with very smaller extensions in the experiments. According to the experimental observations, when the blade is in the 6 and 12 o'clock positions, the destabilisation of the TVC is present. A similar sheet cavitation extension on the leading edge is predicted in the numerical calculations, but the qualitative assessment of its volume is rather difficult. Akin to the previous conditions and incipient TVC, the TVC could not be observed in the CFD predictions.

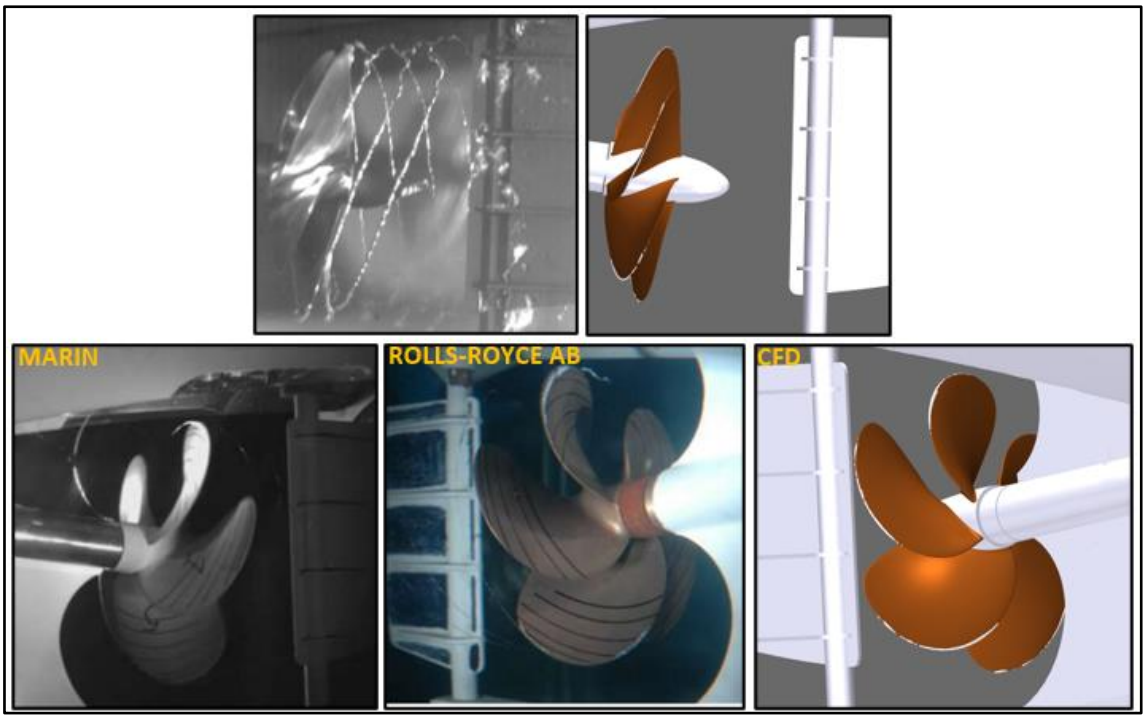

Figure 6.40. Comparison of cavitation extensions at C4 ($\alpha_v = 0.1$).

So far, the CFD predictions are compared with the experiments in terms of the cavitation extension. Although similar sheet cavitation extensions are present between the CFD and experiment at different operating conditions, the incipient and very weak TVC could not be observed in the CFD predictions compared to the experiments at C2, C3 and C4. This is because the incipient and weak TVC observed in the experiments has a very small diameter. Thus, this small diameter of the vortex makes the numerical modelling of TVC in the propeller slipstream difficult using the V-AMR technique. The tip vortex flow is solved more accurately using the V-AMR technique than using base mesh at different operating conditions. However, the V-AMR technique's adopted grid size inside the vortex seems insufficient to observe an incipient and weak TVC in the propeller slipstream using CFD.

In order to show the capabilities of the V-AMR technique, the additional operating condition, which corresponds to the maximum full-scale operating condition (V_S=15.1 knots, n_s=1141.5 rpm, $\sigma_n = 1.05$) is explored. This is because the model scale experiments show a rather stable TVC with a relatively big vortex diameter. The CFD predictions are compared with the experiments in Figure 6.41. A significant amount of sheet and tip vortex cavitation is present at this operating condition. The sheet cavitation covers more blade area when the blade passes in the 12 and 6 o'clock positions. The CFD prediction is in good agreement with the experimental observations in terms of both sheet and tip vortex cavitation. Unlike the previous operating conditions, the TVC could be observed in the propeller slipstream. As the local mesh

refinements are applied in a limited area in the rotating region, the extension of TVC in the CFD is smaller than those of experiments. The TVC in the propeller slipstream can be further extended through the rudder as in the experiment with the overset type grid structure application as the internal interfaces in sliding mesh limits the TVC extension further downstream. Additionally, as the tip vortex strength reduces further downstream, the grid size inside the vortex is required to be decreased.

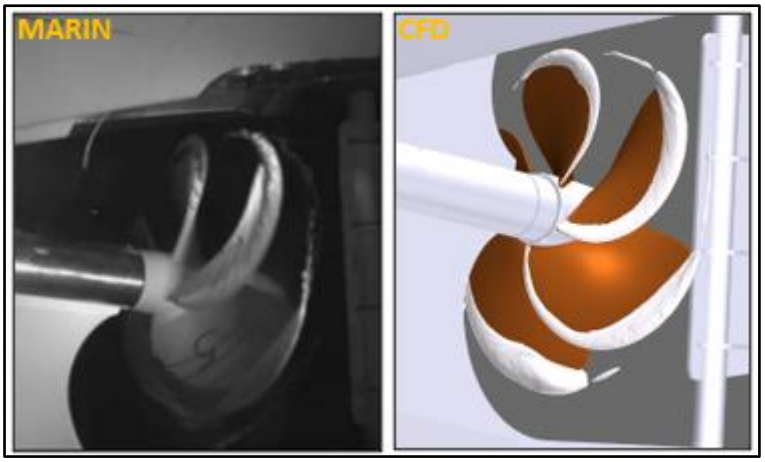

Figure 6.41. Comparison of cavitation extension at additional operating conditions corresponding to the maximum full-scale operating condition (i.e., V_S=15.1 knots, n_s=1142 rpm, $\sigma_n = 1.05$) ($\alpha_v = 0.1$).

It should be noted that the full-scale measurements showed a large extent of suction side sheet cavitation, which was extremely unsteady at maximum full-scale operating conditions. However, the model scale experiments and CFD predictions show smaller suction side sheet cavitation than full-scale with a rather stable formation. Due to this fact, this discrepancy between sea trial observations, experiments and CFD is deemed because of the mismatch of the propeller loading between the model and full-scale propeller.

6.4.3.3 Hull pressure fluctuations

The pressure fluctuations induced by the propeller action are computed at seven different pressure probes during the experiments performed in CNR-INSEAN, as shown in Figure 6.42. The probes are positioned as follows.

- P1 is located at the inner part of the hull, just downstream of the rudder axis
- P2 and P3 are located at symmetrical positions relative to the hull mid-plane between the rudder axis and propeller plane
- P4 and P5 are located at symmetrical positions and propeller planes.
- P6 and P7 are located at symmetrical positions and upstream of the propeller.

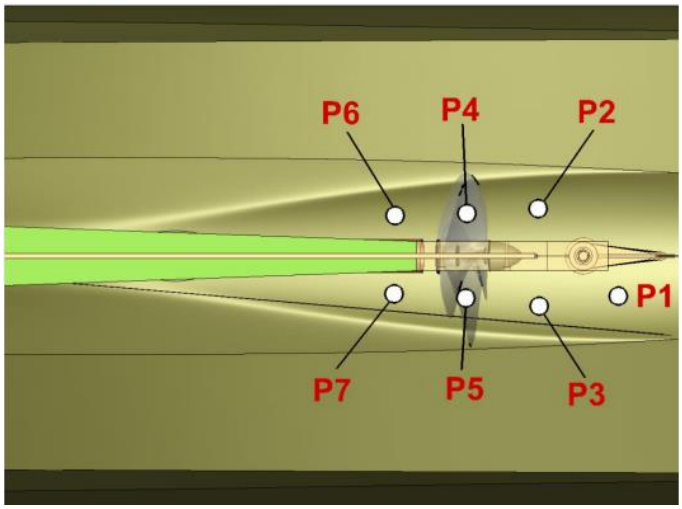

Figure 6.42. Representation of pressure probes' relative positions used in the experiment (Felli et al., 2014).

Akin to the experiments, the four pressure probes are placed in the CFD calculations, and recorded hull pressure fluctuations are compared at four different operating conditions in Figures 6.43, 6.44, 6.45 and 6.46. As shown in these Figures, the CFD predictions generally correlate well with the measurements by means of pressure magnitude at different operating conditions and probe locations. For all operating conditions, the highest pressure fluctuations are found at the probes located above the propeller location (i.e., P4 and P5) both in the CFD predictions and measurements as the linear dynamics are more dominant at the propeller plane. In the experiments, the pressure signals are mainly characterised by spikes, which can be associated with the strong sheet and TVC dynamics and turbulence, especially for the probes located downstream of the propeller (i.e., P2 and P3). The pressure signals predicted by CFD show a rather smooth shape under non-cavitating conditions (i.e., C1, C2 and C3). The predicted sheet cavitation and its dynamics at C4 change the pressure fluctuations characteristics compared to the operating conditions where the cavitation is not present (i.e., C1, C3 and C3). In general, hull-pressure fluctuations are mainly characterised by the spikes created by the strong sheet and TVC dynamics. Also, this might be related to the collapsing of the sheet and tip vortex cavitation. However, the lack of incipient and weak TVC dynamics predicted in the CFD predictions causes the discrepancy between the CFD predictions and measurements in terms of pressure signal shape at four different operating conditions. Figures 6.43, 6.44, 6.45 and 6.46 show a phase shift between CFD predictions and measurements, particularly for P2 and P3 probes. This might be because of the lack of reproduction of cavitation dynamics in the CFD predictions or the exact location of pressure sensors used in the CFD and experiment. The results show that the magnitude of the pressure fluctuations is

similar at four different operating conditions. Thus, the hydrodynamic performance might characterise the intensity of the pressure pulse rather than cavitation extensions.

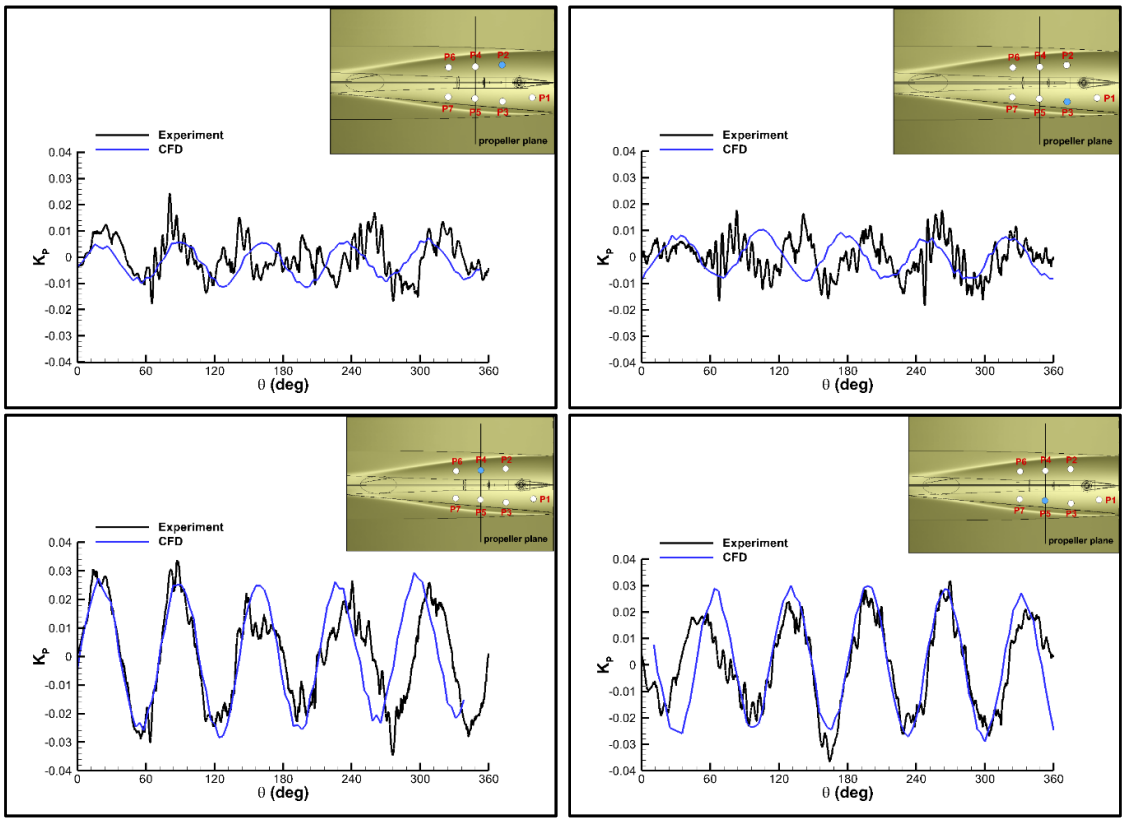

Figure 6.43. Comparison of hull pressure fluctuations at C1.

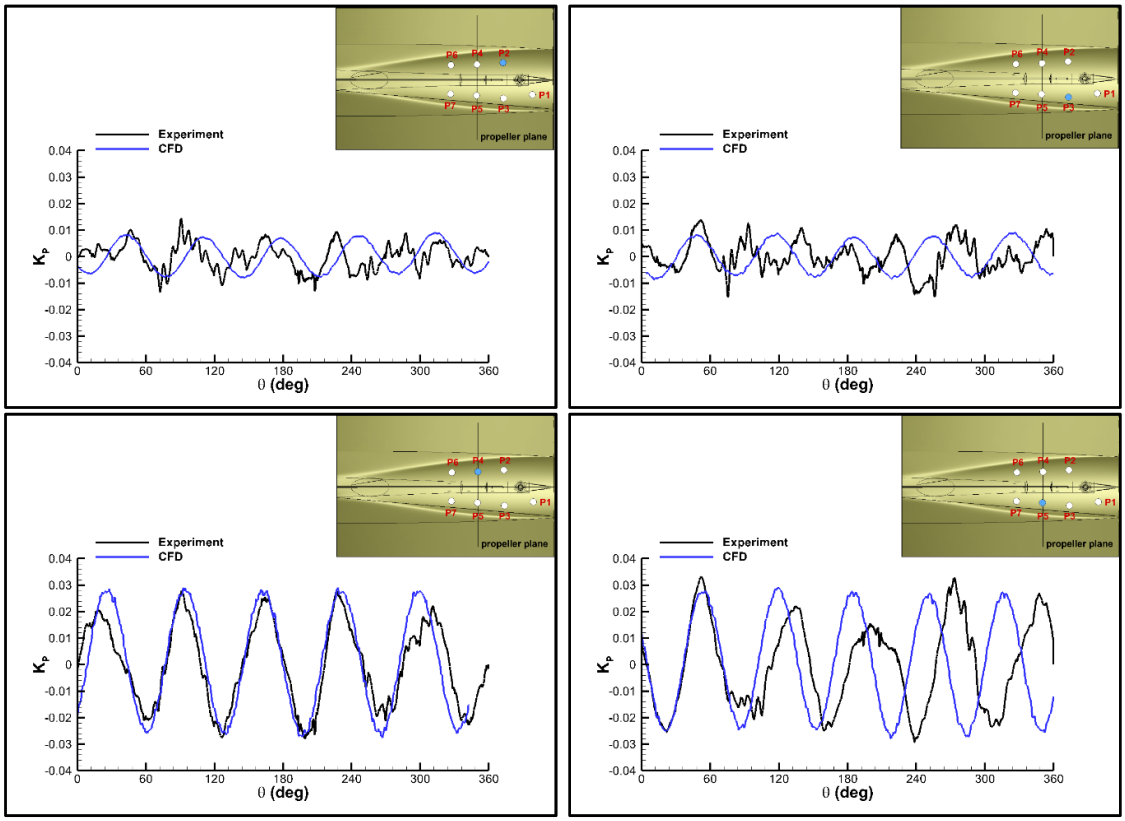

Figure 6.44. Comparison of hull pressure fluctuations at C2.

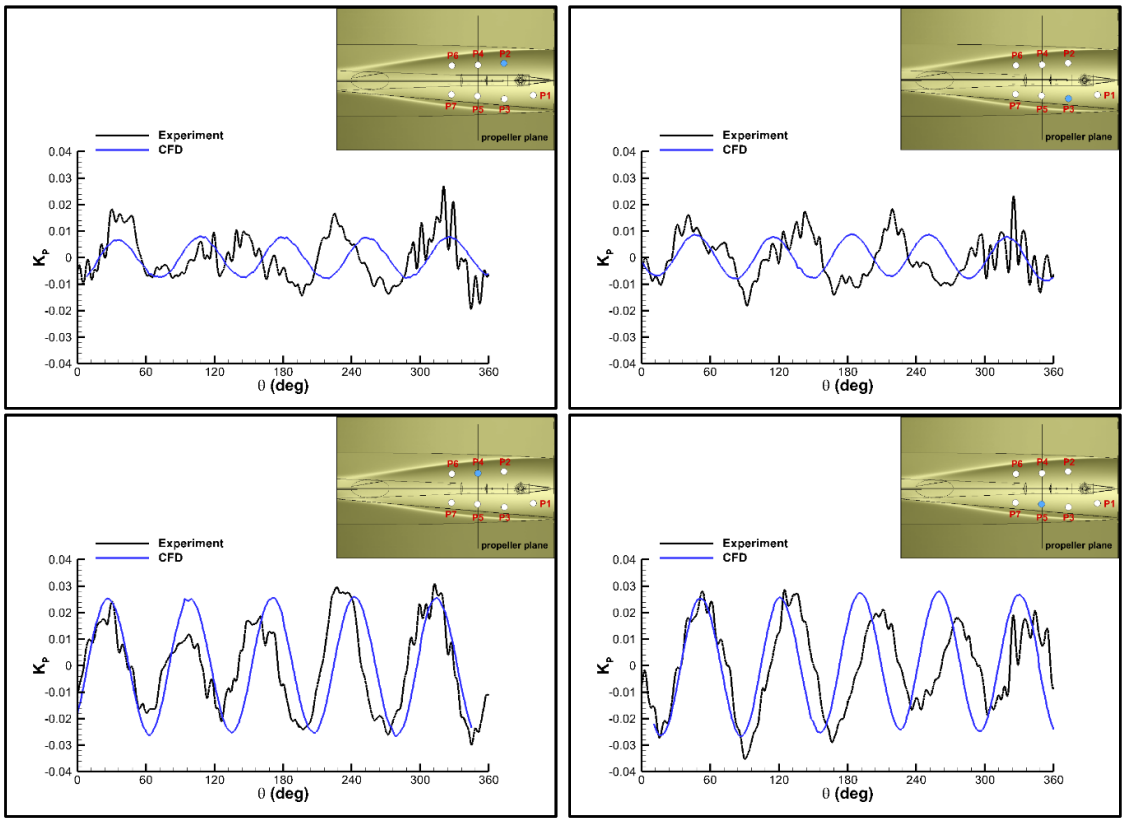

Figure 6.45. Comparison of hull pressure fluctuations at C3.

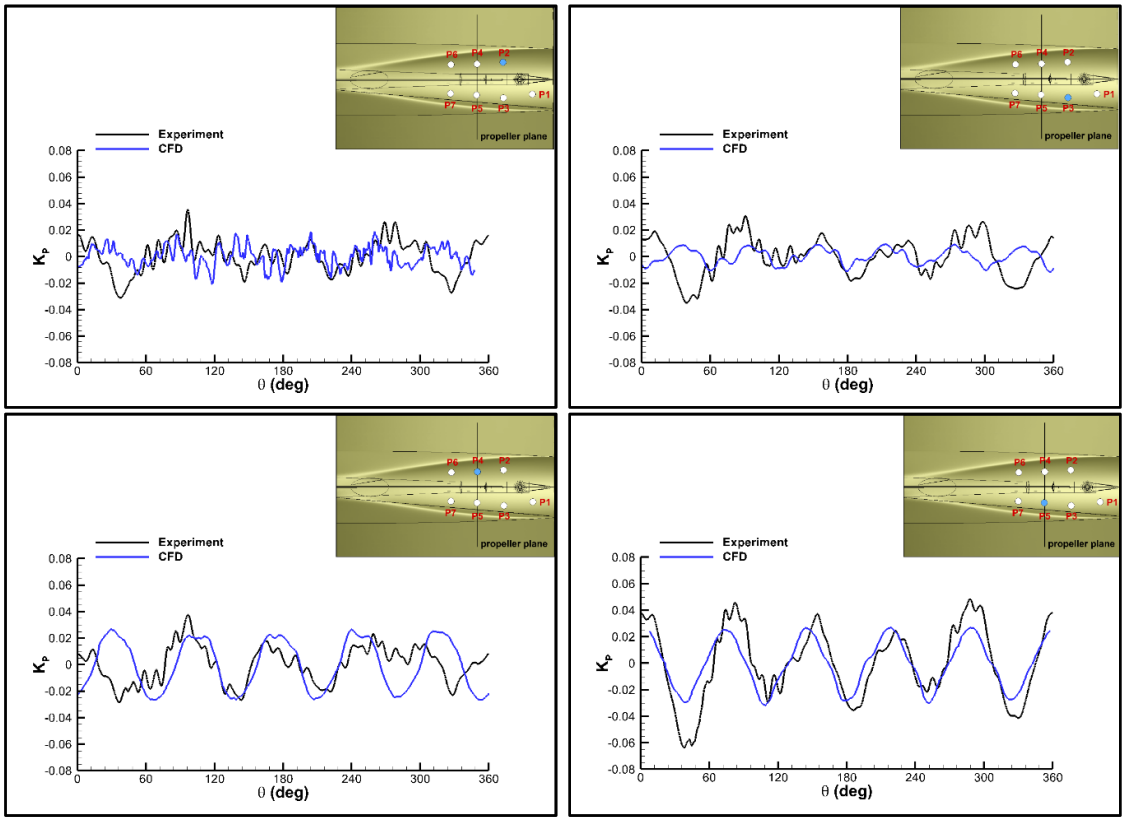

Figure 6.46. Comparison of hull pressure fluctuations at C4.

6.4.3.4 Propeller URN predictions

- **Convergence of the URN predictions**

In the numerical calculations, the permeable formulation of the FWH equation was used to predict the propeller URN. In this formulation, a fictitious surface was placed around the propeller to include the contribution of nonlinear noise sources occurring in the propeller slipstream, including TVC. As stated in Sections 6.2 and 6.3, the selection and placement of permeable surfaces for hydroacoustic problems are not yet known in the literature. Besides, there are no consolidated procedures for selecting and placement of permeable surfaces around the noise source. In this study, the permeable surface was placed based on the flow details in the propeller slipstream, and the permeable surface encapsulated the most energetic part of the vortex structures to account for the contribution of nonlinear noise sources. Nevertheless, as given in Table 6.14, the different permeable surfaces are tested to show the convergence of the solution at C1.

Table 6.14. Dimensions of permeable/porous surfaces.

PDS ID	L/D_{PS}	D_{PS}
1	1.6	1.2D
2	1.9	1.2D
3	2.2	1.2D

Here, L is the length and D_{PS} is the diameter of the permeable surface. The convergence of the solution is first shown in the near field for the receivers located around the propellers, as given in Table 6.15. The NHP1 and NHP2 are located upstream of the propeller and at the propeller plane, respectively.

Table 6.15. Coordinates of near field receivers with respect to the centre of the propeller blades.

Receiver ID	$X\ (m)$	$Y\ (m)$	$Z\ (m)$
NHP1	-0.02	0.00	0.125
NHP2	0.00	0.00	0.125

Figure 6.47 shows the time based acoustic signals recorded using the near field receivers, as given in Table 6.15. As shown in Figure 6.47, the acoustic pressures obtained by different permeable surfaces superimpose each other. In this way, the convergence of the hydroacoustic solution is proven in the near-field.

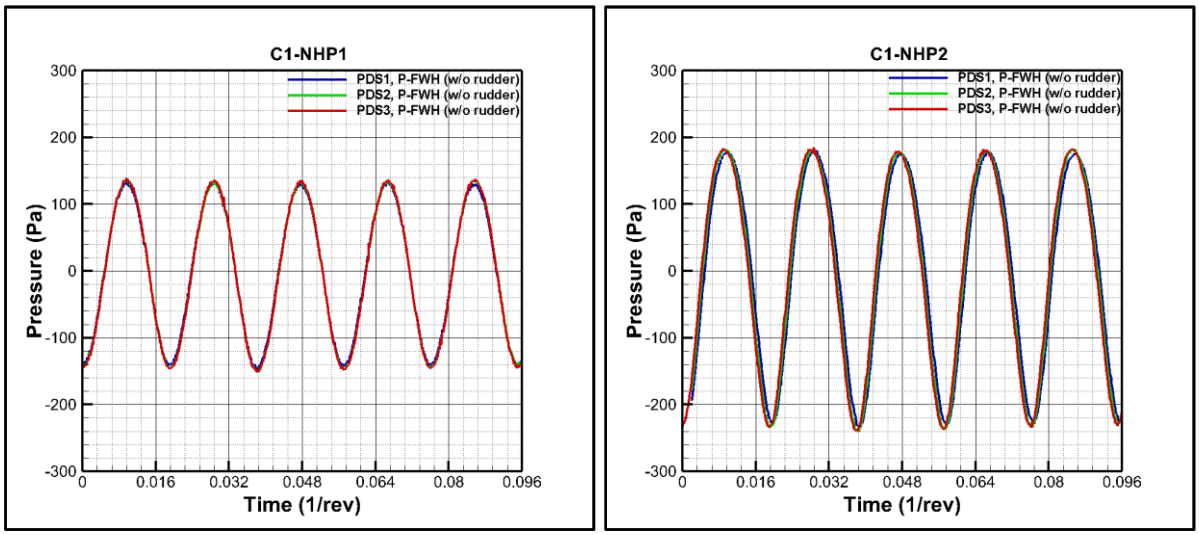

Figure 6.47. Convergence of hydroacoustic results using different permeable surfaces for the receivers located in the near field.

- **Verification of the URN predictions**

Similar to Sections 6.2 and 6.3, the verification of the URN predictions is conducted by comparing the hydrodynamic and hydroacoustic pressures in the near field. Figure 6.48 shows the pressures obtained directly from the hydrodynamic solver (i.e., DES method) and acoustic analogy (i.e., permeable FWH using the PDS3) at the NHP2 for C1, C2, C3 and C4. As shown in Figure 6.48, both pressures agree with each other at different operating conditions. Also, with an increase in propeller rotational speed and blade loading, the hydrodynamic and hydroacoustic pressures increase from C1 to C4. The verification of the results is also valid for different receivers located in the near-field. The agreement between the two pressures also shows the accuracy of the hydrodynamic and hydroacoustic solutions.

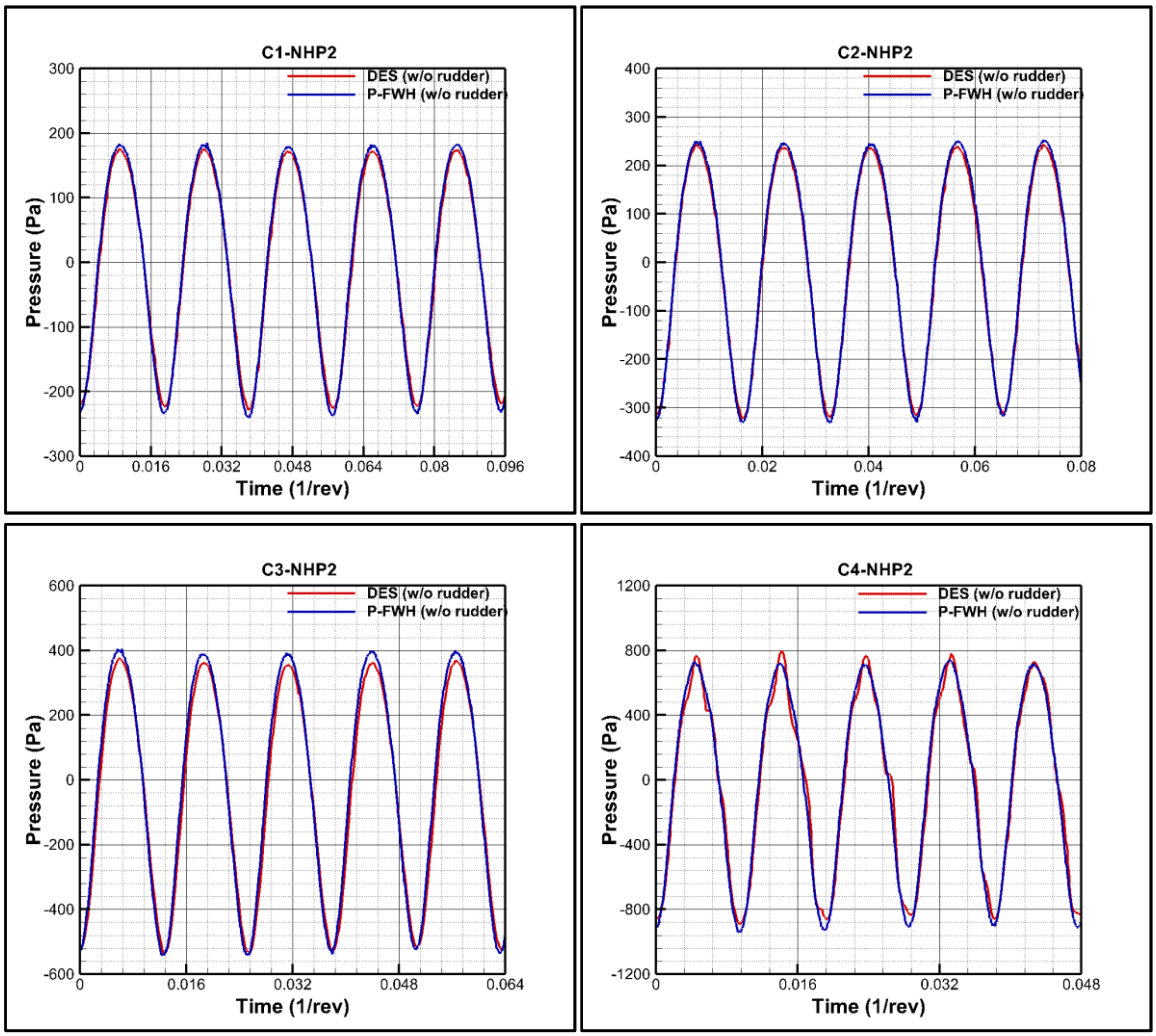

Figure 6.48. Verification of the hydroacoustic results in the near field at NHP2.

- **Validation of the URN predictions**

In the CFD calculations, three different receivers, namely H1, H7 and H8, are placed in the flow field as in the measurements conducted in the CNR-INSEAN. Amongst the receivers, H1 is aligned to the symmetry plane of the model along the prolongation of the propeller axis and 1m downstream of the propeller. The other two receivers are located according to an imaginary sphere centred on the propeller boss, at 1m distance from it, as shown in Figure 6.49.

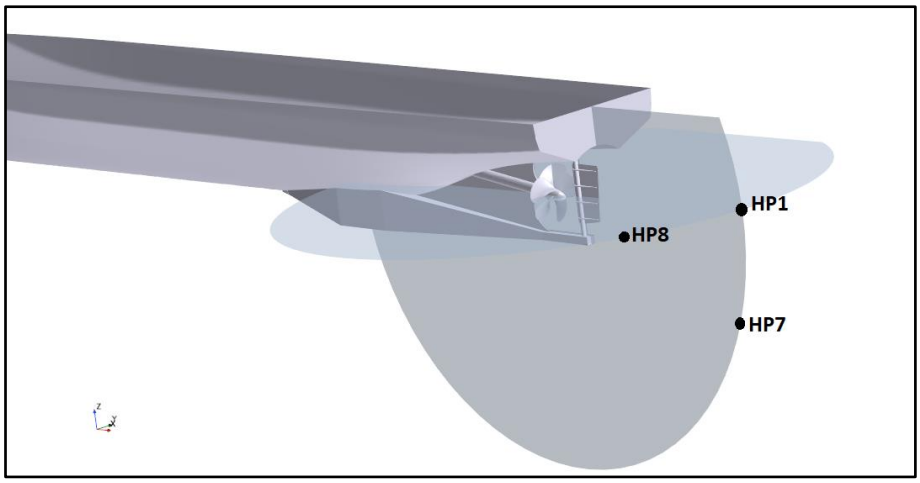

Figure 6.49. Representation of receivers for the URN validation (Figure is not scaled).

Figure 6.50 compares predicted URN levels at H8 and C1 with different permeable surfaces, as given in Table 6.14. In the previous chapter, the convergence of the solution is shown with the time based acoustic pressure signal in the near field in Figure 6.47. Akin to the near field receivers, the noise spectrums obtained by different permeable surfaces are compared with each other in Figure 6.50. As shown in Figure 6.50, the URN levels are predicted similarly using different permeable surfaces with slight differences. Based on the predictions, it seems that a relatively small permeable surface (i.e., PDS1) captures more noise information compared to other permeable surfaces (i.e., PDS2 and PDS3), resulting in higher URN levels, similar to the findings in Section 6.2. Thus, the PDS1 is used as a permeable noise surface for the URN validation with the measurements unless otherwise stated.

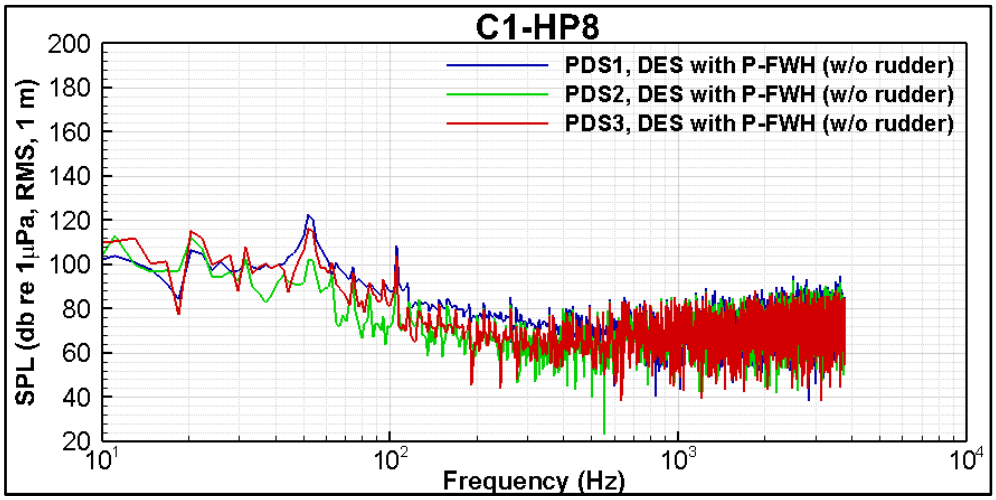

Figure 6.50. Comparison of noise spectrums using different permeable surfaces at HP8 and Condition 1.

The predicted URN levels are compared with the measurements at the HP8 receiver and C1 in Figure 6.51. To explore the effects of the rudder on propeller URN levels, predicted URN levels are also compared with each other in Figure 6.51. The CFD predictions are in good agreement with the measurements until 100Hz and between 1kHz and 3kHz. The numerical calculations underpredicted the URN levels up to 20dB at certain frequencies between 100Hz and 1kHz. As stated in the experimental report (Felli et al., 2014), the background and cavitating propeller noise levels are considerably overlapped in the whole range of analysed frequencies at C1. Therefore, the discrepancy between the 100Hz and 1kHz might be because of the background noise at C1. As shown in Figure 6.51, the rudder causes a slight increase in URN levels. The 1st and 2nd BPF values are well captured in the CFD calculations for the configuration without a rudder, whereas the BPF values disappear for the configuration with the rudder. The break-up of the vortex structures caused by the rudder increase the contribution of nonlinear noise sources at this operating condition, which results in higher noise levels. The increased contribution of nonlinear noise sources due to the break-up phenomenon can be associated with the disappearance of peak values for the configuration of with rudder.

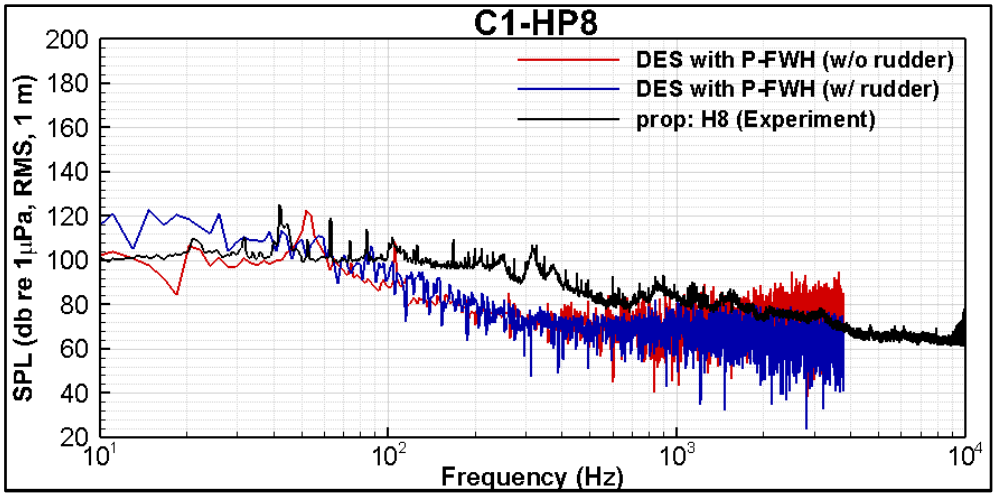

Figure 6.51. Comparison of predicted and measured URN levels at HP8 and Condition 1.

As stated before, the URN measurements were performed with three different receivers, namely HP1, HP7 and HP8. The noise directivity is detected during the measurements according to noise spectrums computed at HP1, HP7, and HP8 for each operating condition, particularly in the low-frequency region. For instance, the noise spectrums at different receiver locations are compared in Figure 6.52 at C1. As shown in Figure 6.52, the low-frequency region of the noise spectrum and some peaks change from HP1 to HP8.

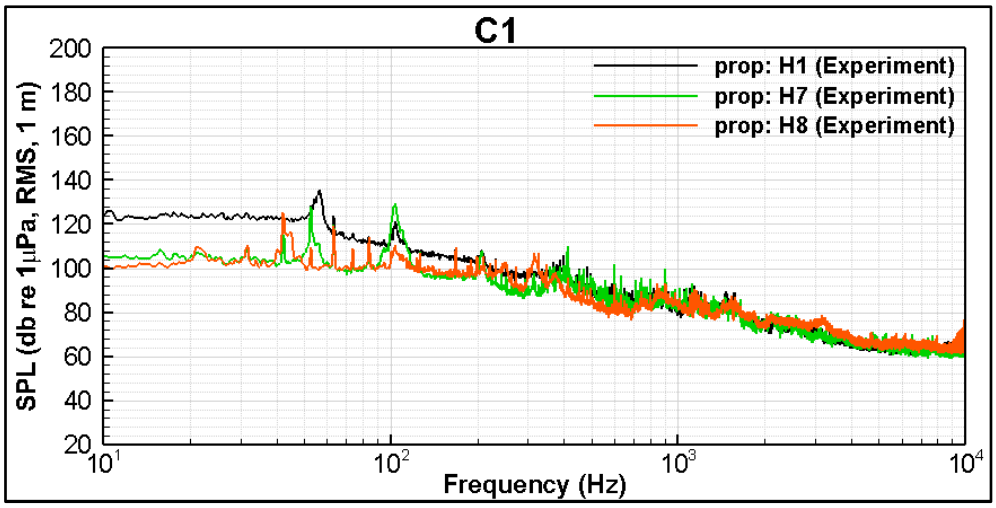

Figure 6.52. The change in noise directivity in the measurements with different receivers at C1.

On the contrary to the measurements, the same noise directivity is not observed in the numerical calculations, and URN levels are found to be rather similar using different receivers at C1, as shown in Figure 6.53. It should be noted that the noise directivity is not still present with the inclusion of rudder in the CFD calculations at all operating conditions.

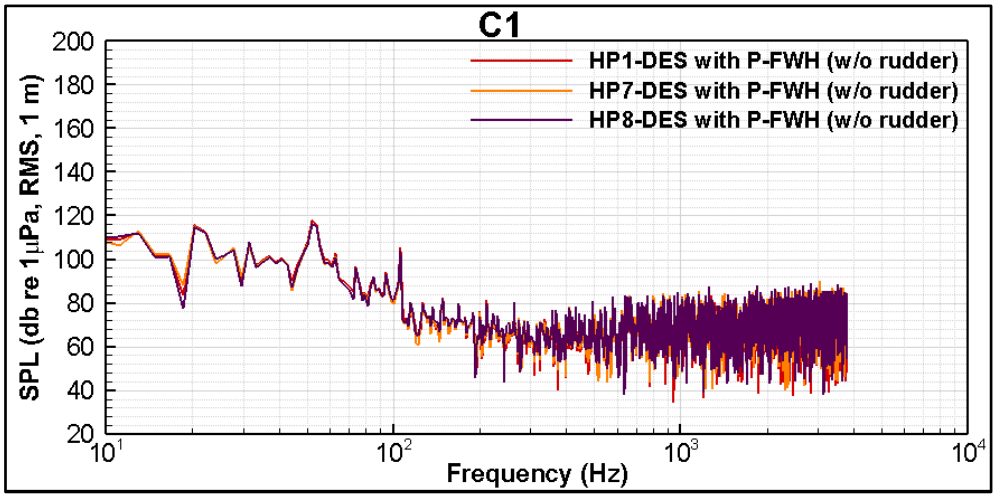

Figure 6.53. The change in noise directivity in the CFD with different receivers at C1.

Figure 6.54 shows the comparison of URN levels obtained by CFD and experiments at C2. The CFD predictions underpredicted the URN levels between 100Hz and 1kHz. At this operating condition, the incipient TVC was observed when the blade was in the 12 o'clock position during the cavitation observations in the tunnel. Although the contribution of the incipient TVC is expected to be not considerable, inevitably, it affects the noise spectrum. Moreover, the incipient TVC slightly manifests itself as a characteristic hump somewhere between 200 and 450Hz in the measurements. However, the same incipient TVC could not be observed in the CFD. Thus, the lack of TVC dynamics captured in the CFD can be the main reason for the URN levels' discrepancy between the CFD and measurements in the frequency region where

the TVC contribution is dominant. Also, the URN levels slightly increase with the inclusion of a rudder, as in the C1.

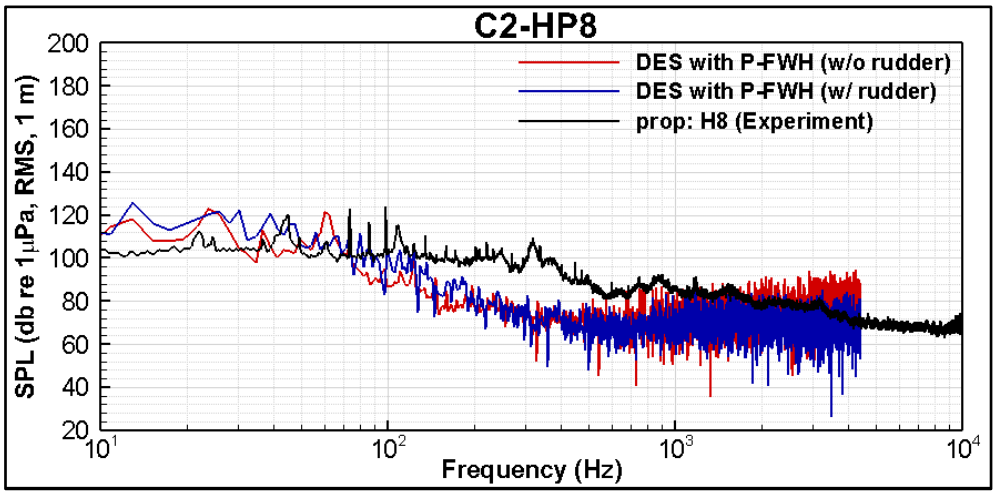

Figure 6.54. Comparison of predicted and measured URN levels at HP8 and Condition 2.

Similar to C2, the URN levels are underpredicted up to 20dB in the CFD calculations compared to the experiments at the mid-frequency range, as shown in Figure 6.55. The least amount of sheet cavitation and weak TVC were observed in the experiments, and these cavitation types could not be captured in the CFD calculations. As the sheet and TVC dynamics are responsible for both the low-frequency region and broadband part of the noise spectrum, the URN level difference is present between the CFD and measurements at C3, as shown in Figure 6.55. Additionally, similar to C1 and C2, the rudder increases the URN levels.

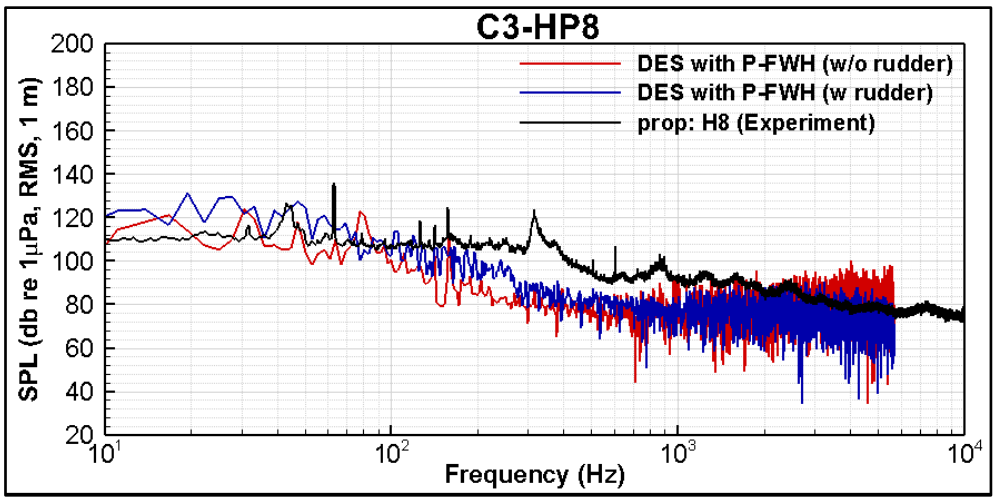

Figure 6.55. Comparison of predicted and measured URN levels at HP8 and Condition 3.

With increased blade loading and ship speed, the URN levels rise from C1 to C4. Figure 6.56 shows the URN levels at the highest loading conditions (i.e., C4). As shown in Figure 6.56, the predicted and measured URN levels are in good agreement with each other. The discrepancy of the URN levels reduces significantly at C4 compared to other operating conditions,

especially in the mid-frequency region of the noise spectrum. Nevertheless, the lack of TVC in the CFD predictions compared to cavitation observations in the experiment can be associated with the URN differences at certain frequencies. The results show that the sheet cavity dynamics are predicted accurately in the CFD compared to the experiment, resulting in a correlation between the CFD and measurements. The characteristic hump originated from the TVC dynamics is not present in the CFD predictions, unlike the experiments, due to the reasons stated before.

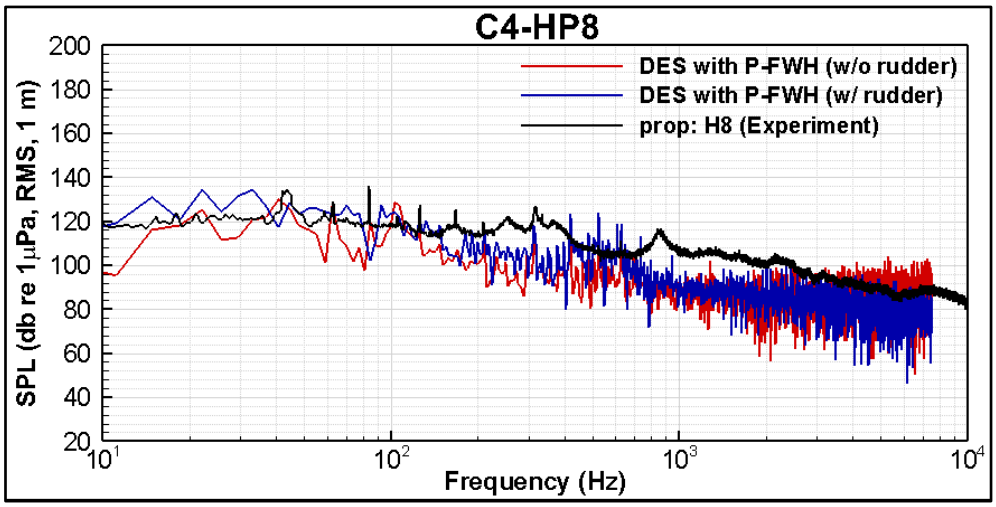

Figure 6.56. Comparison of predicted and measured URN levels at HP8 and Condition 4.

6.5 Chapter summary and concluding remarks

In this chapter, the capabilities of the developed CFD model were demonstrated in predicting the hydrodynamic performance, cavitation, hull pressure fluctuations and URN for the benchmark model and full-scale propeller of The Princess Royal. For this purpose, the selected model scale propeller operated in open water configurations under uniform, inclined and non-uniform (i.e., in the presence of 2D wake screen) flow conditions and in the presence of a scaled 3D full model (with demi-hull). In the numerical calculations, the flow field was solved using the advanced numerical model (i.e., DES), and a permeable formulation of the FWH equation was used as an acoustic analogy for the URN predictions. In order to resolve the tip vortex flow accurately, the newly proposed V-AMR technique, developed in Chapter 5, was applied at different operating conditions. The obtained numerical results were validated comprehensively with the experimental data measured in the cavitation tunnel and sea trial data. The investigations presented important findings summarised in the following:

- The global performance characteristics (i.e., thrust and torque) were found in good agreement with the measured data in open water configurations under uniform, inclined and non-uniform flow conditions. The maximum difference was found at around 8% in the torque coefficient.

- Despite the slight differences in the TVC extension, the cavitation extensions predicted similarly for the uniform and inclined flow conditions in the numerical calculations.

- The comparison of cavitation extensions at different operating conditions in open water configurations under uniform and inclined flow conditions showed that the sheet cavitation was predicted to be similar. Yet, the sheet cavitation was generally slightly more extended towards the inner radii than the experimental observations. Although the TVC was modelled successfully in the propeller slipstream in a wide range of operating conditions, it could not be observed sufficiently when the incipient and weak TVC was present. This can be associated with the inadequate grid resolution adopted in the CFD for capturing such an incipient TVC with a small diameter.

- The hydroacoustic results were verified by comparing the hydrodynamic and hydroacoustic pressures in the near field. Thus, the consistency and accuracy of the solution were shown using the receivers located in the proximity of the permeable surface in open water configurations and behind a scaled model hull.

- The convergence of the propeller URN predictions was also shown using the different permeable noise surfaces located around the propeller for open water configurations and behind a 3D scaled model hull. The numerical results showed that the relatively smaller permeable surface capture more noise information and spectral peaks are more distinct using the relatively smaller permeable surface than other permeable surfaces.

- The CFD approach generally underpredicted the noise levels around 5 and 10dB at certain frequencies between 300Hz and 1kHz in model scale for the open water configurations under uniform flow conditions. However, after 1kHz, the results were in good agreement with the measured data. Although there were spectral humps associated with the tip vortex dynamics in the low-frequency region of the noise spectrum at each operating condition in the measured data, these high amplitude humps could not be observed in the numerical calculations. This might be due to the lack of flow instability, which could be important for the cavitation pulsation and cavitation vortex, and hence

TVC dynamics predicted using the DES method and Scherr-Sauer cavitation model under uniform flow conditions. Thus, the discrepancy in the low-frequency region of the noise spectrum can be considered because of the differences in the TVC dynamics between the CFD approach and experiments.

- The model scale results were extrapolated to full-scale using the ITTC procedure to compare the CFD predictions with the measured data obtained by different facilities in the RR test campaign under uniform flow conditions. Although the trend of the noise spectrum agreed with the measurements, the CFD underpredicted the propeller URN levels compared to the measured data by different facilities. Besides, large discrepancies were also observed between the measured data obtained by different facilities.

- The cavitation extensions, particularly sheet cavitation, were generally predicted to be similar under non-uniform flow conditions, except the highest loading condition, as in the experiment and sea trial observations. Similar to uniform and inclined flow conditions, the small diameter of TVC in the experimental and sea trial observations caused insufficient modelling of TVC in the CFD due to the adopted grid resolution inside the vortex. Therefore, the unstable and strong TVC dynamics could not be observed in the CFD compared to the sea trial observations.

- The propeller URN predictions showed good agreement with the measured data under non-uniform flow conditions, except at the highest loading condition. The large extension of sheet cavitation observed in the CFD led to overprediction of propeller URN levels between 1kHz and 10kHz compared to the measured data.

- Similar to the uniform flow conditions, the numerical results obtained in the model scale were extrapolated to full-scale, and the propeller URN predictions were compared with the full-scale measurements under non-uniform flow conditions. The maximum discrepancy was observed at the lowest loading condition due to the lack of possible bursting phenomenon in the CFD compared to the full-scale measurements. In general, the propeller URN was underpredicted by around 10 and 15dB in the numerical calculations compared to full-scale measurements. At the highest loading condition, the predictions were in good agreement with the full-scale measurements.

- The coherent vortex structures were observed in the ship wake in the presence of a scaled model hull. The rudder broke up the tip vortices in the propeller slipstream compared to the configuration where the rudder was not present.

- Similar to open water configurations, including uniform, inclined and non-uniform flow conditions, the weak and incipient TVC could not be observed in the numerical calculations in the presence of a 3D scaled model hull. Also, the sheet cavitation extensions predicted in the CFD agreed with the experimental observations.

- The hull-pressure fluctuations showed good agreement with measurements in terms of pressure amplitude. As the incipient and weak TVC could not be observed in the CFD, the spikes and irregularities in the pressure signal could not be detected in the CFD predictions for the conditions where the incipient TVC was present in the experiment. Also, there was a phase shift between the CFD and experiment at some probe locations. This might be because the incipient TVC and its dynamics were not present in the CFD predictions compared to the experiment. Also, there might be small differences in the exact probe locations between the CFD and experiment.

- Although the noise directivity was found in the measurements, particularly at the low-frequency region of the noise spectra, this was not present in the CFD predictions for the configurations with and without the rudder.

- The rudder increased the URN levels at all operating conditions due to the break-up of the vortices in the propeller slipstream compared to the configuration where the rudder was not present.

- The numerical results showed that the propeller URN predictions were in good agreement with the measured data behind the 3D (demi) hull model. However, at some operating conditions, there was a discrepancy up to 15dB at certain frequencies and the mid-frequency region of the noise spectrum between the CFD predictions and measured data. This can be related to the lack of reproduction of TVC dynamics and insufficient TVC modelling in the CFD.

7 Hydrodynamic and hydroacoustic performance prediction of benchmark ship propeller in full-scale

7.1 Introduction

As reviewed in Chapter 2, there are only a few studies investigating the capabilities of the CFD approach together with the acoustic analogy for predicting the propeller hydrodynamic performance, including cavitation and URN in full-scale. Hence, this chapter aims to demonstrate the full-scale prediction capability and validity of the developed procedure using the CFD and acoustic analogy at the far-field where the noise data were collected during the SONIC project.

Therefore, Section 7.2 presents the hydrodynamic and hydroacoustic models, respectively. The details of sea trials are given in Section 7.3. Section 7.4 explains the test matrix and numerical modelling of the CFD approach (e.g., computational domain, boundary conditions, grid resolutions, and analysis properties). The propeller hydrodynamic performance predictions, cavitation observations and URN predictions are given with the validation of the sea trial data in Section 7.5. The chapter summary and concluding remarks are given in Section 7.6.

7.2 Theoretical background

7.2.1 Hydrodynamic model

Akin to Chapter 6, the DES method was also used in this chapter. The details of the formulations can be found in Section 6.2.1.

7.2.2 Hydroacoustic model

As used in Chapters 4 and 6, the permeable formulation of the FWH equation was utilised to predict the propeller URN at far-field to include the nonlinear noise sources, including TVC, effectively. Thus, the related formulations can be found in Section 4.2.1 (i.e., hydroacoustic model). As stated earlier, the selection of the porous/permeable surface for the URN prediction is an important subject, and the studies still focus on open water propeller cases to understand the influence of the selection of the noise surfaces on URN levels. As far as the complete full-scale ship case (i.e., ship hull, rudder, propeller, skeg, etc.) and the associated propeller cavitation are concerned, the selection of permeable surface becomes even more critical to

predict the propeller URN accurately. In this investigation, two different permeable surfaces, namely, PS1-FWH and PS2-FWH, are selected. PS1-FWH covers the propeller and its slipstream while the rudder is not included. Whereas PS2-FWH encompasses the whole ship, including the hull, rudder, propeller and the propeller's slipstream, as shown in Figure 7.1.

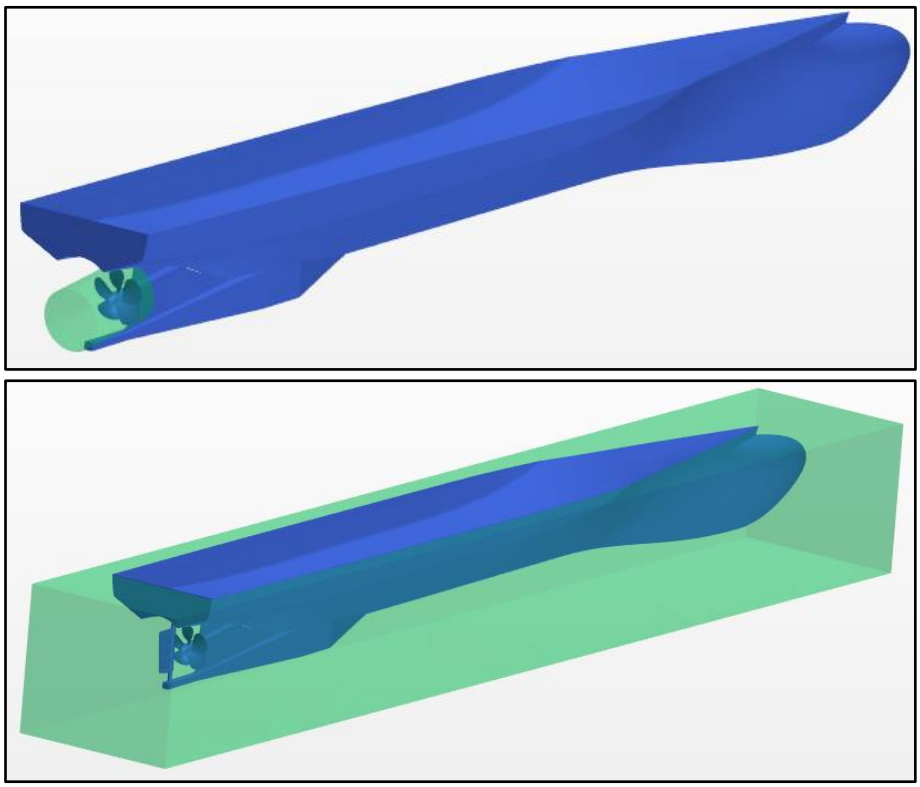

Figure 7.1. Representation of two different permeable surfaces: top is PS1; bottom: PS2 (their boundaries are highlighted by green).

The SONIC (Suppression Of underwater Noise Induced by Cavitation) project, which was funded under the European Union (EU) 7th Framework Programme (FP7), started in 2012 and lasted three years. In this collaborative project, there were thirteen organisations from five European countries, including universities, technical institutes and classification societies (SONIC, 2012). The project funding was provided to meet the requirement of MSFD (EU Marine Strategy Framework Directive) to satisfy the Good Environmental Status (GES) of EU water by 2020. Therefore, exploring the anthropogenic underwater noise, particularly shipping noise, was key to achieving the MFSD requirements. In this regard, the SONIC project focused on the URN induced by the cavitating propeller of ships since the propeller cavitation is the dominant contribution to the URN.

In this project, the first phase was to develop techniques for the accurate prediction of propeller URN using model scale tests, including novel experimental and computational techniques. The second aspect of the project was to investigate the propeller URN radiated by a full-scale ship and conduct sea trials to validate model scale results obtained in the first phase of the project. The last phase of the project was the investigation of noise mitigation. Also, it was aimed to develop an underwater noise propagation model to predict the noise signature of an individual vessel (noise footprint) in the specific region of the ocean where the vessels were passing through this region. In addition to this model, an empirical ship source-level model was developed using the target vessel's URN data obtained during the SONIC project (Brooker and Humphrey, 2014; Brooker and Humphrey, 2016)

The measurements were carried out in September 2013 in the region of Northumberland, where approximately 28km offshore east of Blyth, in the North East coast of England. During the trials, water depth was around 100m, and soft mud sediment conditions were present. The target vessel used in the trials was the catamaran research vessel of Newcastle University, The Princess Royal, designed and commissioned through in-house efforts and locally (Atlar et al., 2013). The target vessel and its specifications can be shown in Figure 7.2 and Table 7.1, respectively. The main characteristics of the vessel propellers were already given in Section 6.2.2.

Figure 7.2. Target vessel: The Princess Royal (Atlar et al., 2013).

Table 7.1. Specifications of the target vessel (Atlar et al., 2013; Turkmen et al., 2017).

Classification	MCA Cat 2
Overall length, (L_{OA}) (m)	18.9
Beam (Full), (B) (m)	7.3
Design draft, (T) (m)	at AP: 1.96 and at FP: 1.76
Displacement (Loaded arrival) (ton)	42 (approximately)
Payload (ton)	5
Max speed (knot)	20
Cruising speed (knot)	15
Engines (BHP)	2 x 602
Gearbox reduction ratio	1.75

The URN measurements were conducted using the deployed vertical hydrophone arrays (3 hydrophones located on each system at different depths of submergences) from a moored support vessel to record the acoustic pressures and URN when the target vessel passed through the hydrophone arrays. The effects of surface wave motion on the hydrophone array were minimised by the help of a spar buoy and using an elastic tether to decouple the array from the support vessel's movement. The different hydrophones were attached to the central rope using a stainless steel protective cage and mounting setup. The hydrophone damage was also prevented using a sloid mounting onto the central rope to keep the distance between hydrophones. Also, the mounting kept fixed the hydrophones away from the central rope and cables to reduce the undesirable self-noise from the turbulence around the array. During the measurements, the GPS data was used for post-processing purposes to define the CPA (Closest Point of Approach) distances between the target and support vessels. The measurements were carried out according to the American National Standard Institute (ANSI) and International Organisation for Standardization (ISO). Also, the measurements were performed in compliance with the Grade-A measurement standard (Turkmen et al., 2017; Brooker and Humphrey, 2016).

In order to perform onboard measurements, several transducers were installed on the target vessel to measure the hull pressure pulses, engine and hull vibration, propeller shaft speed, propeller torque and so on. Also, a baroscope and several cameras were used to capture detailed information about the cavitation at each run. Several partners were involved in the trial, and they used their own measurement capabilities with hydrophone arrays (Turkmen et al., 2017; Brooker and Humphrey, 2016). Amongst them, the setup designed by the University of Southampton (SOTON) and CETENA is shown in Figure 7.3 as the numerical calculations

will be compared with the measurements obtained by SOTON and CETENA in the results section. During the full-scale measurements, the CPA point was 100m. More detailed information about the data acquisition system and trials can be found in the study by Brooker and Humphrey, 2016.

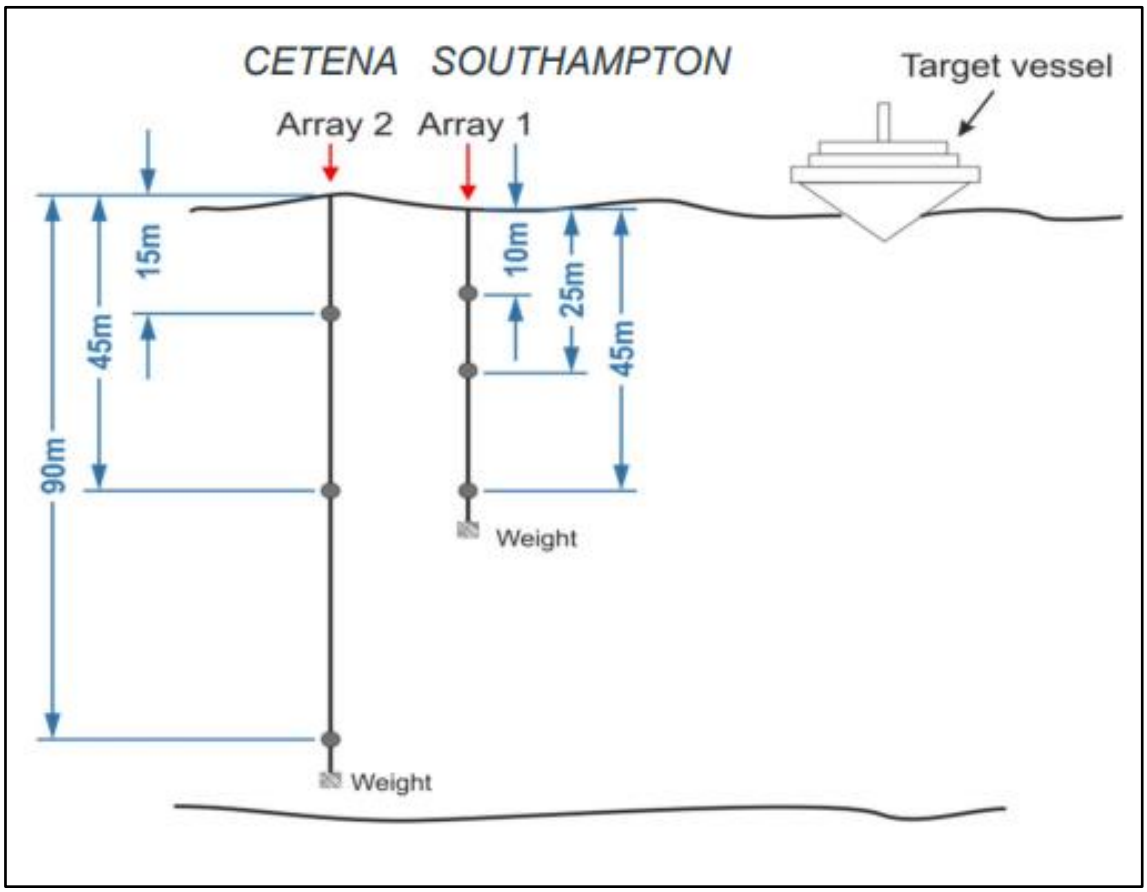

Figure 7.3. The measurements setup (Humphrey and Brooker, 2019).

7.3 Numerical modelling

7.3.1 Test matrix

The operating conditions in the numerical calculations were determined according to full-scale trials carried out in the scope of SONIC projects. These four conditions correspond to the engine speeds of 900, 1200, 1500, and 2000rpm with a gear ratio of 1:1.75. A brief summary of the selected conditions is given in Table 7.2.

Table 7.2. Chosen full-scale operating conditions for the target vessel (The Princess Royal) (Aktas et al., 2016b)

Data/particulars	Values			
Condition name	C1	C2	C3	C4
Dynamic draught T_A/T_F, m	1.95/1.57	1.95/1.57	1.95/1.57	1.95/1.57
Ship speed through water (STW) (V_S), knot	7.1	9.35	10.53	15.11
Engine speed, (n), rpm	900	1200	1500	2000
(Set on the wheelhouse by the skipper)				
Propeller speed, (n), rpm (Port-side in full-scale)	514.2	685.7	856.2	1142
Cavitation number (σ_n)	0.53	0.30	0.19	0.11
Torque coefficient $(10K_Q)$	0.336	0.318	0.323	0.318

The Ship speed Through Water (STW) values was recorded during the trials at each run. The runs were also repeated several times, and it was found that current significantly affected the STW according to recorded values in the trial datasheet. This resulted in higher blade loading conditions compared to the given values in Table 7.2. Thus, the STW values were reduced by around 12% in the numerical calculations for each condition to match the operating conditions between the numerical calculations and sea trials. This modification was also done during the model scale measurements with the demi-hull to match the operating conditions and hence the cavitation extensions between full-scale and model-scale (e.g., Sampson et al., 2015).

7.3.2 Computational domain and boundary conditions

Figure 7.4 shows the computational domain and boundary conditions used in the numerical calculations. The inlet boundary condition was located at $3L_{OA}$ from the forepeak of the vessel, whereas the outlet boundary was located at $5L_{OA}$ from the aft peak of the target vessel. The sides and bottom parts of the domain were extended by $1.2L_{OA}$ from the centreline. The inlet and outlet were defined as velocity inlet and pressure outlet, respectively. The symmetry boundary condition was defined for the side and bottom of the computational domain. In order to avoid the excessive number of grids for the accurate resolution of free surfaces, the free surface was neglected, and hence it was defined as a symmetry boundary condition. Although The Princess Royal is a catamaran, one of the demi-hulls was modelled (i.e., as a monohull) in the numerical calculations to decrease the computational cost.

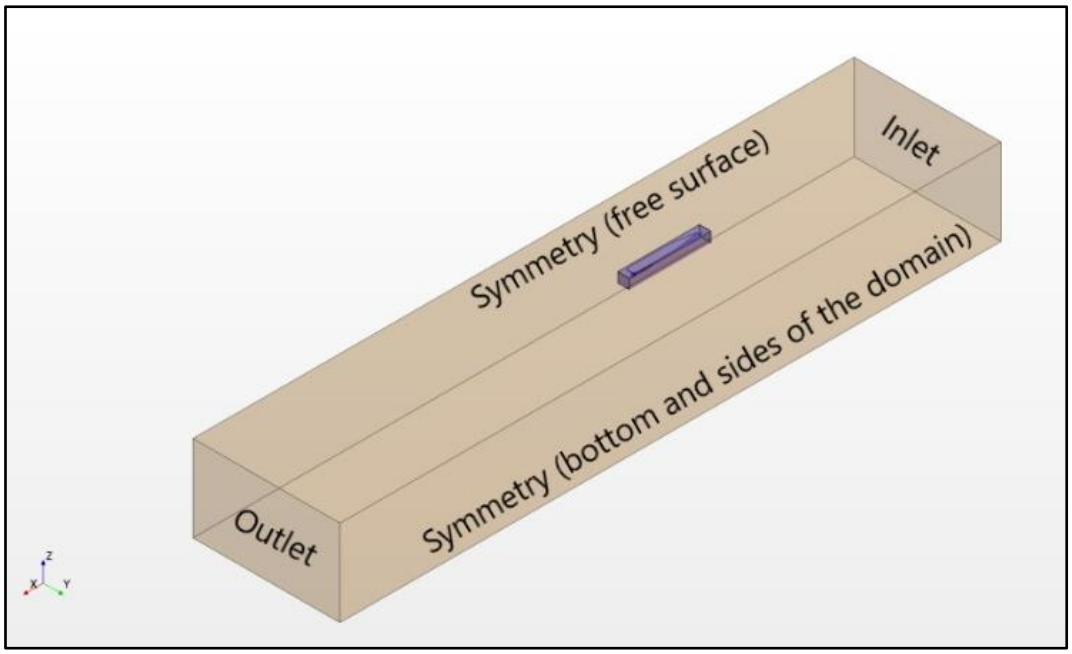

Figure 7.4. Representation of computational domain used in the numerical calculations.

7.3.3 Grid generation

The unstructured grid was adopted within the facilities of Star CCM+ 14.06, 2019 mesh together with hexahedral elements were used to discretise the computational domain. Additional mesh refinements were utilised around the hull and ship wake to decrease the numerical diffusion and hence solve the turbulence field and vortex structures accurately. This also enabled us to meet the grid resolution requirements for the regions where the LES method was applied. The grid was refined in the wall-normal direction to resolve the boundary layer itself (i.e., $y^+ < 1$) for the propeller.

The tip vortex cavitation (TVC) in the propeller slipstream was modelled using the V-AMR technique, as explained in Chapter 5. According to a comprehensive investigation performed in Chapter 5, it was found that the grid size inside the vortex should be between 0.2mm and 0.25mm for the model scale propellers for the better realisation of TVC in the propeller slipstream. When the full-scale propeller's TVC characteristics are concerned, the tip vortex diameter will inevitably be larger than that of a model scale propeller. Thus, the grid size will not have to be in the same order as the model scale propellers to prevent a considerable increase in the computational cost. Nevertheless, the grid size in full-scale propellers for the TVC resolution should be in a similar order to that of the model scale propeller. Based on our recent findings for the model scale propeller of this benchmark propeller, the grid size in the vortex region was enlarged with the scale ratio for the full-scale propeller.

In addition to the TVC application and local mesh refinement around the hull and propeller, the uniform grid was used to avoid possible numerical noise issues created by the abrupt mesh changes by taking crucial findings of Chapter 4 (Section 4.2) into account. Also, the permeable surfaces around the hull and propeller were placed in a region where the fine grid resolution was present. In this way, it was aimed to decrease the information loss due to the numerical diffusion created by the grid resolution for the accurate prediction of propeller URN. During the mesh adaptation process, the fine grid resolution is adopted for the regions where the permeable surfaces are located, as shown in Figure 7.5. As the permeable surface for the PS1 configuration is smaller than PS2, the relatively fine grid resolution is adopted for the PS1 configuration. However, the same grid resolution could not be implemented for the PS2 configuration as the permeable surface covers the whole hull. The implementation of the same grid resolution in PS2 as in the PS1 would result in an excessive amount of element counts. Eventually, the total number of cells was calculated at around 45M (for PS1) and 50M (for PS2). Figure 7.5 shows the grid resolutions for different numerical setups with two different permeable surfaces (i.e., PS1 and PS2).

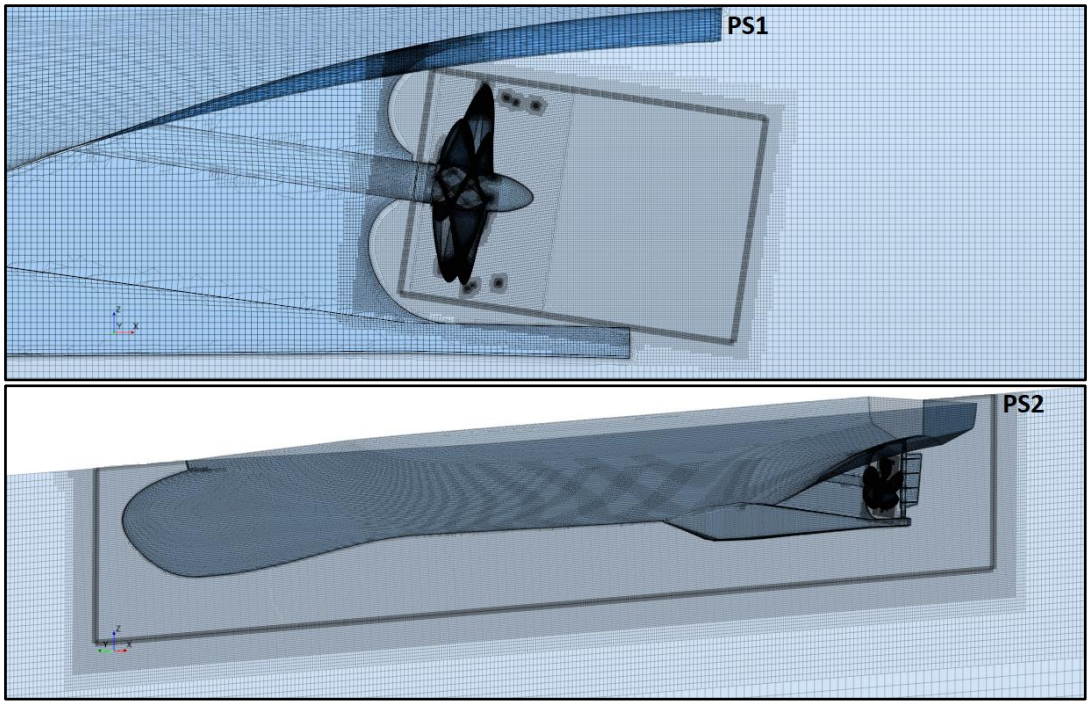

Figure 7.5. Representation of grid distribution in the computational domain for two different numerical setups.

7.3.4 Analysis properties

Figure 7.6 shows the regions, which can be visualised using the DES correction factor (i.e., F_{DES}) in the solver, where the RANS and LES methods are used. The details of the DES correction factor can be found in Section 6.2.1. As shown in Figure 7.6, there is a thin URANS region around the ship hull, and hence boundary layer solution is provided by the RANS method as expected in the DES method. On the other hand, the LES method is utilised in the ship wake.

The permeable surfaces, shown with black lines in Figure 7.6, are placed around the propeller and the whole ship to account for the contribution of nonlinear noise sources embedded in the propeller slipstream. Thus, the regions inside the computational domain, where the LES method is used for the flow field solution, enable the suitable placement of the permeable surfaces around the ship and propeller. Thus, the permeable surfaces are placed based on our understanding of the flow field in full-scale, which is supported by Figure 7.6 and our experience obtained using the applications for the model scale propeller operating under uniform and non-uniform flow conditions (i.e., Chapter 6). Besides, as stated in Chapter 6, there is no consensus and practical guideline for suitable permeable surface location and size for hydroacoustic applications.

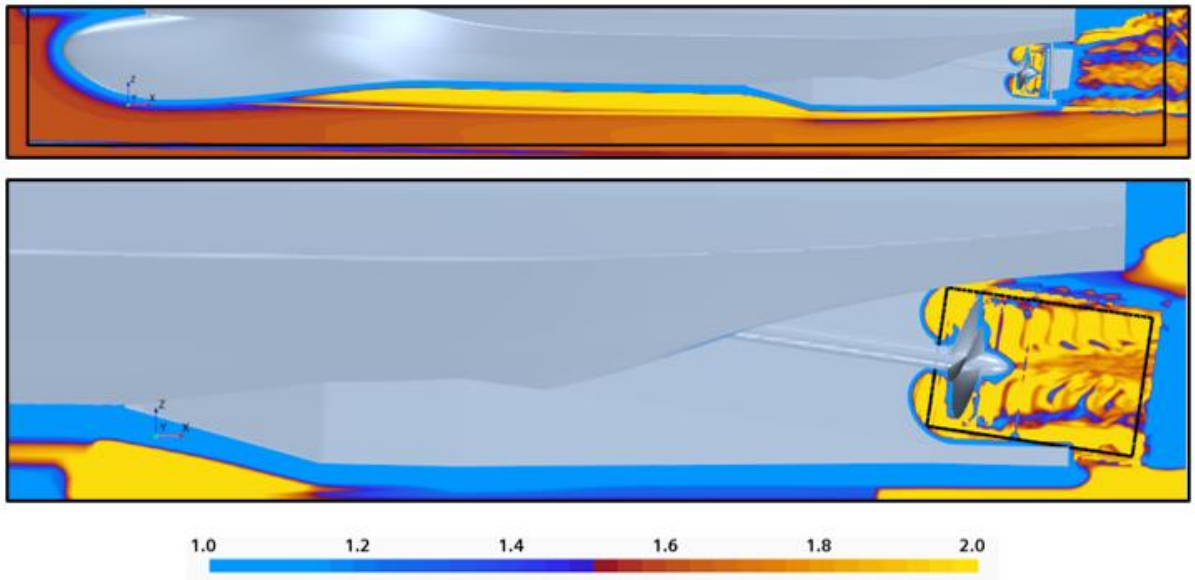

Figure 7.6. Visualisation of RANS and LES regions in the DES method (RANS is $F_{DES} = 1$ and LES is $F_{DES} > 1$).

In the numerical calculations, different numerical schemes were used, and they are summarised as follows:

- A segregated flow solver and a SIMPLE algorithm were used to compute the velocity and pressure.
- For the segregated solver, the Hybrid Bounded Central Differencing Scheme (Hybrid-BCD) was used to discretise convection terms in the momentum equations.
- The second-order discretisation scheme was utilised for the convection of turbulence terms.
- The second-order implicit numerical scheme was used for the time discretisation.
- For the convection term of the VOF approach, High-Resolution Interface Capturing (HRIC) was used to track the sharp interfaces between phases.
- The time step was set to 0.5^{o} of propeller rotational rate for each sea-trial condition.
- Inner iteration was set to 15 for each time step.
- Moving Reference Frame (MRF) and Rigid Body Motion (RBM) were used to model the propeller rotational motion.

Similar to Chapter 6, the DES method was initialised with a steady-state RANS approach using the k-ω SST turbulence model. At this initialisation stage with the steady RANS method, the Moving Reference Frame (MRF) technique was used to model the propeller rotational motion. In this way, the DES method's robustness was increased. After initialising with the RANS method, the solver was switched to the DES method by activating the cavitation. When the solver was switched to the DES method, the propeller rotational motion technique was changed with the Rigid Body Motion (RBM). During the first propeller rotation, the timestep was set to 1^{o} of propeller rotational rate, and then it was reduced to 0.5^{o} of propeller rotational rate. In this way, any possible stability issues related to cavitation phenomena were avoided.

The Schnerr- Sauer mass transfer model based on the reduced Rayleigh-Plesset equation was used to model the cavitation. In this model, the customisable cavitation parameters (i.e., nuclei density and diameter) were taken based on the investigation of the formation of sheet and tip vortex cavitation for the full-scale propellers. Thus, the nuclei density and diameter were set to 10^{10} $(1/m^{3})$ and 10^{-6} (m), respectively. The acoustic analogy was activated when the flow field converged to collect the acoustic pressures at the specified points using the receivers. The acoustic data were collected during the eight propeller revolutions.

7.4 Numerical results

7.4.1 Hydrodynamic performance prediction

The numerical calculations are first compared with the sea trial data in terms of the torque coefficient measured during the noise measurements for all operating conditions explored in this study. Table 7.3 shows the differences in the torque coefficient between the CFD and sea trials. The maximum difference for the torque coefficient between CFD and sea-trial was 12%. This might be due to the slightly different operating conditions between the CFD and sea trials. A similar discrepancy between the CFD and sea trials in terms of thrust and torque values was also seen in other studies conducted using different full-scale vessels (e.g., Ponkratov and Zegos, 2015).

Table 7.3. Comparison of torque coefficient between CFD and sea-trial at different operating conditions.

Operating Condition (Engine Speed, n)	Sea-trial ($10K_Q$)	CFD ($10K_Q$)	Absolute difference (%)
C1 (900rpm)	0.336	0.330	1.681
C2 (1200rpm)	0.318	0.338	6.271
C3 (1500rpm)	0.323	0.364	12.752
C4 (2000rpm)	0.318	0.348	9.431

In order to show the resolution of turbulence vortex structures in the ship wake, the vortex structures are visualised using the iso-surface of Q criterion in Figure 7.7 for C2. The vortex structures are visualised with the threshold value of Q criterion 2500 1/s^2. As shown in Figure 7.7, the helical vortex structures in the near field of the propeller slipstream are well resolved for both configurations. However, these structures disappear further downstream because of the insufficient grid resolution applied further downstream. The small eddies also appear at the bottom of the skeg. As expected, the hub vortex is present for the PS1 configuration, whereas the hub vortex disappears for the PS2 configuration. The rudder leads to the partial break-up of the vortices, which can be considered one of the main nonlinear noise sources further downstream. The coherent vortex structures are more dominant in the PS1 configuration than those in the PS2 configuration. This is because the grid size is smaller in the former configuration than in the latter, as explained in Section 7.4.3. Therefore, relatively coarse grid resolution applied for the PS2 configuration causes to fade away of the vortex structures in a short distance downstream of the rudder compared to those of PS1.

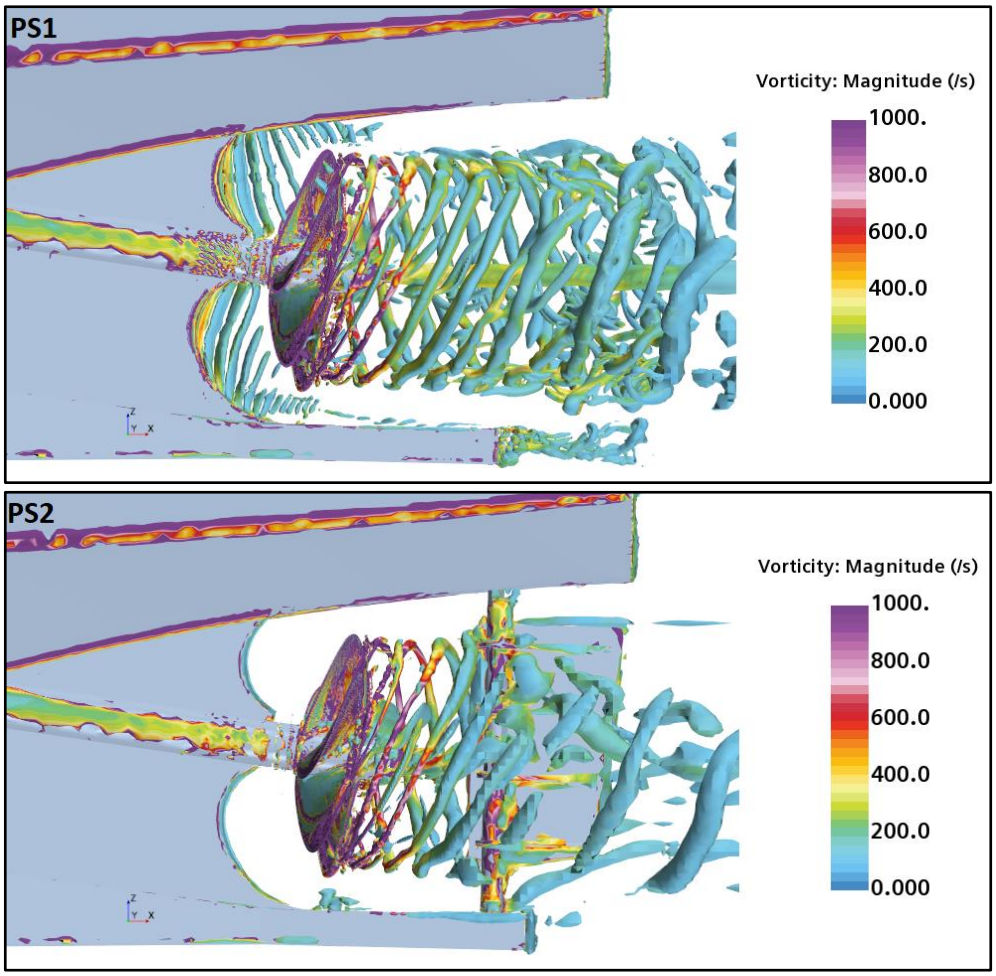

Figure 7.7. The vortex structures in the ship wake for PS1 and PS2 configurations (Q=2500 1/s^2) at C2.

7.4.2 Cavitation observations

Figure 7.8 compares cavitation extensions observed during the sea trials and numerical calculations at different operating conditions.

- As shown in Figure 7.8, the cavitation observed at C1 during the sea trials is characterised by the leading-edge vortex cavitation and its extended downstream of the propeller. Also, the strong cavitation dynamics seem to be present with some bursting phenomena at this operating condition. The leading-edge cavitation is also present in the numerical calculations, but its extension in the propeller slipstream could not be observed. This is because the vortex diameter is rather small and the adopted grid size for the vortex core using the V-AMR technique seems to be not enough to capture the TVC in the propeller slipstream, as observed in Chapter 6.

- The rather thicker vortex cavitation and strong sheet cavitation with some bubbles are observed in the sea trials at C2 compared to C1, as shown in Figure 7.8. The roll-up mechanism terminates the sheet cavitation, which emanates from the entire blade leading edge at the tip, and hence the cloudy trailing tip vortex cavitation formation occurs. In the numerical calculations, the sheet cavitation rather correlates with the sea trial observation without bubbles and strong cavitation dynamics at C2. The sheet cavitation extends towards the inner radii, similar to sea trial observations. However, the trailing tip vortex cavitation is not present in the numerical calculations at C2 due to the similar reasons explained above for C1.
- During the sea-trial observations, the sheet cavitation volume and its intensity increased at C3 compared to C2. Similar to C2, the sheet cavitation terminates the blade tip by rolling up, forming rather strong and unsteady trailing tip vortex cavitation. This TVC breaks up periodically, so cloud cavitation is observed. Similar sheet cavitation is observed in the numerical calculations with less violent cavity dynamics. The sheet cavitation forms trailing tip vortex cavitation by rolling up at the tip. Although the TVC is observed in the propeller slipstream in the numerical calculations, its extension and unsteady behaviour are not the same compared to the full-scale observations.
- The strongest sheet and TVC dynamics are observed at the highest loading condition (i.e., C4). Also, the interaction between two cavitation types is rather complex. The suction side sheet cavitation covers almost 25-30% of the blade area, and unsteadiness is dominant. The sheet cavitation is seen with a cloudy appearance. The sheet cavitation extension is observed slightly less than the sea trial observations in the numerical calculations. However, the strong sheet cavitation dynamics, especially cloudy appearance, are not present in the numerical calculations compared to sea trial observations. The sheet cavity breaks at the tip in the numerical calculations and forms an unstructured vortex. Moreover, the second vortex appears at the sheet cavitation trailing edge. The TVC is observed in the propeller slipstream with less extension than sea trial observations.

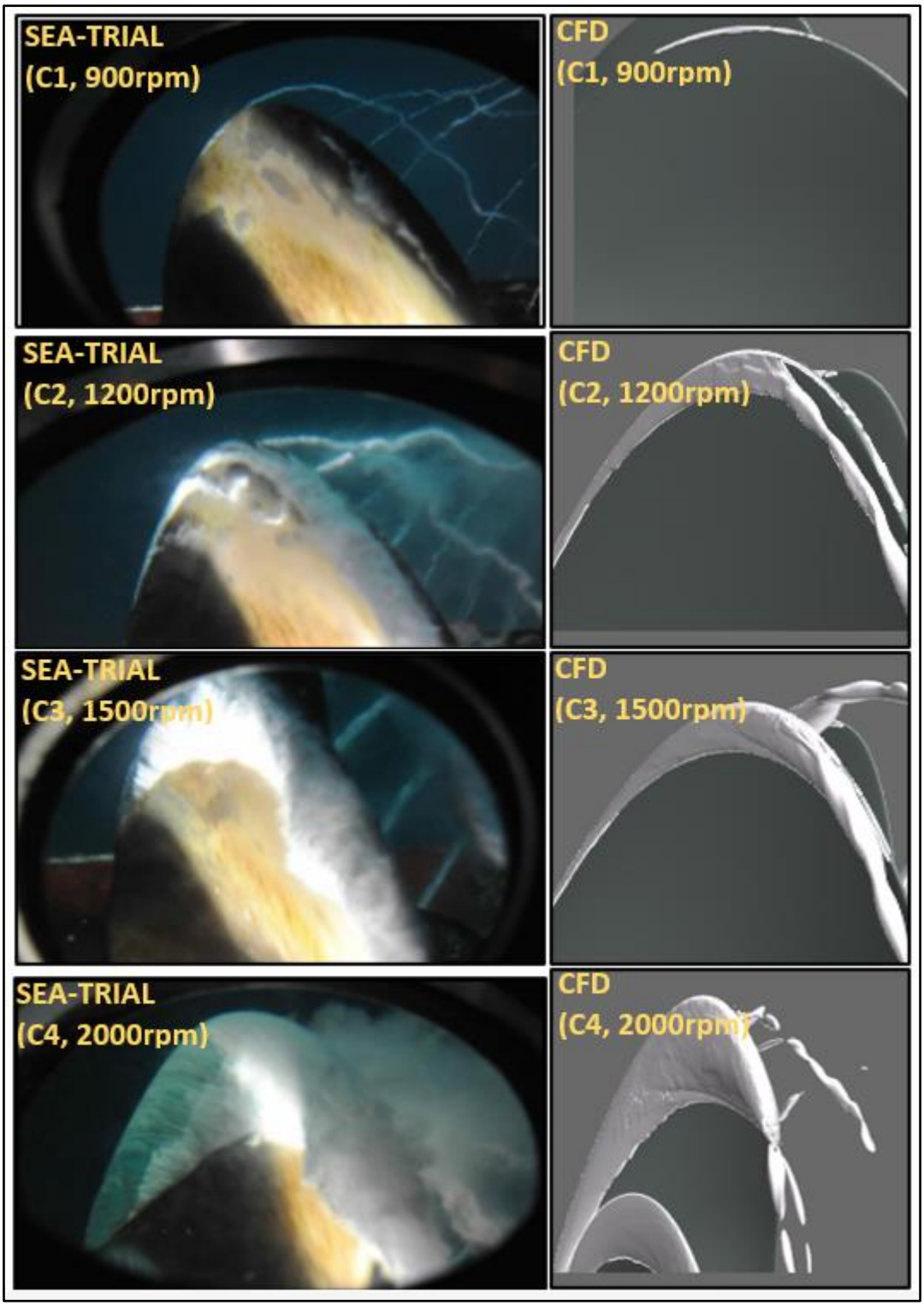

Figure 7.8. Comparison of cavitation extensions between CFD ($\alpha_{vapor} = 0.1$) and sea trials (Sampson et al., 2015).

In addition to comparing cavitation observations between CFD and sea trials, the cavitation patterns are also compared between the PS1 and PS2 configurations to show the influence of the rudder on cavitation extensions, as shown in Figure 7.9. As expected, the sheet and tip vortex cavitation formations are not affected in the presence of the rudder. Thus, similar sheet

and tip vortex cavitation formations are present in both configurations. The thicker and continuous hub vortex cavitation is observed during the sea trials at C3 and C4. In contrast, very little hub vortex cavitation at the tip of the hub is observed in the numerical calculation at C4 for PS2 configuration. As shown in Figure 7.9, the only difference between the two configurations is the extension of hub vortex cavitation.

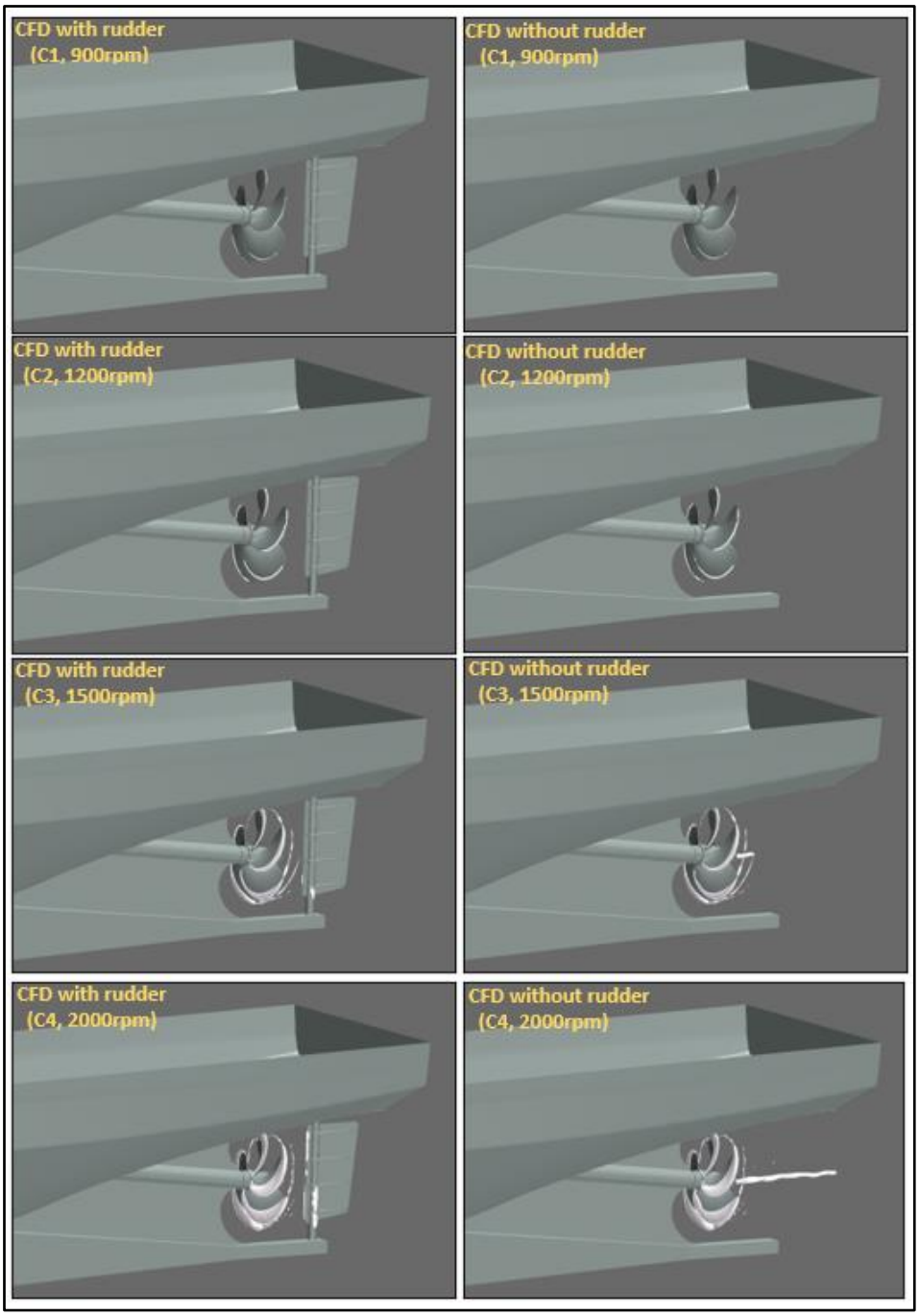

Figure 7.9. Comparison of cavitation extensions between PS1 (right) and PS2 (left) configurations at four different operating conditions ($\alpha_{vapor} = 0.1$).

It is important to note that the TVC in the propeller slipstream can be further extended with the aid of overset type grid using a relatively smaller grid size for the vortex core despite its high computational cost, as explained in Section 6.3.

7.4.3 URN predictions

7.4.3.1 Verification of the hydroacoustic results

The numerical URN predictions are first verified in the near field. However, as the total element count is considerably high in the present case, it is not possible to conduct verification studies using the standard procedures for the hydrodynamic part. In any case, the verification study should be conducted for the hydroacoustic part of the solution, similar to Chapters 4 and 6. This can be achieved by comparing hydrodynamic and hydroacoustic pressures in the near field, as explained in Chapter 6. Even though the incompressible assumption denies the sound propagation because of the infinite sound speed, the low Mach number for marine propellers makes the comparison still meaningful at near/mid fields and worthwhile to show the accuracy of hydrodynamic and hydroacoustic solutions (Ianniello et al., 2013; Sezen and Kinaci, 2019; Testa et al., 2021).

Figure 7.10 compares both pressures in the near field where the receiver NHP1 is placed at X=-0.0682, Y=0.0, Z=0.42625 from the propeller rotational axis for PS1 configuration. As shown in Figure 7.10, there is a good agreement between the pressures directly obtained by the incompressible DES method and acoustic analogy (i.e., porous FWH) for all operating conditions. The pressures are mainly characterised by the BPF (Blade Passing Frequency) in the near field as the linear noise terms are still dominant. Also, with an increase in engine speed or blade loading, although the pressures increase significantly from C1 to C4, the correlations of the hydrodynamic and hydroacoustic pressures are still very good, confirming the validity of the incompressibility assumption in the near field.

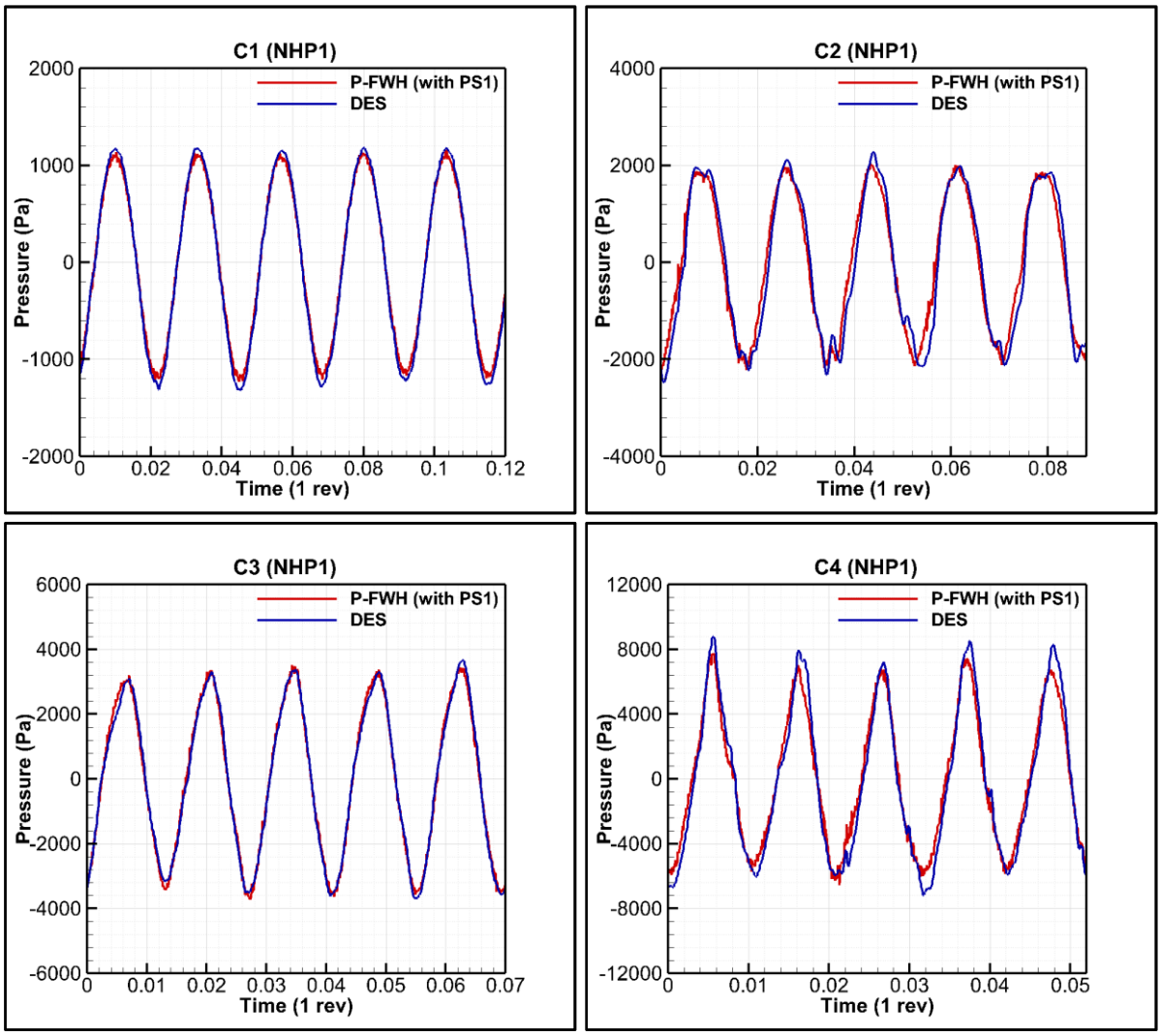

Figure 7.10. Comparison of hydrodynamic and hydroacoustic pressures in the near field at four different operating conditions.

7.4.3.2 URN predictions versus sea trial measurements

The numerical predictions obtained by DES with permeable FWH formulation are compared with the full-scale measurements at C1, C2 and C3 conditions in Figures 7.11, 7.12 and 7.13. The full-scale measurements are presented in terms of narrowband mean square pressure spectral density levels (i.e., Pa^2/Hz) and average of three hydrophones (or receiver) deployed by SOTON and CETENA. It should be noted that the data digitiser software was utilised to obtain the full-scale measurement data in the report of the SONIC project (SONIC, 2012).

As shown in Figures 7.11, 7.12 and 7.13, the agreement of the measurements obtained by the SOTON and CETENA array is very good and similar noise levels are recorded during the measurements. Similar to full-scale measurements obtained by CETANA and SOTON, the predicted noise levels with two hydrophone arrays are similar in the numerical calculations.

Therefore, the numerical predictions obtained by averaged SOTON arrays are presented and compared with the full-scale measurements in the following Figures. Also, the missing starboard propeller was taken into account by adding 3dB in the numerical calculations. This was because the monohull and only one propeller were modelled in the numerical calculations.

Figure 7.11 compares predictions and full-scale measurements at C1 (i.e., 900rpm engine speed). The noise levels in the numerical calculations are generally underpredicted up to 20dB across the noise spectrum compared to full-scale measurements, especially until 1kHz. Between 1kHz and 3kHz, the discrepancy between the numerical prediction and full-scale measurement reduces. At this operating condition, the weak leading-edge vortex cavitation extending propeller slipstream and possible bursting phenomena observed during the sea trials could not be predicted in the numerical calculations. Hence, the lack of cavitation volume and its dynamics in the numerical calculations are considered to be the main reason for the discrepancy, especially until 1kHz. Concerning numerical calculations, two different porous surfaces are utilised. The 1st and 2nd BPF values are well predicted in the numerical calculations using the PS1 configuration. Similar to PS1, the 1st and 2nd BPF values are also predicted using the PS2 configuration with low amplitude and slightly shifted frequencies. As shown in Figure 7.11, the noise spectra obtained by PS1 and PS2 configurations are slightly different after the 2nd BPF. The predicted cavitation using the CFD on and off the blades is rather weak at this operating condition. For this reason, the noise spectrum might be greatly dominated by the contribution of nonlinear noise sources. The PS2 configuration includes the contribution of vortices' throughout the hull and skeg compared to PS1. Even though the tip vortex emanating from the propeller's blade tip is considered to be the important nonlinear noise source, the formation of additional vortices throughout the hull, partial break-up of the vortices due to the rudder and their interaction seem to be the main reason for the noise difference between the two configurations.

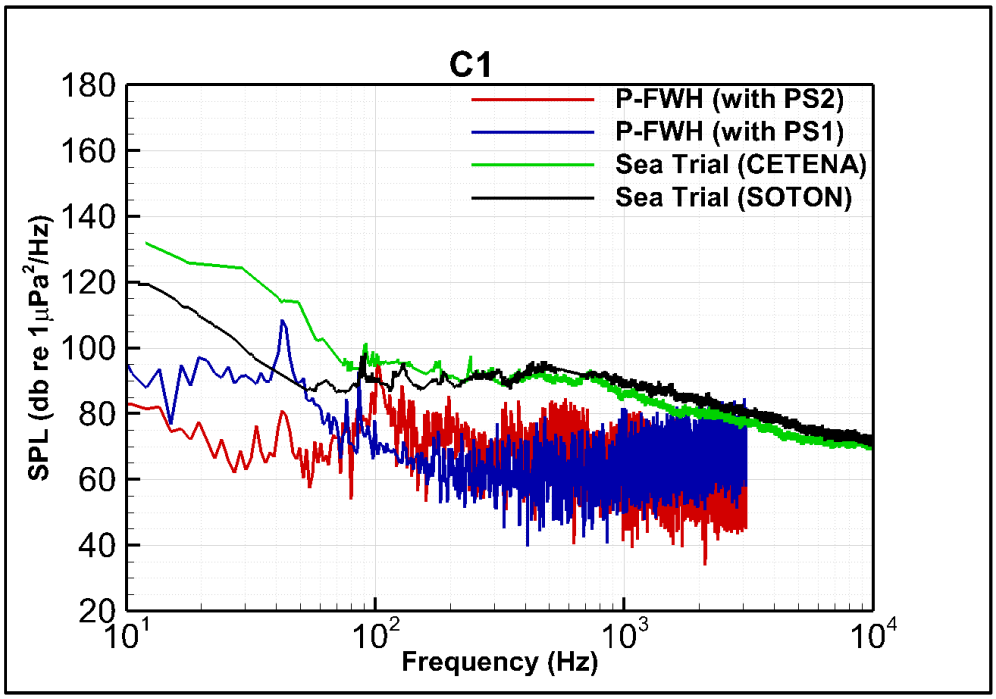

Figure 7.11. Comparison of CFD predictions and full-scale measurements at C1.

Another comparison of URN levels between CFD and full-scale measurements is carried out at C2 (i.e., 1200rpm engine speed) in Figure 7.12. Unlike the previous operating condition (i.e., C1), the discrepancy between the CFD predictions and full-scale measurements decreases by around 10dB at certain frequencies at C2. Although the sheet cavitation on the blades correlates with the full-scale cavitation observations, except for bubbles and cloudy appearance, there is still a lack of TVC in the numerical calculations compared to the full-scale measurements. Therefore, this lack of reproduction of cavity dynamics and TVC, which are expected to significantly contribute to the overall URN level, in the numerical calculations are still the main reason for noise difference for both low and high-frequency regions of the noise spectrum. Akin to the previous operating condition, the first two BPF values are well captured in the CFD using PS1 and PS2 configurations. Yet, the amplitude of the 2nd BPF is significantly higher in PS2 configuration than those of PS1. Remarkably, the predictions obtained by PS2 configuration show a distinct spectral hump similar to full-scale measurements between 100Hz and 300Hz. However, the URN levels at this characteristic hump are overpredicted up to 10dB in the numerical calculations compared to full-scale measurements. This hump is also present to a certain extent for PS1 configuration. In general, TVC is deemed one of the main noise sources, especially if the bursting phenomenon is present. Also, it characterises the noise spectrum with the sheet cavitation interaction and manifests itself as a characteristic hump depending on its dynamic behaviour. However, a similar TVC could not be observed using the V-AMR technique due to the small diameter of the vortex, as explained before. Although the

TVC could not be observed at this operating condition, the accuracy of the tip vortex flow is increased with the application of the V-AMR technique. This is because the pressure inside the vortex is reduced considerably using the V-AMR technique. The detailed investigation of the noise components at this operating condition (i.e., C2) showed that this hump was mainly generated by the pseudo loading term. Thus, apart from the hull interference or scattering due to the hydrodynamic load induced on the ship hull by the propeller, the interaction between the sheet cavitation with resolved tip vortex and nonlinear noise sources around the hull might cause this characteristic hump for PS2 configuration as it encapsulates the whole hull compared to PS1.

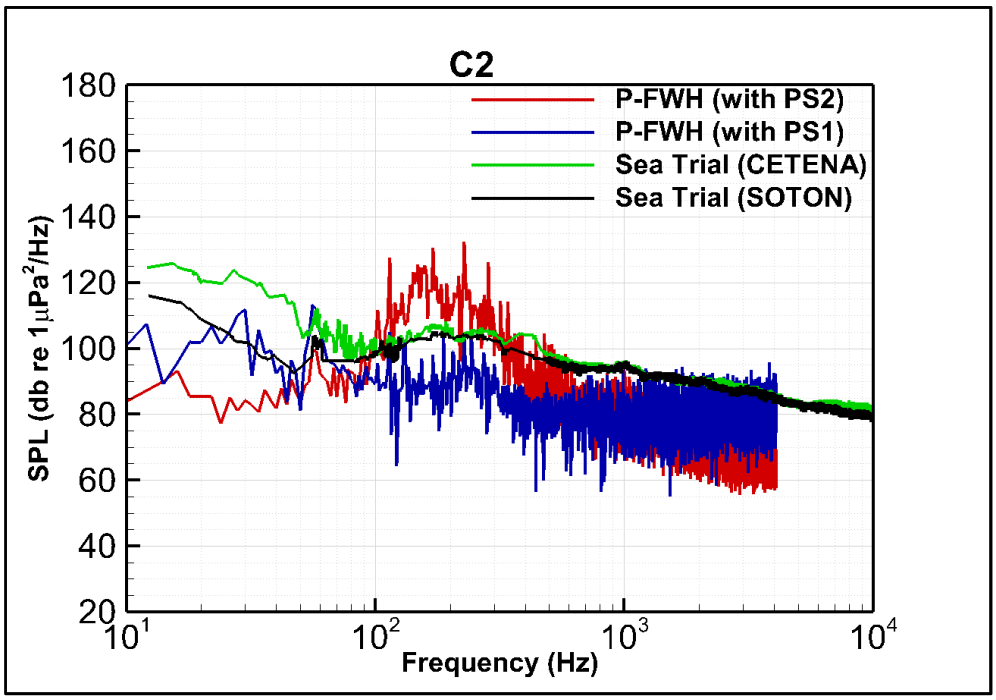

Figure 7.12. Comparison of CFD predictions and full-scale measurements at C2.

Figure 7.13 compares CFD predictions and full-scale measurements at higher loading conditions (i.e., C3, 1500rpm engine speed). As the vessel speed increase, the URN levels increase, corresponding to the increased cavitation extension and intensity. At this higher operating condition, several narrowband peaks are present in the full-scale measurements, and they are related to BPF, engine firing rate and higher harmonics of these sources. At frequencies between approximately 100Hz and 500Hz, the spectrum is mainly represented by tonal noise sources of different noise sources. The highest URN level across the entire noise spectrum occurs in this frequency range because of the strong sheet and TVC dynamics. As expected, the tonal peaks due to the additional noise sources (i.e., main engine, etc.) are not present in the CFD predictions. Akin to the previous operating conditions (i.e., C1 and C2), the noise

levels are generally underpredicted up to 10dB in the CFD calculations compared to full-scale measurements. The lack of cavitation dynamics, the possible bursting phenomena and the insufficient resolution of the nonlinear noise sources can be considered the main driven sources of the noise discrepancy between the prediction and measurements. Similar to C2, the noise spectrum is characterised by the hump between 100Hz and 400Hz for PS2 configuration. This is probably because the TVC is observed in the propeller slipstream in the numerical calculations with less violent dynamics. The appearance of TVC seems to manifest itself as a characteristic hump in numerical calculations similar to full-scale measurements. Yet, the URN levels are slightly higher at the frequency region where the hump appears. Surprisingly, the same characteristic hump due to the TVC dynamics could not be observed for the numerical calculations conducted using the PS1 configuration, which includes only the propeller in the absence of the rudder. Thus, akin to the C2, the interaction of cavity dynamics and nonlinear noise sources around the hull, included inside for the PS2 configuration, might make distinct this characteristic hump compared to PS1, even though the hull interference might contribute to the amplitude of this hump.

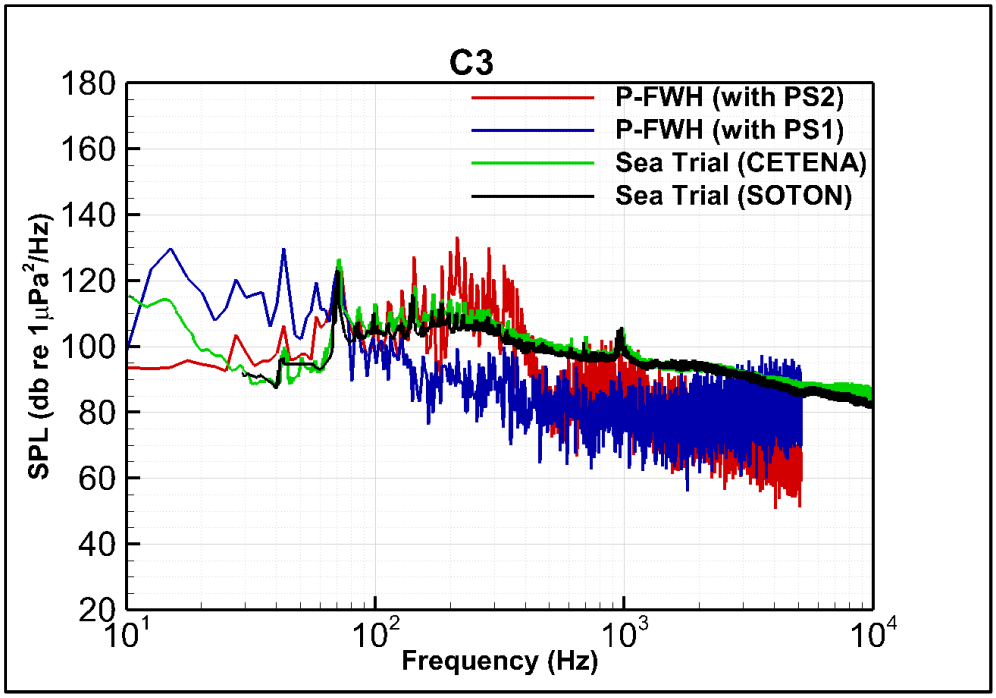

Figure 7.13. Comparison of CFD predictions and full-scale measurements at C3.

7.5 Chapter summary and concluding remarks

In order to achieve the aim of this chapter, the numerical calculations were conducted in full-scale using the DES and permeable formulation of the FWH equation. The V-AMR technique, developed in Chapter 5, was also utilised for the accurate solution of the flow field inside the vortex and hence better realisation of TVC in the propeller slipstream. Two different permeable noise surfaces were located around the propeller and ship to explore possible differences in terms of propeller URN. The numerical results were validated with the sea trial data through the torque coefficient, cavitation extensions and propeller URN. Based on the numerical investigations, the findings can be summarised as follows:

- The comparisons of results showed a good agreement between the CFD and sea trial data in terms of torque coefficient, particularly at C1 and C2. However, the maximum difference between the CFD and sea trial data was around 12% at the highest loading condition. This can be a slightly different operating condition used in the CFD calculations compared to sea trial data due to the possible differences in the service condition.

- The comparison of cavitation extensions between the CFD and sea trial observations showed that the sheet cavitation extension was rather similar at C1, C2 and C3. However, it was underpredicted in the CFD compared to sea-trial at C4. The foamy and strong bubbles could not be predicted in the CFD compared to the sea trial.

- Application of the V-AMR technique enabled TVC observation in the propeller slipstream in full-scale at C3 and C4. However, as expected, the same tip vortex dynamics could not be observed in the CFD compared to sea trial observations. Also, as the sliding mesh was used in this study, the TVC could not be extended towards the rudder. Nevertheless, the deformation and extension of TVC were successfully predicted using the V-AMR technique.

- The verification study was performed with the comparison of hydrodynamic and hydroacoustic pressures in the near field. The results showed that the hydrodynamic and hydroacoustic pressures were in good agreement, and the accuracy of the solution was shown.

- The propeller URN predictions showed that the maximum deviation up to 20dB at certain frequencies was observed at C1, where the incipient TVC, including the bursting phenomenon, was present. However, a similar leading edge tip vortex cavitation was not present in the CFD. Thus, this resulted in an underprediction of the propeller URN levels in the CFD compared to sea trial data. Nevertheless, at this operating condition, the first two BPF values were well captured, particularly using the PS1 configuration.

- The differences in the propeller URN levels were reduced at C2 between the CFD predictions and the sea trial. Although the TVC could not be observed in the CFD, the PS2 configuration showed a spectral hump with higher amplitudes, mainly associated with the TVC dynamics, as in the sea trial data. Yet, this spectral hump was not present for the CFD predictions obtained by PS1. The V-AMR technique was used for better modelling of TVC and accurate solution of the tip vortex flow. Thus, the cavitation dynamics together with the nonlinear noise sources occurring inside the PS2 might cause the hump compared to PS1, even though the hull interference might contribute to the amplitude of this hump considerably.

- The URN predictions were satisfactorily good agreement with the sea trial data at C3. The 1st BPF value was well captured in the CFD predictions. As the TVC was observed with less violent dynamics in the CFD, the spectral hump with high amplitudes due to the TVC dynamics was observed for the CFD predictions obtained by PS2, as in the sea trial. Similar to C2, this hump was not present for the predictions carried out by PS1. Thus, this might be related to the possible interaction of cavity dynamics and nonlinear noise sources around the hull for the PS2 configuration, apart from the possible hull interference effects on induced pressures.

- It should be emphasised that the qualitative comparison of the numerical results with the sea trial data is rather difficult. Many factors can influence the noise measurements at sea, which are not present in the CFD simulations. Moreover, the recorded acoustic signals certainly include several contributions during the measurements. Also, the cavitation dynamics are certainly different in the CFD predictions compared to sea trial data due to the assumptions in the numerical calculations. Therefore, it is not possible to expect complete agreement between the predictions and full-scale measurements. However, the general trend of the noise spectrum predicted in the CFD calculations encouraged us to use the proposed CFD method for full-scale applications.

8 Further investigation into the effect of TVC on the propeller URN performance

8.1 Introduction

Since TVC is one of the most important noise sources contributing to the propeller URN, this chapter aims to investigate the contribution of TVC to overall propeller URN levels, including its accurate CFD modelling aspects, using the model and full-scale test cases for validating and supporting the investigation of this contribution. This is achieved by modelling only sheet and sheet and tip vortex cavitation together at the same operating conditions. In this way, the contribution of TVC to the overall propeller URN could be distinguished.

Therefore, the theoretical background of the chapter is given in Section 8.2. The details of the numerical modelling, propeller geometry, and test matrix are explained in Section 8.3. In Section 8.4, the hydrodynamic results, cavitation extensions and propeller URN predictions are given, respectively. Finally, the concluding remarks are given in Section 8.5.

8.2 Theoretical background

8.2.1 Hydrodynamic model

Akin to Chapters 6 and 7, the DES method was used in this Chapter. The details of the formulations can be found in Section 6.2.1.

8.2.2 Hydroacoustic model

As used in Chapters 4, 6 and 7, the permeable formulation of the FWH equation was utilised to explore the influence of TVC on the propeller URN performance. A relatively small permeable surface was used in this study based on our understanding of the flow field and verification studies conducted with different permeable surfaces in Section 6.2.

8.3 Numerical modelling

8.3.1 Propeller geometry and test matrix

Akin to Chapters 6 and 7, the benchmark Princess Royal propeller was used in this Chapter to predict the propeller hydrodynamic characteristics, cavitation extensions, and propeller URN in conditions where only sheet and sheet and tip vortex cavitation were present. The details of the benchmark propeller's main characteristics can be found in Section 6.2.

In order to explore the influence of TVC on the propeller induced URN further, the propeller was operating under uniform, inclined and non-uniform flow conditions both in model and full-scale. These conditions were determined according to the experiments conducted in the round-robin (RR) test campaign and available sea trial data. For the non-uniform flow configurations, the wake field, given in Section 6.3, was used. The wake field was measured in the Ata Nutku towing tank of Istanbul Technical University (ITU) using the Princess Royal vessel (Korkut and Takinaci, 2013). Thus, the complete hull, including appendages, was not modelled, simplifying the numerical solution and reducing the computational cost.

The operating conditions used in this study are summarised in Table 8.1. Here, J is advance ratio, β is the shaft or inclination angle, n is propeller rotational rate (rps), σ_N is the cavitation number which is calculated based on the propeller rotational rate.

Table 8.1. Operating conditions for model and full-scale propellers.

Uniform and Inclined Flow Conditions				
Condition ID	J	Shaft Angle (β^o)	n (rps)	σ_N (-)
C1	0.4	0	35	1.30
C2	0.4	5	35	1.30
C3	0.4	0	19.025	1.06
C4	0.5	0	19.025	1.06
Non-uniform Flow (behind wake) Conditions				
Condition ID	Engine RPM	STW (kn)	n (rps)	σ_N (-)
C5	2000	15.11	35	1.07
C6	2000	15.11	19.025	1.07

Using the operating conditions given in Table 8.1, the propeller is operating in a condition where only sheet cavitation is present and also where the sheet and TVC are present together. This enables to separate the contribution of TVC on overall propeller URN.

8.3.2 Computational domain and boundary conditions

The computational domain and its dimensions are created according to the University of GENOA cavitation tunnel (UNIGE) test section to replicate the same conditions in the numerical calculations for the model scale propeller, similar to Sections 6.2 and 6.3. According to the test section, the total length of the domain was set to 2.2m with 0.57m height and 0.57m width. As shown in Figure 8.1, the positive X direction is defined as velocity inlet, whereas the negative X direction is defined as pressure outlet. The remaining surfaces, including blades, hub, and shaft, are defined as walls with no-slip boundary conditions. The computational domain is divided into three different regions. A cylinder, which serves as a rotating region, is created around the propeller to define the propeller's rotational motion. Also, another relatively big cylinder, which serves as a permeable surface, is placed around the propeller, and it encapsulates some part of the propeller slipstream. Another region is the static region, where the non-rotating part of the domain is embedded. The transitions between static and noise regions and between rotating and noise regions are provided with the internal interfaces. The constant velocity is assumed at the inlet of the computational domain under uniform and inclined flow conditions, the wake field is imposed at the inlet of the domain for non-uniform flow configurations. The computational domain was also created separately for the full-scale propeller. The domain was extended 4D towards the inlet and 16D towards the outlet from the blade centre. The radial distance was also set to 5D. Similar boundary conditions were used as in the model scale.

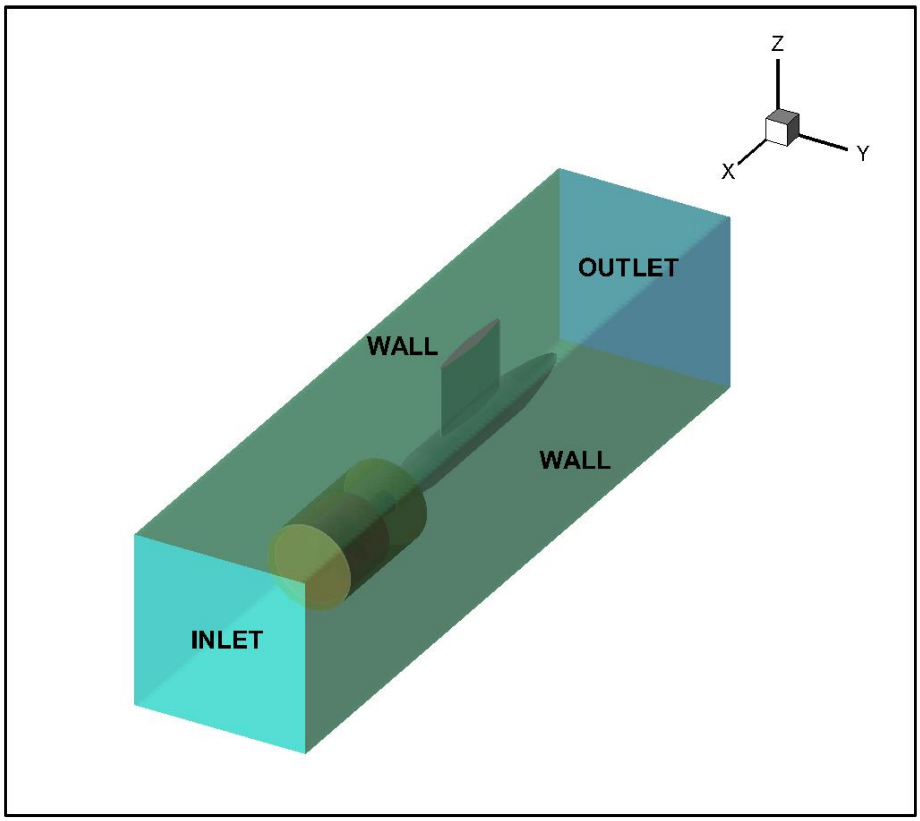

Figure 8.1. Representation of computational domain used in the numerical calculations.

8.3.3 Grid generation

The same grid structure was adopted, as given in Sections 6.2 and 6.3, within the facilities of the commercial CFD solver (Star CCM+ 14.06, 2019). Also, the same V-AMR technique, explained in Chapter 5, was used. Further details can be found in Section 6.2.2 and Section 5.3.3. The boundary layer was directly resolved for model scale applications, whereas the wall function was utilised for the boundary layer solution in full-scale applications. The total element count for model and full-scale propellers was calculated at approximately 24M and 32M, respectively. The numerical calculations were conducted with V-AMR (i.e., modelling sheet and tip vortex cavitation) and without the V-AMR technique (i.e., modelling only sheet cavitation) at all operating conditions to separate the contribution of TVC on overall URN. Other grid properties were kept constant between the solutions obtained with and without the V-AMR technique. The grid structure used in the numerical calculations with and without the V-AMR technique can be seen in Figure 8.2.

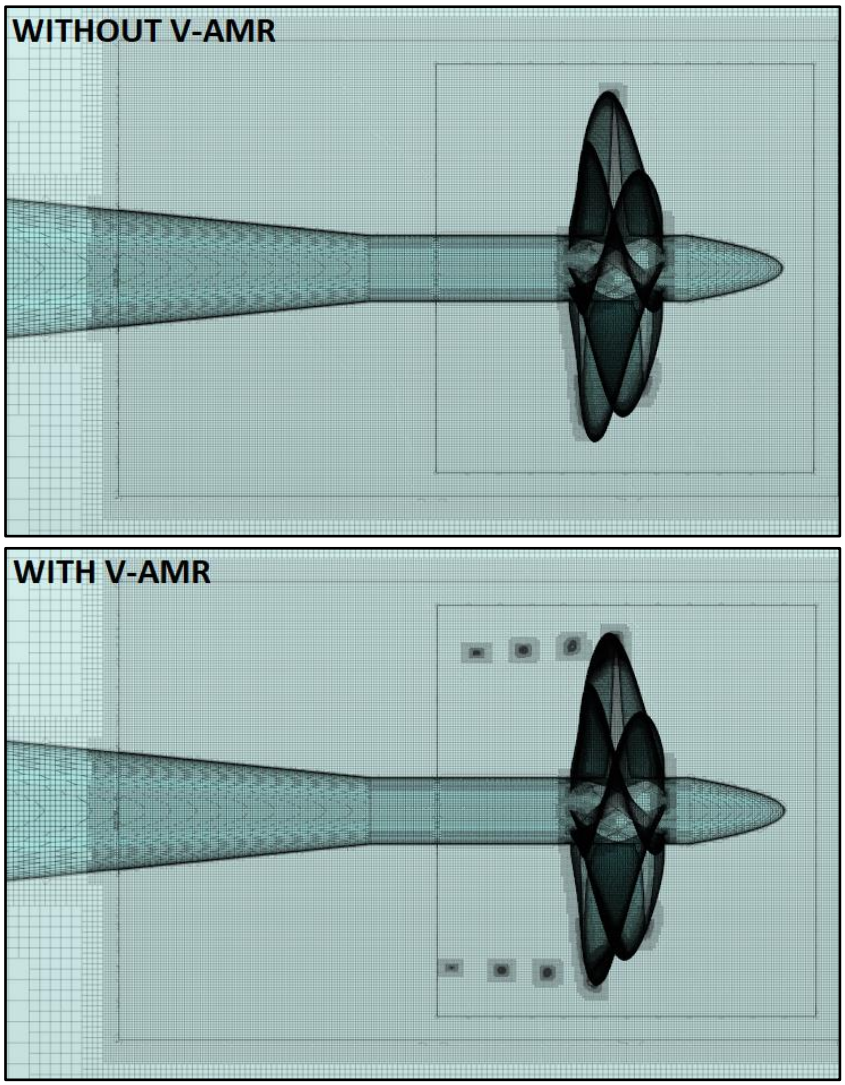

Figure 8.2. Representation of grid resolution with and without V-AMR technique.

8.3.4 Analysis properties

Akin to Section 6.2, the same solution strategy was adopted in the numerical calculations for the model scale propeller. Also, as used in Section 7, the same solution strategy was utilised for the full-scale propeller. The details of the analysis properties can be found in Section 6.2.2 and Section 7.4.4 for model and full-scale propellers, respectively.

8.4 Numerical results

8.4.1 Hydrodynamic performance prediction

The hydrodynamic performance coefficients obtained by CFD are compared with the available experimental and sea trial data at different operating conditions for model and full-scale propellers in Table 8.2. As shown in Table 8.2, the difference between CFD and experiment is

found around 7% for thrust and torque coefficients under uniform and inclined flow conditions (i.e., C1 and C2) for model scale propeller. This is because the model experiments were performed based on thrust identity and advance ratio identity by different facilities during the RR test campaign. However, in the numerical calculations, the advance ratio identity (i.e., for C1 and C2) was used to eliminate the several iterative runs to find the same thrust coefficient as in the experiment.

The torque identity was used for the non-uniform flow conditions (i.e., C5) in the model experiments. As the torque identity was not completely applied for CFD calculations at C5, the difference between CFD and the experiment was found to be around 8% in terms of torque coefficient. The discrepancy between CFD and sea trial data was also found at 10% for torque coefficient at C6. As the experimental and sea trial data is not available for the full-scale propeller operating under uniform flow conditions (i.e., C3 and C4), only CFD results are given in Table 8.2.

Table 8.2. Operating conditions for model and full-scale propellers.

	EXPERIMENT & SEA TRIAL		**CFD**	
Condition	K_T	$10K_Q$	K_T	$10K_Q$
C1	0.244	0.341	0.262	0.365
C2	0.245	0.341	0.262	0.368
C3	-	-	0.257	0.356
C4	-	-	0.203	0.289
C5	-	0.318	0.237	0.346
C6	-	0.318	0.234	0.352

The vortex structures in the propeller slipstream are compared with and without the V-AMR technique at C1 in Figure 8.3. The iso-surface of the Q criterion was used to visualise the vortex structures. Also, the threshold value of the Q criterion is set to 5000 $1/s^2$ in Figure 8.3. As shown in Figure 8.3, the V-AMR technique is applied inside the rotating region, and the area is shown green. With the application of the V-AMR technique, the pressure inside the vortex reduces compared to the base mesh (i.e., without the V-AMR technique). It is expected that the reduced pressure inside the vortex will enable observation of the TVC in the propeller slipstream. Additionally, the thinner vortex diameter is observed with the V-AMR technique as the actual TVC diameter is smaller than the tip vortex diameter. With the application of the V-AMR technique, two vortex structures emanating from the propeller's blade tip occur

compared to the base mesh. Nevertheless, similar and persistent vortex structures can be seen with and without the V-AMR technique in Figure 8.3.

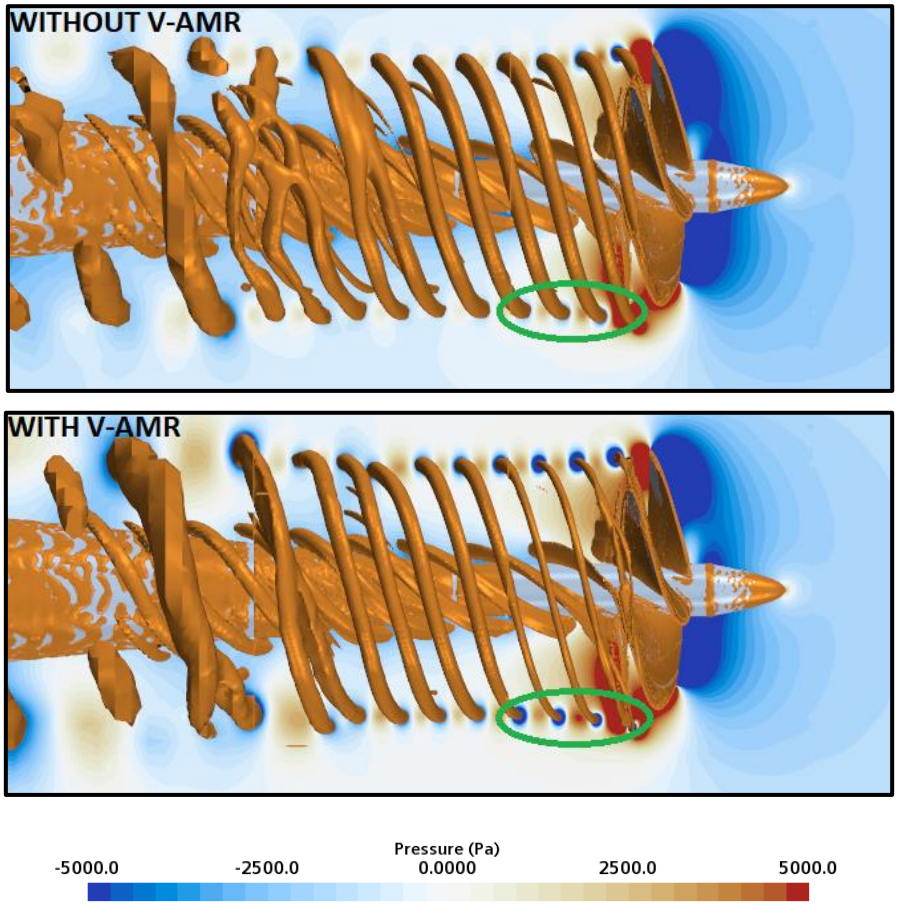

Figure 8.3. Comparison of vortex structures with and without the V-AMR technique at C1.

8.4.2 Cavitation observations

The predicted cavitation extensions in the CFD were compared with the experiments conducted in the University of Genoa Cavitation tunnel and sea trial observations at different operating conditions. The numerical comparisons were performed in the presence of only sheet cavitation (i.e., without V-AMR technique) and sheet and TVC (i.e., with V-AMR technique) using iso-surface of volume fraction 0.1 ($\alpha_V = 0.1$).

Figures 8.4 and 8.5 compare the cavitation observations between CFD and experiment under uniform and inclined flow conditions (i.e., C1 and C2) for the model-scale propeller. Figures 8.4 and 8.5 show that slightly more extended sheet cavitation towards the inner radii is observed in the CFD predictions compared to the experiment. As shown in Figures 8.4 and 8.5, the stable TVC is successfully observed in the propeller slipstream with the V-AMR technique in both conditions. Similar cavitation extensions are observed at C1 and C2. Thus, the effects of shaft

inclination on cavitation extension are not considerable. However, the cavitation dynamics can be stronger for the inclined flow condition (i.e., C2) than for the uniform flow condition (i.e., C1).

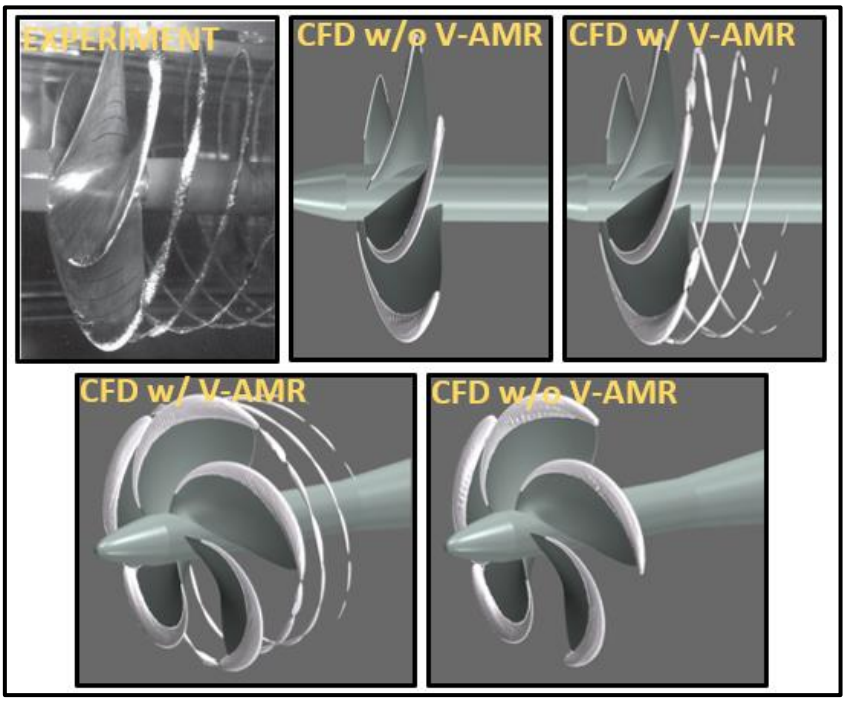

Figure 8.4. Comparison of cavitation observations between experiment and CFD together w/ and w/o V-AMR at C1 ($\alpha_V = 0.1$).

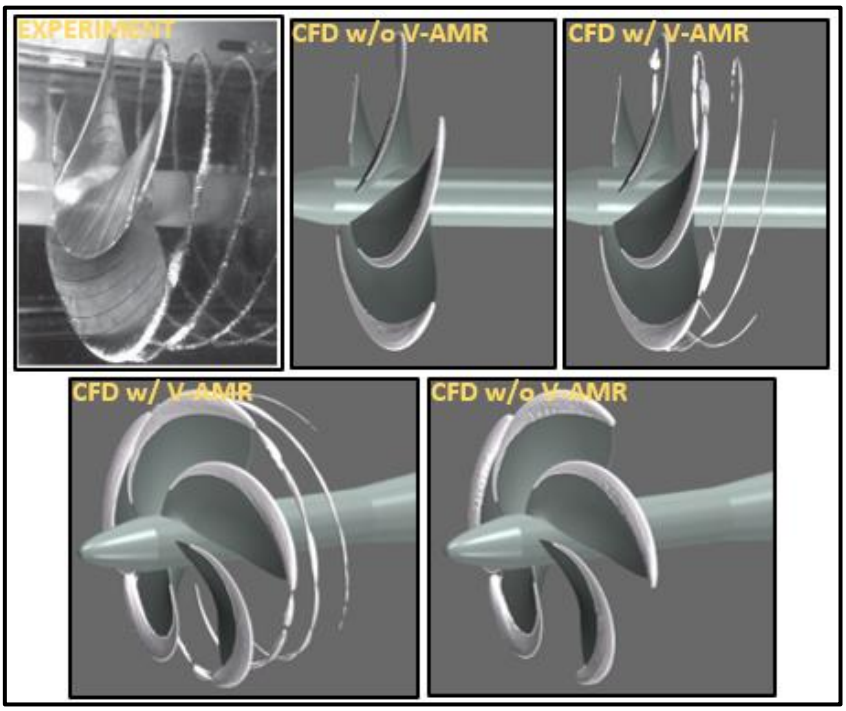

Figure 8.5. Comparison of cavitation observations between experiment and CFD together w/ and w/o V-AMR at C2 ($\alpha_V = 0.1$).

Figure 8.6 shows the cavitation extensions under uniform flow conditions (i.e., C3 and C4) for the full-scale propeller. As shown in Figure 8.6, the higher blade loading manifests itself as a larger suction side sheet cavitation at C3 than C4. Similar to model scale cavitation observations, applying the V-AMR technique enables TVC observation in the propeller slipstream. The stable and structured TVC is observed at J=0.5 (i.e., C4). However, the TVC is rather unstable and unstructured at J=0.4 (i.e., C3) due to the increased blade loading. It is expected that this consequently influences the cavitation dynamics and associated URN.

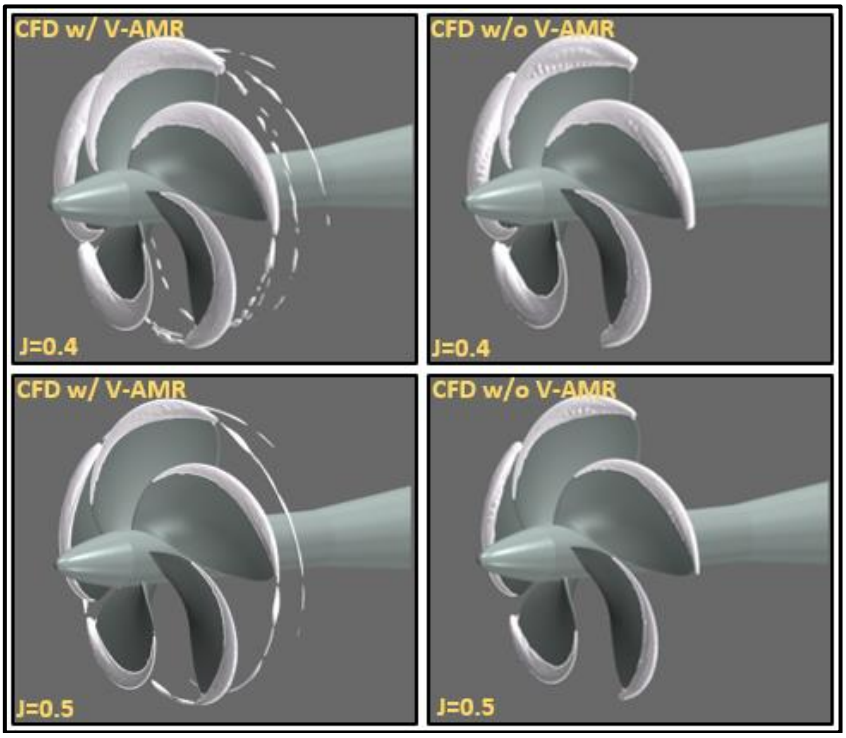

Figure 8.6. Comparison of cavitation observations between w/ and w/o V-AMR at C3 and C4 ($\alpha_V = 0.1$).

Figures 8.7 and 8.8 show the cavitation extensions between CFD, experiment, and sea trial data at C5 and C6. It should be recalled that C5 is the condition corresponding to the same full-scale operating condition (i.e., C6) in the model scale. According to sea trial observation, as shown in Figure 8.8, the suction side sheet cavitation is large and covers around 25-30% of the propeller blades. Also, the cloudy and foamy sheet and TVC are present during the sea trial observations. The cavitation observation is compared between the CFD and experiment at C5 in Figure 8.7. The CFD calculations overpredict the sheet cavitation compared to the experiment as the sheet cavitation is present towards the inner radii in the CFD. Similar TVC patterns are captured using CFD with shorter extensions in the propeller slipstream. However, the unstable and cloudy appearance of TVC could not be predicted in the model scale experiment and CFD calculations compared to the sea trial observations.

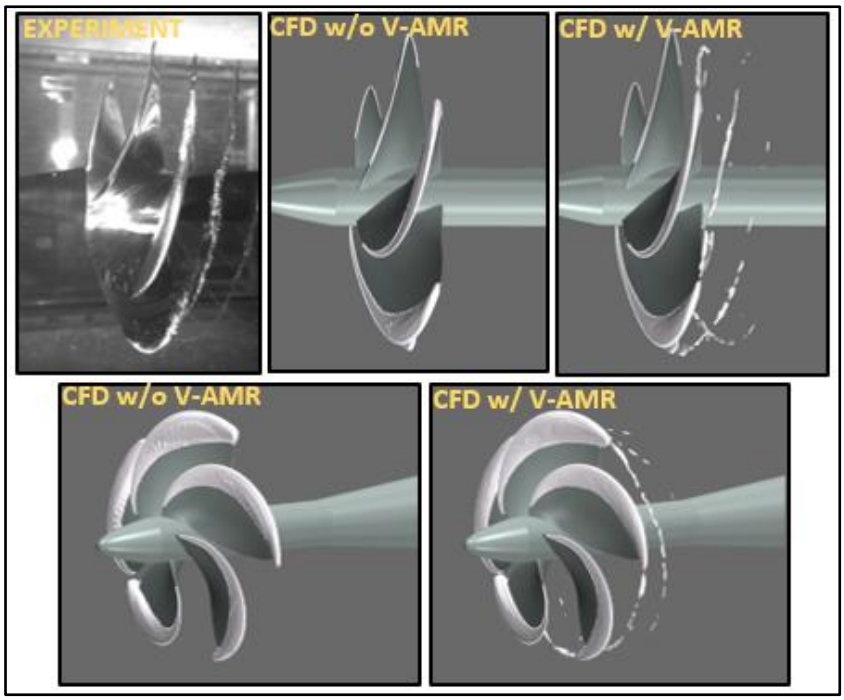

Figure 8.7. Comparison of cavitation observations between experiment and CFD together w/ and w/o V-AMR at C5 ($\alpha_V = 0.1$).

Figure 8.8 also shows the comparison of CFD predictions with the sea trial observations in full-scale. Akin to the model scale predictions, the unstable cavitation dynamics could not be predicted in the CFD. In addition to this, the sheet cavitation is slightly underpredicted in the CFD compared to sea trial observation. The V-AMR technique enables observation of TVC with much less intense vortex dynamics as well as the diameter than in the sea trial observation.

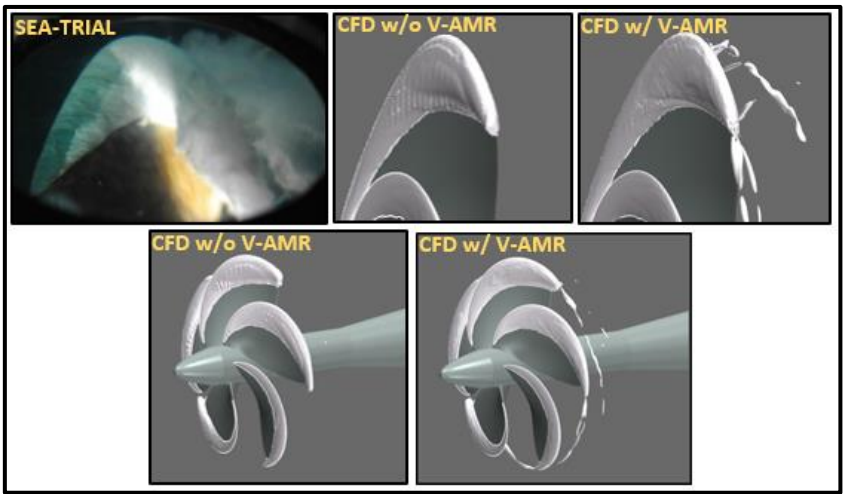

Figure 8.8. Comparison of cavitation observations between experiment and CFD together w/ and w/o V-AMR at C6 ($\alpha_V = 0.1$).

8.4.3 URN predictions

8.4.3.1 Verification of the URN results

Similar to Chapters 6 and 7, the URN predictions can be verified by comparing the hydrodynamic and hydroacoustic pressures in the near-field. Within this framework, as an example, Figure 8.9 shows the comparison of both pressures in the near field (i.e., z=0.17m at the propeller plane from the centre of the blades) at C1. As shown in Figure 8.9, both pressures are in agreement with each other, and the acoustic signal is purely characterised by BPF (Blade Passage Frequency). It should be noted that this agreement is valid everywhere in the near fields around the permeable surface for different operating conditions.

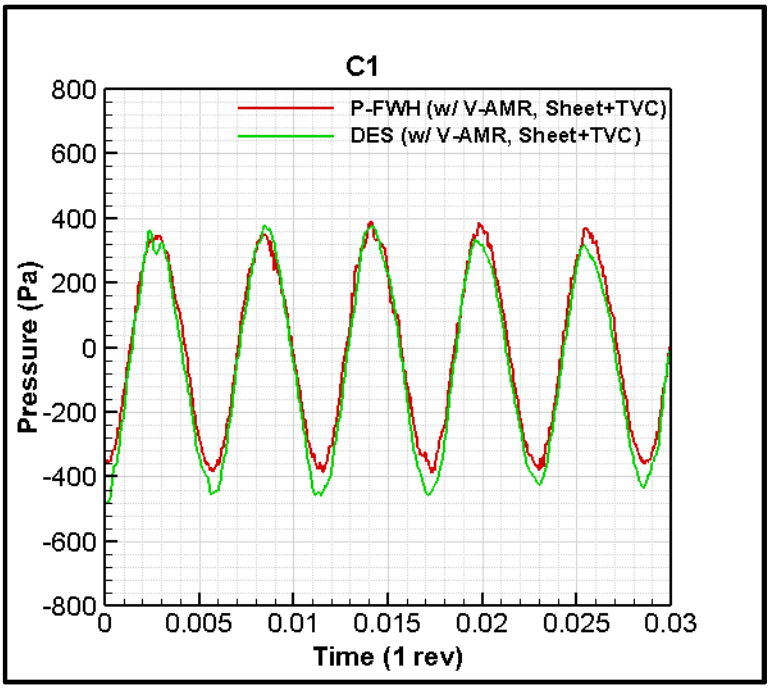

Figure 8.9. Comparison of hydrodynamic and hydroacoustic pressures in the near field (z=0.171m at the propeller plane from the propeller blades' centre).

8.4.3.2 URN predictions with and without TVC in the time domain in the near field

In this section, the acoustic pressures obtained by only sheet cavitation and sheet and tip vortex cavitation were compared to show the influence of TVC on the overall acoustic pressure levels in the near field. The pressures were recorded at the propeller plane, and the locations of the receivers were z=0.171m and z=0.5814m from the propeller blades' centre for model and full-scale propellers, respectively.

Figure 8.10 shows the change in acoustic pressure levels in terms of amplitude and waveform at C1, C3, C4, C5, and C6. As shown in Figure 8.10, the overall cavitating acoustic pressure signals are rather similar in a condition where only sheet cavitation is present and where the sheet and tip vortex cavitation is present at C1 for model scale and at C4 for the full-scale propeller. This is because the stable tip vortex dynamics are observed in the cavitation observations at C1 and C4 (see Figures 8.4 and 8.6). Contrary to C1 and C4, the cavitating pressure signal changes with the contribution of TVC at C3, C5, and C6, where the unstable and more intense TVC are present. As shown in Figure 8.10, the overall acoustic pressure signal shows higher amplitudes with the larger spikes (or irregularities) at C3, C5, and C6 (i.e., uniform and non-uniform flow conditions). These spikes can be associated with the possible bursting phenomena or large and violent cavitation dynamics, even though they could not be modelled as same in the experiment and full-scale measurements using the CFD method. This results in an increase in noise levels over a broad frequency range. In addition to the TVC dynamics, the interaction of sheet and TVC can also be important for the increased noise level in the presence of TVC. Although the uniform flow condition is imposed at C3 and C4 for the full-scale propeller, the intense cavity dynamics observed at C3 cause irregularities with the TVC compared to C4.

In the study by Aktas et al., 2018, the investigation of cavitating pressure signals with different propellers was also performed experimentally to gain further insight into the noise driving mechanisms with suitable signal processing methods. The authors adopted synchronised pressure pulse and noise measurements with the cavitation observations and explored the change in time-based pressure signal according to cavitation dynamics. Akin to the present study, the unstable and intense TVC created spikes in the acoustic signal at different operating conditions, and this was also considered due to the major cavitation events and cavitation collapse. Thus, the experimental study further supports the numerical findings of the present study on the influence of TVC in the time domain.

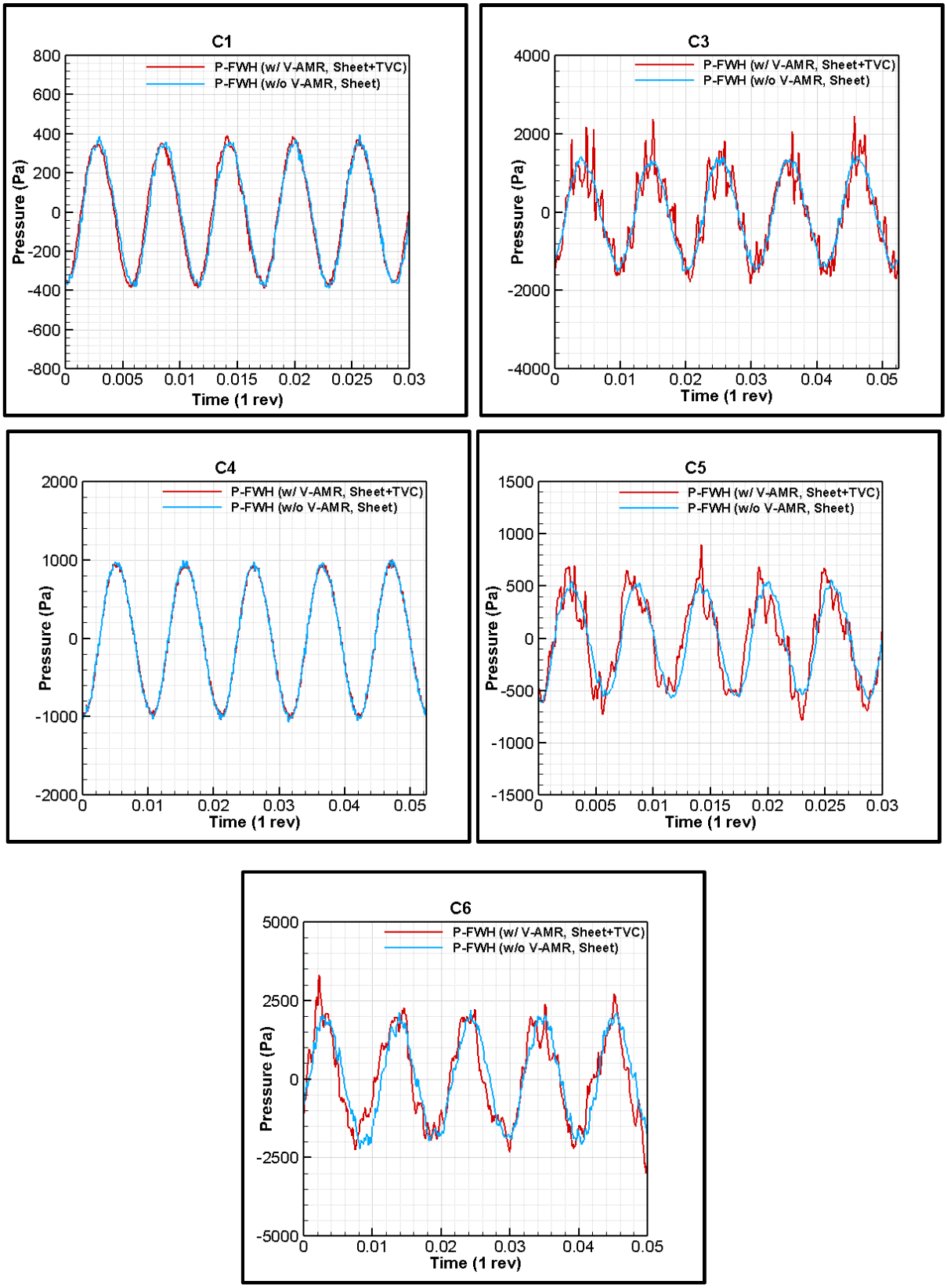

Figure 8.10. Comparison of cavitating acoustic signals in the time domain with and w/o TVC in the near field.

8.4.3.3 URN predictions with and without TVC in the frequency domain

The noise measurements and predictions are always presented with the noise spectrum in the frequency band. During the RR test campaign, the measurements were conducted by different facilities, and obtained results were compared with each other under uniform and inclined flow conditions (Tani et al., 2019b). Amongst the different facilities, in the present study, the numerical predictions for the model scale propeller were compared with the measurements performed in the University of Genoa Cavitation Tunnel due to the availability of the data for uniform, inclined and non-uniform flow conditions. As shown in Section 6.2 in Figure 6.11, three receivers, namely H1, H2, and H3, were located inside and outside (i.e., in an acoustic chamber) the cavitation tunnel. Hence, akin to the experimental setup and receiver locations, the same receivers were positioned in the numerical calculations to replicate the experiment. The receiver H3 was utilised for C1 and C2, whereas the receiver H1 was used at C5. In order to extrapolate the results from H3 to 1m and H1 to 1m, the spherical acoustic relationship was used in the numerical calculations due to the lack of data for the transfer functions used in the measurements.

Also, in the scope of the SONIC project (SONIC, 2012), the noise measurements were conducted with the Princess Royal vessel at different operating conditions, and a comprehensive database was obtained, as explained in Chapter 7. The full-scale measurements were carried out with three receivers deployed at different depths, as shown in Chapter 7 (see Figure 7.3). Later on, the results were corrected at 1m using the extrapolation procedure. Thus, the full-scale propeller URN predictions were compared with the full-scale measurements. In addition to the receivers positioned according to the model experiments, two more receivers were utilised, located at the propeller plane at 1m and 5.5m from the propeller blades' centre, to show the influence of TVC on overall cavitating propeller URN.

The noise spectrums are presented as power spectra (Pa^2) for model scale propeller (i.e., at C1 and C2) as in the experimental data, whereas the noise spectrums for the full-scale propeller at different operating conditions are presented as power spectral density (Pa^2/Hz) (i.e., C3, C4, C5 and C6). Also, the URN levels are presented in a 1/3 octave band.

It is to be noted that the details of the noise measurements and analysis procedures can be found in the studies by Tani et al., 2019a and Brooker and Humphrey, 2016 for cavitation tunnel tests and full-scale measurements, respectively.

Figure 8.11 compares the URN predictions with the measured data in the model scale at C1, C2, and C5. As shown in Figure 8.11, in the noise measurements, there is a high amplitude peak of around at 740Hz at C1, C2, and C5. Tani et al., 2017 stated that this noise component is most likely because of the vibration of one of the foils supporting the receiver inside the tunnel. The detailed information can be found in Chapter 6.

Figure 8.11 compares predicted URN results with the measured data at C1, C2, and C5. As shown in Figure 8.11, the noise results are underpredicted in the low-frequency region of the noise spectrum at C1 and C2. Yet, the agreement between the CFD and measured data is good after 1kHz. The underprediction of URN levels can be associated with the differences in the cavitation dynamics predicted in the CFD calculations compared to the experiment at C1 and C2. Also, the mechanical noises in the tunnel can also be the reason for the discrepancy at certain frequencies. At C5, the numerical calculations overpredict the URN levels after 1kHz. This can be related to the larger extension of sheet cavitation predicted in the CFD calculations compared to the experiment. At the medium-frequency range, the spectral hump, which is present in the measurement, dominates the noise spectrum. In contrast, the amplitude of the spectral hump is low in the numerical calculations at C5. This results in an underprediction of URN levels in the CFD calculations compared to the measured data in the low-frequency region of the noise spectrum.

The influence of TVC on overall URN levels can also be seen in Figure 8.11 at C1, C2, and C5. In general, the sheet and tip vortex cavitation are stable under uniform flow conditions and do not generate large cavitating volume variations. Hence, the sheet cavitation produces higher noise levels at the broadband part of the noise spectrum, and this can be accounted for by the breakup and collapse of small cavities shed by the sheet at the trailing edge of the propeller blades. In this situation, the stable tip vortex can produce a high and narrowband peak at the low-medium frequency region because of the vortex cavity pulsation. However, the spectral peak characteristics depend on the operating conditions and vortex dynamics. The vortex pulsation can be considered the main noise mechanism when the large and persistent vortices are present in the propeller slipstream. Also, when the other mechanisms such as cavitation volume variations because of the wake flow, cavity collapses, and bursting phenomena are dominant, the severity of the peak can be less, and the created acoustic energy with the other noise mechanisms is distributed over the noise spectrum. Eventually, the noise spectrum characterised by the only TVC or together with the sheet cavitation can be found in different forms depending on the dynamic of vortices and cavitation (Tani et al., 2019a). As shown in

Figure 8.11, akin to the near field cavitating propeller signal, the contribution of TVC on overall propeller URN is not considerable at C1, where the uniform flow and stable TVC are present. At C2, the shaft inclination creates cavitation volume variations and instability, and it manifests itself in higher URN levels in the numerical calculation in the presence of TVC. When the non-uniform wakefield is concerned (i.e., C5), which is the main noise-producing mechanism because of the change in cavitation volume of sheet and vortex cavitation, the influence of TVC on overall URN levels can be clearly seen over the noise spectrum in Figure 8.11. The URN levels increase up to 15dB by the contribution of TVC compared to the URN predictions in the presence of only sheet cavitation. Moreover, the spectral hump, characterised by the vortex dynamics as explained above, can be seen in the URN predictions obtained by CFD between 600Hz and 1kHz at C5, whereas it is not distinct at C1 and C2 as same as at C5.

In the past, cavitation tunnel experiments were conducted by Pennings et al., 2015 to explore the relation of tip vortex cavity dynamics with the cavitating propeller URN using the two-bladed model propeller. The results showed that the tip vortex cavity observed under uniform flow conditions did not generate noise with considerable amplitude above the tunnel background. However, a significant broadband contribution was observed due to the cavity dynamics when the tests were carried out under non-uniform flow conditions. Thus, the experimental study also supports the present study's finding in terms of TVC influence on propeller URN under uniform and non-uniform flow conditions for the model scale propeller.

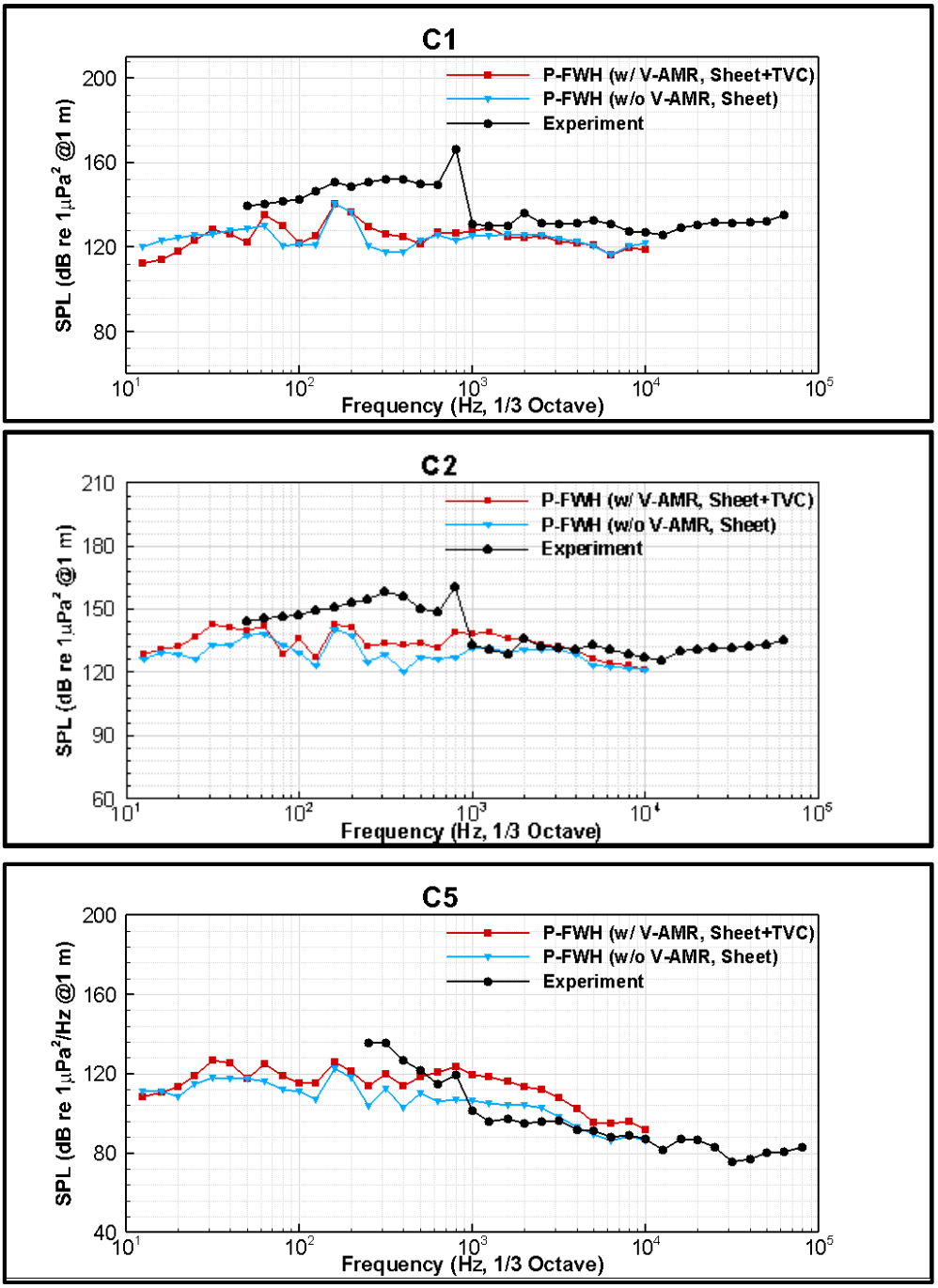

Figure 8.11. Comparison of URN levels between CFD and measured data at 1m and CFD predictions w/ and w/o the TVC at C1, C2 and C5

The full-scale propeller URN predictions are compared with each other at C3 and C4 to explore the influence of TVC on overall propeller URN in Figure 8.12. As shown in this figure, with an increase in blade loading, associated cavitation extensions, and its dynamics, the URN levels increase from C4 to C3. Similar to the model scale propeller operating under uniform flow conditions (i.e., C1), at C4, stable TVC dynamics do not produce considerable sound compared to the URN predictions in the presence of only sheet cavitation. However, unlike the model scale propeller URN predictions under uniform flow conditions (i.e., C1) and C4, the TVC

increases the URN levels considerably at C3 (i.e., under uniform flow conditions). This is because the rather unstable and irregular TVC dynamics are present at C3 compared to the cavitation dynamics observed at C4. Although the larger cavitation volume variations are not expected under uniform flow conditions, the breakup of the cavitation vortices together with the sheet cavitation interaction seems to be one of the reasons for the considerable URN increase with the TVC at C3. This breakup of vortices can further contribute to the nonlinear noise sources. Also, the intense cavity dynamics might be the another source of spectral hump around 600Hz and 1kHz at C3 in full-scale.

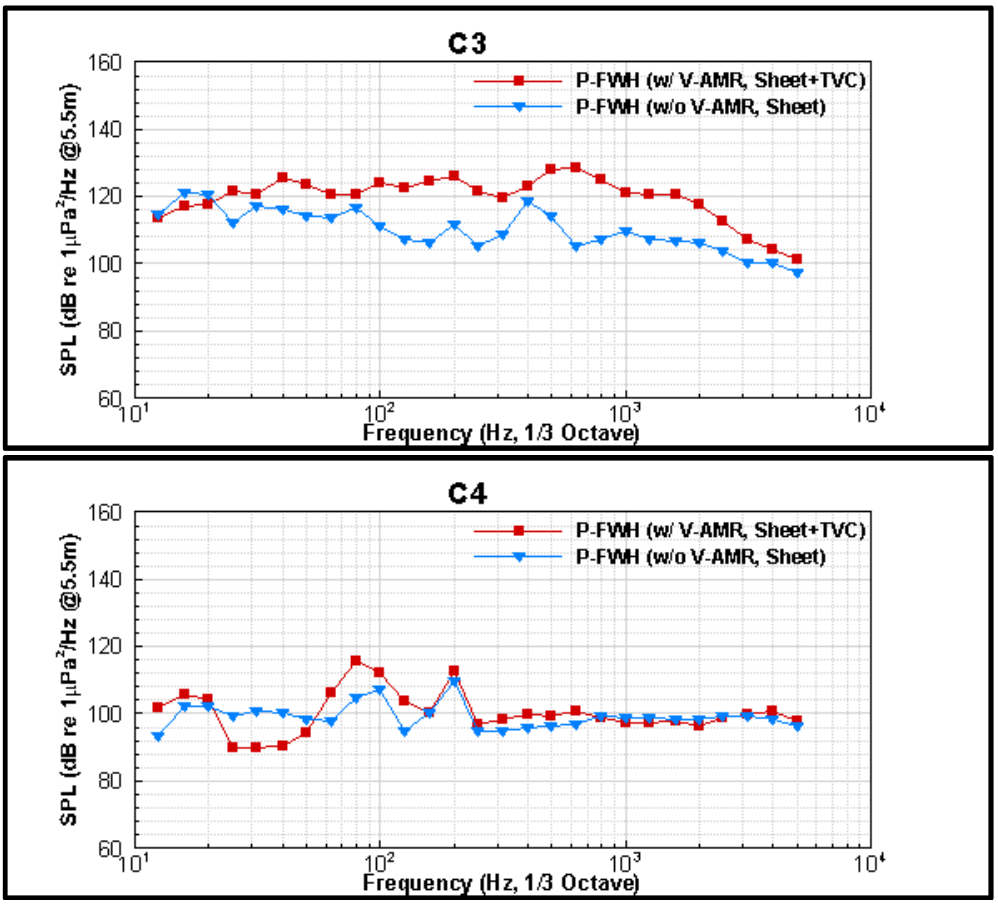

Figure 8.12. Comparison of URN levels between the CFD predictions w/ and w/o the TVC at C3 and C4.

Figure 8.13 shows the comparison of URN predictions with the full-scale measurements at C6. As shown in Figure 8.13, the results are in good agreement with each other up to 1kHz. After 1kHz, the numerical calculations underpredict the URN levels compared to full-scale measurements. This can be associated with the lack of nonlinear noise sources represented by turbulence and vorticity, and the lack of TVC dynamics predicted in the CFD calculations. Similar to model scale URN predictions in the presence of TVC (i.e., C5), the non-uniform flow increases the URN levels by introducing the TVC in the numerical calculations. The

characteristics hump is also somewhat present in the mid-frequency range in the numerical predictions in the presence of TVC, as in the full-scale measurements.

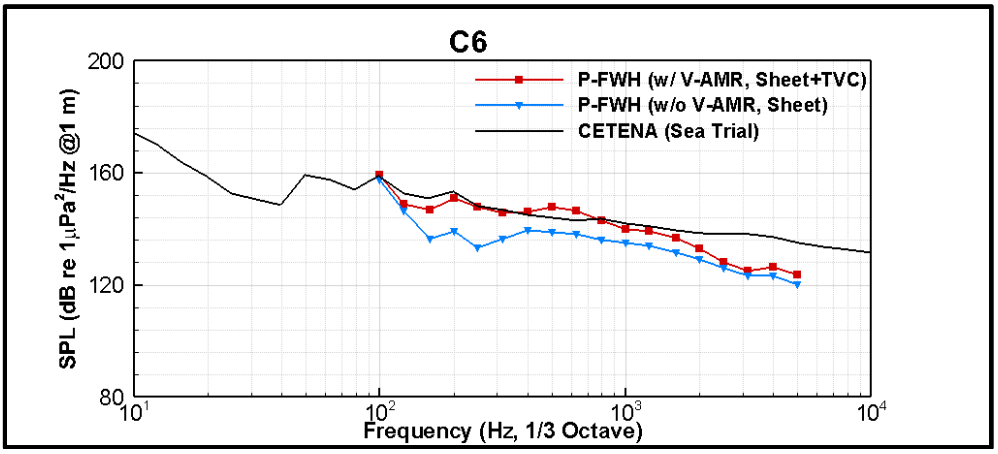

Figure 8.13. Comparison of URN levels between CFD and full-scale measurements data at 1m and CFD predictions w/ and w/o the TVC at C6.

8.5 Chapter summary and concluding remarks

To shed further light on the contribution of the TVC to the propeller hydrodynamic and hydroacoustic performance, this chapter presented a more in-depth investigation of the effect of TVC in the model and full-scale using the DES and permeable FWH acoustic analogy. In the numerical calculations, model and full-scale benchmark propeller, The Princess Royal, operated under uniform, inclined and non-uniform flow conditions. The verification study was conducted for the hydroacoustic part of the solution. The propeller performance characteristics, cavitation extensions, and propeller URN predictions were comprehensively validated with the experimental and sea trial data. The main finding of this chapter can be summarised as follows:

- The hydrodynamic results showed that the thrust and torque coefficients in the model scale under uniform and inclined flow conditions were overpredicted by around 7% in the CFD compared to the experiment as the advance ratio similarity was used in the CFD. Also, as the torque identity was not satisfied completely in the numerical calculations, the difference between the CFD and experiment/sea trial data was found to be around 8% under non-uniform flow conditions.

- The application of the V-AMR technique did not change the vortex structures. Similar vortex structures were observed in the propeller slipstream between the base mesh and the V-AMR technique.

- Similar sheet cavitation extensions were observed between the CFD and experiment. However, the sheet cavitation was slightly more extended towards inner radii in the CFD compared to the experiment under uniform and inclined flow conditions (i.e., C1 and C2).

- Under non-uniform flow conditions in the model scale (i.e., C5), the sheet cavitation extension predicted in the CFD was in good agreement with the sea trial data. However, its extension was overpredicted compared to the experiment. The sheet cavitation was slightly underpredicted in the CFD compared to sea trial data in full-scale (i.e., C6).

- The TVC could be observed in the propeller slipstream at all operating conditions in model and full-scale. As expected, the TVC could not be observed without the V-AMR technique in the numerical calculations.

- The time based acoustic pressures showed that the stable TVC dynamics, as observed at C1 and C4, did not create a considerable change in the waveform and amplitude of the signal compared to the configuration where only the sheet cavitation was modelled. However, when the propeller was operating in inclined and non-uniform flow conditions, the TVC created larger spikes in the acoustic pressures, which can be associated with strong cavity dynamics, cavitation events and possible bursting phenomena, compared to the configuration where the only sheet cavitation was modelled.

- The comparison of the propeller URN predictions showed that the noise results were underpredicted in the CFD compared to the experimental results under uniform and inclined flow conditions, particularly up to 1kHz. However, due to the larger sheet cavitation observed in the CFD compared to the experiment, the propeller URN levels were overpredicted in the CFD compared to measured data under non-uniform flow conditions (i.e., C5) in the model scale. The full-scale URN comparison showed that there was a good agreement between the CFD and full-scale measurements.

- The comparisons obtained with the configurations with and without the TVC in the noise spectrums showed that the stable TVC did not create significant vortex pulsation, and hence the propeller URN levels did not show a considerable change with the contribution of TVC in the numerical calculations. Yet, the propeller URN levels increased considerably when the cavitation volume variations and pulsation were

stipulated with the unstable TVC, as in C2, C3, C5 and C6. The maximum increase with the contribution of TVC was observed at C5 and C6, where the non-uniform wake field was present.

- The unstable TVC and its dynamics manifested themselves as a spectral hump in the noise spectrum at the medium frequency range, particularly at C3, C5 and C6.

9 Investigation of biofouling roughness on propeller hydrodynamic and hydroacoustic performance

9.1 Introduction

As stated in Chapter 2, the current knowledge on the effect of roughness, particularly that of biofouling, on the propeller performance and especially on the cavitation and URN is scarce and almost non-existent for propeller URN. Therefore, this chapter aims to model the effect of the roughness and combine it with the earlier developed CFD procedure to predict and explore the effects of biofouling roughness on the propeller hydrodynamic performance, including cavitation and propeller URN in the model and full-scale to make a novel contribution to the state-of-the-art.

Therefore, each sub-section of the chapter first presents theoretical background within the above framework. This is followed by the details of numerical modelling (i.e., propeller geometry, test matrix, computational domain, boundary conditions, grid structure and solution strategy). After the numerical modelling, the numerical results are presented in detail.

More specifically, Section 9.2 presents the effects of homogenously distributed roughness on the blades for the benchmark INSEAN E779A model scale propeller, with a particular emphasis on propeller hydrodynamic performance, cavitation and propeller URN. The investigations are further extended for the benchmark, The Princess Royal, propeller in the model and full-scale by applying heterogeneously distributed roughness on the blades to explore the effective roughness application area in Section 9.3. Similar to the roughness application on the propeller blades, Section 9.4 presents the effects of roughness applied on the hub, emphasising the hub vortex and hub vortex cavitation. Finally, Section 9.5 includes a summary of the chapter and concluding remarks on the investigations conducted in the chapter.

9.1.1 Theoretical background

9.1.1.1 Hydrodynamic model

Similar to Chapter 5, the RANS method together with the Schnerr-Sauer cavitation model was used in this Section. The details of the model can be found In Chapter 5.

9.1.1.2 Hydroacoustic model

As used in Chapters 4, 6, 7 and 8, the permeable formulation of the FWH equation was utilised for the URN predictions. The details of the formulations can be found in Section 4.2.1.

9.1.1.3 Roughness model

The flow around the roughness elements can be solved in two different approaches. In the first approach, the roughness geometries can be modelled physically and included in the computational domain as part of the surface. Although this approach gives a more realistic solution to the flow around the roughness elements, it requires a high number of grids. Hence, it increases the computational cost of the solution. On the other hand, the second approach uses the roughness functions within the CFD software's wall function. Although this approach simplifies the geometry of roughness elements and the flow physics may not be modelled accurately compared to resolving the roughness elements itself, it is the more effective and computationally affordable approach to include the roughness effects in the calculations (Asnaghi et al., 2020b). Thus, the wall function approach was used to model the influence of roughness. As shown in Figure 9.1, the given roughness conditions are assumed to imply that the flow is in the fully rough regime. Therefore, the velocity distribution in the log-law region can be described by Equation 9.1

$$U^+ = \frac{1}{\kappa} ln(y^+) + B - \Delta U^+ \tag{9.1}$$

where, κ is the von Karman constant, y^+ is the non-dimensional normal distance from the boundary, B is the smooth log law intercept. Roughness causes a downward shift in the velocity profile, which is commonly known as "Velocity Loss Function" or "Roughness Function" and is denoted by ΔU^+, (e.g. Schultz and Swain, 2000). The roughness function can be written as a function of the roughness Reynolds number as given in Equation 9.2.

$$k^+ = \frac{kU_\tau}{\nu} \tag{9.2}$$

where U_τ is the friction velocity, k is the roughness height, and ν is the kinematic viscosity. It is important to note that the roughness function vanishes for the smooth case ($\Delta U^+ = 0$), whereas it is determined experimentally for the rough cases.

The flow over the rough wall can be divided into three flow regimes: hydraulically smooth, transitionally rough and fully rough, depending on the roughness Reynolds number. When the roughness elements are small and embedded in the viscous sublayer, the flow regime is assumed as hydraulically smooth. In this flow regime, the frictional drag is not affected by the roughness elements and the roughness function (i.e., ΔU^+) becomes zero. If the roughness elements partially penetrate beyond the viscous sublayer, the flow regime is called a transitional regime. When most of the roughness elements penetrate the linear sublayer, the flow regime becomes fully rough. Thus, the skin friction becomes independent of the Reynolds number, and viscous effects start to be no longer important (Flack and Schultz, 2010; Schultz and Swain, 2000).

The roughness functions related to varying rough surfaces are given in the literature to reflect its effects on the hydrodynamic performance of the ship hull and propeller. The widely used roughness functions can be classified into inflectional-behaviour functions with three flow regimes and single expression functions. The single expression functions are generally called Colebrook/Grigson-type, initially proposed by Colebrook, 1939 and adopted by Grigson, 1992 (Andersson et al., 2020). The Colebrook/Grigson-type roughness functions are based on a single definition to identify the roughness function given below.

$$\Delta U^+ = \frac{1}{\kappa} ln(1 + k) \tag{9.3}$$

The roughness functions used in this PhD thesis were obtained by Uzun et al., 2020 to represent "barnacle" type biofouling roughness. In these authors' study, the flat plates covered with 3D printed artificial barnacle tiles in different sizes, coverages, and settlement patterns were towed in a towing tank. Then, the roughness functions were derived based on the overall method proposed by Granville, 1978. The obtained barnacle type roughness functions (or biofouling roughness functions) showed good agreement with the Colebrook type roughness functions of Grigson, 1992, as shown in Figure 9.1.

Table 9.1 shows the representative roughness length scales and corresponding configurations with different barnacle sizes and coverage densities. In the CFD model, roughness functions provided in Uzun et al., 2020, were implemented within the CFD solver's wall function. Detailed information about the roughness functions can be found in the study by Uzun et al., 2020. In Table 9.1, Mix and NS Mix are surface names obtained from the study by Uzun et al., 2020; h is barnacle height (mm), k_G is the representative hydrodynamic roughness length scale (μm) that give the same roughness Reynolds numbers with corresponding roughness function values of Grigson, 1992. It should be noted that these representative hydrodynamic roughness length scales, k_G, are not a function of measurable surface properties and may be termed as experimentally obtained equivalent roughness height.

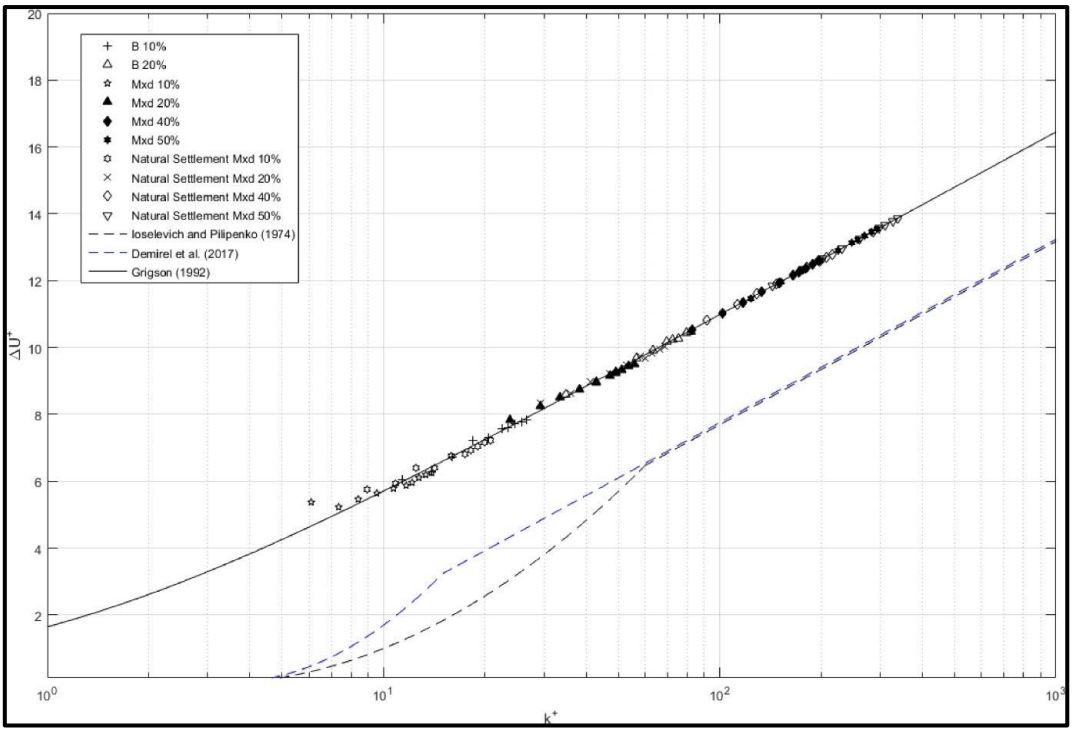

Figure 9.1. Roughness functions for various test surfaces, adapted from Uzun et al., 2020.

Table 9.1. Representative roughness length scales of test surfaces (Uzun et al., 2020).

Test Surfaces	Surface Coverage (%)	Barnacle Height h (mm)	Representative roughness length scale k_G (μm)
Mix	10	5, 2.5, 1.25	94
NS Mix	10	5, 2.5, 1.25	136
Mix	20	5, 2.5, 1.25	337
NS Mix	20	5, 2.5, 1.25	408

9.1.2 Numerical modelling

9.1.2.1 Propeller geometry and test matrix

The benchmark INSEAN E779A propeller geometry was selected to investigate the influence of roughness on the propeller hydrodynamic characteristics, cavitation, and hydroacoustic performance. The main particulars and general view of the four-bladed CNR-INSEAN benchmark propeller can be found in Chapter 4.

Table 9.2 tabulates the selected test cases. Under non-cavitating conditions, the propeller rotational rate (n) was kept constant at around 12rps in correspondence to the experiment and inflow velocity (V_A) was set according to the advance ratio (J). Under cavitating conditions, the propeller rotational rate was set to 36rps as in the experimental conditions, and vapour pressure was kept constant (P_V) as 2337Pa. The hydroacoustic performance of the propeller was predicted under cavitating conditions. The four different roughness configurations (M10, M20, NSM10 and NSM20) were implemented for each case under non-cavitating and cavitating conditions, as given in Table 9.2.

Table 9.2. Description of the test matrix.

	Non-cavitating cases	Cavitation and URN cases	
Condition	J	J	σ
Smooth Rough	0.397; 0.498; 0.596; 0.795	0.71	1.763

9.1.2.2 Computational domain and boundary conditions

The same computational domain and boundary conditions, as described in Chapter 4, are also used in this chapter. The details of the computational domain dimensions can be found in Section 4.2.2.

9.1.2.3 Grid structure

The grid structure was adopted within the facilities of the commercial solver, Star CCM+ (Star CCM+ 14.06, 2019), to solve the flow around the propeller. As described in Chapters 4 and 5, the same grid procedure and the V-AMR technique were followed for the flow field's accurate solution. The details of the grid structure can be found in Chapters 4 and 5. Figure 9.2 shows the grid structure around the propeller. As shown in Figure 9.2, the V-AMR procedure described in Chapter 5 was adopted for better modelling of TVC in the propeller slipstream.

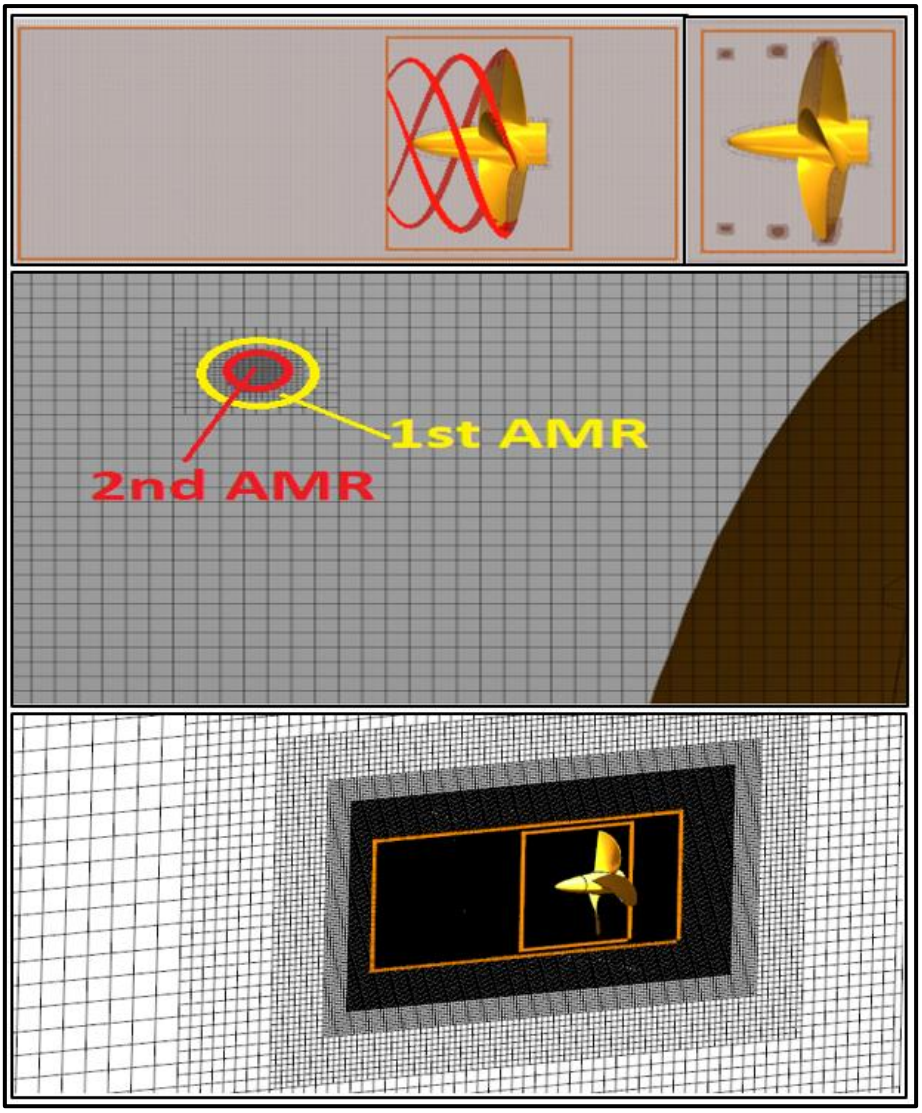

Figure 9.2. Representation of grid resolution in the computational domain.

Table 9.3 indicates the total element counts and grid properties inside the vortex used for cavitation and noise predictions. As the trimmer mesh transition is 1:2, the cell size is divided into two at the 2nd stage of the V-AMR technique.

Table 9.3. Grid properties and total element counts.

	Surface size in the vortex core (mm)	Refinement Factor	Number of Cells (Million)
1st V-AMR	0.00175D	Cell Size/4	16.001.134
2nd V-AMR	0.000875D	Cell Size/8	16.942.008

9.1.2.4 Analysis properties

In the numerical calculations, the RANS method with k-ω SST turbulence model was used for both hydrodynamic and hydroacoustic simulations using all the y^+ wall treatment methodology. The second-order scheme was used for the convection term and temporal discretisation. The segregated flow model was used with a SIMPLE type algorithm between continuity and momentum equations. For propeller rotational motion, MRF and RBM techniques were utilised for propeller hydrodynamic and hydroacoustic simulations, respectively.

In order to include the effects of roughness on the numerical calculations, the selected y^+ value needs to be higher than 30 and higher than k^+ values recommended by Star CCM+ 14.06, 2019. In other words, the distance of the first grid node to the wall must exceed the roughness height; otherwise, the roughness effect cannot be imposed on the numerical calculations. Thus, the y^+ was set according to maximum roughness height into account.

The Schnerr-Sauer cavitation model was employed with the VOF approach to model the phase change in the cavitation simulations. The customisable cavitation parameters such as nuclei diameter and density are available in the facilities of Star CCM+ 14.06, 2019. Based on comprehensive investigations in Chapter 5, the consistency of default values was presented for the model scale propeller. Thus, the default values provided by the commercial solver were selected as 10^{-6} and 10^{12} for nuclei diameter and density, respectively.

9.1.3 Numerical results

9.1.3.1 Uncertainty study

The GCI (Grid Convergence Index) technique, which is suggested for the CFD validation studies in the ITTC procedure (ITTC, 1999), was employed to determine the uncertainty level of the numerical solution and sufficient grid spacing for the simulations, as used in Chapters 4 and 5.

Table 9.4 shows the total element counts and solution scalars for the uncertainty study of non-cavitating hydrodynamic simulations. Here, N_1, N_2 and N_3 refer to element counts of fine, medium and coarse meshes, respectively. Based on the numerical results, the fine mesh was selected for the rest of the analysis under non-cavitating conditions for both smooth and rough conditions.

Table 9.4. Spatial converge study for non-cavitating hydrodynamic simulations at J=0.397.

	K_T	$10K_Q$
N_1	6.725.353	
N_2	2.962.544	
N_3	1.121.426	
φ_1	0.380	0.646
φ_2	0.376	0.645
φ_3	0.369	0.637
r_{f21}	1.314	
r_{f32}	1.382	
ε_{21}	-0.004	-0.001
ε_{32}	-0.007	-0.008
po	1.613	7.518
q	-0.196	-0.196
s	1	1
${e_a}^{21}$	0.010	0.0015
${e_{ext}}^{21}$	0.019	0.0002
${\varphi_{ext}}^{21}$	0.387	0.646
R	0.517	0.125
GCI_{FINE} (%)	2.376	0.028

Table 9.5 shows the parameters of the uncertainty calculations and the total element counts used for the cavitation and hydroacoustic simulations. Here, the uncertainty study was conducted using an initial mesh (i.e., without AMR) to decrease the computational cost as the TVC does not affect the propeller global performance characteristics in the numerical calculations, as shown in Chapter 5. Similarly, a lack of effect of TVC on thrust and torque coefficients was found in the studies of Krasilnikov, 2019 and Gaggero et al., 2014. Consequently, the fine grid structure was selected for the cavitation and hydroacoustic simulations, both in smooth and rough conditions, by implementing the V-AMR technique. Apart from the uncertainty study, the fine grid resolution is also most suitable for propeller URN predictions due to the reduced non-physical numerical noise sources, as explained in Section 4.2.

Table 9.5. Spatial converge study for cavitating and hydroacoustic simulations.

	K_T	$10K_Q$
N_1	12.188.667	
N_2	4.641.416	
N_3	1.842.196	
φ_1	0.2380	0.4340
φ_2	0.2384	0.4353
φ_3	0.2389	0.4616
r_{f21}	1.379	
r_{f32}	1.360	
ε_{21}	0.0004	0.0012
ε_{32}	0.0005	0.0263
po	0.817	9.600
q	0.051	0.051
s	1	1
${e_a}^{21}$	0.0017	0.0028
${e_{ext}}^{21}$	0.0056	0.0001
${\varphi_{ext}}^{21}$	0.237	0.434
R	0.80	0.05
GCI_{FINE} (%)	0.698	0.016

9.1.3.2 Hydrodynamic results

- **Non-cavitating condition**

Smooth case

Figure 9.3 shows the validation of numerical open water test results with the experimental data at several advance coefficients in smooth conditions. As shown in Figure 9.3, there is a good agreement between numerical and experimental results despite the underestimation of K_T and hence η_0 values at higher J. The absolute differences between CFD and experiment are also given in Table 9.6.

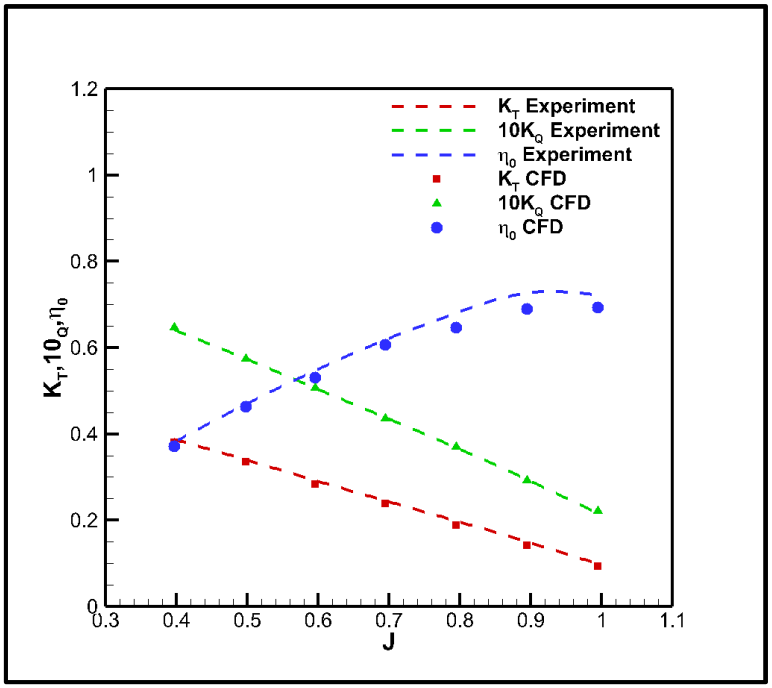

Figure 9.3. Validation of global performance characteristics in smooth condition.

Table 9.6. The absolute differences between CFD and experiment for thrust, torque and efficiency values.

J	K_T (%)	$10K_Q$ (%)	η_0 (%)
0.397	1.809	0.724	2.514
0.498	1.722	0.025	1.697
0.596	1.670	0.073	1.598
0.695	2.388	0.429	1.967
0.795	3.885	0.860	3.051
0.895	5.920	0.913	5.053
0.995	5.980	2.232	3.833

Rough case

Figures 9.4 and 9.5 show the change in the propeller global performance characteristics in the presence of roughness with different representative roughness scales, given in Table 9.1. In these Figures, zero roughness height indicates the smooth condition. As expected, the roughness, depending on its height, will influence the boundary layer and, hence, will significantly impact the hydrodynamic characteristics of propeller blade sections, including the drag and lift. The roughness leads to an increase in the drag coefficient of the blade's sections, while it reduces the lift coefficient due to the reduction in the circulation distribution around the propeller blades. Consequently, it reduces the thrust coefficient of the propeller, as shown in Figure 9.4.

The decrease in the K_T values are predicted between around 5% and 18% at different advance coefficients due to the roughness. It is to be noted that the percentage decrease in the thrust coefficient remains almost similar (i.e., between 5% and 11%) at the first three advance coefficients. In contrast, the maximum decrease is observed at the highest advance ratio due to the relatively smaller K_T value in smooth condition.

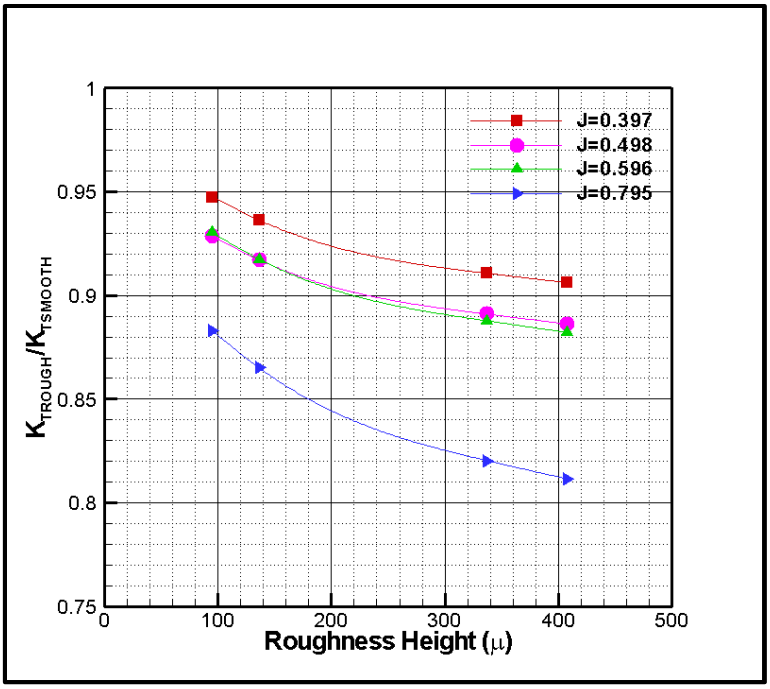

Figure 9.4. Change in K_T values with different roughness conditions.

Figure 9.5 indicates the change in the torque coefficient with different roughness heights. Since the roughness directly contributes to the shear and viscous forces in the linear sublayer, it causes an increase in torque. Additionally, the drag increase in the propeller section increases the torque, reducing the thrust. The increase in the K_Q values are predicted between around 4% and 18% at different advance coefficients with an increase in roughness height. Similarly, the increase in the torque coefficient changes approximately from 4% to 12% at J =0.397, 0.498, and 0.596 with different roughness heights, while the maximum increase is computed at J =0.795 and more severe roughness conditions (i.e., around 18%).

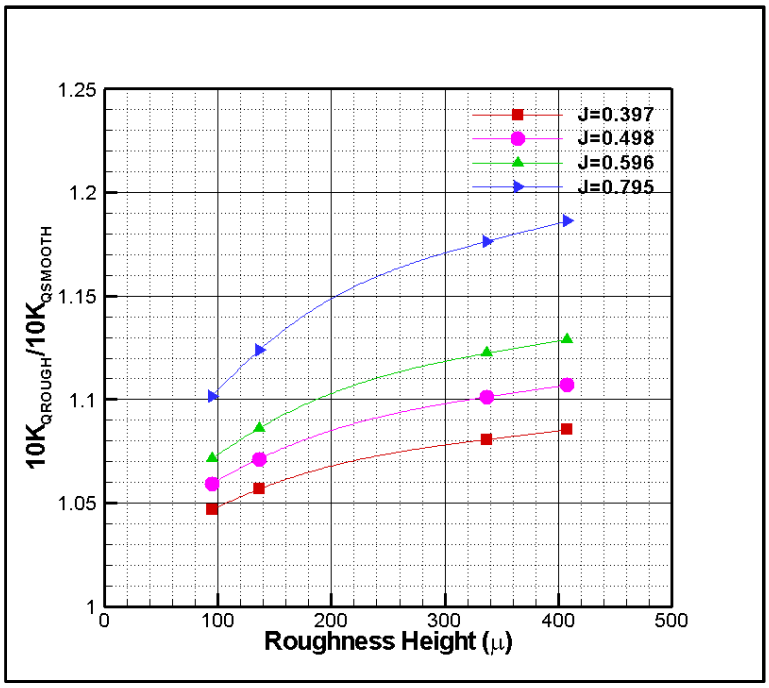

Figure 9.5. Change in $10K_Q$ values with different roughness conditions.

Inevitably, an increase in torque and a decrease in thrust values cause a detrimental impact on propeller efficiency. The loss of propeller efficiency due to roughness can be seen in Figure 9.6 for different advance ratios and rough conditions. Depending on the roughness severity, the roughness increases the efficiency loss due to the increased viscous friction effect. Therefore, it is crucial to keep the propeller blades as smooth as possible from an efficiency point of view (Glover, 1987; ITTC, 2011).

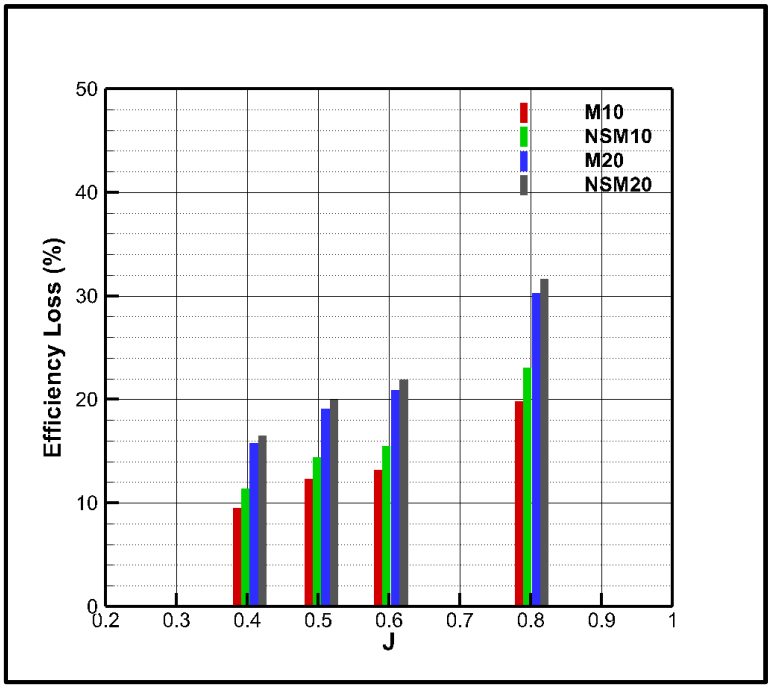

Figure 9.6. Efficiency loss due to roughness at different advance coefficients.

A significant loss can also be expected in propulsive efficiency due to the decrease in propeller efficiency in the presence of roughness. Therefore, ship operators should regularly take the required precautions for polishing their ships' propellers. However, this may not be convenient and cost economical because of the dry-docking times or diver needs (Mosaad, 1986). Instead of cleaning or polishing the propeller, the propeller coating applications can be favourable to minimise or completely prevent efficiency loss since coating can control the fouling growth effectively by providing smooth surface condition as long as it stays on the blade surface (Atlar et al., 2002).

Figure 9.7 shows the non-dimensional pressure contours at different sections of the propeller at J =0.397. The great majority of the thrust is commonly generated between the non-dimensional radius of r/R=0.3 and r/R=0.8 for a typically fixed pitch propeller. Thus, it is appropriate to investigate the impact of the roughness on the pressure distribution of these sections. As the surface roughness accelerates the transition of the laminar boundary layer into the turbulent flow, it results in more frictional losses (Asnaghi et al., 2019). The transition of the boundary layer also changes the pressure distributions at all propeller blade sections, which causes a decrease in thrust. As shown in Figure 9.7, the roughness influences the pressure distributions both at the back (suction) and face (pressure) sides until r/R=0.7 , resulting in a change in the lift and thrust generated by the propeller blades. The effects on the pressure distribution are more prominent towards the trailing edge (TE) of the sections starting somewhere from the 1st quarter of the chord for both the suction and pressure sides. This can

be attributed to the increasing boundary layer thickness activity toward the tail ends depending upon the shape and location of the maximum thickness of the sections. These latter parameters also reflect on the pressure coefficients of the outer blade sections (i.e., r/R=0.7 - 0.8).

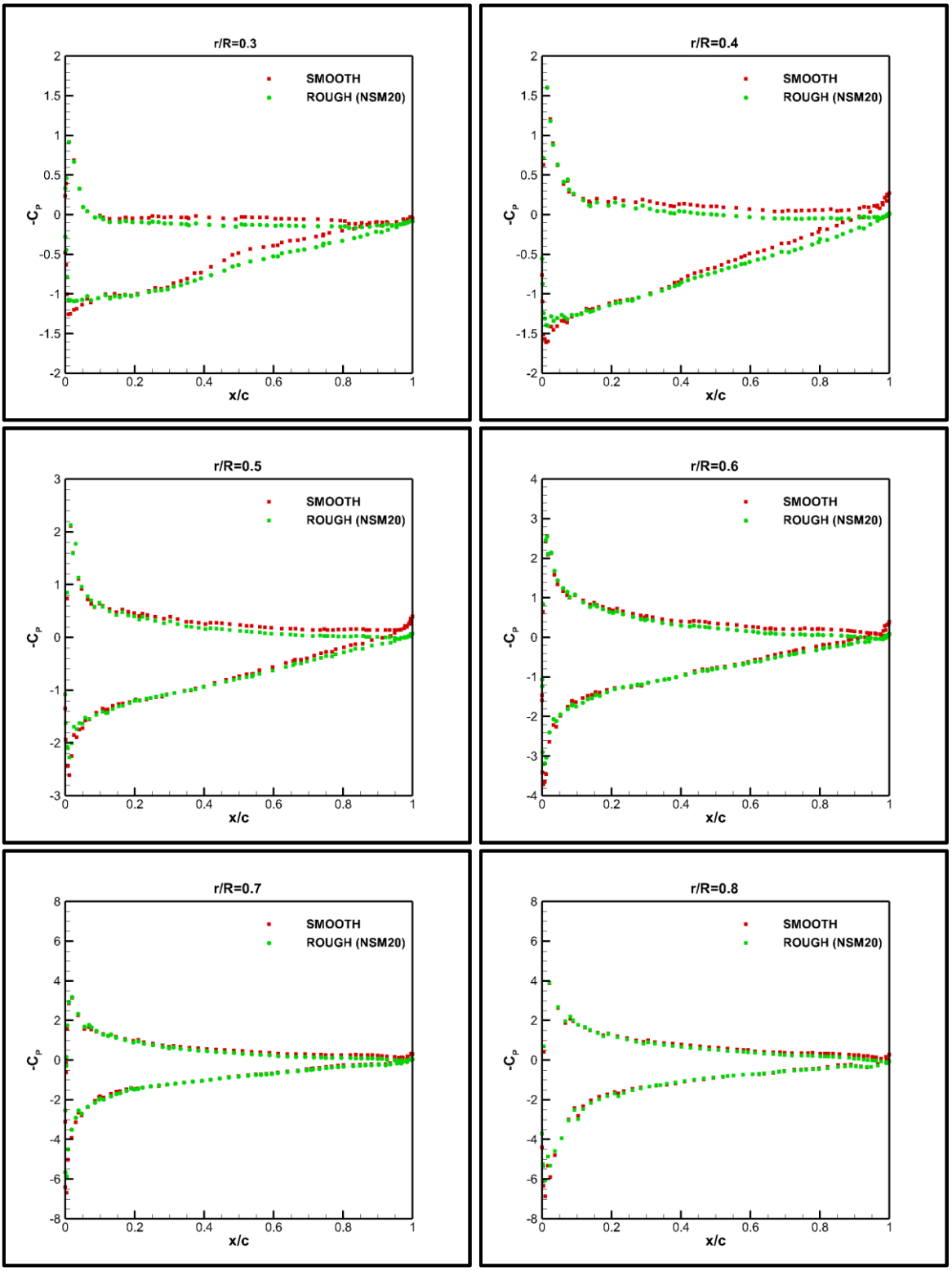

Figure 9.7. Effects of roughness on pressure distributions at different sections at J=0.397.

- **Cavitating condition**

Smooth case

Cavitation formations and their inceptions are critical, and the boundary layer development plays a crucial role in predicting and analysing these characteristics, especially for the TVC. The change of the near-wall grid properties (i.e., boundary layer) influences propeller performance characteristics (i.e., thrust and torque) and the development of cavity bubbles. The prediction of TVC depends on the accurate solution of the flow field inside the vortex core by reducing the numerical diffusion, as shown in Chapter 5.

As explained in Chapter 5, by implementing the V-AMR technique locally with a proper resolution of boundary layer properties, the helical structure of the cavitating tip vortex becomes visible at the propeller blade tips. Then, the roll-up phenomenon, which occurs due to the trailing vortex sheet and the interaction between the sheet and tip vortex cavitation, can be predicted. During this process, it should be noted that the initial tip vortex evolution and roll-up phenomenon are very sensitive to the boundary layer resolution, especially for the RANS based methods (Hsiao and Chahine, 2008; Kim and Rhee, 2004; Qiu et al., 2013; Gaggero et al., 2014).

Bearing in mind the above background information, for the cavitating propeller in smooth condition, the first grid point was shifted to the viscous sublayer (i.e., around y^+=1) by increasing the number of prism layers for better modelling the boundary layer (i.e., resolving the boundary layer without wall function). The remaining properties of the grid were kept constant, including the V-AMR procedure. In this way, the cavitation extensions are compared with the experimental observation, as shown in Figure 9.8. The comparison indicates that the sheet cavitation is slightly over predicted, while the prediction of the hub vortex cavitation is quite good, including the prediction of the roll-up phenomenon as observed in the experiments. As shown in Figure 9.8, the accurate prediction of the roll-up phenomenon enables the extension of TVC further downstream.

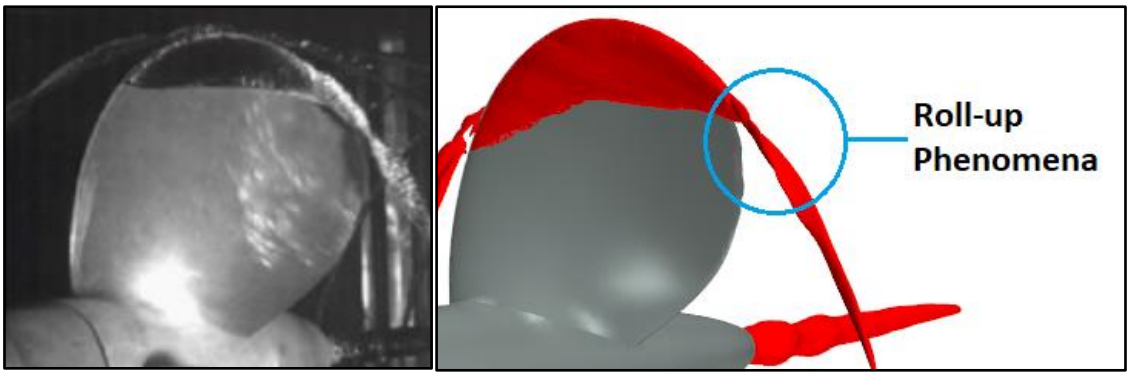

Figure 9.8. Comparison of cavity shape with the experimental observation (α =0.1, J=0.71, σ=1.76).

Rough case

The strength and fluid properties of the vortex core (such as velocity and pressure) are determined by the close interaction of boundary layers on the suction and pressure sides of the propeller in addition to trailing vortices (Asnaghi et al., 2019). As stated above, the evolution of tip vortex formation strongly depends on the boundary layer development on the propeller blades. Thus, the flow around the smooth propeller was resolved again using the determined near wall-properties (i.e., $y^+ > k^+$) to make a fair comparison between smooth and rough cases. For this reason, the number of prism layers was decreased, and the average y^+ value was tuned from y^+=1 to around y^+=280 to satisfy the criteria of the wall function model (i.e., $y^+ > k^+$) in the smooth condition by taking the maximum roughness height into account. The reason behind this was to show the effects of roughness on the cavitation phenomenon, especially for TVC, since the boundary layer modelling is considerably important for the initial formation of TVC and its extension, as shown in Chapter 5. It is to be noted that the y^+=280 was used in the smooth condition for uncertainty study for cavitation and noise simulations. Hereafter, the simulations were conducted using the near-wall properties (i.e., y^+=280) for cavitation and hydroacoustic part unless otherwise stated.

Table 9.7 shows the validation of propeller hydrodynamic performance characteristics with the experimental data under cavitating conditions when the propeller blades are smooth. The influence of roughness on the propeller hydrodynamic performance is also given in Table 9.7. As shown in Table 9.7, the difference between the CFD and experimental is found to be around 5% for thrust and torque coefficients.

As far as the effect of the roughness is concerned, similar to the non-cavitating case, the roughness has a degradation impact on the propeller performance; as such, the thrust coefficient reduces, whereas the torque coefficient increases with an increase in roughness height.

Table 9.7. Validation and influence of roughness on the propeller performance characteristics (J=0.71, σ=1.763).

Roughness Type	K_T	$10K_Q$	η_0
Experiment (Smooth)	0.255	0.460	0.626
SMOOTH ($y^+ \cong 1$)	0.242	0.438	0.624
SMOOTH (y^+=280)	0.238	0.434	0.619
M10	0.214	0.467	0.517
NSM10	0.210	0.474	0.502
M20	0.202	0.491	0.464
NSM20	0.201	0.497	0.458

Figure 9.9 shows the cavitation patterns, both in smooth and rough conditions. As stated in the previous section, the change of cavitation extension in the smooth case is because of the change in near-wall properties. The cavitating volume decreases since the tip vortex, and sheet cavitation becomes thinner for the rough propellers than the smooth propeller. As the roughness stimulates the transition of the boundary layer from laminar to turbulent and changes the near-wall flow structures, it leads to the deterioration of the tip vortex strength. The turbulence triggered by the roughness can destabilise the tip vortex formation and causes its breakdown, which consequently results in a decrease in TVC compared to the smooth condition .A similar destabilisation process was also observed using the tubercles on the leading edge of a foil in the experiment (Shi, 2017). The roughness on the propeller blades also causes a slight decrease in the sheet and hub vortex cavitation. As shown in Figure 9.9, the cavitation volume reduces mainly due to the TVC with the increase in roughness length scales.

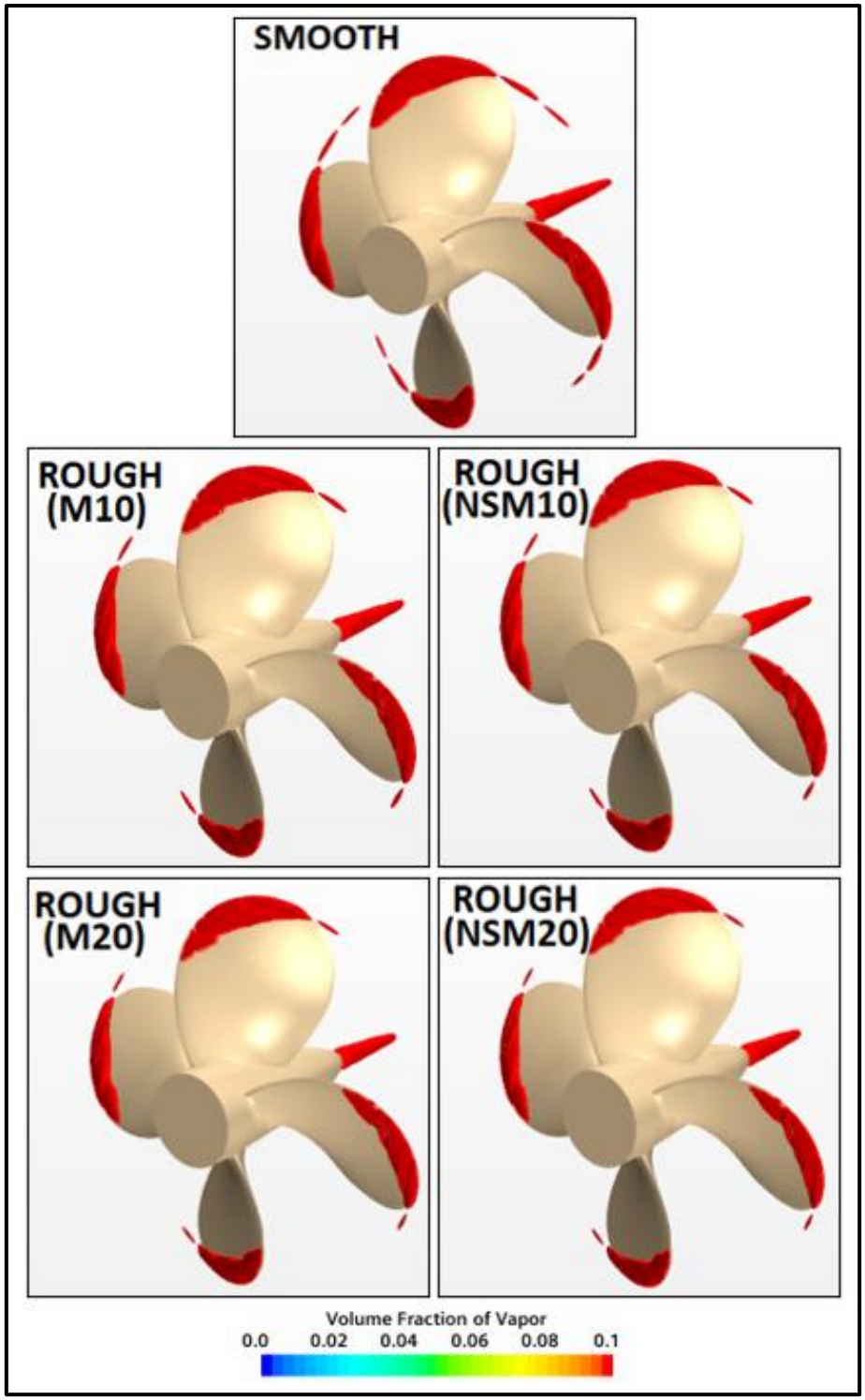

Figure 9.9. The change in sheet, hub, and tip vortex cavitation with different roughness conditions at J=0.71 and σ=1.763.

Figure 9.10 shows the change in vorticity and velocity distribution in the propeller slipstream in smooth and rough conditions. The roughness has a considerable influence on the vortex strength and velocity field. Due to the additional viscous stresses between the roughened tip surface and tip vortex, the circumferential momentum of the vortex structure is converted to turbulence kinetic energy. Hence, turbulence kinetic energy and dissipation rate increase considerably due to the roughness (Krüger et al., 2016). Consequently, the significant amount of vorticity in the propeller's slipstream disappears with an increase in roughness height. Due to the considerable momentum loss stemming from the roughness, the pressure inside the vortex core increases.

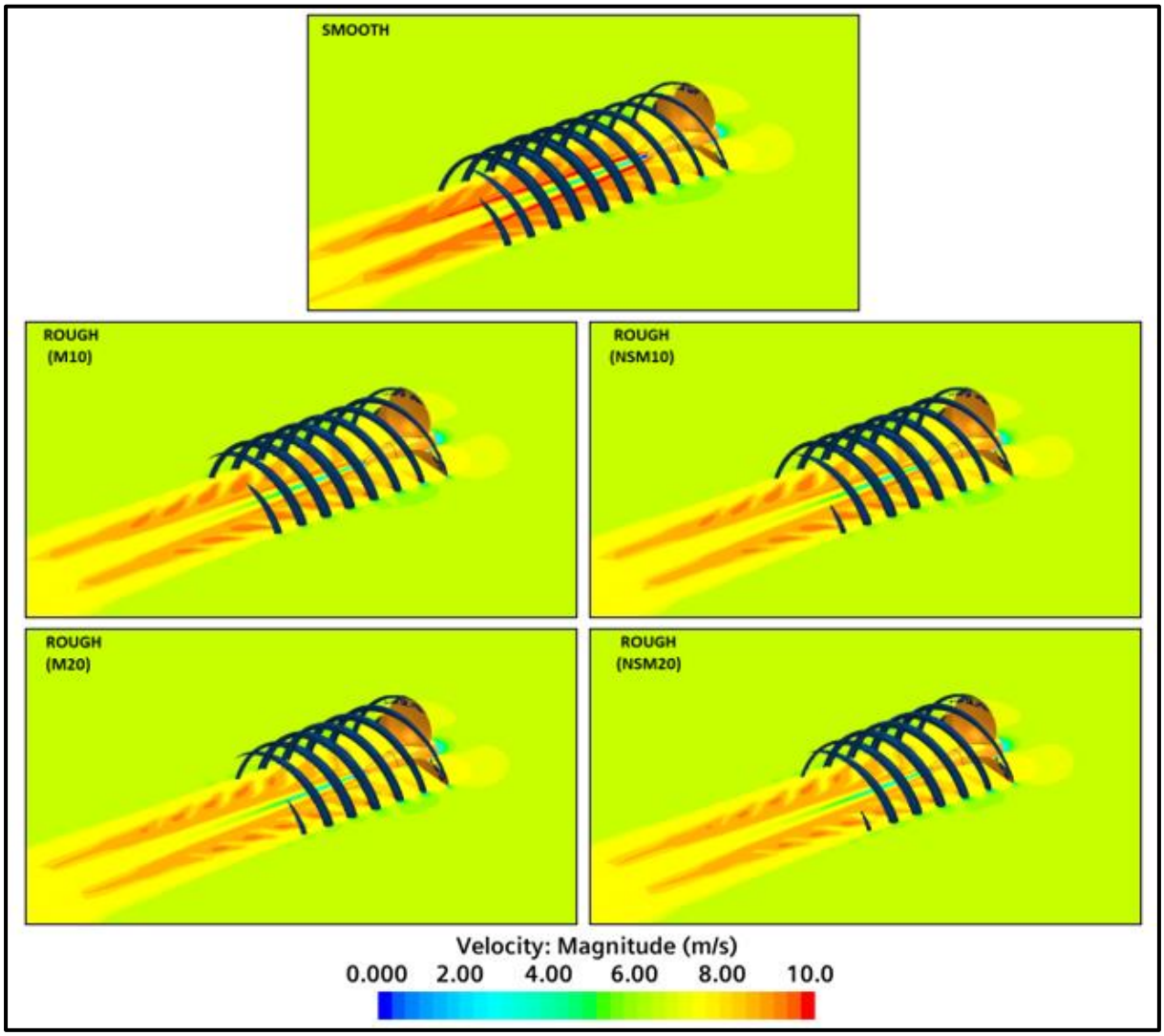

Figure 9.10. The change in vorticity and velocity fields with different roughness conditions at J=0.71 and σ=1.763 ($Q_c = 4000\ 1/s^2$).

9.1.3.3 Hydroacoustic results

- **Cavitating condition**

Smooth case

Figure 9.11 shows the integral noise surface around the benchmark propeller, extending approximately 3D downstream, similar to Chapter 4.

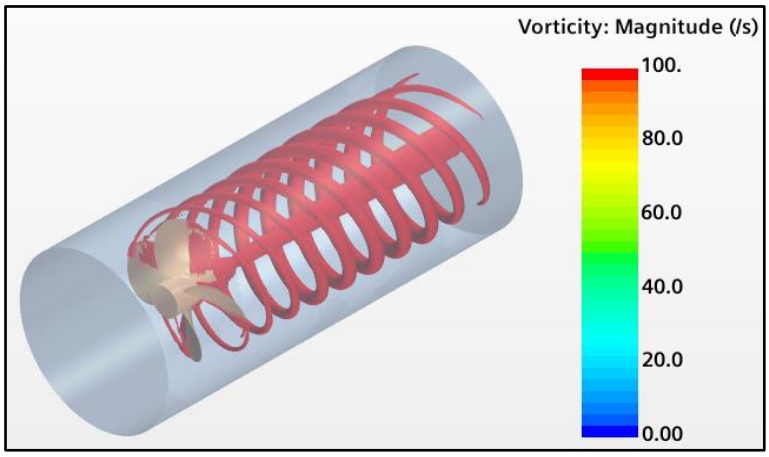

Figure 9.11. The representation of integral surface for URN predictions ($Q_c = 4000\ 1/\mathrm{s}^2$).

As there is no available experimental noise data for the selected benchmark propeller, the verification study should be conducted by comparing the hydrodynamic and hydroacoustic pressures in the near field, similar to Chapters 4,6,7 and 8. Thus, the reliability of the numerical solution gives confidence for the accurate evaluation of the URN in the far-field. Figure 9.12 and Table 9.8 are shown the representation and location of the receivers in the near field, respectively. Receiver 2 (R2) is located at the propeller plane, whereas Receiver 1 (R1) and Receiver 3 (R3) are located upstream and downstream of the propeller, respectively.

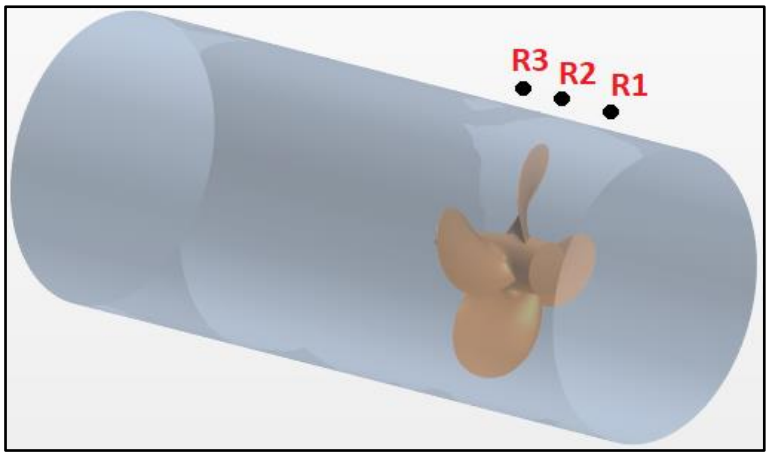

Figure 9.12. Representation of near-field receivers (Figure is not scaled).

Table 9.8. Location of the near- field receivers.

Receiver	X (m)	Y (m)	Z (m)
1	0.06	0	0.1704
2	0	0	0.1704
3	-0.04	0	0.1704

The verification of the near-field pressures is shown in Figure 9.13. Since the receivers are located in the vicinity of the propeller, the overall shape of the signal is smooth and purely characterised by the BPF (i.e. four peaks associated with the four blades). Besides, the contribution of the monopole and dipole (linear) noise terms of the FW-H equation is higher than the quadrupole (i.e. non-linear) noise term for the near-field receivers. The agreement between the hydrodynamic and hydroacoustic pressures is quite good at three different locations. As expected at R2, located at the propeller plane, the pressure fluctuations are higher than the remaining receiver locations since the linear noise terms are more dominant than the non-linear noise terms.

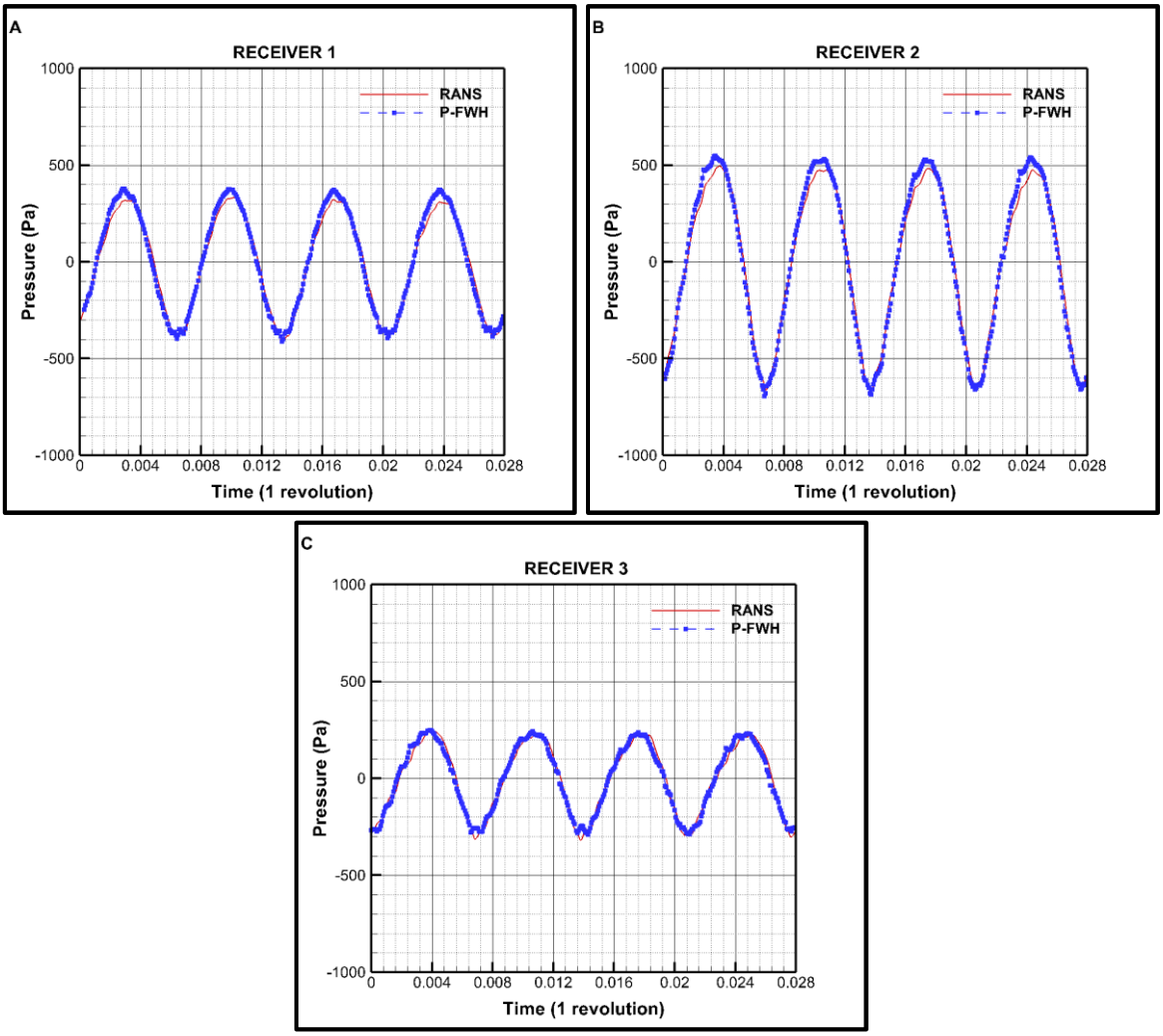

Figure 9.13. Verification of hydrodynamic and hydroacoustic pressures in the near field.

Rough case

As shown in the hydrodynamic results section, the cavitation extensions in the presence of roughness displayed a significant change in the cavitation volume. The maximum change was observed with the maximum roughness length scale (i.e., NSM20). Therefore, URN predictions were conducted using the NSM20 roughness type in the near and far-field.

Figure 9.14 shows the roughness effects on the propeller URN performance in the near field using the receivers, as given in Table 9.8, under cavitating conditions. Comparing the predicted acoustic pressure levels in the near field shows that the roughness does not lead to considerable change in pressure amplitudes in the near field and low-frequency region of the noise spectrum.

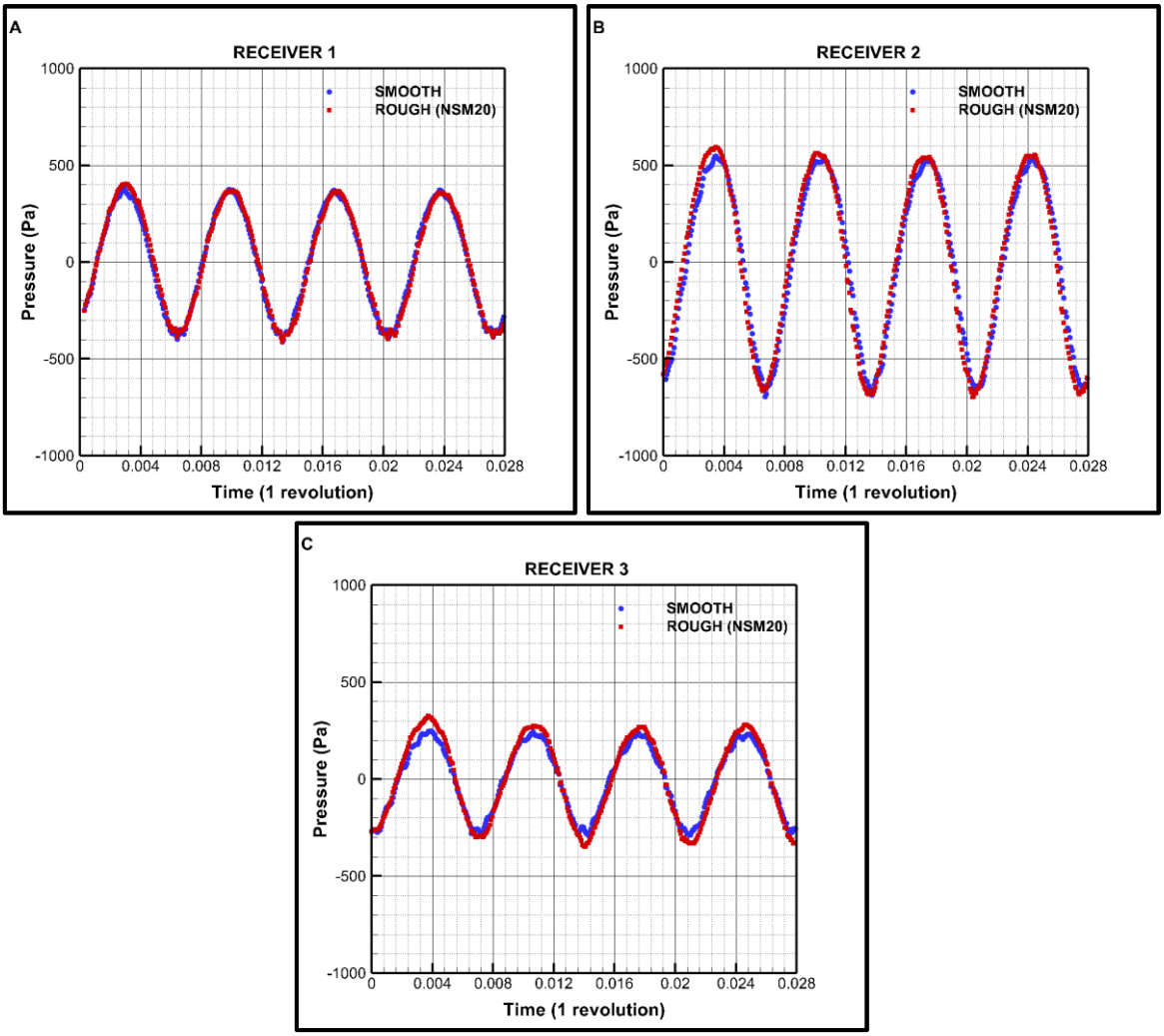

Figure 9.14. Comparison of acoustic pressures both in smooth and rough conditions in the near field.

The noise sources' contribution in the near and far-field can be different. The effects of the non-linear noise terms become dominant when the receivers are located in the far-field. Thus, the changes in the boundary layer properties and the cavitation dynamics caused by the roughness can be analysed more effectively in the far-field using the noise spectrum. Three receivers were located at a distance of 1m (i.e., around 4.4D), 5.675m (i.e., approximately 25D) and 22.7m (i.e., around 100D) away from the intersection point of the propeller plane with the shaft centre. In this way, the effects of roughness on the propeller URN levels were investigated in the far-field.

Figure 9.15 shows the change in noise levels in the presence of roughness at three different receiver locations. By concentrating on the broadband frequency range of the spectrum up to 6.5kHz, Figure 9.15 indicates that the roughness decreases the URN levels between the 1kHz and 2kHz regardless of the receiver locations (see zoomed zones in Figure 9.15). The URN levels decrease up to approximately 10dB at certain frequencies in this frequency range. Above

2kHz, the roughness effect disappears, and similar URN levels are observed between the smooth and rough propellers. This can be associated with increased turbulence activity, even though the cavitation volume reduces.

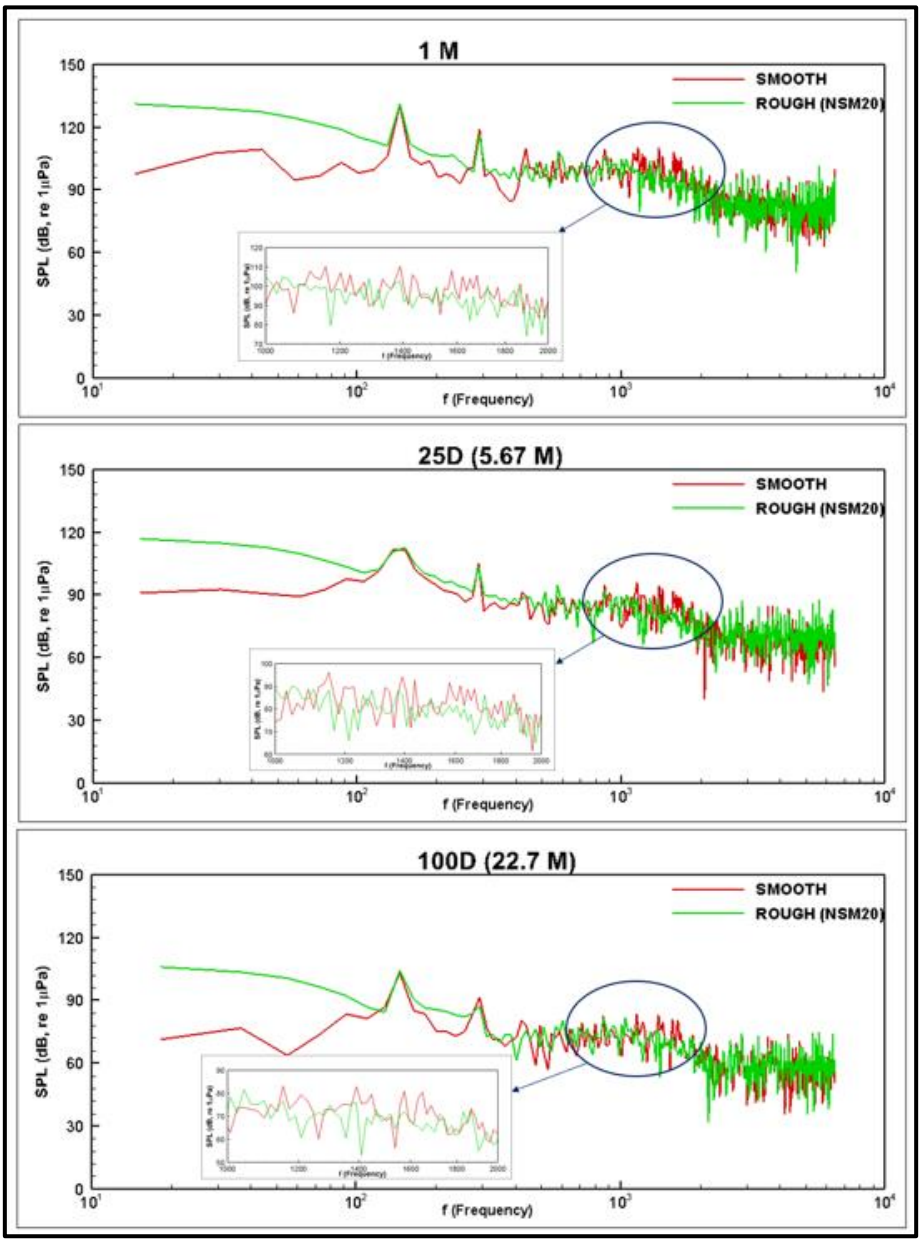

Figure 9.15. The influence of roughness on propeller URN in the far-field.

The change in URN levels at the BPF values is shown in Figure 9.16 for the smooth and rough propeller blades at three different receiver locations. The noise levels at the BPFs include contributions from the non-cavitating and the cavitating sources. The former is related to the fluctuating blade loading and thickness related noise contributions, while the latter is associated with the additional sheet cavitation volume variations, acting as a monopole source. As shown in Figure 9.16, the noise level at the 1st BPF is not significantly affected by the roughness. However, the noise levels at the 2nd and 3rd BPFs reduce with the roughness between 1-7 dB.

This can be associated with the change in TVC volume in the presence of roughness. However, this trend reverses at the 4th BPF value with slightly increased noise levels in the rough condition. The reason behind this is that the increased turbulence activity may cause an increase in URN levels at high order BPFs.

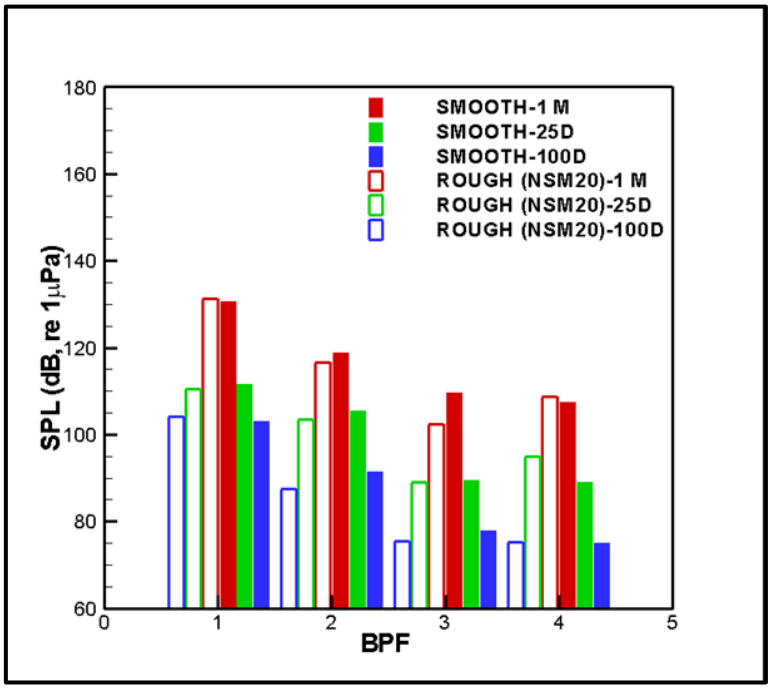

Figure 9.16. The change in BPF values with the roughness application.

9.2 Heterogeneously distributed roughness on propeller blades

9.2.1 Theoretical background

9.2.1.1 Hydrodynamic model

In the numerical calculations, akin to Chapters 6, 7 and 8, the DES approach and the k-ω SST turbulence model were used to solve the flow field around the model and full-scale propellers. Also, the Schnerr Sauer cavitation model was utilised as a mass transfer model for the cavitation modelling in the numerical solver. The details of the mathematical formulations can be found in Section 6.2 and the CFD solver user guide (Star CCM+ 14.06, 2019).

9.2.1.2 Roughness model

In order to include the effects of roughness in the calculations, the wall function of CFD software was utilised, as in Section 9.2. Also, the same biofouling roughness functions were used, as used in Section 9.2. The details of the roughness model and derivation of the roughness functions with the help of experiments can be found in Section 9.2 and Uzun et al., 2020.

9.2.2 Numerical modelling

9.2.2.1 Propeller geometry and test matrix

In the numerical calculations, the Newcastle University's (UNEW) Deep-V type catamaran research vessels' propeller (i.e., The Princess Royal), which is the recently introduced benchmark propeller, was selected (Atlar et al., 2013), as used in Chapters 6,7 and 8. Thus, the main characteristics of the propeller can be found in Section 6.2.2.

Table 9.9 shows the selected uniform, inclined and non-uniform operating conditions for model and full-scale propellers. The operating conditions were determined according to the experiments conducted in the University of Genoa Cavitation Tunnel (UNIGE) in the scope of the round-robin (RR) test campaign for The Princess Royal propeller (Tani et al., 2019b). In Table 9.9, β is the shaft or inclination angle (^{o}), J is advance ratio, n is propeller rotational rate (rps), σ_N is the cavitation number based on the propeller rotational rate, υ is kinematic viscosity (m^2/s).

Table 9.9. Test cases under uniform and inclined flow conditions.

	Loading Condition	Shaft Angle (β, ^{o})	J (-)	n (rps)	Reynolds Number ($Re = \frac{nD^2}{\upsilon}$)	σ_N (-)
MODEL SCALE	C2	0	0.4	35	1.58 x 10^6	1.30
	C6	0	0.5	35	1.58 x 10^6	1.13
	C8	5	0.4	35	1.58 x 10^6	1.30
	C12	5	0.5	35	1.58 x 10^6	1.13
FULL-SCALE	C13	0	0.4	19.025	1.00 x 10^7	1.06
	C14	0	0.5	19.025	1.00 x 10^7	1.06

In addition to uniform and inclined flow conditions, the numerical computations were also performed in the presence of a simulated non-uniform wakefield based on the measured wakefield data in the Ata Nutku Towing tank of Istanbul Technical University (Korkut and Takinaci, 2013). In this way, the realistic flow conditions were modelled for the Princess Royal propeller. The same wakefield was used in this section as used in Chapters 6 and 8. Hence, the wake distribution can be found in Section 6.3. The operating conditions are also given in Table 9.10 for model and full-scale propellers under non-uniform wakefield. In Table 9.10, V_S is the ship speed (knot), K_Q is non-dimensional torque coefficient of the propeller.

Table 9.10. Test cases under the non-uniform wakefield.

	Condition	Engine RPM	n (rps)	V_S(knot)	$10K_Q$	Reynolds Number $(Re = \frac{nD^2}{\upsilon})$	σ_N
Model Scale	C15	2000	35	15.11	0.318	1.58 x 10^6	1.07
Full-Scale (Sea Trial)	C16	2000	19.025	15.11	0.318	1.00 x 10^7	1.07

The four different representative roughness length scales, given in Table 9.1, were applied to the propeller blades with uniform and non-uniform roughness distributions to find the optimum roughness area. Figure 9.17 shows the roughness application areas on the propeller blades in black colour. Also, Table 9.11 summarises the location of roughness patterns. Here, r/R is the section of blades.

Table 9.11. The explanations of roughness application area on the propeller blades.

ID.	The roughness application area
SM	Smooth blade.
FS+BS	Face and backside of the blades
FS	Face side of the blades
BS	Back side of the blades
FS09+BS09	Face and backside of the blades between $0.9 \leq r/R \leq 1$
FS09	Face side of the blades between $0.9 \leq r/R \leq 1$
BS09	Back side of the blades between $0.9 \leq r/R \leq 1$

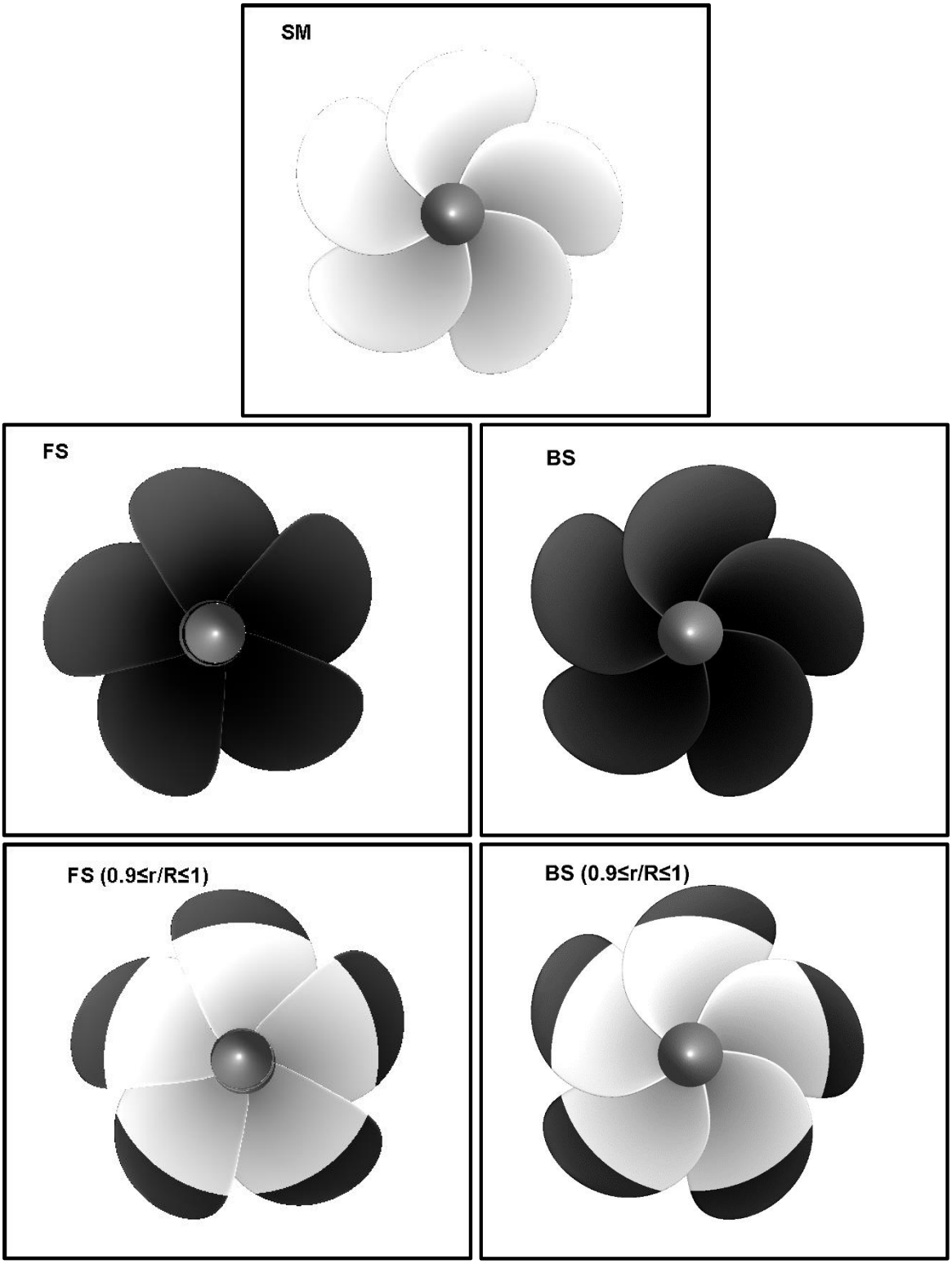

Figure 9.17. Representation of roughness application areas on the propeller blades.

9.2.2.2 Computational domain and boundary conditions

Figure 9.18 shows the computational domain used in the numerical calculations in the model scale. In the numerical calculations, all propeller blades were modelled to reflect the realistic test configuration both in model and full-scale. The computational domain dimensions were set according to the measurement section of the cavitation tunnel dimensions for model-scale propeller, as in Chapter 6, and free field conditions for full-scale propeller, as in Chapter 8.

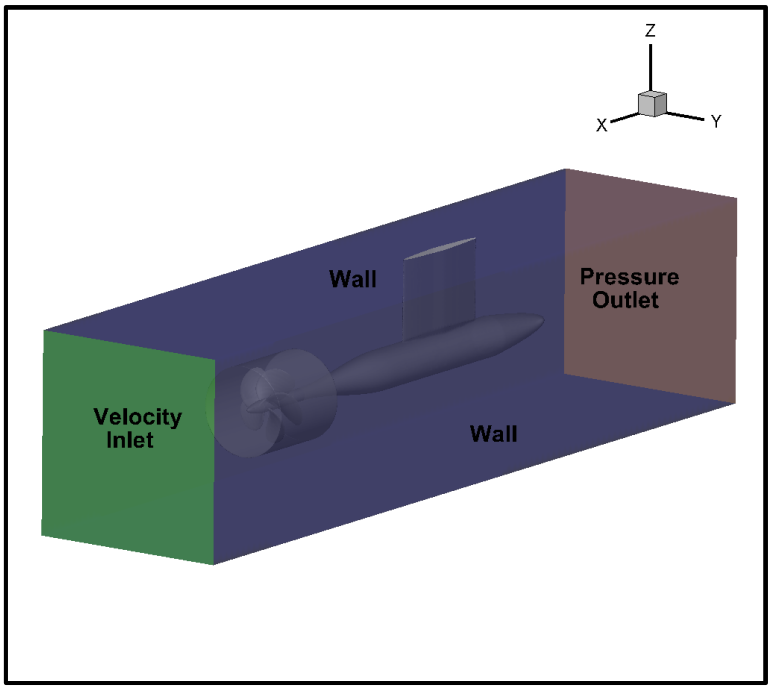

Figure 9.18. Perspective view of the computational domain for the model-scale propeller.

9.2.2.3 Grid structure

The quality of the grid structure is important for an accurate solution with less amount of dissipation. Hence, the grid should be sufficient to solve the complex flow phenomena around the propeller blades under cavitating conditions. As the tip vortex flow solution is more dependent on the grid resolution, the numerical dissipation should be significantly reduced in the propeller slipstream by increasing the grid resolution, particularly around the tip vortex area. Thus, as used in Chapters 6 and 7, the same V-AMR technique, which was described in Chapter 5, was adopted to model the TVC in the propeller slipstream.

The unstructured grid with the trimmer mesh algorithm was utilised to discretise the computational domain using the Star CCM+ 14.06, 2019). The suitable transitions and mesh alignment was adopted between rotating and static region to remove the additional numerical issues. The high cell quality and uniform mesh in all directions were imposed by avoiding highly skewed cells in the computational domain. The full-scale propeller grids were scaled

with additional mesh refinements from the model scale grids. Figure 9.19 indicates the propeller blades' grid structure with the local mesh refinement using the V-AMR procedure. Also, the grid properties are given for both the model and full-scale propeller, as shown in Table 9.12.

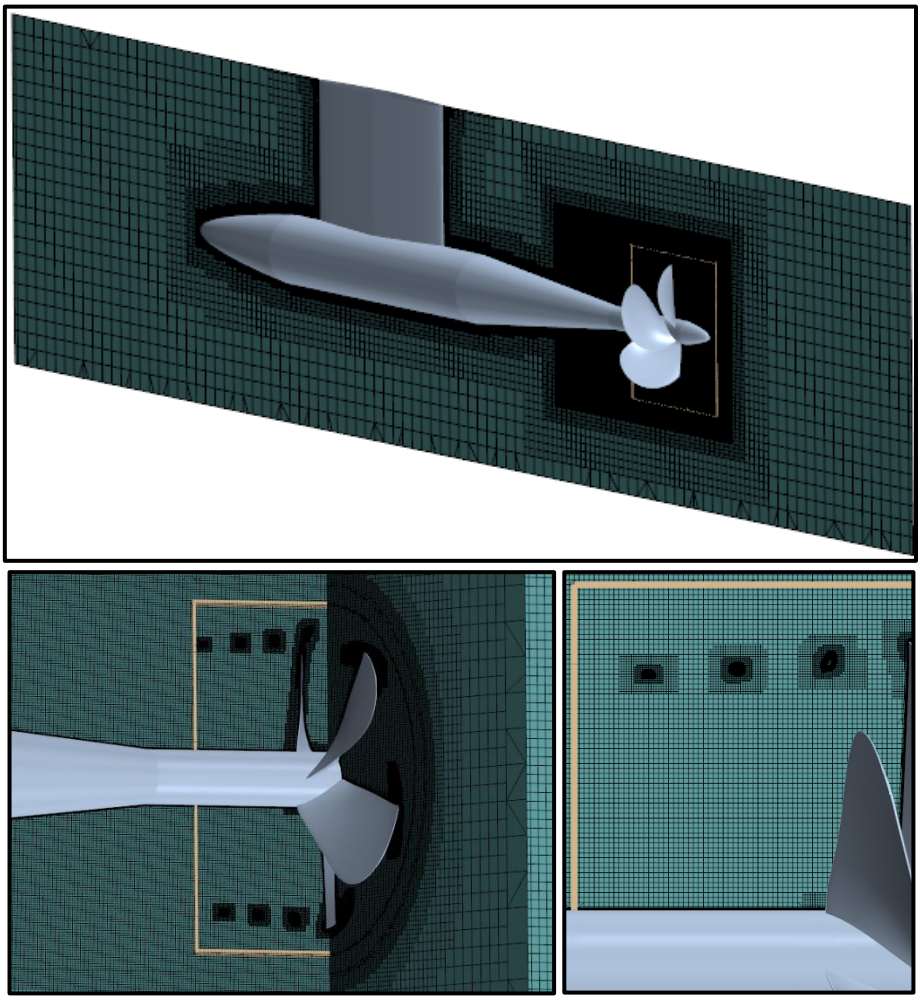

Figure 9.19. Grid structure around the propeller blades.

Table 9.12. Grid properties for both model and full-scale propellers.

	1st V-AMR size (mm)	2nd V-AMR size (mm)	Total Number of Cells (Million)
Model Scale	0.40	0.20	23.5
Full-Scale	1.36	0.68	27

9.2.2.4 Analysis properties

In the numerical calculations, the k-ω SST turbulence model was used with all y^+wall treatment methodology for the DES approach. The DDES variant of the DES approach was used in the numerical calculations, as used in Chapters 6, 7 and 8. The second-order scheme, which is more suitable and advisable for the DES approach, was used to discretise the convection term. Additionally, the second-order implicit unsteady scheme was employed for the time discretisation with the 0.5^o propeller rotational rate for each test case. The SIMPLE algorithm (Semi-Implicit Method for Pressure-Linked Equations) was utilised for the velocity and pressure coupling. In this approach, the discretised momentum pressure correction equations are solved implicitly (Star CCM+ 14.06, 2019). The average y^+ value was calculated between 250 and 290 depending on the operating condition for the model scale propeller. It was also calculated between 380-420 depending on the operating condition of the full-scale propeller. In this way, the roughness effects were imposed on the calculations by satisfying the criteria of the wall function approach (i.e., $k^+ < y^+$).

The sliding mesh or Rigid Body Motion (RBM) technique was used to model the propeller rotational motion. Nevertheless, the Moving Reference Frame (MRF) approach, which is used to solve the problem in a steady-state condition, was also used at the initial stage of the solution with the RANS approach in a steady manner to accelerate the convergence process, as in Chapters 5,6,7 and 8. The simulations were run around 10 propeller rotations by taking the convergence of the solution into account

9.2.3 Numerical results

In this section, the cavitation extensions and propeller hydrodynamic performance characteristics are validated with the experimental and sea trial data in smooth conditions. Following this, the uniformly and non-uniformly distributed roughness are applied on the propeller blades in the model scale, and the most effective roughness area and length scale are determined. The variation of flow properties in the tip vortex, cavitation volume reduction and efficiency loss is explored for model and full-scale propellers in the presence of roughness.

9.2.3.1 Smooth propeller

Figure 9.20 compares cavitation extensions between the numerical computation and experimental observation in the model scale under uniform and inclined flow conditions. Here, α_v is the vapour volume fraction. As shown in Figure 9.20, C2, C6, C8 and C12 show similar cavitation phenomena and dynamics with slight differences in the cavitation extensions. Even though the regular and stable tip vortex cavitation is observed for all conditions, the tip vortex cavitation diameter is stronger in C2 and C8 conditions than in C6 and C12 because of the higher blade loading. The sheet cavitation is extended towards the inner radii with an increase in blade loading. The stable tip vortex cavitation dynamics were observed with the V-AMR technique in the numerical calculations. The numerical results agree with the experimental observations with slight differences in the sheet cavitation extension towards the inner radii.

Table 9.13 shows the comparison of thrust coefficients (K_T) obtained by CFD and experiment. The differences were found at around 7%. The reason being is that the thrust coefficient identity approach, which corresponds to J=0.4 and J=0.5, was used during the measurements at the UNIGE tunnel. In contrast, the CFD calculations were conducted according to the J identity. Also the cavitation extensions and propeller performance characteristics showed good agreement at the same conditions as those of other experimental data obtained by different facilities in the scope of the round-robin (RR) test campaign (e.g., Tani et al., 2020).

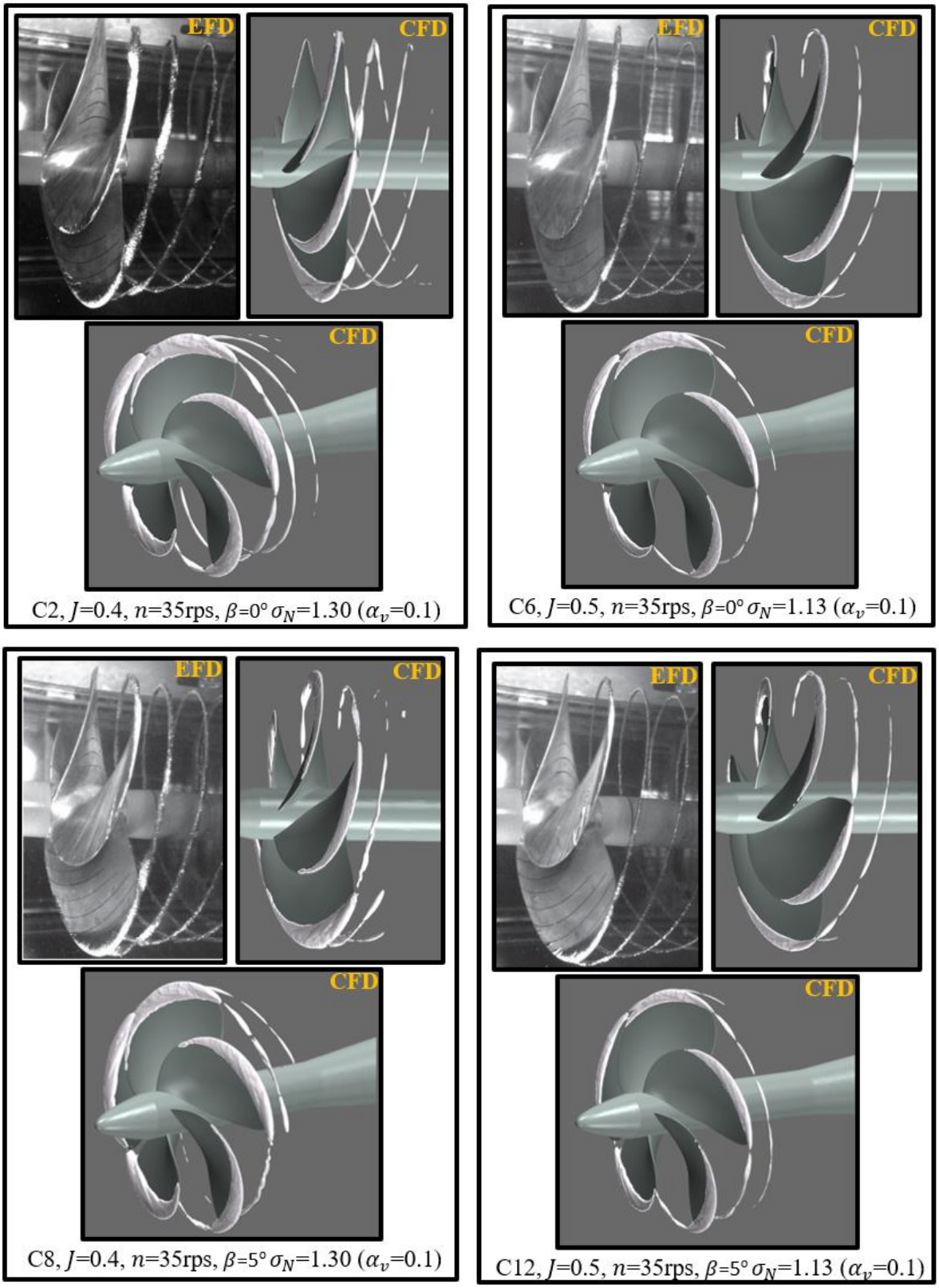

Figure 9.20. Comparison of cavity patterns between CFD and experiment (EFD).

Table 9.13. Comparison of thrust coefficients between CFD and experiment.

Condition	K_T(CFD)	K_T(EFD)
C2	0.263	0.244
C6	0.206	0.191
C8	0.256	0.245
C12	0.207	0.192

The sheet and tip vortex cavitation obtained by CFD, model experiments and sea trial data are also compared for both model and full-scale propeller under the non-uniform flow conditions (i.e., conditions 15 and C16), as shown in Figure 9.21. During the sea trials, a large extent of suction side sheet cavitation (i.e., around 25-30% of the blade area) was observed. The model experiment shows that two tip vortex structures emanate the propeller blade tips. The first tip vortex structure occurs because the sheet cavity breaks up, forming an unstructured and cloudy vortex. In contrast, the second vortex formation starts at the trailing edge's (inner) end with a more distinct vortex core. The close interaction between the two vortex structures is present. These cavity dynamics are also somewhat observed in the numerical calculations using the V-AMR technique for the model and full-scale propeller. Additionally, the complex cavity dynamics associated with the cloudy appearance observed in the sea trial could not be observed in the model and full-scale numerical calculations and the model experiments. It is to be noted that the cavitation extension could not be compared at each blade angle between the CFD, model experiment and sea trial due to the lack of experimental and sea trial observation.

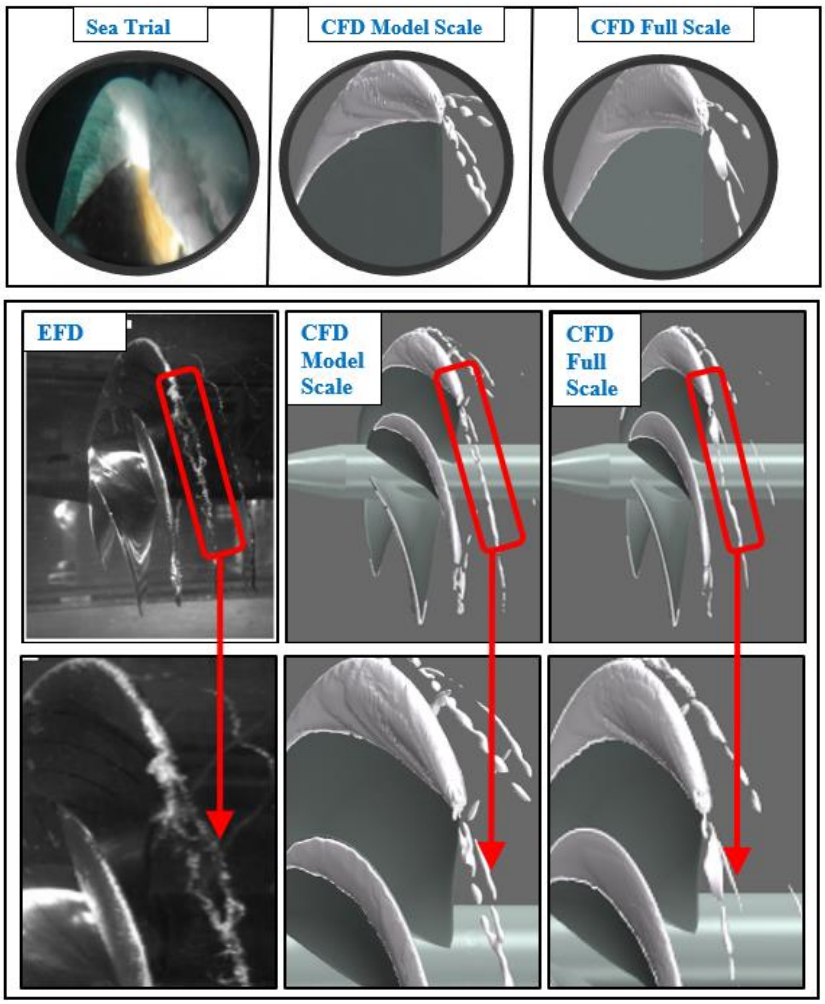

Figure 9.21. Comparison of cavity patterns between CFD, model experiment (EFD) and sea-trial data at C15 and C16 (α_v=0.1). (The sea trial and experimental cavitation observations were taken from Sampson et al., 2015, Tani et al., 2019a, respectively).

Table 9.14 compares the torque coefficients between the CFD, model experiment and sea trial data. The propeller operational condition was defined according to the torque coefficient and cavitation number identity to represent the sea trial condition in the model experiment. As shown in Table 9.14, the difference between the CFD and sea trial data is found to be around 13% for torque coefficient. The discrepancy between CFD and sea trial data might be due to the dissimilarities of the wake distribution used in the numerical calculation. Also, the boundary layer solution imposed by the roughness can cause this difference as the prediction of torque coefficient is strongly dependent on the boundary layer solution.

Table 9.14. Comparison of torque coefficients between CFD, experiment (EFD) and sea trial data.

Condition	Parameter	CFD	Sea Trial	EFD
C15 (Model Scale)	$10K_Q$	0.361	-	0.318
C16 (Full-Scale)	$10K_Q$	0.362	0.318	-

9.2.3.2 Rough propeller

- **Model scale propeller**

Variation of flow details in the tip vortex with the roughness

The tip vortex flow around the marine propeller was investigated to understand the influence of roughness on the flow details inside the tip vortex in the model scale at Condition 6. For this reason, the face and backside of the propeller (i.e., FS+ BS) were covered with uniformly distributed roughness, which has different representative roughness length scales as given in Section 9.2 (see Table 9.1). The axial plane is located in the propeller slipstream to investigate the roughness effects on the velocity components inside the tip vortex, as given in Figure 9.22. The axial and tangential velocity profiles are extracted from the black-dashed lines between the purple-solid lines shown in Figure 9.22.

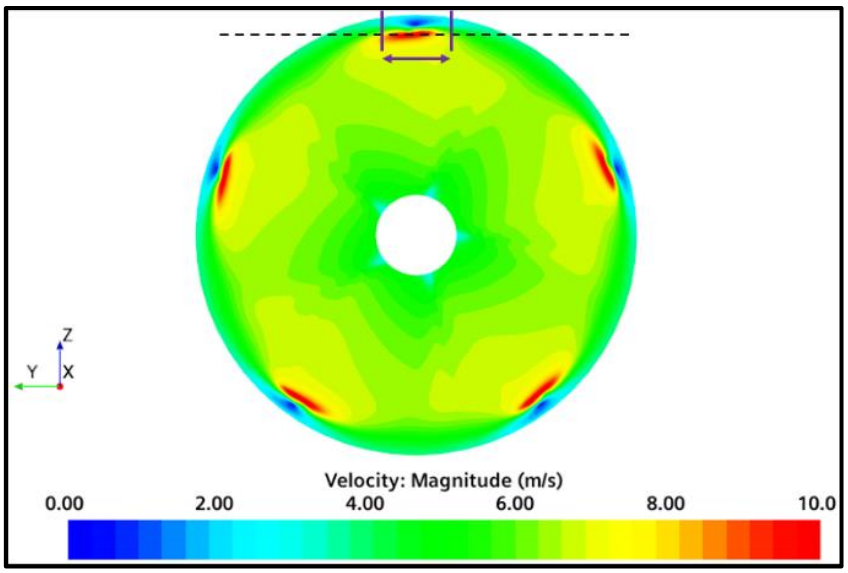

Figure 9.22. The velocity field in the propeller slipstream at x=-0.031 m.

Figure 9.23 compares the axial and tangential (azimuthal) velocity profiles between the smooth and rough conditions. The axial and tangential velocities were normalised with the inflow velocity. The vortex core diameter can be considered the distance between the maximum and minimum velocities' locations in the azimuthal velocity profiles. As shown in Figure 9.23, the axial and azimuthal velocities' magnitudes reduce in the presence of roughness compared to

the smooth condition, particularly around the vortex core. Interestingly, velocity profiles outside the vortex core are similar in smooth and rough conditions. The vortex core radius and axial velocity peak slightly change with the roughness application. The increase in the roughness height causes more reduction in the velocity magnitudes. Having a lower axial and tangential velocity will consequently increase the pressure inside the tip vortex.

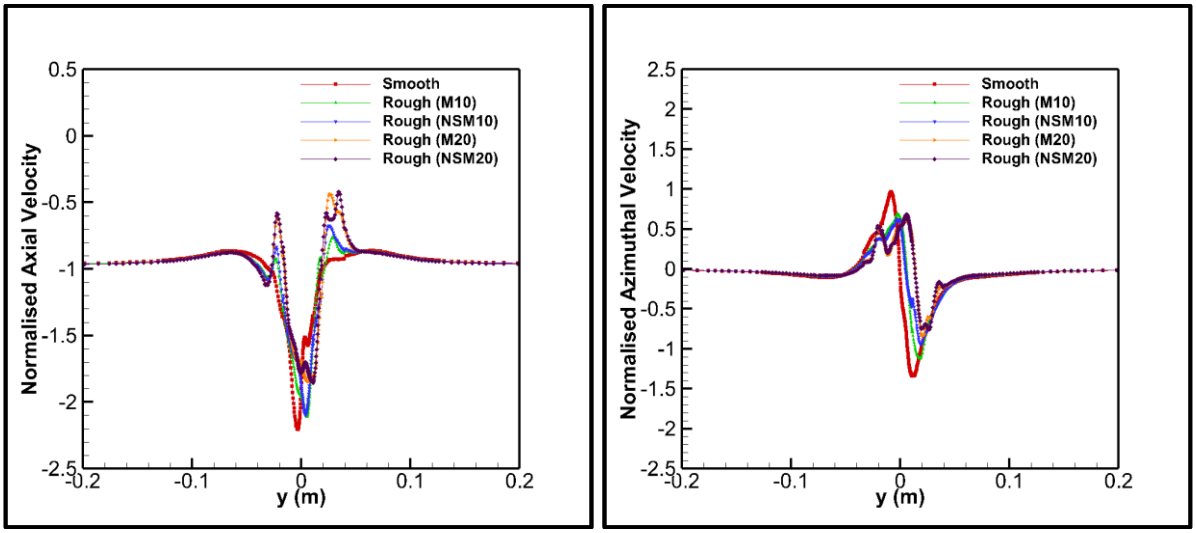

Figure 9.23. The change in normalised axial and azimuthal velocities with the roughness.

Figure 9.24 indicates the turbulent kinetic energy around the vortex region in smooth and rough conditions. As shown in Figure 9.24, the turbulent kinetic energy's maximum value appears at the vortex core centre for rough and smooth conditions. This is because the additional viscous stresses between the tip vortex and roughened blade surface transform the vortex's circumferential momentum into turbulent kinetic energy. With an increase in roughness height, turbulent kinetic energy increases considerably compared to the smooth condition.

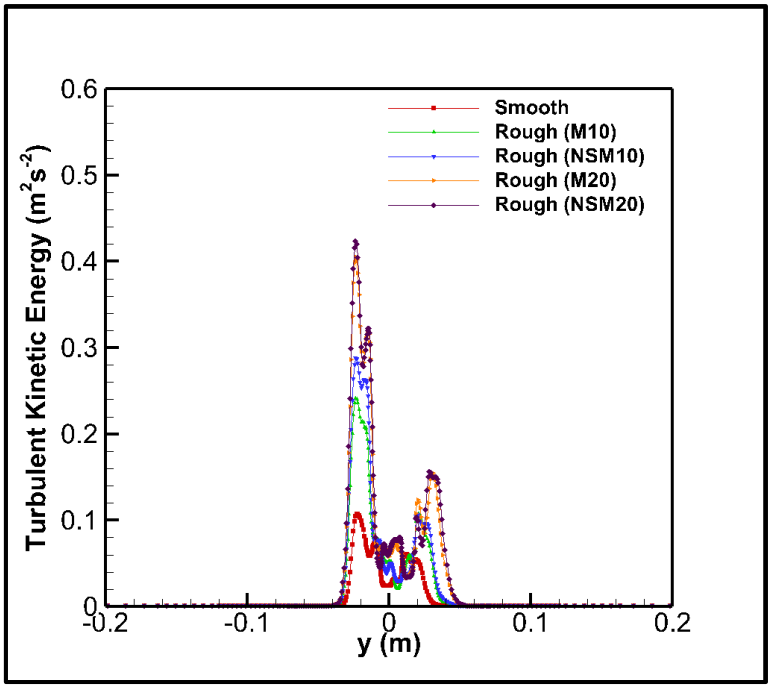

Figure 9.24. The change in resolved turbulent kinetic energy with the roughness (the data was obtained at the location as given in Figure 9.22).

Determination of optimum roughness application area and roughness length scale

The previous chapter shows that the roughness elements interfere with the tip vortex's velocity and pressure field. It enables a decrease in the velocities' magnitude (i.e., increase in pressure) inside the vortex core. However, this favourable impact on tip vortex flow negatively affects the blade sections' hydrodynamic characteristics. In the presence of roughness, the blade sections' drag increases, whereas the lift of the blade sections decreases due to reduced circulation distribution around the propeller blades. Inevitably, this will cause a decrease in thrust value and an increase in torque, resulting in efficiency loss for the propeller. Due to this reason, the roughness application area should be optimised to find a compromise between TVC mitigation and efficiency loss.

In order to find the optimum location on the propeller blades, the uniformly and non-uniformly distributed roughness configurations with different length scales were applied in the model scale at Condition 6, as given in Section 9.2 (see Table 9.1) and Table 9.11. Figure 9.25 shows the change in cavitation volume and efficiency loss with different roughness configurations and length scales concerning the smooth condition. In all configurations of Figure 9.25, the roughness increases the torque coefficient. The maximum increase is found at around 35% at the highest roughness height (i.e., NSM20) when the uniformly distributed roughness is applied at both sides of the propeller blades (i.e., FS+BS configuration). Yet, the roughness decreases

the thrust coefficient for all configurations, except FS and FS09+BS09 configurations. The maximum thrust decrease is also found at around 24% for BS configuration. When the roughness is applied to the blades using the FS and FS09+BS09 configurations, the thrust coefficient increases by around 3%. However, the torque coefficient's substantial increase results in efficiency loss even if the propeller thrust increases. When the roughness is only applied on the propeller blade tips (i.e., FS09, BS09 and FS09+BS09 configuration), the thrust and torque coefficient change are smaller than those of other configurations.

As expected, applying the uniform roughness on the propeller blades shows the maximum performance degradation even if the cavitation volume reduction is higher than those of other configurations with an increase in roughness length scale. On the other hand, the non-uniformly distributed roughness has a favourable impact on the propeller efficiency loss. In this regard, applying the roughness only on the propeller blade tips (i.e., FS09, BS09 and FS09+BS09) reduces the efficiency loss. Amongst these configurations, the roughness application only on the suction side (or backside) of the propeller blade tips (i.e., BS09) enables a significant reduction in efficiency loss. In this way, the efficiency loss can be decreased by approximately 20-32% depending on the roughness length scale compared to uniformly distributed roughness on all propeller blades (i.e., FS+BS configuration).

Regarding the cavitation volume change, applying the roughness on the propeller blades reduces the cavitation volume for all configurations with respect to the smooth case, except the FS and FS09. Remarkably, applying the roughness on the pressure side (or face side) (i.e., FS and FS09) shows the opposite trend and increases the cavitation volume. This opposite trend becomes more pronounced with an increase in roughness height. The reduction of cavitation volume is mainly due to the mitigation of TVC as the roughness increases the pressure inside the vortex. This TVC mitigation further increases with an increase in the roughness height.

The several roughness application areas enable understanding the influence of roughness on the propeller efficiency and cavitation volume reduction. To achieve a compromise between the propeller efficiency loss and the cavitation volume reduction, the BS09 is selected as an optimum roughness application area. Regarding the optimum representative roughness length scale (k_G), the change in the efficiency loss between $k_G = 337\mu m$ and $k_G = 408\mu m$ roughness length scales are found below 1%. Yet, the cavitation volume reduction is found to be around 5% higher in the 408μm roughness length scale than those of 337μm. Hence, $k_G =$

$408\mu m$ (i.e., NSM20) is selected as an optimum representative roughness length scale in this study.

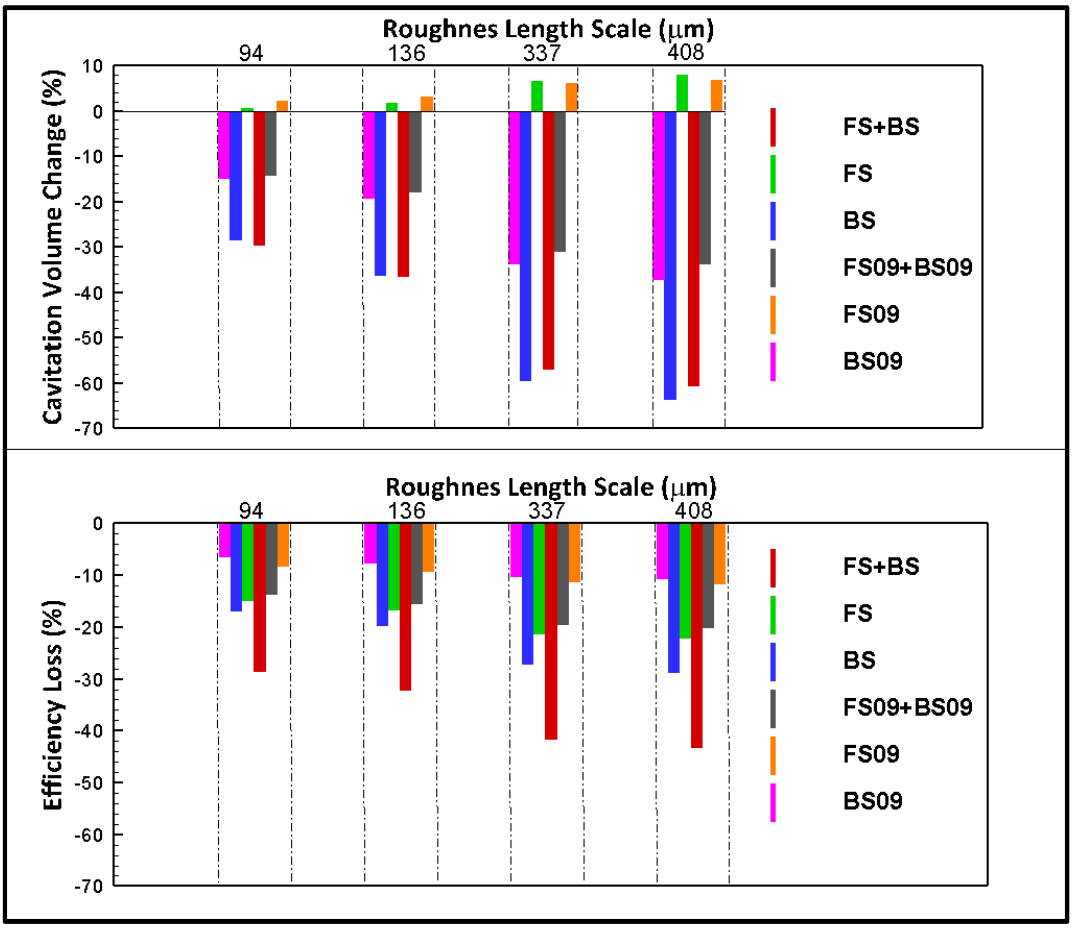

Figure 9.25. The cavitation volume and efficiency variation with different roughness configurations and length scale with respect to smooth condition at C6.

As stated before, the roughness disrupts the tip vortex structure and provides TVC mitigation. For example, the comparison of TVC extension in the propeller slipstream between rough and smooth propellers is given in Figure 9.26 for FS+BS and determined optimum roughness area (i.e., BS09) configurations. As shown in Figure 9.26, the more the roughness height, the more the TVC mitigation can be achieved for both configurations.

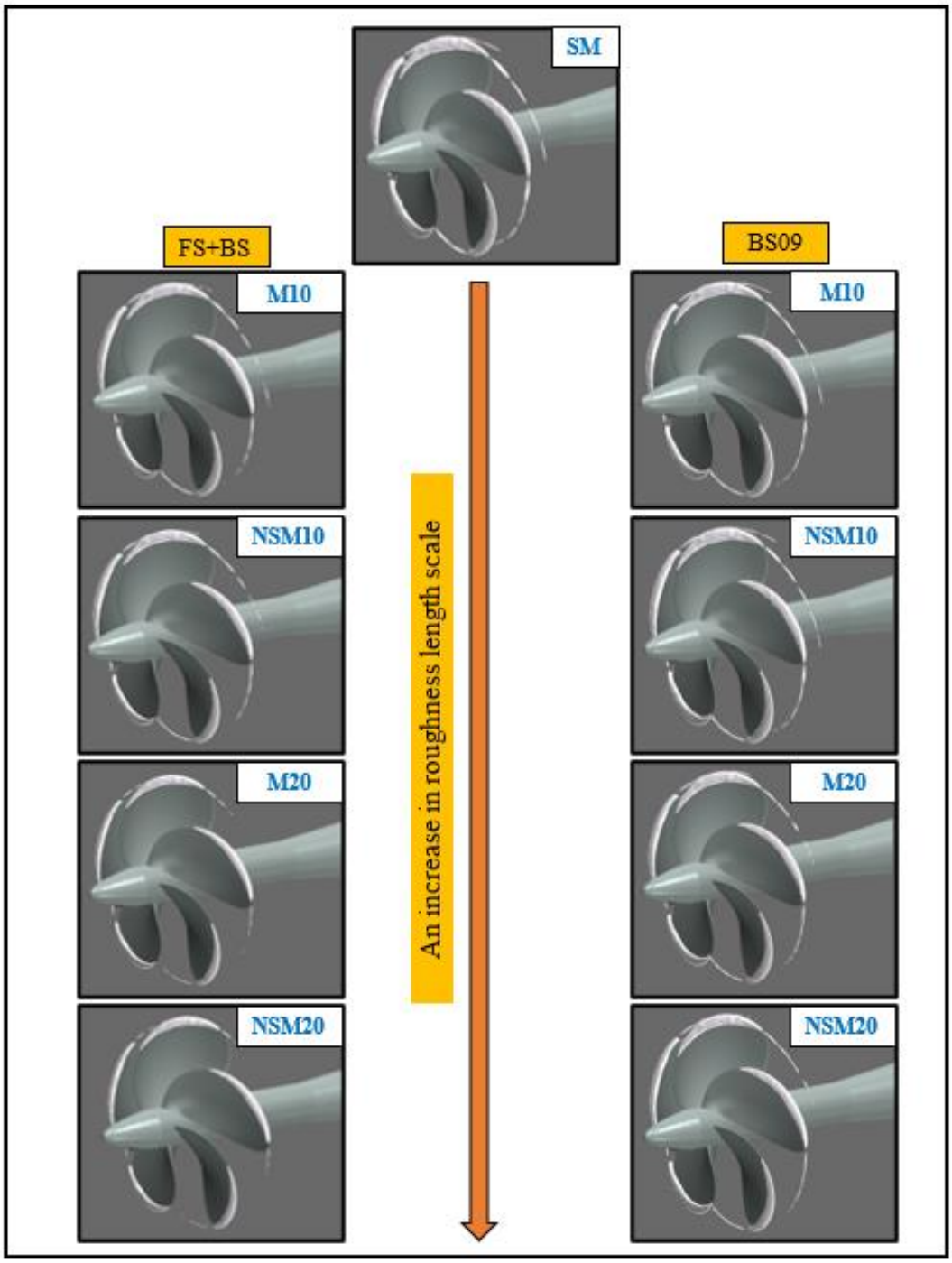

Figure 9.26. The change in TVC with an increase in roughness length scale at C6 (α_v=0.1).

Application of roughness on the optimum area using the optimum length scale for different operating conditions

The optimised roughness area (i.e., BS09) and the selected roughness length scale (i.e., NSM20, $k_G = 408\mu m$) were tested for a wide range of operating conditions (i.e., C2, C8, C12 and C15) to show its effectiveness for the TVC mitigation and efficiency loss in the model scale. Figure 9.27 compares the cavitation extensions between the smooth and roughened

blades. Akin to the C6, the roughness has a favourable impact on mitigating the stable and well-developed TVC emanating the blade tips under uniform (i.e., C2) and inclined flow conditions (i.e., C8 and C12) as given in Figure 9.27.

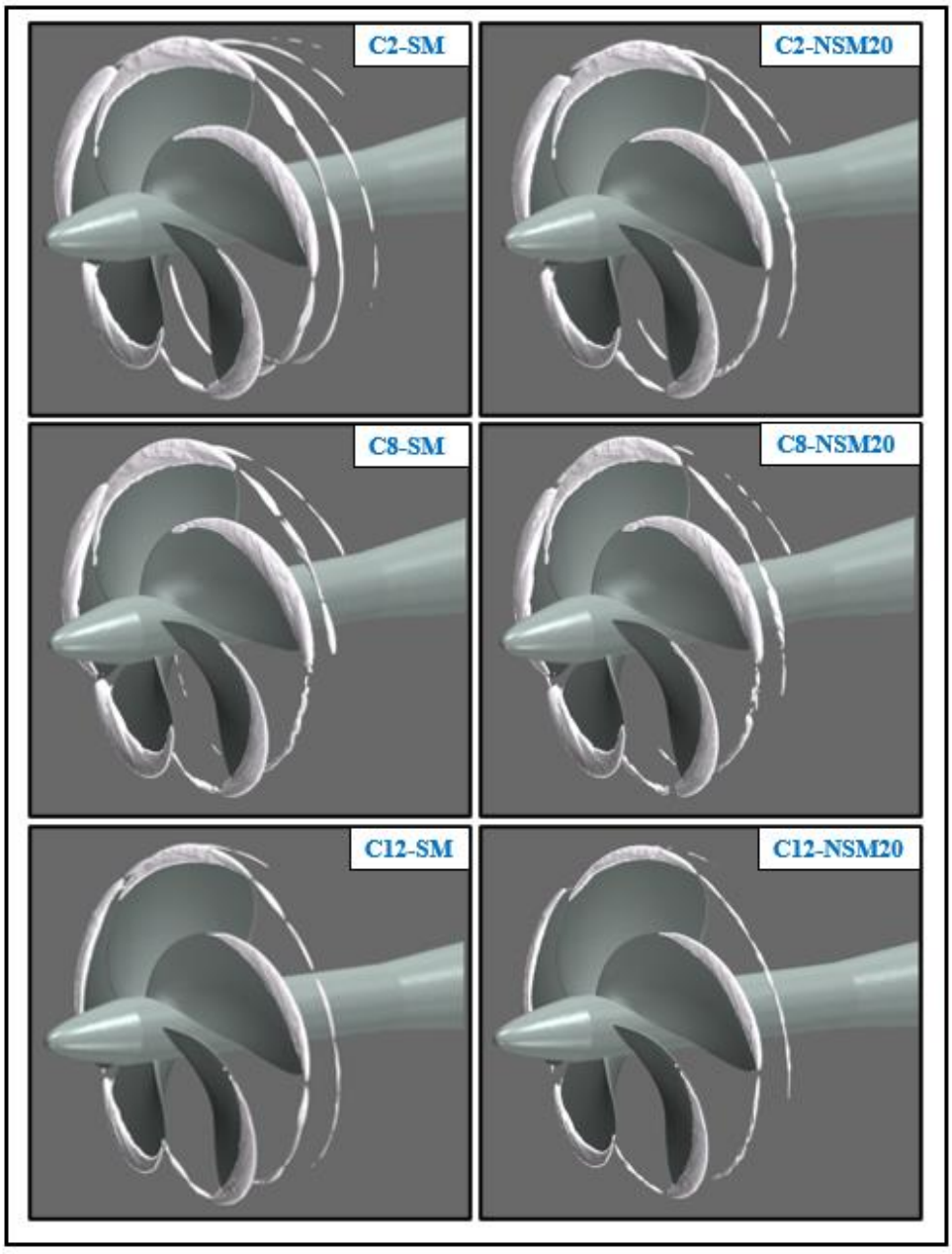

Figure 9.27. The change in TVC at different operational conditions in model scale (α_v=0.1).

Figure 9.28 also compares the variation of TVC between the rough and smooth cases under non-uniform flow conditions. As shown in Figure 9.27, although the stable and structured TVC is observed under uniform and inclined flow conditions, the tip vortex breaks up in the propeller slipstream. It presents somewhat different dynamics under the non-uniform flow conditions in comparison with the uniform flow conditions. This break-up phenomenon and complex structure and dynamics of TVC are disrupted with the roughness application compared to a

smooth case. Moreover, the strength of the first vortex formation, which occurs because of the sheet cavity break up, reduces with the roughness.

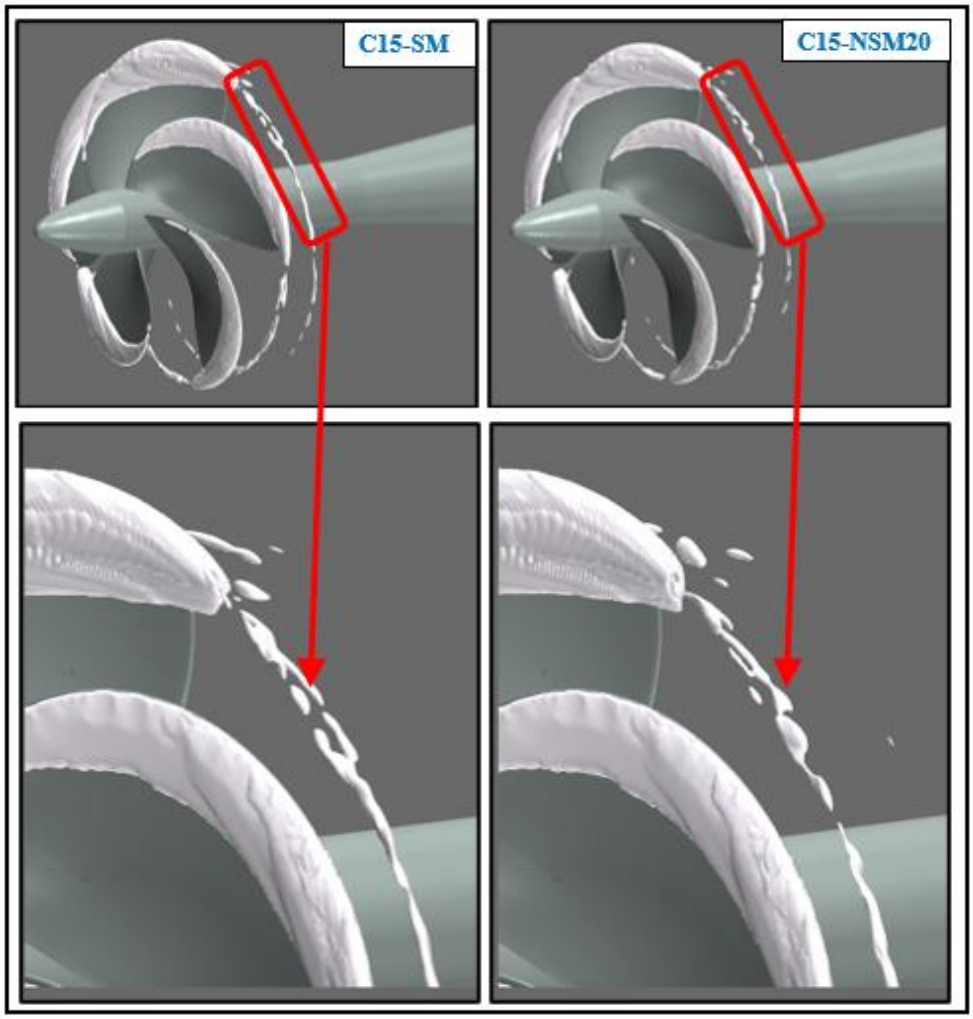

Figure 9.28. The variation of TVC structure with the roughness at C15 (α_v=0.1).

Table 9.15 shows the variation of the global performance characteristics in the presence of roughness with respect to the smooth condition. As shown in Table 9.15, the thrust coefficient decreases, whereas the torque coefficient increases with roughness for all operating conditions. The maximum thrust reduction was 6.82% at C6, while the minimum torque increase was 1.53% at C2. The decrease in thrust and increase in torque coefficient leads to propeller efficiency loss, as shown in Figure 9.29; hence, the maximum efficiency loss was found to be around 10% for C6 and C12 conditions. Contrary to the uniform and inclined flow conditions, the performance degradation is small under the non-uniform flow conditions (i.e., C15).

Regarding the cavitation volume, the maximum reduction achieved is approximately %37 at C6. Although this is around 5% under non-uniform flow conditions (i.e., C15) in the presence of roughness, the roughness also moderates the strength of the unstructured vortex, particularly in the roll-up process. Consequently, these results suggest that the overall cavitation volume reduction is greatly affected by roughness when operating in conditions where the stable and well-developed TVC is present (e.g., C2, C6, C8 and C12) as opposed to an unstructured and unstable TVC (e.g., C15).

Table 9.15. The change in thrust and torque coefficients in the presence of roughness with respect to smooth condition for model scale propeller.

Condition	K_T (%)	$10K_Q$ (%)
C2	-4.85	1.53
C6	-6.82	4.25
C8	-4.66	1.99
C12	-6.70	3.97
C15	-3.03	1.69

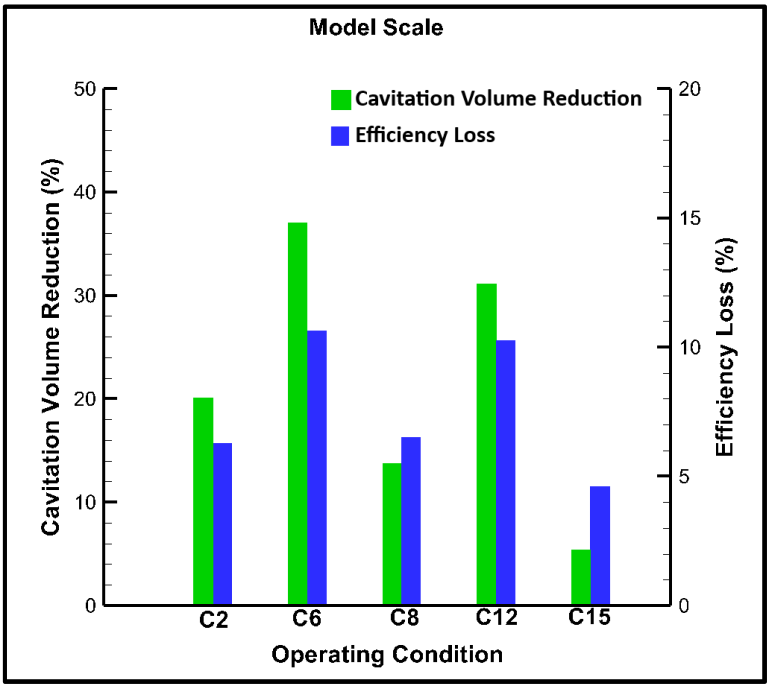

Figure 9.29. The cavitation volume reduction and efficiency loss in the presence of roughness with respect to smooth conditions at different operating conditions in model scale.

- **Full-scale propeller**

The optimum roughness area (i.e., BS09) is also used to investigate roughness effects on the full-scale propeller in terms of the performance degradation and mitigation of TVC at different operating conditions, as given in Tables 9.9 and 9.10. The scaling law for the roughness is dependent on the wall shear velocity at the propeller blade tips. This requires the selection of a larger roughness length scale in the model scale than the full-scale propeller. Yet, as stated in the study by Krüger et al., 2016, to represent the same hydrodynamic effects with roughness, the roughness height must be in almost the same order in the model and full-scale propeller. Also, the geometric and dynamic similarity may not be possible between the model and full-scale propeller in the presence of roughness. Thus, the same representative roughness length scale (i.e., NSM20, $k_G = 408\mu m$) was also used for the full-scale propeller.

Figure 9.30 shows the comparison of TVC between the smooth and roughened full-scale propellers under uniform flow conditions at J=0.4 and J=0.5, respectively. As shown in Figure 9.30, the suction side sheet cavitation covers a larger blade area at C13 (i.e., J=0.4) than C14 (i.e., J=0.5) because of the high blade loading. Also, an increase in blade loading deteriorates the TVC structure in the propeller slipstream in smooth condition. The stable and structured TVC is present at C14. However, this coherent vortex structure deteriorates with an increase in blade loading, which results in the variation of the TVC dynamics in the propeller slipstream. Similar to non-uniform flow conditions, two different vortex structures emanating the propeller blade tips are present at C13. Figure 9.31 also indicates the differences between the smooth and roughened full-scale propeller under non-uniform flow conditions. In all configurations, akin to the model scale operating conditions, the roughness weakens the tip vortex structure, providing TVC mitigation. Table 9.16 shows the change in thrust and torque coefficients in the presence of roughness with respect to the smooth condition. Unlike the model scale propeller, the increase in torque coefficient reduces for the full-scale propeller in the presence of roughness. However, inevitably, the thrust decrease results in efficiency loss for all operating conditions. The efficiency loss and cavitation volume reduction are given in Figure 9.32 in the presence of roughness. The results show that the efficiency loss predicted in the full-scale propeller is smaller than those of the model scale propeller.

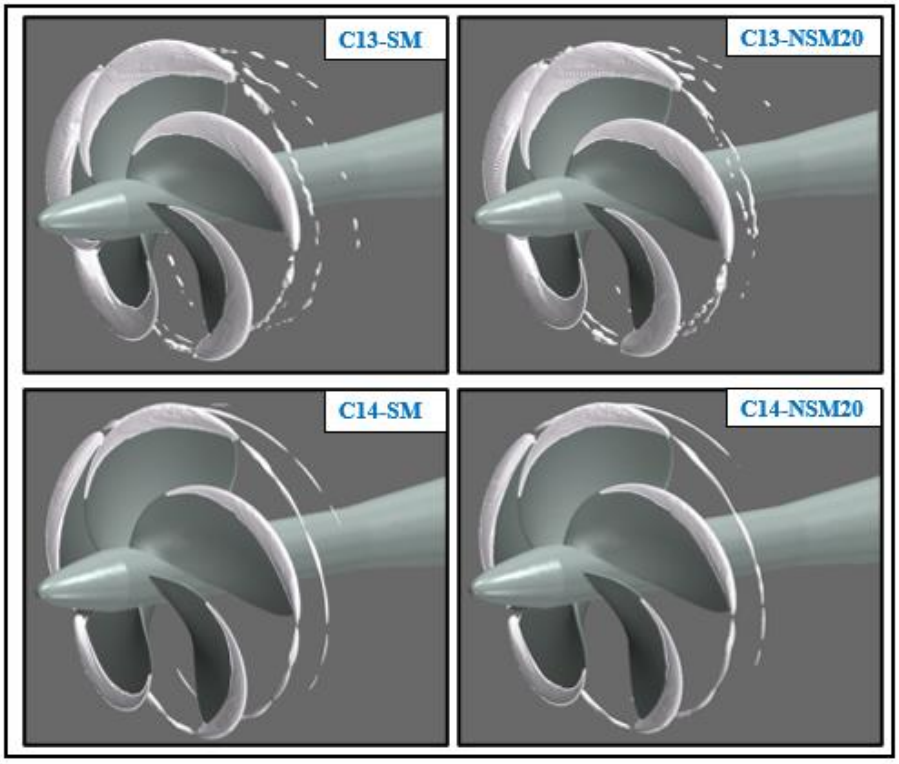

Figure 9.30. The change in TVC with the roughness under uniform flow conditions in full-scale (α_v=0.1).

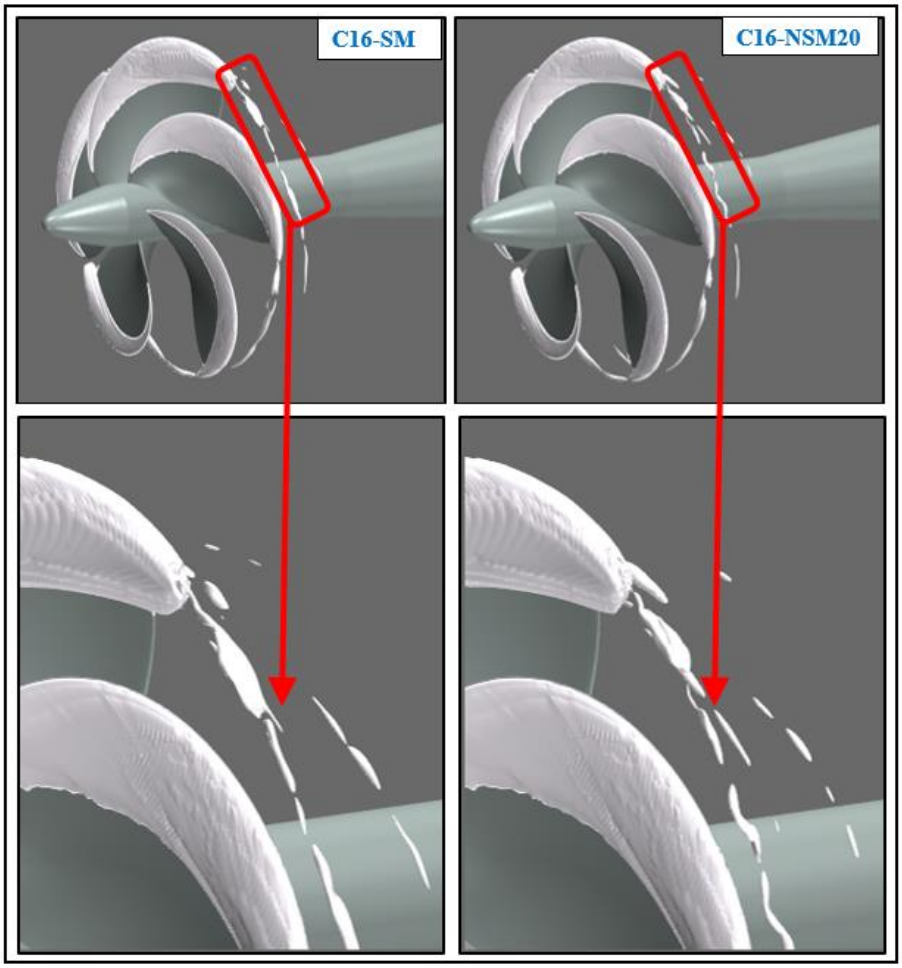

Figure 9.31. The change in TVC structure with the roughness at C16 (α_v=0.1).

Table 9.16. The change in thrust and torque coefficients in the presence of roughness with respect to smooth condition for the full-scale propeller.

Condition	K_T (%)	$10K_Q$ (%)
C13	-2.05	0.38
C14	-5.87	0.06
C16	-2.80	0.28

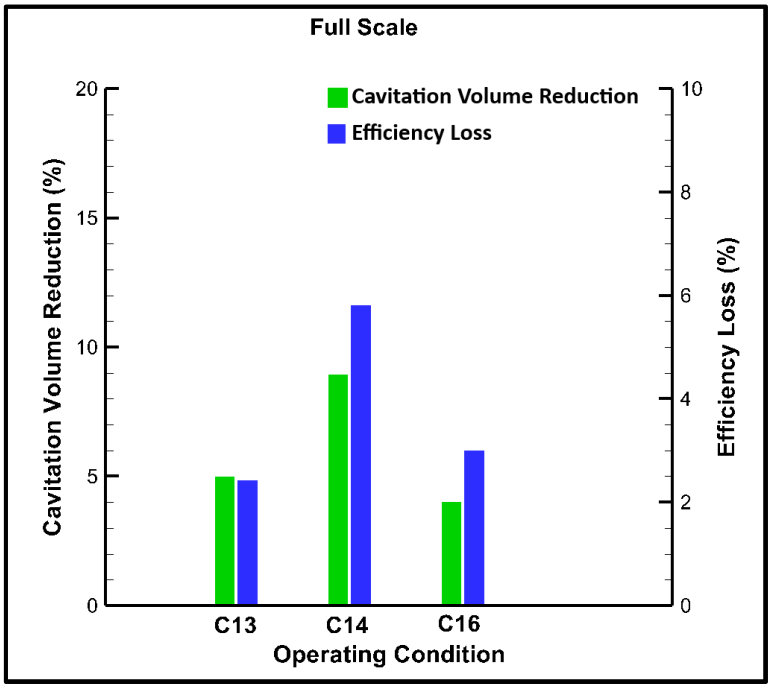

Figure 9.32. The cavitation volume reduction and efficiency loss in the presence of roughness with respect to smooth conditions at different operating conditions in full-scale.

9.3 Application of roughness on the propeller hub

9.3.1 Theoretical background

9.3.1.1 Hydrodynamic model

The unsteady RANS method with k-ω SST turbulence model was used to solve cavitating flow around the propeller, as used in Section 9.2. Also, the Schnerr Sauer cavitation model based on the reduced Rayleigh Plesset equation was used with the VOF (Volume of Fluid) approach to model the liquid and vapour phases, as used in Sections 9.2 and 9.3. Also, further details of the cavitation model and governing equations can be found in the user guide of CFD solver Star CCM+ 14.06, 2019.

9.3.1.2 Roughness model

Roughness functions provided in Uzun et al., 2020 were implemented in the wall function of the CFD software, Star CCM+ 14.06, 2019, to explore its effects on the hub vortex cavitation of a propeller. As used in Sections 9.2 and 9.3, barnacle type roughness was used to represent the surface roughness. The roughness length scales of test surfaces obtained by Uzun et al., 2020 can be found in Section 9.2 and Table 9.1.

9.3.2 Numerical modelling

9.3.2.1 Propeller geometry and test matrix

As used in Chapters 4, 5 and Section 9.2, the four-bladed benchmark INSEAN E779A model propeller was used in the numerical calculations. Table 9.17 summarises the test condition explored in this section.

Table 9.17. Operating conditions for the INSEAN E779A propeller.

Parameter	Symbol and Unit	Value
Advance ratio	J (-)	0.71
Rotation Rate	n (rps)	36
Inflow averaged velocity	V_A (m/s)	5.8
Cavitation number	σ (-)	1.763
Vapour pressure	P_V (Pa)	2337

Figure 9.33 shows the roughness application area on the hub and the smooth propeller. Here, the black colour shows the area where the roughness is applied in this research study. As given in Table 9.1 (Section 9.2), the four different roughness configurations are applied to the black area to investigate the mitigation of hub vortex cavitation with an increase in roughness length scale.

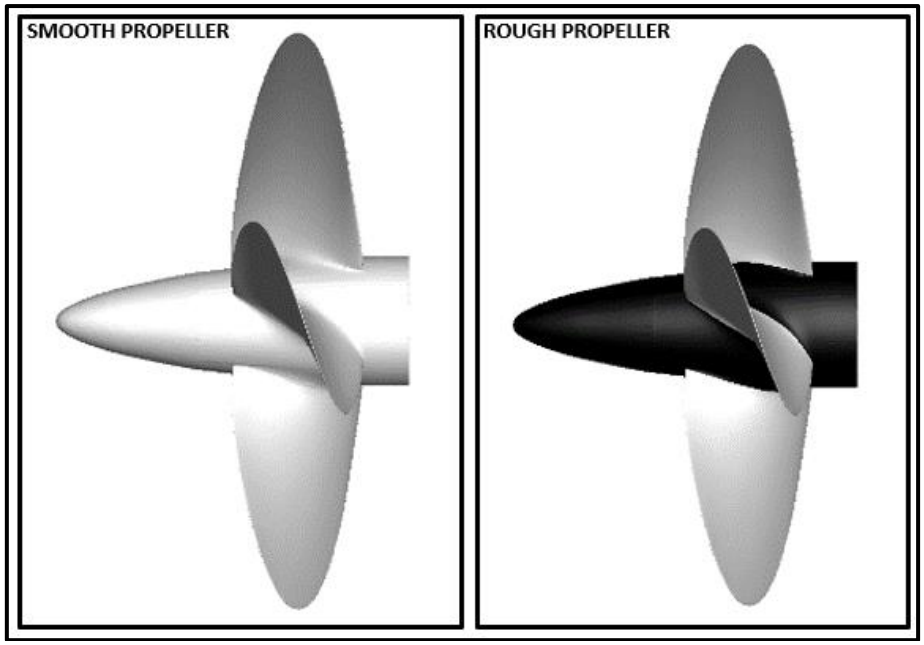

Figure 9.33. Representation of the roughness application area on the hub (black colour represents the area where the roughness was applied).

9.3.2.2 Computational domain and boundary conditions

As used in Section 9.2, the same computational domain and boundary conditions were used here. The details of the computational domain and boundary conditions can be found in Section 9.2.2.

9.3.2.3 Grid structure

The uniform grid resolution was adopted, and additional mesh refinement was applied to the blades. As the main interest of this study is hub vortex cavitation and its mitigation with roughness application, the V-AMR (Vorticity-based Adaptive Mesh Refinement) technique, as described in Chapter 5, was not implemented here for the observation of tip vortex cavitation (TVC) in the propeller slipstream. This also enabled a reduction of the computational cost of the solution. As the uncertainty study was conducted with the selected propeller at the same operating condition in Chapter 5 and Section 9.2, the uncertainty study was not repeated. This is because a similar grid structure was adopted. The total element count was calculated at around 10M. The grid resolution inside the computational domain is shown in Figure 9.34.

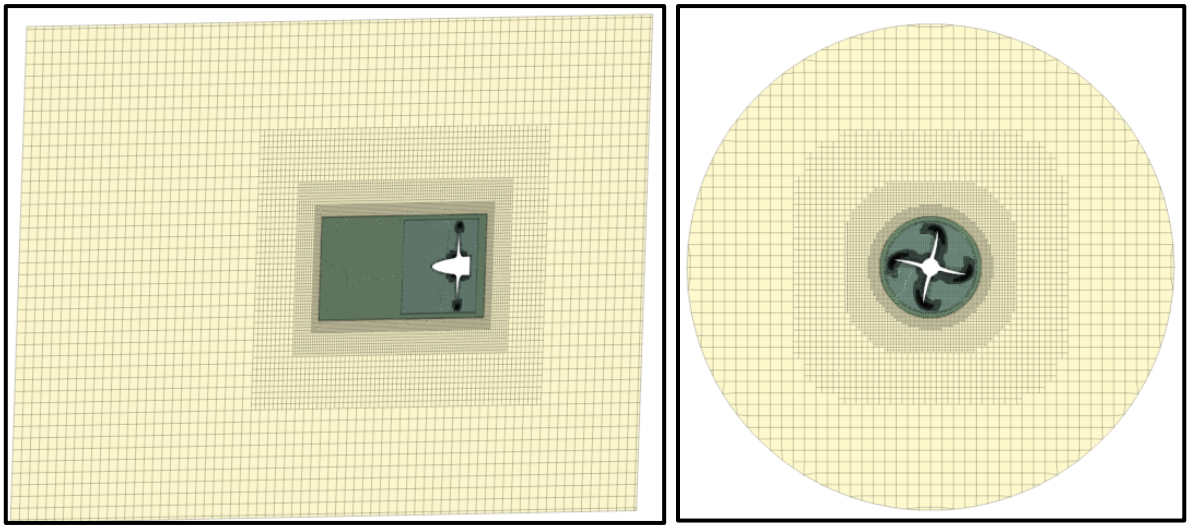

Figure 9.34. Grid resolution inside the computational domain.

9.3.2.4 Analysis properties

Akin to Section 9.2, similar analysis properties were utilised in this Section. The details can be found in Section 9.2.2.

9.3.3 Numerical results

9.3.3.1 Validation of the numerical results in smooth condition

Table 9.18 compares the propeller's global performance characteristics (i.e., thrust and torque) predicted using CFD with the experiment in the smooth condition. As shown in Table 9.18, the difference between the CFD and experiment is approximately 6% for thrust and torque coefficients.

Table 9.18. The comparison of thrust and torque coefficients between the experiment and CFD at J=0.71, σ=1.763 in smooth condition.

Parameter	Experiment (Salvatore et al., 2009)	CFD
K_T	0.255	0.240
$10K_Q$	0.460	0.435

The cavitation extension predicted in the CFD calculations is compared with the experiment at J=0.71, σ=1.763 in the smooth condition in Figure 9.35. In the CFD predictions, the iso-surface of volume fraction is taken as 0.1 ($\alpha_v = 0.1$). As shown in Figure 9.35, the sheet and hub vortex cavitation are predicted similarly in the numerical calculations and the experiment. Compared to the experiment, the sheet cavitation extension on the blades is slightly overpredicted in the CFD calculations. The sheet cavitation rolls up into a thick and strong tip vortex cavitation in the experiment. This TVC extends further downstream of the propeller.

In the numerical calculations, as the V-AMR technique is not applied in this section and the hub vortex cavitation is of great interest, a similar TVC could not be predicted in the CFD calculations. Nevertheless, to recall the capabilities of the V-AMR technique for the TVC modelling, the cavitation observation obtained by RANS in Chapter 5 (Sezen and Atlar, 2021) at the same operating condition is shown in Figure 9.35.

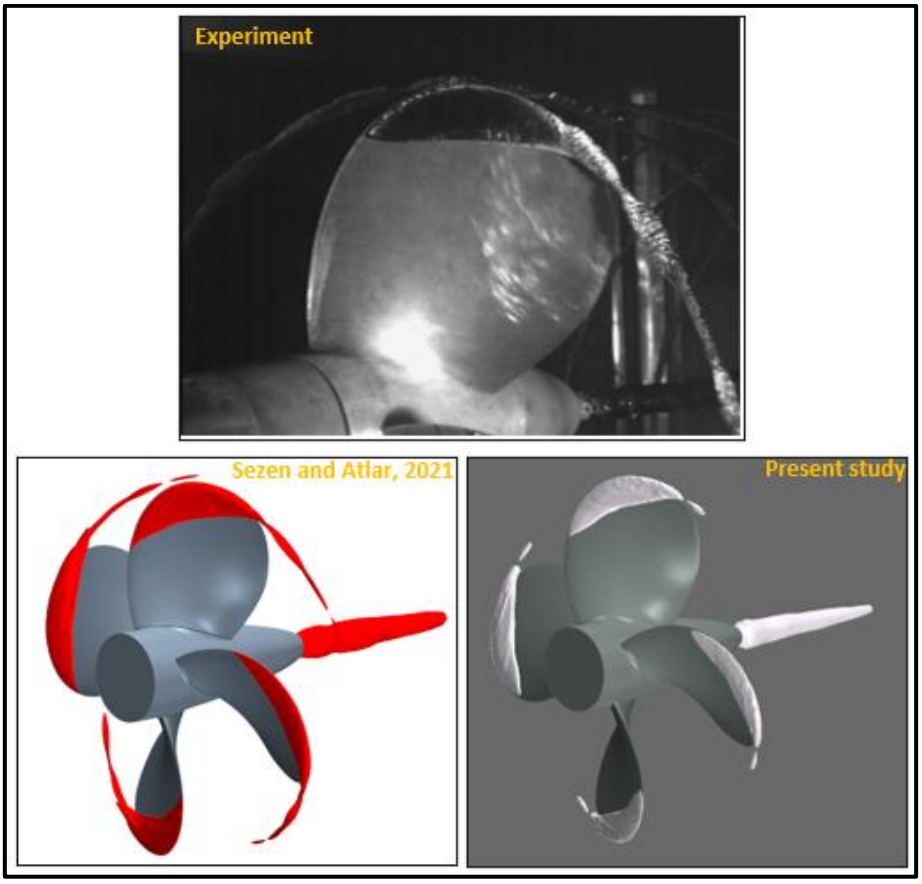

Figure 9.35. Comparison of cavitation extensions between CFD and experiment at J=0.71, σ=1.763 in smooth condition ($\alpha_v = 0.1$).

9.3.3.2 Influence of roughness on propeller hydrodynamic performance and cavitation extension

Figures 9.36 and 9.37 show the change in thrust coefficient (i.e., K_T) and torque coefficient in the presence of roughness with the different roughness length scales, as given in Table 9.1 (see Section 9.2). Here, the smooth condition is shown with zero roughness height. With the application of roughness, the thrust coefficient decreases with an increase in roughness length scale due to the increased drag and reduced lift, as shown in Figure 9.36. As expected, the thrust decrease is smaller with the roughness application on the hub compared to roughness application on the blades, as explored in Section 9.2. The maximum thrust reduction is found at around 2% with respect to the smooth condition.

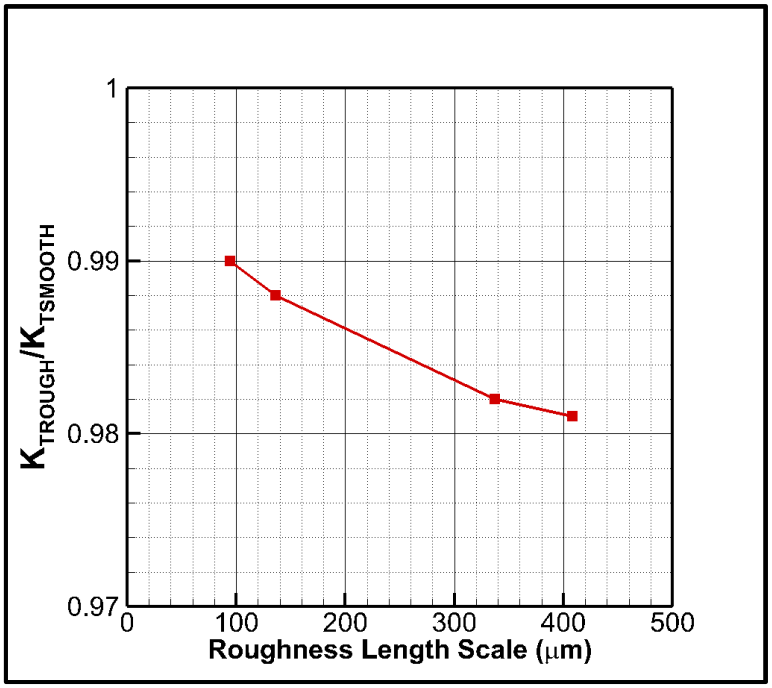

Figure 9.36. Change in thrust coefficient (K_T) with the roughness.

The change in torque coefficient (i.e., $10K_Q$) with the roughness is also shown in Figure 9.37. Similar to thrust coefficient, roughness applied on the hub has a degradation effect on the torque coefficient of the propeller. The maximum reduction is found to be approximately 1.5% at the maximum roughened condition.

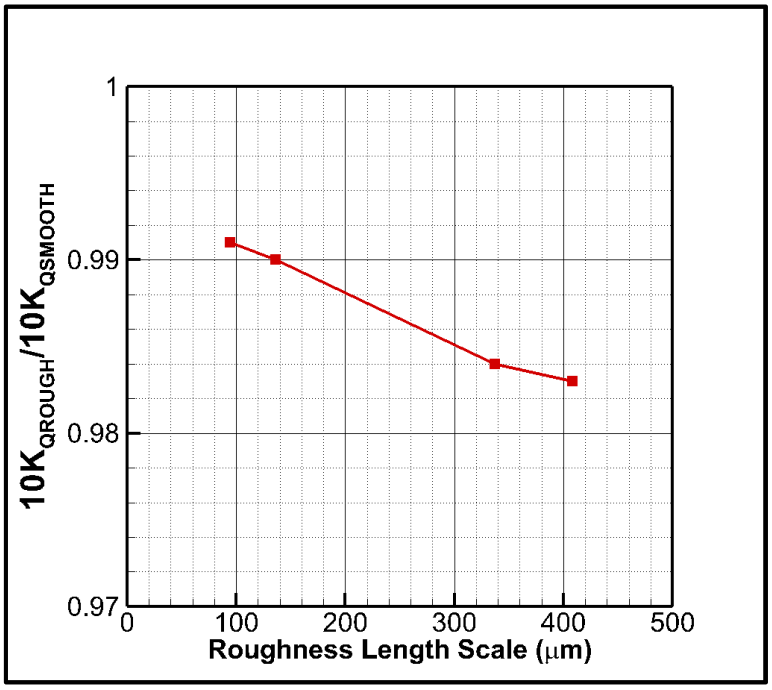

Figure 9.37. Change in torque coefficient ($10K_Q$) with the roughness.

The decreased thrust and torque coefficients with roughness application lead to efficiency loss, as shown in Figure 9.38. This is the main difference between the roughness and typical PBCF applications since the increased thrust in BPCF enables efficiency gain due to recovering the energy loss. Nevertheless, the efficiency loss is not high with roughness on the propeller's hub, and the maximum efficiency loss is around 0.25%, while the cost of applying roughness and PBCF is another parameter for the decision on which one to go for.

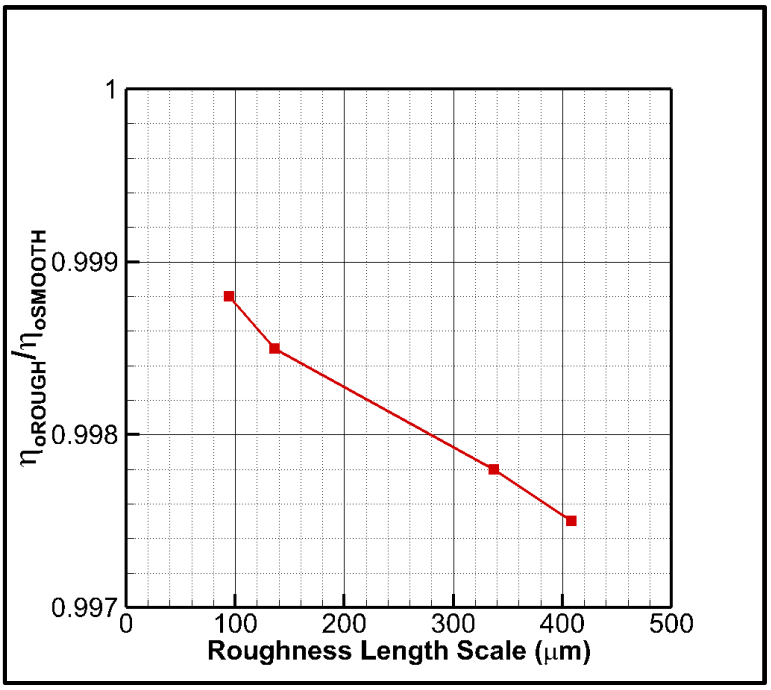

Figure 9.38. Efficiency (η_0) loss with the roughness.

Figure 9.39 compares wall shear stresses on the hub between smooth and rough conditions. As expected, the roughness applied to the hub increases the wall shear stresses.

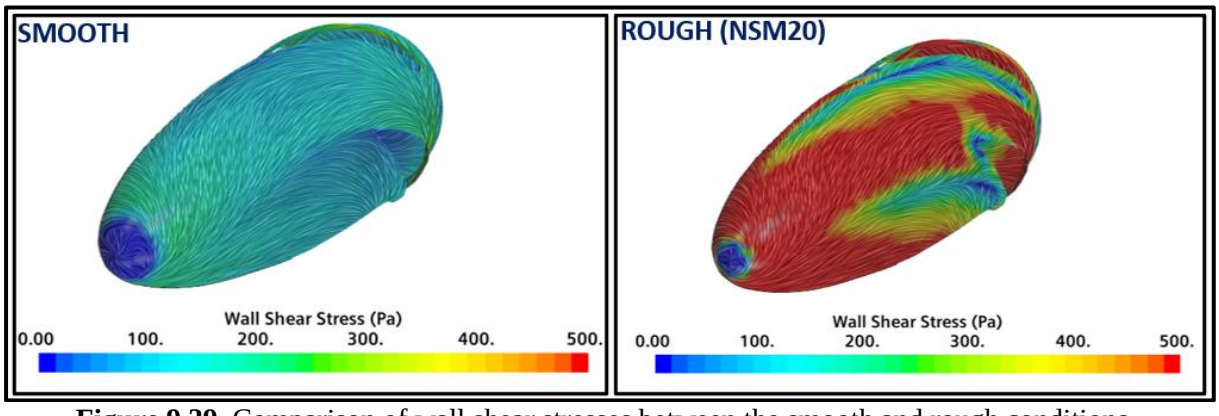

Figure 9.39. Comparison of wall shear stresses between the smooth and rough conditions.

The detailed flow analysis is carried out in the propeller slipstream to show the influence of roughness on the hub vortex and hub vortex cavitation. Figure 9.40 shows the change in turbulent kinetic energy with roughness. As shown in Figure 9.40, the turbulent kinetic energy increases considerably with the roughness due to the transformation of the vortex's circumferential momentum into turbulent kinetic energy.

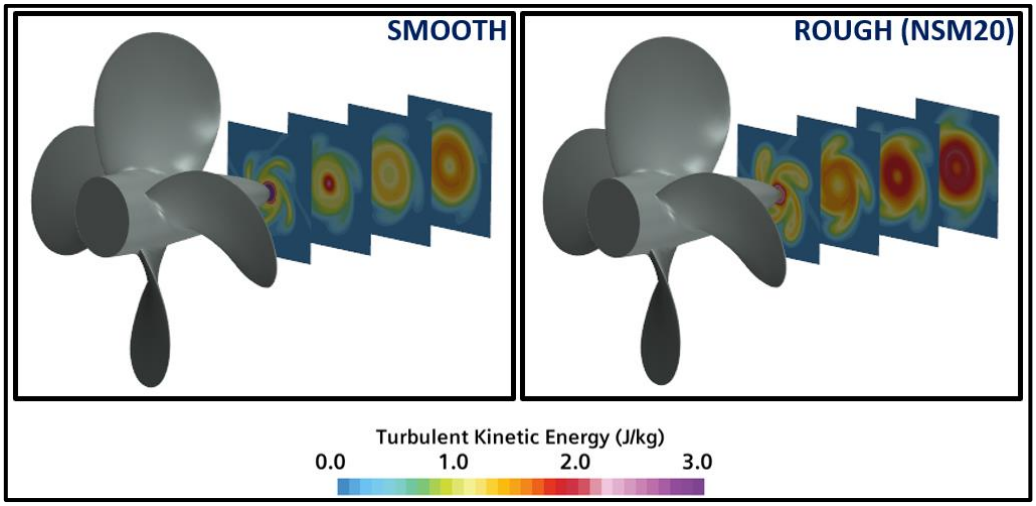

Figure 9.40. Change in turbulent kinetic energy with the roughness.

The change in magnitude of the vortex structures with the roughness is shown at different sections in the propeller slipstream in Figure 9.41. Applying the roughness reduces the strength of the hub vortex with respect to the smooth condition. The reduced vortex strength enables the destabilisation process of the hub vortices, and hence hub vortex disappears with the roughness application.

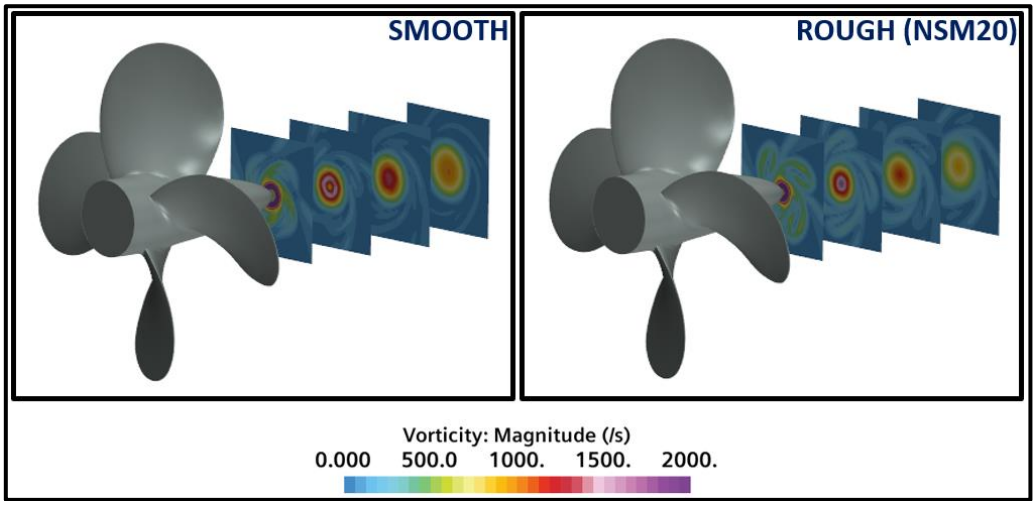

Figure 9.41. Change in magnitude of the vortex structures in the propeller slipstream with the roughness.

Figure 9.42 compares the distribution of the non-dimensional pressure coefficient ($C_p = P/0.5\rho(nD)^2$) between the rough and smooth conditions. The roughness elements around the hub interact with the hub vortices and change their velocity and pressure fields. The roughness decrease the velocity magnitudes, and hence the pressure inside the vortex core and its surroundings increase significantly. With the application of roughness, the pressure inside the hub vortex increases, resulting in the reduction of hub vortex strength and hub vortex cavitation, as shown in Figure 9.42.

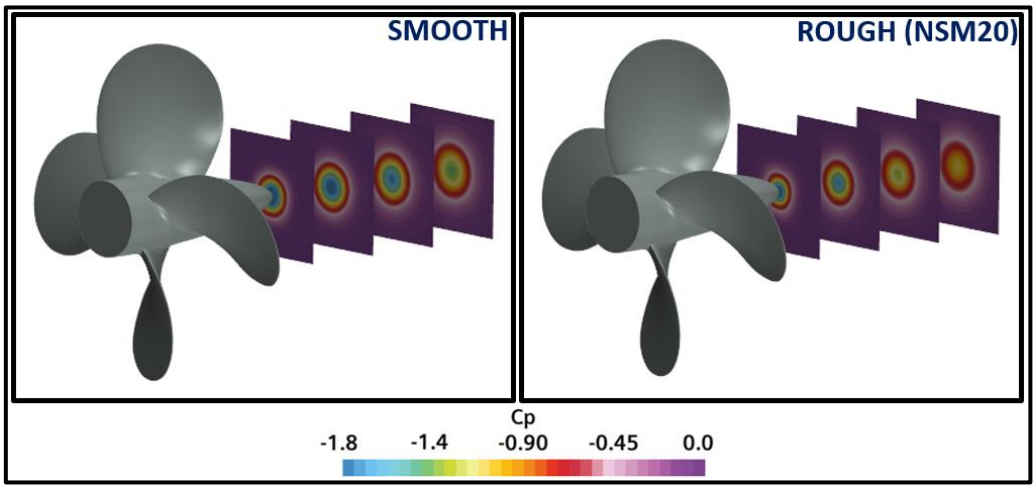

Figure 9.42. Change in non-dimensional pressure distribution with the roughness.

Applying roughness leads to destabilisation of the hub vortex strength, which results in an early breakdown of the hub vortex in the propeller slipstream. The reduced strength of the hub vortex due to the increased pressure inside the vortex core results in hub vortex cavitation mitigation with the roughness application, as shown in Figure 9.43. With an increase in roughness length scale from M10 to NSM20, the hub vortex cavitation is further reduced. The maximum hub vortex cavitation volume reduction due to the roughness is computed at around 50% with respect to the smooth condition. As the roughness is solely applied to the propeller hub and boss cap, the sheet cavitation is not affected by the roughness application.

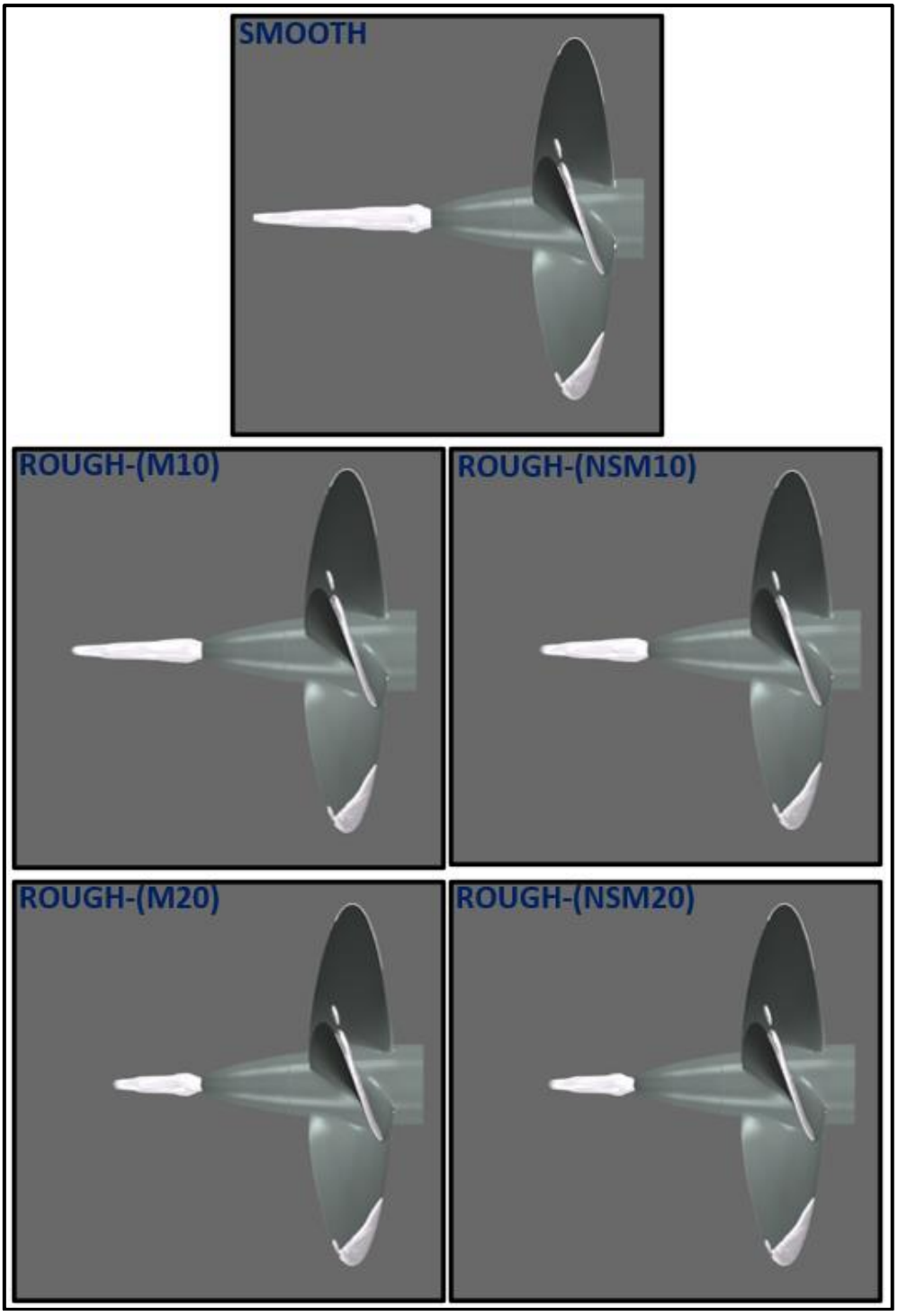

Figure 9.43. Change in hub vortex cavitation with the roughness ($\alpha_v = 0.1$).

9.4 Chapter summary and concluding remarks

In this chapter, the influence of a particular type of biofouling roughness on propeller hydrodynamic performance, cavitation and propeller URN were explored using two different benchmark propellers (i.e., INSEAN E779A and The Princess Royal). As far as the author's knowledge is concerned, the effect of roughness on the propeller induced URN was the first time explored in this thesis using CFD (Sezen et al., 2021).

In the numerical calculations conducted by model scale INSEAN E779A model propeller, the RANS method was utilised to solve the flow field around the propeller. On the other hand, the DES method was used for the calculations carried out by The Princess Royal propeller in model and full-scale.

Under cavitating conditions, the Schnerr Sauer mass transfer model was used to model the cavitation on and off the blades. As explained in Chapter 5, the V-AMR technique was implemented to better model the TVC in the propeller slipstream. The verification study was carried out using the GCI method to calculate the uncertainty of the numerical solution. Also, the verification of the hydroacoustic part of the solution was conducted by comparing the hydrodynamic and hydroacoustic pressures in the near field. The obtained global performance characteristics (i.e., thrust, torque and efficiency) were validated with the experimental data. Also, the sheet, tip and hub vortex cavitation extensions were validated with the experimental observation in smooth conditions. Following this, the roughness functions obtained by the experimental study of Uzun et al., 2020 were imposed in the calculations using the wall function of the CFD solver. The change in propeller hydrodynamic and hydroacoustic performance was investigated in the presence of roughness in a wide range of operating conditions. This chapter suggested some novel and important findings, as summarised below:

- The numerical results showed that the global performance characteristics and cavitation extensions were found to agree with the experimental data for the selected benchmark propellers in smooth conditions.

- Applying roughness homogenously on the propeller blades for INSEAN E779A model scale propeller decreased the thrust and increased the torque. Thus, this resulted in considerable efficiency loss between 8% and 30% depending on the roughness length scale under non-cavitating and cavitating conditions.

- Despite the degradation effects of applying roughness homogenously on the propeller blades for INSEAN E779A model scale propeller, the roughness showed a favourable impact on reducing the cavitation, particularly TVC. The cavitation volume was further reduced with an increase in roughness length scale. The reduced cavitation volume resulted in the mitigation of propeller URN. Although the time based acoustic pressure signal in the low-frequency region did not show remarkable change with the roughness application, the URN levels decreased up to approximately 10dB at certain frequencies between 1kHz and 2kHZ. Also, the URN levels at the 2^{nd} and 3^{rd} BPF decreased from 1 to 7 dB depending on the distance between the receiver and propeller. This interesting and novel finding suggests that the roughness can be used as the cavitation and hence URN mitigation tool.

- Similar to homogeneously distributed roughness, applying roughness heterogeneously led to a reduction in thrust and increase in torque of the Princess Royal propeller in model and full-scale. However, the substantial efficiency loss observed applying roughness homogenously was reduced considerably with the heterogeneous roughness distributions on the blades. With the same roughness length scale, the unfavourable impact of the roughness on the propeller efficiency was smaller in the full-scale propeller than that of the model-scale propeller under uniform and inclined flow conditions. The findings indicated that the cavitation volume reduction, mainly due to the TVC mitigation, was by approximately 6-38%, with a 5-10% efficiency loss in the model scale, while these figures were 4-10% and 2-5%, respectively, for the full-scale propeller under the uniform and non-uniform flow conditions.

- The detailed investigations inside the vortex showed that the roughened blade surfaces decreased the magnitude of the axial and tangential velocities inside the tip vortex. Also, the turbulent kinetic energy increased because of the momentum transfer in the presence of roughness. Thus, the pressure inside the tip vortex increased, resulting in the suppression of the TVC due to the roughness.

- Applying a uniformly distributed roughness pattern on the propeller blades provided maximum TVC mitigation. However, this also caused a substantial efficiency loss for the propeller due to the increased torque and decreased thrust. Therefore, it was concluded that the non-uniform (i.e., strategically and partially applied) distribution of the roughness was critical to minimise the efficiency loss. Hence, the suction side (or

backside) of the propeller blade tips (i.e., $0.9 \leq r/R \leq 1$) was found to be the strategically most favourable area to apply the roughness and minimise the efficiency loss.

- Applying the roughness on strategic areas on the propeller blades with optimum roughness length scale enabled considerable cavitation volume mitigation at the operating conditions where stable and well-developed TVC dynamics are present. However, when the propeller operated in a condition where the unstable TVC dynamics were present, the strategic areas on the blades should be further optimised to mitigate the cavitation volume, similar to the condition where the stable TVC was present.

- Similar to roughness application on the blades, the roughness on the propeller hub caused efficiency loss. However, the unfavourable impact of roughness applied on the hub was less than applying homogenously and heterogeneously distributed roughness on the blades. The maximum efficiency loss was found at 0.25% with respect to the smooth condition in the presence of roughness on the propeller hub.

- Akin to the change in tip vortex dynamics with the roughness, applying roughness on the hub affected the hub vortex dynamics and increased the pressure inside the hub vortex. This increased pressure resulted in a reduction of hub vortex and hub vortex cavitation up to 50% with respect to smooth conditions depending on the roughness length scale.

10 Conclusion and future works

10.1 Introduction

This final chapter aims to provide an overall review of the research study presented in the thesis to rationalise its aims and objectives, including the study's main conclusions and contributions made to the state-of-the-art subject research and recommendations for future work. Therefore, Section 10.2 presents the overall review of the subject research study emphasising its specific objectives that are justified to achieve the aim of the thesis. Next, the main conclusions are stated in Section 10.3, and the associated novelties and contributions of the research study are highlighted and rationalised in Section 10.4. Then, some recommendations for future works are presented in Section 10.5, and a list of research outputs produced and led by the author associated with the research study is given in Section 10.6. Finally, the summary of the chapter is presented in Section 10.7.

10.2 Overall review of the thesis

In this thesis, the propeller hydrodynamic performance, including cavitation, hull pressure fluctuations, and propeller URN was explored comprehensively by addressing the more realistic physics behind these phenomena, particularly URN, to achieve the main aim of the research study. The more realistic physics can be detailed by including the contribution of non-linear noise sources, accurate modelling of tip vortex flow and TVC, and the blade and hub roughness effect in full-scale conditions. The numerical investigations were carried out practically by using the commercial CFD solver, Star CCM+.

The specific objectives of the research study and a summary of the thesis chapters to achieve these objectives are listed and rationalised as in the following:

- Objective 1: To conduct a state-of-the-art literature survey related to propeller cavitation, URN and roughness by identifying the current research gaps and hence justify the aims and objectives of the study.

This first objective was addressed in Chapter 2 by performing a comprehensive critical literature review on related subjects of the thesis by surveying the state-of-art research studies conducted in the literature. The surveying enabled the author to identify the research gaps in the current literature to justify and firm the aims and objectives of the research study.

- Objective 2: To develop a CFD method for investigating the influence of grid resolution on propeller hydrodynamic and hydroacoustic performance and understanding the non-linear noise sources under non-cavitating conditions.

According to the literature survey conducted in Chapter 2, the accuracy and sensitivity of the acoustic analogy have still been explored and hence debated in the current literature for its use in combination with CFD as the application of the hybrid methods is relatively new to predict the propeller induced URN (e.g., Lidtke et al., 2019; Testa et al., 2021). Within this framework, among the different numerical parameters related to accurate propeller URN predictions using CFD, there is no specific study to explore the effects of grid resolution and non-physical numerical noise issues in the numerical solvers. Thus, this research gap in the current literature motivated the author to conduct more in-depth investigations in this field. Also, the role of non-linear noise sources, mainly represented by turbulence and vorticity, is of utmost importance for the accurate prediction of propeller URN. Although there are several research studies conducted using different numerical methods to investigate the flow details in a propeller's wake, these studies have only focussed on the dissimilarities in the propeller's wake field from the hydrodynamic point of view (e.g., Guilmineau et al., 2015; Baek et al., 2015). However, these dissimilarities, which are also important as nonlinear noise sources, have not been associated with the propeller induced URN predictions yet. Thus, this research study aimed to fill this gap by investigating the flow field, particularly the propeller's wake field (slipstream) and understanding the primary nonlinear noise sources in the propeller URN predictions by using the different eddy viscosity turbulence models. Within this context, Objective 2 was also specified and achieved in Chapter 4 by developing a CFD model to conduct the numerical calculations for a benchmark propeller operating under non-cavitating conditions. The influence of the grid resolution on propeller hydrodynamic and hydroacoustic performances was first investigated. The nonphysical numerical noise sources, changes in propeller global performance characteristics, and URN predictions were shown by using the different grid resolutions. The different eddy viscosity turbulence models were explored in order to understand the influence of the nonlinear noise sources on the overall propeller URN and the flow field around the propeller, including the propeller's wake. The relation between the change in the propeller's wake field and propeller URN predictions were examined to identify the essential nonlinear noise sources in the propeller slipstream.

- Objective 3: To develop a new advanced meshing technique to accurately solve the tip vortex flow and model the TVC emanating from all propeller blades in the propeller slipstream by an enhanced method.

As reviewed in Chapter 2, the numerical investigations conducted for modelling the propeller cavitation are generally limited with the sheet cavitation due to the modelling complexity of TVC. Although there have been recent numerical studies to model the TVC in the propeller slipstream, the computational cost of the current methods is still high (e.g., Yilmaz et al., 2019, Krasilnikov 2019); thus, a single blade is usually modelled (e.g., Lloyd et al., 2017). Modelling the single blade, extensive grid numbers and associated computational resources used in the current methods would inevitably limit expanding these techniques for complex scenarios, including full-scale propeller modelling, which is one of the aims of this thesis. Therefore, this motivated the author to develop a more computationally efficient new TVC modelling technique emanating from all propeller blades and incorporating with the propeller URN prediction method by using a commercial CFD solver to tackle the aim of this research study. Also, to the best of the author's knowledge, the influence of the different numerical methods (e.g., RANS, DES, LES) and that of some key computational prediction parameters such as grid resolution, timestep and water quality parameters (e.g., nuclei number and nuclei density) on the TVC has not been comprehensively investigated together yet. Therefore, Objective 3 was specified and achieved in Chapter 5 by developing an advanced meshing technique (i.e., V-AMR) for accurately solving the tip vortex flow and better realisation of the TVC in the propeller slipstream. Also, the capabilities of different numerical models (i.e., RANS, DES and LES) and numerical modelling parameters (i.e., grid and timestep resolution, cavitation modelling parameters, boundary layer solution) were investigated extensively to apply the developed technique for different model and full-scale propeller applications and incorporate with the propeller URN predictions. This developed V-AMR technique applied in subsequent chapters (i.e., Chapter 5 and afterwards)

- Objective 4: To develop a more accurate and basic mathematical model for investigating the propeller hydrodynamic performance, cavitation and propeller URN using CFD, including comprehensive verification and validation study for the benchmark propeller operating under uniform, inclined and non-uniform flow conditions.

To achieve Objective 4, the author developed a CFD model to combine the hydrodynamic and hydroacoustic parts to investigate the propeller hydrodynamic performance, cavitation, hull-pressure fluctuations and propeller URN, particularly for the propeller operating under cavitating conditions. As reviewed in Chapter 2, verifying and validating the numerical results with the experimental data is one of the necessary reservations of the current numerical studies in the literature, especially for propeller URN. Therefore, the access to a comprehensive model test database was the initial motivation of the author to verify and validate the propeller hydrodynamic characteristics, cavitation extensions, hull pressure fluctuations, and propeller URN. In this regard, the numerical results were verified and validated with the experimental and sea trial data through the propeller hydrodynamic performance, cavitation extensions, hull-pressure fluctuations and propeller URN for the propeller operating under uniform, inclined and non-uniform flow conditions.

- Objective 5: To apply the developed CFD methodology to a full-scale benchmark vessel at several operating conditions and validate the numerical results with the full-scale measurements.

To meet the requirements of Objective 5, the author applied the developed CFD method for the full-scale vessel (*The Princess Royal*) to show the effectiveness of the method since the full-scale propeller URN predictions are rather scarce in the literature. Therefore, Objective 5 was achieved in Chapter 7 by validating the numerical results with the full-scale measurements in terms of propeller hydrodynamic performance characteristics (i.e., torque coefficient), cavitation extensions and propeller URN in far-field where the full-scale noise data were collected during the sea trials.

- Objective 6: To explore the influence of TVC on propeller URN using the developed CFD model and advanced meshing technique in a wide range of operating conditions in model and full-scale.

Following the numerical investigations using the developed CFD methods and V-AMR technique, the author explored the influence of TVC on propeller URN. To the best of the author's knowledge, the influence of TVC on the propeller hydroacoustic performance has not been explored in detail yet using CFD methods. Therefore, Objective 6 was tackled in Chapter 8 by investigating the influence of TVC on overall propeller URN for the propeller operating under uniform, inclined and non-uniform flow conditions in model and full-scale. The numerical calculations were performed first by modelling only sheet cavitation and then the

sheet and tip vortex cavitation in combination. This provided further insight into the understanding and separating the contribution of TVC induced noise on the propeller URN in a wide range of operating conditions.

- Objective 7: To develop a CFD method of a model and full-scale propellers to investigate the effects of roughness applied on the propeller blades and hub on propeller hydrodynamic performance, cavitation and propeller URN under uniform, inclined and non-uniform flow conditions.

This last and seventh objective of this research study was addressed in Chapter 9. As the surface roughness effect is mainly explored on the hull performance, the information on the propeller hydrodynamic performance is relatively rare, while the hydroacoustic performance is non-existent, using the CFD method. This research gap, the effect of roughness on propeller hydrodynamic performance, cavitation extensions and propeller URN motivated the author to develop a CFD model to investigate the roughness at different operating conditions in the model and full-scale. The CFD method's wall function was utilised to represent roughness applied to the propeller blades and hub. The special emphasis of the roughness application was given to the performance degradation, cavitation volume, particularly tip and hub vortex cavitation, and the associated URN mitigation.

10.3 Main conclusions

The main conclusions of this research study can be summarised as follows.

- According to the numerical investigations conducted in Chapter 4, it can be concluded that accurate propeller URN prediction is strongly dependent on the grid resolution used in the numerical calculations. The grid resolution, designed specifically for propeller hydrodynamic performance predictions (i.e., thrust and torque), is not suitable for accurate propeller URN prediction. The insufficient grid resolution causes nonphysical numerical noise sources and can contaminate the overall acoustic prediction, resulting in miscalculated propeller URN levels.

- The numerical results obtained in Chapter 4 also concluded that the vortex structures as nonlinear noise sources in the propeller's wake dominate the overall propeller URN in the near and far-field. In particular, the dissimilarities in the propeller's wake cause discrepancies in the overall propeller URN at higher blade loading conditions. The break-up of the vortices and associated vortex instability are the main nonlinear noise sources that can dominate the propeller URN in the far-field.

- In order to solve the tip vortex flow accurately and model the TVC in a better way in the propeller slipstream, the advanced meshing technique (i.e., V-AMR) was developed in Chapter 5. It was found that the proposed V-AMR technique provides a better solution for tip vortex flow and associated cavitation (TVC) with a minimum computational cost. The best modelling of the TVC can be achieved using DES and LES methods due to the several disadvantages of the standard RANS methods. The V-AMR technique can be easily applied for model and full-scale propellers.

- From the numerical results obtained in Chapter 6, the propeller hydrodynamic performance characteristics, cavitation extensions, hull pressure fluctuations and propeller URN were predicted with good accuracy compared to experiments and sea trial data using the developed CFD method. The numerical results showed that the V-AMR technique could struggle to predict the weak and incipient TVC in the propeller slipstream in non-uniform flow conditions (i.e., in the presence of non-uniform wake and 3D model hull). However, based on the comprehensive validation of propeller URN data, it was found that the developed CFD method is a capable tool, in general, to predict the propeller URN under uniform and non-uniform flow conditions that present well developed TVC compared to the experimental and sea trial data.

- The numerical results obtained in Chapter 7 showed that the cavitation dynamics are predicted to be similar but with less violence (in detail) compared to full-scale observations. Also, the propeller URN predictions showed good agreement with the full-scale measurements in terms of the general trend of the noise spectrum with some discrepancies at certain frequencies. The numerical results indicated that the permeable noise surface, which encapsulates the complete hull, might capture more details related to non-linear noise sources around the hull, propeller, rudder and TVC dynamics than the permeable noise surface placed around the propeller. This resulted in a better prediction of the spectral hump contributed by the TVC dynamics.

- Based on the numerical results obtained in Chapter 8, it was concluded that the stable TVC observed in uniform flow conditions does not affect the overall propeller URN levels considerably. The numerical results showed that the contribution of TVC on overall propeller URN levels increases rapidly when the propeller operates under inclined and non-uniform flow conditions where the cavitation volume variations, significant cavitation events, and cavity collapse might be more dominant.

- From the numerical results obtained in Chapter 9, it was found that applying roughness homogenously on the propeller blades has degradation effects on propeller hydrodynamic performance, resulting in an efficiency loss. However, the results showed that roughness has a favourable impact on cavitation, particularly TVC and propeller URN. Applying roughness on the blades enables propeller URN mitigation up to 10dB at specific frequencies.

- The numerical results obtained in Chapter 9 showed that the degradation effects of roughness on propeller hydrodynamic performance could be minimised considerably by applying roughness to strategic areas on the blades. This enables a compromise between the efficiency loss and cavitation volume mitigation due to the TVC and hence the hydroacoustic propeller performance. The investigations showed that applying roughness on the hub also has favourable impacts on hub vortex cavitation mitigation. The hub vortex cavitation can be minimised up to 50% depending on the representative roughness length scale. The results highlighted that roughness on the blades and hub could be used as a passive noise control concept for silent propeller designs.

10.4 Novelties and contributions

The research study introduces several novelties and makes important contributions to the current state-of-art literature in the subject field.

To the best of the author's knowledge, the below list includes the main novelties of this research study:

- It is the first time that grid resolution has been comprehensively investigated, and its importance is shown for the accurate prediction of propeller URN. Also, a numerical technique called the time derivative of the pressure is proposed to visualise the nonphysical numerical noise sources in numerical calculations.

- Also, it is the first time that the propeller's wake field is associated with the propeller URN predictions to understand the contribution of nonlinear noise sources dominating the overall propeller URN in the far-field.

- The study presented the most computationally affordable advanced meshing technique for a better resolution of tip vortex flow and accurate realisation of the TVC in the propeller slipstream.

- The contribution of TVC to the overall propeller URN was demonstrated for the first time over a wide range of operating conditions using CFD. This further explains the interaction between the TVC and propeller URN.

- It is also the first time that the surface roughness effects on the propeller URN levels is explored using CFD.

- Similarly, the first time that roughness is applied to the hub to explore if the roughness can be used for the hub vortex cavitation mitigation using CFD.

The thesis also made several new and useful contributions to the literature in the fields of propeller hydrodynamics, hydroacoustic, cavitation and roughness, as summarised in the following:

- In Chapter 4, the developed CFD method was used to investigate the RANS method's capabilities by decreasing the numerical diffusion through the propeller URN predictions using the receivers located downstream. As the RANS method is generally blamed for insufficient extension of vortex structures in the propeller slipstream, the results can provide important knowledge for understanding the capabilities of the RANS method for the propeller URN predictions, especially for the receivers located downstream of the propeller.

- In Chapter 5, several numerical modelling parameters (i.e., grid, timestep resolution, turbulence modelling and water quality) were investigated comprehensively to develop the V-AMR technique. The findings are useful to understand the influence of these important parameters on the solution of tip vortex flow and hence TVC in the propeller slipstream.

- Chapter 6 presented the first-ever comprehensive verification and validation study in model scale, particularly for the propeller URN predictions, under uniform, inclined and non-uniform flow conditions. As the current numerical investigations have lacked verification and validation data in the relatively new applications of the CFD methods in the hydroacoustic field, the numerical results give an insight into the literature to understand the capabilities and validity of the state-of-art CFD method for predicting the propeller URN.

- In Chapter 7, the investigations were extended to the full-scale to show the effectiveness of the CFD method for predicting the propeller hydrodynamic performance, cavitation extensions and propeller URN predictions. As there are only two studies (e.g., Fujiyama and Nakashima, 2017; Li et al., 2018) in the literature investigating the cavitating propeller URN in full-scale in the presence of TVC, the comparison of the results with the sea trial data are useful to show the effectiveness of the CFD method for full-scale applications.

- In Chapter 8, the developed V-AMR technique was applied for another benchmark propeller (*The Princess Royal*) to show its capabilities in full-scale and explore the effects of TVC on propeller URN. The idea behind the change in grid size inside the vortex with respect to propeller diameter can be useful to tune the grid size for different full-scale propellers with varying diameters.

- Chapter 9 presented the numerical study investigating the effects of homogeneously and heterogeneously distributed roughness on the blades and hub on propeller hydrodynamic performance, cavitation extension and URN for the model and full-scale propellers operating under uniform and non-uniform flow conditions. The numerical findings will be useful to apply the roughness to strategic areas on the blades and hub as a passive noise control concept for mitigating the propeller URN for retrofit projects.

10.5 Recommendations for future work

Although this research study covered several research gaps in the literature, some investigations could not be carried out due to the scope, time and resource limitations that are usually inherent in a PhD study. Therefore, the following tasks can be recommended for future work to advance this research study further:

- In Chapter 5, the new V-AMR technique was developed for accurate solution of tip vortex flow and hence TVC. Although this technique successfully modelled the TVC in the propeller slipstream in a wide range of operating conditions for model and full-scale propellers, there were conditions where the incipient and weak TVC were present, and hence the technique was not as successful as applying for the well-developed TVC cases. Therefore, the technique needs to be further investigated and improved by applying it dynamically during the propeller revolutions at each physical timestep.

- The nonlinear noise sources outside the permeable noise surfaces were neglected for the propeller URN predictions in this study due to the high computational cost (i.e., Chapters 4, 6, 7, 8 and 9). Inevitably, neglecting the sources outside the permeable surfaces might create spurious noise sources, and this might be important, particularly for the receivers located downstream of the propeller. Therefore, a piece of work might be to further explore this spurious noise issue in the numerical solvers, including the non-linear noise sources outside the permeable surface or developing a practical correction method combined with the permeable FWH formulation.

- In Chapter 9, the biofouling type roughness was applied to the blades and hub to explore its effects on propeller hydrodynamic performance, cavitation extensions, and propeller URN. However, it is a well-known fact that the effect of the hull wake on the propeller performance is critical not only for propulsive efficiency but also for cavitation, vibration and URN. When one considers including the effect of the hull wake on the propulsive performance in the presence of roughness, the roughness will not only affect the propeller's performance through the propeller's open water efficiency, and it will also affect the propeller-hull interaction coefficients through the hull wake. Consequently, the roughness on the hull wake will also change the propeller advance coefficient, which inherently changes the propeller efficiency as well as the hull and relative-rotative efficiencies. As a result, the propeller's cavitation inception and cavitation patterns, propeller induced hull vibrations and the URN of the propeller will

be all affected. Therefore, it is recommended to explore propeller hydrodynamic, including cavitation and propeller hydroacoustic performance in the presence of roughened hull surface.

- In Chapter 9, applying roughness on the blades and hub enabled the mitigation of tip and hub vortex cavitation. These two types of cavitation can also cause erosion damage to the rudder. Thus, combining the roughness and developed TVC modelling with the erosion investigations is recommended. It is expected that favourable impacts of roughness applied on the blades and hub will also decrease the rudder erosion due to the tip and hub vortex cavitation. This approach can also be a practical way to mitigate rudder erosion, similar to propeller URN, for retrofit projects.

10.6 Research outputs

Finally, the author published the following peer-reviewed journal and international conference papers in association with the research conducted in this thesis during the course of his PhD study.

Peer-reviewed journal papers (SCI/ SCI-Expanded):

1. Sezen, S., Atlar, M., Fitzsimmons, P., Sasaki, N., Tani, G., Yilmaz, N., Aktas, B., 2020. Numerical cavitation noise prediction of a benchmark research vessel propeller. Ocean Engineering. 211, 107549. https://doi.org/10.1016/j.oceaneng.2020.107549
2. Sezen, S., Cosgun, T., Yurtseven, A., Atlar, M., 2020. Numerical investigation of marine propeller underwater radiated noise using acoustic analogy part 2: The influence of eddy viscosity turbulence models. Ocean Engineering. 220, 108353. https://doi.org/10.1016/j.oceaneng.2020.108353
3. Sezen, S., Cosgun, T., Yurtseven, A., Atlar, M., 2021. Numerical investigation of marine propeller underwater radiated noise using acoustic analogy part 1: The influence of grid resolution. Ocean Engineering. 220, 108448. https://doi.org/10.1016/j.oceaneng.2020.108448
4. Sezen, S., Atlar, M., 2021. An alternative Vorticity based Adaptive Mesh Refinement (V-AMR) technique for tip vortex cavitation modelling of propellers using CFD methods. Ship Technology Research, Vol. 69, Issue 1. https://doi.org/10.1080/09377255.2021.1927590

5. Sezen, S., Atlar, M., Fitzsimmons, P., 2021. Prediction of cavitating propeller underwater radiated noise using RANS & DES-based hybrid method. Ships and Offshore Structures, Vol. 16, No. S1, pp.S93–S105 https://doi.org/10.1080/17445302.2021.1907071
6. Sezen, S., Uzun, D., Ozyurt, R., Turan, O., Atlar, M., 2021. Effect of biofouling roughness on a marine propeller's performance, including cavitation and underwater radiated noise (URN). Applied Ocean Research. 107, 102491. https://doi.org/10.1016/j.apor.2020.102491
7. Sezen, S., Uzun, D., Turan, O., Atlar, M., 2021. Influence of roughness on propeller performance with a view to mitigating tip vortex cavitation. Ocean Engineerng. 239, 109703. https://doi.org/10.1016/J.OCEANENG.2021.109703

International conference papers:

1. Sezen, S., Atlar, M., Fitzsimmons, P., Sasaki, N., Tani, G., Yilmaz, N., Aktas, B., 2019. Numerical cavitation noise prediction of a benchmark research vessel propeller. The Sixth International Conference on Advanced Model Measurement Technology for The Maritime Industry (AMT), Rome, Italy
2. Sezen, S, Atlar, M., Fitzsimmons, P., 2020. Prediction of Cavitating Propeller Underwater Radiated Noise using RANS & DES-based Hybrid Method, International Conference on Ships and Offshore Structures (ICSOS), Glasgow, UK.
3. Sezen, S., Aktas, B., Atlar, M., Fitzsimmons, P., 2021. Numerical Investigation of Full-Scale Cavitating Propeller Underwater Radiated Noise, International Symposium on Cavitation (CAV2021), Daejeon, Korea.

10.7 Chapter summary

This chapter presented an overall review of the research study conducted in the thesis to rationalise its aims and objectives, including the study's main conclusions, novelties and contributions made to the state-of-the-art subject research field and the recommendations for future work.

References

Abe, K., Kondoh, T., Nagano, Y., 1994. A new turbulence model for predicting fluid flow and heat transfer in separating and reattaching flows-I. Flow field calculations. Int. J. Heat Mass Transf. 37, 139–151. https://doi.org/10.1016/0017-9310(94)90168-6

Abrahamsen, K., 2012. The ship as an underwater noise source, in: Proceedings of Meetings on Acoustics. Edinburgh, UK. https://doi.org/10.1121/1.4772953

ABS, 2013. Ship energy efficiency measures advisory. American Bureau of Shipping Houston.

Aktas, B., Atlar, M., Fitzsimmons, P., Shi, W., 2018. An advanced joint time-frequency analysis procedure to study cavitation-induced noise by using standard series propeller data. Ocean Eng. 170, 329–350. https://doi.org/10.1016/j.oceaneng.2018.10.026

Aktas, B., Atlar, M., Turkmen, S., Korkut, E., Fitzsimmons, P., 2016a. Systematic cavitation tunnel tests of a Propeller in uniform and inclined flow conditions as part of a round robin test campaign. Ocean Eng. 120, 136–151. https://doi.org/10.1016/j.oceaneng.2015.12.015

Aktas, B., Atlar, M., Turkmen, S., Shi, W., Sampson, R., Korkut, E., Fitzsimmons, P., 2016b. Propeller cavitation noise investigations of a research vessel using medium size cavitation tunnel tests and full-scale trials. Ocean Eng. 120, 122–135. https://doi.org/10.1016/j.oceaneng.2015.12.040

Aktas, B., Yilmaz, N., Atlar, M., Sasaki, N., Fitzsimmons, P., Taylor, D., 2020. Suppression of tip vortex cavitation noise of propellers using pressurepores technology. J. Mar. Sci. Eng. 8. https://doi.org/10.3390/jmse8030158

AMT'11, 2011. 2nd International Conference on Advanced Model Measurement Technology for the EU Maritime Industry, in: AMT'11,. Newcastle University, Newcastle Upon Tyne.

Anderson, C., Atlar, M., Callow, M., Candries, M., Milne, A., Townsin, R., 2003. The development of foul-release coatings for seagoing vessels. Proc. Inst. Mar. Eng. Sci. Technol. Part B J. Mar. Des. Oper. 4, 11–23.

Andersson, J., Oliveira, D.R., Yeginbayeva, I., Leer-Andersen, M., Bensow, R.E., 2020. Review and comparison of methods to model ship hull roughness. Appl. Ocean Res. 99. https://doi.org/10.1016/j.apor.2020.102119

AQUO, 2012. Achieve Quiter Oceans by shipping noise footprint reduction. 7th framework program, Grant agreement ID: 314227.

Asnaghi, A., 2018. Computational Modelling for Cavitation and Tip Vortex Flows. PhD Thesis, Department of Mechanics and Maritime Sciences, Chalmers University of Technology.

Asnaghi, A., Svennberg, U., Bensow, R.E., 2020a. Large Eddy Simulations of cavitating tip vortex flows. Ocean Eng. 195, 106703. https://doi.org/10.1016/J.OCEANENG.2019.106703

Asnaghi, A., Svennberg, U., Gustafsson, R., Bensow, R.E., 2021. Propeller tip vortex mitigation by roughness application. Appl. Ocean Res. 106, 102449. https://doi.org/10.1016/J.APOR.2020.102449

Asnaghi, A., Svennberg, U., Gustafsson, R., Bensow, R.E., 2020b. Investigations of tip vortex mitigation by using roughness. Phys. Fluids 32, 065111. https://doi.org/10.1063/5.0009622

Asnaghi, A., Svennberg, U., Gustafsson, R., Bensow, R.E., 2019. Roughness Effects on the Tip Vortex Strength and Cavitation Inception, in: Sixth International Symposium on Marine Propulsors,SMP'19. Rome, Italy.

Astolfi, J.A., Billard, J.Y., Dorange, P., Fruman, D.H., 1998. Pressure fluctuations associated with tip vortex and surface cavitation, in: Proceedings of the ASME Fluids Engineering Division Summer Meeting. Washington, DC, USA.

Atlar, M., 2008. An update on marine antifouling, 25th ITTC Group Discussions 3- Global Warming and Impact on ITTC Activities. Fukuoka, Japan.

Atlar, M., Aktas, B., Samspon, R., Fitzsimmons, P., Fetherstonhaug, C., 2013. A multi-purpose marine science and technology research vessel for full-scale observations and measurements, in: 3rd International Conference on Advanced Model Measurement Technologies for the Marine Industry, AMT`13. Gdansk, Poland.

Atlar, M., Glover, E., Candries, M., Mutton, R., Anderson, C., 2002. The effect of a foul release coating on propeller performance, in: Conference Proceedings Environmental Sustainability (ENSUS). pp. 16–18.

Atlar, M., Mutton, R., Glover, E.J., Anderson, C.D., 2003. Calculation of the effects of new generation coatings on high speed propeller performance, in: 2nd International Warship Cathodic Protection Symposium and Equipment Exhibition. Newcastle University.

Atlar, M., Takinaci, A.C., Korkut, E., 1998. On the Efficiency and Cavitation Performance of

a Propeller with Different Boss Caps, in: International Symposium Honouring Tarik SABUNCU On the Occasion of His 75th Birthday, Istanbul Technical University. Istanbul, Turkey.

Baek, D.G., Yoon, H.S., Jung, J.H., Kim, K.S., Paik, B.G., 2015. Effects of the advance ratio on the evolution of a propeller wake. Comput. Fluids 118, 32–43. https://doi.org/10.1016/J.COMPFLUID.2015.06.010

Bagheri, M.R., Seif, M.S., Mehdigholi, H., Yaakob, O., 2017. Analysis of noise behaviour for marine propellers under cavitating and non-cavitating conditions. Ships Offshore Struct. 12, 1–8. https://doi.org/10.1080/17445302.2015.1099224

Barker, S.J., 1976. Measurements of hydrodynamic noise from submerged hydrofoils. J. Acoust. Soc. Am. 59, 1095. https://doi.org/10.1121/1.380963

Bensow, R.E., 2011. Simulation of the unsteady cavitation on the the Delft Twist11 foil using RANS, DES and LES, in: Second International Symposium on Marine Propulsors, SMP'11. Hamburg, Germany.

Bensow, R.E., Bark, G., 2010. Implicit LES predictions of the cavitating flow on a propeller. J. Fluids Eng. Trans. ASME 132, 0413021–04130210. https://doi.org/10.1115/1.4001342

Bensow, R.E., Liefvendahl, M., 2016. An acoustic analogy and scale-resolving flow simulation methodology for the prediction of propeller radiated noise, in: 31st Symposium on Naval Hydrodynamics. Monterey, California, USA, pp. 1–19.

Bosschers, J., 2018. Propeller tip-vortex cavitation and its broadband noise. PhD Thesis, University of Twente, Enschede, Netherlands.

Brentner, K.S., Farassat, F., 2003. Modeling aerodynamically generated sound of helicopter rotors. Prog. Aerosp. Sci. 39, 83–120. https://doi.org/10.1016/S0376-0421(02)00068-4

Brooker, A., Humphrey, V., 2016. Measurement of radiated underwater noise from a small research vessel in shallow water. Ocean Eng. 120, 182–189. https://doi.org/10.1016/j.oceaneng.2015.09.048

Brooker, A., Humphrey, V., 2014. Measurement of Radiated Underwater Noise from a Small Research Vessel in Shallow Water, in: A. Yücel Odabaşı Colloquium Series 1st International Meeting on Propeller Noise and Vibration. Istanbul, Turkey.

Bulat, M.P., Bulat, P.V., 2013. Comparison of turbulence models in the calculation of

supersonic separated flows. World Appl. Sci. J. 27, 1263–1266. https://doi.org/10.5829/idosi.wasj.2013.27.10.13715

Calcagno, G., Di Felice, F., Felli, M., Franchi, S., Pereira, F.J.A., Salvatore, S., 2003. The INSEAN E779a Propeller Test Case: a Database For CFD Validation, in: Proc. of MARNET-CFD Final Workshop. Rome, Italy.

Carlton, J., 2018. Marine Propellers and Propulsion - 4th Edition. Butterworth-Heinemann.

Cazzoli, G., Falfari, S., Bianchi, G.M., Forte, C., Catellani, C., 2016. Assessment of the Cavitation Models Implemented in OpenFOAM® under DI-like Conditions, in: Energy Procedia. Elsevier Ltd, pp. 638–645. https://doi.org/10.1016/j.egypro.2016.11.081

Celik, I.B., Ghia, U., Roache, P.J., Freitas, C.J., Coleman, H., Raad, P.E., 2008. Procedure for estimation and reporting of uncertainty due to discretization in CFD applications. J. Fluids Eng. Trans. ASME 130, 0780011–0780014. https://doi.org/10.1115/1.2960953

Chahine, G.L., Frederick, G.F., Bateman, R.D., 1993. Propeller tip vortex cavitation suppression using selective polymer injection. J. Fluids Eng. Trans. ASME 115, 497–503. https://doi.org/10.1115/1.2910166

Chekab, A.F.M., Gadimi, P., Djeddi, S.R., Soroushan, M., 2013. Investigation of Different Methods of Noise Reduction for Submerged Marine Propellers and Their Classification. Am. J. Mech. Eng. 1, 34–42. https://doi.org/10.12691/ajme-1-2-3

Chou, E., Southall, B.L., Robards, M., Rosenbaum, H.C., 2021. International policy, recommendations, actions and mitigation efforts of anthropogenic underwater noise. Ocean Coast. Manag. 202, 105427. https://doi.org/10.1016/J.OCECOAMAN.2020.105427

Cianferra, M., Petronio, A., Armenio, V., 2019. Non-linear noise from a ship propeller in open sea condition. Ocean Eng. 191. https://doi.org/10.1016/j.oceaneng.2019.106474

Colebrook, C.F., 1939. Turbulent Flow in Pipes, with particular reference to the transition region between the smooth and rough pipe laws. J. Inst. Civ. Eng. 11, 133–156. https://doi.org/10.1680/ijoti.1939.13150

Cong, W.W., Wang, K., Jiang, J.M., Yu, X.Y., Zhang, H.Q., Guo, Y.D., Lv, Z., Gui, T.J., 2019. An experimental investigation of the composite coating for marine propellers on cavitation characteristics and fouling release property, in: IOP Conference Series: Materials Science and Engineering. p. 012030. https://doi.org/10.1088/1757-

899X/504/1/012030

Craft, T.J., Gerasimov, A. V., Iacovides, H., Launder, B.E., 2002. Progress in the generalization of wall-function treatments. Int. J. Heat Fluid Flow 23, 148–160. https://doi.org/10.1016/S0142-727X(01)00143-6

Cruz, E., Lloyd, T., Bosschers, J., Lafeber, F.H., Vinagre, P., Vaz, G., 2021. Study on inventory of existing policy, research and impacts of continuous underwater noise in Europe. EMSA report EMSA/NEG/21/2020, WavEC Offshore Renewables and Maritime Research Institute Netherlands.

Curle, N., 1955. The influence of solid boundaries upon aerodynamic sound. Proc. R. Soc. London. Ser. A. Math. Phys. Sci. 231, 505–514. https://doi.org/10.1098/rspa.1955.0191

Davidson, L., Nielsen, P. V, Sveningsson, A., 2003. Modification of the v2f model for computing the flow in a 3D wall jet. Turbulence, in: Proceedings of the International Symposium on Turbulence, Heat and Mass Transfer. Begell House, October 12 - 17, Antalya, Turkey.

Defraeye, T., Blocken, B., Koninckx, E., Hespel, P., Carmeliet, J., 2011. Computational fluid dynamics analysis of drag and convective heat transfer of individual body segments for different cyclist positions. J. Biomech. 44, 1695–1701. https://doi.org/10.1016/j.jbiomech.2011.03.035

Demirel, Y.K., Uzun, D., Zhang, Y., Fang, H.-C., Day, A.H., Turan, O., 2017. Effect of barnacle fouling on ship resistance and powering. Biofouling 33, 819–834. https://doi.org/10.1080/08927014.2017.1373279

Di Francescantonio, P., 1997. A new boundary integral formulation for the prediction of sound radiation. J. Sound Vib. 202, 491–509. https://doi.org/10.1006/jsvi.1996.0843

DNV, 2010. Rules for Classification of Ships, New Buildings, Part 6 Chapter 24.

Duraisamy, K., Baeder, J.D., 2006. Numerical simulation of the effects of spanwise blowing on tip vortex formation. J. Aircr. 43, 996–1006. https://doi.org/10.2514/1.19746

Durbin, P.A., 1991. Near-wall turbulence closure modeling without “damping functions.” Theor. Comput. Fluid Dyn. 3, 1–13. https://doi.org/10.1007/BF00271513

Epps, B.P., 2017. Review of vortex identification methods, in: AIAA SciTech Forum - 55th AIAA Aerospace Sciences Meeting. American Institute of Aeronautics and Astronautics

Inc. https://doi.org/10.2514/6.2017-0989

Erbe, C., Marley, S.A., Schoeman, R.P., Smith, J.N., Trigg, L.E., Embling, C.B., 2019. The Effects of Ship Noise on Marine Mammals—A Review. Front. Mar. Sci. 6, 606. https://doi.org/10.3389/FMARS.2019.00606

Farassat, F., 2007. Derivation of Formulations 1 and 1A of Farassat, in: NASA/TM-2007-214853. pp. 1–25.

Feder, D.-F., Abdel-Maksoud, M., 2016. Tracking a Tip Vortex with Adaptive Vorticity Confinement and Hybrid RANS-LES. Open J. Fluid Dyn. 06, 406–429. https://doi.org/10.4236/ojfd.2016.64030

Felli, M., Camussi, R., Di Felice, F., 2011. Mechanisms of evolution of the propeller wake in the transition and far fields. J. Fluid Mech. 682, 5–53. https://doi.org/10.1017/jfm.2011.150

Felli, M., Di Felice, F., Guj, G., Camussi, R., 2006. Analysis of the propeller wake evolution by pressure and velocity phase measurements. Exp. Fluids 41, 441–451. https://doi.org/10.1007/s00348-006-0171-4

Felli, M., Falchi, M., Grizzi, S., Mauro, L., Orrico, M., 2014. Suppression of Underwater Noise Induced by Cavitation (SONIC), Deliverable: D1.3-CNR INSEAN, FP7-SONIC Project Report, Grant Agreement No: 314394, December.

Ffowcs Williams, J., 1992. Noise source mechanisms, in: Modern Methods in Analytical Acoustics. Lecture Notes. Springer, Berlin, pp. 313–354.

Ffowcs Williams, J.H., Hawkings, D.L., 1969. Sound generation by turbulence and surfaces in arbitrary motion. Philos. Trans. R. Soc. London. Ser. A, Math. Phys. Sci. 264, 321–342. https://doi.org/10.1098/rsta.1969.0031

Fine, N.E., Kinnas, S.A., 1993. A boundary element method for the analysis of the flow around 3-D cavitating hydrofoils. J. Sh. Res. 37, 213–224.

Flack, K.A., Schultz, M.P., 2010. Review of hydraulic roughness scales in the fully rough regime. J. Fluids Eng. Trans. ASME 132, 0412031–04120310. https://doi.org/10.1115/1.4001492

Fruman, D.H., Aflalo, S.S., 1989. Tip vortex cavitation inhibition by drag-reducing polymer solutions. J. Fluids Eng. Trans. ASME 111, 211–216. https://doi.org/10.1115/1.3243625

Fujiyama, K., 2015. Numerical Simulation of Ship Hull Pressure Fluctuation Induced by Cavitation on Propeller with Capturing the Tip Vortex, in: Fourth International Symposium on Cavitation, CAV2001. Austin, Texas, USA.

Fujiyama, K., Nakashima, Y., 2017. Numerical Prediction of Acoustic Noise Level Induced by Cavitation on Ship Propeller at Behind-Hull Condition, in: Fifth International Symposium on Marine Propulsion, SMP'17. Espoo, Finland.

Gaggero, S., Martinelli, M., 2021. Comparison of different propeller boss cap fins design for improved propeller performances. Appl. Ocean Res. 116, 102867. https://doi.org/10.1016/J.APOR.2021.102867

Gaggero, S., Tani, G., Viviani, M., Conti, F., 2014. A study on the numerical prediction of propellers cavitating tip vortex. Ocean Eng. 92, 137–161. https://doi.org/10.1016/j.oceaneng.2014.09.042

Gaggero, S., Villa, D., 2016. Steady cavitating propeller performance by using OpenFOAM, StarCCM+and a boundary element method: Proc. Inst. Mech. Eng. Part M J. Eng. Marit. Environ. 231, 411–440. https://doi.org/10.1177/1475090216644280

Ge, M., Svennberg, U., Bensow, R.E., 2020. Investigation on RANS prediction of propeller induced pressure pulses and sheet-tip cavitation interactions in behind hull condition. Ocean Eng. 209, 107503. https://doi.org/10.1016/j.oceaneng.2020.107503

Ghassemi, H., Mardan, A., Ardeshir, A., 2012. Numerical analysis of hub effect on hydrodynamic performance of propellers with inclusion of PBCF to equalize the induced velocity. Polish Marit. Res. 19, 17–24. https://doi.org/10.2478/V10012-012-0010-X

Glover, E.J., 1987. Propulsive devices for improved propulsive efficiency. Inst. Mar. Eng. Trans. 99.

Goncalves, E., Decaix, J., Patella, R.F., 2010. Unsteady simulation of cavitating flows in Venturi, in: Journal of Hydrodynamics. China Ocean Press, pp. 753–758. https://doi.org/10.1016/S1001-6058(10)60026-1

Granville, P.S., 1978. Similarity-law characterization methods for arbitrary hydrodynamic roughnesses. Dawid W Taylor Naval Ship Reserach and Development Center, Bethesda, MD. Ship Performance Dept.

Grigson, C., 1992. Drag Losses of New Ships Caused by Hull Finish. J. Sh. Res. 36, 182–196.

Guilmineau, E., Deng, G.B., Leroyer, A., Queutey, P., Visonneau, M., Wackers, J., 2015. Influence of the Turbulence Closures for the Wake Prediction of a Marine Propeller, in: Fourth International Symposium on Marine Propulsors, SMP'15. Austin, Texas, USA.

Hallander, J., Li, D.-Q., Allenstrom, B., Valdenazzi, F., Barras, C., 2012. Predicting Underwater Radiated Noise Due to a Cavitating Propeller in a Ship Wake, in: Proceedings of the 8th International Symposium on Cavitation - CAV2012. Singapore, pp. 1–7.

Higuchi, H., Arndt, R.E.A., Rogers, M.F., 1989. Characteristics of tip vortex cavitation noise, in: Journal of Fluids Engineering, Transactions of the ASME. pp. 495–501. https://doi.org/10.1115/1.3243674

Hildebrand, J.A., 2009. Anthropogenic and natural sources of ambient noise in the ocean. Mar. Ecol. Prog. Ser. 395, 5–20. https://doi.org/10.3354/meps08353

Hirt, C.W., Nichols, B.D., 1981. Volume of fluid (VOF) method for the dynamics of free boundaries. J. Comput. Phys. 39, 201–225. https://doi.org/10.1016/0021-9991(81)90145-5

Hsiao, C.-T., Chahine, G., 2008. Scaling of Tip Vortex Cavitation Inception for a Marine Open Propeller, in: 27th Symposium on Naval Hydrodynamics. Seoul, Korea.

Humphrey, V.F., Brooker, A., 2019. Variability of radiated underwater noise measurements for a small research vessel in shallow water. J. Acoust. Soc. Am. 146, 3061–3061. https://doi.org/10.1121/1.5137625

Hunt, J.C.R., Wray, A.A., Moin, P., 1988. Eddies, streams, and convergence zones in turbulent flows. Cent. Turbul. Res. Proc. Summer Progr. 193–208. https://doi.org/https://doi.org/CTR-S88

Ianniello, S., De Bernardis, E., 2015. Farassat's formulations in marine propeller hydroacoustics. Int. J. aeroacoustics 14, 87–103.

Ianniello, S., Muscari, R., Di Mascio, A., 2014a. Ship underwater noise assessment by the Acoustic Analogy part II: Hydroacoustic analysis of a ship scaled model. J. Mar. Sci. Technol. 19, 52–74. https://doi.org/10.1007/s00773-013-0236-z

Ianniello, S., Muscari, R., Di Mascio, A., 2014b. Ship underwater noise assessment by the acoustic analogy, part III: Measurements versus numerical predictions on a full-scale ship. J. Mar. Sci. Technol. 19, 125–142. https://doi.org/10.1007/s00773-013-0228-z

Ianniello, S., Muscari, R., Di Mascio, A., 2013. Ship underwater noise assessment by the acoustic analogy. Part I: Nonlinear analysis of a marine propeller in a uniform flow. J. Mar. Sci. Technol. 18, 547–570. https://doi.org/10.1007/s00773-013-0227-0

Ianniello, S., Muscari, R., Mascio, A.D., 2012. Hydroacoustic characterization of a marine propeller through the acoustic analogy. Sustain. Marit. Transp. Exploit. Sea Resour. 991–1000.

Ikeda, T., Enomoto, S., Yamamoto, K., Amemiya, K., 2017. Quadrupole Corrections for the Permeable-Surface Ffowcs Williams–Hawkings Equation. AIAA 55, 2307–2320. https://doi.org/10.2514/1.J055328

IMO, 2014. MEPC.1/Circ.833: Guidelines for the Reduction of Underwater Noise from Commercial Shipping to Address Adverse Impacts on Marine Life.

ITTC, 2017a. The Specialist Committee on Hydrodynamic Noise, Final Report and Recommendations to the 28th ITTC-Volume II. Wuxu, China.

ITTC, 2017b. Model-Scale Propeller Cavitation Noise Measurements 7.5-02-01-05.

ITTC, 2014. 27th ITTC Specialist Committee on Hydrodynamic Noise, Noise Discussion Forms.

ITTC, 2011. Specialist Committee on Surface Treatment–Final report and recommendations to the 26th ITTC. Proc. 26th ITTC–Volume II 419–481.

ITTC, 2008. Recommended Procedures and Guidelines, Uncertainty Analysis in CFD Verification and Validation Methodology and Procedures (7.5-03-01-04).

ITTC, 2002a. Testing and Extrapolation Methods Propulsion; Cavitation Description of Cavitation Appearances 7.5 0203-03.2.

ITTC, 2002b. The Specialist Committee on Water Quality and Cavitation, Proceedings of the 23rd ITTC, Volume II.

ITTC, 1999. ITTC-recommended procedures and guidelines 7.5-03.01-0.4, CFD-general CFD verification.

Jang, C.M., Furukawa, M., Inoue, M., 2001. Analysis of vortical flow field in a propeller fan by LDV measurements and LES—Part II: Unsteady nature of vortical flow structures due to tip vortex breakdown. J. Fluids Eng. Trans. ASME 123, 755–761. https://doi.org/10.1115/1.1412566

Jeong, J., Hussain, F., 1995. On the identification of a vortex. J. Fluid Mech. 285, 69–94. https://doi.org/10.1017/S0022112095000462

Ji, B., Luo, X., Wu, Y., Peng, X., Xu, H., 2012. Partially-Averaged Navier–Stokes method with modified k–ε model for cavitating flow around a marine propeller in a non-uniform wake. Int. J. Heat Mass Transf. 55, 6582–6588. https://doi.org/10.1016/J.IJHEATMASSTRANSFER.2012.06.065

Johnsson, C.A., Rutgersson, O., 1991. Leading edge roughness- a way to improve propeller tip vortex cavitation, in: Propeller Shafting Symposium. Virginia Beach, VA, USA, pp. 1–12.

Jonas, D.A., Clarke, D.B., 2010. Fluent code simulation of flow around a naval hull: the DTMB 5415. Maritime Platforms Division Defence Science and Technology Organisation, Report Number: DSTO-TR-2465.

Kanemaru, T., Ando, J., 2013. Numerical analysis of cavitating propeller and pressure fluctuation on ship stern using a simple surface panel method "SQCM." J. Mar. Sci. Technol. 18, 294–309. https://doi.org/10.1007/S00773-012-0208-8/FIGURES/36

Katz, J., Galdo, J.B., 1989. Effect of roughness on rollup of tip vortices on a rectangular hydrofoil. J. Aircr. 26, 247–253. https://doi.org/10.2514/3.45753

Kawamura, T., Ouchi, K., Nojiri, T., 2012. Model and full scale CFD analysis of propeller boss cap fins (PBCF). J. Mar. Sci. Technol. 17, 469–480. https://doi.org/10.1007/S00773-012-0181-2

Kellett, P., Turan, O., Incecik, A., 2013. A study of numerical ship underwater noise prediction. Ocean Eng. 66, 113–120. https://doi.org/10.1016/j.oceaneng.2013.04.006

Kim, S.E., Rhee, S., 2004. Toward high-fidelity prediction of tip-vortex around lifting surfaces—what does it take, in: 25th Symposium on Naval Hydrodynamics. St John`s, Newfoundland, Canada, pp. 62–70.

Kimmerl, J., Mertes, P., Abdel-Maksoud, M., 2021a. Application of Large Eddy Simulation to Predict Underwater Noise of Marine Propulsors. Part 1: Cavitation Dynamics. J. Mar. Sci. Eng. 2021, Vol. 9, Page 792 9, 792. https://doi.org/10.3390/JMSE9080792

Kimmerl, J., Mertes, P., Abdel-Maksoud, M., 2021b. Application of Large Eddy Simulation to Predict Underwater Noise of Marine Propulsors. Part 2: Noise Generation. J. Mar. Sci. Eng. 2021, Vol. 9, Page 778 9, 778. https://doi.org/10.3390/JMSE9070778

Kolář, V., 2007. Vortex identification: New requirements and limitations. Int. J. Heat Fluid Flow 28, 638–652. https://doi.org/10.1016/j.ijheatfluidflow.2007.03.004

Konno, A., Wakabayashi, K., Yamaguchi, H., Maeda, M., Ishii, N., Soejima, S., Kimura, K., 2002. On the mechanism of the bursting phenomena of propeller tip vortex cavitation. J. Mar. Sci. Technol. 6, 181–192. https://doi.org/10.1007/s007730200006

Korkut, E., Atlar, M., 2012. An experimental investigation of the effect of foul release coating application on performance, noise and cavitation characteristics of marine propellers. Ocean Eng. 41, 1–12. https://doi.org/10.1016/j.oceaneng.2011.12.012

Korkut, E., Takinaci, A.C., 2013. 18M Research Vessel Wake Measurements, Faculty of Naval Architecture and Ocean Engineering, Istanbul Technical University. Istanbul, Turkey.

Kowalczyk, S., Felicjancik, J., 2016. Numerical and experimental propeller noise investigations. Ocean Eng. 120, 108–115. https://doi.org/10.1016/j.oceaneng.2016.01.032

Krasilnikov, V., 2019. CFD modelling of hydro-acoustic performance of marine propellers: Predicting propeller cavitation, in: Numerical Towing Tank Symposium, NuTTS'2019. Tomar, Portugal.

Krüger, C., Kornev, N., Greitsch, L., 2016. Influence of propeller tip roughness on tip vortex strength and propeller performance. Sh. Technol. Res. 63, 110–120. https://doi.org/10.1080/09377255.2016.1205293

Kuiper, G., 1981. Cavitation inception on ship ship propeller models. PhD Thesis, Delft University of Technology.

Kumar, P., Mahesh, K., 2017. Large eddy simulation of propeller wake instabilities. J. Fluid Mech. 814, 361–396. https://doi.org/10.1017/JFM.2017.20

Lafeber, F.H., Bosschers, J., Van Wijngaarden, E., 2015. Computational and experimental prediction of propeller cavitation noise. MTS/IEEE Ocean. 2015 - Genova Discov. Sustain. Ocean Energy a New World. https://doi.org/10.1109/OCEANS-GENOVA.2015.7271654

Launder, B.E., Sharma, B.I., 1974. Application of the energy-dissipation model of turbulence to the calculation of flow near a spinning disc. Lett. Heat Mass Transf. 1, 131–137. https://doi.org/10.1016/0094-4548(74)90150-7

Leaper, R., Renilson, M., Ryan, C., 2014. Reducing underwater noise from large commercial ships: Current status and future directions. J. Ocean Technol. 9, 51–69.

Lee, H., Kinnas, S.A., 2004. Application of a boundary element method in the prediction of unsteady blade sheet and developed tip vortex cavitation on marine propellers. J. Sh. Res. 48, 15–30.

Li, D.-Q., Hallander, J., Johansson, T., Karlsson, R., 2015. Cavitation Dynamics and Underwater Radiated Noise Signature of a Ship with a cavitating propeller, in: VI International Conference on Computational Methods in Marine Engineering MARINE 2015. Rome, Italy.

Li, D.Q., Hallander, J., Johansson, T., 2018. Predicting underwater radiated noise of a full scale ship with model testing and numerical methods. Ocean Eng. 161, 121–135. https://doi.org/10.1016/j.oceaneng.2018.03.027

Lidtke, A.K., 2017. Predicting radiated noise of marine propellers using acoustic analogies and hybrid Eulerian-Lagrangian cavitation models, PhD Thesis. University of Southampton.

Lidtke, A.K., Humphrey, V.F., Turnock, S.R., 2016. Feasibility study into a computational approach for marine propeller noise and cavitation modelling. Ocean Eng. 120, 152–159. https://doi.org/10.1016/j.oceaneng.2015.11.019

Lidtke, A.K., Lloyd, T., Vaz, G., 2019. Acoustic modelling of a propeller subject to non-uniform inflow, in: Sixth International Symposium on Marine Propulsors, SMP'2019. Rome, Italy.

Lidtke, A.K., Turnock, S.R., Humphrey, V.F., 2015. Use of acoustic analogy for marine propeller noise characterisation, in: Fourth International Symposium on Marine Propulsors SMP'15. Austin, Texas, USA.

Lighthill, M.J., 1952. On sound generated aerodynamically I. General theory. Proc. R. Soc. London. Ser. A. Math. Phys. Sci. 211, 564–587. https://doi.org/10.1098/rspa.1952.0060

Lloyd, T., Vaz, G., Rijpkema, D., Reverberi, A., 2017. Computational fluid dynamics prediction of marine propeller cavitation including solution verification, in: Fifth International Symposium on Marine Propulsors, SMP'17. Espoo, Finland.

Lloyd, T.P., Lidtke, A.K., Rijpkema, D., Van Wijngaarden, E., Turnock, S.R., Humphrey, V.F., 2015a. Using the FW-H equation for hydroacoustics of propellers, in: 18th Numerical Towing Tank Symposium (NuTTS). Cortona, Italy.

Lloyd, T.P., Rijpkema, D., Wijngaarden, E. Van, 2015b. Marine propeller acoustic modelling: comparing CFD results with an acoustic analogy method, in: 4th International Symposium on Cavitation, CAV2001.

Lloyd, T.P., Rijpkema, D.R., van Wijngaarden, E., 2014. Implementing the Ffowcs Williams-Hawkings acoustic analogy into a viscous CFD solver. 17th Numer. Towing Tank Symp. (NuTTS),Marstrand, Sweden.

Luo, J., Razinsky, E.H., 2008. Conjugate Heat Transfer Analysis of a Cooled Turbine Vane Using the V2F Turbulence Model. ASME Turbo Expo 2006 Power Land, Sea, Air, Am. Soc. Mech. Eng. Digit. Collect. pp. 865–875. https://doi.org/https://doi.org/10.1115/GT2006-91109

Lyrintzis, A.S., 2003. Surface Integral Methods in Computational Aeroacoustics—From the (CFD) Near-Field to the (Acoustic) Far-Field. Int. J. Aeroacoustics 2, 95–128. https://doi.org/10.1260/147547203322775498

Maines, B., Arndt, R.E.A., 1997. The Case of the Singing Vortex. J. Fluids Eng. 119, 271–276. https://doi.org/10.1115/1.2819130

Menter, F.R., 1994. Two-equation eddy-viscosity turbulence models for engineering applications. AIAA J. 32, 1598–1605. https://doi.org/10.2514/3.12149

Mizzi, K., Demirel, Y.K., Banks, C., Turan, O., Kaklis, P., Atlar, M., 2017. Design optimisation of Propeller Boss Cap Fins for enhanced propeller performance. Appl. Ocean Res. 62, 210–222. https://doi.org/10.1016/J.APOR.2016.12.006

Mosaad, M.A.A.-R., 1986. Marine propeller roughness penalties, PhD thesis. Newcastle University.

Moussa, K., 2014. Computational Modeling of Propeller Noise NASA SR-7A, Master Thesis. Waterloo, Ontario, Canada.

Muscari, R., Di Mascio, A., Verzicco, R., 2013. Modeling of vortex dynamics in the wake of a marine propeller. Comput. Fluids 73, 65–79. https://doi.org/10.1016/j.compfluid.2012.12.003

Najafi-Yazdi, A., Brés, G.A., Mongeau, L., 2011. An acoustic analogy formulation for moving sources in uniformly moving media. Proc. R. Soc. A Math. Phys. Eng. Sci. 467, 144–165. https://doi.org/10.1098/rspa.2010.0172

Nitzkorski, Z., 2015. A novel porous Ffowcs-Williams and Hawkings acoustic methodology for complex geometries, PhD thesis, Faculty of the Graduate School of the University of Minnesota.

Ouchi, K., 1992. Effect and Application of PBCF (Propeller Boss Cap Fins). J. MESJ 27(9), 768–778.

Ouchi, K., Ogura, M., Kono, Y., Orito, H., Shiotsu, T., Tamashima, M., Koizuka, H., 1988. A research and Development of PBCF (Propeller Boss Cap Fins). J. Soc. Nav. Archit. Japan 163, 66–78.

Ouchi, K., Tamashima, M., Kawasaki, T., Koizuka, H., 1989. A Research and Development of PBCF (Propeller Boss Cap Fins): 2nd Report: Study on Propeller Slipstream and Actual Ship Performance. J. Soc. Nav. Archit. Japan 165, 43–53.

Owen, D., Demirel, Y.K., Oguz, E., Tezdogan, T., Incecik, A., 2018. Investigating the effect of biofouling on propeller characteristics using CFD. Ocean Eng. 159, 505–516. https://doi.org/10.1016/j.oceaneng.2018.01.087

Park, J., Seong, W., 2017. Novel scaling law for estimating propeller tip vortex cavitation noise from model experiment. J. Hydrodyn. 29, 962–971. https://doi.org/10.1016/S1001-6058(16)60810-7

Peng, H., Qiu, W., Ni, S., 2013. Effect of turbulence models on RANS computation of propeller vortex flow. Ocean Eng. 72, 304–317. https://doi.org/10.1016/j.oceaneng.2013.07.009

Pennings, P., Westerweel, J., Terwisga, T. van, 2016. Cavitation tunnel analysis of radiated sound from the resonance of a propeller tip vortex cavity. Int. J. Multiph. Flow 83, 1–11. https://doi.org/10.1016/j.ijmultiphaseflow.2016.03.004

Pennings, P., Westerweel, J., Van Terwisga, T., 2015. Sound signature of propeller tip vortex cavitation, in: 9th International Symposium on Cavitation (CAV2015). Lausanne, Switzerland.

Philipp, O., Ninnemann, P., 2007. Wirkung von Fluegelrauigkeiten auf Kavitation und Erregung, Maritime Speech Day, Technical University Hamburg.

Platzer, G.P., Souders, W.G., 1981. Tip vortex cavitation characteristics and delay of inception on a three-dimensional hydrofoil, DTNSRDS-81/007. Bethesda, Md.: David W. Taylor Naval Ship Research and Development Center.

Platzer, G.P., Souders, W.G., 1979. Tip vortex cavitation delay with application to marine lifting surfaces, DTNSRDC Technical report 79/051. David W. Taylor Naval Ship Research and Development Center.

Poncet, S., Soghe, R. Da, Facchini, B., 2010. RANS Modeling of Flow in Rotating Cavity System, in: V European Conference on Computational Fluid Dynamics (ECCOMAS CFD 2010). Lisbonne, Portugal.

Ponkratov, D., Zegos, C., 2015. Validation of Ship Scale CFD Self-Propulsion Simulation by the Direct Comparison with Sea Trials Results, in: Fourth International Symposium on Marine Propulsors, SPM'15. Austis, Texas, USA.

Pope, S.B., 2000. Turbulent Flows, Cambridge University Press.

Qiu, W., Peng, H., Ni, S., Liu, L., Mintu, S., Hally, D., Hsiao, C.T., 2013. RANS computation of propeller tip vortex flow. Int. J. Offshore Polar Eng. 23, 73–79.

Queutey, P., Deng, G., Wackers, J., Guilmineau, E., Leroyer, A., Visonneau, M., 2012. Sliding grids and adaptive grid refinement for RANS simulation of ship-propeller interaction. Sh. Technol. Res. 59, 44–57. https://doi.org/10.1179/str.2012.59.2.004

Raestad, A.E., 1996. Tip vortex index-an engineering approach to propeller noise prediction. Nav. Archit. 11–16.

Ramponi, R., Blocken, B., 2012. CFD simulation of cross-ventilation flow for different isolated building configurations: Validation with wind tunnel measurements and analysis of physical and numerical diffusion effects. J. Wind Eng. Ind. Aerodyn. 104–106, 408–418. https://doi.org/10.1016/j.jweia.2012.02.005

Richardson, L.F., 1911. IX. The approximate arithmetical solution by finite differences of physical problems involving differential equations, with an application to the stresses in a masonry dam. Philos. Trans. R. Soc. London. Ser. A, Contain. Pap. a Math. or Phys. Character 210, 307–357. https://doi.org/10.1098/rsta.1911.0009

Roache, P.J., 1998. Verification of codes and calculations. AIAA J. 36, 696–702. https://doi.org/10.2514/2.457

Ross, D., 1976. Mechanics of Underwater Noise. Preninsula Pub.

Sadrehaghighi, I., 2019. Turbulence Modeling, A Review, Report Number:1.86.9.

Salvatore, F., Streckwall, H., Van Terwisga, T., 2009. Propeller Cavitation Modelling by CFD-

Results from the VIRTUE 2008 Rome Workshop, in: First International Symposium on Marine Propulsors, SMP'09. Trondheim, Norway.

Salvatore, F., Testa, C., Ianniello, S., Pereira, F., 2006. Theoretical Modelling of Unsteady Cavitation and Induced Noise, in: Sixth International Symposium on Cavitation, CAV2006. Wageningen, Netherlands.

Sampson, R., Turkmen, S., Aktas, B., Shi, W., Fitzsimmons, P., Atlar, M., 2015. On the full scale and model scale cavitation comparisons of a Deep-V catamaran research vessel, in: Fourth International Symposium on Marine Propulsors, SMP'15. Austin, Texas, USA.

SATURN, 2021. Solutions @ Underwater Radiated Noise Grant Agreement ID: 101006443.

Schnerr, G.H., Sauer, J., 2001. Physical and Numerical Modeling of Unsteady Cavitation Dynamics, in: 4th International Conference on Multiphase Flow. New Orleans, USA.

Schultz, M.P., 2007. Effects of coating roughness and biofouling on ship resistance and powering. Biofouling 23, 331–341. https://doi.org/10.1080/08927010701461974

Schultz, M.P., Bendick, J.A., Holm, E.R., Hertel, W.M., 2011. Economic impact of biofouling on a naval surface ship. Biofouling 27, 87–98. https://doi.org/10.1080/08927014.2010.542809

Schultz, M.P., Swain, G.W., 2000. The influence of biofilms on skin friction drag. Biofouling 15, 129–139. https://doi.org/10.1080/08927010009386304

Seo, K.-C., Atlar, M., Goo, B., 2016. A Study on the Hydrodynamic Effect of Biofouling on Marine Propeller. J. Korean Soc. Mar. Environ. Saf. 22, 123–128. https://doi.org/10.7837/kosomes.2016.22.1.123

Seol, H., Jung, B., Suh, J.C., Lee, S., 2002. Prediction of non-cavitating underwater propeller noise. J. Sound Vib. 257, 131–156. https://doi.org/10.1006/jsvi.2002.5035

Seol, H., Suh, J.C., Lee, S., 2005. Development of hybrid method for the prediction of underwater propeller noise. J. Sound Vib. 288, 345–360. https://doi.org/10.1016/j.jsv.2005.01.015

Sezen, S., Atlar, M., 2021. An alternative Vorticity based Adaptive Mesh Refinement (V-AMR) technique for tip vortex cavitation modelling of propellers using CFD methods. Sh. Technol. Res. 69, 1–21. https://doi.org/10.1080/09377255.2021.1927590

Sezen, S., Bal, S., 2020. Computational and Empirical Investigation of Propeller Tip Vortex

Cavitation Noise. China Ocean Eng. 34, 232–244. https://doi.org/10.1007/s13344-020-0022-8

Sezen, S., Kinaci, O.K., 2019. Incompressible flow assumption in hydroacoustic predictions of marine propellers. Ocean Eng. 186, 106138. https://doi.org/10.1016/j.oceaneng.2019.106138

Sezen, S., Uzun, D., Ozyurt, R., Turan, O., Atlar, M., 2021. Effect of biofouling roughness on a marine propeller's performance including cavitation and underwater radiated noise (URN). Appl. Ocean Res. 107, 102491. https://doi.org/10.1016/j.apor.2020.102491

Shi, W., 2017. Biomimetic improvement of hydrodynamic performance of horizontal axis tidal turbines, PhD Thesis, Newcastle University.

Shih, T.-H., Liou, W.W., Shabbir, A., Yang, Z., Zhu, Ji., 1995. A New k-ε Eddy Viscosity Model for High Reynolds NumberTurbulent Flows Flows. Comput. Fluids 24, 227–238. https://doi.org/10.1007/978-3-319-27386-0_7

Shin, K.W., 2019. CFD Analysis of Ship Propeller Thrust Breakdown, in: Sixth International Symposium on Marine Propulsors, SMP'19. Rome, Italy.

Shin, K.W., Andersen, P., 2018. CFD Analysis of Propeller Tip Vortex Cavitation in Ship Wake Fields, in: 10th International Symposium on Cavitation, CAV2018. Baltimore, Maryland, USA.

Sipilä, T., 2012. RANS analyses of cavitating propeller flows, PhD thesis. Aalto Universtiy School of Engineering.

Song, S., Demirel, Y.K., Atlar, M., 2020. Penalty of hull and propeller fouling on ship self-propulsion performance. Appl. Ocean Res. 94. https://doi.org/10.1016/j.apor.2019.102006

Song, S., Demirel, Y.K., Atlar, M., 2019. An investigation into the effect of biofouling on full-scale propeller performance using CFD, in: Proceedings of the International Conference on Offshore Mechanics and Arctic Engineering - OMAE. https://doi.org/10.1115/OMAE2019-95315

SONIC, 2012. Suppression of underwater noise induced by cavitation. EC-FP7, Grant Agreement No: 2012 314394.

Spalart, P.R., Allmaras, S.R., 1992. A One-Equatlon Turbulence Model for Aerodynamic

Flows, American Institute of, Aeronautics and Astronautics, 30th Aerospace Sciences Meeting and Exhibit. Reno, NV, USA.

Spalart, P.R., Deck, S., Shur, M.L., Squires, K.D., Strelets, M.K., Travin, A., 2006. A new version of detached-eddy simulation, resistant to ambiguous grid densities. Theor. Comput. Fluid Dyn. 20, 181–195. https://doi.org/10.1007/s00162-006-0015-0

Spalart, P.R., Jou, W.-H., Strelets, M., Allmaras, S.R., Research, U.S.A.F.O. of S., 1997. Comments on the Feasibility of LES for Wings, and on a Hybrid RANS/LES Approach, in: First AFOSR International Conference on DNS/LES. Greyden Press, pp. 137–148.

Speranza, N., Kidd, B., Schultz, M.P., Viola, I.M., 2019. Modelling of hull roughness. Ocean Eng. 174, 31–42. https://doi.org/10.1016/j.oceaneng.2019.01.033

Star CCM+ 14.06, 2019. User Guide, Siemens.

Stark, C., Shi, W., 2021. Hydroacoustic and hydrodynamic investigation of bio-inspired leading-edge tubercles on marine-ducted thrusters. R. Soc. Open Sci. 8, 210402. https://doi.org/10.1098/RSOS.210402

Strasberg, M., 1986. Hydrodynamic Cavitation Noise, in: International Symposium on Cavitation and Multiphase Flow Noise, ASME Winter Annual Meeting. Anaheim, California, USA.

Sun, Y., Wu, T., Su, Y., Peng, H., 2020. Numerical Prediction on Vibration and Noise Reduction Effects of Propeller Boss Cap Fins on a Propulsion System. Brodogradnja 71, 1–18. https://doi.org/10.21278/BROD71401

Sundén, B., Fu, J., 2017. Computational Methods for the Investigations of Heat Transfer Phenomena in Aerospace Applications, in: Heat Transfer in Aerospace Applications. pp. 179–196. https://doi.org/10.1016/b978-0-12-809760-1.00010-7

Svennberg, U., Asnaghi, A., Gustafsson, R., Bensow, R.E., 2020. Experimental Analysis of Tip Vortex Cavitation Mitigation By Controlled Surface Roughness. J. Hydrodyn. 2020 1–12. https://doi.org/10.1007/s42241-020-0073-6

Tani, G., Aktas, B., Viviani, M., Atlar, M., 2017. Two medium size cavitation tunnel hydro-acoustic benchmark experiment comparisons as part of a round robin test campaign. Ocean Eng. 138, 179–207. https://doi.org/10.1016/j.oceaneng.2017.04.010

Tani, G., Aktas, B., Viviani, M., Yilmaz, N., Miglianti, F., Ferrando, M., Atlar, M., 2019a.

Cavitation tunnel tests for “The Princess Royal” model propeller behind a 2-dimensional wake screen. Ocean Eng. 172, 829–843. https://doi.org/10.1016/j.oceaneng.2018.11.017

Tani, G., Viviani, M., Felli, M., Lafeber, F.H., Lloyd, T., Aktas, B., Atlar, M., Turkmen, S., Seol, H., Hallander, J., Sakamoto, N., 2020. Noise measurements of a cavitating propeller in different facilities: Results of the round robin test programme. Ocean Eng. 213, 107599. https://doi.org/10.1016/j.oceaneng.2020.107599

Tani, G., Viviani, M., Felli, M., Lafeber, F.H., Lloyd, T., Atlar, M., Seol, H., Hallander, J., Sakamoto, N., Kamiirisa, H., 2019b. Round Robin Test on Radiated Noise of a Cavitating Propeller, in: Proceedings of 6th International Symposium on Marine Propulsors, SPM’19. Rome, Italy.

Testa, C., 2008. Acoustic Formulations for Aeronautical and Naval Rotorcraft Noise Prediction Based on the Ffowcs Williams and Hawkings Equation, PhD thesis. Delft University of Technology, TUD.

Testa, C., Ianniello, S., Salvatore, F., Gennaretti, M., 2008. Numerical approaches for hydroacoustic analysis of marine propellers. J. Sh. Res. 52, 57–70.

Testa, C., Porcacchia, F., Zaghi, S., Gennaretti, M., 2021. Study of a FWH-based permeable-surface formulation for propeller hydroacoustics. Ocean Eng. 240, 109828. https://doi.org/10.1016/J.OCEANENG.2021.109828

Testa, C., Procacchia, F., Greco, L., Muscari, R., 2018. Effectiveness of Boundary Element Method Hydrodynamic Data for Propeller Hydroacoustics, in: A. Yucel Odabasi Colloquium Series 3rd International Meeting-Progress in Propeller Cavitation and Its Consequences. Istanbul, Turkey.

Townsin, R.L., Byrne, D., Svensen, T.E., Milne, A., 1981. Estimating the technical and economic penalties of hull and propeller roughness. Trans. SNAME 89, 295–318.

Tu, J., Yeoh, G.-H., Liu, C., 2018. Practical Guidelines for CFD Simulation and Analysis, in: Computational Fluid Dynamics. Elsevier, pp. 255–290.

Turkmen, S., Aktas, B., Atlar, M., Sasaki, N., Sampson, R., Shi, W., 2017. On-board measurement techniques to quantify underwater radiated noise level. Ocean Eng. 130, 166–175. https://doi.org/10.1016/j.oceaneng.2016.11.070

Urick, R., 1983. Principles of underwater sound. McGraw-Hill Book Company.

Usta, O., Korkut, E., 2018. A study for cavitating flow analysis using DES model. Ocean Eng. 160, 397–411. https://doi.org/10.1016/j.oceaneng.2018.04.064

Uzun, D., 2019. The development of time-dependent biofouling model for ships, PhD thesis, Naval Architecture, Ocean and Marine Engineering. University of Strathclyde.

Uzun, D., Demirel, Y.K., Coraddu, A., Turan, O., 2019. Time-dependent biofouling growth model for predicting the effects of biofouling on ship resistance and powering. Ocean Eng. 191, 106432. https://doi.org/10.1016/j.oceaneng.2019.106432

Uzun, D., Ozyurt, R., Demirel, Y.K., Turan, O., 2020. Does the barnacle settlement pattern affect ship resistance and powering? Appl. Ocean Res. 95, 102020. https://doi.org/10.1016/j.apor.2019.102020

Uzun, D., Sezen, S., Atlar, M., Turan, O., 2021a. Effect of biofouling roughness on the full-scale powering performance of a submarine. Ocean Eng. 238, 109773. https://doi.org/10.1016/J.OCEANENG.2021.109773

Uzun, D., Sezen, S., Ozyurt, R., Atlar, M., Turan, O., 2021b. A CFD study: Influence of biofouling on a full-scale submarine. Appl. Ocean Res. 109, 102561. https://doi.org/10.1016/J.APOR.2021.102561

Van der Kooij, J., 1986. Sound Generation by Bubble Cavitation on Ship Propellers: The effects of Leading Edge Roughness, in: ASME, 2nd International Symposium on Cavitation and Multiphase Flow. Anaheim, California, USA.

Vaz, G., Hally, D., Huuva, T., Bulten, N., Muller, P., Becchi, P., Herrer, J.L.R., Whitworth, S., Macé, R., Korsström, A., 2015. Cavitating Flow Calculations for the E779A Propeller in Open Water and Behind Conditions: Code Comparison and Solution Validation, in: Fourth International Symposium on Marine Propulsors, SMP'15. Austin, Texas, USA.

Versteeg, H.K., Malalasekera, W., 2007. An Introduction to Computational Fluid Dynamics: The Finite Volume Method, 2nd Edition. Pearson.

Viitanen, V., Siikonen, T., 2017. Numerical Simulation of Cavitating Marine Propeller Flows, in: 9th National Conference on Computational Mechanics MekIT-17. Trondheim, Norway.

Wackers, J., Said, K.A., Deng, G.B., Queutey, P., Visonneau, M., 2010. Adaptive Grid Refinement Applied to RANS Ship Flow Computation, in: 28th Symposium on Naval Hydrodynamics. Pasadena, California.

Wang, B., Liu, Z., Peng, X., Liu, D., 2015. Simulations of tip vortex cavitation flows with nonlinear k-ε model, in: Journal of Physics: Conference Series. p. 012187. https://doi.org/10.1088/1742-6596/656/1/012187

Wang, M., Lele, S.K., Moin, P., 1996. Computation of quadrupole noise using acoustic analogy. AIAAJ 34, 2247–2254. https://doi.org/10.2514/3.13387

Wang, X., Walters, K., 2012. Computational analysis of marine-propeller performance using transition-sensitive turbulence modeling. J. Fluids Eng. Trans. ASME 134. https://doi.org/10.1115/1.4005729/456356

Wilcox, D.C., 2006. Turbulence Modeling for CFD, 3rd edition, DCW Industries, Inc., La Canada CA.

Windt, J., Bosschers, J., 2015. Influence of local and adaptive mesh refinement on the tip vortex characteristics of a wing and propeller, in: MARINE 2015 - Computational Methods in Marine Engineering VI. pp. 862–873.

Xiong, Y., Wang, Z., Qi, W., 2013. Numerical study on the influence of boss cap fins on efficiency of controllable-pitch propeller. J. Mar. Sci. Appl. 12, 13–20. https://doi.org/10.1007/S11804-013-1166-9

Yakushiji, R., 2009. Mechanism of Tip Vortex Cavitation Suppression by Polymer and Water Injection. PhD Thesis, Naval Architecture and Marine Engineering, University of Michigan.

Ye, J.M., Xiong, Y., Li, F., Wang, Z.Z., 2012. Numerical prediction of blade frequency noise of cavitating propeller. J. Hydrodyn. 24, 371–377. https://doi.org/10.1016/S1001-6058(11)60257-6

Yeginbayeva, I.A., Atlar, M., 2018. An experimental investigation into the surface and hydrodynamic characteristics of marine coatings with mimicked hull roughness ranges. Biofouling 34, 1001–1019. https://doi.org/10.1080/08927014.2018.1529760

Yilmaz, N., Atlar, M., Khorasanchi, M., 2019. An improved Mesh Adaption and Refinement approach to Cavitation Simulation (MARCS) of propellers. Ocean Eng. 171, 139–150. https://doi.org/10.1016/j.oceaneng.2018.11.001

Yvin, C., Muller, P., 2016. Tip vortex cavitation inception without a cavitation model, in: 19th Numerical Towing Tank Symposium (NuTTS 2016). St Pierre d'Oléron - France.

Zhai, Z.J., Zhang, Z., Zhang, W., Chen, Q.Y., 2007. Evaluation of various turbulence models in predicting airflow and turbulence in enclosed environments by cfd: Part 1—summary of prevalent turbulence models. HVAC R Res. 13, 853–870. https://doi.org/10.1080/10789669.2007.10391459

Zhu, Gao, 2019. A Numerical Investigation of a Winglet-Propeller using an LES Model. J. Mar. Sci. Eng. 7, 333. https://doi.org/10.3390/jmse7100333